**Faculty of Engineering and Science**

# Investigation of Formation and Dissociation Mechanisms of Pure and Mixed CO₂ Hydrates in the Presence of Thermodynamic and Kinetic Promoters using Molecular Dynamics Simulation

**Saied Sinehbaghizadeh**

**0000-0003-1701-6343**

**This thesis is presented for the Degree of**
**Doctor of Philosophy**
**of**
**Curtin University**

**October 2023**

توانا بود هر که دانا بود                 ز دانش دل پیر برنا بود

"Mighty is he who has knowledge; By knowledge the old hearts grow young again." - Ferdowsi (c. 940‑1020)

# Declaration

This thesis contains no material that has been accepted for the award of any other degree or diploma in any university or equivalent institution. To the best of my knowledge and belief, this thesis does not contain any material that has been previously published or written by any other person except where due reference is made. The relative contributions of the respective creators or authors for work based on joint research or publications are duly acknowledged.

I warrant that I have obtained, where necessary, permission from the copyright owners to use any third party copyright material reproduced in the thesis (such as artwork, images, unpublished documents), or to use any of my own published work (such as journal articles) in which the copyright is held by another party (such as publisher, co-author).

Full Name: Saeid Sinehbaghizadeh

Signature:

Date: 29/10/2023

# Copyright

I warrant that I have obtained, where necessary, permission from the copyright owners to use any third-party copyright material reproduced in the thesis (e.g. questionnaires, artwork, unpublished letters), or to use any of my own published work (e.g. journal articles) in which the copyright is held by another party (e.g. publisher, co-author).

**Signature:**               (Saeid Sinehbaghizadeh)

**Date:**                     29/10/2023

# Acknowledgements

This project has been supported by various parties. Therefore, I would like to express my sincere gratitude and special appreciation to:

I foremost dedicate this thesis to my mother and father for their unconditional love, support and encouragement throughout this journey from a long distance.

# Publications arising from the Thesis

**Journal Articles**

    **Chapter 1:**

1. Sinehbaghizadeh, S., Saptoro, A., Mohammadi, A.H., 2022. $CO_2$ hydrate properties and applications: A state of the art. *Progress in Energy and Combustion Science*, 2022, 93, 101026, Elsevier, DOI:  https://doi.org/10.1016/j.pecs.2022.101026 [2021 IF: 35.339, Q1].

    **Chapter 2:**

2. Sinehbaghizadeh, S., Saptoro, A., Amjad, S., Naeiji, P., Tiong, A.N.T., Mohammadi, A.H. A comprehensive review on molecular dynamics simulation studies of phenomena and characteristics associated with clathrate hydrates. *Fuel*, 2023, 338, 127201, Elsevier, DOI: https://doi.org/10.1016/j.fuel.2022.127201 [2021 IF: 8.035, Q1].

    **Chapter 3:**

3. Sinehbaghizadeh, S., Saptoro, A., Naeiji, P., Tiong, A.N.T., Mohammadi, A.H., 2022. Insights into the synergistic effects of metal particles (Ag, Cu, and Fe) and urea on $CO_2$ clathrate hydrate growth using molecular dynamics simulations. *Chemical Engineering Science*, 2022, 264, 118194, Elsevier,  DOI: https://doi.org/10.1016/j.ces.2022.118194 [2021 IF: 4.889, Q1].

    **Chapter 4:**

4. Sinehbaghizadeh, S., Saptoro, A., Amjad, S., Naeiji, P., Tiong, A.N.T., Mohammadi, A.H., 2023. Molecular dynamics simulations of the effects of organic amines on biogas clathrate hydrate formation. *Journal of Molecular liquids*, 2023, 382, 122015, Elsevier, DOI: https://doi.org/10.1016/j.molliq.2023.122015 [2021 IF: 6.633, Q1].

    **Chapter 5:**

5. Sinehbaghizadeh, S., Saptoro, A., Amjad, S., Tiong, A.N.T., Mohammadi, A.H. Molecular dynamics simulation studies on the stability and decomposition of clathrate hydrates of single and double greenhouse gases. *Energy & Fuel*, 2022, 36 (15), 8323-8339, ACS, DOI:https://doi.org/10.1021/acs.energyfuels.2c01396 [2021 IF: 4.654, Q1].

    **Chapter 6:**

6. Sinehbaghizadeh, S., Saptoro, A., Amjad, S., Mohammadi, A.H. Molecular dynamics simulations of the stability and dissociation of structure-H clathrate hydrates in the presence of different amino acids, gas species, and sH hydrate formers, *Energy & Fuels,* 2023, 37 (14), 10550-10566*,* ACS,
DOI: https://doi.org/10.1021/acs.energyfuels.3c01312 [2021 IF: 4.654, Q1].

    **Chapter 7:**

7. Sinehbaghizadeh, S., Saptoro, A., Amjad, S., Mohammadi, A.H. Understanding the influences of different associated gas impurities and the kinetic modelling of biogas hydrate formation at the molecular scale. *Energy*, 2023, 282, 128893, Elsevier, DOI: https://doi.org/10.1016/j.energy.2023.128893 [2021 IF: 8.857, Q1].

**Conferences Papers**

1. Sinehbaghizadeh, S., Saptoro, A., 2022, "Understanding the effects of impurities on the growth rate of biogas hydrate at a molecular level", *3$^{rd}$ Swinburne Sarawak Postgraduate Research Conference (SSPRC)*, Kuching, Malaysia, 11 – 12 August 2022.

2. Sinehbaghizadeh, S., Saptoro, A., 2022, "Molecular dynamics simulations of $CO_2$ clathrate hydrate in the presence of organic components", *Curtin Global Campus Higher Degree by Research Colloquium (CGCHDRC)*, 12 – 13 December 2022.

# Abstract

Global warming is one of the most pressing environmental concerns which correlates strongly with anthropogenic $CO_2$ emissions so that the $CO_2$ decreasing strategies have been meaningful worldwide attention. As an option, natural gas hydrate reservoirs have steadily emerged as a potent source of energy which would simultaneously be the proper places for $CO_2$ sequestration if the method of $CO_2/CH_4$ replacement could be developed. On the flip side, $CO_2$ hydrates as non-flammable solid compounds without an irreversible chemical reaction would contribute to many industrial processes if their approaches could be improved. Toward developing substantial applications of $CO_2$ hydrates, molecular dynamics (MD) investigations at a microscopic scale can aid in understanding their characteristics and mechanisms involved and also complete the laboratory experiments at a macroscopic level.  A variety of industrial applications of hydrate-based $CO_2$ capture and utilization technologies are hindered by the complex and slow formation; however, improving $CO_2$ hydrate kinetics can be facilitated by adding promoters. In this regard, understanding the promotion mechanisms of these components on the hydrate formation and dissociation at the molecular level would assist in either establishing feasible processes or finding more efficient promoters. To increase the impressions of these components, their combinations can also be utilized. To date, hundreds of hydrate promoters from various types ranging from hydrocarbons, surfactants, and inorganic/ organic materials through experimental measurements have been introduced. However, the effects of these substances on pure $CO_2$ or in the gas mixture would be different. Also, the selection of these hydrate promoters for possible industrial applications requires the elucidation of the effectiveness as well as the weaknesses of such components at a microscopic scale (nanoseconds and nanometres) which may not be comprehended by conducting explorations in the laboratory. Such findings can complete the outcome of experimental measurements at the macroscopic level. In this thesis, the pure and mixed $CO_2$ clathrate hydrates in the presence of single and combined kinetic hydrate promoters (KHPs) and thermodynamic hydrate promoters (THPs) have been simulated to elucidate a wide variety of the mechanisms involved during the process of clathrate hydrate formation and dissociation. In this regard, structural, thermo-physical, dynamical, fractional occupancy, thermodynamic, kinetics, heat and mass transfer properties using molecular frameworks at different operating conditions have been investigated. To understand the effects of THPs and KHPs on the formation and the dissociation of Pure/mixed $CO_2$ clathrate hydrates in the form of structure-I/II/H, the MD studies in five different objectives for the simulations were classified:

- Pure $CO_2$ structure-I hydrate growth in the existence of KHPs such as metal Ag, Cu, and Fe particles and urea molecules as well as their hybrid combinations.
- $CO_2+CH_4$ hydrate formation in the presence of pure and binary organic KHPs such as amines and urea molecules.
- The stability and dissociation of $CO_2/ CO_2+CH_4$ hydrates in the inclusion of structure-II THPs selected from different molecular groups or their substituents.
- The stability and decomposition of $CO_2/ CO_2+CH_4/ CO_2+N_2/ CO_2+H_2$ structure-H hydrates in the existence of amino acids, and various THPs known as large molecular guest substances (LMGSs).
- The effects of associated gas impurities (such as $SO_2$, $H_2S$, $N_2$, and $H_2$) on the formation of biogas hydrate and their kinetic modellings.

Through performed MD simulations, this thesis provides various new insights into the characteristics of different hydrate promoters and their effects on the process of hydrate formation as well as the dissociation which can help to accelerate the practical implementations of hydrate-based $CO_2$ capture, sequestration or utilization (CCSU) processes. The outcomes of performed simulations based on the mentioned five objectives for the simulations revealed that:

- Although the mixture of Cu, Ag, and Fe metal particles has positive effects on the rate of hydrate formation, the combination of Cu, Fe, and urea without the inclusion of Ag metal particles possesses the highest promotion effect on the pure $CO_2$ clathrate hydrate growth rate. However, the addition of Cu + Ag and Cu + Fe to the system reduced the orderly movement of water molecules by increasing the potential energy and Brownian motion in the system. In addition, the metal particles and urea promote the formation of new cages at the hydrate solution boundary by decreasing the heat and mass transport resistances of $CO_2$ in water respectively.

- To promote the formation of biogas clathrate hydrates, the promotion effects of small organic amines (methylamine, and dimethylamine) were found to be more kinetically efficient than amine molecules with long chains. Cage analysis shows that the solution including amine molecules with small chains is more capable of building clathrate cages in comparison to pure water. These molecules can also induce guest gases toward being located inside the formed cages more than in pure water and also affect the distribution of $CO_2$ and $CH_4$ molecules during the conversion of the solution phase to hydrate which can be a useful feature to intensify the split fraction of hydrate-based processes.

- The type of large molecular guests in the large cages plays a major role in the stabilization of the clathrate hydrate network. Among studied systems with THPs, cyclopentane, and cyclohexane in comparison with F-promoters (HFC-134a, HCHC-141b, and FCP) seem to be more susceptible to maintaining the stability of $CO_2$ clathrate hydrate. Also, the existence of neopentyl alcohol in large cavities was found to facilitate the process of hydrate dissociation by making new hydrogen bonds between hydroxyl groups and water molecules. Furthermore, the partial occupancy of the cages by increasing the fluctuations in an ordered structure induces the process of hydrate dissociation.

- Among investigated sH hydrate formers as THPs, adamantane and 1,1-dimethyl cyclohexane were identified as the most stable sH hydrates, which suggests that the cyclic hydrocarbons with larger carbon numbers (between six to ten) can help large cages remain integrated. Also, the hydroxyl of amino acids, by attaching to the surrounding water molecules of the sH hydrate, weakens the hydrogen bonds of the water molecules in the sH clathrate. Moreover, unlike $CH_4$ and $N_2$, the presence of $H_2$ molecules in $CO_2$ clathrate hydrate significantly induces the mobility of molecules in the clathrate network. Between the studied amino acids, the order of facilitating sH hydrate dissociation was found to be serine > glycine > L-threonine > Leucine > L-valine. Hence, the side chain and hydrophobicity of amino acids at the molecular scale play a critical role in clathrate hydrate structural changes.

- The presence of gas impurities in the system may slightly increase the arrangement rate of water molecules toward being organized in the clathrate form. In addition, decreasing the gas concentration in the solution phase in comparison with the entrapped gas molecules in the initial hydrate results in a linear reduction of the growth rate. However, their effects on the fraction of the cage occupancy of the formed cavities are found to be insignificant. The growth mechanisms in all cases occur based on two consecutive steps: the diffusion of the gas molecules from the bulk of the solution phase to the solid-liquid interface, followed by the reordering of the water molecules in agreement with the initial hydrate slab. The affinity and decay rate of the model demonstrate that the progress of the hydrate formation is driven by the concept of a thermodynamic driving force which analogously follows the proceeding process based on a natural path.

The simulation results of this thesis can be used to develop the performance of chemical additives in the process optimization and management of hydrate-based $CO_2$ capture, storage/ sequestration, and utilization aims.

# Table of Contents

# Chapter 1: Introduction

In this chapter, the applications and feasibility of gas hydrates in terms of $CO_2$ capture and utilization, the performance parameters, and the role of promoters, phenomena, and properties associated with these technologies have been discussed. Also, the research problem statement and the significance were elaborated to highlight the main aims and objectives. Finally, a summary of the scope of work was schematically shown. Due to the large number of this paper (and its supplementary materials), the brief of the main body from this paper has been extracted for providing this chapter.

Global warming is one of the most pressing environmental concerns which correlates strongly with anthropogenic $CO_2$ emissions so the $CO_2$ decreasing strategies have been meaningful worldwide attention. One of the options that have shown an alternative to utilize is hydrate-based technology. Toward developing substantial applications of these methods, laboratory experiments, process modelling, and molecular dynamics (MD) simulations can aid in understanding their characteristics and mechanisms involved. This review was organized in the form of four distinct sections. The first part reviewed the studies on sequestering $CO_2$ in natural gas hydrate reservoirs. The next section gave an overview of process flow diagrams of $CO_2$ hydrate-based techniques in favour of $CO_2$ Capture and Sequestration & Utilization (CCS&U). The third section summarized the merits, flaws, and different effects of hydrate promoters as well as porous media on $CO_2$ hydrate systems at macroscopic and mesoscopic levels, and also how these components can improve $CO_2$ hydrate properties, progressing toward the feasibility of $CO_2$ hydrate industrial applications. The final sector recapitulated the MD frameworks of $CO_2$ clathrate and semiclathrate hydrates in terms of new insights and research findings to elucidate the fundamental properties of $CO_2$ hydrates at the molecular level.

This paper was published as a review paper in "Progress in Energy and Combustion Science":

Sinehbaghizadeh, S., Saptoro, A., Mohammadi, A.H., 2022. $CO_2$ hydrate properties and applications: A state of the art. *Journal of Progress in Energy and Combustion Science*, 2022, 93, 101026, Elsevier

## 1.1 Introduction

Among the major contributors to global warming, $CO_2$ accounts for about 76% of total greenhouse gas emissions whereas the other participants are $CH_4$, 16%; Nitrous oxide, 6%; and F-gases, 2% respectively. The mitigation of $CO_2$ emissions in the wake of the Kyoto Protocol to control $CO_2$ in the atmosphere has become a critical objective. The concentration of $CO_2$ in the atmosphere since the Industrial Revolution has unprecedentedly increased from 280 ppm to a high of 410 ppm which has resulted in the 0.7 °C global surface temperature rise. Additionally, the prediction of the Intergovernmental Panel on Climate Change (IPCC) revealed that by 2100, the atmospheric $CO_2$ concentration, global temperature, and sea level will have experienced further increases up to 570 ppm, 2 °C, and 38 cm respectively (Masson-Delmotte et al. 2021). Thereby, evidence of $CO_2$ catastrophic consequences indicates that $CO_2$ capture, sequester, or utilization methods are essential to be developed immediately. Figure 1 exhibits the carbon distributions released into the atmosphere, ocean, and land. As is shown, $CO_2$ in the atmosphere is being absorbed into the soils, and terrestrial plants and dissolved into the ocean which leads to altering the ocean chemistry like ocean acidification. This phenomenon is being followed by detrimental effects on the environment like damage to aquatic habitats and marine ecosystems.
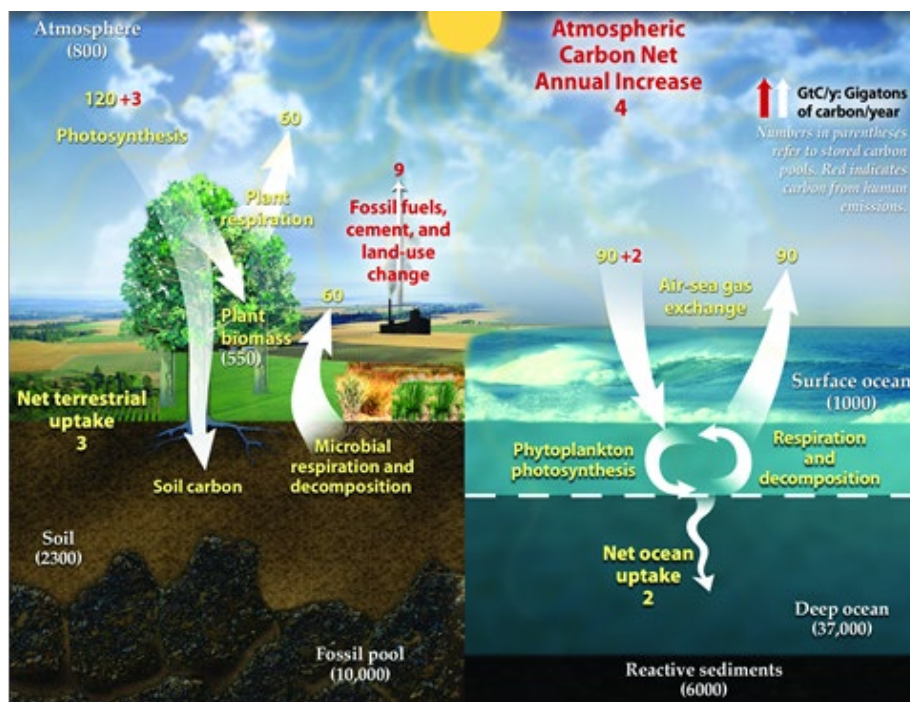


Figure 1: Anthropogenic activities of the carbon cycle in the
atmosphere, ocean, and land (Riebeek 2011).

There are different industrial gas emission sources such as the steelmaking industry, coal power plant, cement industry, refinery, petrochemical industries, and so on, the sum of which accounts for approximately 75% of anthropogenic $CO_2$ emissions. Estimations indicated that a range from 85% to 95% of this content can be eliminated through carbon capture and sequestration & utilization (CCSU) technologies. Broadly speaking, capturing methods in the industry have been classified into post-combustion, pre-combustion, and oxy-fuel combustion, whereas industrial separation methods have been distributed into four main techniques: adsorption, absorption, membrane, and cryogenic. The process of flue gas treatment before being released into the atmosphere is known as a post-combustion in which feed gas consists of $CO_2$ ranging between 15% and 20% and is balanced with $N_2$ and roughly 5% $O_2$. The pre-combustion process refers to the capturing of $CO_2$ from combusted fuel gas including $CO_2$ and $H_2$ with a

proportion of about 40% and 60% respectively. In this type of $CO_2$ capture, the more the content of $CO_2$ in the fuel gas, the higher the efficiency can be achieved. However, pre-combustion is more effective than post-combustion. Once $CO_2$ is captured, transportation, sequestration/ utilization steps must be implemented. In this regard, different viable approaches for CCSU have been suggested.

Figure 2 displays diverse $CO_2$ removal methods. There are many publications in the literature that have reviewed the approaches of $CO_2$ capture and separation, their prospects, and challenges. In the absorption method, $CO_2$ is absorbed from emitted gases into solvents or absorbent materials such as: ionic liquids (Lian et al. 2021; Odunlami et al. 2022), porous materials with high surface area (benzimidazole-based hyper cross-linked poly ionic liquids (HPILs) (Sang and Huang 2020; Yuan et al. 2020), new amine solutions e.g. mono-ethanolamine/1-propanol aqueous biphasic absorbents with rapid absorption rate and low regeneration energy (Rujie Wang et al. 2019), methanol absorbs (Jens et al. 2019). In the adsorption approach, $CO_2$ is adsorbed onto a solid material at high pressure, typically using porous materials like activated carbon (Aghel, Behaein, and Alobaid 2022), carbon-based materials (silica/alumina/zeolites, and metal oxides) (Pardakhti et al. 2019; Dhoke et al. 2021), or metal-organic frameworks (MOFs) (Younas et al. 2020). This can also be performed using sorbents e.g. biochar, and graphene-based adsorbents (Ahmed et al. 2020). However, among $CO_2$ sorptive materials, porous carbon-based biochar and metal-embedded graphyne materials have been considered as promising candidates. (Jung, Park, and Kwon 2019; He et al. 2020). $CO_2$ can also be adsorbed under high pressure/ temperature and released under low pressure/ temperature which is named temperature/ pressure swing adsorption (P/TSA). By utilizing the membrane technologies (Kárászová et al. 2020), specialized membranes allow selective permeation of $CO_2$ over other gases based on size or chemical affinity. Polymeric, ceramic, and mixed matrix membranes are generally used for this purpose. Each method has its advantages and limitations in terms of efficiency, cost, and applicability to different industrial processes. Organic-containing microporous materials can be used for the fabrication of membranes such as metal-organic frameworks, porous organic frameworks, and microporous polymers (Prasetya et al. 2020). Recently, zeolite and zeotype membranes with micropores have received increasing attention for the capture of $CO_2$ (Rahmah et al. 2022). In addition, emerging polymeric membrane materials including a few polymers containing a high content of polar functional groups (i.e., ether oxygen-rich polymers and polymeric ionic liquids), shape-persisting glassy polymers (i.e., perfluoropolymers, and iptycene-containing polymers), and reactive polymers featuring facilitated transport are highly promising options (Han and Ho 2021). Cryogenic technologies for $CO_2$ capture would be a proper alternative in which $CO_2$ can be separated from other gases by cooling the gas mixture to very low temperatures, causing $CO_2$ to condense into a liquid while other gases remain in the gaseous state (C. Song et al. 2019). Although the aforementioned approaches are more conventional, explorations to discover new materials or methods are still on going. For example, the development and application of dual functional materials (DFMs) to capture and convert $CO_2$ to value-added products have recently shown the superiority as an adsorbent to combine with $CO_2$ utilization catalysts owing to its low cost and high $CO_2$ capture capacity (Sun et al. 2021; Omodolor et al. 2020). There are also some biological capturing approaches in which certain microorganisms, like algae or genetically modified bacteria, can capture $CO_2$ from industrial processes. Algae, for example, can be grown in photobioreactors to capture $CO_2$ through photosynthesis (Bhatia et al. 2019; Daneshvar et al. 2022). The gas hydrate-based apprcaches have also been suggested as an appropriate technologies to separate $CO_2$ from other gas species.
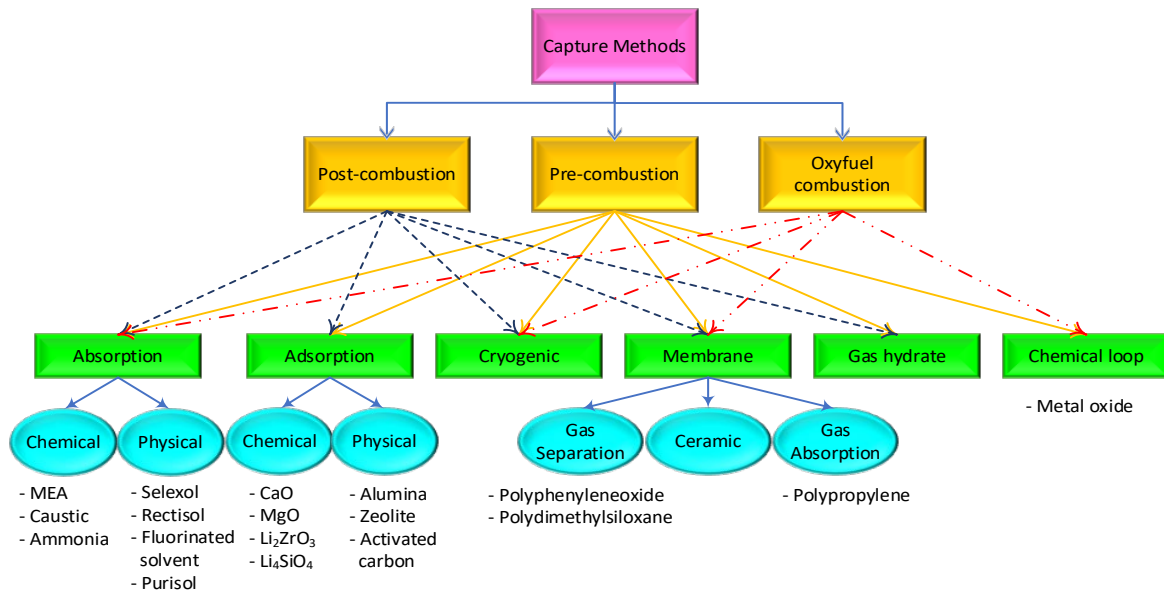
Figure 2: Options for the CO$_2$ capture and separation (D'Alessandro, Smit, and Long 2010; Olajire 2010).

The captured CO$_2$ can then be indirectly utilized in various industries. Worth highlighting for the case of CO$_2$ sequestration through gas replacement in the natural gas hydrate (NGH) fields, the characteristics, and mechanisms of this process should comprehensively be comprehended. Also, to cut down the risks, energy penalties, and costs associated with CCSU techniques, or even find new approaches, a broad range of processes have been suggested. In this regard, hydrate-based CO$_2$ utilization for different technologies has recently received worldwide scientific attention, and subsequently different hydrate-based CCSU processes for industrial applications have been developed/ proposed.

## 1.2    Natural gas hydrate (NGH) deposits

Since several overviews on prospects and challenges of gas production from natural gas hydrates (NGH) as an energy resource have been presented (Li et al. 2016; Chong et al. 2016), the following sub-sections consider the experimental investigations of gas hydrate deposits and replacement phenomena. Evidence demonstrates a tremendous amount of natural gas in the form of hydrate exists in marine and permafrost-associated sediments. In this regard, researchers have revealed that gas reserves in the continental regions and marine sediments are approximately $1 \times 10^{17}$ m$^3$ (Klauda and Sandler 2005), however, this value in other investigations was reported $3 \times 10^{15}$ m$^3$ (Milkov 2004). Although there is no consensus on the NGH estimations, this may be at least greater than worldwide conventional natural gas reserves which were determined around $196 \times 10^{12}$ m$^3$. Therefore, NGH reservoirs could be a future source of energy and, in parallel, suitable sites for CO$_2$ sequestration if the technology of CO$_2$/CH$_4$ gas hydrate exchange could be developed. The concept of coupling both sequestering CO$_2$ and CH$_4$ production can be achieved since the hydrate formation conditions of CO$_2$ are more thermodynamically stable than that in CH$_4$ hydrate. Furthermore, the formation enthalpy of CO$_2$ hydrate is about 20% greater than the dissociation enthalpy of CH$_4$ hydrate. During production and CO$_2$ refilling pore space, it is expected to see that the hydrate mechanical stability is kept constant. Also, the porous media like (clay, zeolite, silica, quartz sand) exhibits various characteristics which significantly impress the hydrate formation mechanism. The main factors affecting the kinetics and thermodynamics of hydrate formation by using a porous medium are particle size, bed height, water saturation, permeability, and porosity (Yang S, Babu H, Sam F, Linga P 2016). The effects of pore and particle size on the process of CO$_2$ hydrate formation have been discussed elsewhere (Ghaedi et al. 2016).

## 1.3    Clathrate gas hydrates

Clathrate hydrates are ice-like materials that can be formed where water molecules as hosts in contact with guest gas species at prevailing pressure-temperature conditions generate a crystalline lattice. Clathrate hydrates are categorized into three types. Structure I, can be usually formed by small guest molecules (with a molecular diameter of 0.4-0.55 nm); Structure II, requires larger guest molecules (0.6-0.7 nm); and Structure H, needs small guest molecules (as a help gas) like those which form sI and large molecule normally liquid hydrocarbons (0.75-0.9 nm) simultaneously. There are, however, some exceptions such as very small guest molecules like $H_2$ and $N_2$ which form structure II clathrate hydrates, and also intermediate guests that generate different structures (sI or sII) depending on pressure and temperature conditions (Sloan and Koh 2008). Figure 3 displays the configuration of cages, and unit cells of clathrate hydrates (Shimada et al. 2005). A unit cells of clathrate hydrates include: structure I, 2 $(5^{12})$.6 $(5^{12}6^2)$: 46 $H_2O$; structure II, 16 $(5^{12})$.8 $(5^{12}6^4)$:136 $H_2O$; and structure H, 3 $(5^{12})$.2 $(4^35^66^3)$.1 $(5^{12}6^8)$: 34 $H_2O$.
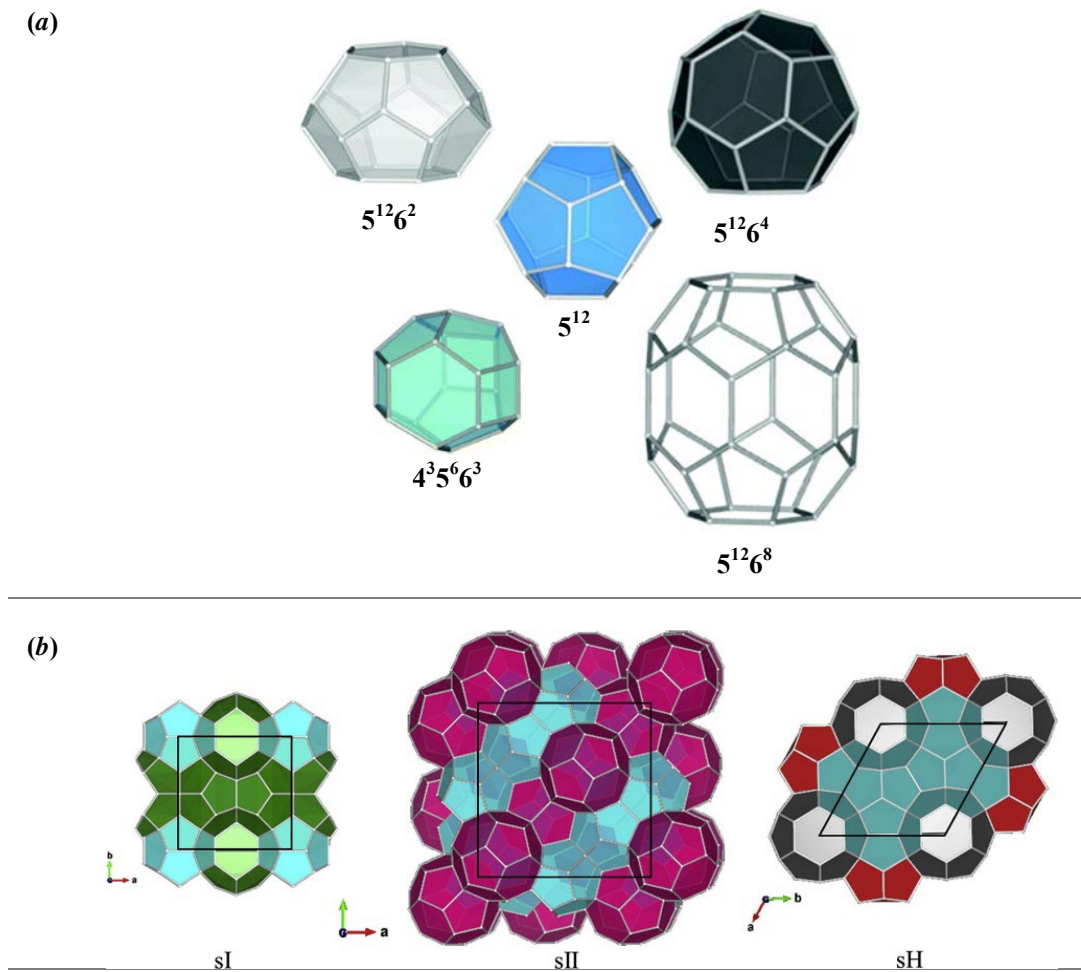


Figure 3: (a), Different cages of clathrate hydrate (Hassanpouryouzband et al. 2020); (b), unit cells of Clathrate hydrates ($5^{12}$, $5^{12}6^2$, $5^{12}6^4$, $4^35^66^{3,}$ and $5^{12}6^8$ cages are in blue, green, magenta, red, and grey) (Ripmeester and Alavi 2016).

## 1.4    Feasibility of Hydrate-based CO₂ capture (HBCC)

Hydrate-based separation techniques mostly operate at medium pressure ranges which can regenerate to separate gas mixtures via a unique mechanism. Estimations suggest a fully loaded sI $CH_4$ hydrate can store 170 volumes of gas (STP) per volume of hydrate. Also, the storage potential of sH $CH_4$ hydrate was determined nearly 201 $m^3$ which would be acceptable in

comparison with the storage capacity of LNG (600 m$^3$ v/v at -160 °C) (Sloan and Koh 2008). However, according to the recent evaluations of the gas-to-hydrate (GTH) method alongside five other technically viable gas transformation technologies, this method may not be the best option for $CH_4$ transformation. The stability condition of different gas species that contribute to the gas mixture also plays a crucial role in gas separation through gas hydrates. The equilibrium phase diagram of diverse pure gas hydrates is presented in Figure 4. At a certain temperature, the corresponding pressure formation conditions of $N_2$, $H_2$, and $CH_4$ hydrates are higher than those in $CO_2$ hydrates. This circumstance can be the basis for the HBCC processes. Thereby, $CO_2$ enrichment by hydrate formation from the gas mixture can be attained. In this context, the higher difference between the hydrate formation pressure of $CO_2$ and other gas species in the mixture could give greater separation efficiency. For example, at 276 K, the minimum pressure to generate pure $CO_2$ $CH_4$, $N_2$, and $H_2$ hydrates are about 1.8, 3.6, 22, and 366 MPa respectively. Accordingly, it is expected to see better performance for the separation of mixed $CO_2$ and $H_2$.
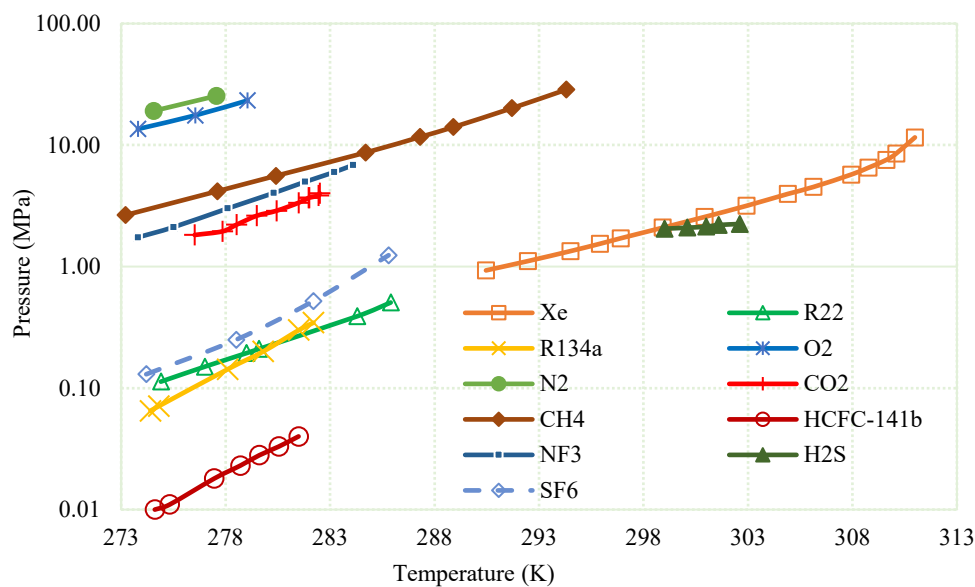


Figure 4: The equilibrium phase diagrams of different gas hydrates (M. Wang et al. 2016; Ohgaki et al. 2000; Jhaveri and Robinson 1965; Hashemi et al. 2015; Sa J, Kwak G, Lee B, Han K, Cho S, Jun L, Ju Dong L 2017; Kim, Choi, and Seo 2018).

The processes of HBCC can be designed in the form of single or multi-stages or combined with other approaches. The advantages of such coupled techniques would be the lower costs or higher efficiencies compared to using standalone. As Figure 4 displays, in the single-stage HBCC, the gas mixture at the first step is fed to the hydrate formation reactor, followed by the routing to the separator to split the associated residual gas from the hydrate slurry. At this stage, $CO_2$ lean gas is separated whereas rich $CO_2$ hydrate is entered into the dissociation reactor. Finally, by changing the operation condition proper for hydrate dissociation, the trapped gas mostly $CO_2$ is released to produce the rich $CO_2$. Experiments have elucidated that the concentration of $CO_2$ in the released gas is at least 5 times higher than that in the feed. To capture $CO_2$ and $H_2S$ from syngas which is derived from natural gas or integrated gasifier combined cycle (IGCC) power plants, the SIMTECHE conceived the low-temperature HBCC continuous process as illustrated in Figure 6.
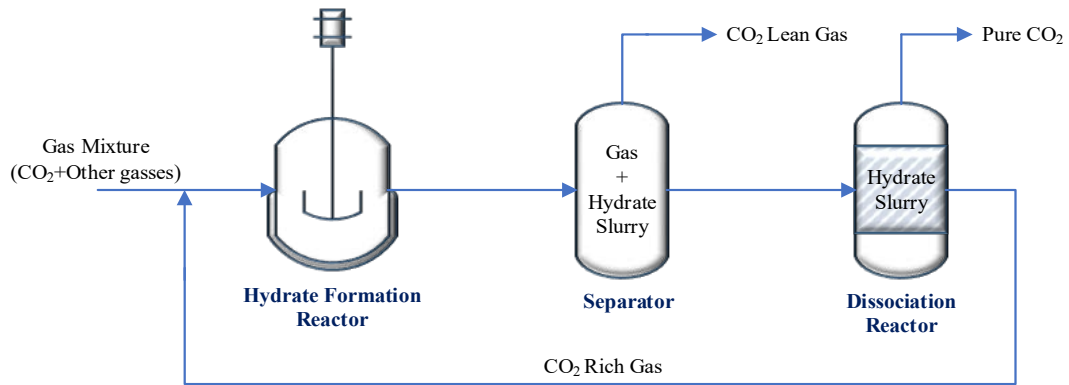
Figure 5: Flow diagram of the HBCC processing unit (Y. Wang, Lang, and Fan 2013).
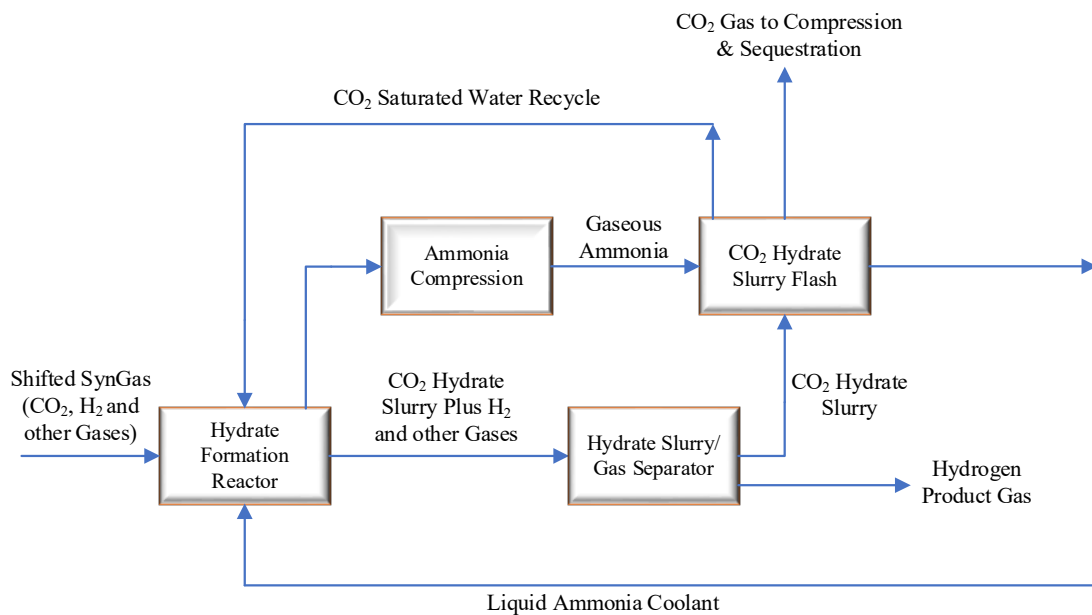


Figure 6: Block flow diagram of the SIMTECHE $CO_2$ capture process (Deppe, G., R. Currier 2003).

### 1.5 Hydrate-based CO₂ utilization alternatives

There are various alternatives that the $CO_2$ hydrate-based approaches to be used for different sections of the industry. Some examples of these technologies are presented as follows:

### A. CO₂ hydrate-based cooling systems

As the world becomes warmer, demand for cooling is expected to soar in major developing economies. To reduce the concerns, the refrigeration industry has been led to minimize the use of greenhouse F-gases and seek novel systems of refrigeration that have a less destructive impact on the environment. One of the solutions researchers have suggested is employing cold thermal energy storage (CTES) and secondary refrigerants supported by a closed refrigeration circuit. CTES refers to an energy storage approach such as phase change materials (PCMs) and chilled water and conserves cooling capacity by extracting heat from a storage medium. Because of the large storage capacity available in a phase transition, among energy storage strategies, latent heat CTES is believed to be superior In this regard, the melting enthalpy of pure $CO_2$ hydrate and ice is 507 kJ/kg and 333 kJ/kg respectively (X. Wang et al. 2021). Stem from the extra latent heat of $CO_2$ hydrates and more thermal capacity in comparison with conventional coolants and commonly-used PCMs showed that they can appear to have obvious advantages and better energy efficiency over many other types of PCM.

7

Figure 7 shows the schematic of hydrate-based secondary refrigeration. The system is charged by gaseous $CO_2$ from a tank gas followed by gas compression through a compressor to pressurize a hydrate formation reactor. Once, the $CO_2$ hydrate slurry is generated, it will be conveyed to the user via a slurry pump. After absorbing thermal energy from the surroundings, hydrate is dissociated into liquid and gas phases which can be separated via a separator.
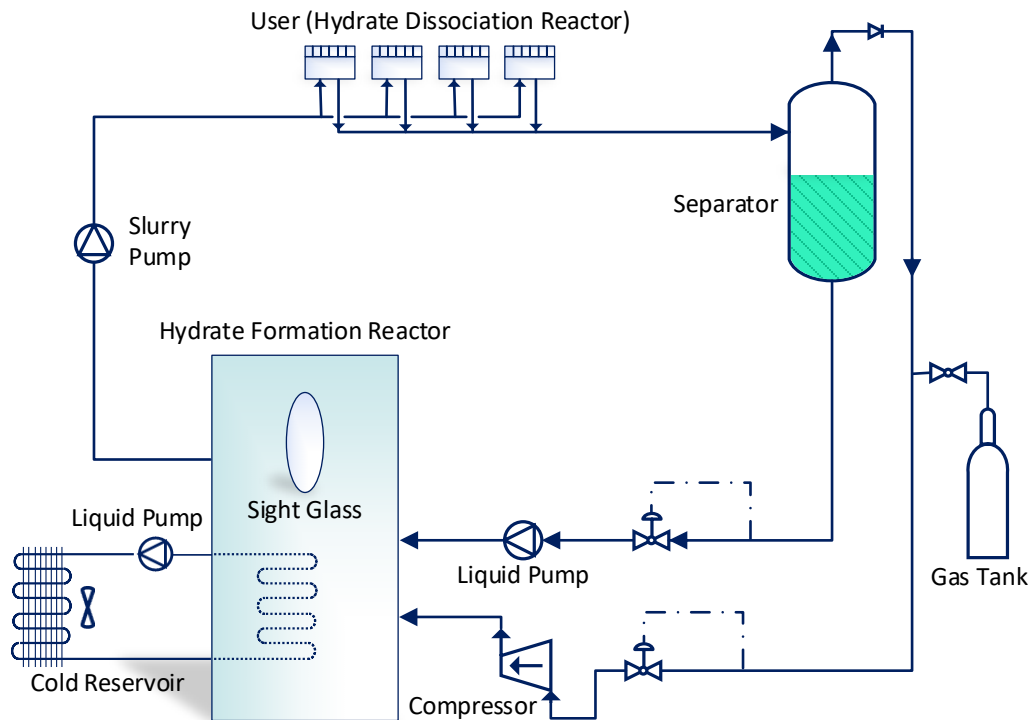


Figure 7: Conceptual diagram of $CO_2$ hydrate refrigeration system (Xie et al. 2019).

## B. Hydrate-based effluent/ heavy metal separation, and desalination

There is an interest in effluent concentration arising from zero liquid discharge (ZLD) operation as the ultimate technique for the prevention of pollution. In the pulp and paper industry, recovering clean water or removing dissolved materials from the effluent is an essential part of a ZLD plant. Processes for water recovery can be carried out by membrane separation, crystallization, and evaporation methods. In this context, generating hydrate crystals followed by their physical separation and then melting formed hydrate has been suggested as a freeze concentration method. Owing to the fact that $CO_2$ clathrate hydrates with promoters e.g. CP (Ho-Van et al. 2019)  can generate hydrates near ambient temperature, the required energy is notably lower than that in the crystallization method which operates at water freezing point. Also, these temperatures are not high enough to cause loss of volatile components or corrosion scaling as is the case with evaporation. In hydrate-based desalination (HBD) or hydrate-based pollutant removal (HBPR) processes, water molecules engage the hydrate former molecules and generate the clathrate hydrate; so that salts and other impurities become excluded. Crystalline hydrate can then be decomposed into potable water and the hydrate former is then recovered and recycled. Since $CO_2$ possesses a dual character, coupled $CO_2$ capture and HBD may become the right choice for both global warming and desalination.  A hybrid process for $CO_2$ capture and seawater desalination is displayed in Figure 8. In this regard, energy consumption, efficiency as well and process safety are found to be critical factors.
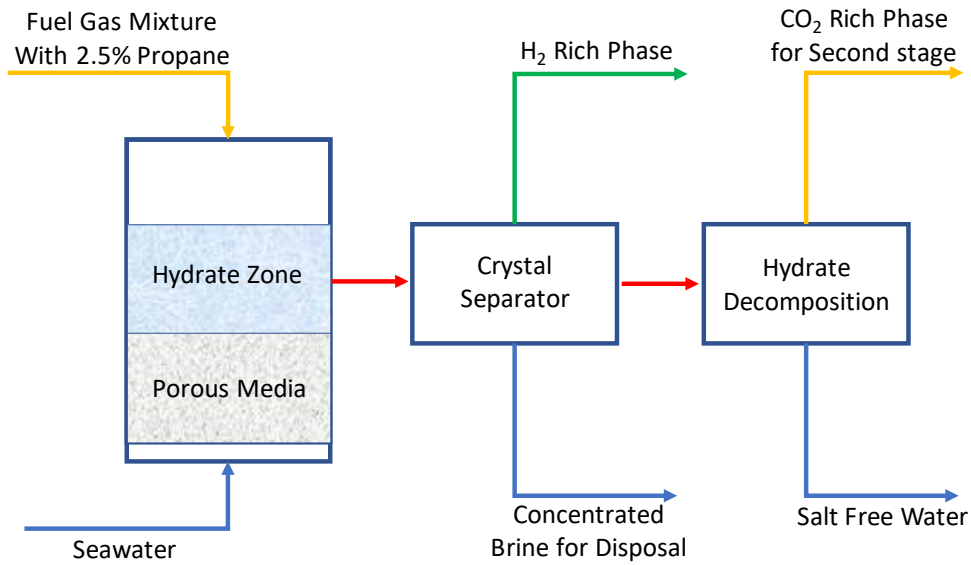
Figure 8: Block flow diagram of the hybrid process for $CO_2$ capture and seawater desalination process (Babu et al. 2018).

## C. Concentration or preservation of food through CO2 hydrates

The products and by-products of the citrus industry play a significant role in the global economy. It was determined that in 2020, over 30 billion liters of fruit juice were related to concentrated juices (Neves et al. 2020). However, the use of a wide array of conventional concentration methods to remove water from fruit juices involves a high level of energy consumption as well as equipment. In this regard, the evaporation method is the one that has been applied to concentrate juices in many cases. To remove extra water from juices at a degree of concentration up to 85%, energy between 180 and 2,160 kJ/kg of water should be provided. For volatile compounds (e.g. aroma) or substances like polyphenols, and heat-sensitive vitamins, evaporation may impair product quality. The membrane concentration method (MCM) is the other alternative but this process technique is associated with the obstruction of the membrane stops which can lead to a high cost for maintenance and a shortening of the membrane's life. Alternatively, gas hydrate technology such as $CO_2$ hydrate in recent years has gained interest in the food industry. Because of the low temperature and moderate pressure condition of $CO_2$ hydrate and low energy consumption to concentrate juices by the use of energy (approximately 252–360 kJ/kg of water), this approach may be more innovative (Seidl et al. 2019).

## D. Nuclear power plants using CO2 hydrate

Evidence suggests a large amount of waste heat from nuclear and thermal power plants is being disposed into oceans, rivers, lakes, and air. On the basis of the heat generated by nuclear reactors, power plants typically have a generation end efficiency of between 33% to 35% while over 60% of generated heat is being wasted. However, in a few cases, such waste heat is used for seawater desalination, farm cultivation, fish farming, etc. Since the location of large-scale nuclear power plants (NPPs) are not close to energy-consuming areas, the effective utilization and recovery of their waste heat is a critical objective. Because small-scale organic Rankine cycle (ORC) power systems (Hu et al. 2020) and small temperature difference power generation using the Carina cycle to convert the waste heat of NPPs into electricity are economically difficult to install, other technologies to obtain higher conversion efficiency should be developed. Given that the efficiency of the gas hydrate power generation system (GGS) is over 20%, it is capable of small temperature difference power generation with energy

9

storage (Obara and Tanaka 2021). Figure 9 displays the configuration of a gas hydrate heat cycle (GHC) where the waste heat is obtained from the condenser by an absorption refrigerator (an absorption chiller).
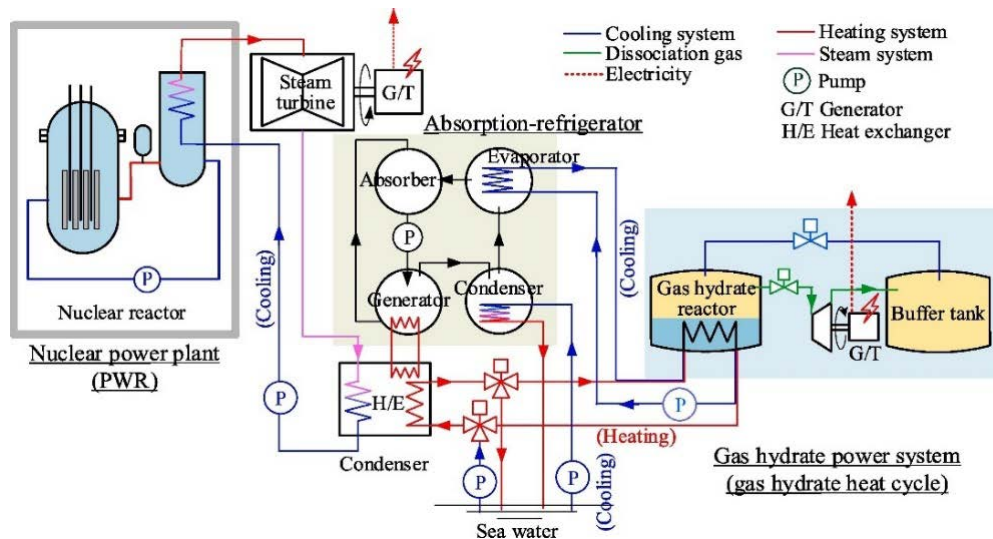


Figure 9: Power plant with exhaust-heat recovery by $CO_2$ hydrate heat cycle (Obara and Tanaka 2021).

### E.  Fire Extinguishment using $CO_2$ hydrate

It was suggested that hydrates utilizing non-flammable gases such as $CO_2$ can be employed as fire extinguishing agents. As previously stated, the dissociation heat of hydrates is comparable to or even larger than that in a fusion of ice. Simultaneously, because of the release of non-flammable gases during hydrate dissociation in the combustion field, this phenomenon can control the flames by reducing the fuel concentration and preventing the supply of oxygen. Additionally, the amount of $CO_2$ hydrate would be much less than that of a conventional fire extinguishing method such as water spraying (Anwar et al. 2018).

### 1.6    Hydrate-based performance parameters and the Role of Promoters

The efficiency of hydrate-based $CO_2$ separation is often described by five specific parameters: hydrate equilibrium pressure, hydrate induction time, gas consumption (G.C.) or Gas uptake, split fraction (S.Fr.), or $CO_2$ recovery and separation factor (S.F.). The major impediment to hydrate-based methods is the sluggish rate of hydrate formation, which originates from the nature of hydrate induction time. Also, the pressure of the system plays a crucial role in the separation efficiency and the formation rate. Problems plaguing the development of these processes are influenced by operating conditions, formation pathways, guest molecule size, and formed hydrate structure. Constant interaction between gas and water is also extremely vital for incessant hydrate formation. In this context, the solution would be the mechanical and chemical bases. The chemical alternative to upgrading the HBCC performance parameters as well as hydrate-based utilization techniques is the addition of hydrate promoters which have been subdivided into kinetic hydrate promoters (KHPs) and thermodynamic hydrate promoters (THPs). The former type mostly boosts gas consumption, rate of formation, and induction time whereas the latter induces the thermodynamic equilibrium conditions. For example, THPs depending on the gas species, by changing the equilibrium pressure of hydrate formation to lower stability conditions play a positive role. Moreover, the utilization of both THPs and KHPs can affect the split fraction as well as the separation factor quite higher than their single utilizations. To date, plenty of additives have been identified, with the addition of which, $CO_2$ hydrate forms at various kinetics and phase equilibrium conditions. Figure 10 shows the list of some of these hydrate promoters and their main impressions.
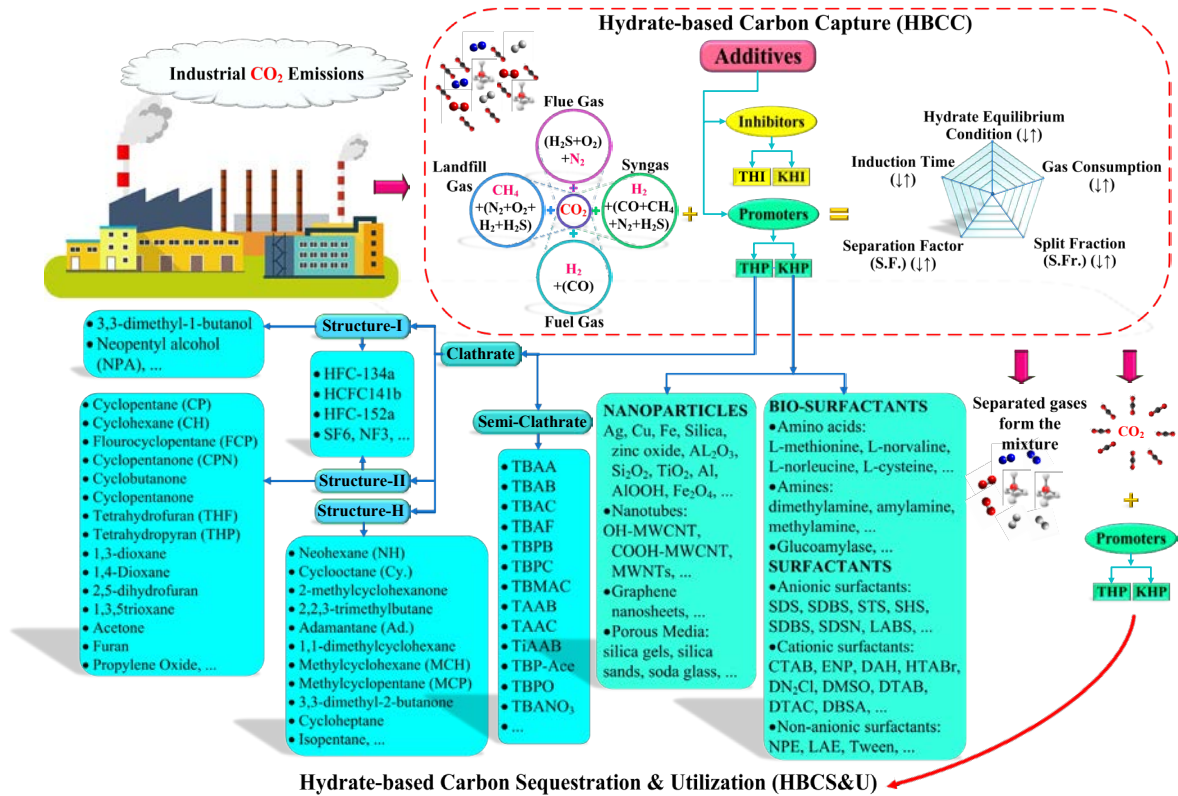
Figure 10: The hydrate promoters identified for hydrate-based CO$_2$ capture, sequestration, or utilization (HBCC/S/U) processes. THI/ KHI are thermodynamic/ kinetic hydrate inhibitor, and THP/ KHP are thermodynamic/ kinetic hydrate promoter respectively; The abbreviation of components are presented in Appendix 1 (Sinehbaghizadeh, Saptoro, and Mohammadi 2022).

Based on Figure 10, understanding the behaviour of a wide variety of promoters to achieve more effective gas separation with less energy consumption needs to be explored. The THPs can be categorized as large molecular guest substances of structure-I/II/H, and semiclathrate components while the KHPs can be mostly classified as inorganic/ organic surfactants (or bio-surfactants), nanoparticles, Nano-tubes/ Nano-sheets and porous components (or porous environments). The most proportion of investigations on gas hydrates in the porous environment e.g. aluminium foam (Fan et al. 2012), metallic packing (Kumar et al. 2015), silica gel (Smith, Wilder, and Seshadri 2002), polyurethane foam (Babu P, Yee D, Linga P, Palmer A, Khoo B, Cheong T, Thiam S, Rangsunvigit P 2013), glass beads (Kono et al. 2002) has been focused on kinetics as well as the storage capacity of gas hydrates. Researchers have certified that kinetic promoters such as activated carbon (Govindaraj et al. 2015), synthetic surfactants (Palodkar and Jana 2020), carbon nanotubes (Y.-M. Song et al. 2021), glass beads and porous silica (Zhang et al. 2021), nanoparticles (Ren Wang et al. 2019), and sand grains (Hyodo et al. 2017) through enhancing surface activity can improve the gas molecules to resolve or disperse in the solution and higher hydrate formation rate. The ion environment, carbon chain, and head group of the surfactant structure as well as hydrate surface property play a crucial role in the surfactant adsorption (Salako et al. 2013). This produces a proper wettability on the reactor sidewall which may cause upward hydrate growth toward hydrate propagation (Hayama et al. 2016).

Although most conventional surfactants may not be environmentally acceptable, the use of bio-surfactants (e.g. amines and amino acids) possesses favourable characteristics such as better stability, lower cost, less toxicity, and biologically degradable. Generally speaking, amino acids comprise amine groups, carboxylic acid, and a side chain, ranging from a polar alkyl

chain (hydrophobic) to a negative or positive charge moiety (hydrophilic) with their physical and chemical properties vigorously depending on the particular side chain. The dual-functional behaviour of amino acids and their role in $CO_2$ capture and sequestration have already been reviewed (Bhattacharjee and Linga 2021). The first research that denoted the capability of natural amino acids (leucines) in promoting hydrate at low concentrations (up to 1 wt%) of amino acids was reported in 2015 (Liu et al. 2015). Compared to hydrophilic amino acids, hydrophobic ones show stronger flue gas hydrate promotion capability (Veluswamy et al. 2017). In this regard, hydrophobic amino acids e.g. L-valine, L methionine, L-histidine, and L-arginine (3000 ppm concentrations) have near similar promotion capabilities as SDS on flue gas (Pandey et al. 2020). These components depending on their physical and chemical properties have also shown a large $CO_2$ gas storage potential in the form of hydrates, even under a non-stirred configuration (Cai et al. 2017). Recent experiments exhibited that 78% water conversion, an average $CO_2$ uptake of 114 v/v, and a significant decline of induction time with the utilization of only 300 ppm l-tryptophan can be attained (Khandelwal H, Qureshi M, Zheng J, Venkataraman P, Barckholtz T, Mhadeshwar A, Linga P 2021). It was also clarified that a higher increase in L-tryptophan concentration cannot result in significant additional improvement. Since strong polar ionic promoters quickly form dense hydrate layers, this phenomenon at the liquid-gas interface hinders the gas diffusion from the gas phase to the bulk solution (Xu et al. 2017); hence, polarity plays a critical role. It seems that most polar amino acids such as serine, threonine, phenylalanine, and glutamine are generally kinetic hydrate inhibitors (KHIs) (Pires et al. 2021). Also, the gas uptake in the presence of weakly polar or non-polar promoters is dependent on the dissolution characteristics between the different components in the system (Xu et al. 2017). Regarding the exothermic and thermal-inhibition properties of gas hydrate formation, researchers have suggested the use of Nano-fluids (such as Nano $Al_2O_3$, Ag, Cu, Fe and so on) with high thermal conductivity to promote gas hydrate formation. These tiny particles by improving heat and mass transfers, providing numerous hydrate nucleation sites, decreasing the wetting angle and interfacial tension of the hydrates can dramatically decline the induction time along with upgrade the gas consumption (Rahmati-Abkenar, Manteghian, and Pahlavanzadeh 2017).

Despite some positive impacts of single promoters, more improvements in all aspects of performance parameters should be fulfilled. Besides, the HBCC separation factor could not be evaluated through experiments in the previous section. Hence, to find a proper energy-saving and time-efficient path, investigations on the synergic influence of additives like those in the preceding part which have proved themselves as effective promoters would be beneficial. In this regard, the coupled promoters can be classified into three kinds: KHP+THP, THP+THP, and KHP+KHP. The maximum enhancement of THP, KHP, and THP+KHP in comparison with the absence of these components is shown in Figure 11.
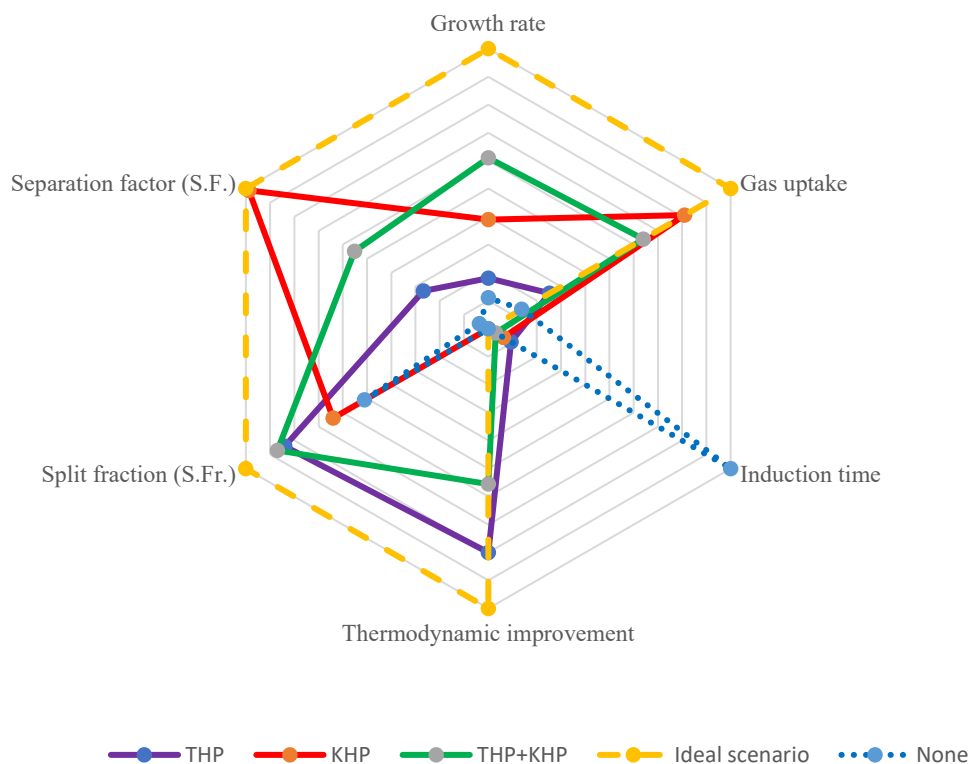
Figure 11: Maximum improvements of THP, KHP, and THP+KHP on performance parameters of mixed $CO_2$ hydrates. (The ideal scenario could be a growth rate: 100 (mmole/ mole.min), gas uptake: 0.174 (mole $CO_2$/ mole $H_2O$), IT: 0 min, S.F.: 250 e.g. $CO_2(40\%)+CH_4(60\%)$, and S.Fr.: 1) (Sinehbaghizadeh, Saptoro, and Mohammadi 2022).

In this thesis, the type of promoters for performing MD simulations was selected based on considering two points: the newly introduced promoters in the literature which have been recently discovered and are environmentally acceptable. Since the organic KHPs would be environmentally friendly and acceptable for the development of hydrate-based $CO_2$ capture, sequestration, or utilization processes, newly introduced hydrate promoters such as amines, and amino acids were selected for the simulations of the hydrate formation. Moreover, metal nanoparticles were also chosen to better understand the synergistic effects of promoters from various types. Also, there are many THPs that can form the structure I/II/H of the clathrate hydrate family. Because the behaviour of these components and their interactions are relevant to the shape and type of these molecules, different THPs from the structure I/II/H which have a cyclic or branched molecular shape with carbon numbers ranging between 5 to 10 were considered. Also, the effects of the combination of THPs were investigated. The molecular impressions of these components on pure and mixed $CO_2$ hydrates using MD simulations can reveal the positive and negative aspects of utilizing different promoters.

The purification of biogas/ syngas/ flue gas and fuel gas would be the feed for the processes of hydrate-based $CO_2$ capture. Since the inclusion of hydrate promoters either for these processes or the sequestration/ utilization of the purified $CO_2$ is required, investigations of the effects and mechanisms of promoters in the processes of CCUS at the molecular scale can complete the experimental findings of these processes during the formation and dissociation phenomena at the macroscopic scale.

### 1.7 Phenomena and properties associated with $CO_2$ hydrate technologies

To develop $CO_2$ hydrate-based technologies, various phenomena, and characteristics associated with $CO_2$ hydrates have been extensively explored through experimental investigations. In this regard, the hydrate formation and dissociation and their properties would be the most important specifications of hydrate-based methods which can directly contribute to the efficiency of these approaches. To understand the main features of these phenomena and properties of $CO_2$ hydrates, explorations can be conducted at three different scales: macroscopic, mesoscopic, and microscopic. Since The mesoscopic and microscopic scales of investigations can significantly affect the characteristics of the macroscopic level, conducting diverse analyses at all scales needs to be implemented. Although the two first scales can be studied by employing laboratory equipment, analysis at the microscopic level may either require highly expensive facilities or sometimes be impossible. For example, when the scales are in order of nano-second and nano-meter or selecting harsh operating conditions (e.g. several GPa or near zero Kelvin) to be considered, the other alternative should be chosen. In this regard, molecular dynamics (MD) simulations as an effective tool can be applied. As a computational framework in the fields of science and engineering, MD simulations have received attention due to their power to calculate the details of motions of individual molecules or atoms and relate these to equilibrium and kinetic properties of bulk phases. MD simulations at the molecular scale aid in achieving knowledge concerning the dynamical as well as structural properties of components in either simple or a mixture of gases and liquids. Using classical MD, large-scale simulations (i.e. thousands of particles) for multiple phases over relatively long times (i.e. hundreds to thousands of nanoseconds) can be performed to investigate a wide variety of physical and chemical processes associated with $CO_2$ hydrates. These simulations can answer many different questions such as the mechanisms of surface absorption, crystal growth, phase separation, etc. There are also different parameters that researchers have applied to investigate the microscopic mechanisms/ phenomena, intermolecular behaviours, and properties of $CO_2$ hydrate crystals. The list of analysis parameters as well as software employed for a variety of hydrates is exhibited in Figure 12.

| LAMMPS | VESTA | MDynaMix | Quantum-Espresso |
|---|---|---|---|
| DL_POLY | SIESTA | MXDORTO | WinMASPHYC |
| DL-CLASSIC | VASP | MCCCS Towhee | CHARMM |
| Pydlpoly | CPMD | MOLDY | GEMS |
| GROMACS | NAMD | MODYLAS | NBO |
| GROMOS | DMol$^3$ | CRITIC2 | SHARC |
| DYNAMO | AIMD | CP2K | GCMC |
| Materials Studio | AMBER | TINKER | Gaussian |

**Initial Configuration**

**MD Software**

**Coding for Simulation**

**Analysis Parameters**

**Phase equilibrium, Physical properties**
Coexistence equilibrium, melting temperature
Densities of states (DOS), Surface Density of Water Cages, Viscosity
Diffusion coefficient, self-diffusion, Fickian diffusivity, relative concentration
Cp and Cv, Specific heat capacity, thermal conductivity
Isothermal compressibility, thermal expansion coefficient
Interfacial transition layer/thermal resistance (ITR)

**Stress, Tension**
Tensile/strain/compressive stress, stress-strain relationships
Contact/torsion/tilt angle, Surface/interfacial tension
Shear/bulk modulus, strain energy, shear strain
Gruneisen parameter, crystal defect
Elastic moduli, shear elastic constant
Crystal anisotropy (anisotropy index), asymmetric stretch

**Hydrogen bond (H-bond)**
No./angle distribution/distance of H-bonds, H/O-H bond stretching
H-bond density/length/energy/lifetime/probability

**Unit Cell and Cage**
Unit cell volume and length
Cell size/lattice constant variation
Fractional cage occupancy (occupation ratio)
Hydration/coordination No.
Refined fractional coordinates/structural parameters
No. of crystal unit cell/polygons
Cage rigidity/deformation, radius change
Seed-nucleus/critical nuclei size
Cross nucleation, critical nuclei size
Persistence of individual cages (e.g. $5^{12}6^3$)

**Energy**
Potential/kinetic/dynamic energy
Interaction energy (conf./elect./vdW energy)
Gibbs/Helmholtz free energy
Excess chemical potential/enthalpy/entropy
Cohesive/surface/internal/adsorption energy
Activation/stabilization/binding energy
Unit-cell configurational energy, DFT energy
Free energy barrier

**Rate**
Growth/formation Rate
Decomposition/decay/melting rate
Gas uptake/release rate
Nucleation/conversion rate
Occupancy rate, storage capacity
Time evolution of the blobs, time decay of OACF
Survival time of cages, nucleus lifetime
Mean first-passage/induction/relaxation time
No. of water/guest molecules in cluster/bubbles
Hydrate crystallinity/thickness

**Rotation, Fluctuation, Distribution**
Heat flux autocorrelation function (HCACF)
Rotational autocorrelation function (RACF)
Velocity autocorrelation function (VACF)
Orientation Auto-Correlation Function (OACF)
Residence autocorrelation function (RACF)
Angular probability distribution function (APDF)
Mean Square Displacement (MSD)
Root mean squared deviation (RMSD)
Root mean squared fluctuation (RMSF)
Axial distribution function (ADF)
Radial displacement function (RDF)
Potential of mean force (PMF)
Mean First-Passage Time (MFPT)
Face-saturated incomplete cage analysis (FSICA)
Mutually coordinated guest order parameter (MCG-OP)
Differential scattering cross-section (DCS)
Orientational/dihedral/angular order parameter (AOP)
Differential scattering cross-section (DCS)
Distribution of the torsion angle/asphericity
Radius of gyration/rotation angle

**Spectrum**
IR/Power/vibrational/translational spectra
Vibrational frequency/density, guest/host vibration
Variation of the lattice vector length
Molecular/net dipole moment
Wave No., Wave/transient moving velocity
13C NMR lineshape, abundance ratio
Phonon mean free path velocity, Phonon dispersion
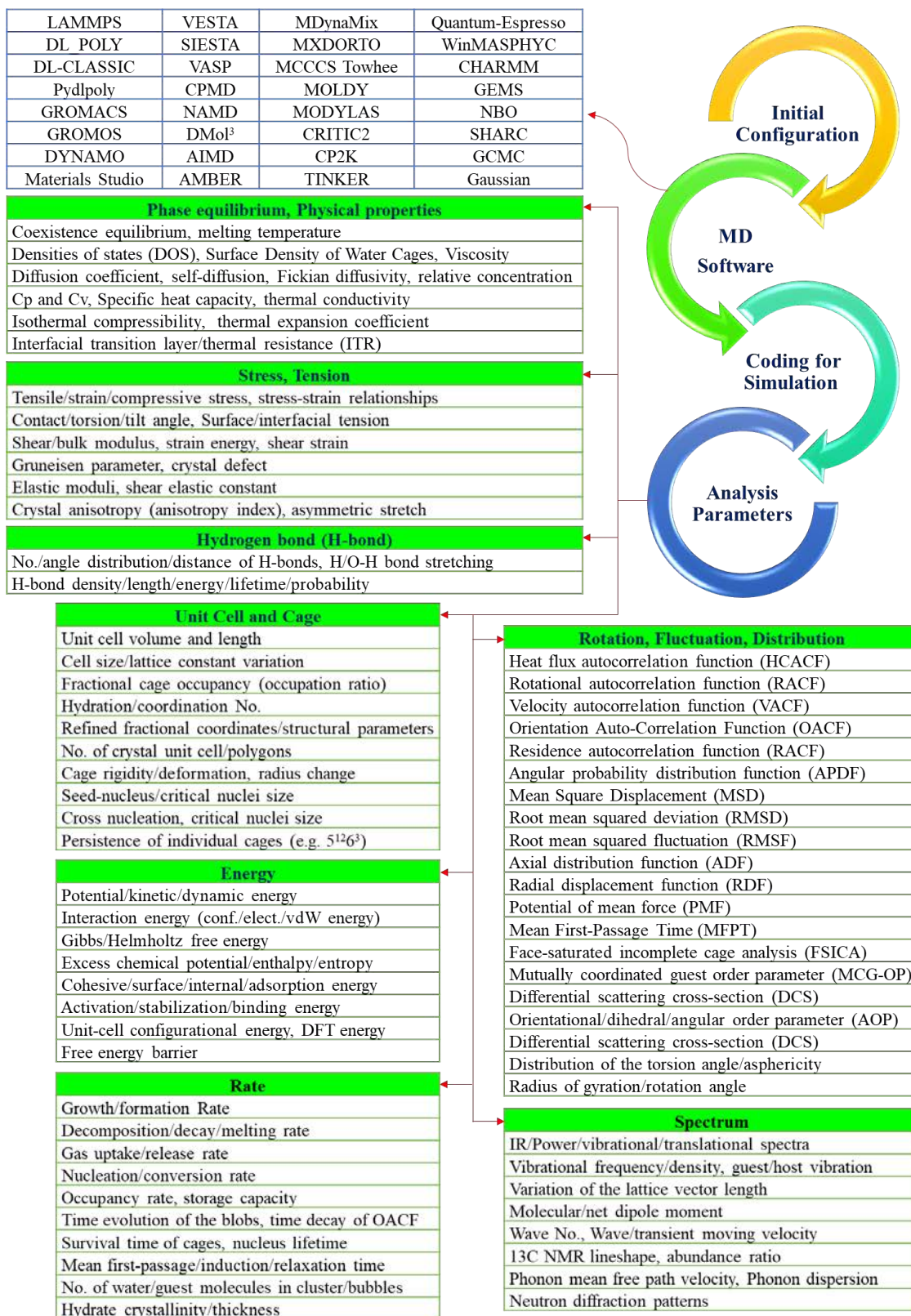Neutron diffraction patterns

Figure 12: Analytical characteristics of gas hydrate systems (Sinehbaghizadeh, Saptoro, and Mohammadi 2022).

## 1.8    Research problem statement

To upgrade the process of hydrate-based $CO_2$ capture, sequestration, or utilization for desalination, secondary refrigeration, or cold storage, and the performance evaluation of the safe preservation and transportation, finding highly efficient promoters is the main target of the researchers. In this regard, microscopic studies on new and environmentally friendly promoters have been experimentally and more recently introduced by scholars. It will also help to understand their promotion effects, progressing toward the next generation of hydrate-based industrial applications. Hence, insights into the crystal growth, stability, and dissociation of $CO_2$ hydrates in the presence of new promoters at the molecular level will elucidate their characteristics and mechanisms which will be fruitful for either upgrading the existing technologies or helping to seek new environmentally friendly promoters. It is worth mentioning, that the microscopic MD investigations on these systems of $CO_2$ hydrates plus new promoters are either too few in the literature or have not been performed yet.

## 1.9    Novelty and significances

The experimental measurements of $CO_2$ hydrate systems in the presence of new single or coupled promoters specified in chapters 3, 4, 5, and 6 of this thesis have been recently performed. Although these new promoters are effective for pure $CO_2$ hydrate and gas mixture hydrate including $CO_2$, MD simulations of these systems to identify their characteristics at the microscopic level to the best of our knowledge have not been carried out. Hence, understanding hydrate formation and dissociation of these systems at the molecular level will aid in developing different $CO_2$ hydrate-based applications and increase the possibility of finding more effective promoters. Accordingly, for such systems, new frameworks of MD analysis will be proposed and then microscopic mechanisms of them will be investigated. The outcomes will elucidate how suggested promoters can induce crystal growth, reduce the formation time, and affect the stability and dissociation conditions of pure and mixed $CO_2$ hydrates. Also, the guest roles of both help-gas species and large molecular guest substances (LMGSs) in hydrate dissociation will be specified and the key parameters will be introduced. The expected new knowledge from the study will reveal the molecular interactions between water, $CO_2$, other gas species, and promoters; and understand microscopic mechanisms of the promotion effects on both the formation and dissociation of $CO_2$ hydrate systems. The results will help develop the industrial feasibility of different applications of hydrate-based technologies.

## 1.10    Research questions

1) What are the effects of the synergistic kinetic promoters (metal nanoparticles and urea) on the crystal growth and properties of $CO_2$ hydrates? And how they can eliminate the mass and heat transfer buriers of $CO_2$ crystallization?
2) What are the strengths and weaknesses of the presence of amines as kinetic promoters in biogas hydrate formation?
3) What are the impacts of different greenhouse F-gas species and large molecular substances (LMGs) as hydrate promoters on thermodynamic/ thermophysical properties, stability, and dissociation of pure/ mixed sI, sII $CO_2$ hydrates for hydrate-based utilization aims?
4) What are the influences of different sH hydrate formers as THPs and polar and non-polar amino acids as kinetic promoters on the stability and dissociation of pure $CO_2$ and mixed $CO_2+N_2$/ $H_2$/ $CH_4$ sH hydrates?
5) What are the effects of gas impurities such as $SO_2$, $H_2S$, $N_2$, and $H_2$ on biogas hydrate during the formation? and how such systems can be kinetically modelled?

## 1.11    Aims and objectives

There is a gap at microscopic level explorations for the effects of single or synergistic promoters on $CO_2$ hydrate systems which need to be carried out. Hence, the MD investigations

of $CO_2$ hydrates in the existence of promoters have not been well developed which is the main aim of this project. To understand the effects of promoters on $CO_2$ hydrate properties such as structural, thermophysical, thermodynamic, kinetic, heat, and mass transfer characteristics at the molecular level which can be useful for industrial applications of hydrate-based $CO_2$ capture and utilization or sequestration technologies (CCUS), the main objectives of this research project are laid out as follows:

**Objective 1:** To provide new MD frameworks and to analyse the molecular formation mechanisms of $CO_2$ hydrate systems in the existence of pure/ mixed KHPs such as metal nanoparticles and urea.

**Objective 2:** To determine the role of organic KHPs (amines and urea) in promoting biogas ($CO_2$+$CH_4$) hydrate formation during the hydrate formation.

**Objective 3:** To specify the impacts of guests and THPs on the stability and the dissociation of pure/ mixed sI, sII $CO_2$ clathrate hydrates at different thermodynamic conditions.

**Objective 4:** To identify the effects of polar and non-polar amino acids on $CO_2$ sH hydrate dissociation. Also, to understand the key influences of sH hydrate formers as THPs on pure/ mixed $CO_2$ sH hydrates.

**Objective 5:** To recognize the impressions of associated gas impurities such as $SO_2$, $H_2S$, $N_2$, and $H_2$ on biogas hydrates during the formation. Also, to develop the kinetic modelling for these hydrate systems based on the parameters obtained from MD simulation results.

## 1.12    Research Hypothesises
In this thesis, the following hypotheses are considered:

1- It is expected that the inclusion of several kinetic hydrate promoters at the same time can enhance the rate of hydrate growth in comparison with their standalone addition to the solution phase.
2- It is assumed that since THPs reduce the thermodynamic hydrate operation, they can improve the resistivity of $CO_2$ hydrates against being decomposed.

## 1.13    Summary of the scope of work
The graphical summary of objectives is presented in Figure 13. All $CO_2$ hydrate-based processes include the formation and dissociation stages. Hence, the results of this project can contribute to the multiple aspects of these technologies.
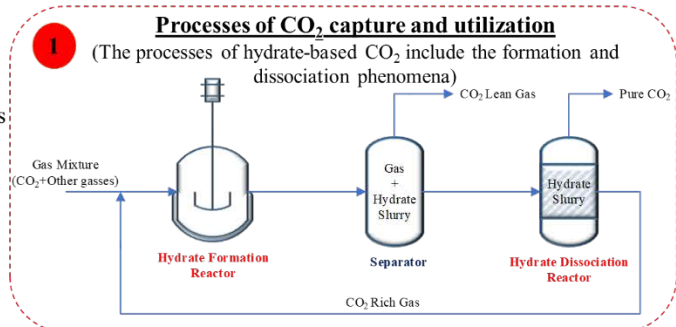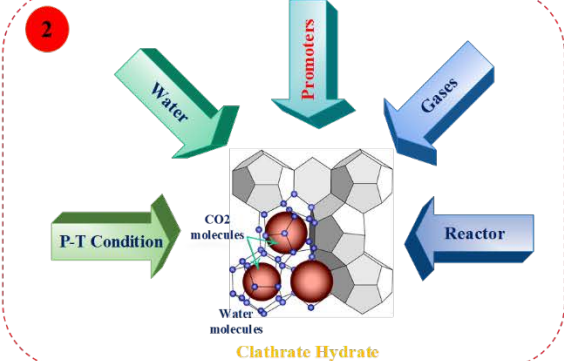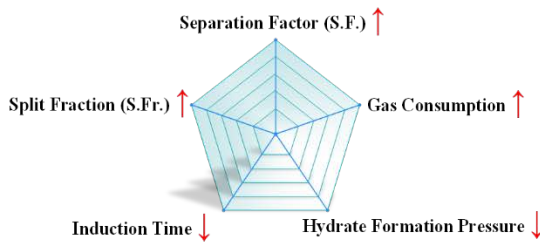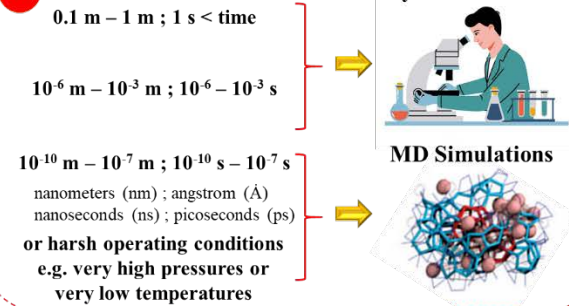
Figure 13: Graphical summary of the phases in this project.
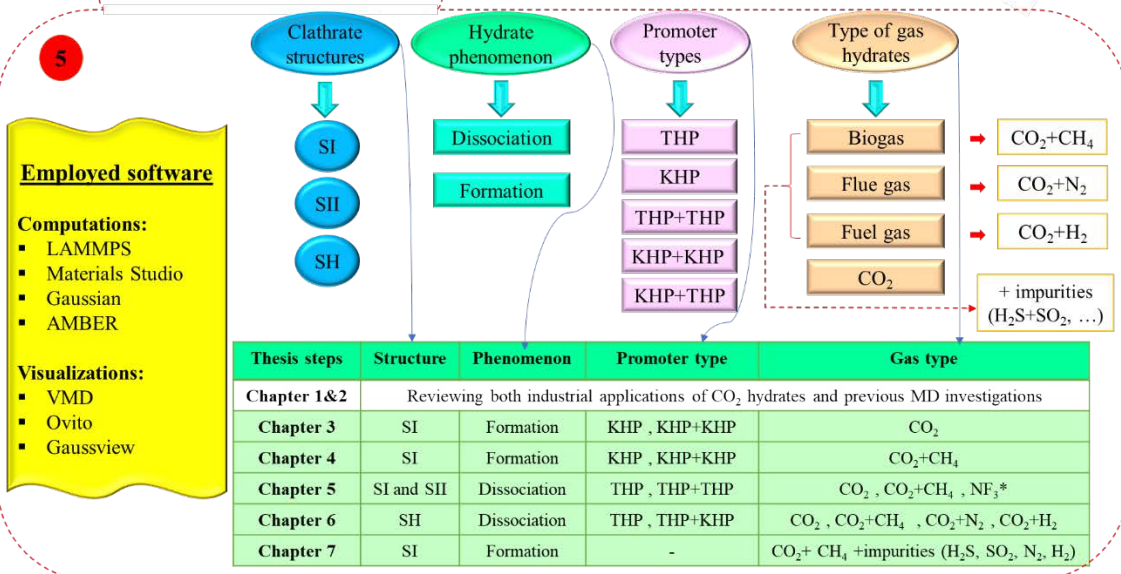
Note: To fully understand the scope of this thesis, two different comprehensive literature reviews have been carried out. The first was performed to overview the $CO_2$ hydrate properties and applications and the second was to review all MD simulations of gas hydrates including $CO_2$ hydrate systems.

## 1.14    Definitions

Table 1: In this thesis, the definition of important items is as below.

| Item | Definition |
|---|---|
| Hydrate promoter | There are two types of hydrate promoters: Thermodynamic hydrate promoters (THP): Components that contribute to the hydrate phase so that the thermodynamic formation of $CO_2$ hydrate can be reduced to lower pressure at a certain temperature or vice versa. Kinetic hydrate promoters (KHP): Components along which the hydrate phase can be formed easily and faster than in their absence. |
| Hydrate inhibitor | These components thermodynamically (THI) or kinetically (KHI) inhibit/ prevent the formation of gas hydrates. they are inversely proportional to the above description. |
| Hydrate Cage | Water cages can be created through hydrogen-bonded water molecules. Indeed, the hydrogen bonds between the oxygen and hydrogen atoms of water molecules induce them to be oriented in specific locations which results in the formation of cages with pentagonal and hexagonal shapes. |
| Clathrate hydrate | Different types of cages together create the unit-cell of hydrate and the allocation of several unit-cells in the neighboring sides form the clathrate hydrate network. |
| Hydrate stability | Under the prevailing thermodynamic conditions, the gas hydrate can remain unchanged. This situation is known as the hydrate stability of gas hydrates. |
| Hydrate formation (hydrate growth) | Under the prevailing thermodynamic conditions, the crystalline shape of water molecules which is similar to the ice can be formed and grown. |
| Hydrate dissociation | Outside of the prevailing thermodynamic conditions, where the water network of clathrate hydrate cannot remain constant, it will be dissociated. |
| Induction time | The time at which gas molecules can be dissolute in the water phase and allocation of water molecules until the initial formation of crystals and creation of the water network (cages) around gas molecules which finally results in the clathrate solid phase. |
| F3 parameter | By calculating this parameter, the trend of crystal growth and the water molecular arrangements as a function of simulation time can be monitored. |
| F4 parameter | To analyse the degree of the hydrates with these components which exhibited desirable improvements during the process of crystal growth. |
| Mean square displacement (MSD) | Atoms in particle diffusion systems tend to diffuse into space. Therefore, the MSD of atoms shows their diffusion and mobility in a system. Since particles cannot freely diffuse through the solid state, the MSD of components in liquid and gas phases is significantly higher than in the solid (hydrate) phase. |
| Radial distribution function (RDF) | To determine the degree of order in the hydrate structure and describe the configuration of the formed clathrate, the calculation of the RDF parameter can be highly useful. |

## Reference

Aghel, Babak, Sara Behaein, and Falah Alobaid. 2022. "CO2 Capture from Biogas by Biomass-Based Adsorbents: A Review." *Fuel* 328 (November): 125276. https://doi.org/10.1016/j.fuel.2022.125276.

Ahmed, Rafay, Guijian Liu, Balal Yousaf, Qumber Abbas, Habib Ullah, and Muhammad Ubaid Ali. 2020. "Recent Advances in Carbon-Based Renewable Adsorbent for Selective Carbon Dioxide Capture and Separation-A Review." *Journal of Cleaner Production* 242 (January): 118409. https://doi.org/10.1016/j.jclepro.2019.118409.

Anwar, M N, A Fayyaz, N F Sohail, M F Khokhar, M Baqar, W D Khan, K Rasool, M Rehan, and A S Nizami. 2018. "CO2 Capture and Storage: A Way Forward for Sustainable Environment." *Journal of Environmental Management* 226 (August): 131–44. https://doi.org/10.1016/j.jenvman.2018.08.009.

Babu P, Yee D, Linga P, Palmer A, Khoo B, Cheong T, Thiam S, Rangsunvigit P, . 2013. "Morphology of Methane Hydrate Formation in Porous Media." *Energy & Fuels* 27 (6): 3364–72. https://doi.org/10.1021/ef4004818.

Babu, Ponnivalavan, Abhishek Nambiar, Tianbiao He, Iftekhar A Karimi, Ju Dong Lee, Peter Englezos, and Praveen Linga. 2018. "A Review of Clathrate Hydrate Bbased Desalination to Strengthen Energy–Water Nexus." *ACS Sustainable Chemistry & Engineering* 6 (7): 8093–8107. https://doi.org/10.1021/acssuschemeng.8b01616.

Bhatia, Shashi Kant, Ravi Kant Bhatia, Jong-Min Jeon, Gopalakrishnan Kumar, and Yung-Hun Yang. 2019. "Carbon Dioxide Capture and Bioenergy Production Using Biological System – A Review." *Renewable and Sustainable Energy Reviews* 110 (August): 143–58. https://doi.org/10.1016/j.rser.2019.04.070.

Bhattacharjee, Gaurav, and Praveen Linga. 2021. "Amino Acids as Kinetic Promoters for Gas Hydrate Applications: A Mini Review." *Energy & Fuels* 35 (9): 7553–71. https://doi.org/10.1021/acs.energyfuels.1c00502.

Cai, Yuanhao, Yulong Chen, Qijie Li, Liang Li, Haoxin Huang, Suying Wang, and Weixing Wang. 2017. "CO2 Hydrate Formation Promoted by a Natural Amino Acid L-Methionine for Possible Application to CO2 Capture and Storage." *Energy Technology* 5 (8): 1195–99. https://doi.org/10.1002/ente.201600731.

Chong, Zheng Rong, She Hern Bryan Yang, Ponnivalavan Babu, Praveen Linga, and Xiao-Sen Li. 2016. "Review of Natural Gas Hydrates as an Energy Resource: Prospects and Challenges." *Applied Energy* 162 (January): 1633–52. https://doi.org/10.1016/j.apenergy.2014.12.061.

D'Alessandro, Deanna M, Berend Smit, and Jeffrey R Long. 2010. "Carbon Dioxide Capture: Prospects for New Materials." *Angewandte Chemie International Edition* 49 (35): 6058–82. https://doi.org/10.1002/anie.201000431.

Daneshvar, Ehsan, Rebecca J. Wicker, Pau-Loke Show, and Amit Bhatnagar. 2022. "Biologically-Mediated Carbon Capture and Utilization by Microalgae towards Sustainable CO2 Biofixation and Biomass Valorization – A Review." *Chemical Engineering Journal* 427 (January): 130884. https://doi.org/10.1016/j.cej.2021.130884.

Deppe, G., R. Currier, and D. Spencer. 2003. "CO2 Hydrate Process For Gas Separation." *Nexant, Inc.(US)*.

Dhoke, Chaitanya, Abdelghafour Zaabout, Schalk Cloete, and Shahriar Amini. 2021. "Review on Reactor Configurations for Adsorption-Based CO 2 Capture." *Industrial & Engineering Chemistry Research* 60 (10): 3779–98. https://doi.org/10.1021/acs.iecr.0c04547.

Fan, Shuanshi, Liang Yang, Xuemei Lang, Yanhong Wang, and Donglai Xie. 2012. "Kinetics and Thermal Analysis of Methane Hydrate Formation in Aluminum Foam." *Chemical Engineering Science* 82 (September): 185–93. https://doi.org/10.1016/j.ces.2012.07.040.

Ghaedi, Hosein, Muhammad Ayoub, A H Bhat, Syed Mohammad Mahmood, Saeed Akbari, and Ghulam Murshid. 2016. "The Effects of Salt, Particle and Pore Size on the Process of Carbon Dioxide Hydrate Formation: A Critical Review." In , 60001. https://doi.org/10.1063/1.4968128.

Govindaraj, Varun, Deepjyoti Mech, Gaurav Pandey, R Nagarajan, and Jitendra S Sangwai. 2015. "Kinetics of Methane Hydrate Formation in the Presence of Activated Carbon and Nano-Silica Suspensions in Pure Water." *Journal of Natural Gas Science and Engineering* 26 (September): 810–18. https://doi.org/10.1016/j.jngse.2015.07.011.

Han, Yang, and W.S. Winston Ho. 2021. "Polymeric Membranes for CO2 Separation and Capture." *Journal of Membrane Science* 628 (June): 119244. https://doi.org/10.1016/j.memsci.2021.119244.

Hashemi, Hamed, Saeedeh Babaee, Amir H Mohammadi, Paramespri Naidoo, and Deresh Ramjugernath. 2015. "Experimental Measurements and Thermodynamic Modeling of Refrigerant Hydrates Dissociation Conditions." *The Journal of Chemical Thermodynamics* 80 (January): 30–40. https://doi.org/10.1016/j.jct.2014.08.007.

Hassanpouryouzband, Aliakbar, Edris Joonaki, Mehrdad Vasheghani Farahani, Satoshi Takeya, Carolyn Ruppel, Jinhai Yang, Niall English, et al. 2020. "Gas Hydrates in Sustainable Chemistry." *Chemical Society Reviews* 49 (15): 5225–5309. https://doi.org/10.1039/C8CS00989A.

Hayama, Hiroaki, Makoto Mitarai, Hiroyuki Mori, Jonathan Verrett, Phillip Servio, and Ryo Ohmura. 2016. "Surfactant Effects on Crystal Growth Dynamics and Crystal Morphology of Methane Hydrate Formed at Gas/Liquid Interface." *Crystal Growth & Design* 16 (10): 6084–88. https://doi.org/10.1021/acs.cgd.6b01124.

He, Chaozheng, Ran Wang, Dan Xiang, Xiuyuan Li, Ling Fu, Zengyun Jian, Jinrong Huo, and Shuo Li. 2020. "Charge-Regulated CO2 Capture Capacity of Metal Atom Embedded Graphyne: A First-Principles Study." *Applied Surface Science* 509 (April): 145392. https://doi.org/10.1016/j.apsusc.2020.145392.

Ho-Van, S, B Bouillot, J Douzet, S Maghsoodloo Babakhani, and J M Herri. 2019. "Cyclopentane Hydrates – A Candidate for Desalination?" *Journal of Environmental Chemical Engineering* 7 (5): 103359. https://doi.org/10.1016/j.jece.2019.103359.

Hu, Shuozhuo, Jian Li, Fubin Yang, Zhen Yang, and Yuanyuan Duan. 2020. "Multi-Objective Optimization of Organic Rankine Cycle Using Hydrofluorolefins (HFOs) Based on Different Target Preferences." *Energy* 203 (July): 117848. https://doi.org/10.1016/j.energy.2020.117848.

Hyodo, Masayuki, Yang Wu, Koji Nakashima, Shintaro Kajiyama, and Yukio Nakata. 2017. "Influence of Fines Content on the Mechanical Behavior of Methane Hydrate-Bearing Sediments." *Journal of Geophysical Research: Solid Earth* 122 (10): 7511–24. https://doi.org/10.1002/2017JB014154.

Jens, Christian M., Leonard Müller, Kai Leonhard, and André Bardow. 2019. "To Integrate or Not to Integrate—Techno-Economic and Life Cycle Assessment of CO 2 Capture and Conversion to Methyl

Formate Using Methanol." *ACS Sustainable Chemistry & Engineering*, July, acssuschemeng.9b01603. https://doi.org/10.1021/acssuschemeng.9b01603.

Jhaveri, Jaysukh, and Donald B Robinson. 1965. "Hydrates in the Methane-Nitrogen System." *The Canadian Journal of Chemical Engineering* 43 (2): 75–78. https://doi.org/10.1002/cjce.5450430207.

Jung, Sungyup, Young-Kwon Park, and Eilhann E. Kwon. 2019. "Strategic Use of Biochar for CO2 Capture and Sequestration." *Journal of CO2 Utilization* 32 (July): 128–39. https://doi.org/10.1016/j.jcou.2019.04.012.

Kárászová, Magda, Boleslav Zach, Zuzana Petrusová, Vojtěch Červenka, Marek Bobák, Michal Šyc, and Pavel Izák. 2020. "Post-Combustion Carbon Capture by Membrane Separation, Review." *Separation and Purification Technology* 238 (May): 116448. https://doi.org/10.1016/j.seppur.2019.116448.

Khandelwal H, Qureshi M, Zheng J, Venkataraman P, Barckholtz T, Mhadeshwar A, Linga P, . 2021. "Effect of L-Tryptophan in Promoting the Kinetics of Carbon Dioxide Hydrate Formation." *Energy & Fuels* 35 (1): 649–58. https://doi.org/10.1021/acs.energyfuels.0c03709.

Kim, Eunae, Wonjung Choi, and Yongwon Seo. 2018. "Thermodynamic Phase Equilibria and Cage Occupancy of NF3 Hydrate." *Fluid Phase Equilibria* 471 (September): 55–60. https://doi.org/10.1016/j.fluid.2018.04.013.

Klauda, Jeffery B, and Stanley I Sandler. 2005. "Global Distribution of Methane Hydrate in Ocean Sediment." *Energy & Fuels* 19 (2): 459–70. https://doi.org/10.1021/ef049798o.

Kono, Hisashi O, Sridhar Narasimhan, Feng Song, and Duane H Smith. 2002. "Synthesis of Methane Gas Hydrate in Porous Sediments and Its Dissociation by Depressurizing." *Powder Technology* 122 (2–3): 239–46. https://doi.org/10.1016/S0032-5910(01)00420-X.

Kumar, Asheesh, Tushar Sakpal, Praveen Linga, and Rajnish Kumar. 2015. "Enhanced Carbon Dioxide Hydrate Formation Kinetics in a Fixed Bed Reactor Filled with Metallic Packing." *Chemical Engineering Science* 122 (January): 78–85. https://doi.org/10.1016/j.ces.2014.09.019.

Li, Xiao-Sen, Chun-Gang Xu, Yu Zhang, Xu-Ke Ruan, Gang Li, and Yi Wang. 2016. "Investigation into Gas Production from Natural Gas Hydrate: A Review." *Applied Energy* 172 (June): 286–322. https://doi.org/10.1016/j.apenergy.2016.03.101.

Lian, Shaohan, Chunfeng Song, Qingling Liu, Erhong Duan, Hongwei Ren, and Yutaka Kitamura. 2021. "Recent Advances in Ionic Liquids-Based Hybrid Processes for CO2 Capture and Utilization." *Journal of Environmental Sciences* 99 (January): 281–95. https://doi.org/10.1016/j.jes.2020.06.034.

Liu, Yao, Biyu Chen, Yulong Chen, Shihao Zhang, Weiqi Guo, Yuanhao Cai, Bien Tan, and Weixing Wang. 2015. "Methane Storage in a Hydrated Form as Promoted by Leucines for Possible Application to Natural Gas Transportation and Storage." *Energy Technology* 3 (8): 815–19. https://doi.org/10.1002/ente.201500048.

Masson-Delmotte, Valérie, Panmao Zhai, Anna Pirani, Sarah Connors, Clotilde Péan, Yang Chen, Leah Goldfarb, and Melissa I. Gomis. 2021. "'Climate Change 2021: The Physical Science Basis.' Contribution of Working Group I to the Sixth Assessment Report of the Intergovernmental Panel on Climate Change." *Cambridge University Press*. https://doi.org/10.1017/9781009157896.

Milkov, Alexei V. 2004. "Global Estimates of Hydrate-Bound Gas in Marine Sediments: How Much Is Really out There?" *Earth-Science Reviews* 66 (3–4): 183–97. https://doi.org/10.1016/j.earscirev.2003.11.002.

Neves, Marcos Fava, Vinícius Gustavo Trombin, Vitor Nardini Marques, and Leticia Franco Martinez. 2020. "Global Orange Juice Market: A 16-Year Summary and Opportunities for Creating Value." *Tropical Plant Pathology* 45 (3): 166–74. https://doi.org/10.1007/s40858-020-00378-1.

Obara, Shin'ya, and Ryu Tanaka. 2021. "Waste Heat Recovery System for Nuclear Power Plants Using the Gas Hydrate Heat Cycle." *Applied Energy*, March, 116667. https://doi.org/10.1016/j.apenergy.2021.116667.

Odunlami, O.A., D.A. Vershima, T.E. Oladimeji, S. Nkongho, S.K. Ogunlade, and B.S. Fakinle. 2022. "Advanced Techniques for the Capturing and Separation of CO2 – A Review." *Results in Engineering* 15 (September): 100512. https://doi.org/10.1016/j.rineng.2022.100512.

Ohgaki, Kazunari, Takeshi Sugahara, Masaru Suzuki, and Hitoshi Jindai. 2000. "Phase Behavior of Xenon Hydrate System." *Fluid Phase Equilibria* 175 (1–2): 1–6. https://doi.org/10.1016/S0378-3812(00)00374-5.

Olajire, Abass A. 2010. "CO2 Capture and Separation Technologies for End-of-Pipe Applications – A Review." *Energy* 35 (6): 2610–28. https://doi.org/10.1016/j.energy.2010.02.030.

Omodolor, Ibeh S., Hope O. Otor, Joseph A. Andonegui, Bryan J. Allen, and Ana C. Alba-Rubio. 2020. "Dual-Function Materials for CO 2 Capture and Conversion: A Review." *Industrial & Engineering Chemistry Research* 59 (40): 17612–31. https://doi.org/10.1021/acs.iecr.0c02218.

Palodkar, Avinash V, and Amiya K Jana. 2020. "Clathrate Hydrate Dynamics with Synthetic- and Bio-Surfactant in Porous Media: Model Formulation and Validation." *Chemical Engineering Science* 213 (February): 115386. https://doi.org/10.1016/j.ces.2019.115386.

Pandey, Daas, Solms, Jyoti Shanker Pandey, Yousef Jouljamal Daas, Nicolas von Solms, Pandey, Daas, and Solms. 2020. "Screening of Amino Acids and Surfactant as Hydrate Promoter for CO2 Capture from Flue

Gas." *Processes* 8 (1): 124. https://doi.org/10.3390/pr8010124.

Pardakhti, Maryam, Tahereh Jafari, Zachary Tobin, Biswanath Dutta, Ehsan Moharreri, Nikoo S. Shemshaki, Steven Suib, and Ranjan Srivastava. 2019. "Trends in Solid Adsorbent Materials Development for CO 2 Capture." *ACS Applied Materials & Interfaces* 11 (38): 34533–59. https://doi.org/10.1021/acsami.9b08487.

Pires, Jéssica Pereira, Alessandro da Silva Ramos, Christian Ferreira Mattos, Marcelo Ketzer, and Rogerio Vescia Lourega. 2021. "Analysis of the Effect of Organic Salts Derived from L-Phenylalanine Amino Acid as Kinetic Promoters/Inhibitors of CO2 Hydrates." *Energy & Fuels* 35 (9): 8095–8101. https://doi.org/10.1021/acs.energyfuels.1c00140.

Prasetya, Nicholaus, Nurul F. Himma, Putu Doddy Sutrisna, I G. Wenten, and Bradley P. Ladewig. 2020. "A Review on Emerging Organic-Containing Microporous Material Membranes for Carbon Capture and Separation." *Chemical Engineering Journal* 391 (July): 123575. https://doi.org/10.1016/j.cej.2019.123575.

Rahmah, W., G.T.M. Kadja, M.H. Mahyuddin, A.G. Saputro, H.K. Dipojono, and I.G. Wenten. 2022. "Small-Pore Zeolite and Zeotype Membranes for CO2 Capture and Sequestration – A Review." *Journal of Environmental Chemical Engineering* 10 (6): 108707. https://doi.org/10.1016/j.jece.2022.108707.

Rahmati-Abkenar, Mahboubeh, Mehrdad Manteghian, and Hassan Pahlavanzadeh. 2017. "Nucleation of Ethane Hydrate in Water Containing Silver Nanoparticles." *Materials & Design* 126 (July): 190–96. https://doi.org/10.1016/j.matdes.2017.04.051.

Riebeek, Holli. 2011. "The Carbon Cycle." Earth Observatory. 2011. https://earthobservatory.nasa.gov/features/CarbonCycle.

Ripmeester, John A, and Saman Alavi. 2016. "Some Current Challenges in Clathrate Hydrate Science: Nucleation, Decomposition and the Memory Effect." *Current Opinion in Solid State and Materials Science* 20 (6): 344–51. https://doi.org/10.1016/j.cossms.2016.03.005.

Sa J, Kwak G, Lee B, Han K, Cho S, Jun L, Ju Dong L, . 2017. "Phase Equilibria and Characterization of CO2 and SF6 Binary Hydrates for CO2 Sequestration." *Energy* 126 (May): 306–11. https://doi.org/10.1016/j.energy.2017.03.039.

Salako, O, C Lo, A Couzis, P Somasundaran, and J W Lee. 2013. "Adsorption of Gemini Surfactants onto Clathrate Hydrates." *Journal of Colloid and Interface Science* 412 (December): 1–6. https://doi.org/10.1016/j.jcis.2013.09.007.

Sang, Yafei, and Jianhan Huang. 2020. "Benzimidazole-Based Hyper-Cross-Linked Poly(Ionic Liquid)s for Efficient CO2 Capture and Conversion." *Chemical Engineering Journal* 385 (April): 123973. https://doi.org/10.1016/j.cej.2019.123973.

Seidl, P., S. Loekman, M. Sardogan, E. Voigt, T. Claßen, J. Ha, G. Luzi, et al. 2019. "Food Technological Potentials of CO2 Gas Hydrate Technology for the Concentration of Selected Juices." *High Pressure Research* 39 (2): 344–56. https://doi.org/10.1080/08957959.2019.1597077.

Shimada, Wataru, Motoo Shiro, Hidemasa Kondo, Satoshi Takeya, Hiroyuki Oyama, Takao Ebinuma, and Hideo Narita. 2005. "Tetra-n-Butylammonium Bromide–Water (1/38)." *Acta Crystallographica Section C Crystal Structure Communications* 61 (2): 65–66. https://doi.org/10.1107/S0108270104032743.

Sinehbaghizadeh, Saeid, Agus Saptoro, and Amir H. Mohammadi. 2022. "CO2 Hydrate Properties and Applications: A State of the Art." *Progress in Energy and Combustion Science* 93 (November): 101026. https://doi.org/10.1016/j.pecs.2022.101026.

Sloan, E Dendy, and Carolyn A Koh. 2008. *Clathrate Hydrates of Natural Gases*. 3rd Ed. CRC Press, Taylor & Francis Group, Boca Raton.

Smith, Duane H, Joseph W Wilder, and Kal Seshadri. 2002. "Methane Hydrate Equilibria in Silica Gels with Broad Pore-Size Distributions." *AIChE Journal* 48 (2): 393–400. https://doi.org/10.1002/aic.690480222.

Song, Chunfeng, Qingling Liu, Shuai Deng, Hailong Li, and Yutaka Kitamura. 2019. "Cryogenic-Based CO2 Capture Technologies: State-of-the-Art Developments and Current Challenges." *Renewable and Sustainable Energy Reviews* 101 (March): 265–78. https://doi.org/10.1016/j.rser.2018.11.018.

Song, Yuan-Mei, Ru-Quan Liang, Fei Wang, Dan-Hui Zhang, Liu Yang, and Deng-Bo Zhang. 2021. "Enhanced Methane Hydrate Formation in the Highly Dispersed Carbon Nanotubes-Based Nanofluid." *Fuel* 285 (February): 119234. https://doi.org/10.1016/j.fuel.2020.119234.

Sun, Shuzhuang, Hongman Sun, Paul T. Williams, and Chunfei Wu. 2021. "Recent Advances in Integrated CO 2 Capture and Utilization: A Review." *Sustainable Energy & Fuels* 5 (18): 4546–59. https://doi.org/10.1039/D1SE00797A.

Veluswamy, Hari Prakash, Pei Yit Lee, Kulesha Premasinghe, and Praveen Linga. 2017. "Effect of Biofriendly Amino Acids on the Kinetics of Methane Hydrate Formation and Dissociation." *Industrial & Engineering Chemistry Research* 56 (21): 6145–54. https://doi.org/10.1021/acs.iecr.7b00427.

Wang, Mao, Zhi-Gao Sun, Cheng-Hao Li, Ai-Jun Zhang, Juan Li, Cui-Min Li, and Hai-Feng Huang. 2016. "Equilibrium Hydrate Dissociation Conditions of CO2 + HCFC141b or Cyclopentane." *Journal of*

*Chemical & Engineering Data* 61 (9): 3250–53. https://doi.org/10.1021/acs.jced.6b00333.

Wang, Ren, Tianle Liu, Fulong Ning, Wenjia Ou, Ling Zhang, Zhen Wang, Li Peng, et al. 2019. "Effect of Hydrophilic Silica Nanoparticles on Hydrate Formation: Insight from the Experimental Study." *Journal of Energy Chemistry* 30 (March): 90–100. https://doi.org/10.1016/j.jechem.2018.02.021.

Wang, Rujie, Shanshan Liu, Lidong Wang, Qiangwei Li, Shihan Zhang, Bo Chen, Lei Jiang, and Yifeng Zhang. 2019. "Superior Energy-Saving Splitter in Monoethanolamine-Based Biphasic Solvents for CO2 Capture from Coal-Fired Flue Gas." *Applied Energy* 242 (May): 302–10. https://doi.org/10.1016/j.apenergy.2019.03.138.

Wang, Xiaolin, Shufan Yang, Hai Zhang, Xingguang Xu, Colin D. Wood, and Wojciech Lipiński. 2021. "Amine Infused Hydrogel-Based CO2 Gas Storage Technology for CO2 Hydrate-Based Cold Thermal Energy Storage." *Journal of CO2 Utilization* 53 (November): 101705. https://doi.org/10.1016/j.jcou.2021.101705.

Wang, Yanhong, Xuemei Lang, and Shuanshi Fan. 2013. "Hydrate Capture CO2 from Shifted Synthesis Gas, Flue Gas and Sour Natural Gas or Biogas." *Journal of Energy Chemistry* 22 (1): 39–47. https://doi.org/10.1016/S2095-4956(13)60004-2.

Xie, Nan, Chenghua Tan, Sheng Yang, and Zhiqiang Liu. 2019. "Conceptual Design and Analysis of a Novel CO2 Hydrate-Based Refrigeration System with Cold Energy Storage." *ACS Sustainable Chemistry & Engineering* 7 (1): 1502–11. https://doi.org/10.1021/acssuschemeng.8b05255.

Xu, Chun-Gang, Yi-Song Yu, Ya-Long Ding, Jing Cai, and Xiao-Sen Li. 2017. "The Effect of Hydrate Promoters on Gas Uptake." *Physical Chemistry Chemical Physics* 19 (32): 21769–76. https://doi.org/10.1039/C7CP02173A.

Yang S, Babu H, Sam F, Linga P, . 2016. "Carbon Dioxide Hydrate Kinetics in Porous Media with and without Salts." *Applied Energy* 162 (January): 1131–40. https://doi.org/10.1016/j.apenergy.2014.11.052.

Younas, Mohammad, Mashallah Rezakazemi, Muhammad Daud, Muhammad B. Wazir, Shakil Ahmad, Nehar Ullah, Inamuddin, and Seeram Ramakrishna. 2020. "Recent Progress and Remaining Challenges in Post-Combustion CO2 Capture Using Metal-Organic Frameworks (MOFs)." *Progress in Energy and Combustion Science* 80 (September): 100849. https://doi.org/10.1016/j.pecs.2020.100849.

Yuan, Rongrong, Zhuojun Yan, Alateng Shaga, and Hongming He. 2020. "Solvent-Free Mechanochemical Synthesis of a Carbazole-Based Porous Organic Polymer with High CO2 Capture and Separation." *Journal of Solid State Chemistry* 287 (July): 121327. https://doi.org/10.1016/j.jssc.2020.121327.

Zhang, Xuemin, Jinping Li, Qingbai Wu, Jiaxian Wang, Yingmei Wang, and Yang Li. 2021. "Influence of Pressure on the Formation Process of CH4 Hydrate in Porous Media below the Freezing Point." *Environmental Progress & Sustainable Energy*, February. https://doi.org/10.1002/ep.13601.

# Chapter 2: Literature review of molecular dynamics simulation studies of clathrate hydrates

In the first chapter, the applications of hydrate-based technologies for $CO_2$ capture, sequestration and utilization (CCSU) and the main objectives of performing MD simulations in this field of study were specified. Since this thesis deals with the MD simulations of gas hydrates, a large proprtion of the previous MD studies ranging from many hydrate formers/ additives and sorounded environments of gas hydrates were overviewed.

In this chapter, a large number of the performed MD simulations in the field of gas hydrates have been reviewed. To fully recognize the capabilities of MD methodologies, various systems of gas hydrates encompassing pure/ mixed hydrates and the effects of the presence of promoters, inhibitors, and mineral components revealed from the previous MD simulations in the literature were reviewed. Furthermore, there are various phenomena associated with gas hydrate applications, the most important of which are nucleation, crystal growth (formation), stability, dissociation, aggregation, memory effect, and self-preservation. Moreover, the vital elements of the aforesaid phenomena such as thermo-physical, mechanical, thermodynamic, kinetics, morphology/ structural analysis, dynamical and vibrational behaviour, the coexistence of phases, storage capacity, heat, and mass transfer properties were reviewed. Also, performing this chapter shed light on the required analysis parameters as well as the features of the MD simulations for doing objectives in this thesis.

This chapter was published as a research paper in Fuel Journal:

Sinehbaghizadeh, S., Saptoro, A., Amjad, S., Naeiji, P., Tiong, A.N.T., Mohammadi, A.H. A comprehensive review on molecular dynamics simulation studies of phenomena and characteristics associated with clathrate hydrates. *Fuel Journal*, 2023, 338, 127201, Elsevier.
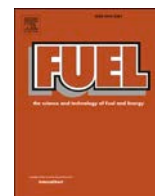
Review article

# A comprehensive review on molecular dynamics simulation studies of phenomena and characteristics associated with clathrate hydrates

Saeid Sinehbaghizadeh [a,*], Agus Saptoro [a,*], Sepideh Amjad-Iranagh [b], Parisa Naeiji [c], Angnes Ngieng Tze Tiong [a], Amir H. Mohammadi [d,*]

[a] Department of Chemical and Energy Engineering, Curtin University Malaysia, CDT 250 Miri, Sarawak 98009, Malaysia
[b] Department of Materials and Metallurgical Engineering, Amirkabir University of Technology, Tehran 15875-4313, Iran
[c] GFZ German Research Centre for Geosciences, Telegrafenberg, 14473 Potsdam, Germany
[d] Discipline of Chemical Engineering, School of Engineering, University of KwaZulu-Natal, Howard College Campus, King George V Avenue, Durban 4041, South Africa

ABSTRACT

Clathrate hydrates or gas hydrates have received worldwide attention due to their potential to be utilized in various sustainable technologies. The hydrate-based industrial applications as well as developing green technologies or safely extracting natural gases stored in the nature require profound comprehension of the phenomena associated with gas hydrates. On the flip side, identifying the characteristics of different hydrate formers and the effects of a wide range of introduced additives to these technologies is the critical objective, so that needs to be deeply investigated at both macroscopic and microscopic scales. The expensive experiments and limited availability of facilities at the nanoscale encourage researchers to apply novel computational methods and simulation approaches. For three decades, molecular dynamics (MD) simulations in the field of gas hydrates have been widely used to mathematically analyse the physical movements of molecules and the evolution of atomic positions in time. In this work, the mechanisms involved in the pure, binary, and mixed gas hydrates, and the impressions of promoters/inhibitors/minerals on gas hydrates were briefly reviewed. Also, the phenomena and properties associated with gas hydrates such as nucleation, growth, stability, dissociation, cage occupancy, storage capacity, morphology analysis, guest role, thermo-physical and mechanical properties, dynamical and vibrational behaviours of gas hydrates were reviewed. This work aims to provide readers with an extensive overview of MD simulations of gas hydrates to stimulate further research on this riveting field.

## 1. Introduction

Gas hydrates are ice-like compounds that can be inherently formed under certain thermodynamic conditions within a gas/water mixture where hydrogen-bonded water molecules create a crystalline lattice around the gas molecules. Clathrate hydrates are categorized into three types of structures I, II, and H. Gas species known as small guests with molecular diameters between 0.4 and 0.55 nm are able to form structure I; components like hydrocarbons with larger sizes mostly between 0.6 and 0.7 nm can generate structure II of clathrate hydrate; while for the formation of structure H, simultaneous presence of both small guests and large molecular guests (LMGs) normally liquid hydrocarbons with a molecular diameter of 0.75–0.9 nm are needed [1]. Aside from the clathrate hydrates, there are some substances such as tetra-

alkylammonium salts/halides e.g. tetra-nbutylammonium bromide (TBAB), with which the guest gases like $CH_4$, $CO_2$, $N_2$, $H_2$, etc. can generate semiclathrate hydrates [2,3]. Due to the innovative applications of hydrates, they can be at the centre of research within sustainable chemistry. The early era of hydrate explorations was dominated by pipeline blockage and flow assurance, however, the idea of using this phenomenon for sustainable development, supporting the economy, and make to a cleaner atmosphere has recently received widespread attention. So that the processes such as hydrate-based $CO_2$ capture and sequestration, gas storage and transportation, secondary refrigeration, water desalination, gas separation, and energy recovery have been the upsurge of research in this field. Fig. 1 shows some suggested industrial applications of hydrate-based methods. The scope of these technologies in the context of a new master plan with concerted collaborative endeavour between various disciplines e.g. engineering, energy,

---

## Nomenclature

| | |
|---|---|
| HBGS | Hydrate-Based Gas Separation |
| NPE | Nonyl Phenol Ethoxylates |
| HBCC | Hydrate-Based Carbon Capture |
| LAE | Lauryl Alcohol Ethoxylates |
| NGH | Natural Gas Hydrate |
| SDS | Sodium Dodecyl Sulfate |
| InSAR | Interferometric Synthetic Aperture Radar |
| SL | Sulfonated Lignin |
| MRI | Magnetic Resonance Imaging |
| SHS | Sodium Hexadecyl Sulfate |
| 13C NMR | Carbon-13 Nuclear Magnetic Resonance |
| STS | Sodium Tetradecyl Sulfate |
| COC | Cyclic Organic Compounds |
| SDBS | Sodium Dodecyl Benzene Sulfonate |
| CN | Coordination Number |
| DMSO | Di-Methyl Sulf-Oxide |
| GHSZ | Gas Hydrate Stability Zone |
| TMS | Tetra-Methylene Sulfone |
| CSMHYD | Colorado School of Mines Hydrate |
| SWNT | Single-Walled carbon Nano-Tube |
| T/KHI | Thermodynamic/Kinetic Hydrate Inhibitor |
| MWCNT | Multi-Walled Carbon Nano-Tube |
| T/KHP | Thermodynamic/Kinetic Hydrate Promoter |
| Na-MMT | Sodium Mont-Morillonite |
| LMGs | Large Molecule Guests |
| SW-CNTs | Single-Walled Carbon Nano-Tubes |
| AIMD | Ab Initio Molecular Dynamics |
| SAMs | Self-Assembled Monolayers |
| TMO | Tri-Methylene-Oxide |
| TMS | Tetra-Methylene Sulfone |
| FA | FormAldehyde |
| EO | Ethylene Oxide |
| CB | CycloButane |
| LHA | Leonardite Humic Acid |
| MWCNT | Multi-Walled Carbon Nano-Tube |
| ACF | Auto-Correlation of the Fluctuations |
| THT | Tetrahydrothiophene |
| AOP | Angular Order Parameter |
| THF | TetraHydroFuran |
| APDF | Angular probability distribution function |
| PMF | Potential of Mean Force |
| CGMC | Grand Canonical Monte Carlo |
| OACF | Orientation Auto-Correlation Function |
| DFT | Density Functional Theory |
| QLD | Quasi-harmonic Lattice Dynamics |
| DWC | Dodecahedral Water Cluster |
| TCF | Time Correlation Function |
| FSICA | Face-Saturated Incomplete Cage Analysis |
| VACF | Velocity Auto-Correlation Function |
| HCACF | Flux AutoCorrelation Function |
| RDF | Radial Displacement Function |
| MCG-OP | Mutually Coordinated Guest Order Parameter |
| RACF | Rotational Auto-Correlation Function |
| MCG | Mutually Coordinated Guest |
| RPMD | Ring Polymer Molecular Dynamics |
| MSD | Mean Square Displacement |
| RMSF | Root Mean Square Fluctuation |
| NEMD | Non-Equilibrium Molecular Dynamics |
| RPMD | Ring Polymer Molecular Dynamics |
| MFPT | Mean First-Passage Time |
| SL | Sulfonated Lignin |
| MRI | Magnetic Resonance Imaging |
| SHS | Sodium Hexadecyl Sulfate |
| 13C NMR | Carbon-13 Nuclear Magnetic Resonance |
| STS | Sodium Tetradecyl Sulfate |
| COC | Cyclic Organic Compounds |
| SDBS | Sodium Dodecyl Benzene Sulfonate |
| CN | Coordination Number |
| DMSO | Di-Methyl Sulf-Oxide |
| GHSZ | Gas Hydrate Stability Zone |
| TMS | Tetra-Methylene Sulfone |
| CSMHYD | Colorado School of Mines Hydrate |
| SWNT | Single-Walled carbon Nano-Tube |
| T/KHI | Thermodynamic/Kinetic Hydrate Inhibitor |
| MWCNT | Multi-Walled Carbon Nano-Tube |
| T/KHP | Thermodynamic/Kinetic Hydrate Promoter |
| Na-MMT | Sodium Mont-Morillonite |
| LMGs | Large Molecule Guests |
| SW-CNTs | Single-Walled Carbon Nano-Tubes |
| AIMD | Ab Initio Molecular Dynamics |
| SAMs | Self-Assembled Monolayers |
| TMO | Tri-Methylene-Oxide |
| TMS | Tetra-Methylene Sulfone |
| FA | FormAldehyde |
| EO | Ethylene Oxide |
| CB | CycloButane |
| LHA | Leonardite Humic Acid |
| MWCNT | Multi-Walled Carbon Nano-Tube |
| ACF | Auto-Correlation of the Fluctuations |
| THT | Tetrahydrothiophene |
| AOP | Angular Order Parameter |
| THF | TetraHydroFuran |
| APDF | Angular probability distribution function |
| PMF | Potential of Mean Force |
| CGMC | Grand Canonical Monte Carlo |
| OACF | Orientation Auto-Correlation Function |
| DFT | Density Functional Theory |
| QLD | Quasi-harmonic Lattice Dynamics |
| DWC | Dodecahedral Water Cluster |
| TCF | Time Correlation Function |
| FSICA | Face-Saturated Incomplete Cage Analysis |
| VACF | Velocity Auto-Correlation Function |
| HCACF | Flux AutoCorrelation Function |
| RDF | Radial Displacement Function |
| MCG-OP | Mutually Coordinated Guest Order Parameter |
| RACF | Rotational Auto-Correlation Function |
| MCG | Mutually Coordinated Guest |
| RPMD | Ring Polymer Molecular Dynamics |
| MSD | Mean Square Displacement |
| RMSF | Root Mean Square Fluctuation |
| NEMD | Non-Equilibrium Molecular Dynamics |
| RPMD | Ring Polymer Molecular Dynamics |
| MFPT | Mean First-Passage Time |

chemistry, and physics have recently been developed.

Recent experimental results have revealed the variety of properties associated with hydrate-based technologies. Although such investigations can cover the required scientific data and reveal the mechanisms at macroscopic and mesoscopic levels, the microscopic mechanisms and molecular characteristics of these systems cannot mostly be explored in the laboratory. In addition, investigating under the harsh operating pressure–temperature conditions may be the other limitation. In this regard, the utilization of molecular dynamics simulations would be the desirable option by which the vast majority of such characteristics can be probed. These new computational techniques may respond to many questionable issues in the involved engineering processes. The number of reviews on the computational studies of gas hydrates is not substantial. Liang and Kusalik provided an overview of explorations of gas hydrate crystal growth [4]. English and MacElroy conducted a review on thermodynamics, equilibrium properties, thermal conductivity, nucleation, growth, dissociation, electromagnetic fields, energy storage, and $CO_2$ sequestration [5]. Also, English and Waldron discussed the prospects and challenges of external electric fields in molecular simulations [6]. Ripmeester and Alavi overviewed the nucleation, dissociation, and memory effect of clathrate hydrates [7]. Somewhat more recently, Alavi and Ripmeester conducted a review focusing on computational studies of $H_2$ storage in clathrate hydrate phases [8]. Recently, we also reviewed the new research findings of $CO_2$ clathrate hydrates which have been revealed from the molecular dynamics (MD) simulations [9]. Nonetheless, there is still a lack of comprehensive review discussion in the literature on the investigated gas hydrates from the molecular perspective which can be useful for further progress in hydrate-based industrial applications. Therefore, in this work, the phenomena and characteristics of all clathrates (sI, sII, and sH) and semiclathrate hydrates at the molecular level ranging from pure, binary, mixed hydrate systems, and gas hydrates in the presence of promoters, inhibitors, and minerals will be reviewed. Hence the following sections are organized to review the performed MD investigations of various gas hydrate systems (in section 2); explored hydrate phenomena and properties at microscopic scale (in section 3); and the proportions of conducted MD studies of gas hydrates and the future research suggestions (in section 4).

## 2. Molecular dynamics (MD) simulation theory

Due to the power in calculating the motion and equilibrium of each molecule or atom, molecular dynamics (MD) simulations in diverse fields of science and engineering have received worldwide attention. The knowledge concerning the structural as well as dynamic properties of substances in either gas, liquid, and solid states can be achieved by MD simulations at molecular or atomic scales [10]. The common applications of MD are either to provide explanations by determining the mechanisms involved or to predict the properties of materials. In classical MD, to predict the energies of molecules and equation of motions at thermodynamic conditions, the laws of mechanics are applied. The positions and velocities in molecular systems are dependent on P-T condition and the chemical structure of the simulated system. Empirical interatomic potentials including a long-range Coulombic force and short-range repulsive/attractive force are usually used to describe the atomic interactions. Generally, two approaches can be used to conduct the MD simulations; the first is the non-equilibrium mode in which the system away from the equilibrium is stimulated and the system response is followed while in the equilibrium model, the macroscopic property of interest during the simulation is calculated from the time average of that property [11–13]. The theories, approaches, and outputs of MD simulations are displayed in Fig. 2.

As exhibited, solving the Schrödinger equation is the basis of the calculations of quantum mechanics; more details of this equation have been given elsewhere [14]. Density functional theory (DFT) is an exact theorem that was developed in the physics community. This method carries out energy calculations and electronic structure using the approximation of Kohn – Sham [15] which can be employed for many practical calculations. Besides, DFT can be combined with the HF method which is known as a Hybrid function [16–18]. Worth highlighting that, against semi-empirical methods, *ab initio* calculations can determine atomic interactions accurately in which the calculations are based on principles of quantum mechanics. However, limitations to treating nanoscale and macroscale decisions are substantial. Many properties that are of critical importance to process performance cannot yet be integrated into process design and computer-aided molecular problems. In this context, the interplay between process design and the design of materials and molecules has been discussed elsewhere [19].
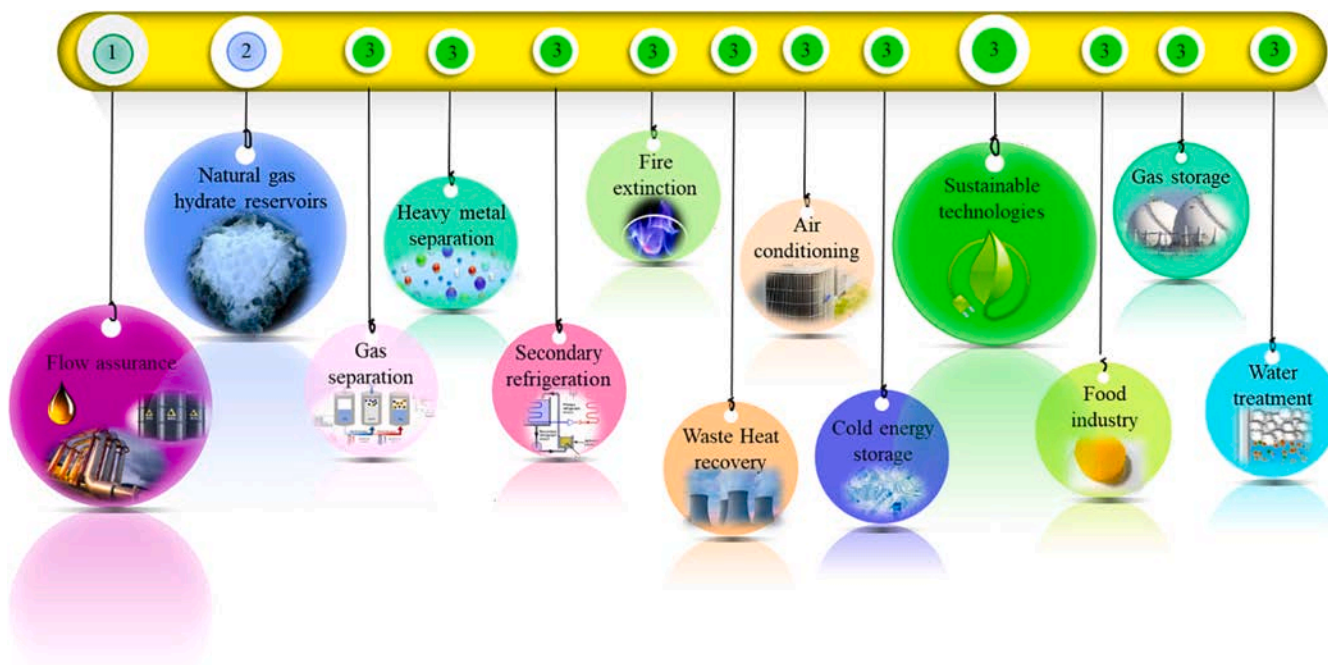


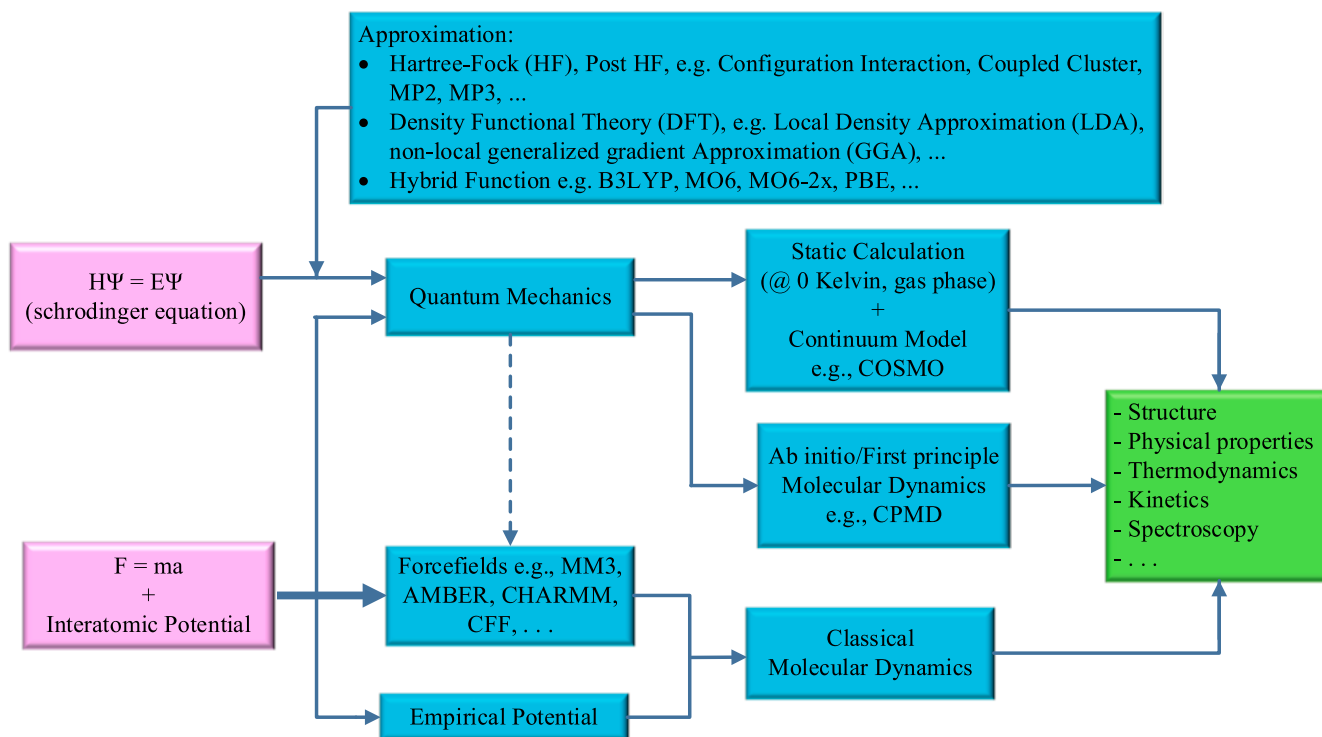**Fig. 1.** Gas hydrate industrial applications.

**Fig. 2.** The theories, approaches, and outputs of molecular simulations.

Using MD analysis, many different questions about the molecular mechanisms of phase separation, crystal growth, surface absorption, etc. can be addressed. In this regard, the combination of Monte Carlo and MD can also be employed [20–29]. It should be pointed out that Monte Carlo simulations can be regarded as classical mechanics methods.

### 2.1. MD simulations of gas hydrate systems

Various aspects of gas hydrates through MD approaches e.g. Free-energy methods, classical MD, potential models, massively parallel MD, DFT, and *ab initio* calculations have been evaluated. It is conceivable that these studies can be rewarding for either hydrate-based gas separation or other utilization approaches of gas hydrates. The phenomena and properties associated with hydrates explored by applying MDs are shown in Fig. 3. Generally, the workflow of MD simulations consists of three steps: pre-processing, MD simulations, and post-processing. The first step includes the preparation of simulation box setup and initial configuration, adjustments of the force field (FF) for each molecule, and energy minimization of the system. To provide the initial hydrate structure, the X-ray diffraction analysis for the initial positions of water molecules in the hydrate structure has been reported [30]. However, the coordinates of water molecules and cages for sI, sII, and sH clathrate hydrates specified using TIP4P potential are presented elsewhere [31]. These water molecular orientations of guest-free cages were determined based on a net-zero dipole moment as well as the lowest potential energy. The next step is a production run in which the system is equilibrated under specific thermodynamic ensembles to obtain the desired results. The final step is analysing the parameters along which the properties or phenomena can be evaluated. To study the intermolecular behaviours, properties, phenomena, and microscopic mechanisms, there are many analysis parameters (target parameters) to employ. Fig. 3 exhibits the list of these parameters along with MD steps and employed software in gas hydrate field.

The classical mechanic's methods can be developed based on intermolecular and intramolecular interactions described by empirical potential energy parameters which are the so-called force field (FF). As a fundamental issue underlying all atomistic simulations, Force-field development has drawn considerable attention. A few examples of developed general force fields are MM3, MM4, Dreiding, SHARP, VAL-BON, UFF, CFF93, AMBER, CHARMM, OPLS, and MMFF. The FFs shown in Fig. 3 are also the set of corresponding parameters for a single molecule and the specific force functions for inter/intra-molecular forces. Over decades, several force fields for classical MD simulations have been developed. Therefore, a wide variety of potential models for components has been proposed. As an example, water models to study the characteristics of gas hydrates are: SPC [32–37], SPC/E [38–43], F-SPC [44], SPC/Fw [45,46], TIPS2 [47], TIP3P [48], TIP4P [4,44,49–58], TIP4P/2005 [59–63], TIP4P-Ew [22,26,64], TIP4P/Ice [27,65–77], TIP4P-FQ [44,78,79], TIP4P/F [80], TIP5P [81,82]; polarizable force fields: AMOEBA [83], COS [84], COS/G2 [85], Stillinger-Weber (SW) model [86–88], mW model [89–95], and KKY potential [96].

These potential approaches can simply be applied to water molecules as employed in many studies due to their computational efficiencies, however, their performances for different systems and operating conditions are dissimilar. For instance, notwithstanding the SPCE/OPLS-UA model that indicated no $CH_4$ hydrate formation at 230–260 K and 30 MPa, the formation of $CH_4$ hydrate using the SPC/TSE model was observed [97]. To analyse the accuracy of the coarse-grained mW model, it was compared with TIP4P + OPLS-AA and SPC + OPLS-UA $CH_4$ models at 250 K and 6 MPa. Based on the results, the mW model was found to be more accurate at recreating structural properties but it has a limitation in identifying small details in the RDFs. This is so that, the utilization of the coarse-grained model depends on what phenomenon is of interest [98]. The coarse-grained method to determine the surface tension at the interface of $CH_4$ and water, melting temperature, and the hydration number of sI and sII clathrate hydrate may estimate the $CH_4$ and water diffusivity, however, it overrates the mobility of guests in solution. Also, it was revealed that the density temperature evolution depends on the ability of a water model in reproducing the solubility of hydrophobic molecules [99].

By comparing $CH_4$ Hydrate properties using polarizable AMOEBA

| Force field type | Example |
|---|---|
| Pairwise potentials | Lennard-Jones, Buckingham, Morse, Born-Mayer-Huggins, Yukawa, soft, class 2 (COMPASS), hydrogen bond, tabulated |
| Charged pairwise potentials | Coulombic, point-dipole |
| Manybody potentials | EAM, Finnis/Sinclair EAM, modified EAM (MEAM), embedded ion method (EIM), Stillinger-Weber, Tersoff, AI-REBO, ReaxFF, COMB |
| Electron force field (eFF) | eFF potential |
| Coarse-grained potentials | DPD, GayBerne, REsquared, colloidal, DLVO |
| Mesoscopic potentials | Granular, Peridynamics |
| Bond potentials | Harmonic, FENE, Morse, nonlinear, class 2, quartic (breakable) |
| Angle potentials | Harmonic, CHARMM, cosine, cosine/squared, cosine/periodic, class 2 (COMPASS) |
| Dihedral potentials | Harmonic, CHARMM, multi-harmonic, helix, class 2 (COMPASS), OPLS |
| Improper potentials | Harmonic, cvff, umbrella, class 2 (COMPASS) |
| Polymer potentials | All-atom, united-atom, bead-spring, breakable |
| Water potentials | TIP3P, TIP4P, SPC |
| Long-range Coulombics and dispersion | Ewald, PPPM (similar to particle-mesh Ewald), Ewald/N for long-range Lennard-Jones |

**Analysis Parameters**

**MD software**

| | |
|---|---|
| LAMMPS | VESTA |
| DL_POLY | SIESTA |
| DL-CLASSIC | VASP |
| GROMACS | CPMD |
| Materials Studio | NAMD |
| GROMOS | DMol³ |
| DYNAMO | AIMD |
| NBO | AMBER |
| SHARC | CHARMM |
| Gaussian | GEMS |
| Pydlpoly | Desmond |
| MDynaMix | CRITIC2 |
| MXDORTO | CP2K |
| MCCCS Towhee | TINKER |
| MOLDY | Spartan |
| MODYLAS | WinMASPHYC |

**Rotation, Fluctuation, Distribution**

Heat flux autocorrelation function (HCACF)
Rotational autocorrelation function (RACF)
Velocity autocorrelation function (VACF)
Orientation Auto-Correlation Function (OACF)
Residence autocorrelation function (RACF)
Angular probability distribution function (APDF)
Mean Square Displacement (MSD)
Root mean squared deviation (RMSD)
Root mean squared fluctuation (RMSF)
Axial distribution function (ADF)
Radial displacement function (RDF)
Potential of mean force (PMF)
Mean First-Passage Time (MFPT)
Face-saturated incomplete cage analysis (FSICA)
Mutually coordinated guest order parameter (MCG-OP)
Differential scattering cross-section (DCS)
Orientational/dihedral/angular order parameter (AOP)
Differential scattering cross-section (DCS)
Distribution of the torsion angle/asphericity
Radius of gyration/rotation angle

**Energy**

Potential/ kinetic/ dynamic energy
Interaction energy (conf./ elect./ vdW energy)
Gibbs/ Helmholtz free energy
Excess chemical potential/ enthalpy/ entropy
Cohesive/ surface/ internal/ adsorption energy
Activation/ stabilization/ binding energy
Unit-cell configurational energy - DFT energy
Free energy barrier

**Spectrum**

IR/ Power/ vibrational/ translational spectra
Vibrational frequency/ density - guest/ host vibration
Variation of the lattice vector length
Molecular/ net dipole moment
Wave No., Wave/ transient moving velocity
13C NMR lineshape, abundance ratio
Phonon mean free path velocity - Phonon dispersion
Neutron diffraction patterns

**Rate**

Growth/ formation Rate
Decomposition/ decay/ melting rate
Gas uptake/ release rate
Nucleation/conversion rate
Occupancy rate - storage capacity
Time evolution of the blobs - time decay of OACF
Survival time of cages - nucleus lifetime
Mean first passage/ induction/ relaxation time
No. of water/ guest molecules in cluster/ bubbles
Hydrate crystallinity/ thickness

**Phase equilibrium, Physical properties**

Coexistence equilibrium, melting temperature
Densities of states (DOS), Surface Density of Water Cages, Viscosity
Diffusion coefficient - self diffusion - Fickian diffusivity - relative concentration
Cp and Cv - Specific heat capacity - thermal conductivity
Isothermal compressibility, thermal expansion coefficient
Interfacial transition layer/ thermal resistance (ITR)

**Unit Cell and Cage**

Unit cell volume and length
Cell size/ lattice constant variation
Fractional cage occupancy (occupation ratio)
Hydration/ coordination No.
Refined fractional coordinates/ structural parameters
No. of crystal unit cell/ polygons
Cage rigidity/ deformation - radius change
Seed-nucleus/ critical nuclei size
Cross nucleation - critical nuclei size
Persistence of individual cages (e.g. $5^{12}6^3$)

**Stress, Tension**

Tensile/ strain/ compressive stress - stress-strain relationships
Contact/ torsion/ tilt angle - Surface/ interfacial tension
Shear/bulk modulus - strain energy - shear strain
Gruneisen parameter - crystal defect
Elastic moduli - shear elastic constant
Crystal anisotropy (anisotropy index) - asymmetric stretch

**Hydrogen bond (H-bond)**

No. of angle distribution/ distance of H-bonds - bond stretching
H-bond density/ length/ energy/ lifetime/ probability
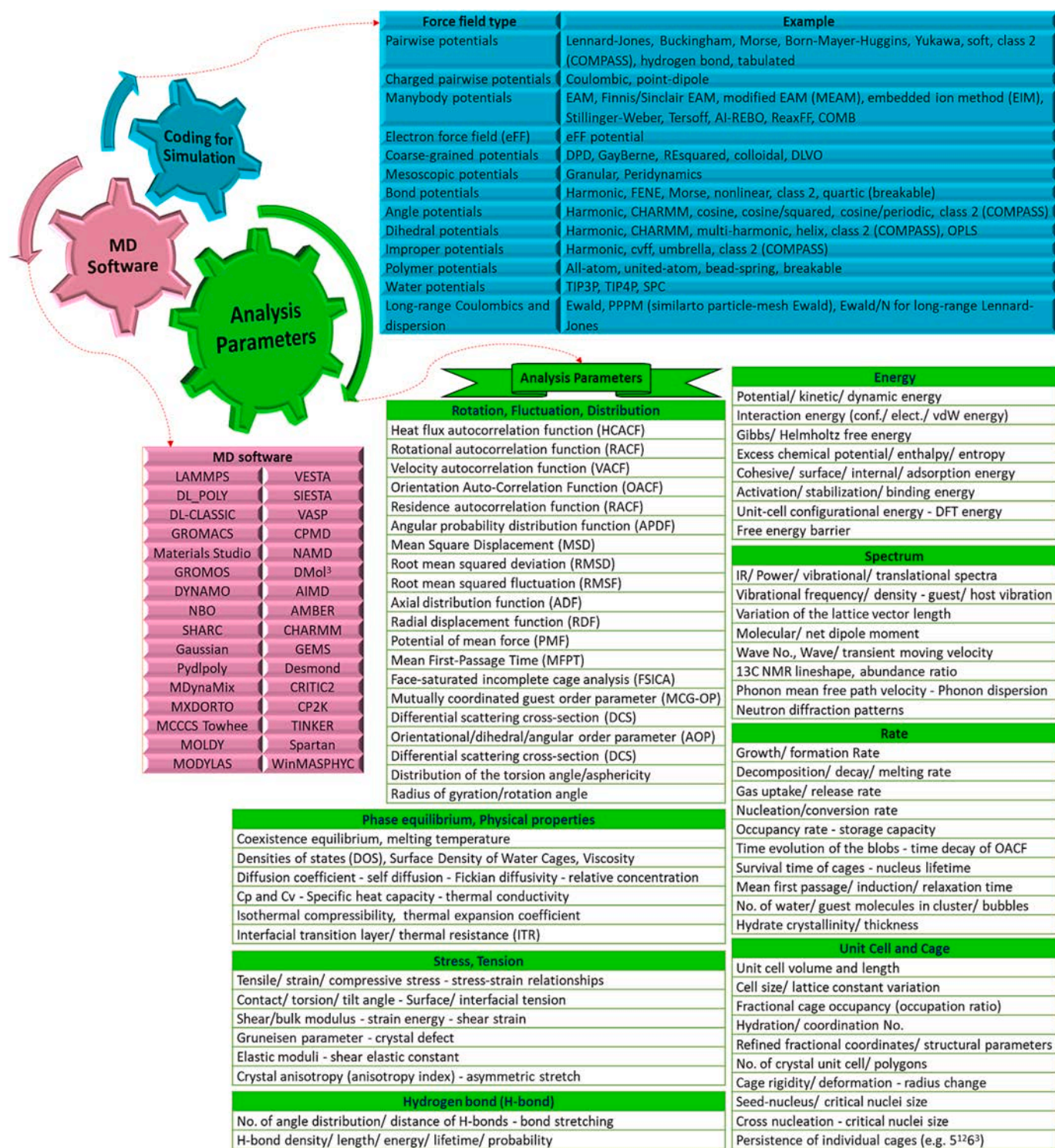
**Fig. 3.** Molecular simulation steps, analysis parameters, and employed software to study gas hydrate systems.

and COS/G2 force fields with TIP4P and TIP4P-FQ models, it was clarified that AMOEBA and COS/G2 models are better at reproducing the experimental data than TIP4P and TIP4P-FQ models that do not explicitly account for polarization [83]. To simulate the hydrate properties of full occupied $CH_4$ hydrate at low-temperature ranges, the performance of TIP4P-FQ intramolecular was found to be higher than the other four-site potential models [44,50]. Also, the TIP4P-FQ model outperforms F-SPC, TIP4P, SPC, and SPC/E force fields in predicting the experimental velocity spectrum [44]. Previously, using rigid/non-polarizable SPC/E, TIP4P-Ew, and the rigid/polarizable TIP4P-FQ

potentials, thermal conductivity, and diffusivity of $CH_4$ hydrate were evaluated. Although the predicted thermal expansion using polarizable force fields and isothermal compressibility in comparison with experiments were in agreement, the deviations are substantial at very low temperatures [84]. MD simulations of Metastable sI and sII hydrates showed that in describing the liberational region of the spectra, the polarizable force-fields outperform non-polarisable models [100]. Also, to describe differences in the spectroscopy of clathrate hydrates, a combination of anharmonic bond potentials and accurate molecular electrostatics can be applied [101]. The thermal conductivities

estimated from MD simulations were found to be independent of pressure. In addition, with decreasing cage occupancy, the simulations predicted a slight increase in thermal conductivity [79]. The three coexistence phases (H-L$_W$-V) of $CO_2$ hydrate by examining the performance of TIP4P/Ice, TIP4P/2005, MSM, EPM2, TraPPE, and ZD molecular models showed that the combination of TraPPE and TIP4P/Ice potential models gives a striking accuracy to predict the experiments of $CO_2$ phase equilibrium up to 200 MPa [102]. Also, TIP4P/Ice and mW models can more accurately reproduce the three-phase coexistence than SPC, SPC/E, TIP4P/2005, and TIP4P force fields [39]. Previously, heat capacity, thermal expansion coefficient, and compressibility of $CH_4$ + $CO_2$ hydrate using TIP5P, TIP4P, TIP3P, TIP4P2005, TIP4PIce, TIP4-PEw, SPC/E for water, DACNIS-UA, TKMAA, OPLS-UA for $CH_4$, and rigid three-site TraPPE, EPM2, EPM potentials for $CO_2$ were simulated. Using the combination of TraPPE $CO_2$ rigid potential, DACNIS united-atom $CH_4$ potential, and TIP4P/2005 water models, the most accurate results compared to experimental values were obtained [48].

The assumptions of the vdWP theory using MD analysis determined that changes in the configurational energy by the nonplanar TIP5P model are higher than the planar SPC [82]. The selected potential model can also affect the estimation of hydrate fractional occupancies. For instance, by employing Gubbins (MG) and OPLS potential models, the accommodation of 2 and 5 $CH_4$ molecules in large cages of sH hydrate at 300 K and 2 GPa were estimated respectively [103]. Recently, it was shown that the stability of $CO_2$ hydrate is quite relevant to the water molecular interactions in which the order of different FF for this hydrate stability would be TIP4P/Ice > TIP4P/2005 > SPC/E > SPC/Fw [104]. Simulations displayed that the type of water force field quantitatively affects the estimated hydrogen bonding but does not affect the qualitative trends. Also, a stronger electrostatic interaction with the guests and neighbour water molecules was observed for TIP4P/ice potential compared to the SPC/E model [105]. Simulation of the $CH_4$ hydrate in conditions of oceanic sediments showed that the SPC/E water model requires a shorter simulation time than the TIP4P model [41]. However, the impacts of potential models on $CH_4$ hydrate dissociation conditions in the other research were found to be negligible. [106]. Although the deviation of MD predictions by TIP4P/Ice and OPLS-UA force fields was approximately 3 K below the experimental values, calculated $CH_4$ solubility was found in good agreement with continuum scale models [107]. According to an evaluation of the accuracy of TIP4P/Ice, GAFF, and OPLS-AA force fields in predicting the phase equilibrium and enthalpy of TBAB semiclathrate at various temperatures, it was concluded that compared to the experimental data, the OPLS-AA outperforms the GAFF. Also, TIP4P/Ice model can more accurately describe the interactions of water molecules in TBAB semiclathrate (type B) [108]. MD analysis of hydrogen bonding and guest conformation of 1-propanol hydrate showed that a larger value of the dihedral angle obtained from the single crystal XRD measurement than the value predicted by the MD simulation might be related to the approximate nature of the intramolecular dihedral potential in the force fields [109]. It should be noted that for intermolecular separations higher than 50 % of the unit cell length, Lennard-Jones interactions can assume to be zero [35]. Table S1 presents the list of force fields for hydrate formers and promoter/inhibitor additives employed in different gas hydrate simulations.

Generally, the gas hydrates based on hydrate formers and additives which contribute into the solid phase and solution phase can be classified into pure, binary, and mixed gas hydrates, and the impressions of promoters/inhibitors/minerals on gas hydrates. The MD simulations of these hydrate systems are briefly reviewed in the following sub-sections.

### 2.2. Pure gas hydrates

Many MD studies have focused on determining the crystallization/dissociation mechanisms and contributing factors that govern the nucleation, dissociation rate, guest–host interactions, molecular mobility, cage occupancy, and cage preference. In this context, it was reported that at the same thermodynamic conditions, dissimilar cage preferences and occupancy of $CH_4$ and $C_2H_6$ may result from their differences in size and shape [110]. MD simulations confirmed that the two-steps dissociation model which was introduced by Sloan [1] is reliable for the mechanism of hydrate dissociation [81] in which the dissociation rate directly depends on the fractional occupancy [111]. Also, expanding the water-hydrate interfacial contact area and higher initial temperature can effectively promote hydrate dissociation [112]. It was proved that the thermal-driven breakup of $CH_4$ hydrate is controlled by the diffusion of $CH_4$ molecules from the hydrate surface to the liquid phase; additionally, break-up for empty hydrate was determined about an order of magnitude faster than filled clathrate hydrate [78]. Also, $CH_4$ in the gas-like fluid transforms from high-density to low-density while reversely occurs for dissolved water in an ice-like phase. This phenomenon is more dominant at an upper melting temperature [40]. Monitoring hydrate dissociations confirmed the formation of nano-bubbles when the mole fraction of dissolved $CH_4$ in the water phase is at least 0.044 [71]. MD simulations also revealed an approximately similar growth mechanism for $CO_2$ and $CH_4$ hydrates [113]; water molecules that are adsorbed and tend to complement the open large cavities induce the rearrangements at the surface of $CH_4$ clathrate hydrate [96]. Also, the nucleus size and relative positions of the guest molecules have bearing on the control of hydrate nucleation [76]. During the induction times, the formation of structural defects within hydrate lattices can also be observed [63]. The MSD analysis elucidated the anomalous diffusion and anisotropic characteristics of the $H_2$ guest molecule [114]. Based on MD findings of thermal expansion, the unit cell volume is significantly dependent on temperature. Also, to analyse the self-preservation mechanism of gas hydrates which takes place at the interface, MD simulations have exhibited that the formation of a layer of solid-like water increases the resistance of mass transfer against guest diffusion from hydrate, consequently, inhibiting further dissociation [54]. MD is also highly useful for investigations at equilibrium conditions that cannot be determined by experiments. For instance, analysing $H_2$ hydrate properties at vigorously high pressure or low temperature (e. g. above several GPa or near 0 Kelvin) cannot be performed by the use of X-ray diffraction patterns but MD verified the existence of different possible structures like (sT′ and C0-II) at such harsh conditions [115]. In a way of more accurate modelling, select force fields respective to guests and simulation techniques are highly crucial. Also, between different ensembles, the sequence of accurate clathrate nucleation was found to be NPT > NVT > NVE; however, the crystallinity sequence is exactly reversed [116]. According to the dissociation of $CO_2$ and $CH_4$ hydrates at 180–280 K, it was concluded that hydrate stability using isochoric conditions is lower than that in isobaric conditions [117]. Although remarkable advances in macroscopic measurements have been accomplished, MD simulations as a powerful technique can provide insights into the fundamental mechanisms of gas hydrates at molecular and atomistic levels. In this regard, computational studies of mixed gas hydrates would be a reasonable alternative.

### 2.3. Binary and mixed gas hydrates

To reveal the interfacial behaviors and characteristics of the mixed gas hydrates which play a central role in developing hydrate applications, investigating molecular interactions can aid in accurately determining the characteristics of their processes. Bearing in mind that a fundamental understanding of different aspects of mixed gas hydrates will be critical for many applications e.g. flow assurance, gas storage, and transportation and MD probes can support the macroscopic experimental studies. MD simulations showed the guest–guest interactions which were ignored by the assumption of vdWP theory, can contribute to the Helmholtz free energy and subsequently bring about some deviation in predicting hydrate equilibrium conditions [82]. It was also found that the mass transfer, memory effect, and guest molecule

chemical potentials are the main controllers of mixed $CO_2 + CH_4$ hydrate in the replacement phenomenon [118]. This phenomenon without structural change occurs first after partial melting of $CH_4$ hydrate surface and followed by partial collapses of large cages at the interface and entering $CO_2$ molecules into them [119]. Worth highlighting that at the macro level, the free water was identified as a significant feature during the replacement [120], however, hydrate growth may become a quasi-static equilibrium at the hydrate-liquid interface rather than in the free gas [121]. Interfacial characteristics of brine water and $CO_2 + CH_4$ mixture indicated that the degree of IFT reduction consistent with experimental evidence is directly proportional to the $CO_2$ concentration [122]. MD simulations can also contribute to molecular level explorations at the early stages of hydrate nucleation and the roles of mixed guest molecules in such phenomena. Cage composition details for $CH_4 + C_2H_6$ and $CH_4 + C_3H_8$ hydrate systems indicated that increasing $CH_4$ composition greatly reduces the appearance of other complete cages whereas grows the formation of standard cages of sI and sII hydrates (i. e., $5^{12}$, $5^{12}6^2$, and $5^{12}6^4$ cages). This suggests that the more stable hydrate nuclei should be obtained with an increasing $CH_4$ percentage. Dissimilar to those mixed systems, $C_2H_6 + C_3H_8$ hydrate exhibited that growing $C_3H_8$ percentage decreases the formation of sI large cages ($5^{12}6^2$), however, promotes the appearance of sII large cages ($5^{12}6^4$). The results of the average composition of cages over the final 30 ns of nucleating trajectories for the aforesaid mixed hydrates are shown in Fig. 4 [123].

The number of complete cages during hydrate nucleation in the $CH_4 + H_2S$ nano-bubble system revealed that forming a nucleus is normally associated with first the emergence of $5^{12}$ and then $5^{12}6^2$ cages, followed by both $4^15^{10}6^2$ and $5^{12}6^3$ cages almost simultaneously. Entropy can also play a critical role in the appearance of specific cage types. For instance, since $5^{12}$ cages are highly symmetric than $4^15^{10}6$ $^m$ and $5^{12}6^n$

cages, they have higher degeneracy and are structurally more consistent with the aqueous phase, resulting in smaller entropic penalty linked with their formation. However, space-filling structures require the appearance of additional cages. Besides, the earlier formation of $5^{12}6^2$ cages because of having higher symmetry than $4^15^{10}6^2$ cages and fewer water molecules than $5^{12}6^3$ cavities is expected to be entropically more favorable [124]. For the sake of a weak $H_2S$-$H_2O$ hydrogen bond, the presence of $H_2S$ in mixed hydrates stabilizes crystal defects in the crystal lattice. These H-bonds are transient with $H_2S$ which typically behaves as the hydrogen bond donor [125].

### 2.4. Gas hydrates in the presence of promoters

For energy storage and transportation purposes, perhaps $CH_4$ and $H_2$ are the most potent candidate. To date, a number of materials/ techniques have been suggested, and a hydrate-based methodology would be the proper option. Since pure $H_2$ hydrate requires uneconomic conditions, the presence of additives as promoters such as TBAB [126], THF [127], or $SF_6$ [128] have been suggested. Given that identifying the key controllers of the kinetics and thermodynamics of gas hydrates in contact with promoters for the suggested hydrate-based applications is particularly critical. As a direct and valuable method, MD investigations have manifested various aspects of microscopic contributors. For example, recent MD simulation results of $CO_2$ double and mixed hydrates showed that the type of large molecular guests in the large cages plays a major role in the stabilization of the clathrate network. In addition, among different types of sII thermodynamic promoters, cyclopentane, and cyclohexane in comparison with greenhouse F-gases (F-promoters) seem to be more susceptible to maintaining the stability of $CO_2$ clathrate hydrate [129]. Gas hydrates can also be useful for gas storage aims, however, the common challenge associated with this is to
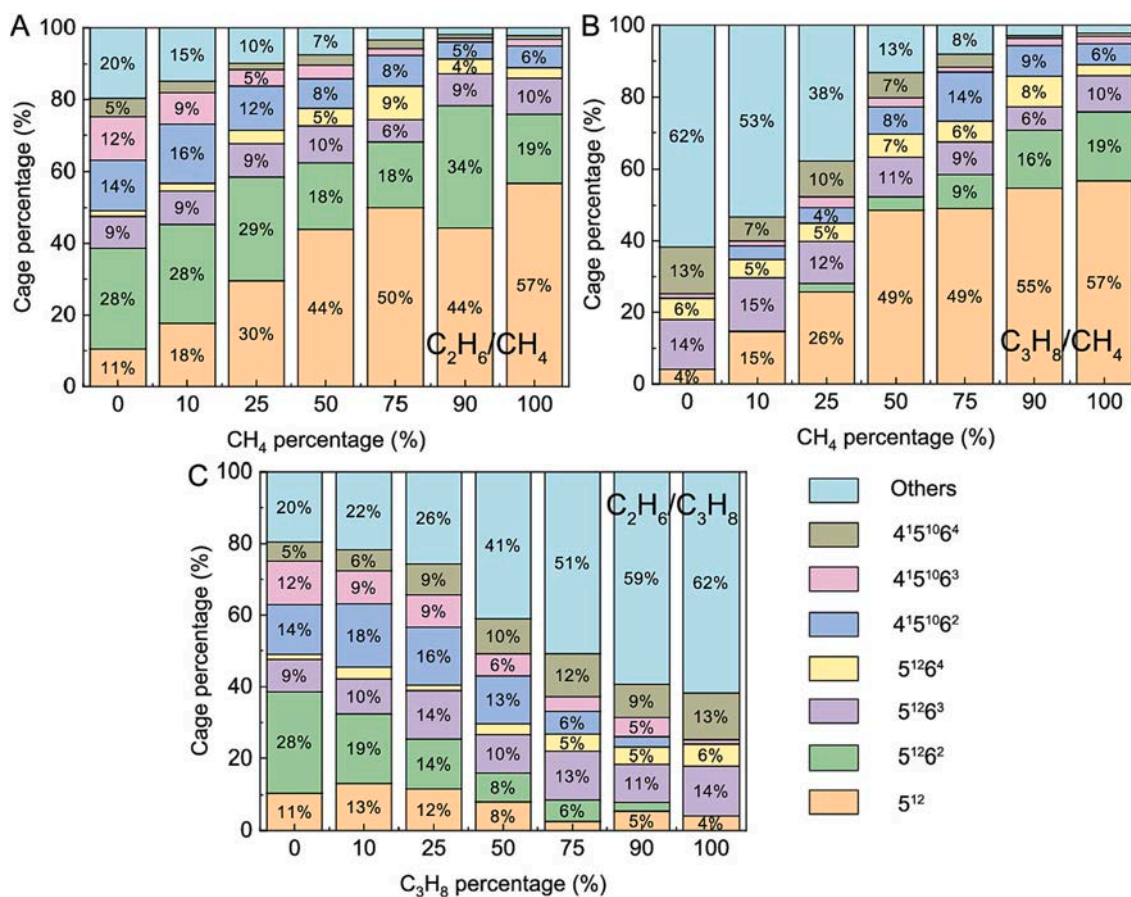


**Fig. 4.** Average composition of cages in (A) $C_2H_6 + CH_4$, (B) $C_3H_8 + CH_4$, and (C) $C_2H_6 + C_3H_8$ mixed hydrates with varying compositions [123].

balance the trade-off between thermodynamic efficiency and $H_2$ storage capacity. Raman spectroscopic measurements revealed that if sII $SF_6$ hydrate is exposed to $H_2$ molecules in the vapor phase, as time proceeds, the $H_2$ concentration in hydrate will hit a peak and then reduce before reaching a stable value [128]. Although this phenomenon cannot be fully explained through spectroscopy experiments, its dynamic process was recently explored through MD simulations in which every large cavity was initially co-occupied by both $SF_6$ and $H_2$ molecules. It was observed that by the end of the simulation time as is shown in Fig. 5 (left), the neighbouring small cavities became partially broken, and then the $H_2$ molecule penetrated them. The red structure shows the initially occupied large cage, and the cyan structure is a partially broken small cage containing an $H_2$ molecule that diffused into it. Also, as Fig. 5 (right) shows, over an enough time, the periodic clathrate turned into an amorphous structure and $H_2$ molecules escaped from their original cavities, gathered, and formed clusters which imply that the large cage co-occupancy of $SF_6$ and $H_2$ molecules could not be the stable configuration. Besides, infiltrating into small and large cages are two main patterns of $H_2$ diffusion as displayed in Fig. 5 (right). The partially broken hydrogen bond ring coloured in green shows the opening through which the $H_2$ molecule can move. Although occupancy of large cages by $H_2$ molecules (once they are filled with $SF_6$) approaches zero, $H_2$ molecules have sufficient space to pass through the hexagonal ring without any cage breaking.

Also, the penetration processes in two special structures of $H_2$ hydrate ($C_0$ and sT') determined that dissimilar to the sT' structure, the number of jumps of $H_2$ molecules among neighbouring channels in the $C_0$ structure is noticeable. However, due to the growth of $H_2$ jumps, with changing temperature from 140 to 260 K, a little acceleration of diffusion can be observed [114]. Generally, pressure and temperature have a critical impact on the growth mechanism, cage occupancy, and storage capacity of $H_2$ + THF hydrate. At 50 MPa and 250 K, the $H_2$ + THF hydrate growth rate can be 3.6 times higher than the pure THF hydrate which implies the kinetics promotion role of $H_2$ molecules. The occupancy of small cages can be enhanced by the presence of $H_2$ molecules while a faster rate of growth can facilitate the formation of $H_2$-filled large cages. However, there is a striking resemblance between the growth behaviour of $H_2$ + THF and pure THF hydrates which indicates that THF is the major controller of the $H_2$ + THF hydrate growth [131]. Recent MD investigations showed that the addition of THF + DMSO can help $CO_2$ molecules diffuse into the $CH_4$ hydrate more readily than either the case with no additive or utilization of a single THF [132]. It was also manifested that in line with experimental results [133], $CO_2$ behaviors in the presence of SDS due to very strong distortion of SDS are quite dissimilar to CH4 interactions with SDS. Both SDS apolar and polar ends lose its shape once it faces $CO_2$ molecules which becomes SDS incapable to exert any substantial driving activity to promote $CO_2$ hydrate formation [134]. The exclusion of SDS and methylene blue (MB) organic molecules from hydrate structure during $CO_2$ hydrate growth indicated that these molecules do not contribute to the crystalline structure [135]. However, the promotion effects of these molecules are different. For example, the urea surfaces make this molecule operate as a catalyst for the formation of $CO_2$ hydrate layers [136]. The role of urea in the growth process was found to be as promoter in mass transfer and catalysation of forming cages at the solid–liquid interface [137]. Recent MD findings for the solution phase including urea and Cu, Fe, Ag metal particles revealed that the mixture of Cu, Fe, and urea (without the inclusion of Ag) possesses desirable promotion effect on the $CO_2$ clathrate hydrate growth rate [138]. The impact of surfactant at near ambient conditions highlighted that the guest molecules can get absorbed into the aggregates during the aggregation process which provides structural flexibility and enhances the aggregation kinetics [139]. In addition, creating hydrate memory effect by organic molecules (e.g. lecithin) may help hydrate be dissociated more slowly when they are adsorbed on the hydrate surface through their hydrocarbon chains crossing and narrowing the available space for water movement and hydrate [140]. Simulating the marine hydrates in contact with protein also confirmed the role of microorganisms in accelerating marine hydrate formation via an approximation mechanism of enzymatic catalysis [141]. $CO_2$ hydrate growth in the presence of metal particles showed that the increase of the concentration of the metal particles can accelerate $CO_2$ hydrate formation but inhibit when their mass fractions were too high which is caused by strong Brownian motion in the solution [142]. The performance of combined promoters may also be more efficient. For instance, the extent of $CH_4$ in the hydrate phase can be increased due to the addition of both DMSO and THF. The ratio of $CH_4$ to $CO_2$ in the existence of THF and THF + DMSO were found to be 1.06 and 1.34 respectively [132]. A combination of absolute thermodynamic and MD modelling for $CO_2$ interactions used to analyse its consequences for hydrate formation revealed that the generate hydrate nearest to the hematite surface possesses lower chemical potential, therefore, it would be thermodynamically favoured to adsorb on hematite [143].

### 2.5. Structure-H of gas hydrates

MD research can be advantageous for determining the micro-scale properties of sH hydrates toward upgrading the hydrate stability and its performances for storage aims. The correlation between the molecular reactivity and stability of $H_2$ + LMGs sH hydrates through analyzing chemical potential and electrophilicity index, electronegativity, and cohesive energy showed that higher hydrate stability corresponds to the larger value of these parameters [144–148]. Studying the stability and chemical activity of 16 promoters on $H_2$ sH hydrates at 230–270 K highlighted that by utilizing alkane components with several heavy atoms less than 7, better stability for $H_2$ sH hydrates can be obtained. Moreover, small cavities have a higher hydrogen-trapping ability than medium ones [149]. Hence, the role of LMGs in sH hydrate nucleation/formation mechanisms, as well as molecular-level factors were found to be unequivocally unique. More recently, it was revealed that compared to a pure $CH_4$ hydrate, 2,2-dimethylbutane (DMB) promotes the formation of $CH_4$ hydrate by at least 5 times faster than its absence. More specifically, the hydration shell of DMB behaves as a
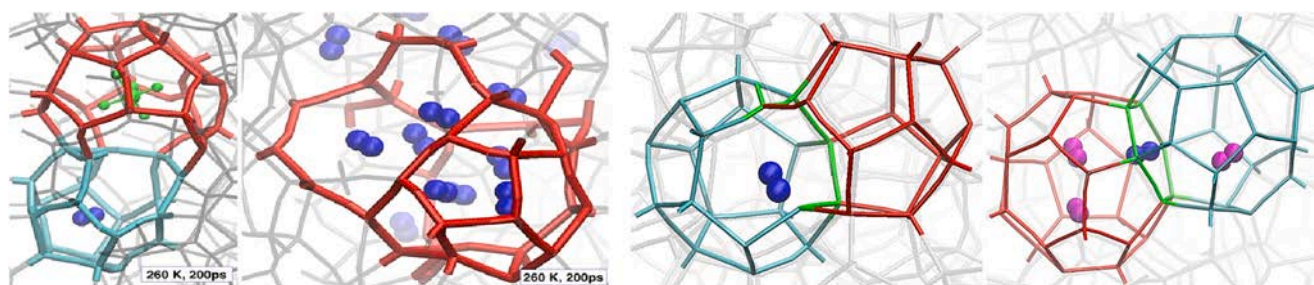


**Fig. 5.** (Left) $H_2$ penetration into neighboring small cavities. (Right) A cluster of $H_2$ molecules in the bulk system; diffusion of $H_2$ molecules from one small cage to another (left) and from one large cage to another (right) [130]. (atoms of $H_2$ and $SF_6$ are in blue and green color respectively). (For interpretation of the references to color in this figure legend, the reader is referred to the web version of this article.)

heterogeneous nucleation site for hydrate formation. This occurs due to the longer residence time of water molecules in the first hydration shell. Indeed, the greater the structural order, the slower the dynamics of DMB relative to that of $CH_4$ [150]. Fig. 6 shows the number of complete cages, the time evolution of the potential energy, and the representative trajectory of $CH_4$ + DMB sH hydrate nucleation. As exhibited, from 200 to 230 ns a sharp increase in the number of $CH_4$ associated with DMB confirmed the first persistent complete cage of the largest cluster. After that more cages were observed to form near the DMB but at 400 ns, the DMB started to form the hydration shell of $CH_4$ + DMB sH hydrate. In this Figure, carbons and hydrogens of DMB are shown in cyan and purple, the water and $CH_4$ molecules are represented as blue and orange spheres, red-dashed lines and red tubes denote the first hydration shells of the associated $CH_4$ molecules and the cages in the largest cluster. Gray lines, green and cyan spheres are also the liquid water, DMB, and $CH_4$ molecules respectively.

Recently, several studies have focused on understanding the effect of guest size and the structural anisotropy which defines the directional dependency of sH hydrate properties [151–153]. In this respect, sH hydrate elastic constants indicated that the type of the LMGs is the main contributor to sH hydrate elastic properties in which LMGs in the large cage of sH hydrate were found to increase its rigidity as well as resistance to shear deformations. Based on DFT calculations, hexagonal sH hydrate compared to hexagonal ice (Ih) possesses higher resistance and stiffness to principal strains [154,155]. To describe the stiffness of materials, calculated values of Young's modulus as one of the key

mechanical properties also demonstrated more resistance of filled sH hydrates to elastic deformation than empty structure. However, compared to sI $CH_4$ hydrate, sH has lower resistance to shear deformations [156,157]. These differences can be linked to the relatively isotropic sI and sII gas hydrates as compared to the anisotropic characteristics of sH and the role of LMGs. Also, the stability of the overall structure strongly depends on both types of guest molecules ($CH_4$ and LMGs) [158]. MD investigation focusing on the impact of guest size and conformation on the structure and stability of sH hydrates showed that tilt angle in the cages, structural flexibility, and guest molecule size can be considered as key parameters of stability of sH hydrates. Generally, in large cages, molecules with shorter lengths have larger tilt angles. Additionally, the width dimension of the LMG may affect the tilt angle. [152]. Also, the sensitivity of cell parameters and thermodynamic properties of sH hydrates to the temperature is higher than the pressure [159]. Structural characterization of sH hydrates (Ar/$CH_4$/$N_2$/Xe + neohexene) at the atomistic level and 0 K revealed that in distinction to nearly isotropic clathrate hydrates, anisotropy is a distinguishing feature of sH hydrate. This structure was found to be more resistive to uniform compression and denser as well as having an isothermal bulk modulus in which the type of help gas plays a crucial role [160]. By analysing the free-energy difference to evaluate the thermodynamic stability conditions of sH hydrates, a strong relationship between the σ parameter of Lennard-Jones and free energy was certified. However, using this method, the highest stable structure for sH hydrate cannot be precisely specified [161].
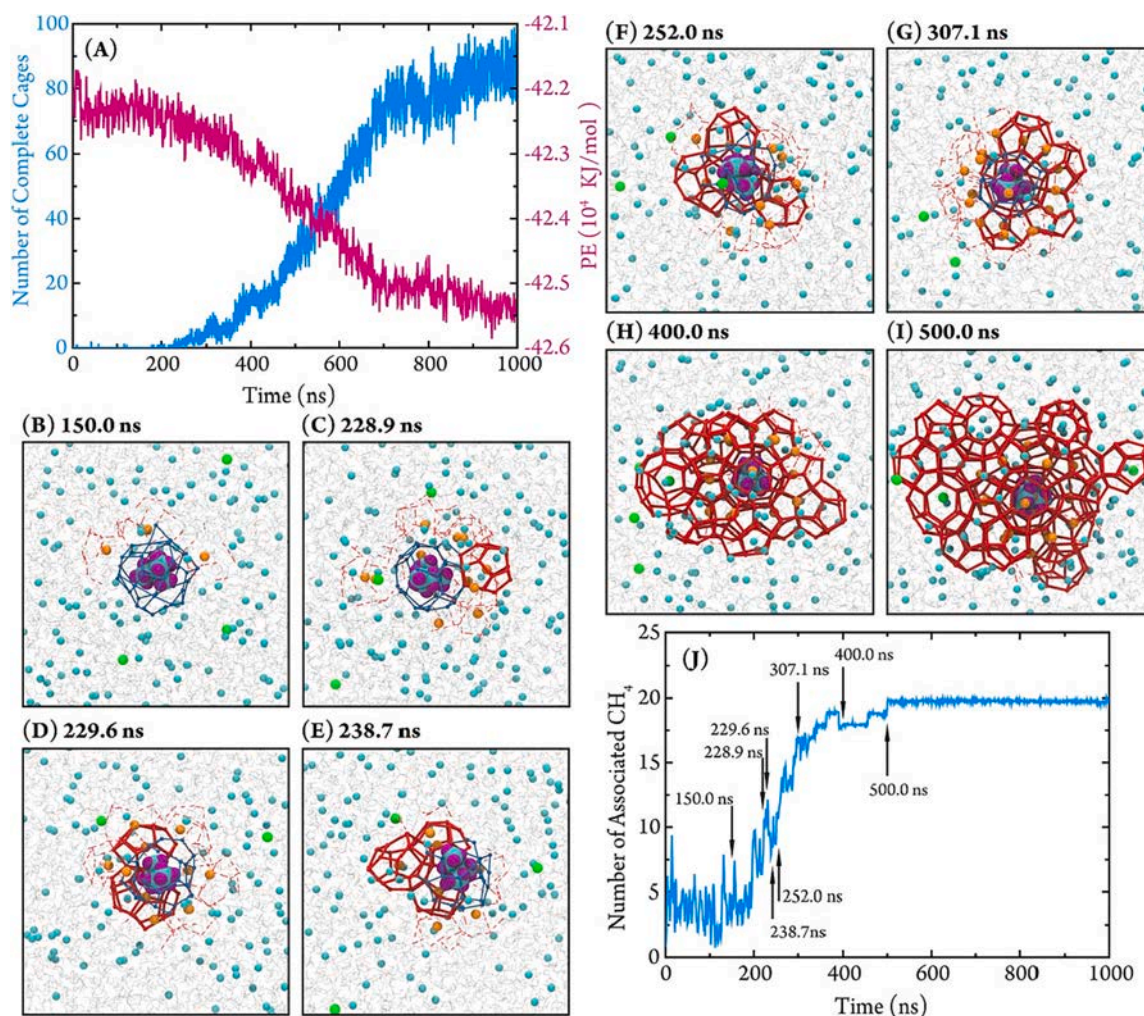


**Fig. 6.** Time evolution of the potential energy, the number of complete cages, and cluster evolution from the trajectory of $CH_4$ + DMB sH hydrate nucleation [150].

## 2.6. Gas hydrates in the presence of inhibitors

Safety and economic concerns caused by pipeline plugging have driven the exploration for finding efficient inhibitors that help to prevent the crystallization of clathrate hydrates. Molecular insights into the dissociation process of gas hydrates under the influence of inhibitors can aid flow assurance experts to find cost-effective and eco-friendly inhibition compounds. In this regard, different MD studies of gas hydrates in the presence of thermodynamic or kinetic organic/inorganic or mixed inhibitors have been conducted. Also, MD simulations can aid to comprehend the factors that play a pivotal role in controlling thermodynamics and adsorption of kinetic inhibitors of gas hydrates. The interactions between hydrate, water, and inhibitor molecules, cohesion and adhesion of hydrate particles, mobility, binding free energy at interfaces, etc., can be accurately analysed via MDs [162]. Evidence suggests hydrate in brine solutions requires a lower dosage of anti-agglomerants (AAs) which keep hydrate particles dispersed in fluids and prevent aggregation [163,164]. In this context, MD simulations showed that salt does not change notably the binding configurations. The free energy of binding with the increase of NaCl concentration from 0 to 10 % becomes more negative which can be attributed to the two individual phenomena. The increase of salt content in the aqueous solution decreases the AA solubility, as a result, AA tends to move into the interfacial region. Additionally, an excess of chloride anions near the hydrate surface establishes a negatively charged interfacial layer which disrupts the network of hydrogen bonding close to the hydrate interface [165]. The influence of surfactants on the clathrate wettability indicated that they can bind to both water-clathrate and oil-clathrate interfaces which promote the nucleation for the former and prevent their coalescence with water droplets as well as an agglomeration of clathrate particles through altering the clathrate wettability from water-wet to

oil-wet for the latter [166]. It was determined that the contact angle of a water droplet at a dodecane-clathrate interface (Fig. 7a) can be $\theta = 34 \pm 2°$ and clathrate covered with a monolayer made of intercalated dodecane and dodecanol or with a pure dodecanol monolayer (Fig. 7b) at the dodecane-clathrate interface can be the same which is consistent with the water wetting angles more than 150° reported in experiments. Also, Fig. 7c shows that being exposed to vapor instead of alkane, the contact angle of dodecanol-covered clathrate can be decreased from 180° to $88 \pm 2°$. This indicates that the van der Waals interactions among alkane and water stabilize the water droplet higher than vapor acts. For a water droplet, even-if surfactants partially cover the clathrate surface, high contact angles will be obtained. Concur with the experiments, the existence of a surfactant monolayer at the oil-clathrate interface by changing the hydrophobicity of the hydrate surface alters the wettability of the clathrate surface to oil-wet as is shown in Fig. 7d. Hence as MD simulations reveal, the coalescence of a bare water droplet cannot be made by the surfactants but the kinetic barrier by their presence will be increased [166]. MD also determined that although the inhibition effect of light oil (toluene, and iron) on the $CH_4$ hydrate growth can be observed, the presence of asphaltenes enhances the hydrate growth rate [167]. Investigation of the surfactant layer impacts at the water–oil-clathrate interface on the melting temperature of sII and sI clarified that the factors which contribute to preventing the clathrate agglomeration are the density of the interfacial layer, the length of molecules of surfactant, and the binding affinity and intensity of surfactant molecules to the surface of the clathrate hydrates [166].

MD also reveals that the inhibition mechanism of organic and inorganic inhibitors is not identical. As an example, in the initial stage, the $CH_4$ hydrate dissociation rate in the NaCl and methanol solutions are slower and faster than that in pure water respectively. However, in the final stage, the NaCl solution finishes the dissociation process earlier than that in pure water. Indeed, methanol in contact with $CH_4$ hydrate lowers the free energy of supersaturation and facilitates the $CH_4$ bubble formation but NaCl due to the strengthening of the hydrophobic interactions can boost the bubble formation more conveniently than pure water [168]. Examining the effect of salt NaCl on the aggregation of $CH_4$ + $C_3H_8$ hydrates showed that with increasing NaCl concentration in solution, the solubility of the anti-agglomerate in the aqueous solution decreases, and the binding free energy becomes more negative [165]. Previously, the structural effect of TBAPS kinetic inhibitor on the interface of $CH_4$ + $C_3H_8$ hydrate was also confirmed, however, the sulfonate group and the hydrophobic end of the molecule make it act as a bi-functional additive [169]. $CH_4$ hydrate formation with kinetic inhibitor indicated that the surface of the crystals can be blocked by hydrophobic inhibitors at the initial stage while hydrophilic ones impose the inhibition effects by disrupting the water structural network [170]. By making a comparison between $CH_4$ hydrate in the absence and presence of 5 % of methanol, it can be implied that although the existence of methanol reduces the equilibrium stability conditions of $CH_4$ hydrate, it can simultaneously boost the diffusion of $CH_4$ molecules at the interface by at least 40 % [171]. $CH_4$ hydrate in the presence of antifreeze proteins (AFPs) showed that the structural aspects of the protein and hydrate surface can contribute to the binding. Also, nonbinding sites are not required for the operation of the protein as a hydrate inhibitor [172]. In addition, simulations of hydrate growth of $CH_4$ in the existence of type I and III antifreeze proteins (AFPs) determined that a type I AFP binding on the hydrate surface can be stabilized by the formation of hydrogen bonds between water molecules and anchoring pendant groups [173]. Moreover, the exchange of hydroxyl groups and amide by mutagenesis may change the hydrogen bonding capability and the side chain shape which implies that the hydrogen bonds are not directly responsible for the activity of AFP III antifreeze [174]. MD simulations revealed that inhibitor molecules e.g. PEO/PVP/PVCap/VIMA that have been found to exhibit more inhibition strength experimentally also possess higher free energies of binding [175]. Investigation of the mechanism of $CH_4$ hydrate growth with combined
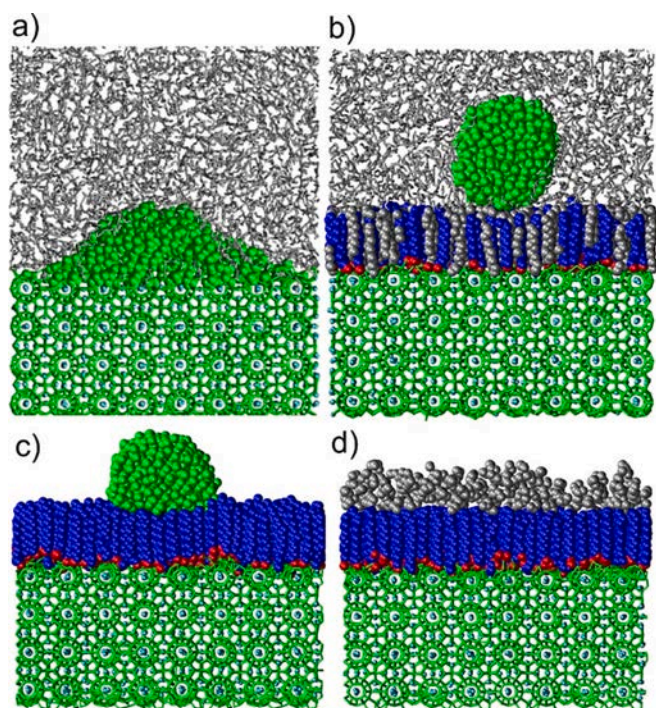
**Fig. 7.** The change of clathrate surface from water-wet to oil-wet by surfactants. (a) Water wets the bare hydrate surface, forming a nonwetting droplet on the surfactant-covered clathrate surface. (b) The clathrate surface is covered with the dodecane-dodecanol interfacial film which repels the water droplet in the alkane oil and behaves as a super-hydrophobic surface. (c) water at the vapor-clathrate interface in the existence of a dodecanol monolayer possesses a less contact angle compared to oil. (d) Dodecane fully wets the clathrate surface [166].

ethylene oxide (EO) and PVCap showed that the amide H-bonds do not contribute to the adsorption, however, dissimilar to antifreeze proteins, PVCap adsorbs on various crystallographic planes of clathrate hydrates [176]. Analysing the effects of amino acids (glycine/alanine/serine/proline) on $CH_4$ hydrate formation at 250 K and 15 MPa revealed that among the simulated amino acids, serine has the highest inhibition influence on the hydrate growth whereas alanine and proline have the lowest. Besides, the more the concentration, the less the hydrate growth rate. However, H-bonds between water molecules and amino acids can mostly damage the cavities [177]. Also, $CH_4$ hydrate in the presence of 8 different oligomer inhibitors (PVPs/amino acids) highlighted that except for asparagine, other inhibitors are absorbed into the interface of $CH_4$-water and suppress the growth of nanoclusters [178]. According to the results of $CH_4$ hydrate formation with PVP/PVCap/PDMAEMA, it was indicated that PVP increases the induction time for the formation of the first hydrate nuclei. Also, the synergistic impact of PVP and PVCap were found to be more efficient than PVCap alone [179] but the existence of PMAEMA reduces the temperature at which sustained hydrate growth can be observed. Hydrate content and the number of H-bonds also can be decreased by increasing the temperature [180]. A molecular study of $CH_4/C_3H_8$ hydrate + PVP/PVCap determined that PVCap kinetically outperforms PVP and such kinetic inhibitors without coming into direct contact with hydrate surfaces can trigger the dissolution of the hydrate [181]. The properties of kinetic hydrate inhibitors (KHIs) on $CH_4$ hydrate growth at 260 K and 80 MPa showed that during the adsorption process, the heterocyclic ring of PVCaps intensively tends to approach the interface of hydrate-liquid [182]. By conducting molecular insights into the kinetic inhibitor adsorption on the surface of $CH_4$ hydrate, although the contribution of the adsorption affinity of hydrogen bonding between water molecules and the amide group of the inhibitor was not observed, a monomer of the KHI (PVCap) was found to be vigorously adsorbed on the surface of $CH_4$ hydrate [183]. GNs in the aqueous phase can also form H-bonds with water at the hydrate surface

which reduces the water activity to obstruct hydrate growth [184].

## 2.7. Gas hydrates in the presence of minerals

For gas hydrates in marine sediments, the zone hydrate formation is an area of sedimentary rock or unconsolidated clay saturated with gas and water in which clay minerals include common constituents of various grain particles in gas hydrate-bearing sediments such as chlorite, kaolinite, illite, montmorillonite, etc. [185,186]. The intercalation of $CO_2$ in minerals within brine aquifers mainly causes significant alteration in the spacing between the mineral layers [187]. The interactions among surrounding sediment grains and hydrates determine the physical properties of the hydrate-sediment matrix. It has been experimentally uncovered that the appearance of the solid surfaces could notably influence hydrate formation [188]. In some studies due to the reduced water activity in confined space, the stronger inhibition compared to the promotion effects has been reported [189,190]. In contrast, experiments revealed that $CH_4$ hydrate formation for conditions milder than that in the bulk can be promoted by the confinement effects of porous materials [191–194]. Due to the experimental challenges associated with quantifying hydrate nucleation and growth, MD simulations were recently applied for examining the $CH_4$ hydrate in hydroxylated silica pores. Based on the results, at relatively milder conditions (at simulation pressures below 10 MPa), confinement impacts can surprisingly induce $CH_4$ hydrate growth. In fact, at constant temperature and in the bulk system, the external pressure governs $CH_4$ hydrate growth whereas in the confinement zone and at pressures less than the minimum expected experimental $CH_4$ hydrate phase equilibria, it grows regardless of the applied external pressure. Fig. 8 displays the initial configuration and lateral growth of the hydrate slab at the water-hydrate interface in which complete cages adjacent to the silica surfaces were replaced by a thin water layer [195]. The formation of a convex-shaped $CH_4$ slab in the first 1 μs is followed by spontaneous lateral hydrate growth for the sake
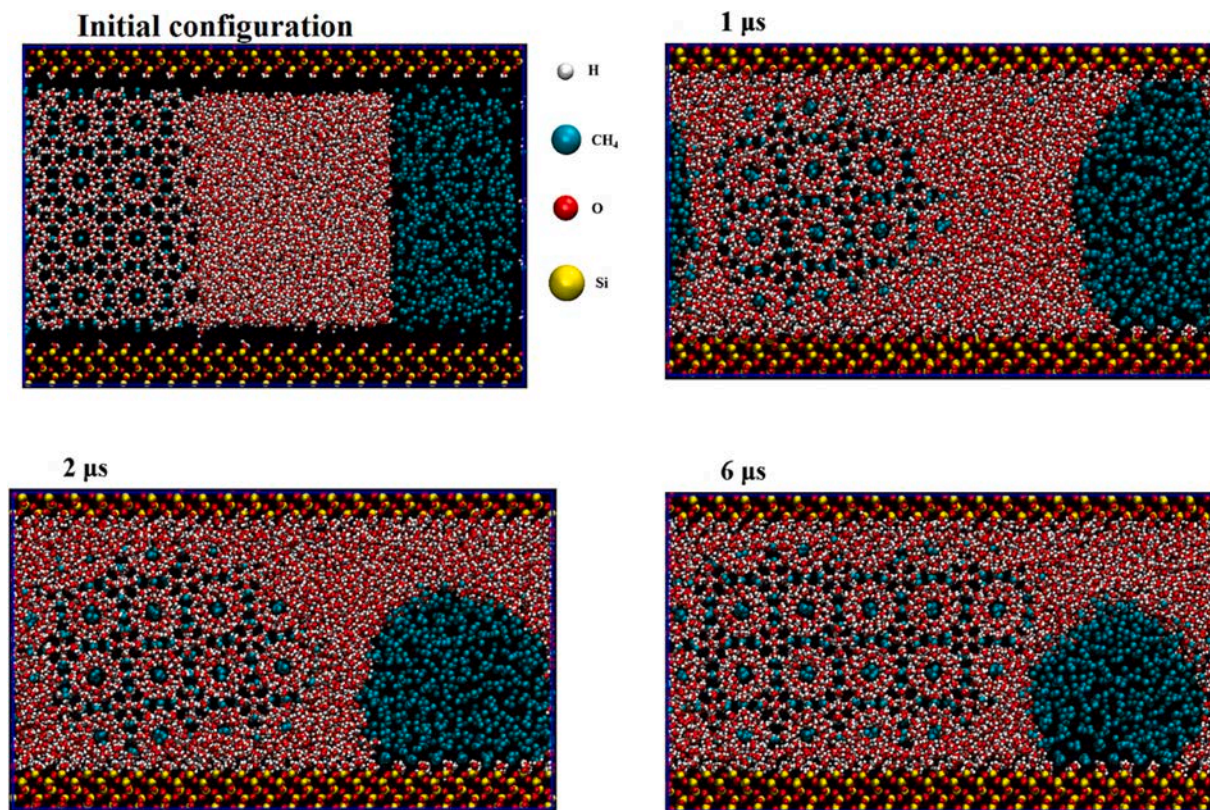
**Fig. 8.** The initial configuration; (1 μs) The transition of $CH_4$ slab into a convex-shaped $CH_4$ bubble, (2 μs) a hemisphere $CH_4$ nanobubble formation, (6 μs) The final snapshot of the simulation. [195].

of $CH_4$ nanobubble formation over 6 μs.

Compared to pure water, bentonite can enhance the hydrate formation of a gas mixture rather than pure $CH_4$. However, by applying MD simulations and neutron scattering experiments, it was found that hydrate formation is insensitive to the addition of impurity particles. Although mineral particles cannot be the most source of heterogeneous nucleation sites, they may do so indirectly if they have a notable impact on gas uptake into solution [196]. Somewhat more recently, MD manifested that kaolinite and illite minerals do not greatly influence the $CO_2$ hydrate phase equilibrium whereas montmorillonite owing to its interlayer cations can shift the equilibrium curve toward lower stability conditions [197]. Besides, the montmorillonite surface by providing nucleation sites can enhance $CH_4$ hydrate nucleation in which the montmorillonite interlayer produces stable $CH_4$ hydrate with $H_2O$ and a basal montmorillonite d-spacing of 24 Å [198]. Also, the increase of basal d-spacing may improve the diffusion coefficients for guest molecules [199]. Since experimental techniques are associated with some limitations of the spatial and temporal resolution to obtain direct evidence of the gas hydrate nucleation and growth behaviour in contact with minerals, MD simulations have therefore emerged as a useful technique for such discoveries. Simulations of the hydrated silica-water interface ($CH_4 + CO_2 + SiO_2$) and the contact angle determined that the density of water in the layers far from the surface is less than the layers adjacent to the silica. Similarly, at the interfaces of liquid and silica, the concentrations of the gases are more than regions in the gas phase [200]. Evaluations of the reaction rate of $CO_2$ hydrate with $Na_2CO_3$ showed that the carbonation of the $Na_2CO_3$ is not mainly affected by the kinetics of the reaction at the surface. In addition, the reaction rate of $Na_2CO_3$ is considerably less than $K_2CO_3$ [201]. Under an external electric field, the migration of NaCl solution in the calcium silicate hydrate (C—S—H) nanochannel showed that bond stability can be weakened by an external electric field. Additionally, the diffusion coefficient of ions confined in pores is around three orders of magnitude less than the mobility of ions in the bulk solution [202]. It was also reported that the cosine oscillation electric field can induce and play positive roles in both dissociation and growth of $CH_4$ hydrate [70].

### 2.8. Semi-clathrate gas hydrates

Aqueous solutions of semiclathrate hydrate formers would be an option for hydrate-based gas separation or cold storage aims. The ionic clathrate hydrates can form from ionic guests such as (TBAB) which have two distinct types of D cages occupied by gas species e.g., $CO_2$, $N_2$, and $CH_4$ [203–207]. Although the cage occupancy and anisotropic angular distribution of $D_A$ and $D_B$ cavities are dissimilar, they have nearly equal volumes. In this regard, MD simulations revealed that CO2 and CH4 molecules prefer to occupy the elongated $D_A$ cavity and the regular quasi-spherical $D_B$ cavity respectively. Although semiclathrate hydrate properties e.g. density, enthalpy, and equilibrium formation conditions have been successfully predicted by the MD approaches, the number of such investigations is quite a few. By analyzing the rotation angle, for $CO_2$ molecules in two cavities at 100–250 K and the lattice structure of $CO_2$ + TBAB, it was revealed that the lattice vibrations of bromide and tetra-*n*-butylammonium groups about their equilibrium positions are small and they are kept in place by electrostatic and van der Waals interactions with the neighbouring water molecules [208]. With the utilization of crystal XRD and MD simulations, $CH_4$ trapped in the two dodecahedral cavities of TBAB semiclathrate hydrate reported that cage occupancies for $CO_2$ and $CH_4$ can be 0.87 and 0.17 in $D_A$ and 0.49 and 0.99 in $D_B$ respectively. [207].

### 3. Hydrate phenomena and properties

Alongside the abovementioned MD simulations of gas hydrate systems, the other characteristics such as structural, energetic, mechanical, physicochemical properties, and dynamical behaviour of gas hydrates

have always been the subject of MD investigations. As exhibited in Fig. 9, there are different gas hydrate characteristics and phenomena which can be investigated through MD methods at the molecular level. In this section, the MD simulations of phenomena and properties of gas clathrate hydrates such as those indicated in Fig. 9 are reviewed.

To study the aforementioned phenomena/properties of gas hydrates, there are several terms such as the dimension of the simulation box, type of ensemble in the final/production phase of simulations, and simulation time MD simulations that need to be properly selected. For example, to obtain a high-ordered hydrate, an NPT ensemble and to observe a critical nucleus as large as possible, an NVE ensemble would be more proper to implement respectively [116]. The nucleation of $H_2S$ hydrate under constant energy conditions (NVE) showed that in the early stages of the nucleation, unlike NPT or NVT which ignored the heat generated by hydrate formation, the NVE simulations can closely mimic experimental conditions [209]. After conducting the simulations, the final step will be the calculations of analysis parameters. Table 1 summarizes some examples of MD simulations studied on different gas clathrate hydrate systems.

### 3.1. Hydrate nucleation and growth

Understanding the phenomena of clathrate hydrates can promote hydrate-based applications [228]. A good illustration of this is a large number of discussions of the hydrate nucleation phenomena [229,230]. Generally, order parameters to analyse and trace the hydrate nucleation are utilized. Analyzing 7 classes of order parameters with a total of 33 individual variants for the nucleation mechanism of hydrate of THF as a water-soluble guest determined that the approximations of order parameters that provide the transition state (TS) and reaction coordinate, based upon water structure are more appropriate than those which are based on guest structure [231]. Also, it was reported that survival probability and mean first-passage time (MFPT) methods can accurately calculate both the $CH_4$ hydrate nucleation rate and critical nucleus size [69]. Using a coarse-grained method for self-assembled monolayers (SAMs), the impacts of hydrophobic and hydrophilic surfaces on THF hydrate nucleation showed that with a homogeneous mechanism in $CH_3$-SAM and OH-SAM, the nucleation rate in OH-SAM due to its higher bulk guest concentration can be faster [232]. To study the structure of clathrate-ice interfaces, conducting four different clathrate and ice nucleation methods revealed that the interfacial transition layer between clathrate and ice is always disordered and could assist in the heterogeneous nucleation of clathrates from ice [213]. A combination method of coarse-grained mW model and the forward flux sampling (FFS) showed that in the vicinity of the water-$CH_4$ interface, hydrate nucleation occurs and then the transition from amorphous to a crystalline structure accelerates its rate [89]. Compelling evidence suggested that hydrates can nucleate through multiple pathways in which direct formation to the globally stable crystalline phase is one of them [233]. The face-saturated incomplete cage analysis (FSICA) method can also be used to identify all possible face-saturated cage compositions in a system [37]. Via examining mutually coordinated guest order parameter (MCG-OP), it was found that both host and guest structuring are crucial to accurately describe the hydrate nucleation [66]. Since MCG-OP considers the effects of both guest and solvent molecules, it can be compatible with defective or hitherto undetected cavity types [234].

Fig. 10 displays a crystallization pathway of clathrate hydrates. As is shown, the crystallization mechanism can be divided into three consecutive stages. The fist step starts with the generation of blobs and the half-cages in which solvent-separated guest molecules and dilute solution are in equilibrium. The next steps are the organization of clathrate cages leading to the amorphous structure and finally the formation of amorphous maturation [235]. Previously, the nucleation mechanisms of sI and sII clathrate hydrate were also investigated by employing the coarse-grained model which demonstrated that the current process occurs first for the small cages followed by large ones [235].
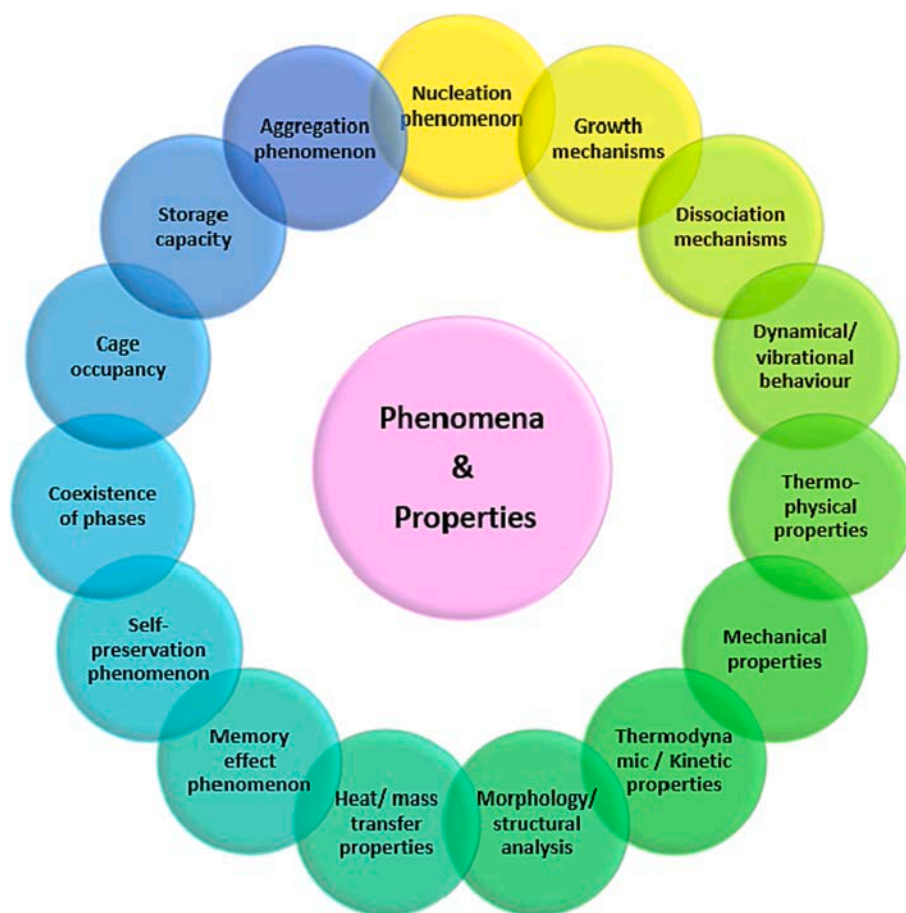
**Fig. 9.** Studied phenomena and properties of hydrates via MD simulations.

The nucleation path in the other study was found to occur in four stages: an increase in the concentration of solvated $CH_4$ via diffusion, formation of an unstructured cluster, a decrease in water content of the nucleus, and finally reordering process of solvated $CH_4$, and water molecules (consistent with the blob hypothesis) [95]. Hence, the hydrate growth rate was found to be due to $CH_4$ solubility and diffusivity in a liquid phase and $CH_4$ adsorption by incomplete water cages at the solid–liquid interface [65,236]. The effect of hydroxylated silica on $CO_2$ kinetic hydrate formation revealed that the process of $CO_2$ hydrate nucleation takes place in 3 stages: the formation of an ice-like layer; intermediate structure and motif layer; and finally, the nucleation seeds can be formed [237]. With the use of massively parallel molecular dynamics for the formation of $CH_4$ hydrate, two distinct steps were recognized for this process: first, the concentration of solvated $CH_4$ clusters increases through penetration from the water-$CH_4$ interface. Then, consistent with the blob hypothesis, the process of re-ordering solvated water and $CH_4$ molecules takes place [93]. To probe hydrate nucleation using forward and backward flux sampling it was demonstrated that the half-cage order parameter describes well the reaction coordinates of hydrate nucleation. Results also suggested that besides the two-step-like mechanism, there exist multiple active transition pathways for hydrate nucleation [94]. Hence, the clathrate nucleation of hydrophobic guests comparable to $CO_2$ and $CH_4$ has suggested that destabilizing the formation of blobs could be a good strategy to apply for the presentation of the nucleation stage [238]. By conducting a two-step method for clathrate structural recognition to identify the nuclei and analyze the relative position of cages, it was observed that 80 % of the enclathrated $CH_4$ molecules at the transition state are contained in sII clathrate-like crystallite. To determine the relative propensity to form sI versus sII motifs, dissipation of the nucleation energy is also essential

[239]. It was revealed that $CH_4$ subcritical clusters can be formed at the initial stage but a higher time is required to aggregate and give the hydrate nucleus which indicates that the aggregation stage is a vital controller of hydrate nucleation [240]. MD simulations also showed the phenomenological similarities between crystallization and protein folding processes [124]. Moreover, high-level kinetic similarities between pure and corresponding mixed hydrate cannot be a reliable basis for predicting the composition of early-stage mixed hydrate nuclei [241]. Somewhat recently, the rugged funnel-shaped potential-energy landscapes and the consistency of structural biased dynamics associated with hydrate nucleation were also studied [124,242]. For the heterogeneous nucleation process, a three-step such as induce, promote, and nucleate mechanisms was suggested as main stages. The heterogeneous nucleation of $CH_4$ hydrate from an aqueous $CH_4$ solution can be facilitated by the interface of hexagonal ice [243]. Nucleation of gas hydrate with high $CH_4$ super-saturation without necessarily allowing enough time for the structure to anneal may enable water cavities to form more quickly [36]. Nucleation of $CH_4$ hydrate indicated that the stability of the initial formation of sII in comparison with sI would be higher [244]. In addition, the equilibrium conditions of the empty and filled lattice of sI and sII $CH_4$ hydrates showed that the cross-nucleation from sI to sII or vice versa needs the formation of $5^{12}6^3$ which is not native to both structures but plays a crucial role [92]. Previously, homogeneous and heterogeneous nucleation of $CH_4$ hydrate using the six-site model for water molecules were analysed that indicated at the early stage of hydrate formation as amorphous intermediate hydrate structures, a set of seven cage types ($5^{12}$, $5^{12}6^2$, $5^{12}6^3$, $5^{12}6^4$, $4^15^{10}6^2$, $4^15^{10}6^3$, $4^15^{10}6^4$) can be formed within the nucleated solids [77]. Probing the $C_2H_6$ hydrate nucleation showed that the full cavity most likely to form first is $4^15^{10}6^2$ which then transforms into both $5^{12}$ and $5^{12}6^2$ cavities [110].

**Table 1**
Molecular simulation studies on different hydrate systems.

| System | Investigated phenomenon/properties | Analysis parameters | P (MPa) | T (K) | Hydrate supercell/ Simulation box (nm³) | Production run time (ns) | Ref. |
|---|---|---|---|---|---|---|---|
| CO$_2$ | Relationship between hydrate occupancy and dissociation | • Density<br>• Energy<br>• Release rate<br>• Dissociation of empty/ filled cages<br>• Interface velocity | 3 | 270–290 | 4 × 4 × 4<br>(10.8 × 4.8 × 4.8) | 50 ns in *NPT* | [111] |
| | NEMD, EMD simulations of the thermal-driven breakup of hydrate | • Fluctuations autocorrelation function (ACF)<br>• No. of hydrate-like CO$_2$ molecules | 20 | 260–320 | 4 × 4 × 4<br>(9.6 × 4.8 × 4.8) | 10 ns in *NPT* | [210] |
| | Three coexistence phases | • Cage occupancy<br>• P-T prediction<br>• potential energy<br>• Density<br>• Cross interaction parameters | 2–500 | 260–295 | 2 × 2 × 2<br>(2.4 × 2.4 × 7.2) | 400 ns in *NPT* | [102] |
| | Homogeneous nucleation mechanism | • No. of cages<br>• Growth rate<br>• Nucleus size<br>• Mutually coordinated guest (MCG) | 50 | 250–273 | (4.8 × 4.8 × 4.8) | 1 µs in *NPT* | [211] |
| CH$_4$ | Surface tension at the interface of CH$_4$, water, hydrate | • Density<br>• Enthalpy<br>• Interaction parameters<br>• RDF | 10 | 300 | 4 × 4 × 4<br>(9.6 × 4.8 × 4.8) | 800 ns in *NPT* | [99] |
| | Cross-nucleation and equilibrium conditions of the empty and filled lattice | • No. of cages<br>• Surface density of cages<br>• Persistence of individual $5^{12}6^3$ cages | 10 | 240–320 | 6 × 6 × 6<br>(14.4 × 7.2 × 7.2) | 400 ns in *NPT* | [92] |
| | Self-preservation mechanism | • Density<br>• Melting rate<br>• Time evolution of total energy | 1–20 | 200–275 | 4 × 4 × 4<br>(9.6 × 4.8 × 4.8) | 100 ns in *NVT/ E* | [54] |
| | Relationship between grain size, mechanical instability, and fracture behavior | • Cohesive energy distributions<br>• Stress–strain relationships | 10–50 | 203–283 | 8 × 8 × 8 | 10 ns in modified *NPT* | [72] |
| | Mechanical properties of monocrystalline hydrate, Young's modulus, and strain rate | • Tensile stress<br>• Compressive stress | 10 | 203–283 | 8 × 8 × 8<br>(9.6 × 9.6 × 9.6) | 1 ns in modified *NPT* | [88] |
| | Interfacial free energy, and stress at the crystal-liquid interface | • Density<br>• Potential energy<br>• Interfacial tension<br>• Excess enthalpy/entropy<br>• RDF | 30 | 271 | 4 × 4 × 10<br>(4.8 × 4.8 × 20.0) | 20 ns in $NP_NAT$* | [46] |
| | Hydrate growth based on non-equilibrium thermodynamics | • Potential energy<br>• No. of guest molecules<br>• RDF<br>• hydrate growth rate | 5–25 | 240–270 | 3 × 3 × 3<br>(3.6 × 3.6 × 11.0) | 10 ns in *NPT* | [212] |
| | Mechanical failure of monocrystalline hydrate | • Tensile stress | 10–20 | 120–325 | 4 × 4 × 12 | 100 ns in *NPT* | [90] |
| | Clathrate hydrate nucleation in the presence of a growing ice front | • Density<br>• Interfacial transition layer<br>• Potential energy<br>• Competing growth | 500 | 250–270 | 8 × 8 × 8<br>9.1 × 10.6 × 36.0) | 10 ns in *NPH* | [213] |
| | Thermo-physical properties of hydrate using AIMD simulations | • Thermal expansion<br>• Compressibility<br>• Total energy<br>• Heat capacity<br>• Elastic moduli | 1–400 | 210–323 | 1 × 1 × 1 | 63 ps in *NVT* | [214] |
| H$_2$ | Special structures of H$_2$ hydrate (C$_0$ and sT') | • MSD | 200–1000 | 140–260 | – | 15 ns in *NPT* | [114] |
| | Vibrational properties, and structural changes | • Enthalpy<br>• Lattice constant<br>• P-T prediction<br>• Density<br>• RDF | 3–100 GPa | 300 | – | 15 ps in *NVT* | [215] |
| | Inter-cage hopping in II clathrate hydrate | • Diffusion coefficient<br>• Activation energy<br>• Cage occupancy | 150 | 80–240 K | 2 × 2 × 2<br>(3.4 × 3.4 × 3.4) | 50 ns in *NVT* | [216] |

**Table 1** (*continued*)

| System | Investigated phenomenon/properties | Analysis parameters | P (MPa) | T (K) | Hydrate supercell/ Simulation box (nm³) | Production run time (ns) | Ref. |
|---|---|---|---|---|---|---|---|
| $H_2$/deuterium ($D_2$) | Molecular scape from hydrate phase | • Inter-cage hopping<br>• No. of guests<br>• Activation energy<br>• Cage occupancy<br>• Binding free energy | 200 | 150–180 | $2 \times 2 \times 2$ ($3.4 \times 3.4 \times 3.4$) | 1 µs in *NPT* | [217] |
| $H_2S$ | Rapid nucleation of hydrate | • Order parameter<br>• Nucleation rate | 50 | 230–265 | $3 \times 3 \times 6$ | 80 ns in *NVE* | [209] |
| $C_2H_6/C_3H_8$ | Dissociation and encapsulation energies | • RDF<br>• Dissociation Enthalpy | 0.1 | 273 | $3 \times 3 \times 3$ (sI)<br>$2 \times 2 \times 2$ (sII) | 1 ns in *NPT* | [218] |
| $CO_2 + CH_4$ | Replacement phenomenon | • Cage-guest Distance Coordination number | 3.2–6.0 | 260–280 | $2 \times 2 \times 4$ | 5 ns in *NPT* | [119] |
| | Replacement and co-growth of $CO_2$ and $CH_4$ hydrates | • No. of adsorbed guests<br>• Cage composition<br>• No. of cages | 2–10 | 250–275 | $3 \times 3 \times 3$ | 1 µs in *NPT* | [219] |
| | Heat capacity, thermal expansion coefficient, and compressibility | • Lattice parameter<br>• Density<br>• Compressibility<br>• Thermal expansion<br>• Specific heat capacity | 10–100 | 271 | $3 \times 3 \times 3$ ($3.6 \times 3.6 \times 3.6$) | 3 ns in *NPT* | [48] |
| $CH_4 + CO_2 + N_2$ | Effect of $N_2$ on the process of $CO_2$/$CH_4$ replacement | • No. of guest molecules in phases<br>• No. of rings<br>• Density | 6 | 280 | $3 \times 2 \times 2$ ($6.5 \times 2.4 \times 2.4$) | 2 µs in *NPT* | [220] |
| $CH_4 + C_2H_6 + C_3H_8$ | Interfacial tension and behavior of mixed hydrocarbons and water | • Density<br>• Angular distribution<br>• Interfacial tension<br>• No. of adsorbed molecules | 10–20 | 275–298 | ($3.2 \times 3.2 \times 10$) | 5 ns in *NVT* | [221] |
| $CH_4 + SDS + CAPB$ | Impact of surfactant on hydrate formation | • No. of guest and host molecules<br>• Distribution of asphericity, acylindricity<br>• ACF | 0.1–5 | 275–298 | – | 3 µs in *NPT* | [139] |
| $H_2 + LMGS$ | Storage capacity of sH hydrate | • Order parameter<br>• Potential energy<br>• Density<br>• No. of guests<br>• Storage capacity | 70–110 | 230–260 | ($5.0 \times 4.2 \times 3.0$) | 2.3 µs in *NPT* | [222] |
| HFC-41/$CH_4$ + pinacolone | Anisotropic expansion of the sH hydrate lattice | • Lattice constant<br>• RDF<br>• MSD<br>• OACF | 0.1 | 90–180 | ■ $3 \times 3 \times 3$ | 25 ps in *NPT* | [223] |
| $CH_4$ + NaCl/KCl/ $CaCl_2$ | Hydrate dissociation, kinetic energy, and transport parameters | • RDF<br>• MSD<br>• Diffusion coefficient<br>• potential energy | – | 273 | $2 \times 2 \times 3$ | 600 ps in *NVT* | [224] |
| $CH_4$ + Ethanol + 1-Propanol/2-Propanol | Hydrate growth in the presence of inhibitors | • Order parameter<br>• Gas uptake<br>• RDF | 0.1 | 100–250 | $2 \times 2 \times 2$ | 500 ps in *NPT* | [225] |
| $CH_4$ + Antifreeze proteins (AFPs) | Hydrate growth in the existence of antifreeze proteins | • RMSD<br>• RMSF<br>• No. of H-bond<br>• Order parameter | 15 | 250 | $7 \times 3 \times 2$ ($8.4 \times 3.6 \times 9.8$) | 30 ns in *NPT* | [173] |
| $CH_4 + SiO_2$ | Thermal conductivity of hydrate in porous media | • Thermal conductivity<br>• Potential energy | 1 | 253–273 | $2 \times 2 \times 3$ | 1 ns in *NVE* | [226] |
| $CH_4$ + clay/kaolinite/ silica nanoparticles | Effects of impurity nanoparticles on hydrate nucleation | • Density<br>• Adsorption energy | 18 | 278–298 | – | 100 ns in *NPT* | [196] |
| $CH_4$ + Na-MMT + fatty acids | Formation and dissociation of hydrate in porous media | • Order parameter<br>• No. of H-bond<br>• No. of cages<br>• RDF<br>• Diffusion coefficient | 50 | 250–303 | $10 \times 6 \times 1$ | 3 µs in *NPT* | [227] |

*: isothermal − isobaric − isointerface area ($NP_NAT$) ensemble.

Explorations of $CO_2 + CH_4$ hydrate nucleation highlighted that stability of $CH_4 + CO_2$ nanobubbles in the water phase and the nucleation rate may be affected by the difference in hydrophobicity between $CO_2$ and $CH_4$ molecules. In addition, the temporary formation of metastable cages such as $4^15^{10}6^2$, $4^15^{10}6^3$, and $4^15^{10}6^4$ was verified [245].

The role of operating conditions is also determinative. The melting temperature and clathrate growth at 260 K specified that a 37 % decrease in the rate of $CO_2$ hydrate growth with increasing pressure from 3 to 100 MPa can be observed while the pressure increase can facilitate the growth rate of $CH_4$ hydrate [113]. In addition, increasing the pressure is less effective than lowering the temperature in promoting hydrate nucleation because the latter induces more water cages to form while the former makes them less prevalent [61]. Additionally, the crystalline structure may grow faster once the sub-cooling is reduced. Also, at moderate temperatures, transient coexistence of crystalline sI and sII may take place [67].
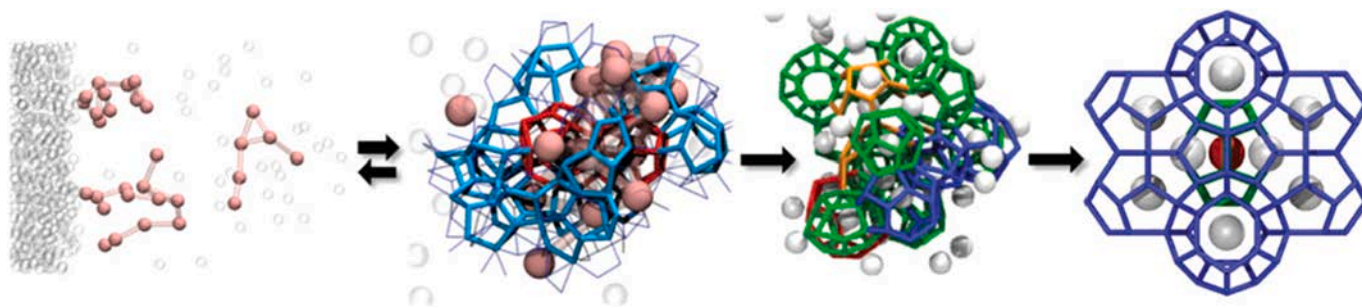
**Fig. 10.** Multi-step blob mechanism of clathrate hydrate crystallization pathway [235].

Homogeneous nucleation mechanism of $CO_2$ hydrate through transition path sampling at 260–273 K revealed that amorphous structures with $4^15^{10}6^2$ cages at low temperature are predominantly formed which is the most abundant, however, increasing temperature above 265 K can change the $4^15^{10}6^2$ to $5^{12}6^2$ cages and help the formation of sI crystalline [211]. In addition, during the nucleation stage, $4^15^{10}6^2$ cavities were found to be the most popular type in the amorphous [246]. By simulating the amorphization of THF hydrate from 1.1 to 1.2 GPa and amorphous densification between 130 K and 170 K, it was found that repulsive interactions between guest and water molecules result in holding a cage structure around the guest [247]. Exploration of the amorphous $CO_2$ hydrate in a water-$CO_2$-silica three-phase system
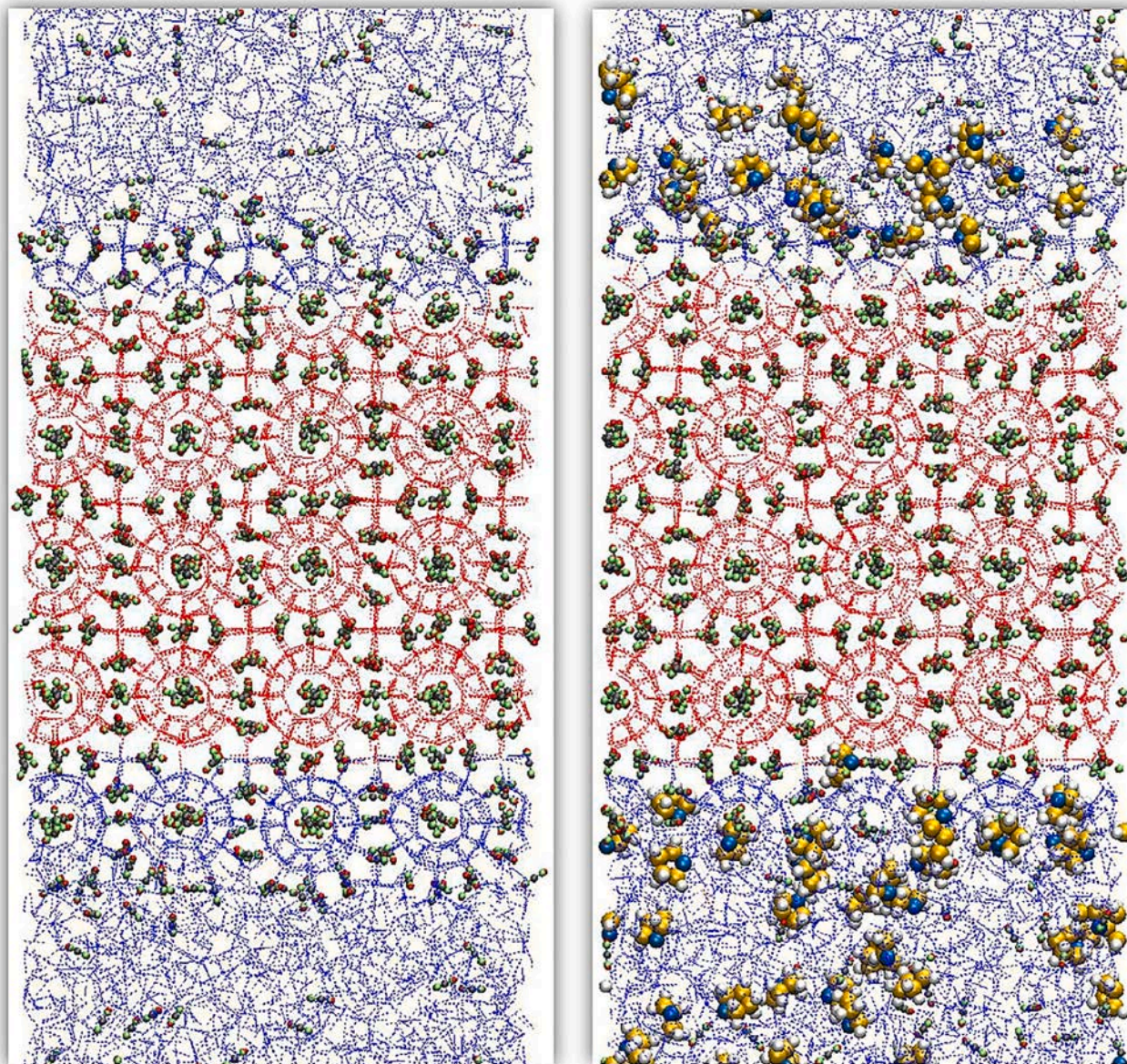


**Fig. 11.** Final trajectories of the hydrate systems including $CO_2$ (left), and $CO_2$ + THF (right) in the aqueous phase [251].

revealed that the nucleation and growth of the nucleus occur mostly near the three-phase contact line. Also, the $SiO_2$ surfaces act as a stabilizer to prolong the lifetime of hydrate cavities. For large cavities, the translational formation of the cage is formed before the rotational structure. However, these occur at the same time for small cavities [248]. Simulation for sI and sII empty hydrate lattices at 150–50 MPa to evaluate their *meta*-stability, and growth mechanism revealed that the empty lattice of sII hydrate can be stable at 275 K and 130 MPa. In addition, the empty sI lattice can nucleate guest-free sII with superior stability. Also, more stability of empty lattice of water clathrates than ice at less than 130 MPa and higher stability than liquid at less than 275 K and negative pressure were confirmed [249]. Based on $H_2$ + $CH_4$ hydrate simulations, the fastest growth rate can be observed at 250 K and 50 MPa. Additionally, at the constant temperature, the more the pressure results in the higher the crystal growth. Also, the temperature above 240 K is directly and inversely proportional to cage occupancies of $CH_4$ and $H_2$ molecules respectively [250]. The growth rate and storage capacity of sII $H_2$ + THF double hydrate at 230–250 K and 10–110 MPa specified that the growth rate of the THF hydrate at 250 K and 50 MPa can be enhanced by the existence of $H_2$ but THF molecules are the main controller of the growth process. Moreover, the increase of pressure leads to the multi-occupancy of large cages, e.g. triple $H_2$ molecules can occupy the cages [131]. By analyzing $CO_2$ storage capacity at 289 K and 2.5 MPa, it was confirmed that, unlike pure $CO_2$ hydrate, $CO_2$ + THF hydrate can be fully stable as displayed in Fig. 11. Furthermore, the growth evolution showed that THF significantly boosts $CO_2$ diffusion at the hydrate-liquid interface [251].

Interestingly, investigation of $CH_4$ hydrates in the presence of cyclic organic compounds (COC) such as cyclohexane, cyclobutanone, and tetrahydropyran revealed that replacing COC molecules with $CH_4$ results in reducing the unit cell stability. Also, the interface of heterogeneous crystal growth of $CH_4$ hydrate indicated a strong affinity for $CH_4$ molecules. In addition, the growth rate for hydrate crystals was found to be four times higher than ice [252]. Analyzing the impact of high solvated $CH_4$ concentration on the nucleation of $CH_4$ hydrate revealed that a very rapid increase of nucleation rate with solvated $CH_4$ concentration can be observed which proved that even beyond bulk super-saturation, $CH_4$ molar fraction is a key that triggers the homogeneous nucleation of clathrate [87]. Analysing the solid–liquid water transition in the presence of a low concentration of $CH_4$ molecules as a hydrophobic guest determined that hydrate growth is dependent on the rate of empty growth lattice and filling of the cages by guest diffusion. Hence, $CH_4$-encaged molecules may act as a catalyst [32,253]. Commonly, thermodynamic properties of $CH_4$ hydrate such as entropy, enthalpy, and kinetic energy during the process of hydrate formation are in accordance with the organized water molecules in the crystal [254]. Based on the non-equilibrium thermodynamics it was also certified that the process of clathrate growth starts by dissolving $CH_4$ molecules to the interface and then arranging water molecules [212]. MD simulations for spontaneous nucleation and growth of $CH_4$ hydrate showed that without an energetically unfavourable interface, uncommon $5^{12}6^3$ cavities facilitate the structural coexistence of two dominant hydrate types (sI and sII) [76]. Also, a simulation of the effect of $CH_4$ adsorption on the lifetime of a dodecahedral water cluster (DWC) showed that the adsorbed $CH_4$ molecules can prolong the DWC lifetime, thereby being more adapted for the DWC [255]. The DWC itself vigorously adsorbs $CH_4$ molecules. As an inherent driving force, shell radii between 6.2 and 8.8 Å is the strong net attraction in DWC which may control the hydrate formation [256]. It was revealed that the stability of the hydrate nucleus on the surface deems to be dependent on the affinity for guest molecules. Dissociation of the hydrate nucleus can also be induced by a strong affinity for guest molecules. [257]. The controllers of cross-nucleation between 4 recognized polymorphs of Frank-Kasper clathrate specified that the sequence of intrinsic growth rate between crystalline polymorphs is sII > TS > HS-I > sI. Among non-identical polymorphs, the formation of an interfacial transition layer mostly prevents cross-nucleation to the quicker growing

polymorph. However, an increase in super-cooling overcomes this barrier [258]. The simulations of hydrate nucleation at a $CH_4$-water Interface indicated that although the nucleated structure was incompatible with the two most common bulk crystal structures, it contains structural elements of both of them [36]. For metastable sI and sII polymorphs of empty hydrate lattices, it was found that the detailed shape of the liberational spectra, and the differences between clathrate spectra and the ice, arise from dynamical correlations between each molecule and its local area [259]. Previously, super-saturation, dynamic and thermodynamic properties of hydrate nuclei were studied using a coarse-grained mW model. It was found that under realistic conditions of formation in industry and nature, homogeneous nucleation of clathrate hydrates does not contribute to their crystallization [91]. The convergence of the nucleation rate is also dependent on the spatial distribution of the spontaneously formed hydrate seeds [89]. Probing the effects of ice on $CH_4$ hydrate nucleation showed that items such as high $CH_4$ concentration near the ice surface, H-bond between the ice surface and hydrate lattices, absorption of released heat from hydrate formation by ice, and finally the preference of cages to occur in the vicinity of ice surface rather than in bulk solution can promote the nucleation of $CH_4$ hydrate [260]. Also, in the direction of fluid − fluid (water-$C_3H_8$) phase separation, high-density fluctuations may promote hydrate nucleation [261]. Investigation of the crystal growth of water-soluble hydrate formers showed that the growth rate of THF hydrate is an order of magnitude less than that of EO and $H_2S$ hydrates. However, the surface trapping effect which leads to the slow growth rate of THF hydrate was not observed for EO hydrate [262]. It should be noted that the growth behaviour and induction time for the gas mixture or in the presence of additives are dissimilar. The sequence of induction time for pure guest hydrate nucleation at a fixed solution composition and the temperature was found to be $C_2H_6$ < $C_3H_8$ < $CH_4$ < $H_2S$. Additionally, there is a strong nonlinear correlation between induction time and guest composition of mixed hydrates [123,263]. The effect of single-walled carbon nanotubes (SWCNTs) on selective separation as well as capturing $CO_2$ molecules from the mixture of $CO_2$ + $H_2$ exhibited that Quasi-one-dimensional (Q1D) hydrates can be an eligible approach aiming at $H_2$ purification from syngas which may offer a safe and clean way to store a large-quantity of $H_2$ [264,265]. It was found that $CH_4$ + THF mixed hydrate has a lower induction time than both pure $CH_4$ and THF hydrates. Also, at the initial stage of crystal growth, $5^{12}$, $5^{12}6^2$, $5^{12}6^3$, and $5^{12}6^4$ cages were observed but in the later stages, a possibility of structural change from sI or sII was confirmed [266].

Insights into the effects of hydrophobic solid surfaces on the formation of gas hydrate determined that at hydrophobic surfaces, the tendency of getting more local ordering of water and interfacial gas enrichment (IGE) gives rise to the promotion of hydrate formation [64]. According to MD simulations to investigate the formation of hydrate at the gas–liquid-metal interface, it was found that the metal surface remarkably accelerates the water conversion to hydrate by facilitating the dissolution of $CH_4$ in THF solution. Increasing the liquid–gas interface curvature can result in a decrease in the energy barrier by 15% [267]. Based on the influence of amino acids on $CH_4$ hydrate growth at 10 MPa and 270 K, the presence of L-histidine in the system was found to markedly boosts $CH_4$ hydrate growth kinetics [268]. Also, analyzing the possible formation of $CH_4$ clathrate attributed to the capability of single SDS (form dimer to solvation sphere) revealed that the folding of SDS in water solutions is the crucial dynamical step to create incipient small cages when the SDS micelle cannot be formed [269]. The presence of hydrophobic nanoparticles can also influence $CH_4$ hydrate crystallization. With the addition of nanoparticles, a trend of hydrate nucleation on the side of the aqueous phase occurs but crystallization on the solid substrate may not be observed [270]. It was found that nanoparticles can facilitate $CO_2$ dissolution by improving the $CO_2$ migration from the bulk of the solution to the interfaces, however, it may physically block the $CO_2$ migration at high concentrations [271]. The spatial distributions and orientations of sH hydrates of $CH_4$ + TBME/NH/MCH showed

that dissimilar to TBME, the hydrophobic interaction of MCH and NH with water restricts the host–guest contact, leading to lower initial kinetics of hydrate formation. The attraction between water and MTBE may also perturb the formation of a hydrate cavity and curb the $CH_4$ occupancy [272]. The effects of 2,2-Dimethylbutane (DMB) on nucleation of $CH_4$ hydrate proved that DMB serves as a nucleation site that promotes the formation of $CH_4$ hydrate so that the presence of a pretty larger hydrocarbon in low concentration notably affects hydrate nucleation [150]. The influence of electrolyte solutions (MgCl2/ NaCl) on hydrate formation of $CO_2$ in terms of ions mobility, density profile, and cage content is also unique. Although the inhibition behaviour of $MgCl_2$ and NaCl on $CO_2$ hydrate growth can be observed, the inhibition effects of $MgCl_2$ compared to NaCl are higher [273]. This may be attributed to their inhibition mechanisms at the initial stages. The kinetic structure and thermodynamic properties of $CH_4$ hydrate from the aqueous phase in the existence of NaCl solution revealed that the hydrate growth rate with the addition of 2 mol% NaCl can be decreased by 30 % to 50 %. Also, the presence of ions affects the $CH_4$ cage occupancy [274]. According to the Hofmeister series, the influence of non-ionic and ionic salts (NaCl/NH4Cl/guanidinium chloride (GdmCl)/methanol) on the growth of $CH_4$ hydrate was explored. At low concentrations e.g. 1 wt %, the promoting effect of a few monovalent salts was the highest for GdmCl while at high concentrations e.g. 10 wt%, methanol showed the slowest hydrate formation kinetics [275]. The growth of $CH_4$ hydrate with ethanol + 1-propanol/2-propanol confirmed that the kinetics of hydrate formation for pure water is faster than the existence of inhibitors [276,277]. $CH_4$ hydrate growth + Na-MMT + leonardite humic acid (LHA) showed that at a high concentration of LHA when the self-aggregation takes place, LHA acts as kinetic inhibition for the hydrate formation on clay minerals [278]. To explore the nucleation of $CH_4$ in the presence of two different kinetic inhibitors, it was revealed that the inhibition impact of KHIs (PVP-A/PVP) on $CH_4$ hydrate at great subcooling decreases significantly and unexpected promotion behaviour can be observed. Under such conditions, KHIs decrease the mass transfer resistance, leading to the nucleation of $CH_4$ hydrate [279]. According to the simulation results of $CH_4$ hydrate in contact with seawater (water with 3.5 wt% NaCl), the inhibition effects of electrolyte ions on nucleation, and orientation of water molecules were certified. Also, ions facilitate the mass transfer of $CH_4$ but suppress simultaneously the penetration of guest molecules [280]. The investigation of $CO_2$ hydrate near silica surfaces revealed that the nucleation of $CO_2$ hydrate tends to occur on relatively less hydrophilic surfaces more easily. Also, the structuring of molecules induced by amorphous solid surfaces is less ordered than that by crystalline surfaces at the initial hydrate growth [281]. The $CH_4$ hydrate sandwiched by hydroxylated silica nanopores showed that the growth of $CH_4$ hydrate in the pore centre is more than on the surfaces where a thin film of water exists. In addition, at pressures lower than that required for the growth of $CH_4$ clathrate in the bulk, $CH_4$ hydrate forms in the nano-pores [195]. The simulation of $CH_4$ hydrate nucleation between hydrophobic graphite and hydrophilic silica surfaces also showed that due to the adsorption of $CH_4$ molecules by graphite surface to form a nanobubble and induce hydrate-like water ordering by graphite near the surface, hydrate nucleation does not occur. In contrast, silanol groups on silica form strong H-bonds which can stabilize the incipient hydrate and facilitate the formation of $CH_4$ hydrate [282]. Also, the effects of impurity nanoparticles (clay/kaolinite/silica nanoparticles) on $CH_4$ hydrate nucleation highlighted that in a similar fashion to heterogeneous ice nucleation, impurity particles for water-soluble guest molecules act as a promoter but $CH_4$ hydrate formation is mostly insensitive to the existence of impurity particles [196]. $CH_4$ hydrate nucleation in the presence of porous sediments showed that the dissolved $CH_4$ molecules migrate to the clay surface where hydroxylated edge sites of clay can facilitate the hydrate nucleation [283]. However, the external surface of clay mineral effects on $CH_4$ hydrate formation demonstrated that unlike the neutral-charge layer, $CH_4$ hydrate nucleation for clay minerals with a negatively

charged layer can occur in the bulk-like region but away from the clay mineral surfaces (water–mineral interface) [284]. According to the simulations of the influence of silica and clay nanoparticles on $CH_4$ hydrate formation, notwithstanding the hydrate nucleation of hydrophilic molecules like $CO_2$ and THF which can be promoted by adding impurity particles, the nucleation of $CH_4$ hydrate is not sensitive to these materials [285]. The impact of organo-minerals such as adsorbed zwitterionic glycine on the sodium montmorillonite surface (Na-MMT) during $CO_2$ hydrate nucleation showed that employing organo-mineral complexes increases the interface area of mineral and water to accelerate the nucleation and crystal growth stages of $CO_2$ hydrate [286].

### 3.2. Hydrate stability and dissociation

To use the hydrate applications, comprehending hydrate stability and dissociation mechanisms would be the critical objective. Previous MD studies of the relationship between hydrate occupancy and dissociation rate and interface velocity showed that identical total occupancy may result in different dissociation behaviour [111]. Also, for pressure ranges up to 500 MPa, it was demonstrated that decay temperature is directly dependent on the cage occupancy [59]. MD simulation of the hydrate cluster dissociation elucidated that the kinetics of atomic dissolution is 5 times faster than crystal hydrate dissolution [42]. Additionally, the kinetic rate of hydrate dissociation was found to be remarkably higher than that in the hydrate formation [287]. Generally, smaller guest molecules than $CH_4$ may have the earlier hydrate dissociation. However, quick dissociation can be observed for those molecules larger than the cage diameter of sI hydrate [288]. According to the MD results of non-equilibrium adiabatic $CH_4$ hydrate dissociation, releasing large amounts of $CH_4$ near a surface increases the formation of bubbles and subsequently the rate of mass transfer [43]. MD also suggests that the dissociation process may occur in four successive stages in which the dissociation process equally undergoes small cages first and next large cavities [289]. The first step of dissociation is the diffusive behaviour of water and cell size increase which leads to fracture of the cages. This is mainly followed by the escape of guest molecules from broken hydrate cages and then aggregating together [81]. Although the resistance of heat and mass transfer during the dissociation increases, it mostly reduces the rate of $CH_4$ hydrate dissociation [112]. Dissociation of partially occupied hydrates is somewhat faster than those of fully occupied hydrates [290]. Also, during the initial homogeneous stages of melting gas hydrate, the aggregation and migration of $CH_4$ molecules are critical [63] and until the threshold of bubble formation, hydrate exists as a metastable superheated solid [62]. Simulations of gas hydrate dissociation in sediments determined that the dissociation occurs layer by layer in a shrinking core manner. In addition, the released $CH_4$ molecules aggregate and subsequently evolve into nanobubbles [291]. Relative to the case where the hydrate is in contact with silica, the presence of a water layer between the silica surface and the hydrate phase increases the hydrate stability [292].

The Non-equilibrium MD (NEMD) simulations methodology to study the acoustic-propagation properties of $CH_4$ clathrate hydrate, and reproduce the P-wave and S-wave velocities in the elastic-response regime of sI and sII $CH_4$ hydrate can be accurately employed [52]. NEMD simulations for $CH_4$ clathrate hydrate dissociation indicated that the dissociation rate of hydrate surrounded by (50% $CH_4$ + 50% $H_2O$) and 100% $CH_4$ are nearly 30% and 55% lower than 100% pure water [78]. Analyzing thermal-driven $CH_4$ hydrate breakup at the water-hydrate interface proved that before the threshold of hydrate dissociation, the fluctuation–dissipation theory is valid and can properly describe the nature of the non-equilibrium [45]. NEMD and EMD simulations of the thermal-driven breakup of $CO_2$ hydrate at 300 K to 320 K demonstrated that Onsager's hypothesis (about the composition-dependence of corresponding dissociation rates above the melting points) is applicable for an initial period of hydrate dissociation [210]. Also, fluctuation–dissipation at the interface plays a critical role [293].

Thermal-driven break-up of $C_3H_8$ hydrate interfaced with liquid water also specified that the Arrhenius equation can predict the dissociation rate of $C_3H_8$ hydrate satisfactorily [294]. According to the dissociation of $H_2 + C_3H_8$ hydrate by NEMD and EMD simulations using pairwise potentials, it was found that different surface-cavity terminations lead to substantial differences in initial break-up rates [295]. NEMD simulations in a range of externally applied electromagnetic fields showed that below a certain intensity threshold, electromagnetic fields cannot bring about structural distortion or dissociation effect on bulk clathrate [296]. However, once a $CH_4$ molecule escapes from a distorted cavity, it is not possible to re-enter them even in the absence of static fields [297]. In the presence and absence of an electric field, release and uptake of sII neon hydrate showed that activation energies for uptake and release of neon in the absence of an electric field were 14.9 and 16.4 kJ/mol which indicated a good agreement with the experimental measurements, however, the release value in the existence of an electric field was declined to 6.5 kJ/mol [298]. By simulating the role of the magnetic field on the formation of $CH_4$ hydrate in the existence of microorganisms (proteins), some evidence of oriented magnetic fields on the hydrate-formation kinetics by a prototypical aromatic peptide was confirmed [299]. Based on exploring the dissociation of $N_2$ hydrate within SWCNT and under the axial electric field, the electric field was found to change the orientations of water dipoles which results in altering the diffusion coefficient and hydrogen-bonding network of the water molecules [300]. Fig. 12 shows the NEMD simulation of $C_3H_8$ hydrate in contact with liquid under the electric field. Analysis of this system revealed that an electric field under 0.7 V $nm^{-1}$ does not lead to dissociation of pre-existing bulk clathrates but field strengths more than that result in significant differences in the initial dissociation rates. In addition, the dissociation rates were observed to be strongly dependent on temperature [301]. It was also revealed that lower frequency and higher intensity may facilitate $C_3H_8$ hydrate dissociation [302]. Based on the results of an external electric field to simulate the dissociation of $CH_4$ hydrate using the non-polarizable models, the presence of an electric field leads to the formation of an ice Ih-type structure while in continuous simulation without the external field, the ice-like structures become disordered. This may result in the separated gas and liquid phases [75].

Based on MD monitoring of the evolution of the $CH_4$ hydrate dissociation in the inclusion of two water reservoirs, it was found that the released $CH_4$ molecules at the initial steps reach the gas phase so that increase the gas pressure on the hydrate phase. As the hydrate dissociates, $CH_4$ molecules aggregate and form nano-bubbles [303]. Moreover, the slow diffusion of $CH_4$ molecules out of the liquid phase results in the agglomeration of $CH_4$ molecules and forms quasi-spherical bubbles with a radius of 11 Å [71]. Concerning the simulation of $CO_2$ and $CH_4$ bubble formation during the dissociation, it was found that when the $CH_4$ and $CO_2$ molecules occupy the small and large cages respectively, the most stable structure can be attained. In addition, the size of formed bubbles during the dissociation for each guest molecule is most likely dependent on solubility conditions of $CH_4$ and $CO_2$ in water [304]. The impact of the grain boundary structures on $CO_2$ hydrate at 220–310 K revealed that the stability of $CO_2$ hydrate somewhat above the bulk melting temperature can remain stable which confirms the relevance of thermal stability of polycrystalline hydrate to the guest's type and the grain boundaries [305]. Simulating the dissociation and encapsulation energies of sI and sII highlighted that the encapsulation energies of guests may stabilize the cavities of sI and sII hydrate but the larger molecules give higher encapsulation energies [218].

The process and behaviour of hydrate dissociation are vigorously relevant to the encaged guest type. By analyzing the diffusion barriers, it was found that the residence of specific cavities and the overall occupancy markedly affect the dissociation of $CO_2$ hydrate. Moreover, unlike $CH_4$ and $CO_2$ molecules, small guests e.g. $H_2$ molecules due to the little penetration barrier can diffuse into the liquid phase during the early stages of the breakup of cavities [306]. MD simulations of $H_2 + THF$ hydrate during dissociation revealed that the encaged THF molecules in large cavities increase the resistance of the diffusion behaviour of $H_2$ molecules, however, THF serves as a strong stabilizer [307]. According to the $NH_3$ hydrate MD analysis, this molecule within temperatures up to 240 K gives more stable host–guest configurations than $CH_4$ [308]. The dissociation conditions and structural change of krypton in the existence
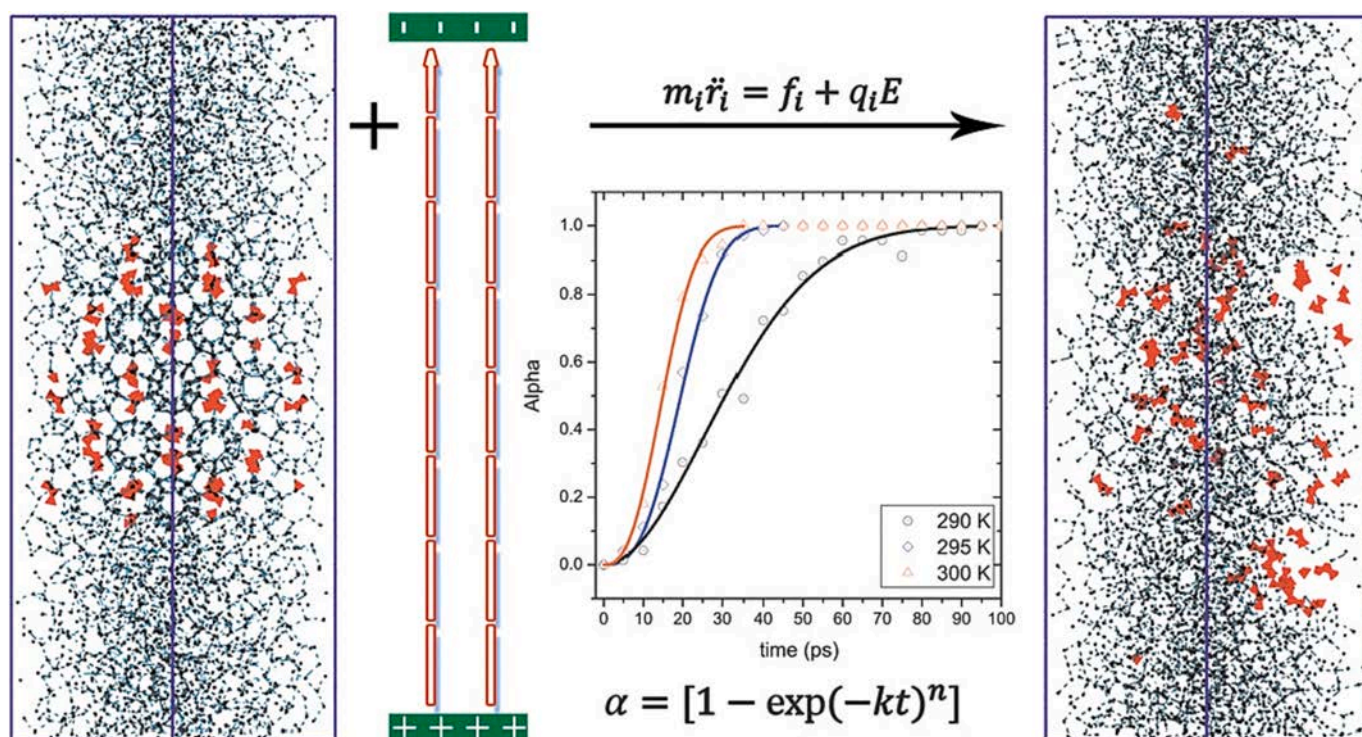


$$m_i \ddot{r}_i = f_i + q_i E$$

$$\alpha = [1 - \exp(-kt)^n]$$

**Fig. 12.** NEMD of both electric field-driven breakup of planar $C_3H_8$ hydrate interfaces with liquid water in electric field intensity [301].

of large molecular guests showed that the cell size of krypton increases with increasing temperature which results in clathrate distortion, small bubble formation, and krypton aggregation in the aqueous phase [309].

By evaluating $CH_4$ hydrate dissociation, kinetic energy, and transport parameters with the utilization of inorganic salts, it was revealed that under the same concentration, the sequence of ion's coordination number (CN) is $Na^+ > Ca^{2+} > K^+$ while $CaCl_2 > KCl > NaCl$ is the order of diffusion coefficients [224]. It was also shown that the generation of $CH_4$ bubbles in dense NaCl solutions near the hydrate interface accelerates the $CH_4$ hydrate dissociation [310]. However, methanol and NaCl through dissimilar mechanisms facilitate the formation of bubbles. In addition, the ions in the solution enhance the hydrophobic interactions and cause non-uniform distribution of dissolved $CH_4$ molecules [168]. With respect to the MD results of the effects of alcohols on the dissociation of $CH_4$ hydrate, it was found that the chain length and the hydrogen number of alcohols are inversely and directly proportional to the $CH_4$ hydrate dissociation respectively [311]. MD investigation of $CH_4$ hydrate dissociation with the addition of methanol indicated that up to 10 MPa and temperatures above 280 K, the effect of pressure would not be tangible. However, the combination of increasing temperature, reducing pressure, and the addition of methanol notably increase the rate of hydrate dissociation [312]. The inhibition capability of alcohols on gas hydrates was also found to be unequal [313]. By probing the $C_3H_8$ hydrate dissociation mechanism with methanol it was found that the hydroxyl and methyl groups of methanol create H-bonds with water molecules that destroy the original H-bonds of water molecules in the hydrate. Also, engaging methanol molecules in small cages may enhance $C_3H_8$ diffusion behaviours and shorten the dissociation time of $C_3H_8$ hydrate [314].

### 3.3. Hydrate cage occupancy and storage capacity

The fraction of gas adsorption into the cages is of great importance for hydrate-based gas separation and gas storage. Results of cage rigidity and the maximum/ optimum cage occupancy for various types of cages using quantum calculations (MP2, M05-2X, and DFT-D) revealed that the maximum and the optimum number of $CO_2$ molecules that can occupy the cavities are: one and one for small cages ($5^{12}$) of all clathrate hydrates, two and one for sI large cages ($5^{12}6^2$), two and two for sII large cages ($5^{12}6^4$), two and one for sH medium cages ($4^35^66^3$) and seven and five for sH large cages ($5^{12}6^8$) [315]. Intermolecular potentials using *ab initio* quantum mechanical to determine the reference energy/ chemical potential of sI $CO_2$ hydrate indicated that the filled fraction for small and large cavities can be around 32%~51% and 98% respectively [316]. Interestingly, by decreasing the fractional cage occupancy from 95% to 85%, the dissociation rate was found to be increased by 30% [317]. However, the size of guest molecules not only affects the fractional occupancy but also changes the unit cell value [60].

Based on free-energy barriers and profiles of $H_2$ hydrate, the energy barriers dramatically decline with increasing the occupancy of small cages by $H_2$ molecules [318]. In addition, the free-energy barriers for $H_2$ molecules from 1 to 5 molecules per large cavity showed a linear decrease for 1 to 3 molecules but become larger for 4 molecules [319,320]. MD simulations indicated that for pressures above 400 MPa, a small number of the large cavities can fill with five $H_2$ molecules [321]. However, the maximum cage occupancies of $H_2$ molecules in sI and sII large cages ($5^{12}6^4$ and $5^{12}6^2$) and small cages ($5^{12}$) were determined as eight, six, and two while in the optimum case were two, two, and one [322]. Also, the negative interaction energy of sI $H_2$ hydrate up to 50% large cage occupancy revealed that $H_2$ hydrate at 150 K and 10 MPa can be metastable which would be competent for $H_2$ storage [323]. MD simulations for sH hydrate storage capacity highlighted that the optimum number of guest molecules in the large cavity for $CH_4$, $C_2H_6$, $C_3H_8$, *n*-butane, and *n*-pentane were determined at 4, 3, 2, 2, 1 respectively [324]. In addition, hydrate systems with small empty cages would have higher stability than that with large empty cages. Also, hydrate stability

in small cages was found to be less sensitive to $CO_2$ molecules compared to $CH_4$ [325]. Somewhat more recently, the effect of cage occupancy, pressure, and the temperature was investigated to reveal the thermophysical properties of $CH_4$ hydrate in the existence of methanol. Cage stability is directly dependent on temperature and inversely proportional to the pressure and cage occupancy. Studying 100% to 75% fractional occupancy at a certain condition indicated that the lower the cage occupancy, the higher the diffusion coefficient [326]. According to MD analysis, the rate of fractional occupancy in the small cavities of sI hydrate at the pressure ranges below 1 MPa was found to be insignificant but gradually increases with elevating the pressure [327]. Recently, the intra-cage behaviour of guest molecules in doubly occupied large cavities of sII hydrates at 100 K was probed by AIMD simulations in which the qualitative consistency of tetrahedral sites with the neutron scattering classical diffusion findings was confirmed [328].

MD investigation of the occupancy and growth of binary $H_2$ + THF clathrate hydrate at 50 MPa and 304–333 K determined that with increasing the super-cooling, more large cages can be filled with $H_2$ molecules but it does not affect the small cavities [329]. Investigation of the structural stability of sII $H_2$ hydrate determined that the increasing temperature reduces the optimum occupancy of large cages [330]. Previously, migration of H-radicals and energy barriers calculated at the MP2 level showed the compatible calculated H-radical migration rates with the actual migration rates [331]. According to the diffusive properties of inter-cage $H_2$ migration in $H_2$ and $H_2$ + THF hydrates at 5 MPa and 200–260 K, it was found that $H_2$ migration does not occur. Also, the diffusivities of $H_2$ in $H_2$ + THF hydrate are an order of magnitude lower than that of pure $H_2$ hydrate [332]. Dynamical cage behaviour and $H_2$ migration in both $H_2$ and $H_2$ + THF hydrates at 200–250 K showed that cage hopping events can be facilitated by temporary openings of small-cage faces with the reformation and relaxation of stabilizing H-bonds [333]. Also, the inter-cage hopping in sII clathrate hydrate showed that although the small cavities remained with only one guest molecule, the large cage occupancy with two and three $H_2$ molecules appeared to be the most stable. The activation energy for guest diffusion was found to be the lowest and the highest for the 4 and 1 occupancy models respectively [216]. Fig. 13 exhibits the hopping and exchange for $CH_4$ molecules between the bubble and large cages. As is shown, initially 2 $CH_4$ molecules occupied cages A and C. Then, the guest molecules hop into the neighbour cages (e.g. cage B). However, the exchange of $CH_4$ molecules between the bubble and the $5^{12}6^3$ cavities is different. During
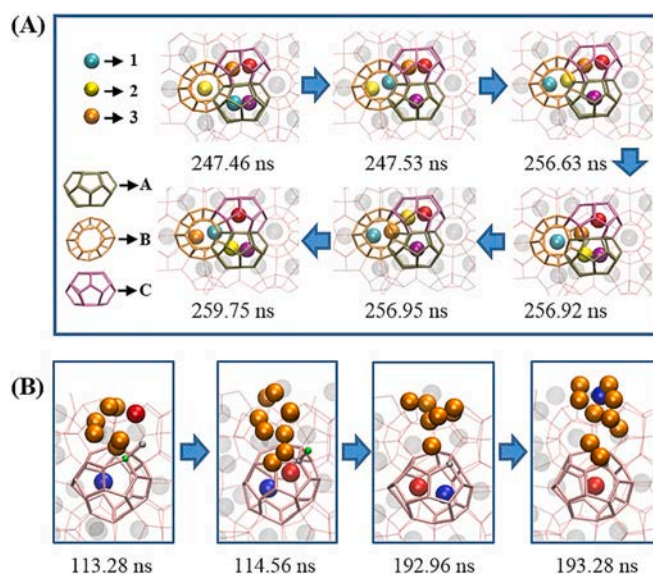


**Fig. 13.** The hopping of $CH_4$ molecules: (A), the hopping and replacement for $CH_4$ molecules between three large cages; (B), the exchange of $CH_4$ molecules between the bubble and large cage [334].

guest hopping between the hydrate cage and bubble, a water molecule in the $5^{12}6^3$ cavities was replaced by another water molecule. In addition, the diffusion rate during the hopping process of $CH_4$ hydrate growth was estimated to be in the order of $10^{-9}$ to $10^{-8}$ $m^2/s$, which is $3 \sim 4$ order of magnitude faster than that during hopping between one-occupied and empty hydrate cages [334].

MD analysis of $H_2 + SF_6$ hydrate revealed that $SF_6$ molecules inhibit the diffusion of $H_2$ molecules and tend to occupy close to 100% of large cages [130]. Newly, the storage capacity of $H_2$ in the $H_2 + THF$ and $H_2 + MCH$ hydrates as a function of temperature and pressure was evaluated. Also, the small cage occupancy is directly proportional to the thermal expansion coefficient and unit cell volume [335]. It was revealed that the cage occupancy is directly and inversely proportional to the pressure and temperature respectively. $H_2$ storage capacity (wt.%) can be reduced by increasing the molecular weight of the promoter [336]. NEMD simulations to study the $H_2$ storage in $C_3H_8$ hydrate revealed that the diffusion coefficient at 273 K is approximately 1.5 times higher than that at 260 K. Based on the experimental and theoretical estimations, $H_2$ content in $C_3H_8$ hydrate can be stored by 1.04 wt% and 1.13 wt% respectively [337]. It was estimated that for the pressure ranges over 270 MPa, double occupancy prevails with the single occupancy of Argon molecules in large cages [338]. MD also specified that under moderate conditions, no double occupancy occurred for the small sI, sII, sH, or medium sH cages but multiple occupancies for the large cages can be observed [339]. Previously, based on MD and vdW-P theory, simulations were performed to study the $CH_4$ content and occupancy in various hydrates. It was proved that multi $CH_4$ occupancies in large cages of sH hydrate are intensively dependent on pressure and temperature. Based on MD analysis of the storage capacity of $H_2 + THF$ sII hydrate and $H_2 + MCP$ sH hydrate at 274 K and up to 500 MPa, it was estimated that large cages at high pressure can be filled with up to 8 $H_2$ molecules whereas small and medium cages can be occupied by just a single molecule. Moreover, the capacity of pure $H_2$, double sII, and sH hydrates were estimated at 3.6 wt%, 1.05 wt%, and 1.4 wt% respectively [340]. To determine $H_2$ storage in sH hydrate at 230–260 K and 70–110 MPa, MD simulations determined that the pressure effects at 250–260 K on the $H_2$ storage capacity are not substantial, however, temperatures below 240 K can at least double the storage capacity of $H_2$ molecules. Also, the main diffusion barriers are found to be the presence of small cages on the boundary layer and the scape of $H_2$ molecules due to the low kinetic energy [222]. Simulations of the $CO_2$ storage in sH hydrate at 100 K and ambient pressure, 273 K and 10 MPa, and also 300 K and 500 MPa revealed that although a single $CO_2$ molecule occupies the small and medium cages, occupancy of 5 and 3 molecules in large cages at the low and high temperatures are the most favoured [341]. Cage occupancy of double hydrates is also found to be slightly dependent on the type of large guests. For example, by simulating $CO_4$ and different large guests, it was determined that the most and least $CH_4$ storage capacity can be 11.9 % and 9.6 % for tetrahydropyran and cyclohexane respectively [342]. However, conducting simulations on the dependency of small guest cage occupancy and LMGs showed no relevance between $CH_4$ occupancy in small cages and the LMGs but the stability of $CH_4$ sH hydrate requires more than 40 % cage occupancies of small and medium cavities by encaged molecules [343]. MD simulations of the sH $H_2 + MTBE$ hydrate at 10–200 MPa revealed that the configurational energy of the unit cell increases when MTBE molecules are replaced by $H_2$ molecules in the large cavities. Also, the volume and energy of the clathrate at the lower temperature are not sensitive to the number of $H_2$ guests in the large cavities [344]. In addition, hydrate guest occupancies in interstitial sites using DFT and MD simulations showed that by occupying interstitial sites, $H_2$ can be incorporated within $H_2 + tert$-butylamine hydrate crystal structures [345]. Also, $CH_4$ may be able to replace MTBE in large cavities. In the absence of large guests, theoretically pure $CH_4$ hydrate requires a pressure higher than 0.5 GPa to form sH clathrate [346]. The simulated double hydrates of $CH_4$ and LMGs at 278 K and up to 1 GPa to investigate the storage capacity determined that the lattice constant can be expanded by increasing the size of LMGs and temperature while it is inversely proportional to the operating pressure. In addition, the fractional occupancy of small cavities by $CH_4$ is entirely related to the type of LMGs. [347]. By computing Quantum free-energy rates of diffusion of $H_2$ molecules at 8 to 200 K it was shown that at temperatures lower than 25 K, the quantum rate is greater than the classical rate whereas it inversely occurs at above 25 K [80]. Theoretically, MD simulations demonstrated that the guest-free sIII clathrate can overtake sII and sH clathrate and emerge at negative pressure e.g. −583 MPa and 0 K or −341 MPa and 300 K [348].

### 3.4. Hydrate guest role

Understanding the structural properties of clathrate hydrates such as metastable clathrate crystals, guest role and size, interstitial defects, structural configurations, and vibrational analysis can be worthwhile either to promote or prevent clathrate formation which has been highly sought after. The elucidation of these specifications has been to some extent uncovered via MD explorations. The anomalous shift in the stretching vibration frequencies of free and guest molecules in small and large cages is not the same. The dynamics and molecular environment of guest molecules can be reflected by the changes in molecular vibrations [349]. Also, the water-guest attraction regulates the nucleus pathway in which weak attraction along with the poor molecule mixing in the interface layer hinders the nucleus from growing in the water phase. In such systems, along with the interface, the hydrate grows but develops toward the gas phase whereas this shift does not occur for the strong attraction [350]. To predict the $^{13}C$ NMR powder lineshapes of the guests, classical MD simulations were performed at the 77–250 K temperature range. A limited range of motion of $C_2H_4$ molecules in the cages at low temperature was observed while with increasing temperature, guest molecules gain greater rotational freedom [351]. Also, estimating the $^{13}C$ NMR lineshape of $CO_2$ at a low temperature is less accurate with experiments [352]. MD simulations showed that the thermal conductivities and speed of sound for $CO_2$ and Xe hydrates are lower than the empty lattice or $CH_4$ hydrate which points out the importance of host–guest coupling [259]. However, the overall nucleation mechanism for all guests was found to be similar and multiple competing channels form the nuclei. The size of guest molecules mostly determines the structure of the nuclei rather than ordering the stable or metastable hydrate crystals or the cage composition [235]. The stability of the hydrate nucleus in the presence of the solid surface to investigate the effect of its affinity indicated that the hydrate nucleus can be stabilized by the slab with a weak affinity for guest molecules which may be correlated with the ordered water structure on the solid surface [257]. As Fig. 14 (left) shows, the free energy of the guest molecules directly corresponds to affinities. Fig. 14 (right) exhibits the initial configuration in that grey plate, cyan balls, silver dots, and red sticks represent the solid slab, guest molecules, liquid water, and the largest hydrate cluster respectively. Based on this Figure, the decline of interaction among the guest molecules and the solid slab weakens the free energy for the guest molecules adsorbed on the slab which is nearly equivalent to that of guest molecules adsorbed on the hydrate nucleus surface for $\varepsilon_{si} = 0.15$ kcal·mol$^{-1}$. This demonstrates the existence of competitive adsorption behaviour among the slab and the hydrate which notably decreases the hydrate nucleus size, leading to the nucleus dissociation. Also, a stronger affinity slab has a shorter hydrate nucleation lifetime.

Although the experimental investigations provide important insights into the hydrate structural analysis and role of guest molecules, some details are not still well-understood whereas MD simulations can systematically be employed to explore such gaps. For example, the effects of guest molecules on hydrate growth showed that the attraction of guest-water molecules may control the nucleus growth rate whereas the size of guest molecules may probably determine the hydrate structure [350].
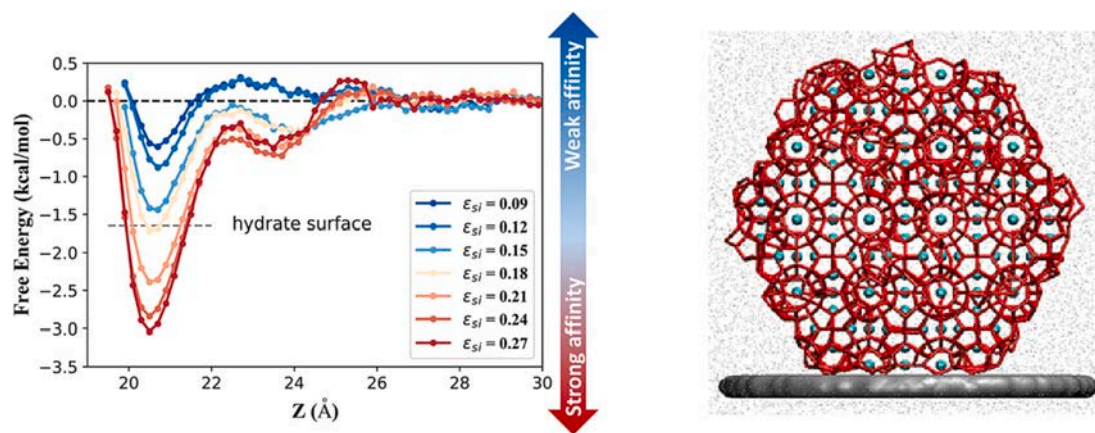
**Fig. 14.** The effect of different guest molecule affinities ($\varepsilon_{si}$ = 0.27–0.09 kcal·mol$^{-1}$) on the free energy of guest molecules adsorbed onto the slabs [257].

### 3.5. Thermo-physical and mechanical properties of gas hydrate

Understanding the mechanical characteristics is of importance for utilizing and predicting the stability of gas hydrate formation. By employing *ab initio* density functional theory (DFT), thermo-physical properties of CH$_4$ hydrate can be accurately calculated [214]. Structural, energetic, and mechanical properties of CO$_2$ hydrate by calculating DFT and MD methodology showed that although the cage distortions are mostly isotropic, a loss in the ideal symmetry of the empty structure is mainly due to the guest molecules [353]. MD indicates the surface tension and intermolecular active forces may decrease with increasing temperature and pressure in the system [354]. Moreover, simulating CH$_4$ hydrate under compression and tension clarified that the tensile stress is lower than maximum compressive stress under the same conditions [49]. Tensile stress and strain rate of calcium silicate hydrate at 300 K demonstrated that the dynamic tensile of calcium silicate hydrate directly depends on water content but it is an inverse function of strain rates [355]. Also, the shear modulus of CO$_2$ and CH$_4$ hydrate directly and inversely depends on temperature [356]. According to the MD results of nucleation of CH$_4$ hydrate sandwiched by elastic silica, the nucleation was found to be dependent on the elasticity of silica in which the weak elastic provides a minimum induction time but in the case of extremely weak elastic, the process of nucleation due to the fluctuation of the layers cannot easily take place [357]. Through MD simulations of acoustic and elastic properties e.g. anisotropy factor, bulk modulus, shear modulus of CH$_4$, C$_2$H$_6$, C$_3$H$_8$, i-butane, and empty hydrates, it was found that the repulsive impact of the guest molecule upon tension and compression can weaken and strengthen the structure of hydrate lattice respectively. The sensitivity of the large cavity to pressure is also more than the small cavity, however, H-bond and O—H bond lengths exhibit the opposite behaviour [157]. MD CH$_4$ hydrate simulations of strain–stress, shear strain, and elastic moduli to investigate the ideal strength under shear deformation showed that CH$_4$ hydrate has no dominant slip system but displays brittle behaviours in terms of its strength [358]. By evaluating the hydrate elasticity and by analyzing the parameters e.g. binding energy, shear elastic constant, and anisotropy index, it was revealed that due to a cage-like structure, gas hydrate frameworks are very isotropic. The presence of highly symmetric proton configurations is one of the reasons for the higher anisotropy of ice *Ih* [359]. The relationship between grain size, mechanical instability, and fracture behaviour of polycrystalline and monocrystalline CH$_4$ hydrates highlighted that CH$_4$ hydrate is highly sensible to cage occupancy changes and environmental conditions. In monocrystalline CH$_4$ hydrate, dislocation-free brittle failure was observed which showed that upon depressurization process, the polycrystalline CH$_4$ hydrate can be destabilized by strain-induced [72]. The determination of mechanical properties of different gas hydrates

indicated that under a uniaxial mechanical load, gas hydrate's stability is critically affected by the polarity, shape, and size of the guest molecules [360]. According to MD insights, the impact of defects on the mechanical property of sI CH$_4$ hydrate was also found to be substantial. Additionally, considerable fluctuations for F$_3$ order parameters just before hydrate structure failure were observed. Also, at a deletion rate of 9%, the mechanical property was decreased [51]. Previously, to analyse the heterogeneous crystal growth of hydrate, a number of defects were observed. Typically, independent of the applied pressure and temperature, around 20% of hydrate cages were unoccupied while some large cages trapped two CH$_4$ molecules [58]. Explored heterogeneous crystal growth of H$_2$S hydrate demonstrated that the growth rate of H$_2$S hydrate is higher than CH$_4$ hydrate, however, in the newly formed crystal of H$_2$S hydrate, a relatively low level of defects was observed [361]. Also, increased gas concentration reduces the induction time for H$_2$S hydrate nucleation while the homogenous nucleation process features the amorphous initial formation more specifically at high super-saturations [362]. Analysis of the dynamic and structural nature of water is also confined in the quasi-two-dimensional pores which is the main binding phase in the cement. It was shown that the defective silicate chains and the interlayer calcium can render a hydrophilic interaction among the C—S—H and confined water. In this regard, the dynamical behaviour of the confined water as a glassy material at an intermediate range up to 4.2 Å was evidenced [363]. To investigate the steady-state heterogeneous crystal growth during the sI crystal formation, an unexpected kind of structural defect (consisting of $5^{12}6^3$ cages) was previously confirmed. Additionally, an in-situ transformation of sI to sK was found to be possible albeit under prevailing operating conditions [57]. it was also revealed that guest–host H-bond leads to the formation of Bjerrum L-defects in the clathrate phase where 2 adjacent water molecules have no covalently bonded hydrogen atom between them. By conducting this simulation, it was determined that an activation barrier for the THF-water defect formation is about 8.3 kJ/mol [364]. NEMD simulations revealed that diffusion of released CH$_4$ from the hydrate surface during dissociation is not homogenous and the solution phase does not necessarily remain isothermal [38]. The examination of the mechanical failure of monocrystalline CH$_4$ hydrate revealed that the failure may take place in two phases: gradual crack growth and quick crack propagation [90]. To investigate the mechanical properties of monocrystalline CH$_4$ hydrate and its intrinsic differences from ice, the impacts of guest occupancy, crystal-orientation temperature, and strain rate at 263 K and 10 MPa highlighted that although the influence of crystal orientation is not significant on monocrystalline CH$_4$ hydrate, mechanical strength greatly depends on temperature, strain rate, and large cage occupancy [88]. The mechanical stress–strain curves of CH$_4$ hydrate under three different strain rates and the directional deformation are presented in Fig. 15.
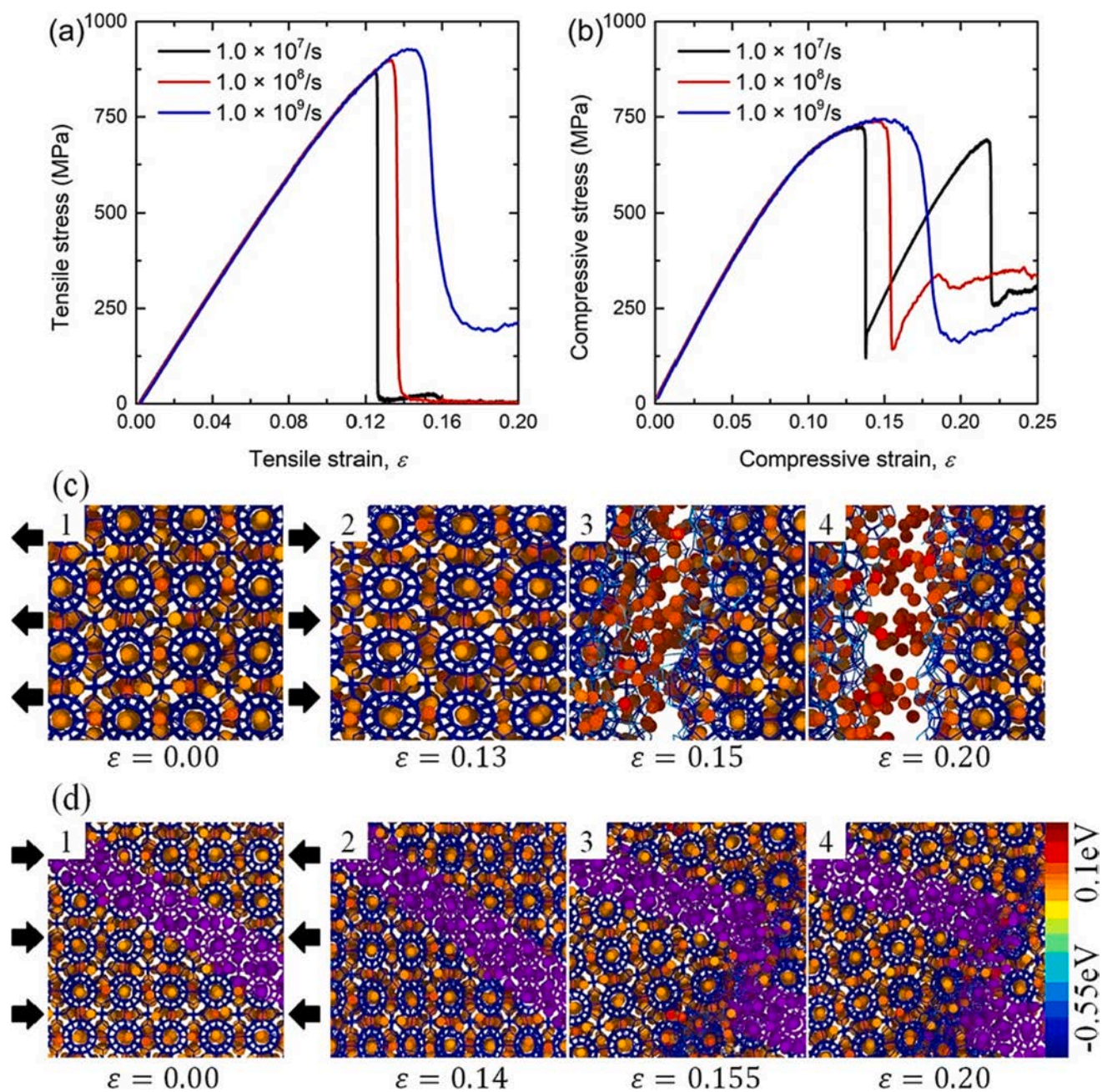
**Fig. 15.** Mechanical properties of CH₄ hydrate for various engineering strain rates. (a) Tensile stress versus strain curves. (b) Compressive stress versus strain. (c) Tensile deformation test conditions. (d) Compressive deformation test conditions [88]. (The color of molecule particles is based on the potential energy. The purple molecules indicate the uniformly structural changes during deformation). (For interpretation of the references to color in this figure legend, the reader is referred to the web version of this article.)

By evaluating the mechanics of CH₄ hydrate at the liquid water-hydrate interface, it was observed that in the region close to the interface, CH₄ molecules due to dense hydrogen-bonded water molecules cannot be soluble. However, the growth of local density and surface excess of CH₄ near the surface indicate anomalous CH₄ adsorption to the CH₄-water interface [365]. Previously, the free energies and thermal expansivity of clathrates showed that the large expansivity of xenon hydrate stems from guest molecules and a difference in oxygen atom arrangement between ice and hydrate plays a minor role [366]. By employing rigid geometry and adopting the non-polarizable model in NEMD simulations it was shown that except at low temperatures (50 K), although the estimated thermal conductivity values are relatively insensitive to the cage occupancy, a small number of defects (1 %) in the

water lattice can result in a large reduction (10 %) in thermal conductivity [85]. The effect of electrostatics methods on the prediction of CH₄ hydrate thermal conductivity showed that the estimated thermal conductivities by non-periodic techniques would be more in agreement with the experiments, however, electrostatic treatments affect thermal conductivity [367]. Thermal conductivity may also depend on both rigidities of the framework and guest–host interactions but the lower thermal conductivity compared to ice *Ih* is because of differences in crystal structures [368]. Studying the mechanisms for thermal conduction of CH₄ hydrate revealed that the guest–host interactions and crystal structure can contribute to glasslike temperature dependence so that they can lower the hydrate thermal conductivity relative to ice *Ih* [369]. Based on MD analysis of the thermal conductivity of CH₄ hydrate in

porous media, it was determined that with increasing temperature, $CH_4$ hydrate-$SiO_2$ thermal conductivity enhances more quickly near the freezing point. Also, at a certain temperature, smaller pore sizes have a larger effect on increasing hydrate thermal conductivity which is several times less than the porous media [226]. Mechanisms for thermal conduction in $H_2$ hydrate demonstrated that dissimilar to $CH_4$, a single occupation of the small cavity by $H_2$ results in more harmonic energy transfer and less resonant scattering [370]. The thermal properties of sI $CH_4$ + LMGs hydrates also showed that at high-temperature ranges, guest molecules with strong host–guest interactions have more thermal expansion but increasing the size of LMGs subsequently decreases the $C_P$, and $C_V$ of hydrate [371]. A correction technique to determine isothermal expansion coefficients and lattice parameters at 287 K and 10–100 MPa highlighted that the isothermal expansion coefficient and specific heat capacity of $C_3H_8$ hydrate are somewhat higher than that in THF hydrate. Furthermore, by comparing $C_3H_8$ + $CO_2$ and $C_3H_8$ + $CH_4$ binary hydrates, it was revealed that the small cages occupied by $CO_2$ molecules dissimilar to $CH_4$ can result in increasing compressibility and expansion coefficient but decreasing the heat capacity [372]. According to structure–mechanical properties of $CH_4$/$Xe$/$N_2$/$H_2$/$Ar$ + neohexene sH hydrates using *ab initio* atomic simulations, the type of help gas was identified as the main contributor to the shear, elastic and anisotropic characteristics of sH hydrate. Also, the brittleness of filled sH hydrate was found to be higher than empty sH hydrate which can be attributed to the role of guests inside cavities. However, wave velocities of ice *Ih* were determined less than sH hydrates [155]. Based on the simulated values of the lattice constants using anisotropic site-site potential models of the $N_2$ + neohexane hydrate, the same tendency as obtained by the powder X-ray diffraction was observed [373]. Moreover, studying the impact of help gas on the crystal lattice of $Ar$/$Kr$/$CH_4$ + neohexane (NH) at different temperatures determined that the order of their crystal lattice as $CH_4 > Kr > Ar$ may be the evidence of the effects and importance of small guest molecular sizes [151]. It was also indicated that the lattice constants and system average volume for xenon hydrate in the presence of cyclopropane and propane are directly related to the guest molecular sizes and pressure [374]. Recently, the lattice expansion of $CH_4$ sII hydrate in the existence of linear and cyclic guest molecules (cyclobutanol and butyraldehyde) with the identical formula of $C_4H_8O$ was studied to figure out the effect of bonding characteristics on hydrate thermal expansion. Based on the results, less lattice expansion in the system consisting of cyclobutanol in comparison with butyraldehyde was observed but the promotion impact of cyclobutanol on hydrate equilibrium was found to be higher [375].

Simulation of the thin liquid film at the hydrate/ $CH_4$ gas interface showed that the thin liquid film makes substantial contributions to the interfacial properties [68]. The interfacial free energy, excess enthalpy, and stress at the crystal-liquid interface by employing a normal pressure-cross-sectional area ($NP_NAT$) ensemble elucidated that interfacial tension is directly and reversely proportional to temperature and pressure respectively [46]. Based on molecular analysis of the interfacial mechanics and thermodynamics at the interface of liquid water and natural gas, it was found that for the pressure range of less than 50 MPa, the increase of pressure and temperature reduces the interfacial tension [376]. Interfacial tension and $CH_4$ hydrate morphologies at the liquid water-hydrate interface showed that the nucleation may take place in the ranked order of film-shaped, cap-shaped, lens-shaped, and homogeneous [377]. By examination of the interfacial tension and behaviour of the single and mixture of $CH_4$, $C_2H_6$, and $C_3H_6$ hydrates, equilibrium molecular dynamics and hydrate formation at the water–gas interface were observed. At the interface, the surface adsorption of gas molecules enhances the gas local concentration but reduces the interfacial tension, however, both of these factors boost the formation of gas clathrate hydrate [221]. To determine the mechanical and key structural properties such as bulk modulus and equilibrium lattice volume for $C_3H_8$, $C_2H_6$ + $C_3H_8$, $CH_4$ + $C_3H_8$, and empty hydrates, it was determined that the equilibrium lattice volumes are directly proportional to the guest size in

double hydrates which may experience the greater increase than pure hydrates [378]. Based on MD analysis of $H_2$ and $D_2$ molecular scape from the hydrate phase using the same force-field parameters at 150 to 195 K, it was also revealed that the stronger collisions between the cage and guest molecules may increase the likelihood of cage distortion which results in the subsequent escape of $D_2$ molecules. Also, the leakage rates of $H_2$ were observed to be lower than those for $D_2$ [217]. In addition, the in-slab translational order parameters of the $CH_4$ hydrate surface in contact with the gas phase determined that the molecules of water in the adlayers and slab surfaces can be periodically arranged while the internal slabs can remain completely rigid [96].

### 3.6. Dynamical and vibrational behaviours

According to MD results, it was confirmed that the power spectra would be a reliable technique to evaluate the vibrational behaviour of guests in the hydrate phase [379]. Previously, the idea of a resonant scattering mechanism for the host–guest phonon interactions in clathrate hydrates was supported by MD simulations [380]. The dynamical behaviour of ice and sI clathrate hydrate showed that the phonon densities in both states are similar which represents the resemblance of their infrared spectra. Also, the phonon density enhancement of selective vibrational modes can be induced by guest species [34]. Phonon scattering off the rotational and vibrational motions of guests was also found to be responsible for the lower thermal conductivity of hydrates relative to ice [381]. According to the exploration of lattice vibrations in clathrate hydrates for Xe at 220 K, vibrational couplings lead to energy exchange between the guest vibrations and the host lattice which results in anomalous glasslike behaviour in the thermal conductivity [382]. Examining anomalous thermal conductivity of clathrate hydrates using EMD, and NEMD simulations revealed that the resonance scattering model is the most likely mechanism of anomalous temperature dependence and low thermal conductivity [383]. Evaluating energetic dynamical and H-bond vibrational properties in sI and sII hydrates demonstrated that H-bond energies are the largest in magnitude in structure I, followed by sII hydrate and then ice *Ih*. However, unlike ice and sII hydrate, energy transfer via H-bonds in sI occurs at higher frequencies [73]. MD calculations for the vibrational spectral band of molecular $H_2$ trapped in hydrate indicated that $H_2$ molecules in large cavities provide a high-frequency peak than those in small cages [384]. With the combination of *ab initio* and classical MD simulations to analyse the host–guest H-bonding in alcohol clathrate hydrates it was found that due to the strong host–guest H-bonding, vibrational spectra of alcohol O—H bonds consistent with experimental Raman spectra displays large frequency shifts. Also, conducting similar investigations of dynamical properties of $H_2S$ revealed that a preferred orientation of the dipole-vector exists at 150 K whereas there is no preferred orientation at 300 K [385]. Interestingly, some alcohol molecules can fit into $5^{12}6^4$ cages of clathrate hydrates [386]. The mechanical and vibrational features of $CH_4$/$Xe$/$CO_2$ + neohexane sH hydrates showed that vibrational frequencies are dependent on interatomic distances of hydrate and pressure. Also, the relations between interatomic distances, H-bond strength, and vibrational frequency shifts, affected by guest–host interactions and guest type were previously certified [387]. Based on the stretching vibrations of sI $CH_4$ hydrate investigated with *ab initio* density functional theory, although the consistency between calculated vibrational frequencies and experiments was confirmed, the computed H—C stretching vibrations are less than in the free molecules [349]. In addition, *ab initio* results to investigate the vibrational spectra of sH $CH_4$ hydrate indicated that asymmetric and symmetric stretching vibrational frequencies of $CH_4$ molecules are higher in small cages of sH hydrate than in medium cavities, however, the H—C bond length in medium cavities is slightly longer [388]. Also, asymmetric and symmetric stretching vibrational frequencies of $CH_4$ molecules are higher in small cavities than in large ones of sI hydrate [389]. Based on the infrared spectra of sII $C_3H_8$, i-butane, $CH_4$ + $C_2H_6$, $CH_4$ + $C_3H_8$, and empty

hydrates using DFT, it was determined that the calculated vibrational frequencies of the guest and host molecules can give comparable results to experimental data which can be useful to detect the presence of gas hydrates [390]. Analysing the properties of multiple occupied $N_2$ clathrate hydrates showed that there is a large vibrational host–guest coupling for both double and single occupancies, however, the frequency range is broader in the former case [391]. To evaluate the mobility of water and $CO_2$ molecules in the hydrate phase, it was elucidated that negligible composition change leads to significant impacts on the mobility of $CO_2$ molecules. For example, altering 3 % cage occupancy may result in two orders of magnitude change in the diffusion coefficient [392]. Molecular $H_2$ mobility within the sII clathrate at 200–265 K demonstrated that on the time scale of the simulations, $H_2$ molecular mobility in the small cavities is not substantial but can be more stable with the presence of THF [393]. By analysing apparent high mobility and transport of interstitial $H_2O$ defects in $CH_4$ hydrate crystal it was concluded that $H_2O$ molecules are somewhat high mobile entities within a gas hydrate. Also, the presence of empty cavities facilitates the pathways for the $H_2O$ molecular transportation between them [394]. In addition, the hydration shell nucleation of guest molecules becomes more ordered with increasing the concentration of guest molecules, resulting in a decline of entropy and guest mobility [395]. The results of first-principles DFT and MD to determine the thermal properties of gas hydrates at very low temperatures confirmed the negative thermal expansion which is similar to the ice [396]. The structural and dynamical properties of $CO_2$, $CH_4$, and Xe hydrates indicated that by elevating the temperature, the lattice expansion of $CO_2$ hydrate is larger than that in Xe and $CH_4$ hydrates. Also, the thermal conductivities of both Xe and $CO_2$ are less than that in $CH_4$ or even empty lattice [397]. With respect to the analysis of structural and energetic properties of the sI and sII CO hydrate it was revealed that increasing the content of CO molecules in the large cages can stabilize the sII but destabilize sI hydrate [398]. Using the rotational autocorrelation function (RACF) to study the host and guest rotational dynamics, it was highlighted that altering the rotational motion of both water and guest molecules affect the proportion of them in mixed $CO_2$ + $CH_4$ hydrate [399]. Dynamical and energetic properties of $H_2$ + THF hydrate through EMD simulations determined that the van der Waals component with the surrounding water molecules in the constituent cavities is the largest contribution to the interaction energy of both guests [400]. By applying first-principles DFT to study the vibrational, structural, and mechanical properties of THF and THF + Xe hydrates, it was found that compared to THF hydrate, THF + Xe hydrate has a larger OH stretching frequency, lattice volume, hydrogen bond length but lower Poisson ratio, density, compressional wave velocity, and hydrogen bond stretching frequency [401].

### 3.7. Coexistence of phases

The phase equilibrium of clathrate hydrates more specifically those at thermodynamically difficult to conduct the experiments in a laboratory can be studied using MD simulations. For example, the thermodynamic stability of sII neon hydrate at 480 MPa and 260 K with employing MD simulations was confirmed [402]. Previously, by employing MDs, a new phase between equilibrium conditions of sT′ and $C_0$-II structures for $H_2$ hydrate was explored which helped to clarify the experimental puzzle of $H_2$ hydrates [115]. In addition, at ambient temperature and 3–130 GPa, the phase diagram of the $C_2$ structure of $H_2$ hydrate was determined [215]. However, the results of MD to determine the three-phase coexistence of $H_2$ hydrate at 90–400 MPa were found to underestimate the experiments by approximately 25 K [403]. The MD predictions of the three-phase coexistence of binary $CH_4$ + $CO_2$ hydrates at 40, 100, and 200 MPa compared to experimental data indicated that the deviation of simulations up to 100 MPa is not significant [404]. MD insights into the stability of CO hydrate at 17.3 MPa and 243 K revealed that CO tends to form sI rather than sII clathrate, however, with increasing pressure and temperature to 10 MPa and 252 K, it would be

more prone to generate sII clathrate hydrate [405]. In addition, *ab initio* intermolecular potentials at the MP2 level to calculate energy surfaces of $CH_4$-$H_2O$ and $CO_2$-$H_2O$ showed that the angle-dependent approach improves the prediction of the $CO_2$ and $CH_4$ hydrates phase equilibrium [406]. MD simulation of three-phase equilibrium suggested that compared to NPT simulation, NVT has two benefits: first, there is no need to control the pressure; second, NVT reduces the number of time steps in simulations. Therefore, it is more suitable to study the phase coexistence of gas hydrates [74]. Moreover, the equilibrium condition can be reached more accurately when the temperature and total energy become constant [407].

### 3.8. Gas exchange phenomenon

Evidence suggests the gas exchange occurs via a transient co-occupation of $CO_2$ and $CH_4$ in cages [408,409]. Both MD simulations as well as Raman spectroscopic confirmed that the process of $CO_2/CH_4$ replacement is the breakup of the cage, the scape of $CH_4$, and finally the cage occupation by $CO_2$ molecules [410]. It was also elucidated that during gas exchange phenomena, replacement takes place at both small and large cages of $CH_4$ hydrate without changing the structure and with the partial collapse in which the hydrate surface is partially melted so that the interface becomes active [119]. MD evidence indicated that the increase of temperature from 250 to 270 K accelerates the kinetics of the $CO_2/CH_4$ replacement by at least 1.5 times, also, a swap of the guest molecules without a breakup of cages was confirmed [409]. Previously, for $CO_2$ capture and storage analysis, Gibbs free energy calculations for $CO_2$ clathrate hydrates in the presence of $H_2S$, $CH_4$, $N_2$, and $SO_2$ were performed. Based on the results, the negative values of ΔG for $SO_2$ and $H_2S$ impurities compared to $CO_2$ showed more stability in the hydrate phase. Although at lower concentrations, these impurities act as promoters, large amounts of them decline the $CO_2$ capture and storage capacity [411]. According to the $CH_4$ + $CO_2$ hydrate formation, the concentration of $CO_2$ plays a key role in the kinetics of $CH_4$ + $CO_2$ hydrate formation. However, increasing $CO_2$ concentration in the aqueous phase cannot give faster growth [412]. It was also revealed that during the gas replacement process, $CO_2$ molecules in mixed bubbles mostly surround the $CH_4$ molecules so that they influence the process of gas exchange specifically at the initial stage [413]. MD investigations of the replacement or co-growth of $CO_2$ and $CH_4$ hydrates indicated that $CH_4$ hydrate in the presence of $CO_2$ gas is more stable than with $CO_2$ solution. It was also estimated that nearly 20 % of the dissociated $CH_4$ hydrates can be replaced by $CO_2$ and most likely $CO_2$ + $CH_4$ mixed hydrates can be formed [219]. Additionally, the guest behaviour in a porous environment would be dissimilar. MD exploration of the transport properties of $CH_4$ and $CO_2$ hydrates in Na-montmorillonite clay determined that increasing $CH_4$ and $CO_2$ molecules in Na-montmorillonite interlayers probably result in a decrease in their self-diffusion coefficients [199]. Also, the formation and dissociation of $CH_4$ hydrate in the clay pore with fatty acids showed that the existence of fatty acids slightly accelerates the breakdown of $CH_4$ hydrate in the heterogeneous sediment [227]. Moreover, the amorphous layer formation was detected as a barrier against mass transfer which results in a slower rate of $CO_2/CH_4$ replacement because as time proceeds, the $CO_2$ amorphous layer forms on the $CH_4$ hydrate surfaces [118].

Another barrier is that since $CH_4$ relative to $CO_2$ possesses a smaller size, it can be more stable in small cages [414]. Also, $N_2$ guests can be used as a carrier gas because it does not compete directly with $CO_2$ during $CH_4$ substitution. In addition, the substitution of $CH_4$ in the small cavities with $N_2$ has positive free energy [415]. The effects of $N_2$ on the process of $CO_2/CH_4$ replacement showed that the addition of $N_2$ aids $CO_2$ penetrate into all $CH_4$ hydrate cages on a broader scale. However, this diffusion is sensitive to the ratio of $CO_2$ to $N_2$ [220]. The $CH_4$ replacement by flue gas in the hydrate phase in the presence of $SO_2$, $H_2S$, $N_2O/NO$, and $CS_2$ revealed that $N_2O$, $SO_2$, and $CS_2$ molecules tend to occupy the large cavities of sII and sI hydrates while NO, and $H_2S$ have

no preference to occupy small or large cavities. It was also confirmed that $CS_2$, $N_2O$, $H_2S$, and $SO_2$ can replace $CH_4$ in the hydrate phase and help the process of gas exchange [416].

### 3.9. Memory effect phenomenon

Another feature of gas hydrate is the observation of a memory effect. In this phenomenon, the resulting solution from the decomposed hydrate is able to form a hydrate more readily with a shorter induction time than a fresh solution. Since a number of studies to test a memory effect have failed to observe this phenomenon, it may be concluded that the memory effect does occur for just specific hydrate systems. Generally, the most popular model for the memory effect is the residual structure hypothesis which assumes the dissociation of gas hydrates leads to the formation of some "hydrate melt". Therefore, residual structures that retain some structural features of the hydrate phase would persist in the liquid water phase for a long time after the dissociation. For example, guest molecules with associated pentagonal rings of hydrogen-bonded water molecules provide nucleation sites for the second formation of gas hydrate when they cooled again [7]. MD simulations of $CH_4$ hydrate pointed out that the lifetime of a hydrogen bond in water is of the order of picoseconds [417]. It was also assumed that the freezing of a bulk hydrate-forming solution occurs similarly to the freezing of bulk water in which the nucleation is mostly heterogeneous and rarely homogeneous in bulk solution [62]. MD investigations of the properties of melting temperature considering the memory effect suggested that the coordination atoms of oxygen in water are an important factor in the memory effect but water molecules near the interface of water-$CH_4$ have fewer memory properties [40]. Moreover, MD modelling of two-step nucleation and memory effect in $CH_4$ hydrate clarified that the areas locally richer by $CH_4$ molecules enhance the apparent nucleation rate more readily. Also, the memory of the crystal for fast recrystallization was found to be insignificant [4].

### 3.10. Self-preservation phenomenon

Self-preservation would be an advantageous property for the transportation and storage of gas hydrates. Quasi-harmonic lattice dynamics (QLD) model considering guest–guest interactions of multiple $H_2$ occupancies to predict self-preservation and the thermodynamic properties of sII $H_2$ hydrate specified that the pressure in the $H_2$ hydrate is more than that in the ice phase but the hydrogen bonds between the ice and hydrate do not allow hydrate to be destroyed, so that, the hydrate phase under heating remains stable [418]. The self-preservation mechanism using the combination of the NVT and NVE method for $CH_4$ hydrate also proved that the coupling of heat and mass transfer resistances is the driving mechanism for self-preservation impact [54]. According to MD simulations, the water self-diffusion coefficient can be changed by altering the temperature and guest concentration [56]. Based on the calculated order parameter, it was found that the order parameter value for ice, hydrate and liquid water phases by partially heating is different but it can be changed at the interfaces of the phases [53]. Through MD exploration of the self-preservation of hydrate dissociation using NVT/E to represent different levels of heat transfer resistance, it was observed that heat transfer resistance facilitates the formation of the solid-like layer which inhibits further hydrate dissociation. Also, the increase in pressure and particularly the decrease in temperature enhances self-preservation [54]. Moreover using MD algorithms, the number and type of cavities in the amorphous and clathrate (sI, sII, HS-I) coexist with ice during $CH_4$ hydrate self-preservation can be monitored [419]. Recently, the sources of the THF hydrate anomalous preservation surrounded by CP hydrate were evaluated outside the stability conditions. The melting temperature of uncoated THF hydrate was determined to be 270 K whereas THF hydrate encapsulated with CP hydrate could not be dissociated up to 290 K. This phenomenon also indicates the transformation of the THF hydrate from heterogeneous to homogeneous

mechanism. As Fig. 16 (a) shows, the potential energy of the coated THF hydrate for the 50 ns at 280 K can remain stable. Fig. 16 (b) indicates the partial breakup of coting layers of THF hydrate at 290 K which results in the liquid layer formation on top of the hydrate phase. With increasing temperature to 300 K, the potential energy suddenly elevates due to the dissociation of all CP hydrate followed by the breakdown of THF hydrate as the inner layer [420].

In the self-preservation phenomenon, the effects of H-bonds are also critical. In this regard, the influence of host–guest H-bond on the properties of $H_2S$/Xe + pinacolone/MTBE sH hydrates showed that MD simulation results are consistent with the observations of X-ray crystallographic at the temperature range from 100 K to 250 K [421]. Based on MD simulations of the halogen bonding in BrCl, mixed $Cl_2$ + $Br_2$, $Cl_2$, and $Br_2$ clathrate hydrates, the short and strong interactions between water molecules and bromine atoms in the sI clathrate hydrates were observed [422]. In addition, halogen bonding in $Cl_2$ and $Br_2$ clathrate hydrates studied via both MD simulations and DFT showed that the obtained halogen-water distances were compatible with values observed in X-ray diffraction [423]. The anomalous halogen bonding interactions between $Cl_2$ and $Br_2$ with water indicated that a combination of the dihalogen interaction with oxygen lone electron pairs may result in the halogen bonding non-bonded interactions between water in the clathrate and guest molecules [424]. To explore the hydrogen bonding in binary sI hydrate at 183–263 K, it was found that although gas molecules in the small cavity do not themselves form hydrogen bonds with water, the THF molecules affect the occurrence of hydrogen bonds. Also, nearest neighbour guest–guest interactions were found to influence the stability and structure of the clathrate network [425]. Hydrogen bonding study of pure and binary $CO_2$ + THF hydrates indicated that a small percentage of hydrogen bond formation between water and THF occurs, however, it cannot be seen through single-crystal X-ray diffraction at low temperatures. Interestingly, the presence of hydrogen bonding guests can increase $CO_2$ migration and boosts the hydrate formation kinetics [426]. MD simulations of the role of the medium and small cage guests on the hydrogen bonding of the large cage guests with the hydrate framework water molecules exhibited that the presence of $CH_3F$ enhances the H-bonding probability of the TBME with the water molecules [427]. Exploring the hydrogen bonding in binary sI hydrate at 100–250 K revealed that ethanol molecules by forming a long-lived proton- accepting and donating hydrogen bonds with water molecules, support the general cage integrity of clathrate hydrate [428]. The hydroxyl groups of inhibitors e.g. ethanol/1-propanol/2-propanol may act as both proton donors and proton acceptors. Also, the probability of H-bond between hydroxyl atoms with water molecules was found to be considerable [225]. By conducting the MD exploration of the microscopic properties of the HFC-41/$CH_4$ + pinacolone hydrate, although the anisotropic expansion of the sH hydrate lattice for sH HFC-41 + pinacolone hydrate was not observed, weak H-bonding of the water and pinacolone molecules was detected [223]. Recently, hydrogen bonding analysis for $CH_4$/HFC-32 + *N*-methylpiperidine (NMP) hydrate determined that for HFC-32 + NMP sH hydrate which was more stable than $CH_4$ + NMP sH hydrate, NMP molecules with water form H-bonds whereas similar hydrogen bonding for $CH_4$ + NMP system was not observed [429].

## 4. Proportions of MD gas hydrate investigations and future research guidelines

Fig. 17 exhibits the proportion of different MD studies that have been conducted on gas hydrates in the literature. As is shown, semiclathrate hydrates possess the least share of these investigations whereas over half of MD studies have been performed on pure gas hydrates. It should be kept in mind that to perceive fundamental microscopic characteristics of gas hydrates, most MD studies have been performed on $CH_4$ hydrate, therefore that is why its percentage is near one-third of the total explorations. In addition, the proportions of insight into the specifications
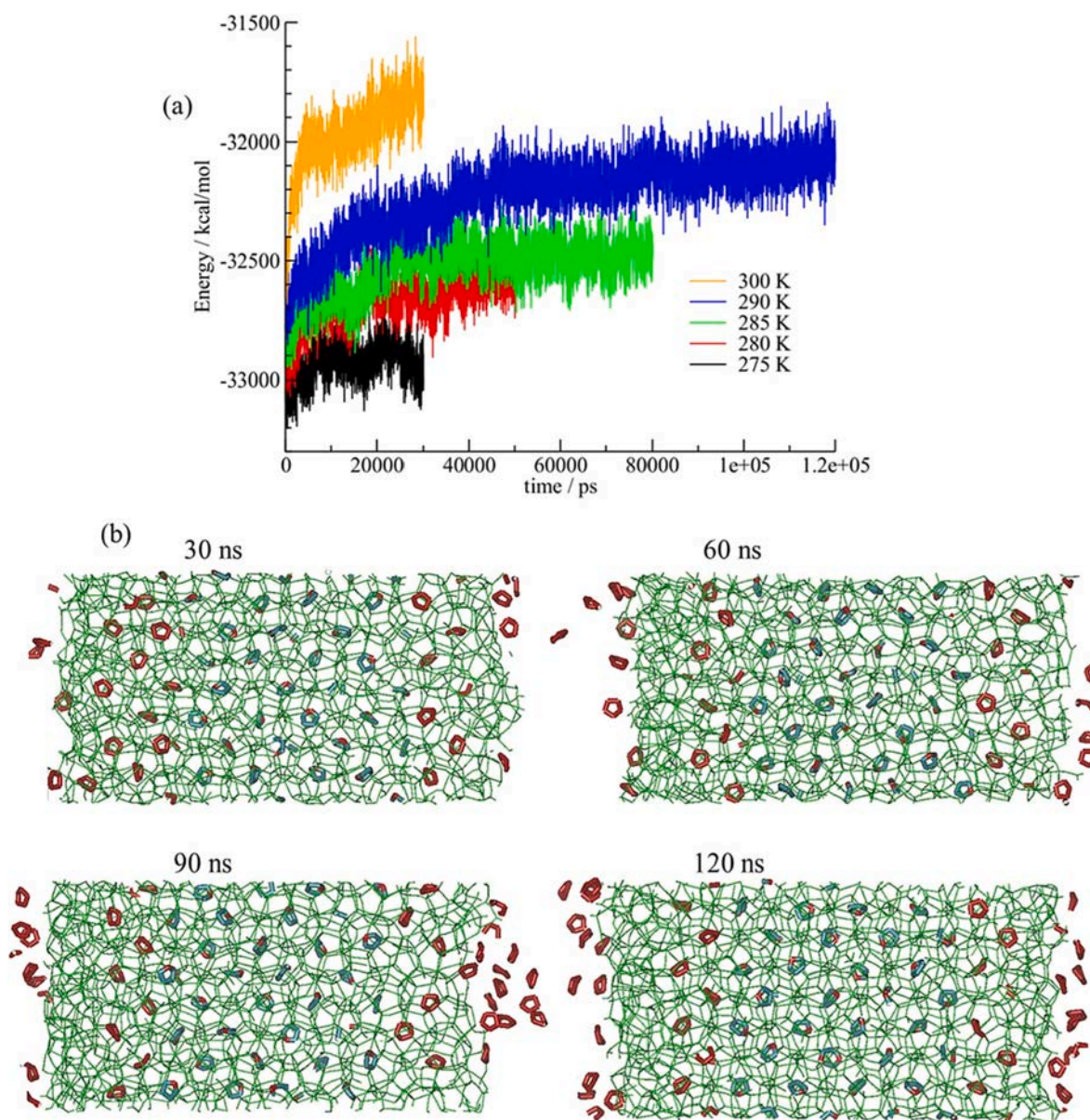
**Fig. 16.** (a), Time evolution of the potential energy of THF hydrate coated by CP hydrate at different temperatures; (b) Snapshots of THF–CP hydrate dissociation at 290 K [420].
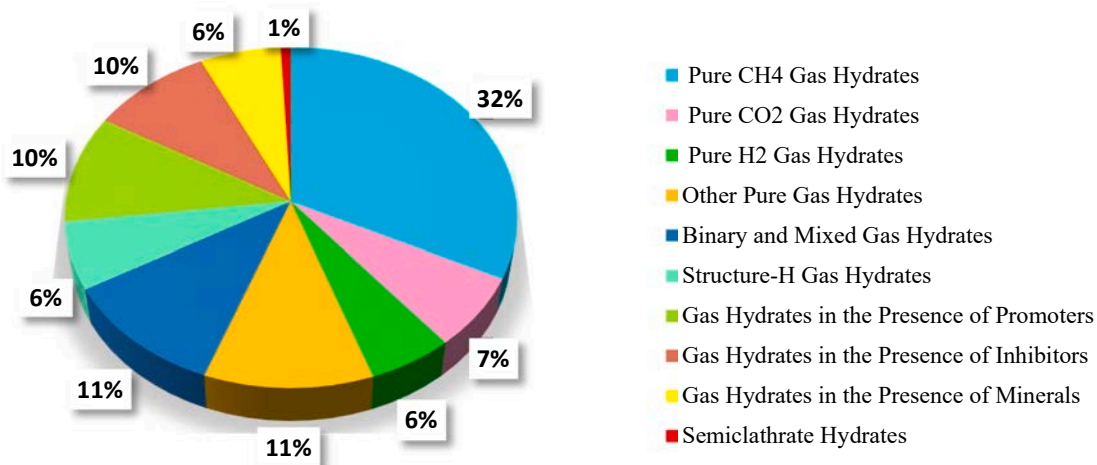


**Fig. 17.** The proportion of MD simulation studies on gas hydrates.

**Table 2**

Investigated phenomena for various hydrate systems using MD simulations.

| Component | | Dynamical and vibrational behaviour | Nucleation/ aggregation | Growth | Dissociation | Thermo-physical properties | Mechanical properties | Thermodynamic/ Kinetic properties | Morphology/ structural analysis (stabilization) | Heat and mass transfer properties | Memory effect | Self-preservation | Coexistence of phases/ Phase equilibrium | Cage occupancy/ capacity | Storage capacity | Ref. |
|---|---|---|---|---|---|---|---|---|---|---|---|---|---|---|---|---|
| Pure hydrates | $CH_4$ | * | * | * | * | * | * | * | * | * | * | * | * | * | * | [4,23,26,27,32–46,49–63,65–79,81,83,85,87–99,107,112,116,212–214,233,234,236,243,244,252–256,260,289,290,296,297,303,317,354,365,367–369,377,379,419,430] |
| | $H_2$ | * | * | * | * | * | * | | * | * | * | | | * | * | [40,114,115,215,217,293,306,330,384,403,418] |
| | $CO_2$ | * | * | * | * | * | * | * | * | * | * | | * | * | * | [25,211,220,246,327,360,426] |
| | $C_2H_4$, $C_2H_6$, $C_3H_8$ | * | * | * | * | * | * | | * | * | * | | * | * | * | [21,110,218,261,294,301,302,351] |
| | Acid gas ($H_2S$, CO, CS, $CS_2$, $SO_2$, $N_2O$) | * | * | * | * | * | | * | * | * | * | | | * | * | [209,239,352,360–362,385,398,405] |
| | Noble gas (Ar, Kr, Xe, Ne, $N_2$) | * | * | * | * | * | * | * | * | * | * | | * | * | * | [162,298,338,339,366,380,382,383,391,395,397,402] |
| | Liquid hydrocarbon (EO, CP, THF, THP, $C_3H_9NO$, $C_2H_4O$, $CH_2O$, $C_3H_6O_2$, $C_3H_8O$) | * | * | * | * | * | * | | * | * | * | | * | * | * | [105,109,231,232,247,249,262,364,381,396] |
| Gas hydrates + KHP/ THP | $CH_4/H_2$/Xe + THP ($C_3H_8$/THF/ TBME/ $C_2H_6$/TMO/ EO/FA/CB/ CP/ISA/ TBAB/$SF_6$/ Asphaltene) | * | * | * | * | * | * | * | * | * | * | | * | * | * | [108,130,131,140,141,167,207,251,266–270,299,307,329,332,333,335,336,346,371,374,386,393,400,401] |
| | $CH_4/H_2/N_2$ + KHP (SDS/ CAPB/ SWCNT/ Protein/ lecithin) | | * | * | * | | * | | * | * | * | * | | * | * | [139,184,265,300] |
| Gas hydrates + KHI/ THI | $CH_4 + C_2H_6$/ $C_3H_8/C_4H_{10}$ + THI (Salt: NaCl/$NH_4$Cl/ KCl/$CaCl_2$)/ (Alcohol: (methanol/ | * | * | * | * | * | * | | * | * | * | | | * | * | [165,168–171,181,224,225,274–276,280,310–314,326] |

28

**Table 2** (*continued*)

| Component | Dynamical and vibrational behaviour | Nucleation/aggregation | Growth | Dissociation | Thermo-physical properties | Mechanical properties | Thermodynamic/Kinetic properties | Morphology/structural analysis (stabilization) | Heat and mass transfer properties | Memory effect | Self-preservation | Coexistence of phases/Phase equilibrium | Cage occupancy/capacity | Storage capacity | Ref. |
|---|---|---|---|---|---|---|---|---|---|---|---|---|---|---|---|
| Ethanol/1-Propanol/2-Propanol/Propanol/Glycerol $CH_4$ + KHI (Na-MMT/LHA/Amino acids/PVPs/PVCap/PDMAEMA/PEO/VIMA/AFPs) | | * | * | * | * | * | | * | | * | | | | * | [166,172–180,182,183,278,279] |
| Mixed gas hydrates $CH_4$ + $C_2H_6$/$C_3H_8$/Acid gas ($H_2S$/CO/NO/$N_2O$/$SO_2$/$CS_2$) | * | * | * | * | * | * | * | * | * | * | | | * | * | [101,123,124,221,241,242,372,376,407,411,416] |
| $H_2$ + $CH_4$/$C_2H_6$/$C_3H_8$ | | * | * | * | * | * | | | | * | | | * | * | [250,264,295,337] |
| $Cl_2$ + BrCl/$Br_2$/$NH_3$ | * | | | | | * | | * | | | | | | | [308,420,422–424,427] |
| sH hydrates $H_2$/$CH_4$/$N_2$/Ar/Kr/Xe/$H_2S$ + LMGs | * | * | * | * | * | * | * | * | * | * | | | * | * | [149,151,155,159,160,222,223,309,340,344,345,373,421] |
| Hydrate + minerals $CH_4$ + NMP/$SiO_2$/Clay/Graphite/Kaolinite | * | * | * | * | * | * | * | * | * | * | | | * | | [29,195,196,202,226,227,282–285,291,292,355,357,363,429] |

29

of other pure, binary, and mixed gas hydrates, the effects of minerals, thermodynamic/kinetic promoters, and inhibitors have been reasonably close together.

In this work, different phenomena and properties of gas hydrates were overviewed. The summary list of MD computational studies conducted on clathrate (sI/II/H) hydrates ranging from pure/binary/mixed components, or in the presence of promoters/inhibitors/minerals is presented in Table 2.

The performed MD frameworks to analyse the phenomena and characteristics associated with hydrate-based applications either for gas separation or utilization can complete or at least support the experimental measurements. Despite a number of MD simulations of gas hydrates reported in the literature, conducting MD simulations to investigate unexplored gas hydrate characteristics can also complete the present findings at the microscopic level. Hence, we aim to highlight some suggestions for future research below:

- Additional MD investigations on the combined effects of various inhibitors and promoters such as KHI + THI and KHP + THP on clathrate hydrates to identify the relationship between hydrate phenomena and the presence of additives can be performed. These simulations may help to comprehend the characteristics connected to the performance parameters of hydrate-based gas separation, $CO_2$ hydrate utilization, or other hydrate-relevant applications.
- More MD simulations to understand some gas hydrate phenomena such as memory effect and self-preservation at different environmental or operating conditions need to be carried out.
- In spite of several experimental suggestions to utilize the semiclathrate hydrates in different processes of hydrate-based applications e.g. secondary refrigeration and air conditioning aims, the least proportion of MD simulations is for this type of gas hydrates. Therefore, a manifold of MD explorations to reveal the molecular mechanisms of semiclathrate hydrate promoters can be conducted.
- Only a few studies focused on clathrate hydrate structural transitions from sI to sII or sH and the coexistence of the phases based on the guest molecular sizes, shapes, and concentrations at the molecular scale. Hence, simulations considering different thermophysical properties during the process of structural transitions need to be performed.
- Heterogeneous nucleation MD simulations with fast mass transfer in the hydrate formation, and analyzing the role of nanobubbles during the nucleation phase can be considered for further research.
- To date, although some MD simulations in porous media have been performed, studying the systems simultaneously including mixed minerals e.g. kaolinite, quartz, montmorillonite, and kaolinite can help to assess the effects of these components on gas hydrate phenomena.
- In order to evaluate the influences of permeability and wettability on hydrate-bearing sediments, more MD studies should be carried out.
- Discrepancies between MD simulations and experimental outcomes in terms of consistency with the real condition can be assessed by providing simulations of the phenomena at larger scales. Therefore, a better understanding of the mutual relationship among mechanisms can be achieved.

## Declaration of Competing Interest

The authors declare that they have no known competing financial interests or personal relationships that could have appeared to influence the work reported in this paper.

## Data availability

Data will be made available on request.

## Acknowledgment

## Appendix A. Supplementary data

Supplementary data to this article can be found online at https://doi.org/10.1016/j.fuel.2022.127201.

## References

[1] Sloan ED, Koh CA. Clathrate hydrates of natural gases. 3rd ed. Taylor & Francis Group, Boca Raton: CRC Press; 2008.

[2] Suginaka T, Sakamoto H, Iino K, Sakakibara Y, Ohmura R. Phase equilibrium for ionic semiclathrate hydrate formed with CO2, CH4, or N2 plus tetrabutylphosphonium bromide. Fluid Phase Equilib 2013;344:108–11. https://doi.org/10.1016/j.fluid.2013.01.018.

[3] Sakamoto J, Hashimoto S, Tsuda T, Sugahara T, Inoue Y, Ohgaki K. Thermodynamic and Raman spectroscopic studies on hydrogen+tetra-n-butyl ammonium fluoride semi-clathrate hydrates. Chem Eng Sci 2008;63:5789–94. https://doi.org/10.1016/j.ces.2008.08.026.

[4] Liang S, Kusalik PG. Explorations of gas hydrate crystal growth by molecular simulations. Chem Phys Lett 2010;494:123–33. https://doi.org/10.1016/j.cplett.2010.05.088.

[5] English NJ, Macelroy JMD. Perspectives on molecular simulation of clathrate hydrates: Progress, prospects and challenges. Chem Eng Sci 2015;121:133–56. https://doi.org/10.1016/j.ces.2014.07.047.

[6] English NJ, Waldron CJ. Perspectives on external electric fields in molecular simulation: Progress, prospects and challenges. Phys Chem Chem Phys 2015;17:12407–40. https://doi.org/10.1039/c5cp00629e.

[7] Ripmeester JA, Alavi S. Some current challenges in clathrate hydrate science: Nucleation, decomposition and the memory effect. Curr Opin Solid State Mater Sci 2016;20:344–51. https://doi.org/10.1016/j.cossms.2016.03.005.

[8] Alavi S, Ripmeester JA. Simulations of hydrogen gas in clathrate hydrates. Mol Simul 2017;43:808–20. https://doi.org/10.1080/08927022.2017.1295456.

[9] Sinehbaghizadeh S, Saptoro A, Mohammadi AH. CO2 hydrate properties and applications: A state of the art. Prog Energy Combust Sci 2022;93:101026. https://doi.org/10.1016/j.pecs.2022.101026.

[10] Sokhan VP, Tildesley DJ. The free surface of water: molecular orientation, surface potential and nonlinear susceptibility. Mol Phys 1997;92:625–40. https://doi.org/10.1080/002689797169916.

[11] Stoddard SD, Ford J. Numerical experiments on the stochastic behavior of a Lennard-Jones gas system. Phys Rev A 1973;8:1504–12. https://doi.org/10.1103/PhysRevA.8.1504.

[12] Rapaport DC. The Art of Molecular dynamics simulation. Cambridge University Press; 2004. 10.1017/CBO9780511816581.

[13] Orsi M. Molecular dynamics simulation of humic substances. Chem Biol Technol Agric 2014;1:10. https://doi.org/10.1186/s40538-014-0010-4.

[14] Alavi S., Ripmeester J. Molecular simulations fundamentals and practice. vol. 1. 2020. 10.1002/9783527699452.

[15] Kohn W, Sham LJ. Self-consistent equations including exchange and correlation effects. Phys Rev 1965;140:1133–8. https://doi.org/10.1103/PhysRev.140.A1133.

[16] Tan H, Li Y, Zhang SB, Duan W. Effect of Hartree-Fock pseudopotentials on local density functional theory calculations. Phys Chem Chem Phys 2018;20:18844–9. https://doi.org/10.1039/C8CP00990B.

[17] Duan X-M, Song G-L, Li Z-H, Wang X-J, Chen G-H, Fan K-N. Accurate prediction of heat of formation by combining Hartree–Fock/density functional theory calculation with linear regression correction approach. J Chem Phys 2004;121:7086–95. https://doi.org/10.1063/1.1786582.

[18] Neese F, Wennmohs F, Hansen A, Becker U. Efficient, approximate and parallel Hartree-Fock and hybrid DFT calculations. A 'chain-of-spheres' algorithm for the Hartree-Fock exchange'. Chem Phys 2009;356:98–109. https://doi.org/10.1016/j.chemphys.2008.10.036.

[19] Adjiman CS, Sahinidis N V, Vlachos DG, Bakshi B, Maravelias CT, Georgakis C. Process systems engineering perspective on the design of materials and molecules. Ind Eng Chem Res 2021:acs.iecr.0c05399. 10.1021/acs.iecr.0c05399.

[20] Papadimitriou NI, Tsimpanogiannis IN, Economou IG, Stubos AK. Monte Carlo simulations of the separation of a binary gas mixture (CH4 + CO2) using hydrates. Phys Chem Chem Phys 2018;20:28026–38. https://doi.org/10.1039/C8CP02050G.

[21] Tanaka H. The thermodynamic stability of clathrate hydrate. III. Accommodation of nonspherical propane and ethane molecules. J Chem Phys 1994;101:10833–42. https://doi.org/10.1063/1.467832.

[22] Qiu N, Bai X, Sun N, Yu X, Yang L, Li Y, et al. Grand Canonical Monte Carlo simulations on phase equilibria of methane, carbon dioxide, and their mixture hydrates. J Phys Chem B 2018;122:9724–37. https://doi.org/10.1021/acs.jpcb.8b04551.

[23] Brumby PE, Yuhara D, Wu DT, Sum AK, Yasuoka K. Cage occupancy of methane hydrates from Gibbs ensemble Monte Carlo simulations. Fluid Phase Equilib 2016;413:242–8. https://doi.org/10.1016/j.fluid.2015.10.005.

[24] Radhakrishnan R, Trout BL. A new approach for studying nucleation phenomena using molecular simulations: Application to CO2 hydrate clathrates. J Chem Phys 2002;117:1786–96. https://doi.org/10.1063/1.1485962.

[25] Ferdows M, Ota M. Molecular simulation study for CO2 clathrate hydrate. Chem Eng Technol 2005;28:168–73. https://doi.org/10.1002/ceat.200407056.

[26] Taylor CE, Link DD, English N. Methane hydrate research at NETL: Research to make methane production from hydrates a reality. J Pet Sci Eng 2007;56:186–91. https://doi.org/10.1016/j.petrol.2005.08.006.

[27] Jin D, Coasne B. Molecular simulation of the phase diagram of methane hydrate: Free energy calculations, direct coexistence method, and hyperparallel tempering. Langmuir 2017;33:11217–30. https://doi.org/10.1021/acs.langmuir.7b02238.

[28] Trinh TT, Waage MH, van Erp TS, Kjelstrup S. Low barriers for hydrogen diffusion in sII clathrate. Phys Chem Chem Phys 2015;17:13808–12. https://doi.org/10.1039/C5CP01713K.

[29] Nath Chakraborty S, Gelb LD. A monte carlo simulation study of methane clathrate hydrates confined in slit-shaped pores. J Phys Chem B 2012;116:2183–97. https://doi.org/10.1021/jp205241n.

[30] Kirchner MT, Boese R, Billups WE, Norman LR. Gas hydrate single-crystal structure analyses. J Am Chem Soc 2004;126:9407–12. https://doi.org/10.1021/ja049247c.

[31] Takeuchi F, Hiratsuka M, Ohmura R, Alavi S, Sum AK, Yasuoka K. Water proton configurations in structures I, II, and H clathrate hydrate unit cells. J Chem Phys 2013;138:124504. https://doi.org/10.1063/1.4795499.

[32] Izadkhah S. Molecular insights into structural properties around the threshold of gas hydrate formation. Pet Sci Technol 2017;34:1964–71. https://doi.org/10.1080/10916466.2016.1235047.

[33] Varini N, English NJ, Trott CR. Molecular dynamics simulations of clathrate hydrates on specialised hardware platforms. Energies 2012;5:3526–33. https://doi.org/10.3390/en5093526.

[34] Tse JS, Klein ML, McDonald IR. Molecular dynamics studies of ice Ic and the structure I clathrate hydrate of methane. J Phys Chem 1983;87:4198–203. https://doi.org/10.1021/j100244a044.

[35] Rodger PM. Stability of gas hydrates. J Phys Chem 1990;94:6080–9. https://doi.org/10.1021/j100378a082.

[36] Hawtin RW, Quigley D, Rodger PM. Gas hydrate nucleation and cage formation at a water/methane interface. Phys Chem Chem Phys 2008;10:4853. https://doi.org/10.1039/b807455k.

[37] Guo G, Zhang Y, Liu C, Li K. Using the face-saturated incomplete cage analysis to quantify the cage compositions and cage linking structures of amorphous phase hydrates. Phys Chem Chem Phys 2011;13:12048. https://doi.org/10.1039/c1cp20070d.

[38] Bagherzadeh SA, Englezos P, Alavi S, Ripmeester J. Molecular simulation of non-equilibrium methane hydrate decomposition process. J Chem Thermodyn 2012;44:13–9. https://doi.org/10.1016/j.jct.2011.08.021.

[39] Conde MM, Vega C. Note: A simple correlation to locate the three phase coexistence line in methane-hydrate simulations. J Chem Phys 2013;138:14–6. https://doi.org/10.1063/1.4790647.

[40] Li Q, Liu C, Chen X. Molecular characteristics of dissociated water with memory effect from methane hydrates. Int J Mod Phys B 2014;28:1450062. https://doi.org/10.1142/S0217979214500623.

[41] Baghel VS, Kumar R, Roy S. Heat transfer calculations for decomposition of structure I methane hydrates by molecular dynamics simulation. J Phys Chem C 2013;117:12172–82. https://doi.org/10.1021/jp4023772.

[42] Baez L, Clancy P. Computer simulation of the crystal growth and dissolution of natural gas hydrates. Ann N Y Acad Sci 1994;715:177–86. https://doi.org/10.1111/j.1749-6632.1994.tb38833.x.

[43] Alavi S, Ripmeester JA. Nonequilibrium adiabatic molecular dynamics simulations of methane clathrate hydrate decomposition. J Chem Phys 2010;132:144703. https://doi.org/10.1063/1.3382341.

[44] English NJ, Macelroy JMD. Structural and dynamical properties of methane clathrate hydrates. J Comput Chem 2003;24:1569–81. https://doi.org/10.1002/jcc.10303.

[45] Li J, Wang Z. Fluctuation–dissipation analysis of nonequilibrium thermal transport at the hydrate dissociation interface. Phys Chem Chem Phys 2019;21:23492–500. https://doi.org/10.1039/C9CP04780H.

[46] Mirzaeifard S, Servio P, Rey AD. Multiscale modeling and simulation of water and methane hydrate crystal interface. Cryst Growth Des 2019;19:5142–51. https://doi.org/10.1021/acs.cgd.9b00578.

[47] Jorgensen WL. Revised TIPS for simulations of liquid water and aqueous solutions. J Chem Phys 1982;77:4156–63. https://doi.org/10.1063/1.444325.

[48] Ning FL, Glavatskiy K, Ji Z, Kjelstrup S, H. Vlugt TJ.. Compressibility, thermal expansion coefficient and heat capacity of CH4 and CO2 hydrate mixtures using molecular dynamics simulations. Phys Chem Chem Phys 2015;17:2869–83. https://doi.org/10.1039/C4CP04212C.

[49] Wang Q, Tang Q, Tian S. Molecular dynamics simulation of sI methane hydrate under compression and tension. Open Chem 2020;18:69–76. https://doi.org/10.1515/chem-2020-0008.

[50] English NJ, MacElroy JMD. Theoretical studies of the kinetics of methane hydrate crystallization in external electromagnetic fields. J Chem Phys 2004;120:10247–56. https://doi.org/10.1063/1.1730092.

[51] Cai S, Tang Q, Tian S, Lu Y, Gao X. Molecular simulation study on the microscopic structure and mechanical property of defect-containing sI methane hydrate. Int J Mol Sci 2019;20:2305. https://doi.org/10.3390/ijms20092305.

[52] Melgar D, Ghaani MR, Lauricella M, O'Brien GS, English NJ. Acoustic-propagation properties of methane clathrate hydrates from non-equilibrium molecular dynamics. J Chem Phys 2019;151:144505. https://doi.org/10.1063/1.5121712.

[53] Li Q, Tang Q, Peng T, Zhang X, Liu C, Shi X. Molecular characteristics of H2O in hydrate/ice/liquid water mixture. Int J Mod Phys B 2015;29:1550185. https://doi.org/10.1142/S0217979215501854.

[54] Bai D, Zhang D, Zhang X, Chen G. Origin of self-preservation effect for hydrate decomposition: Coupling of mass and heat transfer resistances. Sci Rep 2015;5:14599. https://doi.org/10.1038/srep14599.

[55] English N. Massively-parallel molecular dynamics simulation of clathrate hydrates on blue gene platforms. Energies 2013;6:3072–81. https://doi.org/10.3390/en6063072.

[56] Zhang J, Piana S, Freij-Ayoub R, Rivero M, Choi SK. Molecular dynamics study of methane in water: diffusion and structure. Mol Simul 2006;32:1279–86. https://doi.org/10.1080/08927020601039598.

[57] Vatamanu J, Kusalik PG. Unusual crystalline and polycrystalline structures in methane hydrates. J Am Chem Soc 2006;128:15588–9. https://doi.org/10.1021/ja066515t.

[58] Vatamanu J, Kusalik PG. Heterogeneous crystal growth of methane hydrate on its sII [001] Ccystallographic face. J Phys Chem B 2008;112:2399–404. https://doi.org/10.1021/jp077583k.

[59] Smirnov GS, Stegailov VV. Melting and superheating of sI methane hydrate: Molecular dynamics study. J Chem Phys 2012;136:44523. https://doi.org/10.1063/1.3679860.

[60] Docherty H, Galindo A, Vega C, Sanz E. A potential model for methane in water describing correctly the solubility of the gas and the properties of the methane hydrate. J Chem Phys 2006;125:74510. https://doi.org/10.1063/1.2335450.

[61] Guo G-J, Rodger PM. Solubility of aqueous methane under metastable conditions: Implications for gas hydrate nucleation. J Phys Chem B 2013;117:6498–504. https://doi.org/10.1021/jp3117215.

[62] Yagasaki T, Matsumoto M, Andoh Y, Okazaki S, Tanaka H. Effect of bubble formation on the dissociation of methane hydrate in water: A molecular dynamics study. J Phys Chem B 2014;118:1900–6. https://doi.org/10.1021/jp412692d.

[63] Liang S, Yi L, Liang D. Molecular insights into the homogeneous melting of methane hydrates. J Phys Chem C 2014;118:28542–7. https://doi.org/10.1021/jp511362s.

[64] Nguyen NN, Nguyen AV, Steel KM, Dang LX, Galib M. Interfacial gas enrichment at hydrophobic surfaces and the origin of promotion of gas hydrate formation by hydrophobic solid particles. J Phys Chem C 2017;121:3830–40. https://doi.org/10.1021/acs.jpcc.6b07136.

[65] Walsh M, Beckham G, Koh C, Sloan ED, Wu D, Sum A. Methane hydrate nucleation rates from molecular dynamics simulations: Effects of aqueous methane concentration, interfacial curvature, and system size. J Phys Chem C 2011;115:21241–8. https://doi.org/10.1021/jp206483q.

[66] Barnes BC, Knott BC, Beckham GT, Wu DT, Sum AK. Reaction coordinate of incipient methane clathrate hydrate nucleation. J Phys Chem B 2014;118:13236–43. https://doi.org/10.1021/jp507959q.

[67] Jiménez-Ángeles F, Firoozabadi A. Nucleation of methane hydrates at moderate subcooling by molecular dynamics simulations. J Phys Chem C 2014;118:11310–8. https://doi.org/10.1021/jp5002012.

[68] Jiménez-Ángeles F, Firoozabadi A. Induced charge density and thin liquid film at hydrate/methane gas interfaces. J Phys Chem C 2014;118:26041–8. https://doi.org/10.1021/jp507160s.

[69] Yuhara D, Barnes BC, Suh D, Knott BC, Beckham GT, Yasuoka K, et al. Nucleation rate analysis of methane hydrate from molecular dynamics simulations. Faraday Discuss 2015;179:463–74. https://doi.org/10.1039/C4FD00219A.

[70] Xu T, Lang X, Fan S, Wang Y, Chen J. The effect of electric fields in methane hydrate growth and dissociation: A molecular dynamics simulation. Comput Theor Chem 2019;1149:57–68. https://doi.org/10.1016/j.comptc.2018.12.018.

[71] Bagherzadeh SA, Alavi S, Ripmeester J, Englezos P. Formation of methane nano-bubbles during hydrate decomposition and their effect on hydrate growth. J Chem Phys 2015;142:214701. https://doi.org/10.1063/1.4920971.

[72] Wu J, Ning F, Trinh TT, Kjelstrup S, Vlugt TJH, He J, et al. Mechanical instability of monocrystalline and polycrystalline methane hydrates. Nat Commun 2015;6:8743. https://doi.org/10.1038/ncomms9743.

[73] Chakraborty SN, English NJ. Hydrogen-bond vibrational and energetic dynamical properties in sI and sII clathrate hydrates and in ice Ih: Molecular dynamics insights. J Chem Phys 2015;143:154504. https://doi.org/10.1063/1.4932681.

[74] Yuhara D, Brumby PE, Wu DT, Sum AK, Yasuoka K. Analysis of three-phase equilibrium conditions for methane hydrate by isometric-isothermal molecular dynamics simulations. J Chem Phys 2018;148:184501. https://doi.org/10.1063/1.5016609.

[75] Luis DP, Herrera-Hernández EC, Saint-Martin H. A theoretical study of the dissociation of the sI methane hydrate induced by an external electric field. J Chem Phys 2015;143:204503. https://doi.org/10.1063/1.4936214.

[76] Walsh MR, Koh CA, Sloan ED, Sum AK, Wu DT. Microsecond simulations of spontaneous methane hydrate nucleation and growth. Science (80-) 2009;326:1095–8. https://doi.org/10.1126/science.1174010.

[77] Walsh MR, Rainey JD, Lafond PG, Park D-H, Beckham GT, Jones MD, et al. The cages, dynamics, and structuring of incipient methane clathrate hydrates. Phys Chem Chem Phys 2011;13:19951. https://doi.org/10.1039/c1cp21899a.

[78] English NJ, Johnson JK, Taylor CE. Molecular-dynamics simulations of methane hydrate dissociation. J Chem Phys 2005;123:244503. https://doi.org/10.1063/1.2138697.

[79] Rosenbaum EJ, English NJ, Johnson JK, Shaw DW, Warzinski RP. Thermal conductivity of methane hydrate from experiment and molecular simulation. J Phys Chem B 2007;111:13194–205. https://doi.org/10.1021/jp074419o.

[80] Cendagorta JR, Powers A, Hele TJH, Marsalek O, Bačić Z, Tuckerman ME. Competing quantum effects in the free energy profiles and diffusion rates of hydrogen and deuterium molecules through clathrate hydrates. Phys Chem Chem Phys 2016;18:32169–77. https://doi.org/10.1039/C6CP05968F.

[81] Ding LY, Geng CY, Zhao YH, Wen H. Molecular dynamics simulation on the dissociation process of methane hydrates. Mol Simul 2007;33:1005–16. https://doi.org/10.1080/08927020701528524.

[82] Chialvo AA, Houssa M, Cummings PT. Molecular dynamics study of the structure and thermophysical properties of model sI clathrate hydrates. J Phys Chem B 2002;106:442–51. https://doi.org/10.1021/jp012735b.

[83] Jiang H, Jordan KD, Taylor CE. Molecular dynamics simulations of methane hydrate using polarizable force fields. J Phys Chem B 2007;111:6486–92. https://doi.org/10.1021/jp068505k.

[84] Costandy J, Michalis VK, Tsimpanogiannis IN, Stubos AK, Economou IG. Molecular dynamics simulations of pure methane and carbon dioxide hydrates: lattice constants and derivative properties. Mol Phys 2016;114:2672–87. https://doi.org/10.1080/00268976.2016.1241442.

[85] Jiang H, Myshakin EM, Jordan KD, Warzinski RP. Molecular dynamics simulations of the thermal conductivity of methane hydrate. J Phys Chem B 2008; 112:10207–16. https://doi.org/10.1021/jp802942v.

[86] Molinero V, Moore EB. Water modeled as an intermediate element between carbon and silicon. J Phys Chem B 2009;113:4008–16. https://doi.org/10.1021/jp805227c.

[87] Lauricella M, Ciccotti G, English NJ, Peters B, Meloni S. Mechanisms and nucleation rate of methane hydrate by dynamical nonequilibrium molecular dynamics. J Phys Chem C 2017;121:24223–34. https://doi.org/10.1021/acs.jpcc.7b05754.

[88] Cao P, Wu J, Zhang Z, Fang B, Ning F. Mechanical properties of methane hydrate: Intrinsic differences from ice. J Phys Chem C 2018;122:29081–93. https://doi.org/10.1021/acs.jpcc.8b06002.

[89] Bi Y, Li T. Probing methane hydrate nucleation through the forward flux sampling method. J Phys Chem B 2014;118:13324–32. https://doi.org/10.1021/jp503000u.

[90] Sveinsson HA, Malthe-Sørenssen A. Molecular-scale thermally activated fractures in methane hydrates: a molecular dynamics study. Phys Chem Chem Phys 2019; 21:13539–44. https://doi.org/10.1039/C9CP01337G.

[91] Knott BC, Molinero V, Doherty MF, Peters B. Homogeneous nucleation of methane hydrates: Unrealistic under realistic conditions. J Am Chem Soc 2012; 134:19544–7. https://doi.org/10.1021/ja309117d.

[92] Nguyen AH, Jacobson LC, Molinero V. Structure of the clathrate/solution interface and mechanism of cross-nucleation of clathrate hydrates. J Phys Chem C 2012;116:19828–38. https://doi.org/10.1021/jp305468s.

[93] English NJ, Lauricella M, Meloni S. Massively parallel molecular dynamics simulation of formation of clathrate-hydrate precursors at planar water-methane interfaces: Insights into heterogeneous nucleation. J Chem Phys 2014;140: 204714. https://doi.org/10.1063/1.4879777.

[94] Bi Y, Porras A, Li T. Free energy landscape and molecular pathways of gas hydrate nucleation. J Chem Phys 2016;145:211909. https://doi.org/10.1063/1.4961241.

[95] Lauricella M, Meloni S, English NJ, Peters B, Ciccotti G. Methane clathrate hydrate nucleation mechanism by advanced molecular simulations. J Phys Chem C 2014;118:22847–57. https://doi.org/10.1021/jp5052479.

[96] Chihaia V, Adams S, Kuhs WF. Molecular dynamics simulations of properties of a (001) methane clathrate hydrate surface. Chem Phys 2005;317:208–25. https://doi.org/10.1016/j.chemphys.2005.05.024.

[97] Zhang J, Pan Z. Effect of potential energy on the formation of methane hydrate. J Pet Sci Eng 2011;76:148–54. https://doi.org/10.1016/j.petrol.2011.01.004.

[98] Waldron CJ, Lauricella M, English NJ. Structural and dynamical properties of methane clathrate hydrates from molecular dynamics: Comparison of atomistic and more coarse-grained potential models. Fluid Phase Equilib 2016;413:235–41. https://doi.org/10.1016/j.fluid.2015.12.030.

[99] Jacobson LC, Molinero V. A methane−water model for coarse-grained simulations of solutions and clathrate hydrates. J Phys Chem B 2010;114: 7302–11. https://doi.org/10.1021/jp1013576.

[100] Burnham CJ, English NJ. Study of clathrate hydrates via equilibrium molecular-dynamics simulation employing polarisable and non-polarisable, rigid and flexible water models. J Chem Phys 2016;144:164503. https://doi.org/10.1063/1.4947039.

[101] Plattner N, Bandi T, Doll JD, Freeman DL, Meuwly M. MD simulations using distributed multipole electrostatics: Structural and spectroscopic properties of CO and methane containing clathrates. Mol Phys 2008;106:1675–84. https://doi.org/10.1080/00268970802314394.

[102] Míguez JM, Conde MM, Torré J, Blas FJ, Piñeiro MM, Vega C. Molecular dynamics simulation of CO2 hydrates : Prediction of three phase coexistence line Molecular dynamics simulation of CO 2 hydrates : Prediction of three phase coexistence line 2015;124505. 10.1063/1.4916119.

[103] Alavi S, Ripmeester JA, Klug DD. Molecular dynamics study of the stability of methane structure H clathrate hydrates Molecular dynamics study of the stability of methane structure H clathrate hydrates 2007;124708. 10.1063/1.2710261.

[104] Jiao L, Wang Z, Li J, Zhao P, Wan R. Stability and dissociation studies of CO2 hydrate under different systems using molecular dynamic simulations. J Mol Liq 2021;338:116788. https://doi.org/10.1016/j.molliq.2021.116788.

[105] Mohammadi-Manesh H, Ghafari H, Alavi S. Molecular dynamics study of guest–host hydrogen bonding in ethylene oxide, trimethylene oxide, and formaldehyde structure I clathrate hydrates. J Phys Chem C 2017;121:8832–40. https://doi.org/10.1021/acs.jpcc.7b00218.

[106] Iwai Y, Nakamura H, Arai Y, Shimoyama Y. Analysis of dissociation process for gas hydrates by molecular dynamics simulation. Mol Simul 2010;36:246–53. https://doi.org/10.1080/08927020903307529.

[107] Michalis VK, Costandy J, Tsimpanogiannis IN, Stubos AK, Economou IG. Prediction of the phase equilibria of methane hydrates using the direct phase coexistence methodology. J Chem Phys 2015;142:44501. https://doi.org/10.1063/1.4905572.

[108] Veesam SK, Punnathanam SN. Computation of the dissociation temperature of TBAB semiclathrate in an aqueous solution using molecular simulations. J Phys Chem B 2020;124:9195–203. https://doi.org/10.1021/acs.jpcb.0c05238.

[109] Udachin K, Alavi S, Ripmeester JA. Communication: Single crystal x-ray diffraction observation of hydrogen bonding between 1-propanol and water in a structure II clathrate hydrate. J Chem Phys 2011;134:65–8. https://doi.org/10.1063/1.3574393.

[110] Wilson DT, Barnes BC, Wu DT, Sum AK. Molecular dynamics simulations of the formation of ethane clathrate hydrates. Fluid Phase Equilib 2016;413:229–34. https://doi.org/10.1016/j.fluid.2015.12.001.

[111] Sarupria S, Debenedetti PG. Molecular dynamics study of carbon dioxide hydrate dissociation. J Phys Chem A 2011;115:6102–11. https://doi.org/10.1021/jp110868t.

[112] Li J, Liang Z, Wang Z, Bao W. Molecular dynamics simulation of decomposition of methane hydrate and interfacial characteristics in nanostructure region. Int J Thermophys 2020;41:13. https://doi.org/10.1007/s10765-019-2591-4.

[113] Tung Y, Chen L-J, Chen Y, Lin S. Growth of structure I carbon dioxide hydrate from molecular dynamics simulations. J Phys Chem C 2011;115:7504–15. https://doi.org/10.1021/jp112205x.

[114] Smirnov G, Stegailov V. Anomalous diffusion of guest molecules in hydrogen gas hydrates. High Temp 2015;53:829–36. https://doi.org/10.1134/S0018151X15060188.

[115] Smirnov GS, Stegailov VV. Toward determination of the new hydrogen hydrate clathrate structures. J Phys Chem Lett 2013;4:3560–4. https://doi.org/10.1021/jz401669d.

[116] Zhang Z, Liu C-J-J, Walsh MR, Guo G-J-J. Effects of ensembles on methane hydrate nucleation kinetics. Phys Chem Chem Phys 2016;18:15602–8. https://doi.org/10.1039/C6CP02171A.

[117] Sizova A, Sizov V, Brodskaya E. Molecular dynamics simulation of the stability of spherical nanoclusters of methane and carbon dioxide hydrates. Colloid J 2020; 82:180–7. https://doi.org/10.1134/S1061933X2002012X.

[118] Bai D, Zhang X, Chen G, Wang W. Replacement mechanism of methane hydrate with carbon dioxide from microsecond molecular dynamics simulations. Energy Environ Sci 2012;5:7033. https://doi.org/10.1039/c2ee21189k.

[119] Iwai Y, Nakamura H, Hirata M. Molecular dynamics simulation of replacement of methane hydrate with carbon dioxide. Mol Simul 2012;38:481–90. https://doi.org/10.1080/08927022.2011.647817.

[120] Xu C-G, Cai J, Yu Y-S, Chen Z-Y, Li X-S. Research on micro-mechanism and efficiency of CH4 exploitation via CH4-CO2 replacement from natural gas hydrates. Fuel 2018;216:255–65. https://doi.org/10.1016/j.fuel.2017.12.022.

[121] Klapproth A, Piltz RO, Kennedy SJ, Kozielski KA. Kinetics of sII and mixed sI/sII, gas hydrate growth for a methane/propane mixture using neutron diffraction. J Phys Chem C 2019;123:2703–15. https://doi.org/10.1021/acs.jpcc.8b06693.

[122] Yang Y, Narayanan Nair AK, Sun S. Molecular dynamics simulation study of carbon dioxide, methane, and their mixture in the presence of brine. J Phys Chem B 2017;121:9688–98. https://doi.org/10.1021/acs.jpcb.7b08118.

[123] Zhang Z, Guo G-J, Wu N, Kusalik PG. Molecular insights into guest and composition dependence of mixed hydrate nucleation. J Phys Chem C 2020;124: 25078–86. https://doi.org/10.1021/acs.jpcc.0c07375.

[124] Hall KW, Carpendale S, Kusalik PG. Evidence from mixed hydrate nucleation for a funnel model of crystallization. Proc Natl Acad Sci 2016;113:12041–6. https://doi.org/10.1073/pnas.1610437113.

[125] Buch V, Devlin JP, Monreal IA, Jagoda-Cwiklik B, Uras-Aytemiz N, Cwiklik L. Clathrate hydrates with hydrogen-bonding guests. Phys Chem Chem Phys 2009; 11:10245. https://doi.org/10.1039/b911600c.

[126] Chapoy A, Anderson R, Tohidi B. Low-Pressure Molecular Hydrogen Storage in Semi-clathrate Hydrates of Quaternary Ammonium Compounds. J Am Chem Soc 2007;129:746–7. https://doi.org/10.1021/ja066883x.

[127] Strobel TA, Hester KC, Koh CA, Sum AK, Sloan ED. Properties of the clathrates of hydrogen and developments in their applicability for hydrogen storage. Chem Phys Lett 2009;478:97–109. https://doi.org/10.1016/j.cplett.2009.07.030.

[128] Lee BR, Sa J-H, Hong SY, Lee JD, Lee K-H, Seo Y, et al. Guest-Guest interactions and co-occupation by distinct guests in the metastable state of clathrate hydrates. J Phys Chem C 2019;123:3811–6. https://doi.org/10.1021/acs.jpcc.8b08629.

[129] Sinehbaghizadeh S, Saptoro A, Amjad-Iranagh S, Tze Tiong AN, Mohammadi AH. Molecular dynamics simulation studies on the stability and dissociation of clathrate hydrates of single and double greenhouse gases. Energy Fuel 2022;36: 8323–39. https://doi.org/10.1021/acs.energyfuels.2c01396.

[130] Hasegawa T, Brumby PE, Yasuoka K, Sum AK. Mechanism for H2 diffusion in sII hydrates by molecular dynamics simulations. J Chem Phys 2020;153:054706. https://doi.org/10.1063/5.0017505.

[131] Tian H, Zhang Z. Revealing the growth of H2 + THF binary hydrate through molecular simulations. Energy Fuel 2020;34:15004–10. https://doi.org/10.1021/acs.energyfuels.0c03096.

[132] Castillo-Borja F, Bravo-Sánchez UI, Vázquez-Román R, Díaz-Ovalle CO. Biogas purification via sII hydrates in the presence of THF and DMSO solutions using MD simulations. J Mol Liq 2020;297:111904. https://doi.org/10.1016/j.molliq.2019.111904.

[133] Torré J-P, Ricaurte M, Dicharry C, Broseta D. CO2 enclathration in the presence of water-soluble hydrate promoters: Hydrate phase equilibria and kinetic studies in quiescent conditions. Chem Eng Sci 2012;82:1–13. https://doi.org/10.1016/j.ces.2012.07.025.

[134] Albertí M, Pirani F, Laganà A. Carbon dioxide clathrate hydrates: Selective role of intermolecular interactions and action of the SDS catalyst. J Phys Chem A 2013; 117:6991–7000. https://doi.org/10.1021/jp3126158.

[135] Zhang L, Sun L, Lu Y, Kuang Y, Liang Z, Yang L, et al. Molecular dynamics simulation and in-situ MRI observation of organic exclusion during CO2 hydrate growth. Chem Phys Lett 2021;764:138287. https://doi.org/10.1016/j.cplett.2020.138287.

[136] Lim LHV, Lloren AV, Lamorena RB. The effect of urea in the nucleation process of CO2 clathrate hydrates. J Mol Liq 2014;194:245–50. https://doi.org/10.1016/j.molliq.2014.03.003.

[137] Wang P-W, Wu DT, Lin S-T. Promotion mechanism for the growth of CO2 hydrate with urea using molecular dynamics simulations. Chem Commun 2021. https://doi.org/10.1039/D0CC06165D.

[138] Sinehbaghizadeh S, Saptoro A, Naeiji P, Tiong ANT, Mohammadi AH. Insights into the synergistic effects of metal particles (Ag, Cu, and Fe) and urea on CO2 clathrate hydrate growth using molecular dynamics simulations. Chem Eng Sci 2022;264:118194. https://doi.org/10.1016/j.ces.2022.118194.

[139] Hande V, Choudhary N, Chakrabarty S, Kumar R. Morphology and dynamics of self-assembled structures in mixed surfactant systems (SDS + CAPB) in the context of methane hydrate growth. J Mol Liq 2020;319:114296. https://doi.org/10.1016/j.molliq.2020.114296.

[140] Wang L, Jiang G, Zhang X. Modeling and molecular simulation of natural gas hydrate stabilizers. Eur J Remote Sens 2020:1–12. https://doi.org/10.1080/22797254.2020.1738901.

[141] Ghaani MR, Allen C, Skvortsov T, English NJ. Engineering peptides to catalyze and control stabilization of gas hydrates: Learning from nature. J Phys Chem Lett 2020;11:5068–75. https://doi.org/10.1021/acs.jpclett.0c01224.

[142] Liu N, Zhu H, Zhou J, Yang L, Liu D. Molecular dynamics simulations on formation of CO2 hydrate in the presence of metal particles. J Mol Liq 2021;331:115793. https://doi.org/10.1016/j.molliq.2021.115793.

[143] Kuznetsova T, Jensen B, Kvamme B, Sjøblom S. Water-wetting surfaces as hydrate promoters during transport of carbon dioxide with impurities. Phys Chem Chem Phys 2015;17:12683–97. https://doi.org/10.1039/C5CP00660K.

[144] Sinehbaghizadeh S, Javanmardi J, Mohammadi AH. Phase stability conditions of clathrate hydrates in the (methane + 3-methyl-1-butanol + water), (methane + 3,3-dimethyl-2-butanone + water) and (methane + 2,3-dimethyl-2-butene + water) systems: Experimental measurements and thermodynamic modeling. J Chem Thermodyn 2018;125:64–70. https://doi.org/10.1016/j.jct.2018.05.006.

[145] Sinehbaghizadeh S, Javanmardi J, Roosta A, Mohammadi AH. A fugacity approach for prediction of phase equilibria of methane clathrate hydrate in structure H. Phys Chem Chem Res 2017;5(465–81). https://doi.org/10.22036/pcr.2017.69958.1334.

[146] Sinehbaghizadeh S, Roosta A, Rezaei N, Ghiasi MM, Javanmardi J, Zendehboudi S. Evaluation of phase equilibrium conditions of clathrate hydrates using connectionist modeling strategies. Fuel 2019;255:115649. https://doi.org/10.1016/j.fuel.2019.115649.

[147] Sinehbaghizadeh S, Javanmardi J, Roosta A, Mohammadi AH. Estimation of the dissociation conditions and storage capacities of various sH clathrate hydrate systems using effective deterministic frameworks. Fuel 2019;247:272–86. https://doi.org/10.1016/j.fuel.2019.01.189.

[148] Jokar SM, Wood DA, Sinehbaghizadeh S, Parvasi P, Javanmardi J. Transformation of associated natural gas into valuable products to avoid gas wastage in the form of flaring. J Nat Gas Sci Eng 2021::104078. https://doi.org/10.1016/j.jngse.2021.104078.

[149] Liu J, Yan YY, Chen G, Hou J, Yan YY, Liu H, et al. Prediction of efficient promoter molecules of sH hydrogen hydrate: An ab initio study. Chem Phys 2019; 516:15–21. https://doi.org/10.1016/j.chemphys.2018.08.032.

[150] Zhang Z, Kusalik PG, Guo G-J. Might a 2,2-Dimethylbutane Molecule Serve as a Site to Promote Gas Hydrate Nucleation? J Phys Chem C 2019;123:20579–86. https://doi.org/10.1021/acs.jpcc.9b04518.

[151] Murayama K, Takeya S, Alavi S, Ohmura R. Anisotropic lattice expansion of structure H clathrate hydrates induced by help guest: Experiments and molecular dynamics simulations. J Phys Chem C 2014;118:21323–30. https://doi.org/10.1021/jp5058786.

[152] Tezuka K, Murayama K, Takeya S, Alavi S, Ohmura R. Effect of guest size and conformation on crystal structure and stability of structure H clathrate hydrate: Experimental and molecular dynamics simulation studies. J Phys Chem C 2013; 117:10473–82. https://doi.org/10.1021/jp4005899.

[153] Imasato K, Murayama K, Takeya S, Alavi S, Ohmura R. Effect of nitrogen atom substitution in cyclic guests on properties of structure H clathrate hydrates. Can J Chem 2015;93:906–12. https://doi.org/10.1139/cjc-2014-0553.

[154] Huo H, Liu Y, Zheng Z, Zhao J, Jin C, Lv T. Mechanical and thermal properties of methane clathrate hydrates as an alternative energy resource. J Renew Sustain Energy 2011;3:63110. https://doi.org/10.1063/1.3670410.

[155] Daghash SM, Servio P, Rey AD. Elastic properties and anisotropic behavior of structure-H (sH) gas hydrate from first principles. Chem Eng Sci 2020;227:115948. https://doi.org/10.1016/j.ces.2020.115948.

[156] Jendi ZM, Rey AD, Servio P. Ab initio DFT study of structural and mechanical properties of methane and carbon dioxide hydrates. Mol Simul 2015;41:572–9. https://doi.org/10.1080/08927022.2014.899698.

[157] Vlasic TM, Servio PD, Rey AD. Effect of guest size on the mechanical properties and molecular structure of gas hydrates from first-principles. Cryst Growth Des 2017;17:6407–16. https://doi.org/10.1021/acs.cgd.7b01072.

[158] Erfan-Niya H, Modarress H. Molecular dynamics simulation of structure H clathrate-hydrates of binary guest molecules. J Nat Gas Chem 2011;20:577–84. https://doi.org/10.1016/S1003-9953(10)60242-3.

[159] Reshadi P, Modarress H, Dabir B, Amjad-iranagh S. Molecular dynamics simulation for studying the stability of structure H clathrate-hydrates of argon and large guest molecules. J Dispers Sci Technol 2018:1–10. https://doi.org/10.1080/01932691.2018.1446145.

[160] Daghash SM, Servio P, Rey AD. Structural properties of sH hydrate: a DFT study of anisotropy and equation of state. Mol Simul 2019;45:1524–37. https://doi.org/10.1080/08927022.2019.1660326.

[161] Okano Y, Yasuoka K. Free-energy calculation of structure-H hydrates. J Chem Phys 2006;124:24510. https://doi.org/10.1063/1.2150430.

[162] Tanaka H, Kiyohara K. The thermodynamic stability of clathrate hydrate. II. Simultaneous occupation of larger and smaller cages. J Chem Phys 1993;98:8110–8. https://doi.org/10.1063/1.464567.

[163] Kelland MA. History of the development of low dosage hydrate inhibitors. Energy Fuel 2006;20:825–47. https://doi.org/10.1021/ef050427x.

[164] Gao S. Hydrate risk management at high watercuts with anti-agglomerant hydrate inhibitors. Energy Fuel 2009;23:2118–21. https://doi.org/10.1021/ef8009876.

[165] Mehrabian H, Bellucci MA, Walsh MR, Trout BL. Effect of salt on antiagglomerant surface adsorption in natural gas hydrates. J Phys Chem C 2018;122:12839–49. https://doi.org/10.1021/acs.jpcc.8b03154.

[166] Naullage PM, Bertolazzo AA, Molinero V. How do surfactants control the agglomeration of clathrate hydrates? ACS Cent Sci 2019;5:428–39. https://doi.org/10.1021/acscentsci.8b00755.

[167] Zi M, Chen D, Wu G. Molecular dynamics simulation of methane hydrate formation on metal surface with oil. Chem Eng Sci 2018;191:253–61. https://doi.org/10.1016/j.ces.2018.06.070.

[168] Yagasaki T, Matsumoto M, Tanaka H. Effects of thermodynamic inhibitors on the dissociation of methane hydrate: a molecular dynamics study. Phys Chem Chem Phys 2015;17:32347–57. https://doi.org/10.1039/C5CP03008K.

[169] Storr MT, Taylor PC, Monfort J-P, Rodger PM. Kinetic inhibitor of hydrate crystallization. J Am Chem Soc 2004;126:1569–76. https://doi.org/10.1021/ja035243g.

[170] Gómez Gualdrón DA, Balbuena PB. Classical molecular dynamics of clathrate−methane−water kinetic inhibitor composite systems. J Phys Chem C 2007;111:15554–64. https://doi.org/10.1021/jp071959c.

[171] Kvamme B, Selvåg J, Saeidi N, Kuznetsova T. Methanol as a hydrate inhibitor and hydrate activator. Phys Chem Chem Phys 2018;20:21968–87. https://doi.org/10.1039/C8CP02447B.

[172] Bagherzadeh A, Alavi S, Ripmeester JA, Englezos P. Why ice-binding type I antifreeze protein acts as a gas hydrate crystal inhibitor. Phys Chem Chem Phys 2015;17:9984–90. https://doi.org/10.1039/C4CP05003G.

[173] Maddah M, Maddah M, Peyvandi K. Investigation on structural properties of winter flounder antifreeze protein in interaction with clathrate hydrate by molecular dynamics simulation. J Chem Thermodyn 2021;152:106267. https://doi.org/10.1016/j.jct.2020.106267.

[174] Maddah M, Maddah M, Peyvandi K. The influence of a type III antifreeze protein and its mutants on methane hydrate adsorption–inhibition: a molecular dynamics simulation study. Phys Chem Chem Phys 2019;21:21836–46. https://doi.org/10.1039/C9CP03833G.

[175] Anderson BJ, Tester JW, Borghi GP, Trout BL. Properties of inhibitors of methane hydrate formation via molecular dynamics simulations. J Am Chem Soc 2005; 127:17852–62. https://doi.org/10.1021/ja0554965.

[176] Yagasaki T, Matsumoto M, Tanaka H. Adsorption of kinetic hydrate inhibitors on growing surfaces: A molecular dynamics study. J Phys Chem B 2018;122:3396–406. https://doi.org/10.1021/acs.jpcb.7b10356.

[177] Maddah M, Maddah M, Peyvandi K. Molecular dynamics simulation of methane hydrate formation in presence and absence of amino acid inhibitors. J Mol Liq 2018;269:721–32. https://doi.org/10.1016/j.molliq.2018.08.108.

[178] Oluwunmi PA, Finney AR, Rodger PM. Molecular dynamics screening for new kinetic inhibitors of methane hydrate. Can J Chem 2015;93:1043–9. https://doi.org/10.1139/cjc-2015-0003.

[179] Moon C, Hawtin RW, Rodger PM. Nucleation and control of clathrate hydrates: insights from simulation. Faraday Discuss 2007;136:367. https://doi.org/10.1039/b618194p.

[180] Zhang J, Hawtin RW, Yang Y, Nakagava E, Rivero M, Choi SK, et al. Molecular dynamics study of methane hydrate formation at a water/methane interface. J Phys Chem B 2008;112:10608–18. https://doi.org/10.1021/jp076904p.

[181] Kvamme B, Kuznetsova T, Aasoldsen K. Molecular dynamics simulations for selection of kinetic hydrate inhibitors. J Mol Graph Model 2005;23:524–36. https://doi.org/10.1016/j.jmgm.2005.04.001.

[182] Xu J, Li L, Liu J, Wang X, Yan Y, Zhang J. The molecular mechanism of the inhibition effects of PVCaps on the growth of sI hydrate: an unstable adsorption mechanism. Phys Chem Chem Phys 2018;20:8326–32. https://doi.org/10.1039/C8CP00010G.

[183] Yagasaki T, Matsumoto M, Tanaka H. Adsorption mechanism of inhibitor and guest molecules on the surface of gas hydrates. J Am Chem Soc 2015;137: 12079–85. https://doi.org/10.1021/jacs.5b07417.

[184] Li S, Lv R, Wu Y, Huang F, Zhang X, Yue T. Size, aggregation, and oxidization-dependent perturbation of methane hydrate by graphene nanosheets revealed by molecular dynamics simulations. J Phys Chem C 2019. https://doi.org/10.1021/acs.jpcc.9b02659.

[185] Yeon S-H, Seol J, Koh D-Y, Seo Y, Park K-P, Huh D-G, et al. Abnormal methane occupancy of natural gas hydrates in deep sea floor sediments. Energy Environ Sci 2011;4:421–4. https://doi.org/10.1039/C0EE00355G.

[186] Seo Y, Seol J, Yeon S-H, Koh D-Y, Cha M, Kang S-P, et al. Structural, mineralogical, and rheological properties of methane hydrates in smectite clays. J Chem Eng Data 2009;54:1284–91. https://doi.org/10.1021/je800833y.

[187] Myshakin EM, Saidi WA, Romanov VN, Cygan RT, Jordan KD. Molecular dynamics simulations of carbon dioxide intercalation in hydrated Na-montmorillonite. J Phys Chem C 2013;117:11028–39. https://doi.org/10.1021/jp312589s.

[188] Yan L, Chen G, Pang W, Liu J. Experimental and modeling study on hydrate formation in wet activated carbon. J Phys Chem B 2005;109:6025–30. https://doi.org/10.1021/jp045679y.

[189] Kim D, Ahn Y-H, Kim S-J, Lee JY, Lee J, Seo Y, et al. Gas hydrate in crystalline-swelled clay: The effect of pore dimension on hydrate formation and phase equilibria. J Phys Chem C 2015;119:22148–53. https://doi.org/10.1021/acs.jpcc.5b03229.

[190] Kim D, Lee H. Phase behavior of gas hydrates in nanoporous materials: Review. Korean J Chem Eng 2016;33:1977–88. https://doi.org/10.1007/s11814-016-0064-z.

[191] Cuadrado-Collados C, Fauth F, Such-Basañez I, Martínez-Escandell M, Silvestre-Albero J. Methane hydrate formation in the confined nanospace of activated carbons in seawater environment. Microporous Mesoporous Mater 2018;255: 220–5. https://doi.org/10.1016/j.micromeso.2017.07.047.

[192] Borchardt L, Nickel W, Casco M, Senkovska I, Bon V, Wallacher D, et al. Illuminating solid gas storage in confined spaces – methane hydrate formation in porous model carbons. Phys Chem Chem Phys 2016;18:20607–14. https://doi.org/10.1039/C6CP03993F.

[193] Casco ME, Jordá JL, Rey F, Fauth F, Martinez-Escandell M, Rodríguez-Reinoso F, et al. High-performance of gas hydrates in confined nanospace for reversible CH4/CO2 storage. Chem - A Eur J 2016;22:10028–35. https://doi.org/10.1002/chem.201600958.

[194] Casco ME, Silvestre-Albero J, Ramírez-Cuesta AJ, Rey F, Jordá JL, Bansode A, et al. Methane hydrate formation in confined nanospace can surpass nature. Nat Commun 2015;6:6432. https://doi.org/10.1038/ncomms7432.

[195] Bin YK, Yazaydin AO. Does confinement enable methane hydrate growth at low pressures? Insights from molecular dynamics simulations. J Phys Chem C 2020; 124:11015–22. https://doi.org/10.1021/acs.jpcc.0c02246.

[196] Cox SJ, Taylor DJF, Youngs TGA, Soper AK, Totton TS, Chapman RG, et al. Formation of methane hydrate in the presence of natural and synthetic nanoparticles. J Am Chem Soc 2018;140:3277–84. https://doi.org/10.1021/jacs.7b12050.

[197] Park T, Kyung D, Lee W. Effect of organic matter on CO2 hydrate phase equilibrium in phyllosilicate suspensions. Environ Sci Technol 2014;48: 6597–603. https://doi.org/10.1021/es405099z.

[198] Cygan RT, Guggenheim S, Koster van Groos AF. Molecular models for the intercalation of methane hydrate complexes in montmorillonite clay. J Phys Chem B 2004;108:15141–9. https://doi.org/10.1021/jp037900x.

[199] Kadoura A, Narayanan Nair AK, Sun S. Molecular dynamics simulations of carbon dioxide, methane, and their mixture in montmorillonite clay hydrates. J Phys Chem C 2016;120:12517–29. https://doi.org/10.1021/acs.jpcc.6b02748.

[200] Bagherzadeh SA, Englezos P, Alavi S, Ripmeester JA. Influence of hydrated silica surfaces on interfacial water in the presence of clathrate hydrate forming gases. J Phys Chem C 2012;116:24907–15. https://doi.org/10.1021/jp305529d.

[201] Cai T, Johnson JK, Wu Y, Chen X. Toward understanding the kinetics of CO2 capture on sodium carbonate. ACS Appl Mater Interfaces 2019;11:9033–41. https://doi.org/10.1021/acsami.8b20000.

[202] Hou D, Zhang Q, Xu X, Zhang J, Li W, Wang P. Insights on ions migration in the nanometer channel of calcium silicate hydrate under external electric field. Electrochim Acta 2019;320:134637. https://doi.org/10.1016/j.electacta.2019.134637.

[203] Tzirakis F, Stringari P, von Solms N, Coquelet C, Kontogeorgis G. Hydrate equilibrium data for the CO2 + N2 system with the use of tetra-n-butylammonium bromide (TBAB), cyclopentane (CP) and their mixture. Fluid Phase Equilib 2016;408:240–7. https://doi.org/10.1016/j.fluid.2015.09.021.

[204] Sun Q, Guo X, Liu A, Liu B, Huo Y, Chen G. Experimental Study on the Separation of CH4 and N2 via Hydrate Formation in TBAB Solution. Ind Eng Chem Res 2011; 50:2284–8. https://doi.org/10.1021/ie101726f.

[205] Liao Z, Guo X, Zhao Y, Wang Y, Sun Q, Liu A, et al. Experimental and modeling study on phase equilibria of semiclathrate hydrates of Tetra-n-butyl Ammonium Bromide + CH4, CO2, N2, or gas mixtures. Ind Eng Chem Res 2013;52:18440–6. https://doi.org/10.1021/ie402903m.

[206] Muromachi S, Hashimoto H, Maekawa T, Takeya S, Yamamoto Y. Phase equilibrium and characterization of ionic clathrate hydrates formed with tetra- n -butylammonium bromide and nitrogen gas. Fluid Phase Equilib 2016;413: 249–53. https://doi.org/10.1016/j.fluid.2015.09.002.

[207] Muromachi S, Udachin KA, Alavi S, Ohmura R, Ripmeester JA. Selective occupancy of methane by cage symmetry in TBAB ionic clathrate hydrate. Chem Commun 2016;52:5621–4. https://doi.org/10.1039/C6CC00264A.

[208] Muromachi S, Udachin A, Shin K, Alavi SMI, Ohmura R, Ripmeester J. Guest-induced symmetry lowering of an ionic clathrate material for carbon capture. Chem Commun 2014;50:11476–9. https://doi.org/10.1039/C4CC02111H.

[209] Liang S, Kusalik PG. Nucleation of gas hydrates within constant energy systems. J Phys Chem B 2013;117:1403–10. https://doi.org/10.1021/jp308395x.

[210] English NJ, Clarke ET. Molecular dynamics study of CO2 hydrate dissociation: Fluctuation-dissipation and non-equilibrium analysis. J Chem Phys 2013;139: 94701. https://doi.org/10.1063/1.4819269.

[211] Arjun A, Bolhuis PG. Molecular understanding of homogeneous nucleation of CO2 hydrates using transition path sampling. J Phys Chem B 2021;125:338–49. https://doi.org/10.1021/acs.jpcb.0c09915.

[212] Naeiji P, Varaminian F, Rahmati M. The kinetic modeling of methane hydrate growth by using molecular dynamic simulations. Int J Heat Mass Transf 2019; 142:118356. https://doi.org/10.1016/j.ijheatmasstransfer.2019.07.006.

[213] Nguyen AH, Koc MA, Shepherd TD, Molinero V. Structure of the ice–clathrate interface. J Phys Chem C 2015;119:4104–17. https://doi.org/10.1021/jp511749q.

[214] Jendi ZM, Servio P, Rey AD. Ab initio modelling of methane hydrate thermophysical properties. Phys Chem Chem Phys 2016;18:10320–8. https://doi.org/10.1039/C5CP06530E.

[215] Zhang J, Kuo J, Iitaka T. First principles molecular dynamics study of filled ice hydrogen hydrate. J Chem Phys 2012;137:84505. https://doi.org/10.1063/1.4746776.

[216] Krishnan Y, Ghaani MR, Desmedt A, English NJ. Hydrogen inter-cage hopping and cage occupancies inside hydrogen hydrate: Molecular-dynamics analysis. Appl Sci 2020;11:282. https://doi.org/10.3390/app11010282.

[217] Krishnan Y, Ghaani MR, English NJ. Hydrogen and deuterium molecular escape from clathrate hydrates: "Leaky" microsecond-molecular-dynamics predictions. J Phys Chem C 2021;125:8430–9. https://doi.org/10.1021/acs.jpcc.1c00987.

[218] Alavi S, Ohmura R. Understanding decomposition and encapsulation energies of structure I and II clathrate hydrates. J Chem Phys 2016;145:154708. https://doi.org/10.1063/1.4964673.

[219] Wu G, Tian L, Chen D, Niu M, Ji H. CO2 and CH4 hydrates: Replacement or co-growth? J Phys Chem C 2019;123:13401–9. https://doi.org/10.1021/acs.jpcc.9b00579.

[220] Matsui H, Jia J, Tsuji T, Liang Y, Masuda Y. Microsecond simulation study on the replacement of methane in methane hydrate by carbon dioxide, nitrogen, and carbon dioxide – nitrogen mixtures. Fuel 2019;116640. https://doi.org/10.1016/j.fuel.2019.116640.

[221] Naeiji P, Woo TK, Alavi S, Varaminian F, Ohmura R. Interfacial properties of hydrocarbon/water systems predicted by molecular dynamic simulations. J Chem Phys 2019;150:114703. https://doi.org/10.1063/1.5078739.

[222] Wang Y, Yin K, Lang X, Fan S, Li G, Yu C, et al. Hydrogen storage in sH binary hydrate: Insights from molecular dynamics simulation. Int J Hydrogen Energy 2021;46:15748–60. https://doi.org/10.1016/j.ijhydene.2021.02.112.

[223] Kondo Y, Alavi S, Takeya S, Ohmura R. Characterization of the clathrate hydrate formed with fluoromethane and pinacolone: The thermodynamic stability and volumetric behavior of the structure H binary hydrate. J Phys Chem B 2021;125: 328–37. https://doi.org/10.1021/acs.jpcb.0c09818.

[224] Xu J, Gu T, Sun Z, Li X, Wang X. Molecular dynamics study on the dissociation of methane hydrate via inorganic salts. Mol Phys 2016;114:34–43. https://doi.org/10.1080/00268976.2015.1081708.

[225] Alavi S, Takeya S, Ohmura R, Woo TK, Ripmeester JA. Hydrogen-bonding alcohol-water interactions in binary ethanol, 1-propanol, and 2-propanol+ methane structure II clathrate hydrates. J Chem Phys 2010;133:74505. https://doi.org/10.1063/1.3469776.

[226] Guo P, Pan Y-K, Li L-L, Tang B. Molecular dynamics simulation of decomposition and thermal conductivity of methane hydrate in porous media. Chinese Phys B 2017;26:73101. https://doi.org/10.1088/1674-1056/26/7/073101.

[227] Ji H, Chen D, Zhao C, Wu G. Molecular dynamics simulation of methane hydrate formation and dissociation in the clay pores with fatty acids. J Phys Chem C 2018; 122:1318–25. https://doi.org/10.1021/acs.jpcc.7b08808.

[228] Ripmeester JA, Alavi S. Molecular simulations of methane hydrate nucleation. Chem Phys Chem 2010;11:978–80. https://doi.org/10.1002/cphc.201000024.

[229] Christiansen RL, Sloan ED. Mechanisms and kinetics of hydrate formation. Ann N Y Acad Sci 1994;715:283–305. https://doi.org/10.1111/j.1749-6632.1994.tb38841.x.

[230] Sloan ED, Fleyfel F. A molecular mechanism for gas hydrate nucleation from ice. AIChE J 1991;37:1281–92. https://doi.org/10.1002/aic.690370902.

[231] DeFever RS, Sarupria S. Nucleation mechanism of clathrate hydrates of water-soluble guest molecules. J Chem Phys 2017;147:204503. https://doi.org/10.1063/1.4996132.

[232] Defever RS, Sarupria S. Surface chemistry effects on heterogeneous clathrate hydrate nucleation : A molecular dynamics study. J Chem Thermodyn 2017. https://doi.org/10.1016/j.jct.2017.08.021.

[233] Zhang Z, Walsh MR, Guo G-J-J. Microcanonical molecular simulations of methane hydrate nucleation and growth: evidence that direct nucleation to sI hydrate is among the multiple nucleation pathways. Phys Chem Chem Phys 2015;17: 8870–6. https://doi.org/10.1039/C5CP00098J.

[234] Barnes BC, Beckham GT, Wu DT, Sum AK. Two-component order parameter for quantifying clathrate hydrate nucleation and growth. J Chem Phys 2014;140: 164506. https://doi.org/10.1063/1.4871898.

[235] Jacobson LC, Hujo W, Molinero V. Nucleation pathways of clathrate hydrates: Effect of guest size and solubility. J Phys Chem B 2010;114:13796–807. https://doi.org/10.1021/jp107269q.

[236] Tung Y-T, Chen L-J, Chen Y-P, Lin S-T. The growth of structure I methane hydrate from molecular dynamics simulations. J Phys Chem B 2010;114:10804–13. https://doi.org/10.1021/jp102874s.

[237] Bai D, Chen G, Zhang X, Wang W. Microsecond molecular dynamics simulations of the kinetic pathways of gas hydrate formation from solid surfaces. Langmuir 2011;27:5961–7. https://doi.org/10.1021/la105088b.

[238] Jacobson LC, Hujo W, Molinero V. Amorphous precursors in the nucleation of clathrate hydrates. J Am Chem Soc 2010;132:11806–11. https://doi.org/10.1021/ja1051445.

[239] Lauricella M, Meloni S, Liang S, English NJ, Kusalik PG, Ciccotti G. Clathrate structure-type recognition: Application to hydrate nucleation and crystallisation. J Chem Phys 2015;142:244503. https://doi.org/10.1063/1.4922696.

[240] Sarupria S, Debenedetti PG. Homogeneous nucleation of methane hydrate in microsecond molecular dynamics simulations. J Phys Chem Lett 2012;3:2942–7. https://doi.org/10.1021/jz3012113.

[241] Hall KW, Zhang Z, Kusalik PG. Unraveling mixed hydrate formation: Microscopic insights into early stage behavior. J Phys Chem B 2016;120:13218–23. https://doi.org/10.1021/acs.jpcb.6b11961.

[242] Hall KW, Zhang Z, Burnham CJ, Guo G-J, Carpendale S, English NJ. Does local structure bias how a crystal nucleus evolves? J Phys Chem Lett 2018;9:6991–8. https://doi.org/10.1021/acs.jpclett.8b03115.

[243] Pirzadeh P, Kusalik PG. Molecular insights into clathrate hydrate nucleation at an ice–solution interface. J Am Chem Soc 2013;135:7278–87. https://doi.org/10.1021/ja400521e.

[244] Moon C, Taylor PC, Rodger PM. Molecular dynamics study of gas hydrate formation. J Am Chem Soc 2003;125:4706–7. https://doi.org/10.1021/ja028537v.

[245] He Z, Gupta KM, Linga P, Jiang J. Molecular insights into the nucleation and growth of CH4 and CO2 mixed hydrates from microsecond simulations. J Phys Chem C 2016;120:25225–36. https://doi.org/10.1021/acs.jpcc.6b07780.

[246] He Z, Linga P, Jiang J. What are the key factors governing the nucleation of CO2 hydrate? Phys Chem Chem Phys 2017;19:15657–61. https://doi.org/10.1039/C7CP01350G.

[247] Carvalho PH, Mace A, Bull CL, Funnell NP, Tulk CA, Häussermann U. Elucidation of the pressure induced amorphization of tetrahydrofuran clathrate hydrate 2019;204506. 10.1063/1.5083958.

[248] Bai D, Chen G, Zhang X, Wang W. Nucleation of the CO2 hydrate from three-phase contact lines. Langmuir 2012;28:7730–6. https://doi.org/10.1021/la300647s.

[249] Jacobson LC, Hujo W, Molinero V. Thermodynamic stability and growth of guest-free clathrate hydrates: A low-density crystal phase of water. J Phys Chem B 2009;113:10298–307. https://doi.org/10.1021/jp903439a.

[250] Zhang Z, Kusalik P, Guo G. Molecular insight into the growth of hydrogen and methane binary hydrates. J Phys Chem C 2018;122:7771–8. https://doi.org/10.1021/acs.jpcc.8b00842.

[251] Phan A, Schlösser H, Striolo A. Molecular mechanisms by which tetrahydrofuran affects CO2 hydrate growth: Implications for carbon storage. Chem Eng J 2021;129423. https://doi.org/10.1016/j.cej.2021.129423.

[252] Vatamanu J, Kusalik PG. Molecular insights into the heterogeneous crystal growth of sI methane hydrate. J Phys Chem B 2006;110:15896–904. https://doi.org/10.1021/jp061684l.

[253] Małolepsza E, Keyes T. Pathways through equilibrated states with coexisting phases for gas hydrate formation. J Phys Chem B 2015;119:15857–65. https://doi.org/10.1021/acs.jpcb.5b06832.

[254] Naeiji P, Varaminian F, Rahmati M. Comparison of the thermodynamic, structural and dynamical properties of methane/water and methane/water/hydrate systems using molecular dynamic simulations. J Nat Gas Sci Eng 2017. https://doi.org/10.1016/j.jngse.2017.04.010.

[255] Guo G, Zhang Y, Liu H. Effect of methane adsorption on the lifetime of a dodecahedral water cluster immersed in liquid water: A molecular dynamics study on the hydrate nucleation mechanisms. J Phys Chem C 2007;111:2595–606. https://doi.org/10.1021/jp064271t.

[256] Guo G-J, Li M, Zhang Y-G, Wu C-H. Why can water cages adsorb aqueous methane? A potential of mean force calculation on hydrate nucleation mechanisms. Phys Chem Chem Phys 2009;11:10427. https://doi.org/10.1039/b913898f.

[257] Ma R, Zhong H, Li L, Zhong J, Yan Y, Zhang J, et al. Molecular insights into the effect of a solid surface on the stability of a hydrate nucleus. J Phys Chem C 2020;124:2664–71. https://doi.org/10.1021/acs.jpcc.9b09704.

[258] Nguyen AH, Molinero V. Cross-nucleation between clathrate hydrate polymorphs: Assessing the role of stability, growth rate, and structure matching. J Chem Phys 2014;140:84506. https://doi.org/10.1063/1.4866143.

[259] Burnham CJ, English NJ. Communication: Librational dynamics in water, sI and sII clathrate hydrates, and ice Ih: Molecular-dynamics insights. J Chem Phys 2016;144:51101. https://doi.org/10.1063/1.4941330.

[260] Zhang Z, Guo G-J-J. The effects of ice on methane hydrate nucleation: a microcanonical molecular dynamics study. Phys Chem Chem Phys 2017;19:19496–505. https://doi.org/10.1039/C7CP03649C.

[261] Jiménez-Ángeles F, Firoozabadi A. Enhanced hydrate nucleation near the limit of stability. J Phys Chem C 2015;119:8798–804. https://doi.org/10.1021/acs.jpcc.5b01869.

[262] Yagasaki T, Matsumoto M, Tanaka H. Formation of clathrate hydrates of water-soluble guest molecules. J Phys Chem C 2016;120:21512–21. https://doi.org/10.1021/acs.jpcc.6b06498.

[263] Forester TR, McDonald IR, Klein ML. Intermolecular potentials and the properties of liquid and solid hydrogen sulphide. Chem Phys 1989;129:225–34. https://doi.org/10.1016/0301-0104(89)80008-4.

[264] Zhao W, Bai J, Francisco JS, Zeng XC. Formation of CO2 hydrates within single-walled carbon nanotubes at ambient pressure: CO2 capture and selective separation of a CO2/H2 mixture in water. J Phys Chem C 2018;122:7951–8. https://doi.org/10.1021/acs.jpcc.7b12700.

[265] Zhao W, Wang L, Bai J, Francisco JS, Zeng XC. Spontaneous formation of one-dimensional hydrogen gas hydrate in carbon nanotubes. J Am Chem Soc 2014;136:10661–8. https://doi.org/10.1021/ja5041539.

[266] Wu J, Chen L, Chen Y, Lin S. methane + tetrahydrofuran mixed guest hydrate. Phys Chem Chem Phys 2016. https://doi.org/10.1039/C5CP06419H.

[267] Hu P, Wu G, Zi M, Li L, Chen D. Effects of modified metal surface on the formation of methane hydrate. Fuel 2019;255:115720. https://doi.org/10.1016/j.fuel.2019.115720.

[268] Bhattacharjee G, Choudhary N, Kumar A, Chakrabarty S, Kumar R. Effect of the amino acid l-histidine on methane hydrate growth kinetics. J Nat Gas Sci Eng 2016;35:1453–62. https://doi.org/10.1016/j.jngse.2016.05.052.

[269] Albertí M, Costantini A, Laganá A, Pirani F. Are micelles needed to form methane hydrates in sodium dodecyl sulfate solutions? J Phys Chem B 2012;116:4220–7. https://doi.org/10.1021/jp301124z.

[270] Min J, Kang DW, Lee W, Lee JW. Molecular dynamics simulations of hydrophobic nanoparticle effects on gas hydrate formation. J Phys Chem C 2020;124:4162–71. https://doi.org/10.1021/acs.jpcc.9b11459.

[271] Mahmoodi MH, Manteghian M, Naeiji P. Study the effect of Ag nanoparticles on the kinetics of CO2 hydrate growth by molecular dynamics simulation. J Mol Liq 2021;343:117668. https://doi.org/10.1016/j.molliq.2021.117668.

[272] Susilo R, Alavi S, Lang S, Ripmeester J, Englezos P. Interactions between structure H hydrate formers and water molecules. J Phys Chem C 2008;112:9106–13. https://doi.org/10.1021/jp8006848.

[273] Yi L, Liang D, Zhou X, Li D, Wang J. Molecular dynamics simulations of carbon dioxide hydrate growth in electrolyte solutions of NaCl and MgCl2. Mol Phys 2014;112:3127–37. https://doi.org/10.1080/00268976.2014.932454.

[274] Tung Y, Chen L-J, Chen Y, Lin S. Molecular dynamics study on the growth of structure I methane hydrate in aqueous solution of sodium chloride. J Phys Chem B 2012;116:14115–25. https://doi.org/10.1021/jp308224v.

[275] Choudhary N, Kushwaha OS, Bhattacharjee G, Chakrabarty S, Kumar R. Macro and molecular level insights on gas hydrate growth in the presence of hofmeister salts. Ind Eng Chem Res 2020;59:20591–600. https://doi.org/10.1021/acs.iecr.0c04389.

[276] Choudhary N, Kushwaha OS, Bhattacharjee G, Chakrabarty S, Kumar R. Molecular dynamics simulation and experimental study on the growth of methane hydrate in presence of methanol and sodium chloride. Energy Procedia 2017;105:5026–33. https://doi.org/10.1016/j.egypro.2017.03.1008.

[277] Makiya T, Murakami T, Takeya S, Sum AK, Alavi S, Ohmura R. Synthesis and characterization of clathrate hydrates containing carbon dioxide and ethanol. Phys Chem Chem Phys 2010;12:9927. https://doi.org/10.1039/c002187c.

[278] Ji H, Wu G, Zi M, Chen D. Microsecond molecular dynamics simulation of methane hydrate formation in humic-acid-amended sodium montmorillonite. Energy Fuel 2016;30:7206–13. https://doi.org/10.1021/acs.energyfuels.6b01544.

[279] Cheng L, Liao K, Li Z, Cui J, Liu B, Li F, et al. The invalidation mechanism of kinetic hydrate inhibitors under high subcooling conditions. Chem Eng Sci 2019;207:305–16. https://doi.org/10.1016/j.ces.2019.06.032.

[280] Bai D, Wu Z, Lin C, Zhou D. The effect of aqueous NaCl solution on methane hydrate nucleation and growth. Fluid Phase Equilib 2019;487:76–82. https://doi.org/10.1016/j.fluid.2019.01.008.

[281] Bai D, Chen G, Zhang X, Sum AK, Wang W. How properties of solid surfaces modulate the nucleation of gas hydrate. Sci Rep 2015;5:12747. https://doi.org/10.1038/srep12747.

[282] He Z, Linga P, Jiang J. CH4 hydrate formation between silica and graphite surfaces: Insights from microsecond molecular dynamics simulations. Langmuir 2017;33:11956–67. https://doi.org/10.1021/acs.langmuir.7b02711.

[283] Yan K-F, Li X-S, Chen Z-Y, Xia Z-M, Xu C-G, Zhang Z. Molecular dynamics simulation of the crystal nucleation and growth behavior of methane hydrate in the presence of the surface and nanopores of porous sediment. Langmuir 2016;32:7975–84. https://doi.org/10.1021/acs.langmuir.6b01601.

[284] Li Y, Chen M, Liu C, Song H, Yuan P, Zhang B, et al. Effects of layer-charge distribution of 2:1 clay minerals on methane hydrate formation: A molecular dynamics simulation study. Langmuir 2020;36:3323–35. https://doi.org/10.1021/acs.langmuir.0c00183.

[285] Park S-H, Sposito G. Do montmorillonite surfaces promote methane hydrate formation? monte carlo and molecular dynamics simulations. J Phys Chem B 2003;107:2281–90. https://doi.org/10.1021/jp021427q.

[286] Kyung D, Lim H-K, Kim H, Lee W. CO2 hydrate nucleation kinetics enhanced by an organo-mineral complex formed at the montmorillonite–water interface. Environ Sci Technol 2015;49:1197–205. https://doi.org/10.1021/es504450x.

[287] Kvamme B, Graue A, Buanes T, Kuznetsova T, Ersland G. Storage of CO2 in natural gas hydrate reservoirs and the effect of hydrate as an extra sealing in cold aquifers. Int J Greenh Gas Control 2007;1:236–46. https://doi.org/10.1016/S1750-5836(06)00002-8.

[288] Das S, Baghel VS, Roy S, Kumar R. A molecular dynamics study of model SI clathrate hydrates: the effect of guest size and guest–water interaction on decomposition kinetics. Phys Chem Chem Phys 2015;17:9509–18. https://doi.org/10.1039/C5CP00678C.

[289] Yasuoka K, Murakoshi S. Molecular dynamics simulation of dissociation process for methane hydrate. Ann N Y Acad Sci 2006;912:678–84. https://doi.org/10.1111/j.1749-6632.2000.tb06823.x.

[290] English NJ, Phelan GM. Molecular dynamics study of thermal-driven methane hydrate dissociation. J Chem Phys 2009;131:74704. https://doi.org/10.1063/1.3211089.

[291] Fang B, Ning F, Ou W, Wang D, Zhang Z, Yu Y, et al. The dynamic behavior of gas hydrate dissociation by heating in tight sandy reservoirs: A molecular dynamics simulation study. Fuel 2019;258:116106. https://doi.org/10.1016/j.fuel.2019.116106.

[292] Bagherzadeh SA, Englezos P, Alavi S, Ripmeester JA. Molecular modeling of the dissociation of methane hydrate in contact with a silica surface. J Phys Chem B 2012;116:3188–97. https://doi.org/10.1021/jp2086544.

[293] English NJ, Ghaani MR. Hybrid versus global thermostatting in molecular-dynamics simulation of methane-hydrate crystallisation. Chinese J Chem Eng 2019;27:2180–8. https://doi.org/10.1016/j.cjche.2019.02.034.

[294] Ghaani MR, English NJ. Molecular-dynamics study of propane-hydrate dissociation: Fluctuation-dissipation and non-equilibrium analysis. J Chem Phys 2018:114504. https://doi.org/10.1063/1.5018192.

[295] Ghaani MR, English NJ. Hydrogen-/propane-hydrate decomposition: thermodynamic and kinetic analysis. Mol Phys 2019;117:2434–42. https://doi.org/10.1080/00268976.2019.1567845.

[296] Waldron CJ, English NJ. Global-density fluctuations in methane clathrate hydrates in externally applied electromagnetic fields. J Chem Phys 2017;147: 24506. https://doi.org/10.1063/1.4990029.

[297] Waldron CJ, English NJ. System-density fluctuations and electro-dissociation of methane clathrate hydrates in externally-applied static electric fields. J Chem Thermodyn 2018;117:68–80. https://doi.org/10.1016/j.jct.2017.08.016.

[298] Krishnan Y, Ghaani MR, English NJ. Electric-field control of neon uptake and release to and from clathrate hydrates. J Phys Chem C 2019;123:27554–60. https://doi.org/10.1021/acs.jpcc.9b07257.

[299] Ghaani MR, English NJ, Allen CCR. Magnetic-field manipulation of naturally occurring microbial chiral peptides to regulate gas-hydrate formation. J Phys Chem Lett 2020;11:9079–85. https://doi.org/10.1021/acs.jpclett.0c02347.

[300] Li J, Lu H, Zhou X. Electric field triggered release of gas from a quasi-one-dimensional hydrate in the carbon nanotube. Nanoscale 2020;12:12801–8. https://doi.org/10.1039/D0NR01113D.

[301] Ghaani MR, English NJ. Molecular dynamics study of propane hydrate dissociation: Nonequilibrium analysis in externally applied electric fields. J Phys Chem C 2018;122:7504–15. https://doi.org/10.1021/acs.jpcc.7b12238.

[302] Ghaani MR, English NJ. Non-equilibrium molecular-dynamics study of electromagnetic-field-induced propane-hydrate dissociation. J Chem Phys 2018; 149:124702. https://doi.org/10.1063/1.5029457.

[303] Bagherzadeh SA, Alavi S, Ripmeester JA, Englezos P. Evolution of methane during gas hydrate dissociation. Fluid Phase Equilib 2013;358:114–20. https://doi.org/10.1016/j.fluid.2013.08.017.

[304] Kondori J, James L, Zendehboudi S. Molecular scale modeling approach to evaluate stability and dissociation of methane and carbon dioxide hydrates. J Mol Liq 2020;297:111503. https://doi.org/10.1016/j.molliq.2019.111503.

[305] Zhang Z, Kusalik PG, Guo G-J, Ning F, Wu N. Insight on the stability of polycrystalline natural gas hydrates by molecular dynamics simulations. Fuel 2021;289:119946. https://doi.org/10.1016/j.fuel.2020.119946.

[306] Liu Y, Zhao J, Xu J. Dissociation mechanism of carbon dioxide hydrate by molecular dynamic simulation and ab initio calculation. Comput Theor Chem 2012;991:165–73. https://doi.org/10.1016/j.comptc.2012.04.016.

[307] Geng C-Y, Han Q-Z, Wen H, Dai Z-Y, Song C-H. Molecular dynamics simulation on the decomposition of type SII hydrogen hydrate and the performance of tetrahydrofuran as a stabiliser. Mol Simul 2010;36:474–83. https://doi.org/10.1080/08927021003664041.

[308] Alavi S, Shin K, Ripmeester JA. Molecular dynamics simulations of hydrogen bonding in clathrate hydrates with ammonia and methanol guest molecules. J Chem Eng Data 2015;60:389–97. https://doi.org/10.1021/je5006517.

[309] Reshadi P, Modarress H, Dabir B, Amjad-Iranagh S. A study on dissociation of sII krypton hydrate and the effect of hydrocarbon guest molecules as stabilizer by molecular dynamics simulation. Phase Transit 2017;90:1128–42. https://doi.org/10.1080/01411594.2017.1309404.

[310] Yagasaki T, Matsumoto M, Andoh Y, Okazaki S, Tanaka H. Dissociation of methane hydrate in aqueous NaCl solutions. J Phys Chem B 2014;118: 11797–804. https://doi.org/10.1021/jp507978u.

[311] Dai C, Hu Y, Wu Y, Zhao M, Yue T. Effects of structural properties of alcohol molecules on decomposition of natural gas hydrates: A molecular dynamics study. Fuel 2020;268:117322. https://doi.org/10.1016/j.fuel.2020.117322.

[312] Sun X, Zhou G, Zhu J, Wu H, Lu G, Bai D. Molecular dynamics simulation of methane hydrate decomposition in the presence of alcohol additives. ChemPhysChem 2019;20:2553–65. https://doi.org/10.1002/cphc.201900742.

[313] Kondori J, Zendehboudi S, James L. Molecular dynamic simulations to evaluate dissociation of hydrate structure II in the presence of inhibitors : A mechanistic study. Chem Eng Res Des 2019;149:81–94. https://doi.org/10.1016/j.cherd.2019.05.048.

[314] Li K, Shi R, Huang Y, Tang L, Cao X, Su Y, et al. Dissociation mechanism of propane hydrate with methanol additive: A molecular dynamics simulation. Comput Theor Chem 2018;1123:79–86. https://doi.org/10.1016/j.comptc.2017.11.011.

[315] Srivastava HK, Sastry GN. Viability of clathrate hydrates as CO2 capturing agents: A theoretical study. J Phys Chem A 2011;115:7633–7. https://doi.org/10.1021/jp203599g.

[316] Velaga SC, Anderson BJ. Carbon dioxide hydrate phase equilibrium and cage occupancy calculations using Ab initio intermolecular potentials. J Phys Chem B 2014;118:577–89. https://doi.org/10.1021/jp410306v.

[317] Myshakin EM, Jiang H, Warzinski RP, Jordan KD. Molecular dynamics simulations of methane hydrate decomposition. J Phys Chem A 2009;113: 1913–21. https://doi.org/10.1021/jp807208z.

[318] Burnham CJ, English NJ. Free-energy calculations of the intercage hopping barriers of hydrogen molecules in clathrate hydrates. J Phys Chem C 2016;120: 16561–7. https://doi.org/10.1021/acs.jpcc.6b06524.

[319] Burnham CJ, Futera Z, English NJ. Quantum and classical inter-cage hopping of hydrogen molecules in clathrate hydrate: temperature and cage-occupation effects. Phys Chem Chem Phys 2017;19:717–28. https://doi.org/10.1039/c6cp06531g.

[320] Burnham CJ, Futera Z, English NJ. Study of hydrogen-molecule guests in type II clathrate hydrates using a force-matched potential model parameterised from ab initio molecular dynamics. J Chem Phys 2018;148:102323. https://doi.org/10.1063/1.4999909.

[321] Brumby PE, Yuhara D, Hasegawa T, Wu DT, Sum AK, Yasuoka K. Cage occupancies, lattice constants, and guest chemical potentials for structure II hydrogen clathrate hydrate from Gibbs ensemble Monte Carlo simulations. J Chem Phys 2019;150:134503. https://doi.org/10.1063/1.5084785.

[322] Lu Q, He X, Hu W, Chen X, Liu J. Stability, vibrations, and diffusion of hydrogen gas in clathrate hydrates: Insights from Ab initio calculations on condensed-phase crystalline structures. J Phys Chem C 2019;123:12052–61. https://doi.org/10.1021/acs.jpcc.8b11586.

[323] Mondal S, Ghosh S, Chattaraj PK. A molecular dynamics study on sI hydrogen hydrate. J Mol Model 2013;19:2785–90. https://doi.org/10.1007/s00894-012-1625-7.

[324] Liu J, Yan Y, Zhang J, Xu J, Chen G, Hou J. Theoretical investigation of storage capacity of hydrocarbon gas in sH hydrate. Chem Phys 2019;525:110393. https://doi.org/10.1016/j.chemphys.2019.110393.

[325] Sun ZZ, Wang H, Yao J, Bongole K, Zhu X, Liu L, et al. Effect of cage-specific occupancy on the dissociation rate of a three-phase coexistence methane hydrate system: A molecular dynamics simulation study. J Nat Gas Sci Eng 2018;55: 235–42. https://doi.org/10.1016/j.jngse.2018.05.004.

[326] Kondori J, Zendehboudi S, James L. New insights into methane hydrate dissociation: Utilization of molecular dynamics strategy. Fuel 2019;249:264–76. https://doi.org/10.1016/j.fuel.2019.02.125.

[327] Matsuo M, Takii Y, Matsumoto M, Tanaka H. On the occupancy of carbon dioxide clathrate hydrates: Grandcanonical monte carlo simulations. J Phys Soc Japan 2012;81:SA027. 10.1143/JPSJS.81SA.SA027.

[328] English NJ, Burnham CJ. Intra-cage structure, vibrations and tetrahedral-site hopping of H2 and D2 in doubly-occupied 51264 cages in sII clathrate hydrates from path-integral and classical molecular dynamics. Appl Sci 2020;11:54. https://doi.org/10.3390/app11010054.

[329] Song B, Nguyen AH, Molinero V. Can guest occupancy in binary clathrate hydrates be tuned through control of the growth temperature? J Phys Chem C 2014;118:23022–31. https://doi.org/10.1021/jp504852k.

[330] Alavi S, Ripmeester JA, Klug DD. Molecular-dynamics study of structure II hydrogen clathrates. J Chem Phys 2005;123:24507. https://doi.org/10.1063/1.1953577.

[331] Alavi S, Ripmeester JA. Migration of hydrogen radicals through clathrate hydrate cages. Chem Phys Lett 2009;479:234–7. https://doi.org/10.1016/j.cplett.2009.08.044.

[332] Cao H, English NJ, MacElroy JMD. Diffusive hydrogen inter-cage migration in hydrogen and hydrogen-tetrahydrofuran clathrate hydrates. J Chem Phys 2013; 138. https://doi.org/10.1063/1.4793468.

[333] Gorman PD, English NJ, MacElroy JMD. Dynamical cage behaviour and hydrogen migration in hydrogen and hydrogen-tetrahydrofuran clathrate hydrates. J Chem Phys 2012;136:44506. https://doi.org/10.1063/1.3677788.

[334] Liu Y, Chen C, Hu W, Li W, Dong B, Qin Y. Molecular dynamics simulation studies of gas hydrate growth with impingement. Chem Eng J 2021;426:130705. https://doi.org/10.1016/j.cej.2021.130705.

[335] Alavi S, Ripmeester JA, Klug DD. Molecular-dynamics simulations of binary structure II hydrogen and tetrahydrofurane clathrates. J Chem Phys 2006;124: 14704. https://doi.org/10.1063/1.2141506.

[336] Tsimpanogiannis IN, Economou IG, Stubos AK. A practical methodology to estimate the H2 storage capacity of pure and binary hydrates based on monte carlo simulations. J Chem Eng Data 2020;65:1289–99. https://doi.org/10.1021/acs.jced.9b00707.

[337] Ghaani MR, Takeya S, English NJ. Hydrogen storage in propane-hydrate: Theoretical and experimental study. Appl Sci 2020;10:8962. https://doi.org/10.3390/app10248962.

[338] Tanaka H, Nakatsuka T, Koga K. On the thermodynamic stability of clathrate hydrates IV: Double occupancy of cages. J Chem Phys 2004;121:5488–93. https://doi.org/10.1063/1.1782471.

[339] Papadimitriou NI, Tsimpanogiannis IN, Economou IG, Stubos AK. Influence of combining rules on the cavity occupancy of clathrate hydrates by Monte Carlo simulations. Mol Phys 2014;112:2258–74. https://doi.org/10.1080/00268976.2014.902136.

[340] Papadimitriou NI, Tsimpanogiannis IN, Peters CJ, Papaioannou AT, Stubos AK. Hydrogen storage in sH hydrates: A monte carlo study. J Phys Chem B 2008;112: 14206–11. https://doi.org/10.1021/jp805906c.

[341] Alavi S, Woo TK. How much carbon dioxide can be stored in the structure H clathrate hydrates?: A molecular dynamics study. J Chem Phys 2007;126:44703. https://doi.org/10.1063/1.2424936.

[342] Gharebeiglou M, Izadkhah S. Molecular dynamics simulation study on the structure II clathrate-hydrates of methane + cyclic organic compounds 2016; 6466. 10.1080/10916466.2016.1194860.

[343] Susilo R, Alavi S, Ripmeester JA, Englezos P. Molecular dynamics study of structure H clathrate hydrates of methane and large guest molecules. J Chem Phys 2008;128:194505. https://doi.org/10.1063/1.2908074.

[344] Alavi S, Ripmeester JA, Klug DD. Molecular dynamics simulations of binary structure H hydrogen and methyl-tert-butylether clathrate hydrates. J Chem Phys 2006;124:204707. https://doi.org/10.1063/1.2199850.

[345] Grim RG, Barnes BC, Lafond PG, Kockelmann WA, Keen DA, Soper AK, et al. Observation of interstitial molecular hydrogen in clathrate hydrates. Angew Chemie Int Ed 2014;53:10710–3. https://doi.org/10.1002/anie.201406546.

[346] Susilo R, Alavi S, Ripmeester J, Englezos P. Tuning methane content in gas hydrates via thermodynamic modeling and molecular dynamics simulation. Fluid Phase Equilib 2008;263:6–17. https://doi.org/10.1016/j.fluid.2007.09.015.

[347] Erfan-Niya H, Modarress H, Zaminpayma E. Computational study on the structure II clathrate hydrate of methane and large guest molecules. J Incl Phenom Macrocycl Chem 2011;70:227–39. https://doi.org/10.1007/s10847-010-9899-9.

[348] Huang Y, Zhu C, Wang L, Cao X, Su Y, Jiang X, et al. A new phase diagram of water under negative pressure: The rise of the lowest-density clathrate s-III. Sci Adv 2016;2:e1501010.

[349] Tse JS. Vibrations of methane in structure I clathrate hydrate—an ab initio density functional molecular dynamics study. J Supramol Chem 2002;2:429–33. https://doi.org/10.1016/S1472-7862(03)00053-4.

[350] Bai D, Liu B, Chen G, Zhang X, Wang W. Role of guest molecules on the hydrate growth at vapor-liquid interfaces. AIChE J 2013;59:2621–9. https://doi.org/10.1002/aic.14011.

[351] Mohammadi-Manesh H, Alavi S, Woo TK, Najafi B. Computational prediction of temperature dependence of 13C NMR lineshapes of planar molecules in structure I clathrate hydrates. J Iran Chem Soc 2013;10:659–67. https://doi.org/10.1007/s13738-012-0198-9.

[352] Mohammadi-Manesh H, Alavi S, Woo TK, Najafi B. Molecular dynamics simulation of NMR powder lineshapes of linear guests in structure I clathrate hydrates. Phys Chem Chem Phys 2011;13:2367–77. https://doi.org/10.1039/C0CP01920H.

[353] Izquierdo-Ruiz F, Otero-de-la-Roza A, Contreras-García J, Prieto-Ballesteros O, Recio JM. Effects of the CO2 guest molecule on the sI clathrate hydrate structure. Materials (Basel) 2016;9:777. https://doi.org/10.3390/ma9090777.

[354] Naeiji P, Varaminian F, Rahmati M. Thermodynamic and structural properties of methane/water systems at the threshold of hydrate formation predicted by molecular dynamic simulations. J Nat Gas Sci Eng 2016. https://doi.org/10.1016/j.jngse.2016.03.044.

[355] Zhou J, Liang Y. Effect of water on the dynamic tensile mechanical properties of calcium silicate hydrate: Based on molecular dynamics simulation. Materials (Basel) 2019;12:2837. https://doi.org/10.3390/ma12172837.

[356] Jia J, Liang Y, Tsuji T, Murata S, Matsuoka T. Elasticity and stability of clathrate hydrate: Role of guest molecule motions. Sci Rep 2017;7:1290. https://doi.org/10.1038/s41598-017-01369-0.

[357] Hou J, Bai D, Zhou W. Methane hydrate nucleation within elastic confined spaces: Suitable spacing and elasticity can accelerate the nucleation. Langmuir 2018;34:10889–96. https://doi.org/10.1021/acs.langmuir.8b02387.

[358] Jendi ZM, Servio P, Rey AD. Ideal strength of methane hydrate and ice Ih from first-principles. Cryst Growth Des 2015;15:5301–9. https://doi.org/10.1021/acs.cgd.5b00829.

[359] Gudkovskikh SV, Kirov MV. Proton disorder and elasticity of hexagonal ice and gas hydrates. J Mol Model 2019;25:32. https://doi.org/10.1007/s00894-018-3919-x.

[360] Shi Q, Cao P, Han Z, Ning F, Gong H, Xin Y, et al. Role of guest molecules in the mechanical properties of clathrate hydrates. Cryst Growth Des 2018;18:6729–41. https://doi.org/10.1021/acs.cgd.8b01017.

[361] Liang S, Kusalik PG. Crystal growth simulations of H2S hydrate. J Phys Chem B 2010;114:9563–71. https://doi.org/10.1021/jp102584d.

[362] Liang S, Kusalik PG. Exploring nucleation of H2S hydrates. Chem Sci 2011;2:1286. https://doi.org/10.1039/c1sc00021g.

[363] Youssef M, Pellenq R-J-M, Yildiz B. Glassy nature of water in an ultraconfining disordered material: The case of calcium−silicate−hydrate. J Am Chem Soc 2011;133:2499–510. https://doi.org/10.1021/ja107003a.

[364] Alavi S, Susilo R, Ripmeester JA. Linking microscopic guest properties to macroscopic observables in clathrate hydrates: Guest-host hydrogen bonding. J Chem Phys 2009;130:174501. https://doi.org/10.1063/1.3124187.

[365] Mirzaeifard S, Servio P, Rey AD. Molecular dynamics characterization of temperature and pressure effects on the water-methane interface. Colloids Interface Sci Commun 2018;24:75–81. https://doi.org/10.1016/j.colcom.2018.04.004.

[366] Tanaka H, Tamai Y, Koga K. Large thermal expansivity of clathrate hydrates. J Phys Chem B 1997;101:6560–5. https://doi.org/10.1021/jp970511g.

[367] English NJ. Effect of electrostatics techniques on the estimation of thermal conductivity via equilibrium molecular dynamics simulation: Application to methane hydrate. Mol Phys 2008;106:1887–98. https://doi.org/10.1080/00268970802360348.

[368] English NJ, Tse JS. Mechanisms for thermal conduction in methane hydrate. Phys Rev Lett 2009;103:15901. https://doi.org/10.1103/PhysRevLett.103.015901.

[369] English NJ, Tse JS, Carey DJ. Mechanisms for thermal conduction in various polymorphs of methane hydrate. Phys Rev B 2009;80:134306. https://doi.org/10.1103/PhysRevB.80.134306.

[370] English N, Gorman P, MacElroy J. Mechanisms for thermal conduction in hydrogen hydrate. J Chem Phys 2012;136:44501. https://doi.org/10.1063/1.3677189.

[371] Ghafari H, Mohammadi-Manesh H. The thermal properties of binary structure sI clathrate hydrate from molecular dynamics simulation. Mol Simul 2019;45:614–22. https://doi.org/10.1080/08927022.2019.1572142.

[372] Fang B, Ning F, Cao P, Peng L, Wu J, Zhang Z, et al. Modeling thermodynamic properties of propane or tetrahydrofuran mixed with carbon dioxide or methane in structure-II clathrate hydrates. J Phys Chem C 2017;121:23911–25. https://doi.org/10.1021/acs.jpcc.7b06623.

[373] Arai Y, Takeya S, Alavi S, Yamauchi Y, Ohmura R. Effect of nonspherical encapsulated guests on the volumetric behavior of structure H clathrate hydrates. J Phys Chem C 2018;122:27631–9. https://doi.org/10.1021/acs.jpcc.8b09923.

[374] Erfan Niya H, Modarress H, Zaminpayma E. Molecular dynamics simulation of structure II clathrate hydrates of xenon and large hydrocarbon guest molecules. J Clust Sci 2011;22:11–30. https://doi.org/10.1007/s10876-011-0358-6.

[375] Min J, Ahn Y, Baek S, Shin K, Cha M, Lee JW. Effects of large guest molecular structure on thermal expansion. J Phys Chem C 2019;123:20705–14. https://doi.org/10.1021/acs.jpcc.9b04125.

[376] Mirzaeifard S, Servio P, Rey AD. Molecular dynamics characterization of the water-methane, ethane, and propane gas mixture interfaces. Chem Eng Sci 2019;208:114769. https://doi.org/10.1016/j.ces.2019.01.051.

[377] Mirzaeifard S, Servio P, Rey AD. Characterization of nucleation of methane hydrate crystals: Interfacial theory and molecular simulation. J Colloid Interface Sci 2019;557:556–67. https://doi.org/10.1016/j.jcis.2019.09.056.

[378] Vlasic TM, Servio P, Rey AD. Atomistic modeling of structure II gas hydrate mechanics: Compressibility and equations of state. AIP Adv 2016;6:85317. https://doi.org/10.1063/1.4961728.

[379] Greathouse JA, Cygan RT, Simmons BA. Vibrational spectra of methane clathrate hydrates from molecular dynamics simulation. J Phys Chem B 2006;110:6428–31. https://doi.org/10.1021/jp060471t.

[380] Baumert J, Gutt C, Shpakov VP, Tse JS, Krisch M, Müller M, et al. Lattice dynamics of methane and xenon hydrate: Observation of symmetry-avoided crossing by experiment and theory. Phys Rev B 2003;68:174301. https://doi.org/10.1103/PhysRevB.68.174301.

[381] Tse JS, Klein ML, McDonald IR. Computer simulation studies of the structure I clathrate hydrates of methane, tetrafluoromethane, cyclopropane, and ethylene oxide. J Chem Phys 1984;81:6146–53. https://doi.org/10.1063/1.447569.

[382] Tse JS, Shpakov VP, Murashov VV, Belosludov VR. The low frequency vibrations in clathrate hydrates. J Chem Phys 1997;107:9271–4. https://doi.org/10.1063/1.475218.

[383] Inoue R, Tanaka H, Nakanishi K. Molecular dynamics simulation study of the anomalous thermal conductivity of clathrate hydrates. J Chem Phys 1996;104:9569–77. https://doi.org/10.1063/1.471705.

[384] Futera Z, Celli M, del Rosso L, Burnham CJ, Ulivi L, English NJ. Vibrational modes of hydrogen hydrates: A first-principles molecular dynamics and raman spectra study. J Phys Chem C 2017;121:3690–6. https://doi.org/10.1021/acs.jpcc.6b11029.

[385] English NJ, Tse JS. Dynamical properties of hydrogen sulphide motion in its clathrate hydrate from Ab initio and classical isobaric−isothermal molecular dynamics. J Phys Chem A 2011;115:6226–32. https://doi.org/10.1021/jp111485w.

[386] Hiratsuka M, Ohmura R, Sum AK, Alavi S, Yasuoka K. A molecular dynamics study of guest–host hydrogen bonding in alcohol clathrate hydrates. Phys Chem Chem Phys 2015;17:12639–47. https://doi.org/10.1039/C4CP05732E.

[387] Daghash SM, Servio P, Rey AD. From infrared spectra to macroscopic mechanical properties of sH gas hydrates through atomistic calculations. Molecules 2020;25:5568. https://doi.org/10.3390/molecules25235568.

[388] Hiratsuka M, Ohmura R, Sum AK, Yasuoka K. Vibrational modes of methane in the structure H clathrate hydrate from ab initio molecular dynamics simulation. J Chem Phys 2012;137:144306. https://doi.org/10.1063/1.4757914.

[389] Hiratsuka M, Ohmura R, Sum AK, Yasuoka K. Molecular vibrations of methane molecules in the structure I clathrate hydrate from ab initio molecular dynamics simulation. J Chem Phys 2012;136:44508. https://doi.org/10.1063/1.3677231.

[390] Vlasic TM, Servio PD, Rey AD. Infrared spectra of gas hydrates from first-principles. J Phys Chem B 2019;123:936–47. https://doi.org/10.1021/acs.jpcb.8b10223.

[391] Van Klaveren EP, Michels JPJ, Schouten JA, Klug DD, Tse JS. Computer simulations of the dynamics of doubly occupied N2 clathrate hydrates. J Chem Phys 2002;117:6637–45. https://doi.org/10.1063/1.1502645.

[392] Jendi ZM, Servio P, Rey AD. Molecular mobility in carbon dioxide hydrates. Mol Syst Des Eng 2017;2:500–6. https://doi.org/10.1039/C7ME00041C.

[393] Frankcombe TJ, Kroes G-J. Molecular dynamics simulations of type-sII hydrogen clathrate hydrate close to equilibrium conditions. J Phys Chem C 2007;111:13044–52. https://doi.org/10.1021/jp071006e.

[394] Liang S, Kusalik PG. The mobility of water molecules through gas hydrates. J Am Chem Soc 2011;133:1870–6. https://doi.org/10.1021/ja108434h.

[395] Zhang Z, Kusalik P, Guo G-J. Bridging solution properties to gas hydrate nucleation through guest dynamics. Phys Chem Chem Phys 2018;20:24535–8. https://doi.org/10.1039/C8CP04466J.

[396] Mathews SL, Servio PD, Rey AD. Heat capacity, thermal expansion coefficient, and grüneisen parameter of CH4, CO2, and C2H6 hydrates and ice Ih via density functional theory and phonon calculations. Cryst Growth Des 2020;20:5947–55. https://doi.org/10.1021/acs.cgd.0c00630.

[397] Jiang H, Jordan KD. Comparison of the properties of xenon, methane, and carbon dioxide hydrates from equilibrium and nonequilibrium molecular dynamics

simulations. J Phys Chem C 2010;114:5555–64. https://doi.org/10.1021/jp9063406.

[398] Pétuya C, Martin-Gondre L, Aurel P, Damay F, Desmedt A. Unraveling the metastability of the SI and SII carbon monoxide hydrate with a combined DFT-neutron diffraction investigation. J Chem Phys 2019;150:184705. https://doi.org/10.1063/1.5093202.

[399] Cladek BR, Everett SM, Mcdonnell MT, Tucker MG, Ke DJ, Rawn CJ. Molecular rotational dynamics in mixed CH4−CO2 hydrates: insights from molecular dynamics simulations 2019. 10.1021/acs.jpcc.9b06242.

[400] Gorman PD, English NJ, MacElroy JMD. Dynamical and energetic properties of hydrogen and hydrogen–tetrahydrofuran clathrate hydrates. Phys Chem Chem Phys 2011;13:19780. https://doi.org/10.1039/c1cp21882d.

[401] Vlasic TM, Servio PD, Rey AD. THF hydrates as model systems for natural gas hydrates: Comparing their mechanical and vibrational properties. Ind Eng Chem Res 2019;58:16588–96. https://doi.org/10.1021/acs.iecr.9b02698.

[402] Yu X, Zhu J, Du S, Xu H, Vogel SC, Han J, et al. Crystal structure and encapsulation dynamics of ice II-structured neon hydrate. Proc Natl Acad Sci 2014;111:10456–61. https://doi.org/10.1073/pnas.1410690111.

[403] Luis DP, Romero-Ramirez IE, González-Calderón A, López-Lemus J. The coexistence temperature of hydrogen clathrates: A molecular dynamics study. J Chem Phys 2018;148:114503. https://doi.org/10.1063/1.5017854.

[404] Michalis VK, Tsimpanogiannis IN, Stubos AK, Economou IG. Direct phase coexistence molecular dynamics study of the phase equilibria of the ternary methane–carbon dioxide–water hydrate system. Phys Chem Chem Phys 2016;18:23538–48. https://doi.org/10.1039/C6CP04647A.

[405] Zhu J, Du S, Yu X, Zhang J, Xu H, Vogel SC, et al. Encapsulation kinetics and dynamics of carbon monoxide in clathrate hydrate. Nat Commun 2014;5:4128. https://doi.org/10.1038/ncomms5128.

[406] Sun R, Duan Z. Prediction of CH4 and CO2 hydrate phase equilibrium and cage occupancy from ab initio intermolecular potentials. Geochim Cosmochim Acta 2005;69:4411–24. https://doi.org/10.1016/j.gca.2005.05.012.

[407] Erfan-Niya H, Modarress H, Zaminpayma E. Molecular dynamics study on the structure I clathrate-hydrate of methane+ethane mixture. Energy Convers Manag 2011;52:523–31. https://doi.org/10.1016/j.enconman.2010.07.027.

[408] Tung Y-T, Chen L-J, Chen Y-P, Lin S-T. In situ methane recovery and carbon dioxide sequestration in methane hydrates: A molecular dynamics simulation study. J Phys Chem B 2011;115:15295–302. https://doi.org/10.1021/jp2088675.

[409] Zhang K, Qin G. Mechanistic and kinetic study of CO2-CH4 exchange process in methane hydrates using molecular dynamics simulation. Soc Pet Eng - SPE Eur Featur 81st EAGE Conf Exhib 2019 2019:1–15. 10.2118/195457-MS.

[410] Qi Y, Ota M, Zhang H. Molecular dynamics simulation of replacement of CH4 in hydrate with CO2. Energy Convers Manag 2011;52:2682–7. https://doi.org/10.1016/j.enconman.2011.01.020.

[411] Nohra M, Woo TK, Alavi S, Ripmeester JA. Molecular dynamics Gibbs free energy calculations for CO2 capture and storage in structure I clathrate hydrates in the presence of SO2, CH4, N2, and H2S impurities. J Chem Thermodyn 2012;44:5–12. https://doi.org/10.1016/j.jct.2011.08.025.

[412] Nakate P, Ghosh B, Das S, Roy S, Kumar R. Molecular dynamics study on growth of carbon dioxide and methane hydrate from a seed crystal. Chinese J Chem Eng 2019;27:2074–80. https://doi.org/10.1016/j.cjche.2019.02.006.

[413] Liu Y, Zhao L, Deng S, Bai D. Evolution of bubbles in decomposition and replacement process of methane hydrate. Mol Simul 2017;7022:1–13. https://doi.org/10.1080/08927022.2017.1359745.

[414] Geng C, Wen H, Zhou H. Molecular simulation of the potential of methane reoccupation during the replacement of methane hydrate by CO2. J Phys Chem A 2009;113:5463–9. https://doi.org/10.1021/jp811474m.

[415] Dornan P, Alavi S, Woo TK. Free energies of carbon dioxide sequestration and methane recovery in clathrate hydrates. J Chem Phys 2007;127:124510. https://doi.org/10.1063/1.2769634.

[416] Qiu N, Bai X, Xu J, Sun N, Francisco JS, Yang M, et al. Adsorption behaviors and phase equilibria for clathrate hydrates of sulfur and nitrogen containing small molecules. J Phys Chem C 2019;123:2691–702. https://doi.org/10.1021/acs.jpcc.8b05962.

[417] Buchanan P, Soper AK, Thompson H, Westacott RE, Creek JL, Hobson G, et al. Search for memory effects in methane hydrate: Structure of water before hydrate formation and after hydrate decomposition. J Chem Phys 2005;123:164507. https://doi.org/10.1063/1.2074927.

[418] Belosudov RV, Bozhko YY, Zhdanov RK, Subbotin OS, Kawazoe Y, Belosludov VR. Hydrogen hydrates: Equation of state and self-preservation effect. Fluid Phase Equilib 2016;413:220–8. https://doi.org/10.1016/j.fluid.2015.11.031.

[419] Nguyen AH, Molinero V. Identification of clathrate hydrates, hexagonal ice, cubic ice, and liquid water in simulations: the CHILL+ algorithm. J Phys Chem B 2015;119:9369–76. https://doi.org/10.1021/jp510289t.

[420] Naeiji P, Woo TK, Alavi S, Ripmeester JA. Molecular dynamic simulations of clathrate hydrate anomalous preservation: The effect of coating clathrate hydrate phases. J Phys Chem C 2019;123:28715–25. https://doi.org/10.1021/acs.jpcc.9b07769.

[421] Alavi S, Udachin K, Ripmeester JA. Effect of guest-host hydrogen bonding on the structures and properties of clathrate hydrates. Chem - A Eur J 2010;16:1017–25. https://doi.org/10.1002/chem.200902351.

[422] Dureckova H, Woo TK, Alavi S, Ripmeester JA. Molecular dynamics simulation of halogen bonding in Cl2, BrCl, and mixed Cl2/Br 2 clathrate hydrates. Can J Chem 2015;93:864–73. https://doi.org/10.1139/cjc-2014-0593.

[423] Dureckova H, Woo TK, Alavi S. Molecular simulations and density functional theory calculations of bromine in clathrate hydrate phases. J Chem Phys 2016;144:44501. https://doi.org/10.1063/1.4940321.

[424] Dureckova H, Woo TK, Udachin KA, Ripmeester JA, Alavi S. The anomalous halogen bonding interactions between chlorine and bromine with water in clathrate hydrates. Faraday Discuss 2017;203:61–77. https://doi.org/10.1039/C7FD00064B.

[425] Alavi S, Ripmeester JA. Effect of small cage guests on hydrogen bonding of tetrahydrofuran in binary structure II clathrate hydrates. J Chem Phys 2012;137:54712. https://doi.org/10.1063/1.4739928.

[426] Moudrakovski IL, Udachin KA, Alavi S, Ratcliffe CI, Ripmeester JA. Facilitating guest transport in clathrate hydrates by tuning guest-host interactions. J Chem Phys 2015;142:74705. https://doi.org/10.1063/1.4907720.

[427] Trueba AT, Kroon MC, Peters CJ, Moudrakovski IL, Ratcliffe CI, Alavi S, et al. Inter-cage dynamics in structure I, II, and H fluoromethane hydrates as studied by NMR and molecular dynamics simulations. J Chem Phys 2014;140. https://doi.org/10.1063/1.4874636.

[428] Alavi S, Ohmura R, Ripmeester JA. A molecular dynamics study of ethanol–water hydrogen bonding in binary structure I clathrate hydrate with CO2. J Chem Phys 2011;134:54702. https://doi.org/10.1063/1.3548868.

[429] Kondo Y, Alavi S, Murayama K, Ruiz A, Takeya S, Ohmura R. Effect of help-guest size and hydrogen bonding on the stability of N-methylpiperidine structure H clathrate hydrate. J Phys Chem C 2020;124:5978–86. https://doi.org/10.1021/acs.jpcc.9b11910.

[430] English NJ, Tse JS. Pressure-induced amorphization of methane hydrate. Phys Rev B 2012;86:104109. https://doi.org/10.1103/PhysRevB.86.104109.

# Chapter 3 (Objective 1): Pure CO₂ clathrate hydrate growth in

# the presence of pure/ mixed kinetic hydrate promoters

As Figure 13 (step 5) of the chapter 1 indicated, in chapters 1 and 2, the hydrate-based applications for $CO_2$ capture, sequestration, utilization and previous MD simulations reported in the literature were overviewed. In this chapter, the effects of KHPs on $CO_2$ gas hydrates were explored.

Since the slow formation rate and limited storage capacity of gas hydrates obstruct the possible industrial application of this phenomenon, the inclusion of kinetic hydrate promoters (KHPs) would be the most important alternative beside the new mechanical methods. Up until now, handreds of mentioned components from different molecular categories have been introduced in the literature. Between these substances, metal nanoparticles and organic components are environmentally the proper alternatives for the applications of hydrate-based $CO_2$ utilization methods. However, by understanding their single or synergistic impressions, it can be possible to prepare novel and more efficient promoters for upgrading such technologies. In this chapter, the effects of synergistic kinetic hydrate promoters (KHPs) on $CO_2$ clathrate hydrate using molecular dynamics simulations were investigated.

Operating conditions to perform the MD simulations in this chapter were selected from the phase equilibrium curve (P-T curve) of pure $CO_2$ hydrate where it can be formed in the hydrate-liquid-vapor (H-L-V) region. If the pressure and temperature conditions were chosen from this region of the equilibrium cure, it is because analyzing $CO_2$ hydrate formation in this zone of the P-T curve can be useful for different suggested $CO_2$ hydrate-based utilization processes in the industry.

The required equations to perform MD simulations are given in Appendix 2. Also, an example of LAMMPS code for $CO_2$ hydrate in the presence of Cu, Ag, and Fe metal particles and urea molecules is presented in Appendix 3.

This chapter was published as a research paper in the Journal of Chemical Engineering Science:

Sinehbaghizadeh, S., Saptoro, A., Naeiji, P., Tiong, A.N.T., Mohammadi, A.H., 2022. Insights into the synergistic effects of metal particles (Ag, Cu, and Fe) and urea on $CO_2$ clathrate hydrate growth using molecular dynamics simulations. *Journal of Chemical Engineering Science*, 2022, 264, 118194, Elsevier.

# Insights into the synergistic effects of metal particles (Ag, Cu, and Fe) and urea on $CO_2$ clathrate hydrate growth using molecular dynamics simulations

Saeed Sinehbaghizadeh [a,*], Agus Saptoro [a,*], Parisa Naeiji [b], Angnes Ngieng Tze Tiong [a], Amir H. Mohammadi [c]

[a] Department of Chemical and Energy Engineering, Curtin University Malaysia, CDT 250, Miri 98009, Sarawak, Malaysia
[b] GFZ German Research Centre for Geosciences, Telegrafenberg 14473, Potsdam, Germany
[c] Discipline of Chemical Engineering, School of Engineering, University of KwaZulu-Natal, Howard College Campus, King George, V Avenue, Durban 4041, South Africa

## HIGHLIGHTS

- The promotion process of metal particles and urea on $CO_2$ hydrate growth kinetics through molecular dynamics simulations was investigated.
- Hydrate structural analysis revealed that growth kinetics can be enhanced by the combination of metal particles and urea.
- The synergic of Cu + Fe + urea outperforms the mixture of either Cu + Ag + Fe + urea or Cu + Ag + Fe.
- The promotion effects of Cu + Ag and Cu + Fe were not observed.
- The growth kinetic mechanism of $CO_2$ hydrate above and below the water freezing point is different.

## GRAPHICAL ABSTRACT
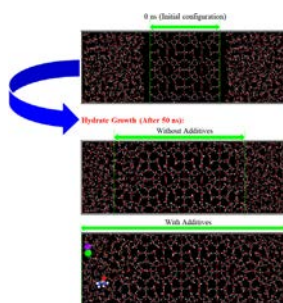
## ABSTRACT

A variety of industrial applications of hydrate-based $CO_2$ capture and utilization technologies are hindered by the complex and slow hydrate formation; however, improving $CO_2$ hydrate formation kinetics can be facilitated by adding the accelerators (promoters). In this regard, understanding the promotion mechanisms of these compounds on the hydrate formation at the molecular level would assist in either establishing feasible processes or finding more efficient promoters. In this work, $CO_2$ hydrate growth and formation in the presence of hybrid metal particles (Ag, Cu, and Fe) and urea molecule has been explored through molecular dynamics (MD) simulation at below and above water freezing point. Different criteria were used to characterize and analyse the $CO_2$ hydrate formation kinetics. The outcomes reveal that, although the mixture of Cu, Ag, and Fe metal particles has positive effects on the rate of hydrate formation above the ice point, the mixture of Cu, Fe, and urea (without the inclusion of Ag) in comparison with the other investigated systems, possesses the highest promotion effect on the clathrate hydrate growth rate. This combination of metal particles creates various functions in the solution phase adjacent to the hydrate surface. The metal particles and urea could promote the formation of new cages at the hydrate-solution boundary by decreasing the heat and mass transport resistances of $CO_2$ in water. In addition, the improvement of combined metal particles and urea under water freezing was found to be less

---

* Corresponding authors.
  *E-mail addresses:* s.baghizadeh@postgrad.curtin.edu.my (S. Sinehbaghizadeh), agus.saptoro@curtin.edu.my (A. Saptoro).

---

**Nomenclature**

| | |
|---|---|
| MD | Molecular Dynamics |
| Ag | Silver |
| Fe | Iron |
| Cu | Cupper |
| PE | Potential Energy |
| MSD | Mean Squared Displacement |
| $F_3$ | Three-body Structural order |
| RDF | Radial Distribution Function |
| $g_{ab}$ | RDF between atoms $a$ and $b$ |
| P | Pressure |
| T | Temperature |
| K | Kelvin |
| MPa | Mega Pascal |
| Å | Angstrom |
| HB | Hydrogen bonds |
| ns | nano-second |
| ps | pico-second |

*Greek letters*

| | |
|---|---|
| $a$ | Atom $a$ |
| $b$ | Atom $b$ |
| $\varepsilon$ | Cross LJ parameters |
| $\sigma$ | Cross LJ parameter |
| $\theta$ | Angle |

*Subscripts*

| | |
|---|---|
| $i$ | Atom $i$ |
| $j$ | Atom $j$ |
| $k$ | Atom $k$ |
| x | x direction |
| y | y direction |
| z | z direction |

---

substantial. However, the behaviours of combined metal particles without urea at different thermodynamic conditions are quite dissimilar.

---

## 1. Introduction

Many industrial countries are committed to controlling the emission of greenhouse gases, more specifically $CO_2$. Cutting down the generated $CO_2$ by optimizing the processes involved in manufacturing divisions, capturing $CO_2$, and developing $CO_2$ utilization/conversion technologies to produce valuable products could sequentially be the most immediate pathway. Although the methods such as adsorption (Ayittey et al., 2020b, 2020a; Dhoke et al., 2021; Saptoro and Huo, 2013; Zhu et al., 2021), absorption (Ayittey et al., 2021; Hafizi et al., 2021; Jiang et al., 2021), membrane (Senatore et al., 2021; Wu et al., 2021; Zhang et al., 2021), and cryogenic (Cann et al., 2021; Machida et al., 2021) for capturing $CO_2$ from the emitted gas mixtures have been proposed, gas hydrate crystallization would also be a novel technique for $CO_2$ separation from the flue gas (Gambelli et al., 2021), fuel gas (Muromachi, 2021), landfill gas (Xu et al., 2019) as well as syngas (Rezaei et al., 2022). Gas hydrate technologies according to the U.S. Department of Energy was known as a promising method for $CO_2$ capture and storage (Elwell and Grant, 2006). Estimations suggest that 1 m³ of hydrate can store 170 m³ of gas at standard conditions (Strobel et al., 2007). Moreover, the separated $CO_2$ can be utilized or sequestered by other hydrate-based applications e.g. refrigeration systems (Xie et al., 2019), seawater desalination (Babu et al., 2018), fruits juice concentration (Rudolph et al., 2021), and gas storage applications (Jokar et al., 2021). This method can also be used for exploiting $CH_4$ from deposited hydrate in oceans or permafrost regions and coincide with sequestering $CO_2$ in the geological sites (Zhang et al., 2017).

Clathrate hydrates are composed of water and suitable size gas molecules entrapped in the cages which are formed by the network of hydrogen-bonded water molecules. Under prevailing thermodynamic conditions and with considering the molecular diameter, and chemical properties of guest molecules, three different clathrate structures of hydrates (sI, sII, and sH) can be formed. Among the different hydrate guests, the $CO_2$ molecule at moderated formation pressure by contributing to the hydrate phase can generate sI of the clathrate (Sloan and Koh, 2008). Although the issue of hydrate formation pressure by adding the second guest namely large molecular liquid hydrocarbons to the water phase can be reduced (Sinehbaghizadeh et al., 2019b, 2019a, 2018, 2017), the rate of $CO_2$ hydrate formation from a kinetic point of view is inappreciable which hinders the hydrate-based processes toward being industrialized. Many investigations have been conducted to discover qualified promotion agents. A good example of this is the addition of nanoparticles which help to enhance the mass transfer at the interface of solid and solution by creating numerous nucleation sites. Evidence suggests the influence of nanoparticles on clathrate hydrate growth is highly complicated and dependent on a variety of influencing factors. Also, the surface functional groups of nanoparticles may determine the promoter or inhibitor effects (Liu et al., 2020; Yu et al., 2016; Zhou et al., 2014). According to an investigation of the kinetics of hydrate formation in contact with Cu, and Ag nanoparticles, it was found that the effects of Cu and Ag nanoparticles are intermediate and insignificant respectively. Also, nanoparticles with high specific areas may enhance the mass transfer and improve gas consumption by activating the interfacial area (Adibi et al., 2020; Said et al., 2016). The equilibrium formation condition for different additives is also unique. For example, the best concentration and condition for $Fe_3O_4$ nanoparticles in contact with the magnetic field were found to be 0.15 wt% at 4 MPa and 274 K respectively (Firoozabadi et al., 2018). Furthermore, the inclusion of the secondary or a couple of substances to the primary solution system may manifold the positive impressions of additives. There are several organic and environmentally harmless components that have been acknowledged as thermodynamic inhibitors but simultaneously strong kinetic promoters. As a low-toxic biological metabolite, the addition of urea can be regarded as a thermodynamic inhibitor for $CO_2$ hydrate (Gong et al., 2022; Muromachi et al., 2015), however, the kinetic effects of urea on $CO_2$ hydrates were found to be substantial and in the macroscopic scale, urea kinetically acts as a promoter for

clathrate hydrate of $CO_2$. It was reported that at 2.7 MPa and 278 K, the inclusion of urea can halve the induction time of $CO_2$ hydrate during crystallization (Chen and Ho, 2017).

Through experimental investigations such as X-ray diffraction (XRD) and Raman or NMR spectroscopy, the distribution of guest molecules in the cages, as well as the crystalline identification of structures can be studied. However, it is difficult to determine the relationship between the nature of components in the system and the process of crystallization at a molecular level as well as initial nanoseconds. To assess and explore the positive and negative aspects of promoters on $CO_2$ hydrate besides the macroscopic experiments, molecular dynamics (MD) simulations can be perfectly employed. We recently reviewed the role of hydrate promoters and MD frameworks of $CO_2$ clathrate hydrates in terms of new insights and research findings to elucidate the fundamental properties of $CO_2$ hydrates at the molecular level (Sinehbaghizadeh et al., 2022b). MD results of $CO_2$ double and mixed hydrates showed that the type of hydrate promoters can play a determinative role in the stabilization of the clathrate hydrate network (Sinehbaghizadeh et al., 2022a). MD simulation trajectories suggested that urea may appear to mediate the *meta*-stable amorphous hydrate and modification of solution characteristics for supporting clathrate hydrate formation (Lim et al., 2014). Also, molecular analysis of $CO_2$ hydrate formation with metal particles (Cu, Fe, and Ag) at various concentrations clarified that such microparticles possess a mixed effect on growth kinetics. Furthermore, the promoting effect of Cu at 1.0 wt% on hydrate growth was found to be higher than either Fe or Ag. Although the effect of Fe particles had a medium promotion, Ag particles were found to be little impact on the growth rate of $CO_2$ hydrate or even act as an inhibitor (Liu et al., 2021). Moreover, the formation rate can be attributed to the operating conditions of the system. Through the MD framework, the $CO_2$ hydrate growth in contact with Ag nanoparticles at 260 K was found to be more rapid than either at 250 K or 270 K. Additionally, Ag additive may facilitate $CO_2$ dissolution as well as diffusion coefficient by increasing the $CO_2$ molecular migration from the solution side to the solid–liquid boundary (Mahmoodi et al., 2021).

Although some MD works in the literature have studied the different aspects of $CO_2$ hydrate formation with promoters, investigations directed toward a better understanding of the synergistic effects of the hydrate promoters from diverse types at the molecular level have mostly remained unexplored and poorly understood. Thus, in this work, the synergistic effects of metal particles and urea on the solution phase in contact with $CO_2$ sI hydrate were studied. To the best of our knowledge, this is the first investigation that analyses the hybrid addition of these materials on $CO_2$ hydrate growth via acting at the solid-solution interface. The simulation results of this work can be useful to understand the mechanisms involved in $CO_2$ hydrate formation in the presence of synergic additives. It is worth mentioning that the interpretation of MD observations may help to accelerate the practical implementations of hydrate-based $CO_2$ capture and utilization (HBCC/U) systems.

## 2. Simulation methodology

### 2.1. Model setup

The simulation system consists of a crystal layer of $CO_2$ sI hydrate sandwiched by a solution of $CO_2$ and water was considered as an initial configuration. The $CO_2$ hydrate slab was employed as the solid substrate for hydrate growth so that it would help to overcome the time lag of initial nucleation. To build the initial hydrate, a unit cell of sI hydrate with a lattice parameter of 12.03 Å was adopted (Takeuchi et al., 2013). To generate a

$2 \times 2 \times 2$ hydrate slab containing 368 water and 64 $CO_2$ molecules, the sI hydrate unit cell was replicated two times in all directions ($24.06 \times 24.06 \times 24.06$ Å$^3$). The $CO_2$ molecules were located at the centre of both small and large cages. Subsequently, the hydrate slab was allocated in the middle of the mixture of 736 water and 128 $CO_2$ molecules, yielding a simulation box length of 72 Å in the Z direction. Also, the solution and hydrate substrate were aligned to the X-Y plane (cross-section area) with the same dimension of 24.06 Å. The periodic boundary conditions in all directions were set so that the hydrate substrate model along the X and Y directions could be effectively infinite. To understand the microscopic effects of the combination of metal particles and molecular impacts of urea, the growth of $CO_2$ hydrates in the presence of such mixtures was evaluated; Table 1 gives the combined additives as well as their concentrations. In addition, the presence of pure Cu metal particles and single urea to make a comparison with mixed additives were also simulated. Each set of the simulation was carried out at two P-T conditions of 2 MPa and 260 K, 3 MPa and 275 K. It is worth noting that the high concentrations of solid metal particles can cause a stronger Brownian motion in the solution. Accordingly, it may increase the activation energy to agglomerate and inhibit orderly intermolecular movements (Liu et al., 2021). Therefore, the low concentrations of these additives in this work were chosen.

### 2.2. Computational details

All MD simulations were carried out with the utilization of LAMMPS software, developed by Sandia National Laboratories which is an open-source code (Steve et al., 2012). The accuracy of MD simulations is dependent upon the force field and the parameters used to define the interactions in the system. Intramolecular interactions are normally described in the energy terms of deformation and coupling terms between deformations of internal coordinates whereas Intermolecular interactions contain the Lennard-Jones function and the electrostatic term (Frenkel and Smit, 2002). Since the TIP4P/Ice force field has been successfully employed to describe the properties of water during hydrate growth (Maddah et al., 2018; Mahmoodi et al., 2021; Phan et al., 2021), water molecules were simulated by this intermolecular model (Abascal et al., 2005). Moreover, it was previously shown that among the different versions of TIP4P water models, the TIP4P/Ice approach yields better agreement with the $CO_2$ hydrate experimental results (Míguez et al., 2015). The $CO_2$ molecules were also modelled using the TraPPE potential model (Eggimann et al., 2014). This force field can quantitatively reproduce the vapor–liquid equilibria (VLE) of the neat/ mixed systems and create a good balance between dispersive and electrostatic (quadrupole–quadrupole) interactions. To model the interactions of urea molecules, the potential approach proposed by Kallies was utilized (Kallies, 2002). Using this force field, the effects of urea on the structure of water and the properties in terms of the extent of the hydrogen-bond network, the interaction energy, and radial profiles of excess coordination numbers have been successfully analysed (Idrissi et al., 2010; Wang et al., 2021). In addition, the Lennard-Jones potential was applied to describe the behaviour of metal particles in the simulated systems. Due to the limitations of computer hardware, single atoms for Cu, Fe, and Ag metal particles instead of metal clusters were considered to reduce the number of calculations (Liu et al., 2021). In the system containing Cu, Fe, and Ag additives, the metal particles were uniformly distributed in the solution. The Lennard-Jones parameters between unlike atoms were calculated from the geometric combination rule [$\varepsilon_{ij}=(\varepsilon_{ii}.\varepsilon_{jj})^{1/2}$ and $\sigma_{ij}=(\sigma_{ii}.\sigma_{jj})^{1/2}$]. The long-range Coulomb interactions were calculated with a cut-off of 12 Å and calculated using the "pppm" algorithm (Hockney and Eastwood,

**Table 1**
List of mixed additives and amounts in the water solution.

| No. | Hydrate additive | No. of metal atom(s)/ molecule in the solution | | | | Content in the solution (wt%) |
|---|---|---|---|---|---|---|
| | | **Cu** | **Fe** | **Ag** | **Urea** | |
| 1 | Pure water | – | – | – | – | – |
| 2 | Urea | – | – | – | 1 | Urea molecule (0.32 %) |
| 3 | Cu | 3 | – | – | – | metal particles [Cu (1.01 %)] |
| 4 | Cu + Ag-(1) | 1 | – | 1 | – | metal particles [Cu (0.33 %) + Ag (0.56 %)] |
| 5 | Cu + Fe-(1) | 1 | 1 | – | – | metal particles [Cu (0.33 %) + Fe (0.29 %)] |
| 6 | Cu + Ag + Fe-(1) | 1 | 1 | 1 | – | metal particles [Cu (0.33 %) + Ag (0.56 %) + Fe (0.29 %)] |
| 7 | Cu + Ag-(2) | 2 | – | 2 | – | metal particles [Cu (0.66 %) + (Ag (1.12 %)] |
| 8 | Cu + Ag + Fe-(2) | 2 | 2 | 2 | – | metal particles [Cu (0.66 %) + Ag (1.12 %) + Fe (0.58 %)] |
| 9 | Cu + Fe + Urea-(1) | 1 | 1 | – | 1 | metal particles [Cu (0.33 %) + Fe (0.29 %)] + Urea molecule (0.32 %) |
| 10 | Cu + Ag + Fe + Urea-(1) | 1 | 1 | 1 | 1 | metal particles [Cu (0.33 %) + Ag (0.56 %) + Fe (0.29 %)] + Urea molecule (0.32 %) |

2021). To constrain the rigidity of water molecules, the Shake algorithm was utilized (Ryckaert et al., 1977). By applying the conjugate gradient algorithm, the energy minimization before each simulation was carried out. The initial configurations at the simulation temperatures were then conducted in the *NVT* canonical ensemble for 40 ps. This step was subsequently followed by performing *NPT* ensemble for at least 150 ns by Nose-Hoover thermostat and barostat with the time step of 1 fs. Implementing *NPT* ensemble can be useful for investigating the hydrate growth phenomenon (Naeiji et al., 2019b, 2019a, 2017, 2016). It should be noted that The *NPT* ensemble was implemented in all directions. To solve the motion equation and obtain the motion trajectory of atoms, the Verlet algorithm was also used (Grubmüller et al., 1991). All simulations were conducted under the prevailing P-T conditions (2 MPa and 260 K; 3 MPa and 275 K) to identify the molecular mechanisms, responsible for the $CO_2$ crystal growth in the absence or presence of combined additives.

## 3. Results and discussion

This section deals with analysing the synergistic impacts of additives on $CO_2$ hydrate growth. However, since the goal of doing simulations was to study the effect of a different set of additives on $CO_2$ hydrate growth, the main focus was not on the interactions of individual additives with water molecules at the surface. To do so, different parameters such as hydrate growth thickness, potential energy, three-body structural order ($F_3$), number of hydrogen bonds (H-bonds), mean squared displacement (MSD), radial distribution function (RDF), and the composition of the solution phase was computed. The results of the impacts of mentioned additives in Table 1 on $CO_2$ hydrate growth at two different thermodynamic conditions are presented in the following sub-sections.

### 3.1. Hydrate growth thickness

Understanding the transport properties of the dense hydrate phase is pivotal in identifying the controller mechanisms of the hydrate formation and stability. Recent experimental reports on the mass transfer mechanism of gas hydrate formation from water droplets via X-ray computed tomography at the mesoscopic level (300 μm) showed that due to the outward permeation of water through capillary pores in the hydrate shell, the initial diffusion regime is controlled by the transport of water through the shell. However, the first occurrence of hydrate protrusions changes the mode of water transport from diffusion to permeation (Liang et al., 2022). The investigations of components in the system in terms of how they affect each other at smaller scales e.g. nanometres and nanoseconds would also help to detect the behaviours of components at very early stages of the hydrate formation. In addi-

tion, analysing the growth evolution at the molecular level would bridge the gap that exists at scales, the experiment is unable to get so close to. MD framework suggested that the crystallization mechanism of clathrate hydrates can be segmented into three different steps. The formation of blobs is the first step in which dilute solution is in equilibrium with solvent-separated guest molecules. Clathrate cages are then organized by the water so that the solution forms the amorphous clathrate and subsequently, critical nucleus growth can occur. This stage is followed by amorphous maturation in the crystalline phase in which hydrate grows around the nucleus (Jacobson et al., 2010). Since the clathrate nucleation from the solution of gas and water is a stochastic event that needs much time to form, two first steps were skipped, and the growth stage of $CO_2$ hydrate was explored in this work. Fig. 1 (a) shows the snapshots of the simulation box up to 400 ns at 2 MPa and 260 K. To better understand the evolution of the solution phase, the simulation box was divided into five different sections in which "Si (i: 1–4)" represents the water/gas solution beside the initial sI crystal. As the simulation time proceeded, the hydrate growth occurred at the interface of the solution phase. This Figure also shows that up to 150 ns, most of the $CO_2$ molecules were entrapped in the hydrate cages and the solution gradually changed from a disordered configuration to an ordered solid hydrate during the simulation time; so that the crystal growth was entirely completed as is shown in the final snapshot after 400 ns. With increasing the regularity of guest–host molecular positions, the formed network structurally remained stable. However, the growth kinetics could be changed once additives were included. Fig. 1(b) displays the growth evolution of $CO_2$ hydrate in the presence of mixed metal particles (Cu and Fe) and urea. It can be observed that the existence of additives significantly promoted the rate of crystallization for $CO_2$ clathrate hydrate. The first snapshot demonstrated that after 25 ns, the S2 and S3 zones were converted to hydrate. Then, the formation of the clathrate layers was extended and almost all the solution regions were converted to hydrate as the simulation time reached 50 ns. The agglomeration of metal particles in the solution is also evident. The snapshot of the simulation box at 150 ns shows that the position of guest–host molecules was changed slightly but such alterations were toward a better arrangement of water molecules in the clathrate structure.

Fig. 2 exhibits the thickness of the $CO_2$ hydrate layer for the first 50 ns of the simulation time. To determine the thickness of the $CO_2$ hydrate layer, image processing was utilized. By growing the hydrate phase as a function of time, the snapshots were generated every 0.5 ns. The thickness of the hydrate slab from two interfaces was analyzed and finally, the results after 10, 30, 50, 100, and 150 ns of simulation time were reported as indicated in Fig. 2. As is shown, the influences of metal particles under different thermodynamic conditions are dissimilar. The addition of combined metal particles to the solution at 260 K seems to be inefficient for the
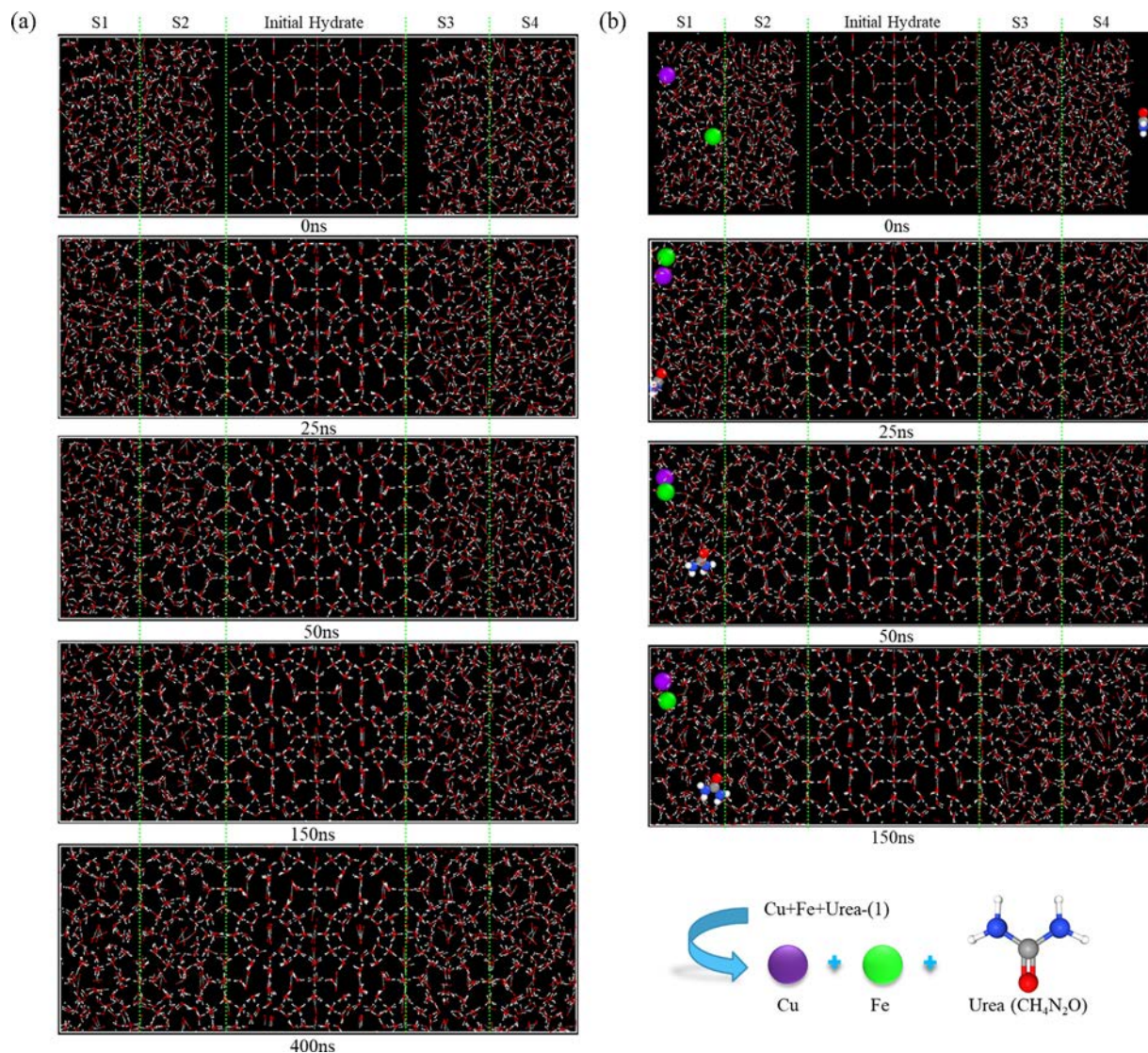
**Fig. 1.** The snapshots of the $CO_2$ hydrate simulation for (a) pure water, and (b) Cu + Fe + Urea-(1) at 260 K and 2 MPa. (white atoms: H; red atoms: O; gray atoms: C).

growth rate of the $CO_2$ hydrate layer. However, the process of hydrate crystallization was positively influenced by the mixture of additives including urea. According to Fig. 2 (b), the thickness of $CO_2$ clathrate above the ice point of water was accelerated when Cu + Ag + Fe metal particles were placed in the solution. Interestingly, the growth rate of the sI slab could even be increased once urea was also included. Although the synergic of additives e.g. mixed metal particles and urea at either below or above water freezing point may positively affect the formation process of $CO_2$ hydrate, the mixed components in some cases cannot be efficient as either stand-alone utilization of these components or even pure water. Therefore, the following analysis parameters discuss the behaviour of these components during the $CO_2$ hydrate growth phenomenon.

### 3.2. The time variation of potential energy analysis

Analysing the potential energy of the simulated systems can help to reflect the thermodynamic stability and circumstance of gas hydrate at different P-T conditions. The energy for an unstable system is generally prone to abrupt changes but the steady-state creates the situation under which the energy of the system fluctu-

ates around a specific value. The potential energy of the simulated $CO_2$ hydrates for the cases of either pure water or the presence of combined additives is shown in Figure S1. The downward trend of curves in all systems implies the growth of the initial hydrate slab due to the rearrangements of the solution phase. The more the decline, the higher the growth rate. This Figure shows that the variation of the potential energy of the system in the presence of Cu + Ag, Cu + Fe, and Cu + Ag + Fe-(1) is slightly higher than that of the pure system at 2 MPa and 260 K which indicates that the metal particles at this temperature could not induce the exothermic formation of $CO_2$ hydrate. Also, the behaviour of Cu + Ag + Fe-(2) in the system is similar to that of pure water. It seems that mixed metal particles under the above-mentioned *T*-P condition are not only unable to boost the $CO_2$ crystal growth, but some of which might even slightly inhibit the hydrate formation. However, the mixture including the urea molecule helped to accelerate the decrease of potential energy. This difference is more visible after 50 ns of the simulation time where the fluctuation of Cu + Ag + Urea-(1) reaches the lower potential energy. It can be inferred that with the addition of urea to the primary metal particles, the stability of partially hydrogen-bonded water molecules was maintained, and on the other hand, the amount of mobility and

**Fig. 2.** Hydrate thickness (a): at 260 K and 2 MPa; (b) at 275 K and 3 MPa.

higher. Since the behaviour of the system including either Cu + Ag or Cu + Fe was quite dissimilar, it can be concluded that the synergistic of metal particles cannot be always successful. Moreover, the thermodynamic condition can also be one of the main contributors. Indeed, the *T*-P condition of the system would be determinative in the performance of additives. By comparing the $CO_2$ hydrate growth at below and above water freezing points, it can be deduced that the growth process in the presence of metal particles is more prone to change than the systems with urea once the thermodynamic condition was altered from 260 K to 275 K. It can also be assumed that metal particles and urea might intrinsically affect heat and mass transfer coefficients of the solution phase respectively. Since the collision of metal particles with water molecules can accelerate the relative motion of the solution phase, a such local disturbance may improve the energy transfer between the original molecules of both $CO_2$ and water in the system which would contribute to creating the effective formation of hydrogen bonds between water molecules.

### 3.3. Hydrogen bonding of $CO_2$ crystal growth

The number of hydrogen bonds (H-bonds) has a close relationship with the ordered crystal of clathrate hydrate. The more conversion of disordered liquid molecules to arranged shapes gives a higher number of H-bonds. The tetrahedral cages are gradually formed by the H-bond connections across water molecules. The time variation of the number of H-bonds during the $CO_2$ hydrate formation in contact with different additives in the solution is shown in Figure S2. For both thermodynamic simulation conditions in this figure, the number of H-bonds from the initial time to 150 ns has been increased from 616 to over 1500 which indicates that the hydrate crystal was steadily growing. The trend of H-bonds reached a plateau value as the process of crystal formation came to the end. As is evident in Figure S2 (*a*1 and *a*2), the highest number of H-bonds was obtained for the system including Cu + Fe + Urea-(1) which properly promoted the $CO_2$ hydrate formation. The average and maximum number of H-bonds for pure water were 1511 and 1603 while that for Cu + Fe + Urea-(1) were 1547 and 1640 respectively. A higher number of H-bonds for the latter system may indicate that an orderly arrangement of the water molecules in the clathrate was upgraded. This might be due to the surface of the urea molecule which creates several hydrogen bonds with two or three adjacent cages of water molecules. The oxygen atom of urea prefers to align slightly towards the hydrate phase. It was found that the oxygen atom in urea is aligned toward the hexagonal face of the large cage. The distance between this atom in urea and cage water was ~ 2.5 Å which indicates the close interactions of this molecule with the hydrate cage. Since urea molecule can help to stabilize the cages at the hydrate surface, the more regular water molecules in the network can be formed. In addition, the undesirable local interactions of Cu and Fe metal particles may be inappreciable due to the lower operating temperature (260 K). However, in the presence of Ag metal, the disturbance motions of Ag compensate the more regular algorithm of water molecules in the clathrate structure of $CO_2$ hydrate. Hence, the inclusion of Ag in this mixture (Cu + Ag + Fe + Urea-( 1)) slightly slowed down the hydrate growth. Based on Figure S2 (*a*1 and *a*2), the promotion effect of the Cu + Fe binary and the Cu + Ag + Fe ternary mixtures in comparison with the pure water system was no longer significant. Also, the addition of Cu + Ag at two different concentrations slightly acted as an inhibitor which resulted in a lower number of H-bonds. However, according to Figure S2 (*b*1 and *b*2), the behaviour of combined additives at 3 MPa and 275 K are somewhat different. Although the presence of pure Cu and urea molecule were quite efficient in increasing the number of H-bonds, the combined Cu + Ag + Fe, Cu + Ag + Fe-Urea-(1), and

consequently atomic movement in the solution was increased. Also, the amount of interatomic distance was probably increased which might create a space in the atomic space and caused more oscillations of the particles. Since the interaction force between particles is inversely proportional to the distance between particles, it can be expected that the number of atomic interactions and the dependence of the particles on each other was reduced by enhancing oscillations. Once, the P-T circumstance was altered to 275 K and 3 MPa, some mixed metal particles appeared differently. As Figure S1 (*b*1 and *b*2) present, the addition of Cu + Ag + Fe-(1) to the system decreased the potential energy to lower values, therefore, showing a positive impact. This alteration emerged evidently after 30 ns. However, the presence of Cu metal shows higher performance in comparison with the metal mixtures. This may be because of the regular creation of the active Brownian motion in the solution phase by Cu metal which boosts the rapid transfer of energy. Generally, metal particles due to their high surface are in a state of overactivation so that they may attract each other to form secondary metal clusters if high numbers of those are in the solution phase. In addition, with the higher concentration of metal particles, Cu + Ag + Fe-(2) was somewhat more inducing the reduction rate of potential energy. The synergy of Cu + Ag + Fe-(1) with urea also accelerated the aforementioned reduction. Interestingly, this enhancement in the absence of Ag was even

Cu + Fe-Urea-(1) by providing plenty of nucleation sites might elevate the effectiveness of the surface area in the solution phase. In contrast, Cu + Ag and Cu + Fe decreased the amount of H-bonds. It should be highlighted that during the process of $CO_2$ hydrate formation, the heat released raises the temperature of the system and subsequently weakens the effective driving force. So that, since metal particles mostly possess high thermal conductivity, they can evenly distribute the generated heat at the local liquid–solid interface. The heat and mass transfer of the solution can also be increased by enhancing the electrical conductivity but the optimal state may give a higher performance. The order of electrical conductivity for the mixed metal atoms from low to high are Cu + Fe, Cu + Ag + Fe, and Cu + Ag respectively (Zuo et al., 2017). Therefore, Cu + Ag + Fe in comparison with two other coupled metal atoms might be closer to the optimum condition. This is indicated that the mixed metal particles have various impacts on the enhancement of the kinetics of the hydrate growth process. In addition, the atomic mass may contribute to the formation of local perturbations. Since the Ag atomic mass (1 0 8) is considerably different from Cu (64) and Fe (56), the Ag atom has a smaller motion speed and ability to promote local convection rather than either Cu or Fe. Based on the results of the simulation, it can be assumed that there is a correspondence relating the potential energy with the number of H-bonds. The higher reduction of potential energy at the final stage of the simulations may give a higher number of H-bonds. Table 2 indicates some information about the correspondence of these two analysis parameters. Therefore, by plotting the evolution of potential energy versus the number of H-bonds, it can be considered that the higher slope of simulated systems than that of pure water may show the promotion impacts of the included additives.

### 3.4. The structural order parameter of clathrate hydrate

Computing the order parameter $F_3$ for water molecules in a specific region or total simulation box as a function of time can help to quantify the $CO_2$ hydrate growth along the Z-axis. This parameter displays the deviation of the oxygen positions in the water triplets from the tetrahedral arrangement in the clathrate. The $F_3$ parameter is defined as the below equation (Bagherzadeh et al., 2012):

$$F_3 = \frac{1}{n} \sum_{i}^{n} \left( |cos\theta_{jik}|cos\theta_{jik} + cos^2(104.52°) \right)^2 \qquad (1)$$

Where $j$, $i$, and $k$ represent three oxygen atoms of water molecules to take into account a tetrahedral arrangement of water molecules that are close together, and atom $i$ is located in the center of a spherical shell of 3.5 Å including atoms $j$ and $k$. The value

(104.52) in the equation is the H—O—H angle of water molecules from the TIP4P/ice model. Once the solution phase was ordered, the $F_3$ order parameter converges to nearly zero whereas the $F_3$ for the liquid phase is around 0.1. Figure S3 reveals the total $F_3$ parameter of the simulation box at two investigated operating conditions. As is evident, values of $F_3$ as a function of time decreased from 0.05 to less than 0.02 by the end of the simulations. This implies that the hydrate formation extends along the simulation box. There is a similarity between the results obtained from the $F_3$ values and those from the potential energy evaluated in the previous section. At 260 K, the decline of the $F_3$ curve for the systems including Cu + Ag and Cu + Ag + Fe was not substantial. Therefore, the slope of the $F_3$ is less than the absence of metal particles. Also, the impression of systems with urea is more apparent when 50 ns of simulation time is passed. Interestingly, the $F_3$ after the aforesaid time was reduced to below 0.015 for the case of Cu + Fe + urea while by adding Ag to this mixture, the performance of the additives was lowered and the $F_3$ value fluctuates between the former case and the system with pure water. This may indicate that Ag reduces the promotion capability of Cu + Fe + urea-(1) by creating uncoordinated movements. Also, the $F_3$ amount for the combined additives which converged to less than 0.015 indicates that the formation of the solid phase is more regular and rapid than in other systems. However, the behaviour of additives at 275 K is not similar to those under the water ice point. Although Cu + Ag and Cu + Fe are unable to desirably reduce the $F_3$ order parameter, the ternary of Cu + Ag + Fe with different concentrations possesses a positive impression on decreasing the $F_3$ parameter. For the lower and higher concentrations of ternary metal additives, the $F_3$ declined at about 60 ns and 40 ns respectively. This may reveal that a greater concentration was closer to the optimized condition. While the $F_3$ drop in the existence of synergistic Cu + Ag + Fe + urea-(1) occurred at 30 ns.

Although the results of the utilization of pure urea are substantial, the Cu + Fe + urea-(1) led the decline time of $F_3$ to around 20 ns which represents the most superior improvement of this combination on the extension of clathrate growth. It should be noted that urea has no particular affinity to the hydrate-solution interface but prefers to stay near the liquid–gas interface. Urea molecule is neither entrapped in the clathrate nor blocks the hydrate growth. However, urea may firstly be entrapped in partially formed cavities and then replaced with guest $CO_2$ molecules to complete the cages as it was certified elsewhere (Wang et al., 2021). It is also essential to consider that in the case of binding additives to the hydrate surface over the characteristic time of clathrate formation, the process of hydrate growth can be hindered. Probably, the residence time of urea near the solid surface is less than the characteristic time of the crystal growth. Therefore, hydrate growth was not blocked by the urea molecule.

**Table 2**
Correspondence relating the potential energy and the number of H-bonds at 3 MPa and 275 K.

|  | pure water | | Cu + Ag-(1) | | Cu + Ag-(2) | | Cu + Fe-(1) | | Cu + Ag + Fe-(1) | |
|---|---|---|---|---|---|---|---|---|---|---|
|  | PE | HB | PE | HB | PE | HB | PE | HB | PE | HB |
| Min. | −16894 | 1286 | −16862 | 1306 | −16831 | 1293 | −16943 | 1288 | −17007 | 1293 |
| Avg. | −16676 | 1481 | −16670 | 1466 | −16642 | 1450 | −16638 | 1460 | −16824 | 1504 |
| Max. | −15620 | 1574 | −15555 | 1542 | −15596 | 1541 | −15712 | 1573 | −15420 | 1614 |
| Y = aX + b | a: −0.27, b: −3013 | | a: −0.26, b: −2817 | | a: −0.25, b: −2708 | | a: -0.26, b: −2920 | | a: −0.28, b: −3321 | |
|  | **Cu + Ag + Fe-(2)** | | **Cu + Fe + Urea-(1)** | | **Cu + Ag + Fe + Urea-(1)** | | **Urea-(1)** | | **Cu** | |
|  | PE | HB | PE | HB | PE | HB | PE | HB | PE | HB |
| Min. | −17034 | 1306 | −17049 | 1329 | −17038 | 1284 | −16994 | 1315 | −17017 | 1288 |
| Avg. | −16837 | 1486 | −16867 | 1519 | −16840 | 1514 | −16803 | 1516 | −16853 | 1515 |
| Max. | −15443 | 1576 | −15229 | 1609 | −15261 | 1592 | −15195 | 1602 | −15320 | 1597 |
| Y = aX + b | a: −0.28, b: −3197 | | a: −0.30, b: −3530 | | a: −0.29, b: −3461 | | a: −0.29, b: −3385 | | a: −0.30, b: −3484 | |

Note: the "PE" and "HB" represent the potential energy and the number of hydrogen bonds respectively; PE in the linear equation (as an X) gives the number of HB.

To further investigations about the effects of additives on the solution segments neighbour the sI slab, analysing the section-wise $F_3$ calculations would be advantageous. Fig. 3 exhibits the $F_3$ parameter in the solution around the hydrate slab for pure water, Cu + Ag + Fe-(2) and Cu + Ag + Fe + Urea-(1) at two different $T$-P conditions. It seems that the reduction of $F_3$ for all systems irre-spective of the operating condition is firstly started from the solu-tion layers just beside the hydrate slab (S2 and S3) and then extended toward the end sides of the Z-axis of the simulation box (S1 and S4). This may be evidence of the inherent growth mechanism of crystallization in contact with the hydrate phase. Consistent with preceding expressions, the decrease of the $F_3$ parameter during simulation time at 260 K for Cu + Ag + Fe and Cu + Ag + Fe + Urea are slower and quicker than pure water respec-tively. However, as Fig. 3 (d) and (f) show, both combinations pos-sess the promotion behaviour in comparison with their absence which is displayed in case (b). By comparing Fig. 3 (a), (c), and (e), it can be observed that although the synergic of Cu + Ag + Fe improves the heat transfer flow, the Brownian motion may act as a disturbance of partially formed cavities near the initial slab. However, the inclusion of urea by facilitating the formation of half cages restrains the disordering motions of water molecules. There-

fore, the growth in Fig. 3 (e) after passing 60 ns can be completed while it did not occur for cases (a) and (c). Fig. 3 (b) also kinetically exhibits that, the process of crystallization for pure water at 275 K was increased which signifies that the lower subcooling may not always give a faster rate of hydrate crystallization. Similar beha-viour can also be seen in cases (d) and (f). In contrast with case (c), the presence of metal particles acted as a vigorous promoter which reduced the drop time of $F_3$ value from over 100 ns in case (b) to slightly above 40 ns in case (d). This time in case (f) was also shortened to 30 ns once urea was included. Interestingly, the pres-ence of urea regardless of thermodynamic condition reduces the fluctuation of the $F_3$ parameter in all fourth regions of the solu-tions. This implies that the urea molecule by alleviating the vibra-tions of ordered water molecules due to inducing the better distribution of $CO_2$ molecules between water molecules may help to extend and then maintain the stability of formed hydrate.

### 3.5. Diffusion behaviour of the particles

Atoms in particle diffusion systems tend to diffuse into space. Therefore, the mean square displacement (MSD) of atoms shows their diffusion and mobility in a system. Since particles cannot
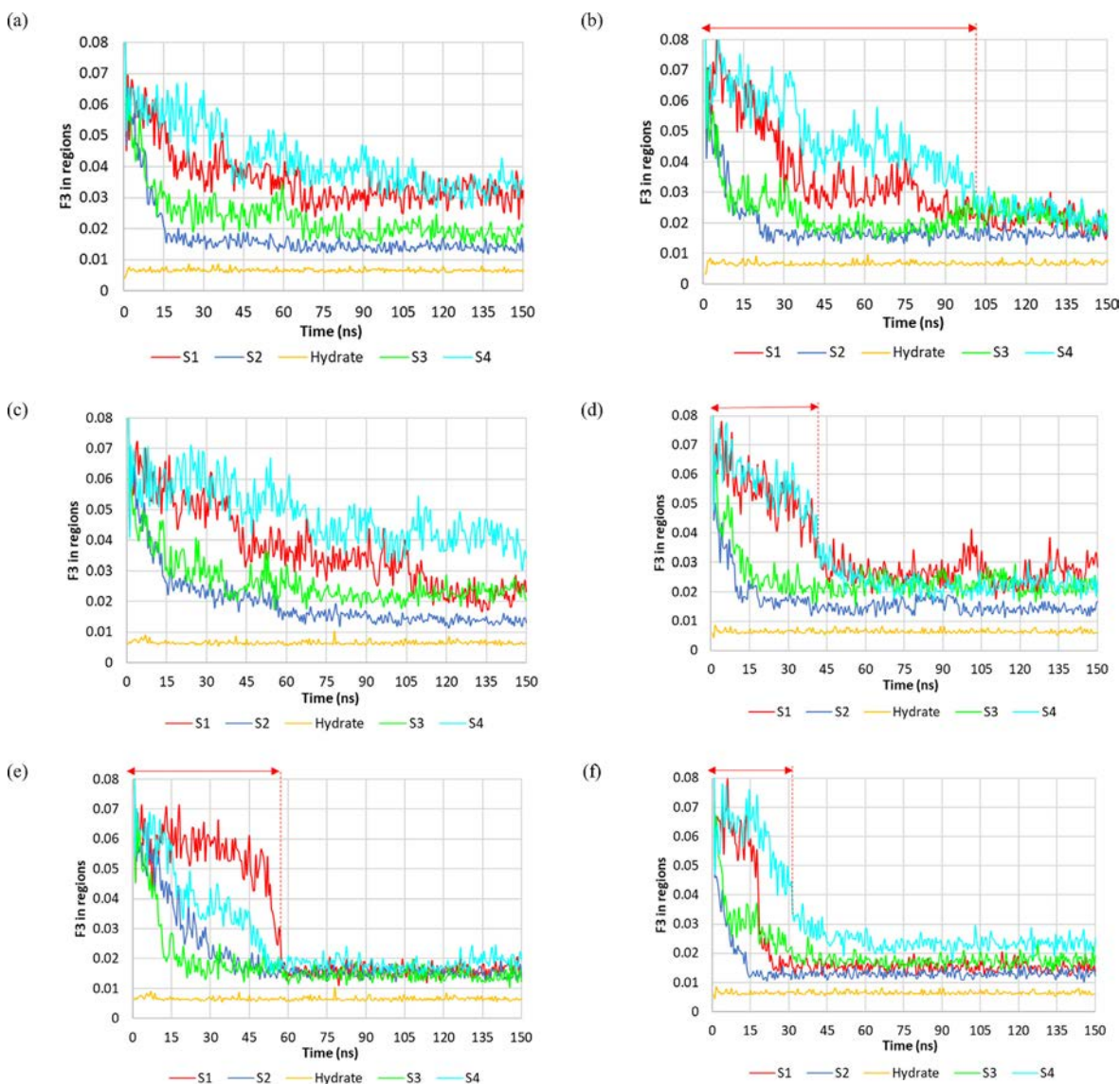


**Fig. 3.** $F_3$ order parameter of $CO_2$ hydrate growth in the different slabs of the simulation box along the $z$-direction for (a) and (b), pure water; (c) and (d), Cu + Ag + Fe-(2); and (e) and (f), Cu + Ag + Fe + Urea-(1). Cases (a), (c), and (e) were performed at 260 K and 2 MPa while (b), (d), and (f) were carried out at 275 K and 3 MPa.

freely diffuse through the solid state, the MSD of components in liquid and gas phases is significantly higher than in the solid (hydrate) phase. To distinguish the phases, this parameter is applied which can be expressed by the following equation (Naeiji et al., 2019a):

$$MSD = \frac{1}{N}\sum_{i=1}^{N}\left|R^i(t) - R^i(0)\right|^2 \qquad (2)$$

Where $R$ is the position of atom $i$ at times $t$ and 0; $N$ represents the total number of atoms. MSD of all molecules in the simulation box for all simulated systems at two different thermodynamic conditions is plotted in Figure S4. As is shown at 260 K, the MSD curve of systems with urea after a specific simulation time reaches a plateau whereas the systems in the presence of metal particles are still unstable. This indicates that the solution for the systems with urea almost converted to the solid state, while the growth process for the systems with metal particles was not fulfilled. Consistent with the results of the previous sections, the behaviour of Cu + Ag + Fe metal

particles at 275 K is quite different and their MSDs after about 40–50 ns approached to the constant value. This is also valid for the solution including pure Cu and urea which occurred at around 30 ns whereas MSD for the combined Cu + Fe + urea-(1) stabilized at 20 ns. Due to the somewhat inhibitor effects of binary combined metal particles, the higher mobility in the system resulted in increasing MSDs above 50 ns while most of the solution phase for the other systems converted into the clathrate hydrate so that their MSDs converged to almost a flat trend.

Analysing the MSD of water molecules can also help to understand how additives change the water arrangement in the solution phase. Fig. 4 manifests the MSD of water molecules in four distinct areas of the solution besides the sI hydrate slab. The mixed additives at 275 K shown in Fig. 4 (a) acted as an accelerator of hydrate formation while the combinations presented in Fig. 4 (b) are found to somewhat prevent the hydrate growth. The smooth slopes of MSD in Fig. 4 (a) reflect that the additives successfully impressed host molecules and locate themselves in guest–host positions of
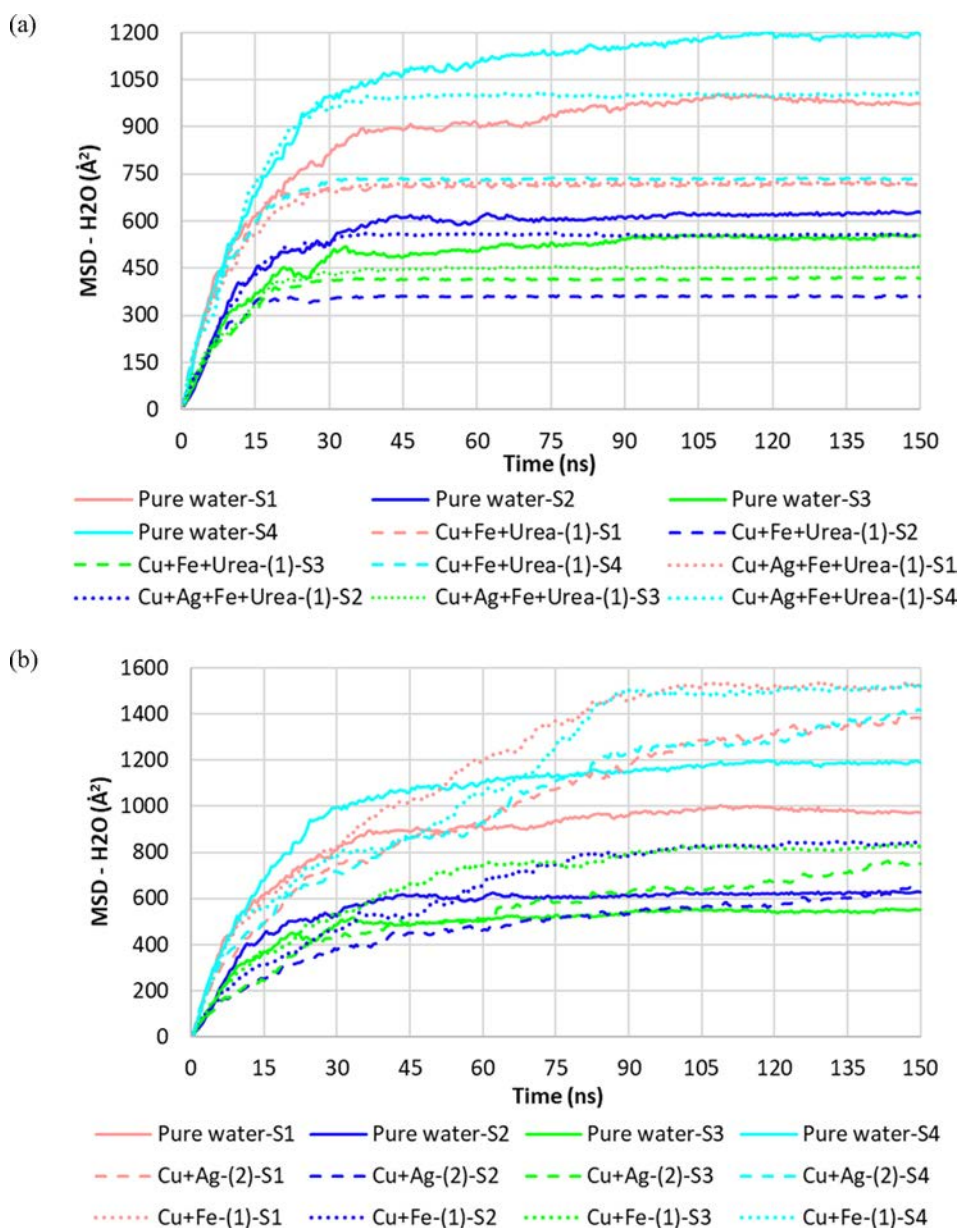


**Fig. 4.** MSD of water molecules in different regions of the simulation box at 275 K and 3 MPa. (a): a combination of metal particles and urea; (b) a binary mixture of metal particles (The regions are defined in Fig. 1).

sI clathrate. Moreover, the ordered arrangement of water molecules began firstly in the S2 and S3 segments of the solution (at nearly 20 ns) and subsequently occurred in S1 and S4 at over 30 ns. Additionally, the MSD approach of systems with additives in all fourth regions was under that of pure water. As Fig. 4 (b) shows, the Cu + Ag and Cu + Fe also inclined the trend of water's MSD when they were included in the solution. This behaviour is also observed in all segments as simulation time passed. It seems that in these systems, the movements caused by the existence of metal particles disturb the local arrangement of water molecules.

### 3.6. Water molecules in the hydrate structure

To determine the degree of ordered molecules in the hydrate structure and describe the configuration of the formed clathrate, the radial distribution function (RDF) was also investigated. The following equation represents the degree of ordered molecules in the system, where the probability of particle β distribution around a given particle α is counted. vs $N_\alpha$, and $N_\beta$ denote the volume of the simulation box, and the number of particles α and β respectively.

$$g_{\alpha\beta} = \frac{V_s}{N_\alpha N_\beta} \left[ \sum_{i=1}^{N_\alpha} \frac{N_{i\beta}(r)}{4\pi r^2 \Delta r} \right] \tag{3}$$

The RDF between oxygen atoms of water molecules in the system is displayed in Figure S5. As is evident, the first significant peak occurred at 2.75 Å which relates to the adjacent $H_2O$ molecule. The second shorter peak at 4.5 Å reflects the tetrahedral nature of the water cage. The lowest peak appeared at 6.45 Å which is the distance between oxygen atoms of $H_2O$ molecules spaced apart in the hydrate cage. It should be pointed out that the calculated RDF in this work is qualitatively in agreement with the reported values in the literature (Liu et al., 2021; Mahmoodi et al., 2021).

By comparing the RDF of water molecules at 260 K and 275 K, it can be concluded that the peak height became slightly greater as well as narrower once the temperature was lowered. This may indicate the more ordered water molecules and higher number of H-bonds in the clathrate. Besides, the similar Peaks of systems with or without additives implies that these components cannot significantly change the local arrangement of water molecules. As Figure S5 (a3) exhibits, the height of the first peak for pure water is located above the systems with metal particles but under the systems with urea. The binary mixture of metal particles in Figure S5 (b3) also seems to be ineffective. In addition, the first RDF peak of $H_2O$ atoms for the system with the presence of Cu + Ag + Fe-(1) remained unchanged when urea was included. There is a striking resemblance between the highest peak of Cu + Fe + urea-(1) and Cu + Ag + Fe-(2), however, both of which were established over the earlier mentioned solution systems. Therefore, it can be deduced that the promotion of a ternary mixture of Cu, Ag, and Fe metal particles at 275 K in ordered water molecules of clathrate hydrate is more appreciable than either utilization of single urea or pure Cu metal particles.

### 3.7. Guest and host distribution in the solution phase

Through MD simulations, it was reported that when urea is present, the relative concentration of $CO_2$ in the water phase is near unity and the $CO_2$ concentration gradient is markedly lowered. It was also estimated that urea increases the mass transfer coefficient of $CO_2$ by nearly 6 times, therefore, this component enhances the mass transport and the formation rate of the system (Wang et al., 2021). It seems that the self-diffusivity of water molecules and CO2 solubility may be boosted when urea is in the system. Presumably, urea catalyses the ring structure of hydrate formation but does not block the crystal growth process. Therefore, the surface of
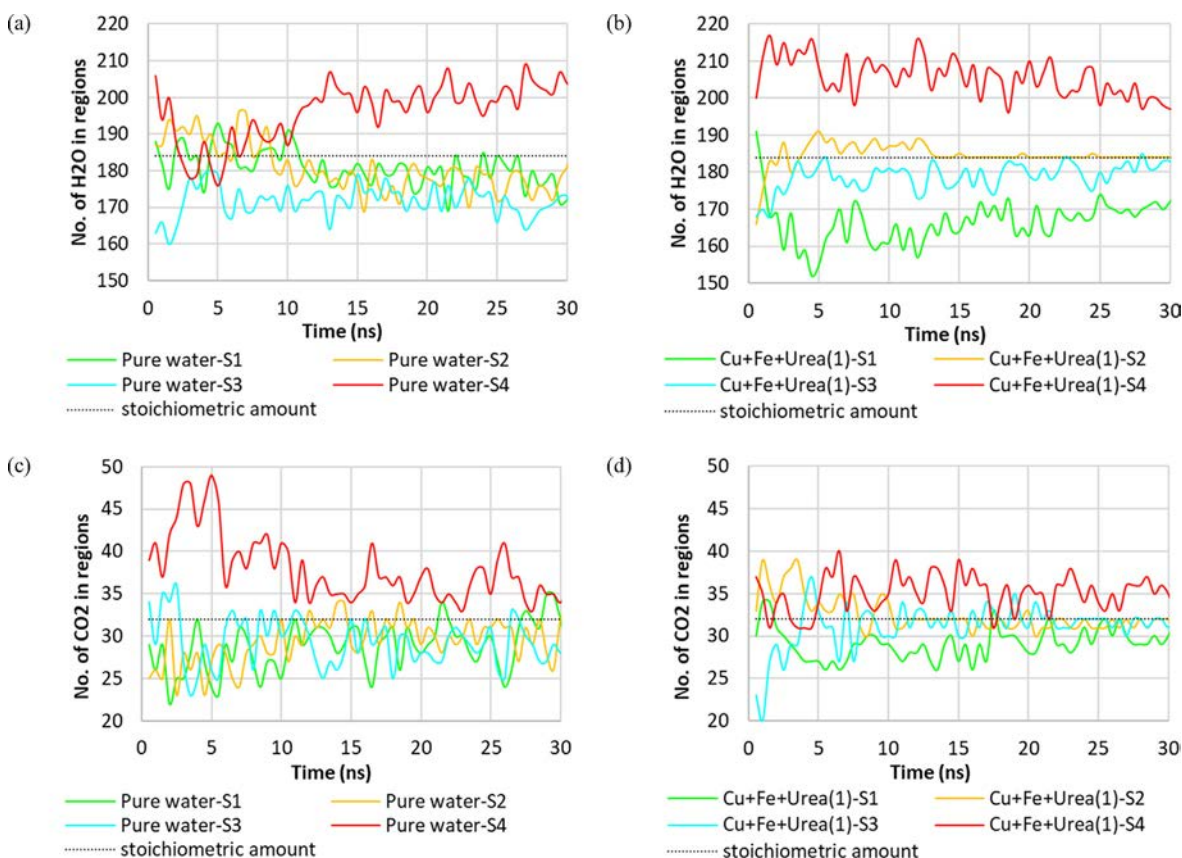


Fig. 5. Comparison of the number of water and $CO_2$ molecules between the systems including (a) and (c) pure water; (b) and (d) Cu + Fe + Urea-(1), at 275 K and 3 MPa.

urea might help water molecules to arrange themselves in form of pentagonal and hexagonal rings. The oxygen and nitrogen atoms in the molecular structure of urea, by dragging the H-bonded water molecule, serve as a hydrogen acceptor. Therefore, the oxygen atoms tend to align towards the hydrate phase. Fig. 5 compares the regional distribution of $CO_2$ and $H_2O$ molecules for pure water and Cu + Fe + Urea-(1) systems at 3 MPa and 275 K. As is shown, there is a pleasant convergence in the oscillation of guest and host molecules for the system with urea. According to the stoichiometric of $CO_2$ sI clathrate hydrate, the number of $CO_2$ and water in each segment of the solution need to be equal to 32 and 184 molecules respectively. Since the growth starts to expand from the boundaries of the solution phase with the sI hydrate slab, the neighbouring solution sides of the hydrate are more prone to form the clathrate structure. Therefore, they converge to the stoichiometric values more quickly than two further sections. These regions in the existence of Cu + Fe + Urea-(1) are almost approaching the stoichiometric amounts of $CO_2$ sI hydrate after passing the first 30 ns. In addition, the aforementioned synergic promoters by increasing the diffusivity of guest and host molecules most likely moderate the irregular distribution of the solution phase.

## 4. Conclusion

Since the synergistic promoters may not always be favourable for the formation of gas hydrates, the main contributors to such combinations need to be investigated to find the optimized circumstances, particularly in terms of studying the types of combined additives, their concentrations in the mixture, and operating conditions. The simulation results of this work demonstrated that the synergic mixtures of metal particles (Cu, Ag, Fe) and urea can accelerate the process of $CO_2$ hydrate growth by increasing the heat and mass transport of the solution at the solid–liquid interface respectively. The formation rate was even maximized when the aforementioned mixed additives without Ag were used. The addition of mixed metal particles and urea can positively induce host and guest molecules in the solution regions and help them be more properly organized. Interestingly, the mentioned synergistic promoters can efficiently work below and above the water ice point. However, the results of the solution systems including just metal particles showed that their behaviour mostly varies depending on the temperature and pressure of the system. The inclusion of Cu + Ag + Fe with two different concentrations in the solution phase enhanced water molecules to locate themselves in the form of hydrogen-bonded crystalline structure above the water solidification point. The addition of Cu + Ag and Cu + Fe to the system either below or above the water freezing point reduced the orderly movement of water molecules by increasing the potential energy and Brownian motion in the system. The growth kinetics of $CO_2$ hydrate in the presence of a single urea molecule and pure Cu metal particles are also close to the cases when their combinations were used. However, the higher arrangement of water molecules in the network of the clathrate hydrate for the mixed metal particles and urea was observed. Furthermore, when higher subcooling (260 K) was imposed, lower $CO_2$ hydrate growth was observed. This implies that the higher subcooling does not always result in quicker crystallization. Also, the crystallization in all simulated cases irrespective of operating conditions and additive types was started from the interface and then expanded in neighbouring layers of the solution.

## CRediT authorship contribution statement

**Saeed Sinehbaghizadeh:** Conceptualization, Methodology, Writing – original draft. **Agus Saptoro:** Conceptualization, Supervi-

sion, Writing – review & editing. **Parisa Naeiji:** Conceptualization, Writing – review & editing. **Angnes Tiong Ngieng Tze:** Supervision, Writing – review & editing. **Amir H. Mohammadi:** Supervision, Writing – review & editing.

## Data availability

Data will be made available on request.

## Declaration of Competing Interest

The authors declare that they have no known competing financial interests or personal relationships that could have appeared to influence the work reported in this paper.

## Appendix A. Supplementary data

Supplementary data to this article can be found online at https://doi.org/10.1016/j.ces.2022.118194.

## References

Abascal, J.L.F., Sanz, E., García Fernández, R., Vega, C., 2005. A potential model for the study of ices and amorphous water: TIP4P/Ice. J. Chem. Phys. 122,. https://doi.org/10.1063/1.1931662 234511.

Adibi, N., Mohammadi, M., Ehsani, M.R., Khanmohammadian, E., 2020. Experimental investigation of using combined CH4/CO2 replacement and thermal stimulation methods for methane production from gas hydrate in the presence of SiO2 and ZnO nanoparticles. J. Nat. Gas Sci. Eng. 103690. https://doi.org/10.1016/j.jngse.2020.103690.

Ayittey, F.K., Obek, C.A., Saptoro, A., Perumal, K., Wong, M.K., 2020a. Process modifications for a hot potassium carbonate-based CO2 capture system: a comparative study. Greenh. Gases Sci. Technol. 10, 130–146. https://doi.org/10.1002/ghg.1953.

Ayittey, F.K., Saptoro, A., Kumar, P., Wong, M.K., 2020b. Parametric study and optimisation of hot K 2 CO 3 -based post-combustion CO 2 capture from a coal-fired power plant. Greenh. Gases Sci. Technol. 10, 631–642. https://doi.org/10.1002/ghg.1983.

Ayittey, F.K., Saptoro, A., Kumar, P., Wong, M.K., 2021. Energy-saving process configurations for monoethanolamine-based CO2 capture system. Asia-Pacific J. Chem. Eng. 16, 1–15. https://doi.org/10.1002/apj.2576.

Babu, P., Nambiar, A., He, T., Karimi, I.A., Lee, J.D., Englezos, P., Linga, P., 2018. A review of clathrate hydrate Bbased desalination to strengthen energy–water nexus. ACS Sustain. Chem. Eng. 6, 8093–8107. https://doi.org/10.1021/acssuschemeng.8b01616.

Bagherzadeh, S.A., Englezos, P., Alavi, S., Ripmeester, J.A., 2012. Molecular simulation of non-equilibrium methane hydrate decomposition process. J. Chem. Thermodyn. 44, 13–19. https://doi.org/10.1016/j.jct.2011.08.021.

Cann, D., Font-Palma, C., Willson, P., 2021. Experimental analysis of CO2 frost front behaviour in moving packed beds for cryogenic CO2 capture. Int. J. Greenh. Gas Control 107,. https://doi.org/10.1016/j.ijggc.2021.103291 103291.

Chen, C.H., Ho, Y., 2017. Measurement of Thermodynamics and Kinetics of Carbon Dioxide Hydrate in the Presence of Urea and 1,3-Cyclohexanebis (methylamine). National Taiwan University.

Dhoke, C., Zaabout, A., Cloete, S., Amini, S., 2021. Review on Reactor Configurations for Adsorption-Based CO 2 Capture. Ind. Eng. Chem. Res. 60, 3779–3798. https://doi.org/10.1021/acs.iecr.0c04547.

Eggimann, B.L., Sunnarborg, A.J., Stern, H.D., Bliss, A.P., Siepmann, J.I., 2014. An online parameter and property database for the TraPPE force field. Mol. Simul. 40, 101–105. https://doi.org/10.1080/08927022.2013.842994.

Elwell, L.C., Grant, W.S., 2006. Technology options for capturing CO2. Power (New York), p. 149.

Firoozabadi, S.R., Bonyadi, M., Lashanizadegan, A., 2018. Experimental investigation of Fe3O4 nanoparticles effect on the carbon dioxide hydrate formation in the presence of magnetic field. J. Nat. Gas Sci. Eng. 59, 374–386. https://doi.org/10.1016/j.jngse.2018.09.013.

Frenkel, D., Smit, B., 2002. Long-Range Interactions. In: Understanding Molecular Simulation. Elsevier, pp. 291–320. 10.1016/B978-012267351-1/50014-6.

Gambelli, A.M., Presciutti, A., Rossi, F., 2021. Review on the characteristics and advantages related to the use of flue-gas as CO2/N2 mixture for gas hydrate production. Fluid Phase Equilib. 541,. https://doi.org/10.1016/j.fluid.2021.113077 113077.

Gong, Y., Mendgaziev, R.I., Hu, W., Li, Y., Li, Z., Stoporev, A.S., Manakov, A.Y., Vinokurov, V.A., Li, T., Semenov, A.P., 2022. Urea as a green thermodynamic inhibitor of sII gas hydrates. Chem. Eng. J. 429,. https://doi.org/10.1016/j.cej.2021.132386 132386.

Grubmüller, H., Heller, H., Windemuth, A., Schulten, K., 1991. Generalized Verlet Algorithm for Efficient Molecular Dynamics Simulations with Long-range Interactions. Mol. Simul. 6, 121–142. https://doi.org/10.1080/08927029108022142.

Hafizi, A., Rajabzadeh, M., Mokari, M.H., Khalifeh, R., 2021. Synthesis, property analysis and absorption efficiency of newly prepared tricationic ionic liquids for CO2 capture. J. Mol. Liq. 324,. https://doi.org/10.1016/j.molliq.2020.115108 115108.

Hockney, R., Eastwood, J., 2021. Computer Simulation Using Particles. CRC Press. https://doi.org/10.1201/9780367806934.

Idrissi, A., Gerard, M., Damay, P., Kiselev, M., Puhovsky, Y., Cinar, E., Lagant, P., Vergoten, G., 2010. The Effect of Urea on the Structure of Water: A Molecular Dynamics Simulation. J. Phys. Chem. B 114, 4731–4738. https://doi.org/10.1021/jp911939y.

Jacobson, L.C., Hujo, W., Molinero, V., 2010. Nucleation pathways of clathrate hydrates: Effect of guest size and solubility. J. Phys. Chem. B 114, 13796–13807. https://doi.org/10.1021/jp107269q.

Jiang, W., Wu, F., Gao, G., Li, X., Zhang, L., Luo, C., 2021. Absorption performance and reaction mechanism study on a novel anhydrous phase change absorbent for CO2 capture. Chem. Eng. J. 420,. https://doi.org/10.1016/j.cej.2021.129897 129897.

Jokar, S.M., Wood, D.A., Sinehbaghizadeh, S., Parvasi, P., Javanmardi, J., 2021. Transformation of associated natural gas into valuable products to avoid gas wastage in the form of flaring. J. Nat. Gas Sci. Eng. 104078. https://doi.org/10.1016/j.jngse.2021.104078.

Kallies, B., 2002. Coupling of solvent and solute dynamics—molecular dynamics simulations of aqueous urea solutions with different intramolecular potentials. Phys. Chem. Chem. Phys. 4, 86–95. https://doi.org/10.1039/b105836n.

Liang, H., Guan, D., Shi, K., Yang, L., Zhang, L., Zhao, J., Song, Y., 2022. Characterizing Mass-Transfer mechanism during gas hydrate formation from water droplets. Chem. Eng. J. 428,. https://doi.org/10.1016/j.cej.2021.132626 132626.

Lim, L.H.V., Lloren, A.V., Lamorena, R.B., 2014. The effect of urea in the nucleation process of CO2 clathrate hydrates. J. Mol. Liq. 194, 245–250. https://doi.org/10.1016/j.molliq.2014.03.003.

Liu, Y., Liao, X., Shi, C., Ling, Z., Jiang, L., 2020. Promoting and inhibitory effects of hydrophilic/hydrophobic modified aluminum oxide nanoparticles on carbon dioxide hydrate formation. Energies 13, 5380. https://doi.org/10.3390/en13205380.

Liu, N., Zhu, H., Zhou, J., Yang, L., Liu, D., 2021. Molecular dynamics simulations on formation of CO2 hydrate in the presence of metal particles. J. Mol. Liq. 331,. https://doi.org/10.1016/j.molliq.2021.115793 115793.

Machida, H., Hashiride, R., Niinomi, R., Yanase, K., Hirayama, M., Umeda, Y., Norinaga, K., 2021. An Alternative CO 2 Capture with a Pressure Swing Amine Process Driven by Cryogenic Pumping with the Unused Cold Energy of Liquefied Natural Gas. ACS Sustain. Chem. Eng. 9, 15908–15914. https://doi.org/10.1021/acssuschemeng.1c05892.

Maddah, M., Maddah, M., Peyvandi, K., 2018. Molecular dynamics simulation of methane hydrate formation in presence and absence of amino acid inhibitors. J. Mol. Liq. 269, 721–732. https://doi.org/10.1016/j.molliq.2018.08.108.

Mahmoodi, M.H., Manteghian, M., Naeiji, P., 2021. Study the effect of Ag nanoparticles on the kinetics of CO2 hydrate growth by molecular dynamics simulation. J. Mol. Liq. 343,. https://doi.org/10.1016/j.molliq.2021.117668 117668.

Míguez, J.M., Conde, M.M., Torré, J., Blas, F.J., Piñeiro, M.M., Vega, C., 2015. Molecular dynamics simulation of CO2 hydrates: Prediction of three phase coexistence line Molecular dynamics simulation of CO 2 hydrates: Prediction of three phase coexistence line 124505. 10.1063/1.4916119.

Muromachi, S., 2021. CO2 capture properties of semiclathrate hydrates formed with tetra-n-butylammonium and tetra-n-butylphosphonium salts from H2 + CO2 mixed gas. Energy 223,. https://doi.org/10.1016/j.energy.2021.120015 120015.

Muromachi, S., Abe, T., Maekawa, T., Yamamoto, Y., 2015. Phase equilibrium for clathrate hydrate formed in methane+water+urea system. Fluid Phase Equilib. 398, 1–4. https://doi.org/10.1016/j.fluid.2015.04.007.

Naeiji, P., Varaminian, F., Rahmati, M., 2016. Thermodynamic and structural properties of methane/water systems at the threshold of hydrate formation predicted by molecular dynamic simulations. J. Nat. Gas Sci. Eng. https://doi.org/10.1016/j.jngse.2016.03.044.

Naeiji, P., Varaminian, F., Rahmati, M., 2017. Comparison of the thermodynamic, structural and dynamical properties of methane/water and methane/water/hydrate systems using molecular dynamic simulations. J. Nat. Gas Sci. Eng. https://doi.org/10.1016/j.jngse.2017.04.010.

Naeiji, P., Varaminian, F., Rahmati, M., 2019a. The kinetic modeling of methane hydrate growth by using molecular dynamic simulations. Int. J. Heat Mass Transf. 142,. https://doi.org/10.1016/j.ijheatmasstransfer.2019.07.006 118356.

Naeiji, P., Woo, T.K., Alavi, S., Ripmeester, J.A., 2019b. Molecular dynamic simulations of clathrate hydrate anomalous preservation: The effect of coating clathrate hydrate phases. J. Phys. Chem. C 123, 28715–28725. https://doi.org/10.1021/acs.jpcc.9b07769.

Phan, A., Schlösser, H., Striolo, A., 2021. Molecular mechanisms by which tetrahydrofuran affects CO2 hydrate growth: Implications for carbon storage. Chem. Eng. J. 129423. https://doi.org/10.1016/j.cej.2021.129423.

Rezaei, N., Mohebbi, V., Feyzi, V., 2022. Hybrid hydrate processes for CO2/H2 mixture purification: A techno-economic analysis. Int. J. Hydrogen Energy 47, 10137–10155. https://doi.org/10.1016/j.ijhydene.2022.01.102.

Rudolph, A., El-Mohamad, A., McHardy, C., Rauh, C., 2021. Concentrating model solutions and fruit juices using CO2 hydrate technology and its quantitative effect on phenols, carotenoids, vitamin C and betanin. Foods 10, 626. https://doi.org/10.3390/foods10030626.

Ryckaert, J.-P., Ciccotti, G., Berendsen, H.J., 1977. Numerical integration of the cartesian equations of motion of a system with constraints: molecular dynamics of n-alkanes. J. Comput. Phys. 23, 327–341. https://doi.org/10.1016/0021-9991(77)90098-5.

Said, S., Govindaraj, V., Herri, J.M., Ouabbas, Y., Khodja, M., Belloum, M., Sangwai, J.S., Nagarajan, R., 2016. A study on the influence of nanofluids on gas hydrate formation kinetics and their potential: Application to the CO2 capture process. J. Nat. Gas Sci. Eng. 32, 95–108. https://doi.org/10.1016/j.jngse.2016.04.003.

Saptoro, A., Huo, K.C., 2013. Influences of Indonesian coals on the performance of a coal-fired power plant with an integrated post combustion CO2 removal system: A comparative simulation study. Energy Convers. Manag. 68, 235–243. https://doi.org/10.1016/j.enconman.2013.01.015.

Senatore, V., Buonerba, A., Zarra, T., Oliva, G., Belgiorno, V., Boguniewicz-Zablocka, J., Naddeo, V., 2021. Innovative membrane photobioreactor for sustainable CO2 capture and utilization. Chemosphere 273,. https://doi.org/10.1016/j.chemosphere.2021.129682 129682.

Sinehbaghizadeh, S., Javanmardi, J., Roosta, A., Mohammadi, A.H., 2017. A fugacity approach for prediction of phase equilibria of methane clathrate hydrate in structure. H. Phys. Chem. Res. 5, 465–481. 10.22036/pcr.2017.69958.1334.

Sinehbaghizadeh, S., Javanmardi, J., Mohammadi, A.H., 2018. Phase stability conditions of clathrate hydrates in the (methane + 3-methyl-1-butanol + water), (methane + 3,3-dimethyl-2-butanone + water) and (methane + 2,3-dimethyl-2-butene + water) systems: Experimental measurements and thermodynamic modeling. J. Chem. Thermodyn. 125, 64–70. https://doi.org/10.1016/j.jct.2018.05.006.

Sinehbaghizadeh, S., Javanmardi, J., Roosta, A., Mohammadi, A.H., 2019a. Estimation of the dissociation conditions and storage capacities of various sH clathrate hydrate systems using effective deterministic frameworks. Fuel 247, 272–286. https://doi.org/10.1016/j.fuel.2019.01.189.

Sinehbaghizadeh, S., Roosta, A., Rezaei, N., Ghiasi, M.M., Javanmardi, J., Zendehboudi, S., 2019b. Evaluation of phase equilibrium conditions of clathrate hydrates using connectionist modeling strategies. Fuel 255,. https://doi.org/10.1016/j.fuel.2019.115649 115649.

Sinehbaghizadeh, S., Saptoro, A., Amjad-Iranagh, S., Tze Tiong, A.N., Mohammadi, A. H., 2022a. Molecular Dynamics Simulation Studies on the Stability and Dissociation of Clathrate Hydrates of Single and Double Greenhouse Gases. Energy & Fuels 36, 8323–8339. https://doi.org/10.1021/acs.energyfuels.2c01396.

Sinehbaghizadeh, S., Saptoro, A., Mohammadi, A.H., 2022b. CO2 hydrate properties and applications: A state of the art. Prog. Energy Combust. Sci. 93,. https://doi.org/10.1016/j.pecs.2022.101026 101026.

Sloan, E.D., Koh, C.A., 2008. Clathrate hydrates of natural gases, 3rd Ed. ed. CRC Press, Taylor & Francis Group, Boca Raton.

Steve, P., Paul, C., T.a.., 2012. Large-scale atomic/molecular massively parallel simulator. LAMMPS. Sandia Natl, Labs, Albuquerque, NM.

Strobel, T.A., Koh, C.A., Sloan, E.D., 2007. Hydrogen storage properties of clathrate hydrate materials. Fluid Phase Equilib. 261, 382–389. https://doi.org/10.1016/j.fluid.2007.07.028.

Takeuchi, F., Hiratsuka, M., Ohmura, R., Alavi, S., Sum, A.K., Yasuoka, K., 2013. Water proton configurations in structures I, II, and H clathrate hydrate unit cells. J. Chem. Phys. 138,. https://doi.org/10.1063/1.4795499 124504.

Wang, P.-W., Wu, D.T., Lin, S.-T., 2021. Promotion mechanism for the growth of CO2 hydrate with urea using molecular dynamics simulations. Chem. Commun. https://doi.org/10.1039/D0CC06165D.

Wu, H., Li, Q., Sheng, M., Wang, Z., Zhao, S., Wang, J., Mao, S., Wang, D., Guo, B., Ye, N., Kang, G., Li, M., Cao, Y., 2021. Membrane technology for CO2 capture: From pilot-scale investigation of two-stage plant to actual system design. J. Memb. Sci. 624,. https://doi.org/10.1016/j.memsci.2021.119137 119137.

Xie, N., Tan, C., Yang, S., Liu, Z., 2019. Conceptual design and analysis of a novel CO2 hydrate-based refrigeration system with cold energy storage. ACS Sustain. Chem. Eng. 7, 1502–1511. https://doi.org/10.1021/acssuschemeng.8b05255.

Xu, C.G., Yan, R., Fu, J., Zhang, S.H., Yan, K.F., Chen, Z.Y., Xia, Z.M., Li, X.S., 2019. Insight into micro-mechanism of hydrate-based methane recovery and carbon dioxide capture from methane-carbon dioxide gas mixtures with thermal characterization. Appl. Energy 239, 57–69. https://doi.org/10.1016/j.apenergy.2019.01.087.

Yu, Y.S., Zhou, S.D., Li, X.S., Wang, S.L., 2016. Effect of graphite nanoparticles on CO2 hydrate phase equilibrium. Fluid Phase Equilib. 414, 23–28. https://doi.org/10.1016/j.fluid.2015.12.054.

Zhang, P., Tong, J., Huang, K., Zhu, X., Yang, W., 2021. The current status of high temperature electrochemistry-based CO2 transport membranes and reactors for direct CO2 capture and conversion. Prog. Energy Combust. Sci. 82,. https://doi.org/10.1016/j.pecs.2020.100888 100888.

Zhang, L., Yang, L., Wang, J., Zhao, J., Dong, H., Yang, M., Liu, Y., Song, Y., 2017. Enhanced CH4 recovery and CO2 storage via thermal stimulation in the CH4/CO2 replacement of methane hydrate. Chem. Eng. J. 308, 40–49. https://doi.org/10.1016/j.cej.2016.09.047.

Zhou, S., Yu, Y., Zhao, M., Wang, S., Zhang, G.-Z., 2014. Effect of graphite nanoparticles on promoting CO2 hydrate formation. Energy & Fuels 28, 4694–4698. https://doi.org/10.1021/ef5000886.

Zhu, X., Ge, T., Yang, F., Wang, R., 2021. Design of steam-assisted temperature vacuum-swing adsorption processes for efficient CO2 capture from ambient air. Renew. Sustain. Energy Rev. 137,. https://doi.org/10.1016/j.rser.2020.110651 110651.

Zuo, X., Zhu, J., An, B., Han, K., Li, R., Wang, E., 2017. Influence of Fe addition on microstructure and properties of Cu-Ag composite. Met. Mater. Int. 23, 974–983. https://doi.org/10.1007/s12540-017-6656-2.

# Supplementary materials

*a*1
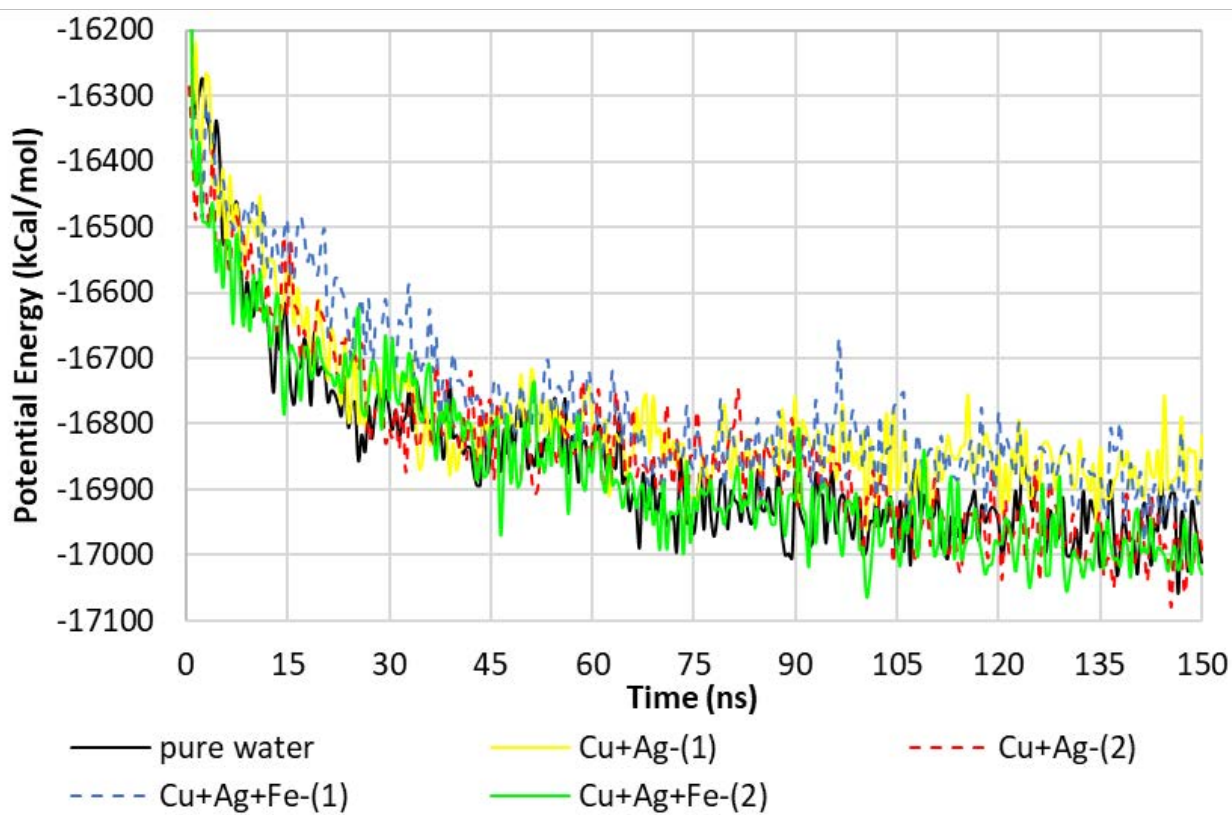


*a*2
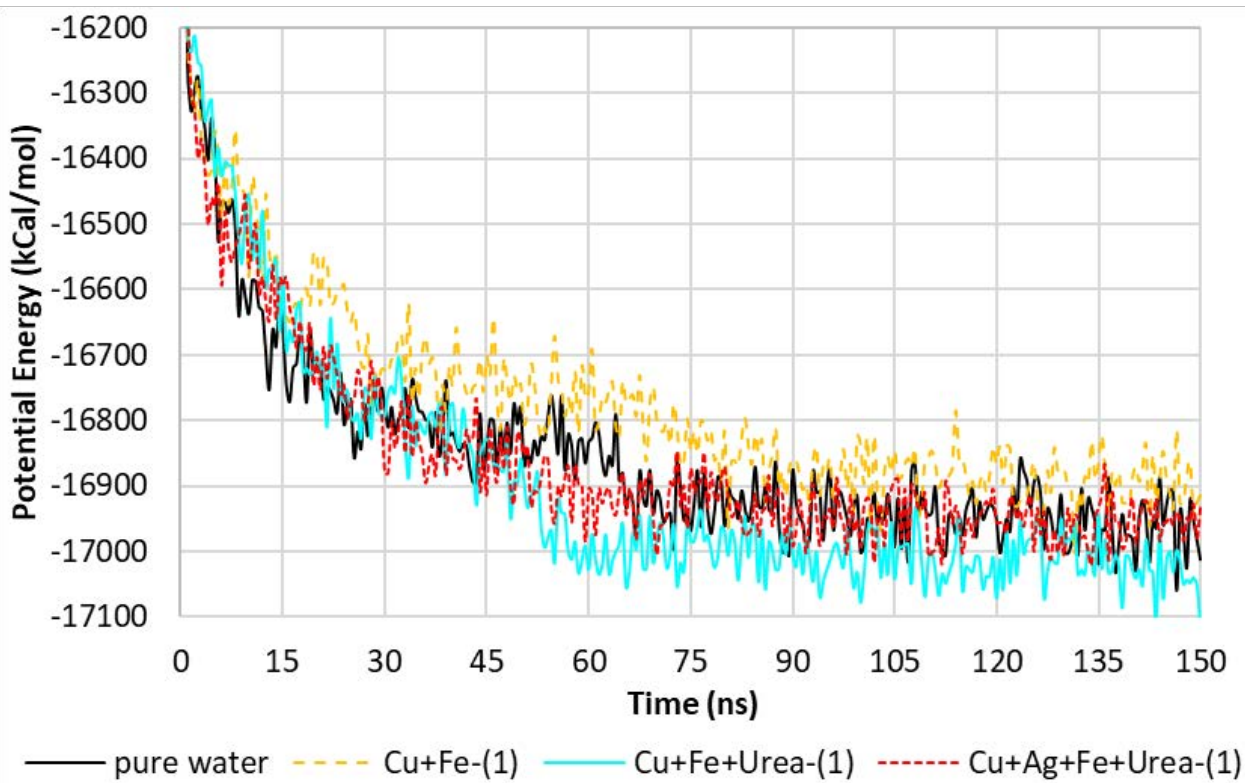
*b*1
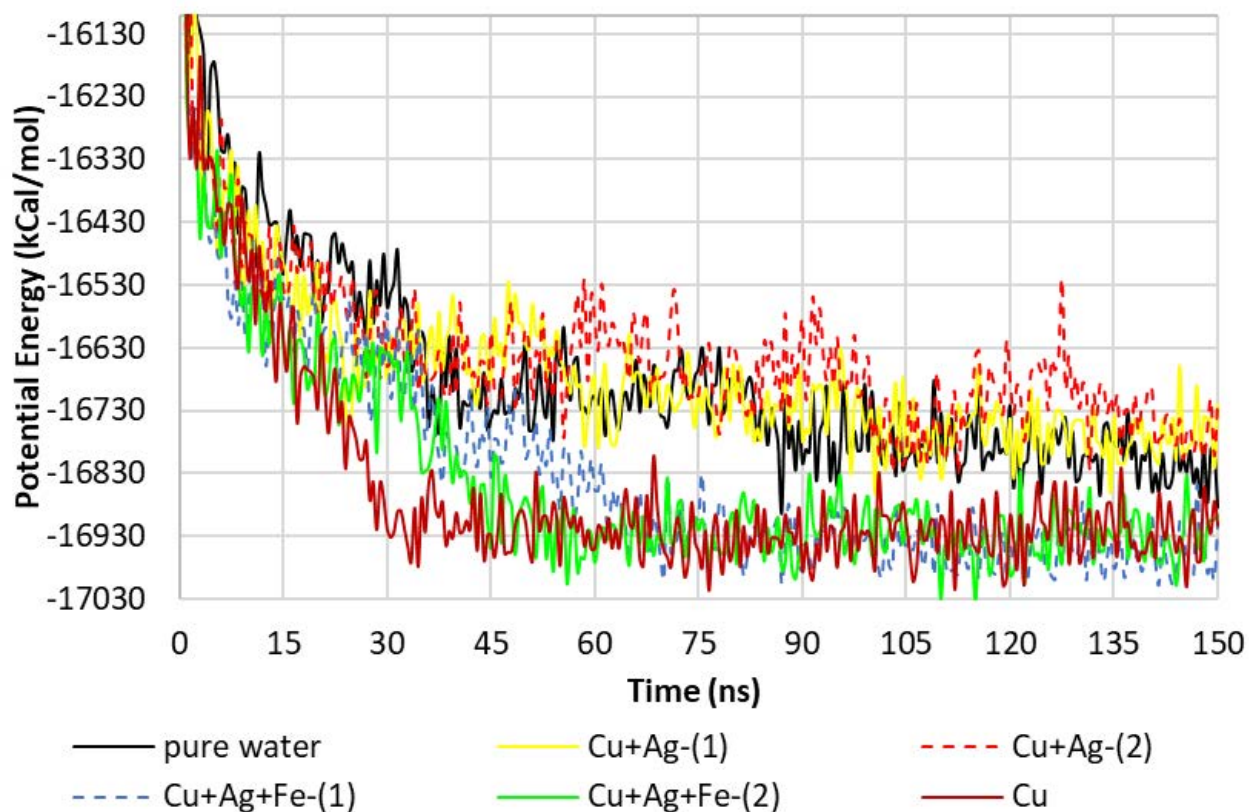


*b*2
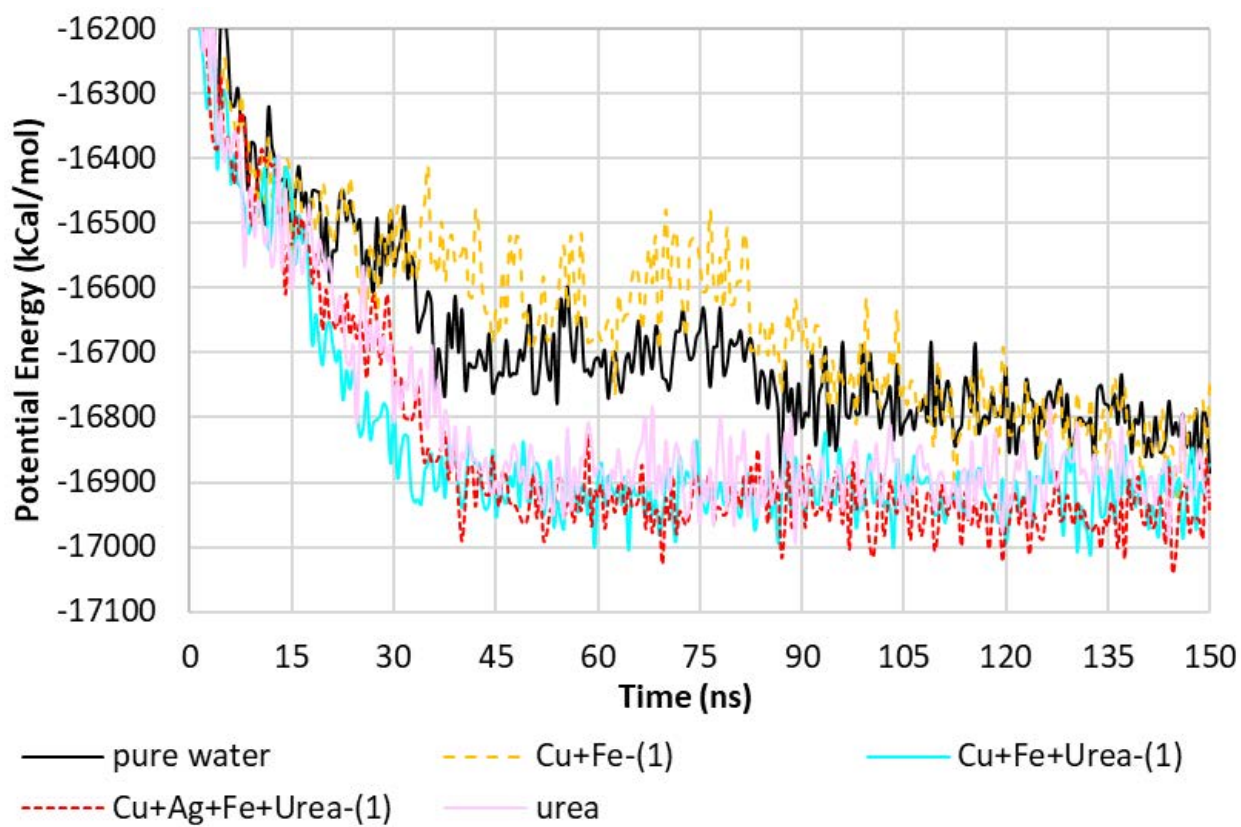


Figure S1: Potential energy, a1 and a2 at 2 MPa and 260 K; b1 and b2 at 3 MPa and 275 K.

*a*1
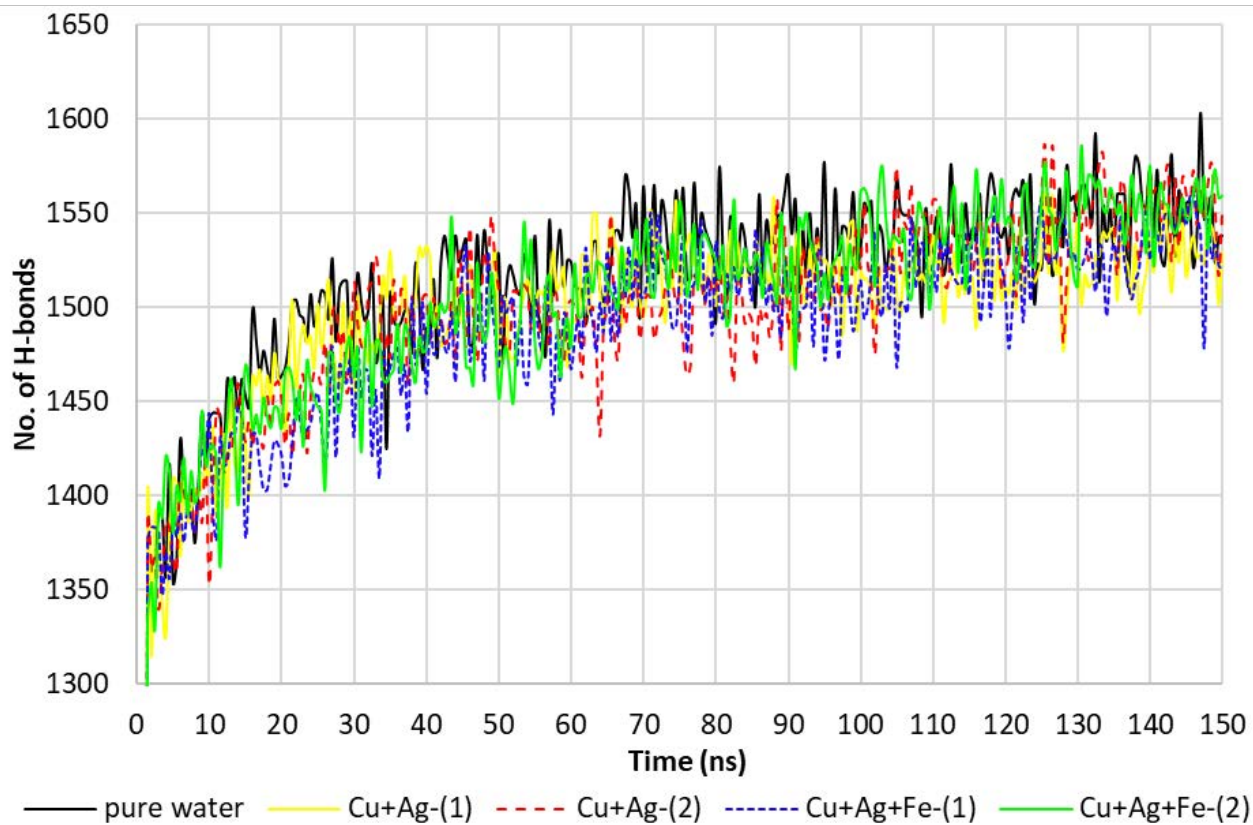


*a*2
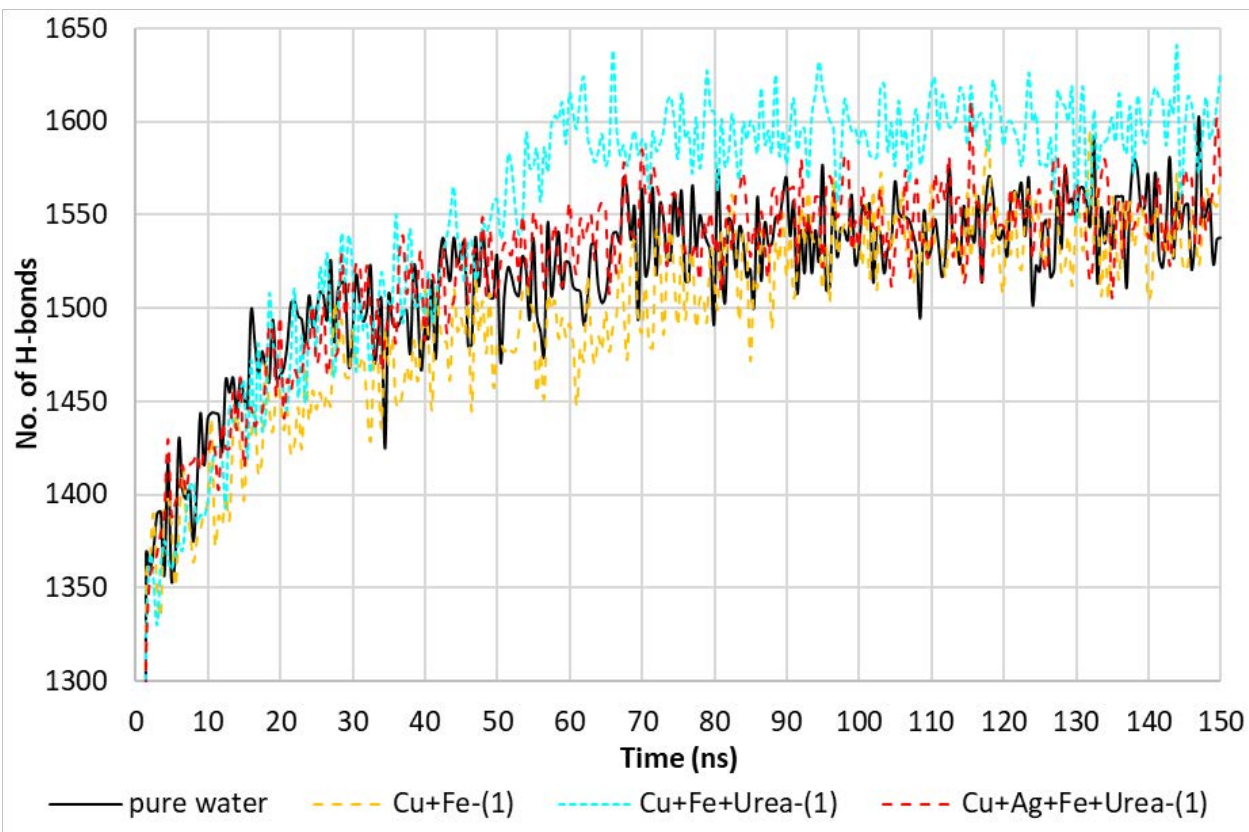
*b*1
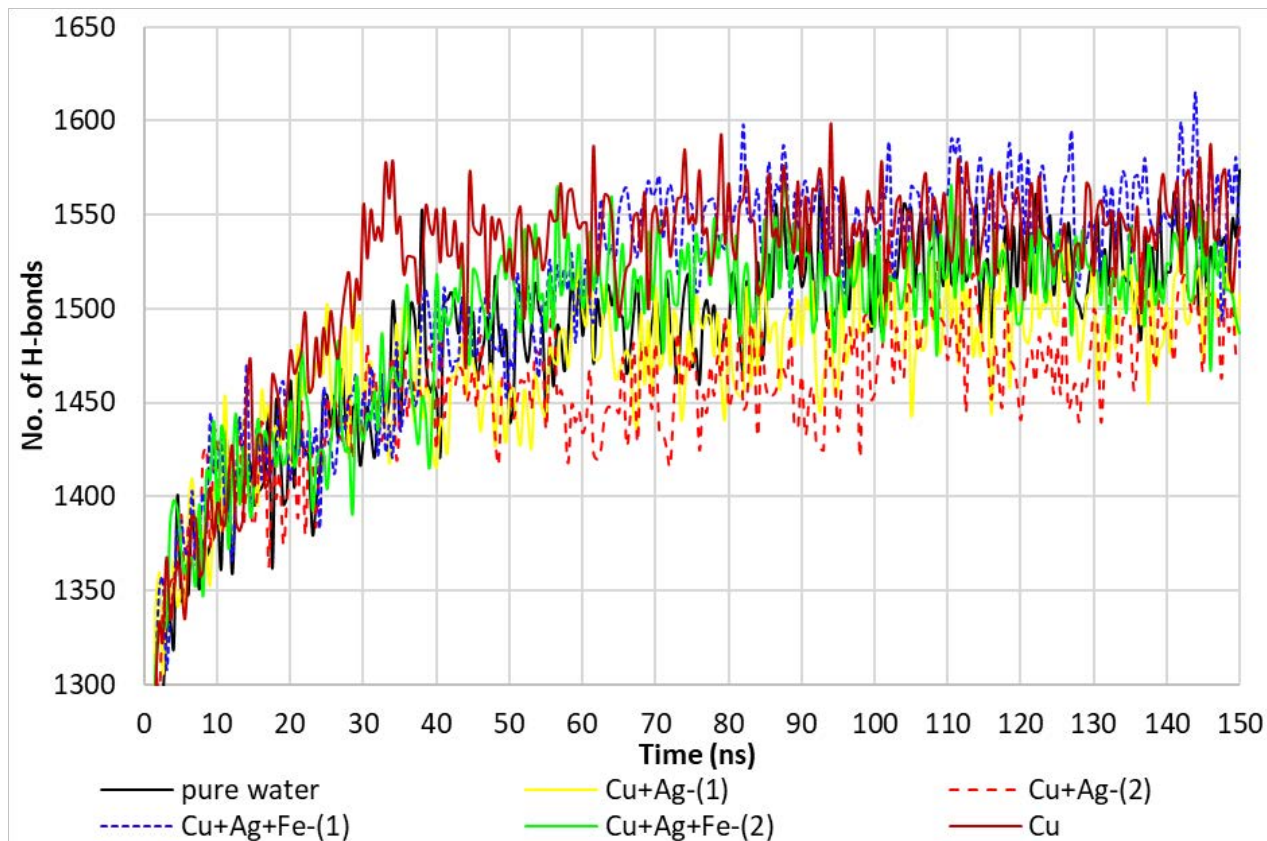


*b*2
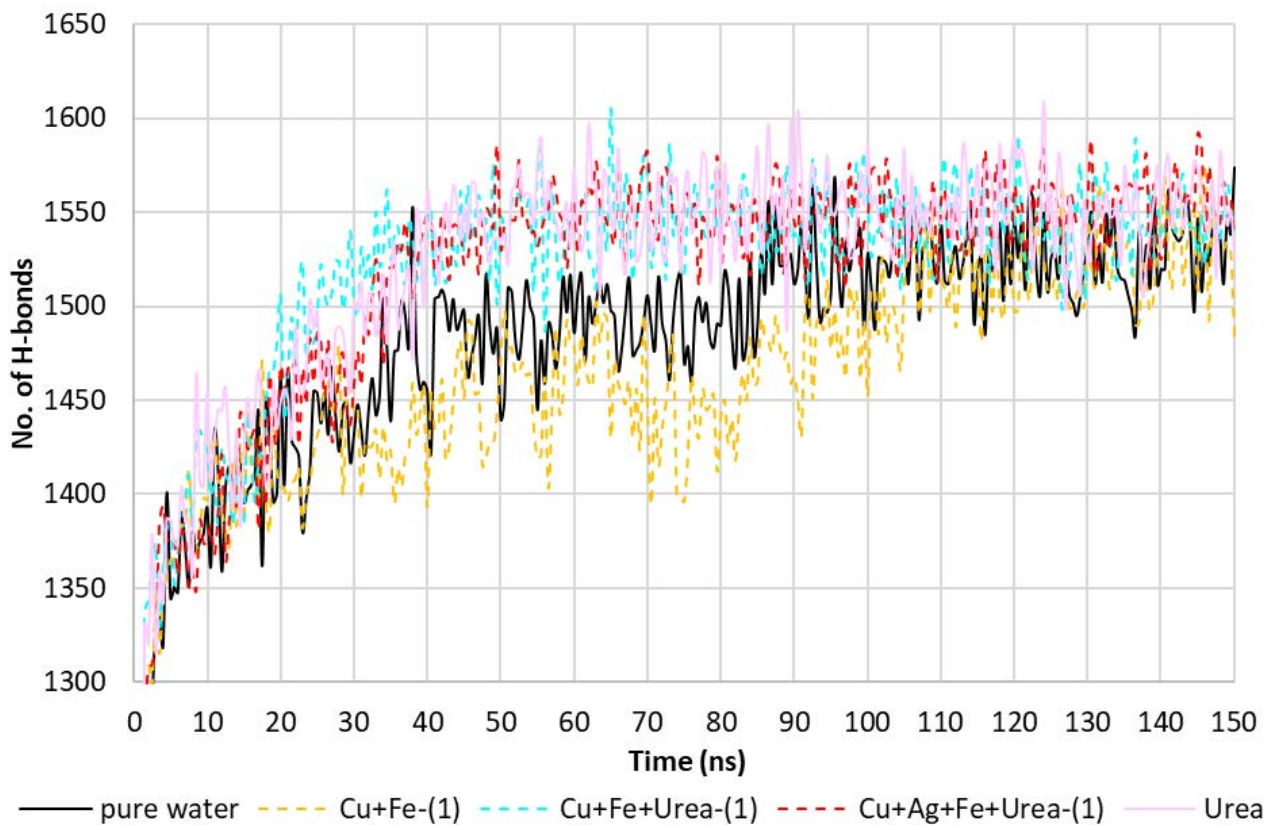


Figure S2: Number of Hydrogen bonds versus the $CO_2$ hydrate growth, a1 and a2 at 2 MPa and 260 K; b1 and b2 at 3 MPa and 275 K.

*a*1
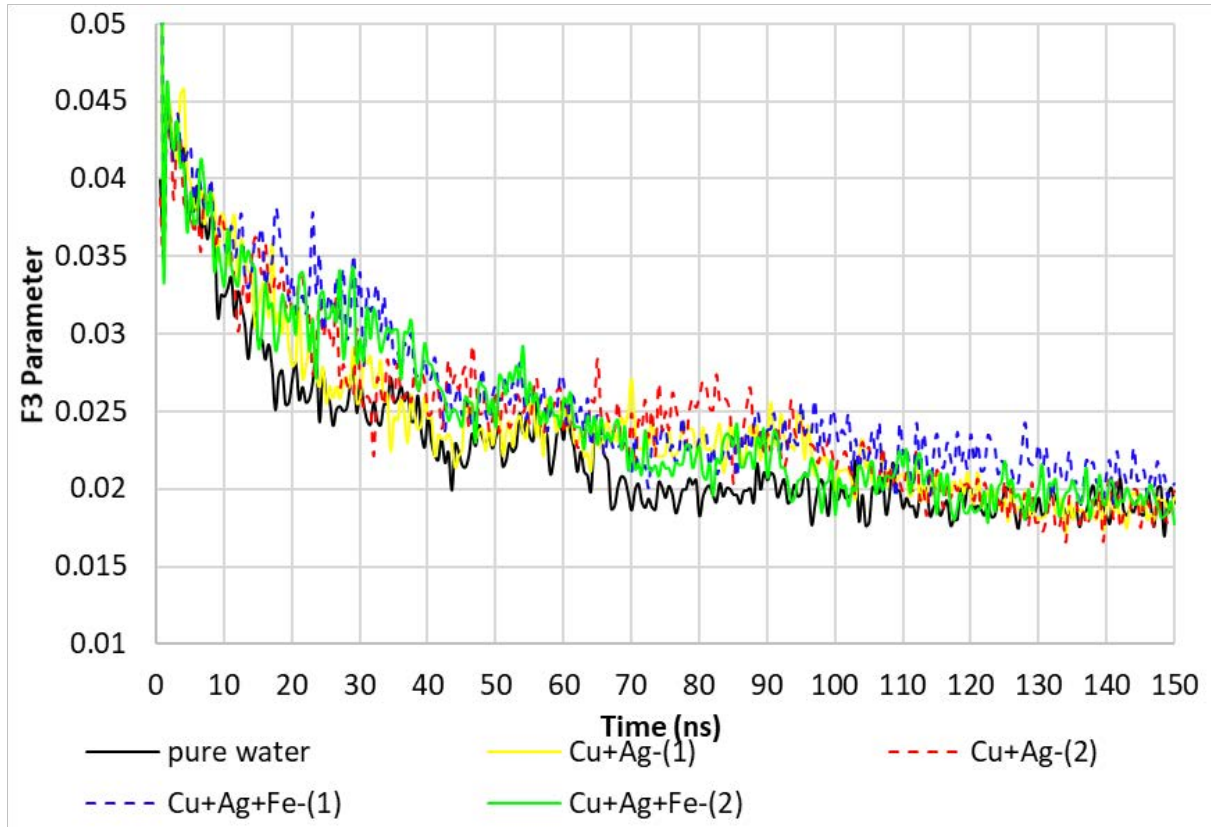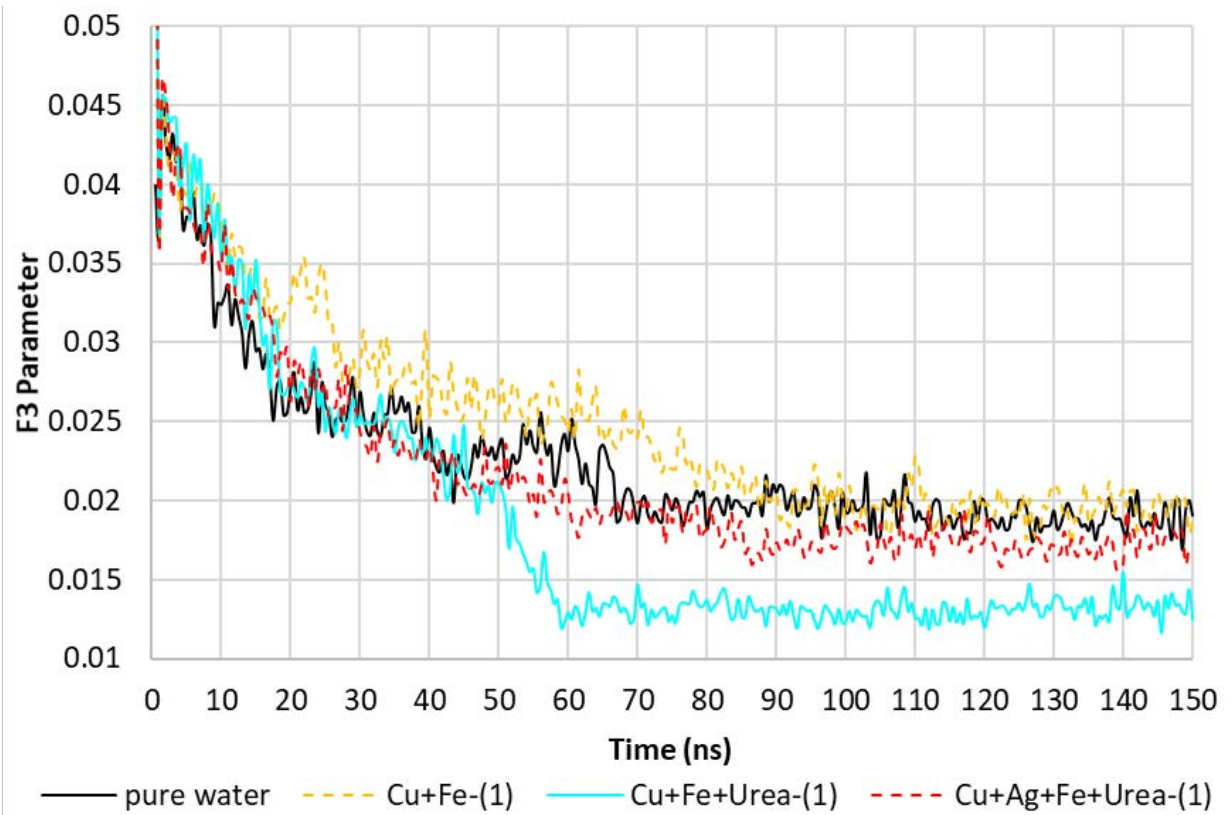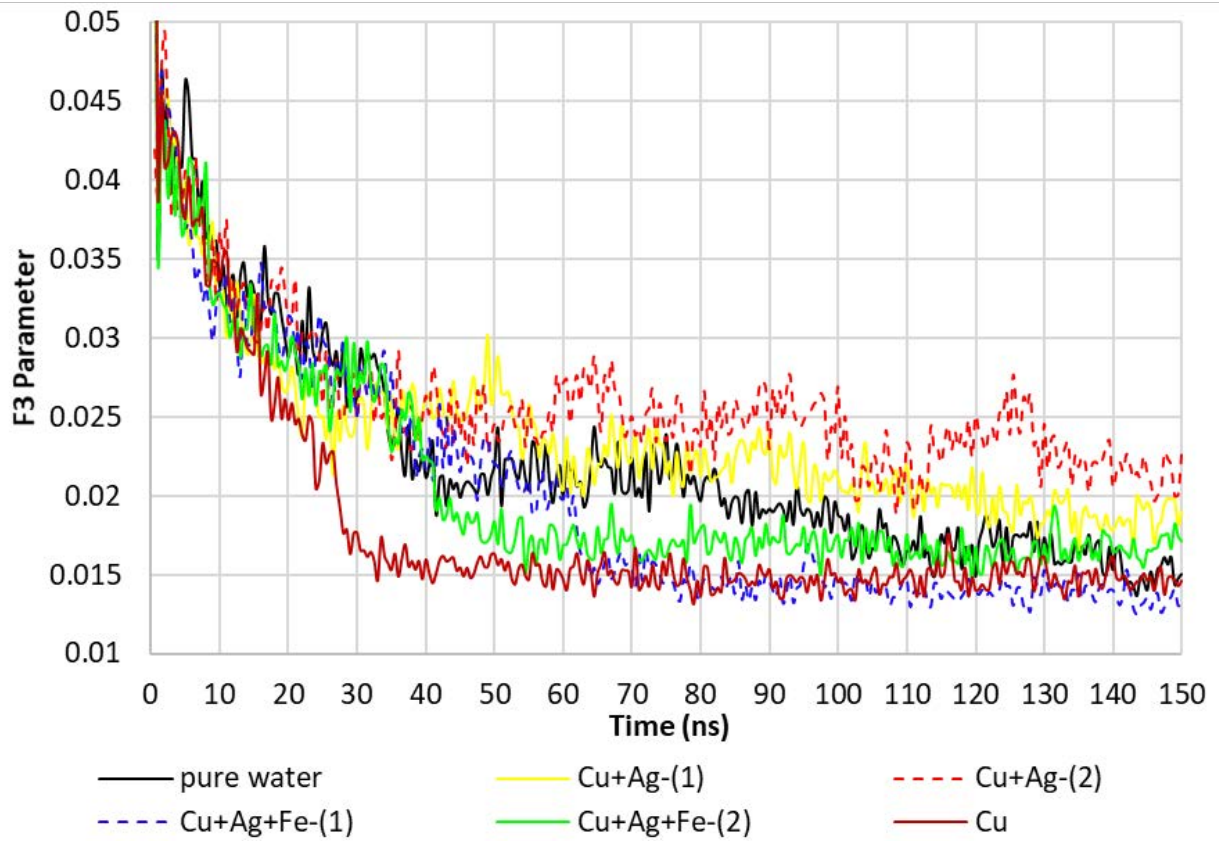


*a*2
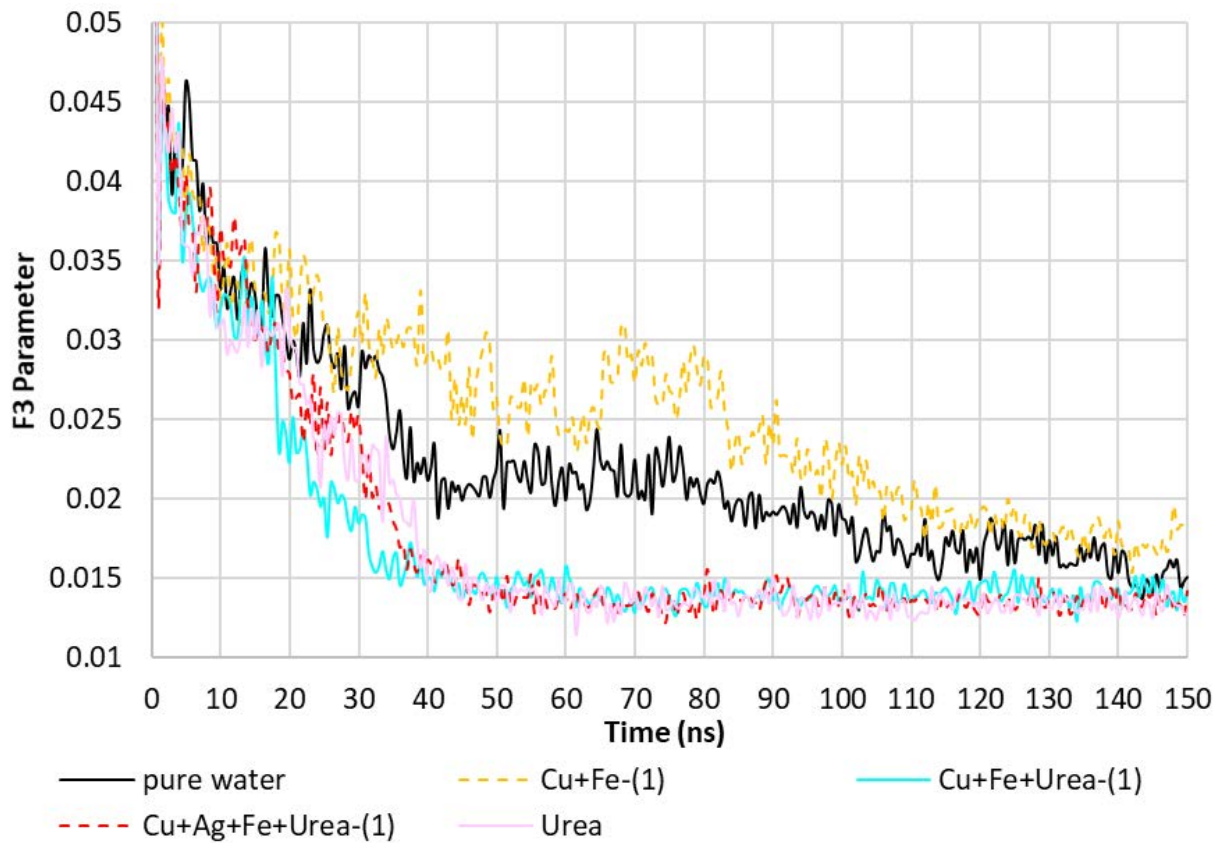
Figure S3: F3 parameter for total simulation box, a1 and a2 at 2 MPa and 260 K; b1 and b2 at 3 MPa and 275 K.
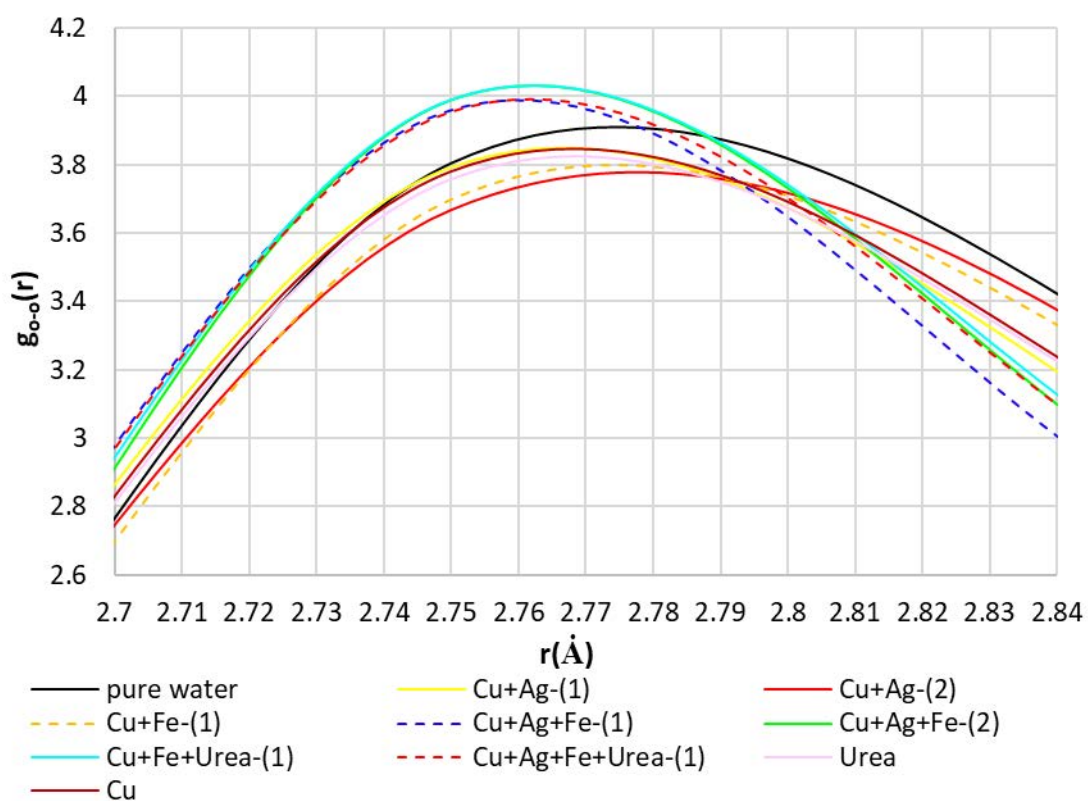
*a*1
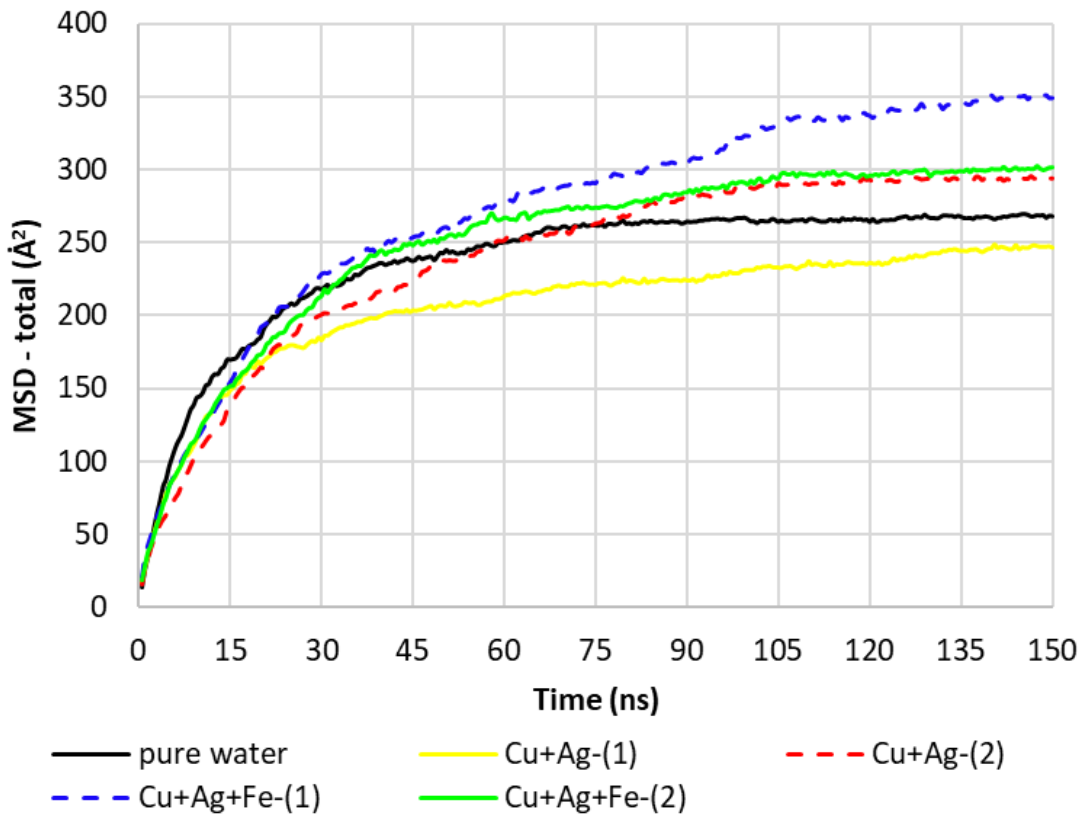
*a*2
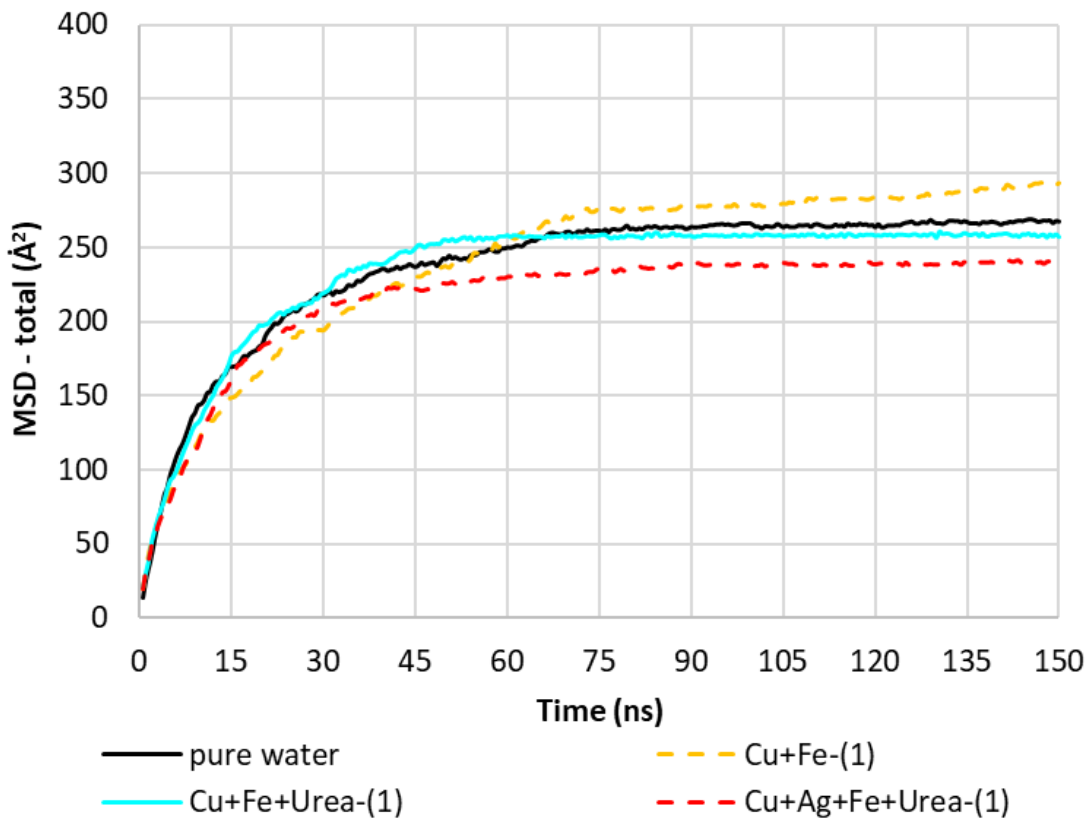
*b*1
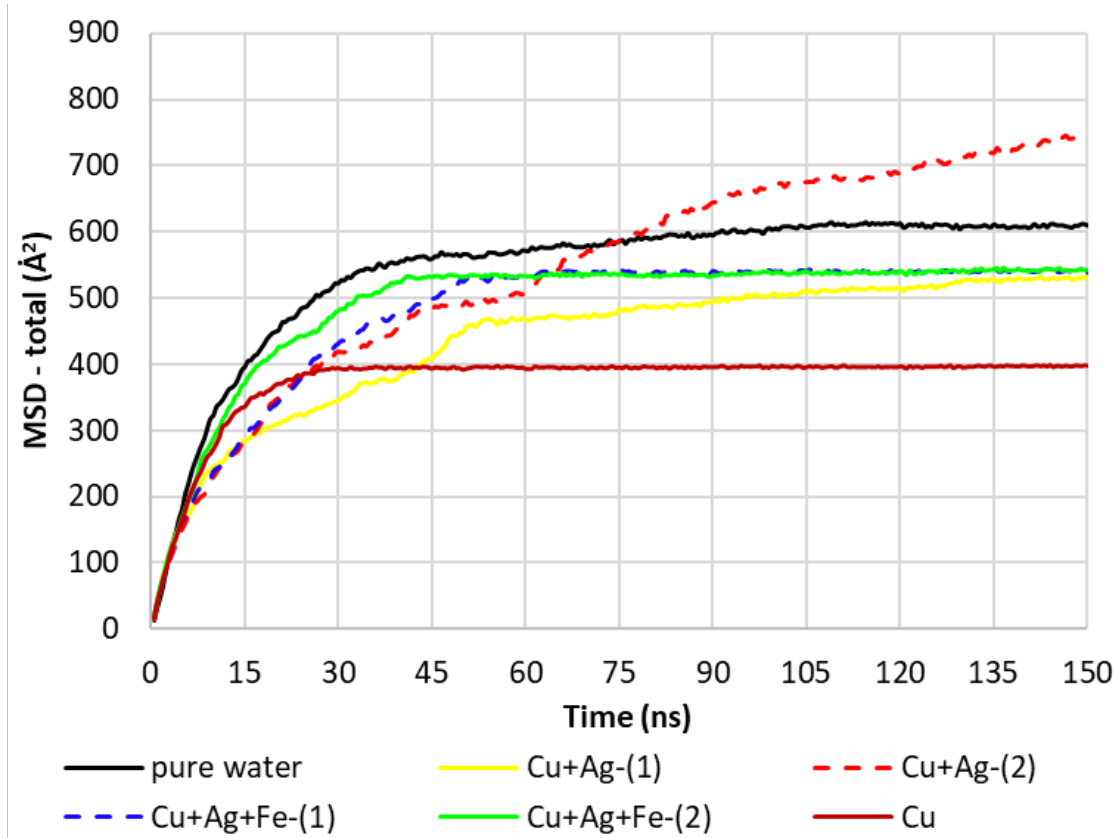


*b*2
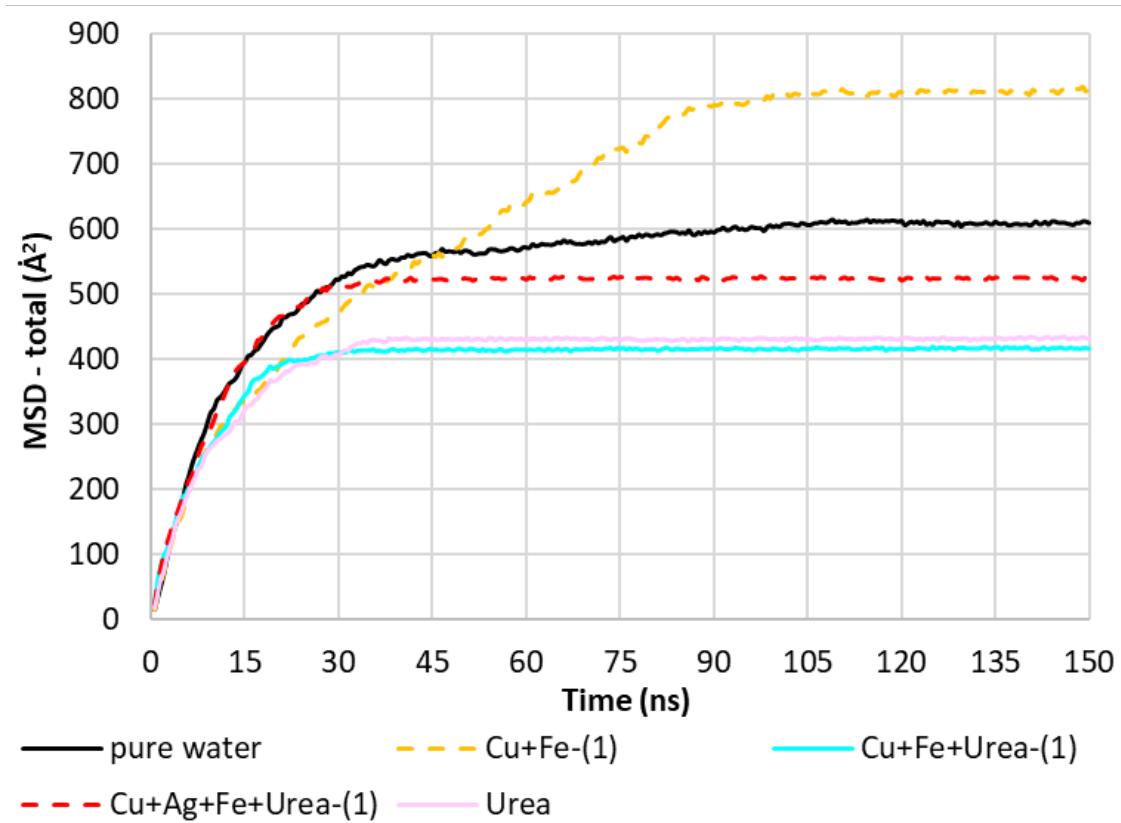


Figure S4: MSD for all molecules in the simulation box, a1 and a2 at 2 MPa and 260 K; b1 and b2 at 3 MPa and 275 K.

*a*1
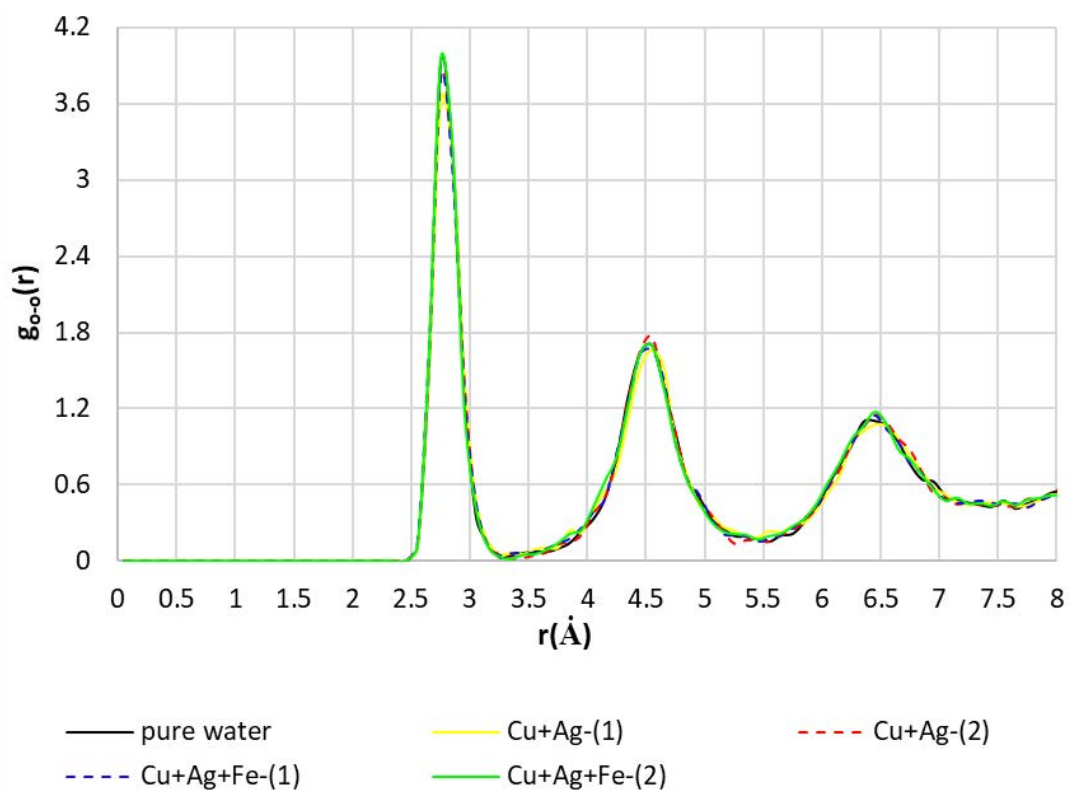


*a*2
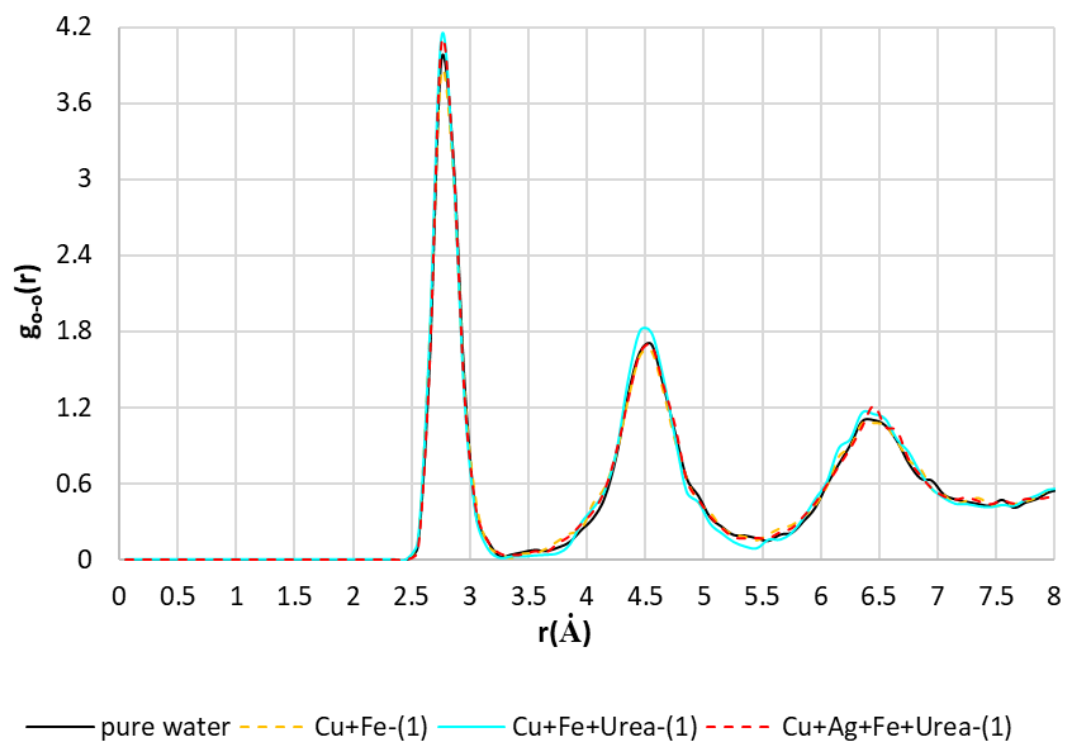
*a*3
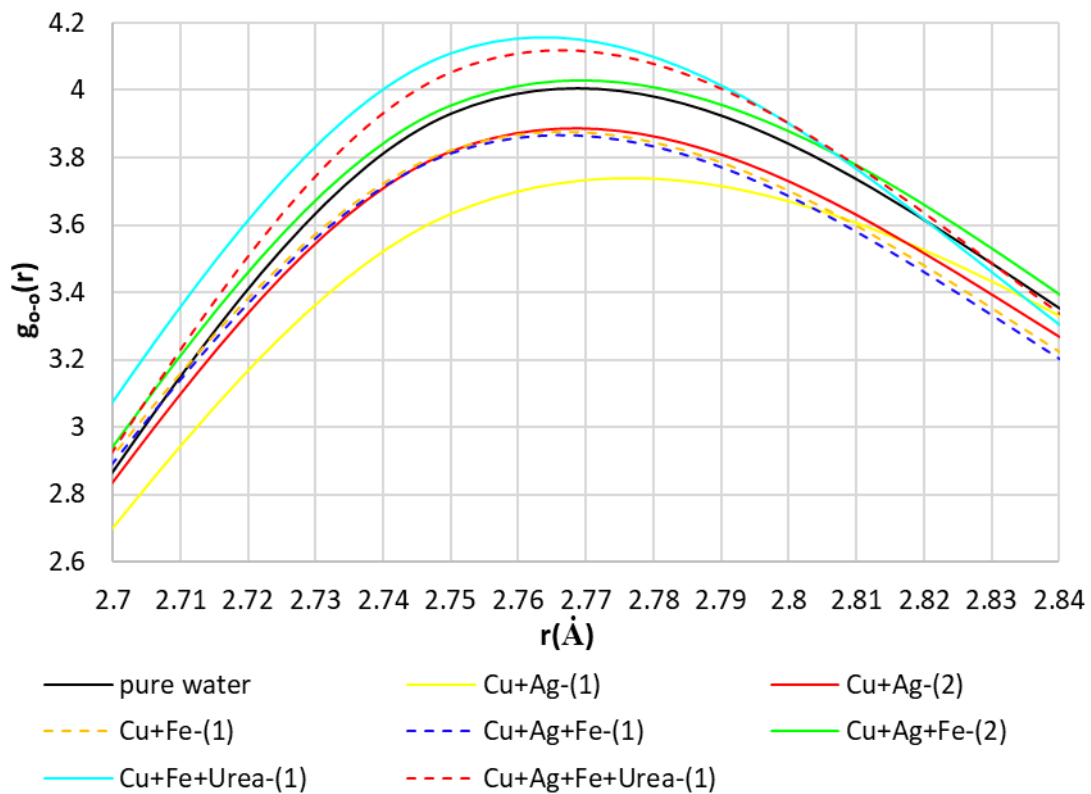


*b*1
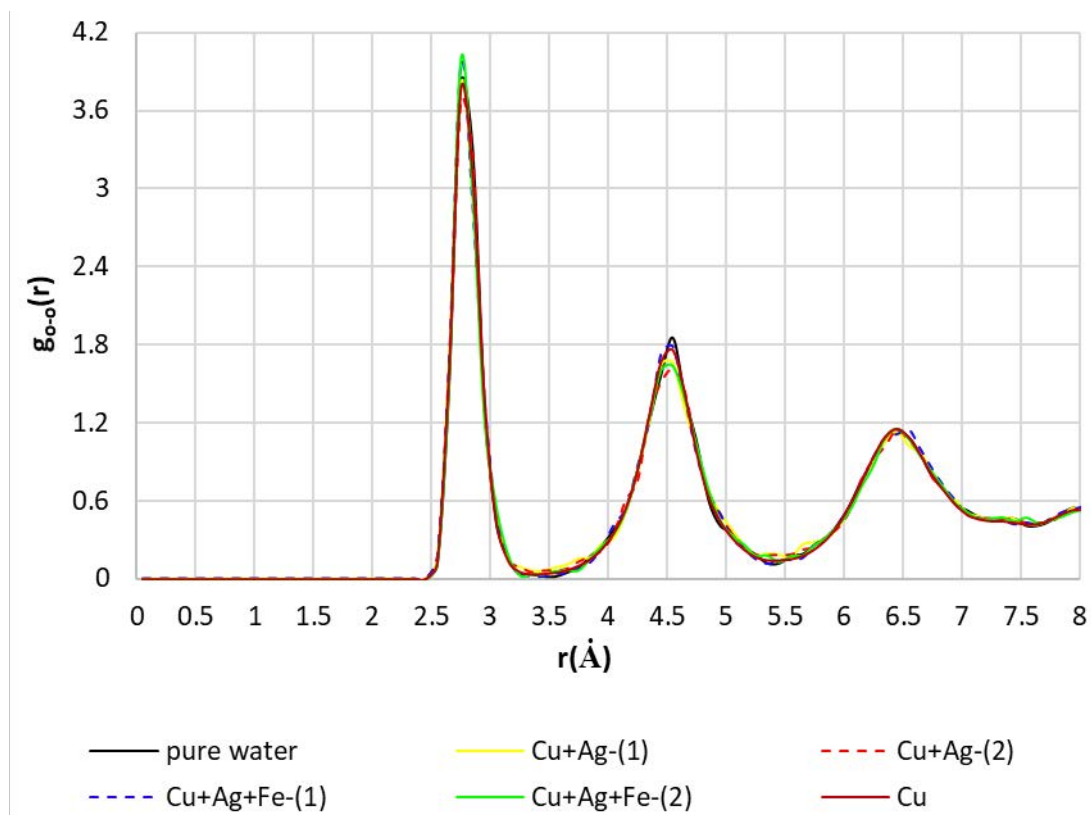
*b2*
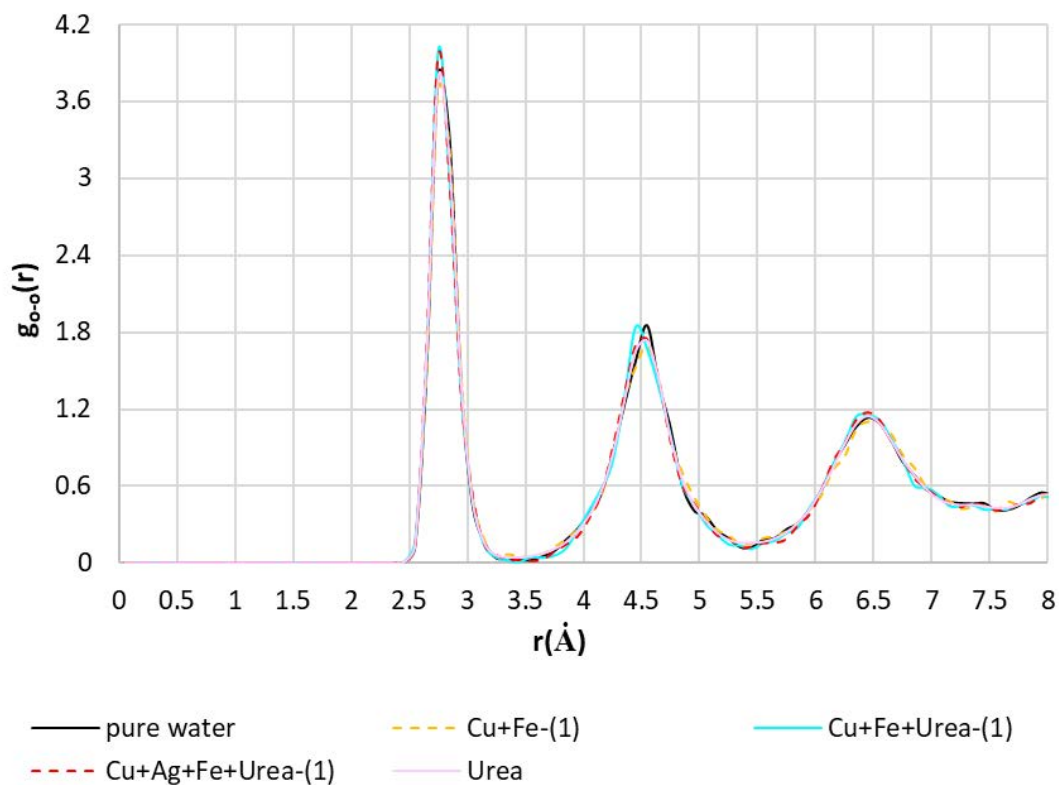


*b3*



Figure S5: RDF between oxygen atoms of water molecules in the system. a1, a2, a3 at 2 MPa and 260 K; b1, b2, b3 at 3 MPa and 275 K.

# Chapter 4 (Objective 2): Biogas hydrate formation in the inclusion of pure/ mixed organic kinetic hydrate promoters

As Figure 13 (step 5) of chapter 1 indicated, the influences of KHPs (pure/ mixed metal particles and urea) on $CO_2$ hydrate formation in the chapter 3 were studied. This chapter considers the effects of pure or mixed organic KHPs such as organic aliphatic amines on the formation of clathrate hydrate of the biogas. These organic compounds contain nitrogen atoms with a lone pair which are derived from ammonia replacing one or more hydrogen atoms by an alkyl or aryl group. Also, the utilization of these components from an environmental perspective would be acceptable.

Since the promotion mechanisms of organic promoters for pure and mixed $CO_2$ hydrate are not the same, conducting this exploration can also complete the finding of the previous chapter in which the pure $CO_2$ hydrate was the basis of the simulations. Also, the difference in the characteristics of organic hydrate promoters can create a complex formation phenomenon so that their combined utilization would be unique. Therefore, it is essential to identify the positive and negative aspects of applying these substances at the initial stage of biogas hydrate growth.

This chapter was published as a research paper in the Journal of Molecular Liquids:

Sinehbaghizadeh, S., Saptoro, A., Naeiji, P., Mohammadi, A.H., 2023. Molecular dynamics simulations of the effects of organic amines on biogas clathrate hydrate formation. *Journal of Molecular liquids*, 2023, 382, 122015, Elsevier.
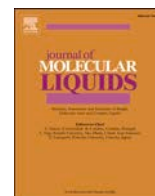
# Molecular dynamics simulations to investigate the effects of organic amines on biogas clathrate hydrate formation

Saeid Sinehbaghizadeh [a,*], Agus Saptoro [a,b,*], Parisa Naeiji [c], Amir H. Mohammadi [d,*]

[a] *Department of Chemical and Energy Engineering, Curtin University Malaysia, CDT 250, Miri 98009, Sarawak, Malaysia*
[b] *Curtin Malaysia Research Institute, Curtin University Malaysia, CDT 250, Miri 98009, Sarawak, Malaysia*
[c] *School of Chemical and Bioprocess Engineering, University College Dublin, Belfield, Dublin 4, Ireland*
[d] *Discipline of Chemical Engineering, School of Engineering, University of KwaZulu-Natal, Howard College Campus, King George V Avenue, Durban 4041, South Africa*

A B S T R A C T

The biological degradation of organic wastes mostly generates biogas including $CO_2$ and $CH_4$. Since both gases may be utilized as feedstock for various industrial applications, the alternative of gas hydrates to separate or enrich such gas species is of particular interest. To promote the hydrate-based (HB) methods, introducing environmentally friendly promoters could either enhance the formation or improve the recovery rates. In this study, the effects of pure and binary organic amines (methylamine, dimethylamine, amylamine) and urea on the kinetics of $CO_2 + CH_4$ hydrate formation through molecular dynamics simulations were explored. To characterize the kinetics of biogas hydrate formation, different analyses such as the three/four-body structural order parameters, determination of hydrate-like cages, number of hydrogen bonds, molecular distributions, and energy variations were investigated. Results indicate that the promotion effects of organic molecules were evident in which the presence of methylamine, dimethylamine, and their mixture was found to be more kinetically efficient than other studied solution systems. These molecules can also induce guest gases toward being located inside the formed cages more than in pure water. Studied molecules can also affect the distribution of $CO_2$ and $CH_4$ molecules during the conversion of the solution phase to a clathrate-like state which could be a useful feature to intensify the split fraction of HB processes. Nonetheless, the addition of urea in either a pure or binary mixture with other amine molecules was not recognized as the observed efficiency of combined methylamine and dimethylamine. This investigation reveals the uncovered characteristics regarding the utilization of long/short-chain amines to upgrade the process of biogas separation through hydrate.

## 1. Introduction

As an environmentally-friendly, renewable energy source, biogas (or landfill gas) is a mixture of different gas species produced when organic matter such as organic waste, food, and municipal rubbish is broken down through the biological degradation processes in biowaste treatment plants. For this to take place, microorganisms in the absence of oxygen degrade the organic waste which is called anaerobic digestion. Biogas mainly includes $CH_4$ and $CO_2$ ranging between 50%-75% mole and 25%–50% mole, respectively. Both gases are greenhouse gases so that essential to control their emissions. The $CH_4$ as a clean energy source should be enriched to enhance the calorific value. Also, the separated $CO_2$ can be used for different industrial utilizations or

converted into valuable products. There are many different technologies to perform the enrichment of biogas such as chemical absorption, cryogenic separation, solvent scrubbing, physical absorption, membrane, and pressure swing adsorption [1]. However, one of the negative aspects of these methods is their high energy costs. Moreover, future technologies and ideas which would be environmentally and efficiently more acceptable need to be developed. Another alternative would be the hybrid of the present and new methodologies. Therefore, the new ecologically safe methods in this respect are highly essential. One of the new eco-friendly processes for biogas separation is the utilization of the clathrate hydrate formation phenomenon.

Clathrate gas hydrates are crystalline shapes formed through hydrogen-bonded water molecules while trapping the gas molecules inside the cages of a lattice. The three known structures of the clathrate

* Corresponding authors at: Department of Chemical and Energy Engineering, Curtin University Malaysia, CDT 250, Miri 98009, Sarawak, Malaysia (A. Saptoro).
  *E-mail addresses:* s.baghizadeh@postgrad.curtin.edu.my (S. Sinehbaghizadeh), agus.saptoro@curtin.edu.my (A. Saptoro), amir_h_mohammadi@yahoo.com (A.H. Mohammadi).

---

**Nomenclature**

| | |
|---|---|
| TE | Total Energy |
| MSD | Mean Squared Displacement |
| $F_3$ | Three-body Structural order parameter |
| $F_4$ | Four-body structural order parameter |
| HB | Hydrate-based |
| MA | Methylamine molecule |
| DMA | Dimethylamine molecule |
| AA | Amylamine molecule |
| Ur | Urea molecule |
| THF | Tetrahydrofuran |
| DMSO | Dimethyl sulfoxide |
| SDS | Sodium dodecyl sulfate |
| SL | Sulfonated lignin, |
| SDBS | Sodium dodecyl benzene sulfonate |

| | |
|---|---|
| ns | nano-second |
| ps | pico-second |
| Å | Angstrom |

*Greek letters*

| | |
|---|---|
| $a$ | Atom $a$ |
| $b$ | Atom $b$ |
| $\varepsilon$ | Cross LJ parameters |

*Subscripts*

| | |
|---|---|
| $i$ | Atom $i$ |
| $j$ | Atom $j$ |
| $k$ | Atom $k$ |
| $x$ | x direction |
| $y$ | y direction |
| $z$ | z direction |

---

gas hydrates are sI, sII, and sH [2]. The size and geometry of cavities in these structures are not the same. Also, the mixture of $CO_2$ and $CH_4$ molecules can fill the cages (both small and large types) of either sI or sII of clathrate hydrates, however, the prominent clathrate structure is sI. To identify the distribution of these molecules in the cavities and crystalline structure, the most popular techniques are powder X-ray diffraction (PXRD) and Raman spectroscopy. Based on experiments of these methods, it was revealed that the tendency to fill the large cavities with $CO_2$ molecules in comparison with $CH_4$ is higher [3]. Since the number of large to small cavities for sI hydrate is 3, it is expected to capture $CO_2$ molecules more than $CH_4$ in the hydrate state. Nevertheless, the recovery of the process of hydrate-based (HB) biogas treatment is pertinent to different factors such as $CO_2/CH_4$ ratio, P-T condition, hydrate formation reactor, number of designed stages, etc. [4,5]. It is worth highlighting that by employing similar HB processes, the enriched $CO_2$ can be used for seawater desalination, fruit juice concentration, refrigeration systems, and so on. Recently, we have reviewed almost all applications and practical properties of these methodologies [6].

To do the commercially viable HB methods, one of the main impediments is the longtime of induction time as well as the low conversion rate of gas to form hydrate. For this reason, a wide variety of kinetic additives to find effective promoters have been tested. These components can also be used as thermodynamic promoters [7–10]. Experimental measurements demonstrated that the inclusion of dimethyl sulfoxide (DMSO) by increasing the solubility of $CO_2$ in water can markedly promote the hydrate formation rate [11]. Kinetic promoters e. g. sodium dodecyl sulfate (SDS) by reducing the surface tension in the solution solubilize the gases so that it decreases the induction time [12]. Surfactants like dodecyl trimethyl ammonium chloride (DTAC) can also improve the hydrate formation kinetics if it exceeds its critical micellar concentration and form the micelle phenomenon [13]. Although the aforementioned promoter looks good for the HB processes, they are mostly not compatible with the latest criteria used for the environment.

Recently practical explorations have revealed the possible utilization of organic components such as organic amines, proteins, and amino acids as strong kinetic hydrate promoters [14–16]. PXRD and NMR studies revealed that some amines such as dimethylamine and ethylamine play as sI hydrate former while in the presence of $CH_4$, structural transition to sII hydrate can occur [17]. In another experimental investigation, it was demonstrated that $CH_4$ sI hydrate with the inclusion of di-isopropyl amine and diethyl amine can be changed into the sH clathrate hydrate [18]. In the industry, chemical absorption using liquid amines by reacting with $CO_2$ can capture it in the aqueous amine scrubbing which is known as acid gas removal from natural gas. However, this process leaves a considerable carbon footprint. A new $CO_2$ sorbent using organic amine-infused hydrogels showed that in

comparison with commonly aqueous amine solutions, $CO_2$ can rapidly be captured with higher overall uptake [19]. This method using amine diethanolamine-infused hydrogels combined with a $CO_2$ HB cold thermal energy storage even gave a very effective $CO_2$ absorber [20]. The $CO_2$ splitting from the gas mixture through hydrate growth with the presence of two tertiary amines (tri-ethanolamine and tri-isopropanolamine) showed that these additives can contribute to the better $CO_2$ selectivity so that 65% increase in the process for capturing $CO_2$ [21]. Since the positive impressions of amines for various hydrate-based applications have been recorded in the literature, finding organic and eco-friendly amines to upgrade their processes would be practical. These components can act as both thermodynamic or kinetic promoters. Exploration of ^{13}C NMR spectra and synchrotron high-resolution powder diffraction determined that by introducing cyclopentyl amine into $CH_4$ hydrate, the P-T formation equilibrium conditions can be significantly improved [22]. Recently, the kinetic effects of short and long-chain organic aliphatic amines (decylamine, amylamine, and methylamine) on $CO_2$ hydrate nucleation and growth at 274 K and 3.5 MPa were evaluated [14]. The water to hydrate conversion and $CO_2$ uptake for 1 wt% methylamine, and 5 wt% amylamine, and decylamine were found to be significantly higher than pure water.

To gain a better comprehension of clathrate hydrates in contact with kinetic promoters, analyzing their different characteristics at the molecular scale can also be profitable. In this regard, molecular dynamics (MD) simulations as an effective method can either cover the experimental results or reveal more details about the microscopic mechanisms of promoters. In this respect, we have reviewed a large number of MD-studied phenomena and properties associated with clathrate hydrates [23]. MD study of $CH_4$ hydrate with the inclusion of five different amino acids uncovered that electrostatic and van der Waals interactions of these components with water significantly influence the hydrogen bonding of the water network as well as guest solubility [24]. It was determined that the ratio of $CH_4$ to $CO_2$ in the hydrate phase can be increased by 34% according to the MD outcomes of biogas hydrate growth with the utilization of tetrahydrofuran and dimethyl sulfoxide [25]. Also, the MD investigation of $CO_2$ + $CH_4$ hydrates with thermodynamic promoters showed that these components would be the main conductors of hydrate structural properties [26]. Recently, it was revealed that the addition of mixed kinetic promoters such as Cu and Fe metal particles with urea can efficiently decrease the mass and heat transport resistances of $CO_2$ in the solution [27]. Therefore, kinetic promoters have been widely acknowledged to aid more efficient hydrate formation.

In the literature, few experimental investigations pertinent to the influences of organic aliphatic amines on hydrate growth at the macroscopic scale could be found [14]. However, the effects of their

**Table 1**
The simulation sets used in this work including the organic molecules added to the solution phase.

| Case | Solution system | No. of molecules in the solution | Content in the solution (wt%) |
|------|-----------------|----------------------------------|-------------------------------|
| S1   | Pure water      | –                                | –                             |
| S2   | MA1             | 1                                | 0.23                          |
| S3   | MA2             | 2                                | 0.46                          |
| S4   | DMA1            | 1                                | 0.34                          |
| S5   | DMA2            | 2                                | 0.68                          |
| S6   | AA1             | 1                                | 0.66                          |
| S7   | AA2             | 2                                | 1.32                          |
| S8   | Ur1             | 1                                | 0.45                          |
| S9   | Ur2             | 2                                | 0.90                          |
| S10  | MA + DMA        | 1 + 1                            | 0.57                          |
| S11  | MA + AA         | 1 + 1                            | 1.11                          |
| S12  | MA + Ur         | 1 + 1                            | 0.68                          |
| S13  | DMA + AA        | 1 + 1                            | 1.00                          |
| S14  | DMA + Ur        | 1 + 1                            | 0.79                          |
| S15  | AA + Ur         | 1 + 1                            | 1.11                          |

Note: MA: Methylamine; DMA: Dimethylamine; AA: Amylamine; Ur: Urea.

presence on hydrate growth at the molecular level are still poorly understood and have not been reported. Understanding these effects may assist in the better identification of organic amines for either HB biogas processing, HB gas enrichment, and other HB $CO_2$ utilization methods. This paper is therefore presented to elucidate the molecular level mechanism of mixed $CO_2$ + $CH_4$ hydrate growth in the existence of pure and mixed amines such as methylamine (MA), dimethylamine (DMA), amylamine (AA), and urea (Ur) through MD simulations. MA molecule includes a primary aliphatic amine group that has a strong odor similar to fish. Commonly, it exists in several plant foods such as cabbages, tea, carrots, barley, soybeans, and common grapes. As a secondary amine and off-flavor compound, DMA molecule mainly results from microbial enzymatic and metabolite activities in fish, squid, and shellfish [28]. AA is a primary aliphatic amine group and fishy-tasting compound that can be found in bell peppers, apples, and cabbages. Organic amines can also be found in shallow subsea sediments [29]. It should be noted that the results of this work may also help to find appropriate organic amines for biogas hydrate formation.

## 2. Simulation methodology

In this study, the influences of amines and urea and their various combinations through fifteen sets of simulations were performed as summarized in Table 1. All simulations were carried out using the LAMMPS parallel software [30]. To build the initial configuration of the hydrate slab at the centre of the simulation box, the initial positions of hydrogen and oxygen atoms of water molecules were orientationally specified from the work of Takeuchi et al. [31]. The guest molecules at the centre of sI hydrate cages were then allocated using the determined cartesian coordinates of the sI hydrate unit cell. Worth mentioning that these positions based on the ice rules give a net zero dipole moment while having the least potential energy configuration for the protons. To provide a composition similar to the landfill gas [32], we selected the same number of molecules for both $CH_4$ and $CO_2$ in all simulation sets. Thus, the initial hydrate slab was constructed by 2 × 2 × 2 hydrate supercells including 368 water, 32 $CO_2$, and 32 $CH_4$ molecules respectively. The surrounding solution phase of this slab was composed of 736 water, 64 $CO_2$, and 64 $CH_4$ molecules with or without the additive. The initial solution phase was created using the Packmol code [33] which is a computer program designed to generate initial configurations for molecular dynamics simulations. It also guarantees that the short-range repulsive interactions do not disrupt the simulations. Packmol uses a random placement algorithm to position the gas and water molecules within the simulation box. Since the $CO_2$ solubility in water is several times more than $CH_4$ [34], its fraction in the hydrate phase would be

higher, however, it depends on operating conditions and the absence/presence of other additives in the system, etc. [3]. On the other hand, biogas includes $CH_4$ rather than $CO_2$. Due to the fact that these two effects may compensate for each other, the equal number of $CO_2$ and $CH_4$ molecules in both the initial hydrate and the solution phase was considered. Also, the organic molecules were placed on the right side of the simulation box. The XY surface of the initial hydrate slab on both sides was placed in contact with two solution regions with a thickness of 24 Å along the z-axis. The size of the initially established simulation box (similar to our previous work) was set equal to 24 Å×24 Å×72 Å [27]. Since the lattice constant of sI hydrate is around 12 Å [35], the dimension of the simulation box can be consistent with this value. Hence, each solution region was considered the same as the initial hydrate slab which is equal to 2 × 2 × 2 hydrate supercells. Also, the Z-direction after the total conversion of all solution phases to the hydrate phase can be around 72 Å or a chain of eight unicells. The amine/urea molecules were located in the liquid phases about 3 Å away from the hydrate surface.

The inter/intramolecular interactions including the electrostatic, Lennard-Jones functional, and coupling terms between internal coordinates were modelled using specific force fields. To determine the behaviours of both gases ($CO_2$ and $CH_4$ molecules), TraPPE force fields (transferable potentials for phase equilibria) were chosen [36]. The $H_2O$ molecules were also represented by the utilization of TIP4P-ice potential [37]. The structure of amine and urea molecules (MA, DMA, AA, and Ur) was geometrically optimized by the Gaussian 09 package at the B3LYP/cc-ρVDZ theory [38] and then their force fields were adopted by the GAFF (General AMBER Force Field) simulation package [39]. The cross-molecular Lennard-Jones parameters were calculated via the Lorentz-Berthelot mixing rule [40]. The interactions were calculated as the sum of long-range Coulomb potentials and the van der Waals by employing the Ewald summation technique [41] with a k-space cut-off of $1 \times 10^{-4}$. In addition, a spherical cut-off of 11.0 Å was truncated for all intermolecular interactions. The SHAKE algorithm was also employed to restrain the angle and bond of water molecules.

Three directions of the simulation system are set as periodic boundary conditions. For all simulated systems, a time step of 1 fs was considered. The solution phase was then equilibrated over the frozen hydrate state by NVT ensemble for 40 ps. To relax the system and energy minimization of the molecules in the hydrate phase, a short simulation time (40 ps) was implemented using the NPT ensemble. Eventually, all molecules inside the simulation box under the NPT ensemble at 273 K and 3 MPa were performed for at least 75 ns which were fixed by the Nose-Hoover thermostat and barostat. The hydrate and solution phases at the initial configuration were detached by spatial gaps to prevent two overlap segments, but after the equilibration stage, they were removed and therefore didn't influence the process of hydrate growth. The constructed systems were finally subjected to the MD simulation and the hydrate slab was unrestrained in performing both NVT and NPT stages so that all molecules were permitted to naturally evolve in the production stage of performed simulations. The MD trajectories were finally applied for different analyses.

## 3. Results and discussion

### 3.1. The growth process of clathrate hydrate

Characteristics of amines can contribute to the growth mechanisms of $CO_2$ + $CH_4$ clathrate hydrate. In this work, we have selected three different aliphatic amines which can be found in nature. From the chemical perspective, polarity and hydrophilicity are two important characteristics of these components. Generally, the polarity is the result of remarkable electronegativity differences between atoms in the molecule. Also, molecules that have a propensity for being dissolved by water through attaching to water molecules are found to be a hydrophile property. For the MA molecule, there is a lone pair of electrons on the
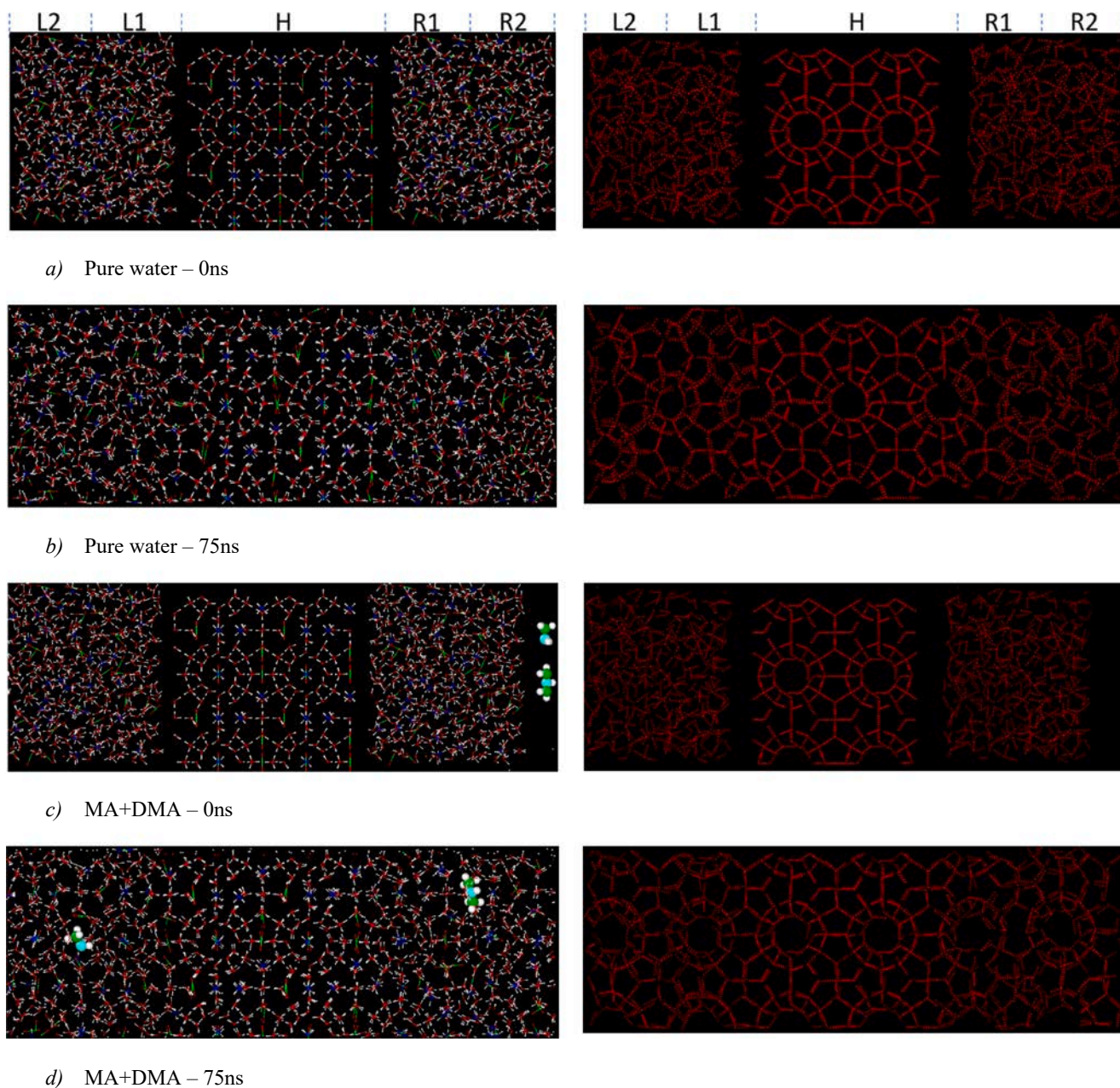
a) Pure water – 0ns

b) Pure water – 75ns

c) MA+DMA – 0ns

d) MA+DMA – 75ns

**Fig. 1.** Snapshots of $CO_2$ + $CH_4$ hydrate growth with or without amines (right side snapshots show the hydrogen bonds of water molecules in the simulation box).

nitrogen atom because nitrogen is a more electronegative element than carbon so the dipole moment on the C-N bond will be towards nitrogen while the dipole moment on the N–H bond adds up due to the higher electronegativity of the nitrogen than connected hydrogens. Therefore, the dipole moment due to the lone pair of electrons on the N atom will be in an upward direction so that MA, DMA, and AA molecules are known as polar compounds. Also, it was determined that methyl groups attached to an N atom, rather enhance hydrophilicity but do not promote hydrophobicity. Indeed, guest molecules including hydrophilic and polar functional groups have stronger affinities for water than hydrocarbons.

For all explored cases, the $CH_4$ + $CO_2$ hydrate formation during the simulation time intervals (every 0.5 ns) was measured by different criteria. To be more precise, the Z-direction of the simulation box was segmented into 5 regions as is shown in Fig. 1a. The snapshots of the simulation were provided by OVITO [42] and VMD [43] molecular visualization software. Layers L1 and L2 are the gas/water aqueous

solution on the left side while layers R1 and R2 are on the right side of the initial hydrate. Also, layer H indicates the initial hydrate slab. During the simulation, gas molecules initially migrate to the solid-solution interfaces and then the ordering of water molecules around the gas molecules starts to take place while the diffusion of dissolved gas in the hydrate-like phase regularly occurs. Fig. 1b displays the final configuration of mixed gas hydrate with pure water. It is evident that the solid state grows at 75 ns. In addition, the asymmetric growth in the L2 segment of Fig. 1b is also evident which may be due to the formation of irregular sI hydrate cages. The initial simulation box of the binary MA + DMA added to the pure water case is also displayed in Fig. 1c. By making a comparison with final snapshots of the formed hydrate (Fig. 1d), it can be deduced that these components improve the regular distribution of gas and water molecules along the solution regions by conducting water molecules to form a clathrate-like structure.
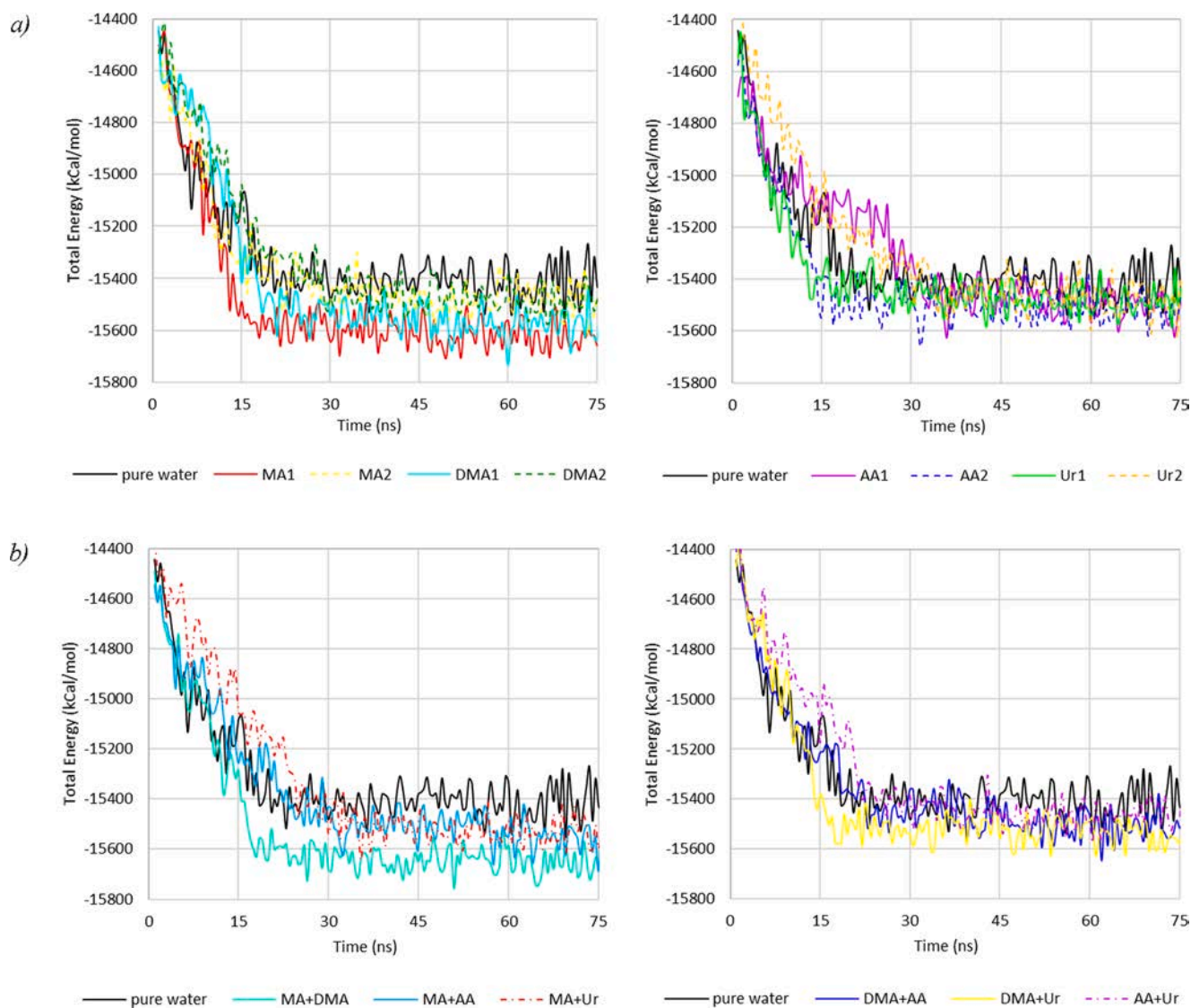
**Fig. 2.** Total energy of $CO_2 + CH_4$ clathrate hydrates with (*a*) single and (*b*) binary organic components.

## 3.2. The transformation of total energy

Analysing the variations of energy reflects the prone of unstable molecules to abrupt changes. Since the process of hydrate growth is exothermic, the system energy must decline to lower ranges as time proceeds during the simulation trajectory. The hydrate growth can be certified by viewing snapshots taken through molecular visualization software. Therefore, faster hydrate formation can be expected with more decline in the trend of the energy curve. Fig. 2 exhibits the total energy changes of $CO_2 + CH_4$ hydrate growth with single and binary organic components respectively. As is shown, the initial descent of MA1, DMA1, AA2, and MA + DMA are sensibly more than the pure water as a base case. However, the differences for other cases are not substantial. In the previous work [27], we simulated the growth of $CO_2$ hydrate with urea which showed very effective due to the increasing diffusivity of $CO_2$ while it is evident in Fig. 2a that this component cannot considerably induce the mobility of mixed $CO_2$ and $CH_4$ molecules. It seems that increasing the concentration of urea (Ur2) even plays as a weak inhibitor. Also, the effects of the combination of AA with other studied amines on the hydrate growth do not work as their standalone utilization. Also, some cases which include combined amine and urea could create disturbances between water molecules so that they may influence the formation of hydrogen bonds in the network. Based on the curve fitting

**Table 2**
Curve fitting results of total energy for all simulated systems.

| Solution system | Trendline equation and R-squared value | Solution system | Trendline equation and R-squared value |
|---|---|---|---|
| Pure water | y = -217.3Ln(x)-14582, $R^2$ = 0.7678 | AA1 | y = -228.3Ln(x)-14457, $R^2$ = 0.8931 |
| MA1 | y = -309.1Ln(x)-14439, $R^2$ = 0.7891 | AA2 | y = -301.9Ln(x)-14684, $R^2$ = 0.7983 |
| MA2 | y = -261.4Ln(x)-14551, $R^2$ = 0.8199 | Ur1 | y = -272.4Ln(x)-14708, $R^2$ = 0.7688 |
| DMA1 | y = -307.4Ln(x)-14367, $R^2$ = 0.8293 | Ur2 | y = -207.5Ln(x)-14252, $R^2$ = 0.9131 |
| DMA2 | y = -258.2Ln(x)-14327, $R^2$ = 0.8784 | DMA + AA | y = -261.4Ln(x)-14481, $R^2$ = 0.8904 |
| MA + DMA | y = -305.3Ln(x)-14535, $R^2$ = 0.8328 | DMA + Ur | y = -278.9Ln(x)-14489, $R^2$ = 0.7869 |
| MA + AA | y = -267.9Ln(x)-14451, $R^2$ = 0.8952 | AA + Ur | y = -236.3Ln(x)-14286, $R^2$ = 0.8867 |
| MA + Ur | y = -243.4Ln(x)-14160, $R^2$ = 0.9031 | | | |

results shown in Table 2, it can be inferred that the lower slope in the reduction of total energy than pure water arises from the fewer mass transfer barriers in the solution phase.
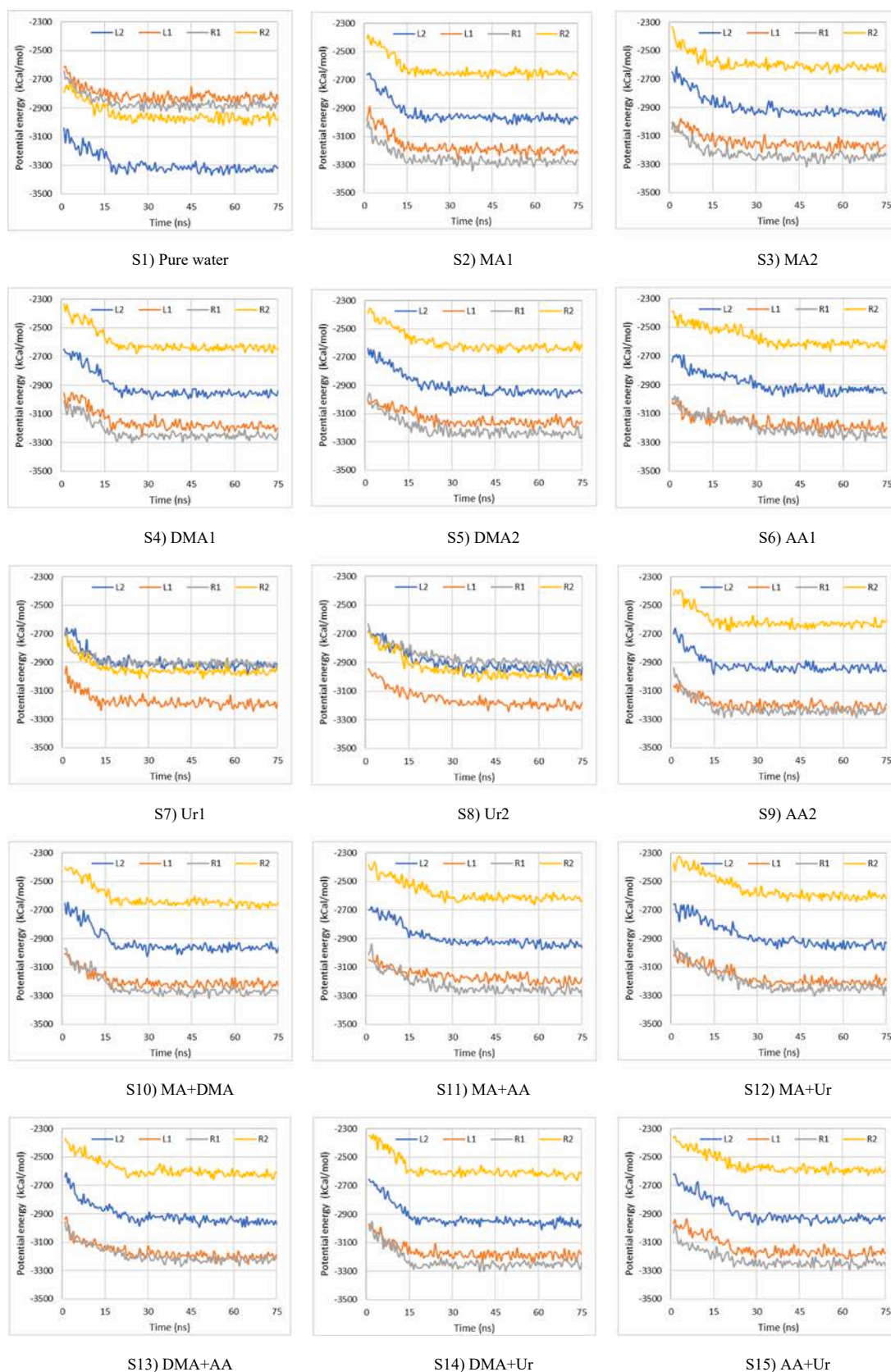
**Fig. 3.** Potential energy of $CO_2 + CH_4$ clathrate hydrates with or without amines/urea in different layers of the solution phase.

**Table 3**
The number of formed H-bonds during the performed simulations.

| Solution system | H-bonds (Avg.) | AD% | Solution system | H-bonds (Avg.) | AD% |
|---|---|---|---|---|---|
| pure water | 1465 | – | AA1 | 1536 | 4.8% |
| MA1 | 1557 | 6.3% | AA2 | 1507 | 2.9% |
| MA2 | 1509 | 3.0% | Ur1 | 1512 | 3.2% |
| DMA1 | 1498 | 2.3% | Ur2 | 1501 | 2.4% |
| DMA2 | 1509 | 3.1% | DMA + AA | 1486 | 1.4% |
| MA + DMA | 1532 | 4.5% | DMA + Ur | 1515 | 3.4% |
| MA + AA | 1557 | 6.3% | AA + Ur | 1487 | 1.5% |
| MA + Ur | 1544 | 5.4% | | | |

Note: "Avg." denotes the average number of H-bonds at the final stage of the hydrate growth. "AD%" stands for the average difference percentage of the simulated system in comparison with pure water (base case).

Such slope descent of potential energy in the solution layers at the early stage of the simulation time can also be observed in Fig. 3. Based on the potential energy of each layer, the lower values for L1 and R1 in the cases involving organic molecules demonstrated the more convenient formation of the hydrate layer from the centre toward the Z-direction of the simulation box. Moreover, in the early step of simulation time (e.g. initial 15 ns), the slope of potential energy for MA1, DMA1, AA2, MA + DMA, and DMA + Ur is steeper than either pure water or other investigated solution systems.

### 3.3. Hydrogen bonding analysis of clathrate growth

One of the main mechanisms of organic additives might be to affect the hydrogen bonds (H-bonds) of local water molecules. The geometrical criterion for calculating H-bond is that the maximum angle is $30°$ and the distance between an acceptor and a donor is lower than 3.5 Å. The structural arrangement of solvation water in the vicinity of the binding surface of the organic molecules may overlap with the solvation water of hydrate and contribute to the clathrate phase. The number of formed H-bonds during amorphous fragments (preferentially appeared at initial simulation time) and shaped regular water cavities at the next stage was recorded. Obtained results indicated that the number of H-bonds increases exponentially during the crystal hydrate growth. The average formed H-bonds for the performed simulations are summarized in Table 3. As can be observed, there is a significant difference between the number of H-bonds of systems including MA molecule. This improvement is still maintained when MA with DMA, AA, and Ur molecules was added to the solution. However, that is not the case for the systems encompassing AA + DMA or AA + Ur.

The neighbouring hydrophilic organic molecules have the potential for hydrogen bonding and site-directed mutagenesis in hydrate binding. Generally, the polar side of organic molecules belonging to the hydrophilic is possible to form several hydrogen bonds with water. For detailed consideration, the final configuration of amine/urea molecules between surrounding water molecules was exhibited separately in Fig. 4. During the simulation of $CO_2 + CH_4$ hydrate with pure water and after 25 ns, the formation of two to four sII large cages ($5^{12}6^4$) was detected by the cage analysis. This may be a reason for reducing the regular formation of sI clathrate hydrate in the presence of pure water. From the simulations with amines, it is certified that MA molecule can contribute to the hydrate phase and occupy the sI large cage. However, dissimilar cage occupation was observed when DMA and AA molecules were included in the solution. The final configuration of the formed clathrate network in the presence of DMA molecule revealed that this molecule can participate in the hydrate phase but form an unusual cage-like structure ($5^96^27^1$) involving 22 water molecules. Also, AA molecule in the clathrate phase due to the larger molecular size than two other studied amines forms $4^15^96^7$ cages containing 30 water molecules which is an uncommon cage. This may occur as a consequence of some local interactions with surrounding water molecules. However, from Fig. 4 it

can be seen that MA, DMA, and AA molecules have fewer H-bonds linked to the water framework than Ur. In addition, the number of donor and acceptor atoms as a result of the mutant in the urea molecule is dissimilar. The number of H-bonds between the urea and water molecules due to the mutagenesis of the amide group in urea is markedly more than the studied amine molecules. It can be assumed that the shape complementarity and steric capability to interact with water molecules are responsible for the activity of these organic molecules. The water molecules may also act as an H-bond bridge between $CO_2$ and amines so that they can form two complex H-bonds: the hydrogen atom of water molecules with the oxygen atom of $CO_2$; and the oxygen atom of water molecules with the hydrogen atom of amines. Thus, water molecules may serve as a proton donor to $CO_2$ and a proton acceptor from organic amines. Probably the formation of H-bond bridges between the studied organic amines and $CO_2$ provides a cooperative binding effect in which the bridging may decrease the N–C distance between the amine group interacting with $CO_2$. Accordingly, an H-bond bridge between amines and $CO_2$ would drag the two molecules closer together, therefore it could facilitate the proton transfer. Due to this effect, the bond angle of $CO_2$ in the water cavities can be less than $180°$. Also, the higher amount of H-bond from the two water molecules can shorten the N–C distance which results in a stronger direct amine to $CO_2$ interaction.

### 3.4. Dynamical properties of formed hydrates

The time evolution of guest molecules captured in the hydrate phase can be dynamically analysed through the transmission displacement of molecules in the system. To this end, the mean square displacement (MSD) of guest and host molecules is calculated which is expressed by the following equation [44]:

$$MSD = \frac{1}{N} \sum_{i=1}^{N} \left| \gamma^i(t) - \gamma^i(0) \right|^2 \tag{1}$$

Where the total number of atoms is described by $N$. Also, $\gamma$ stands for the position of atom $i$ at simulation time. This parameter in the simulation model can be employed to distinguish gas, liquid, and solid-like structures. Fig. 5 displays the calculated MSD profile of $CO_2$, $CH_4$, water, and all molecules along the simulation box. As shown, the trend of MSDs for the solutions including organic molecules increases before being level-off at which they approach specific values and change into a smooth line shape. In contrast, such conversion from the liquid to the solid state does not occur for the pure water case during the chosen simulation time. In addition, the solutions comprising MA1, DMA1, AA2, and MA + DMA possess the sooner occurrence of smooth line shape which indicates the rapid conversion of clathrate hydrate formation in their interfaces. Hence, the presence of amine molecules can markedly facilitate the diffusivity of guests due to the stronger interactions with water molecules as well as opening pathways for guest molecules to move longer distances; so that they would expedite both $CH_4$ and $CO_2$ dynamics in the clathrate network. The diffusion of all molecules can also be affected by the concentration of additives. It seems that the lower and higher mass fraction of promoters respectively for small and large organic amines can be more effective. For example, the twice concentration of AA can visibly facilitate the extension of the clathrate hydrate-like network from 40 ns to 20 ns. Probably, it may be pertinent to the less mobility of AA molecule rather than MA, DMA, and Ur molecules.

Similar results can also be certified by Fig. 6 where the MSD of water in different segments of the solution are presented. As is displayed, in almost all cases encompassing organic molecules, the trend of MSDs after specified values is levelled off which indicates that both host and guest molecules may locate at positions comparable to the structured clathrate hydrate network.
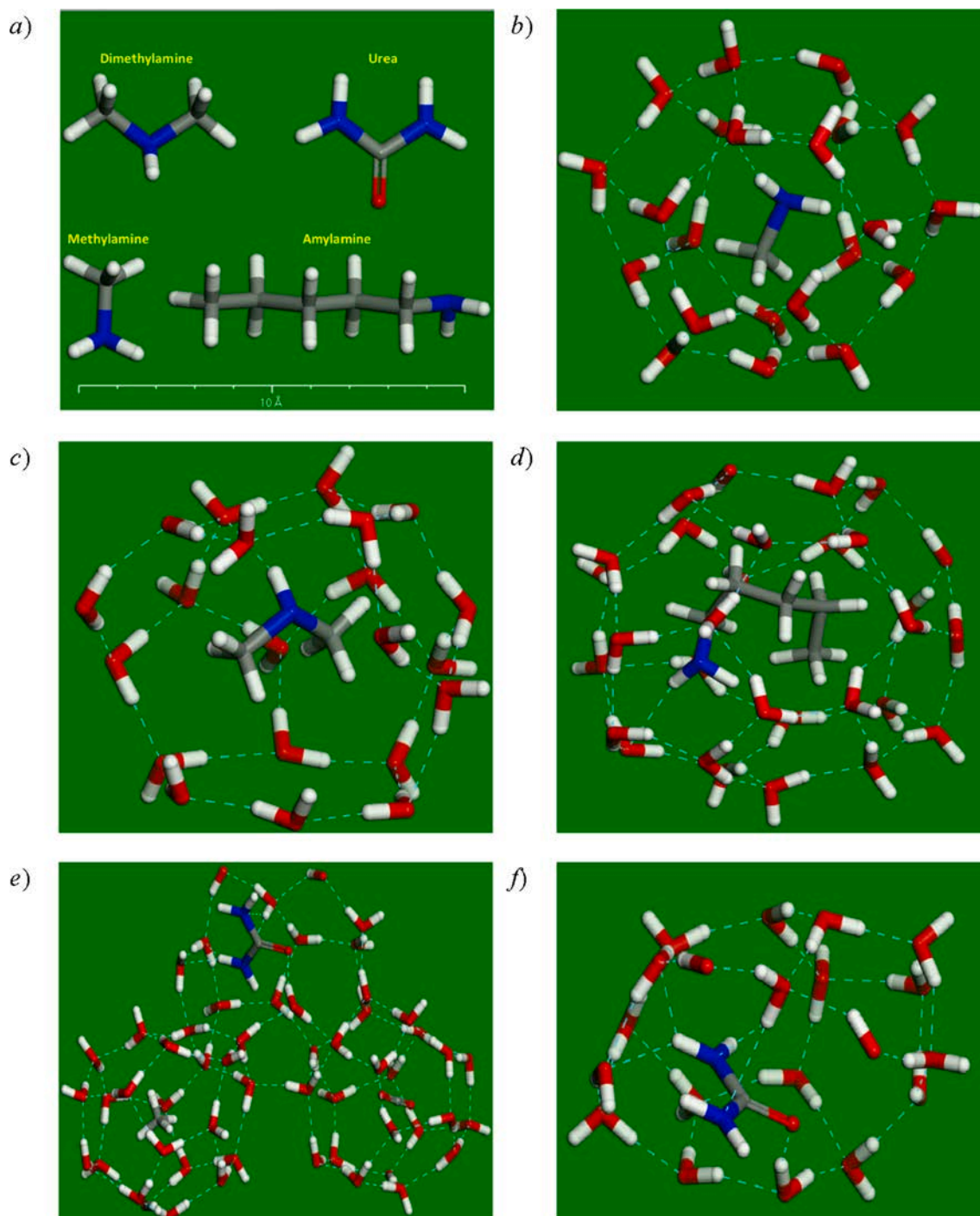
**Fig. 4.** Final position of studied organic molecules in the clathrate hydrate large cages: (*a*), studied organic molecules; (*b*), MA; (*c*), DMA; (*d*), AA; and (*e*,*f*) Ur respectively. (Hydrogen bonds are shown as light blue dash-lines).

### 3.5. The molecular order of the clathrate network

Computing the structural order parameter of clathrate hydrate to distinguish between various orders of clathrate-like water structures can be beneficially utilized [45]. In this study, monitoring the evolution of nucleation and growth of clathrate hydrates was performed by different designed order parameter algorithms. Also, two qualified order parameters which can accurately probe the clathrate-like structure were used. Characterization of the water molecular local arrangements of the hydrate phase was determined by the $F_3$ order parameter as specified below [46]:

$$F_{3,i} = \left\langle \left[ cos\theta_{jik} \left| cos\theta_{jik} \right| + cos^2 109.47 \right]^2 \right\rangle_{j,k} = \left\{ \begin{array}{l} 0.1 \, liquid \, water \\ 0.0 \, ice \, or \, hydrate \end{array} \right\} \tag{2}$$

In this equation, oxygen atoms of three neighbour water molecules create an angle as indicated by $\theta_{jik}$ where atom *i* is located at the centre of a spherical shell with a 3.5 Å radius including atoms *k* and *j*. Indeed, the $F_3$ order parameter is an average over all the neighbours of the oxygen atom *i* of each water molecule that exists within this radius. With changing the orientations of water molecules from liquid state to hydrate state, the $F_3$ parameter reduces to lower values (near zero) which represents the highly tetrahedral structure of the formed water network.
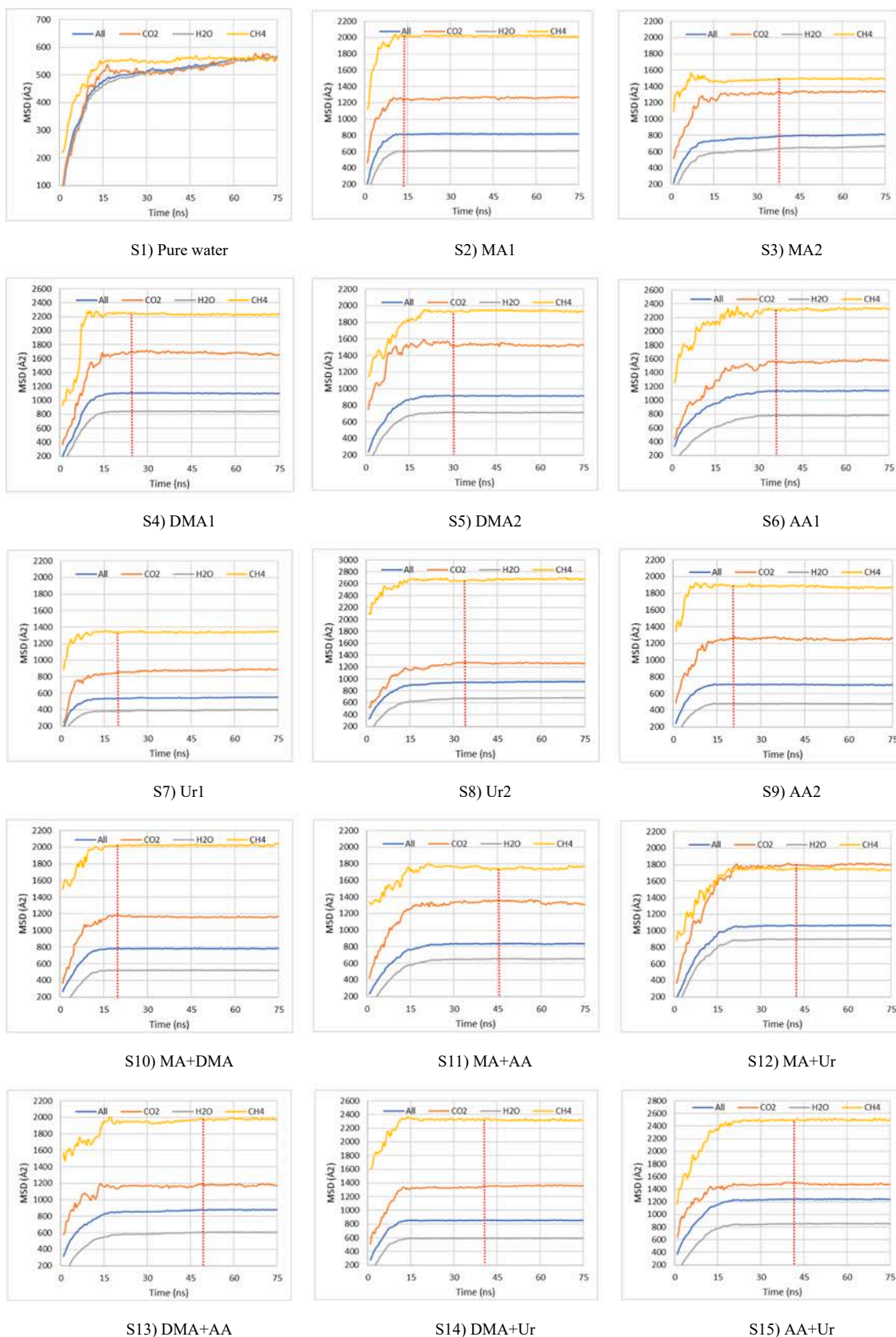
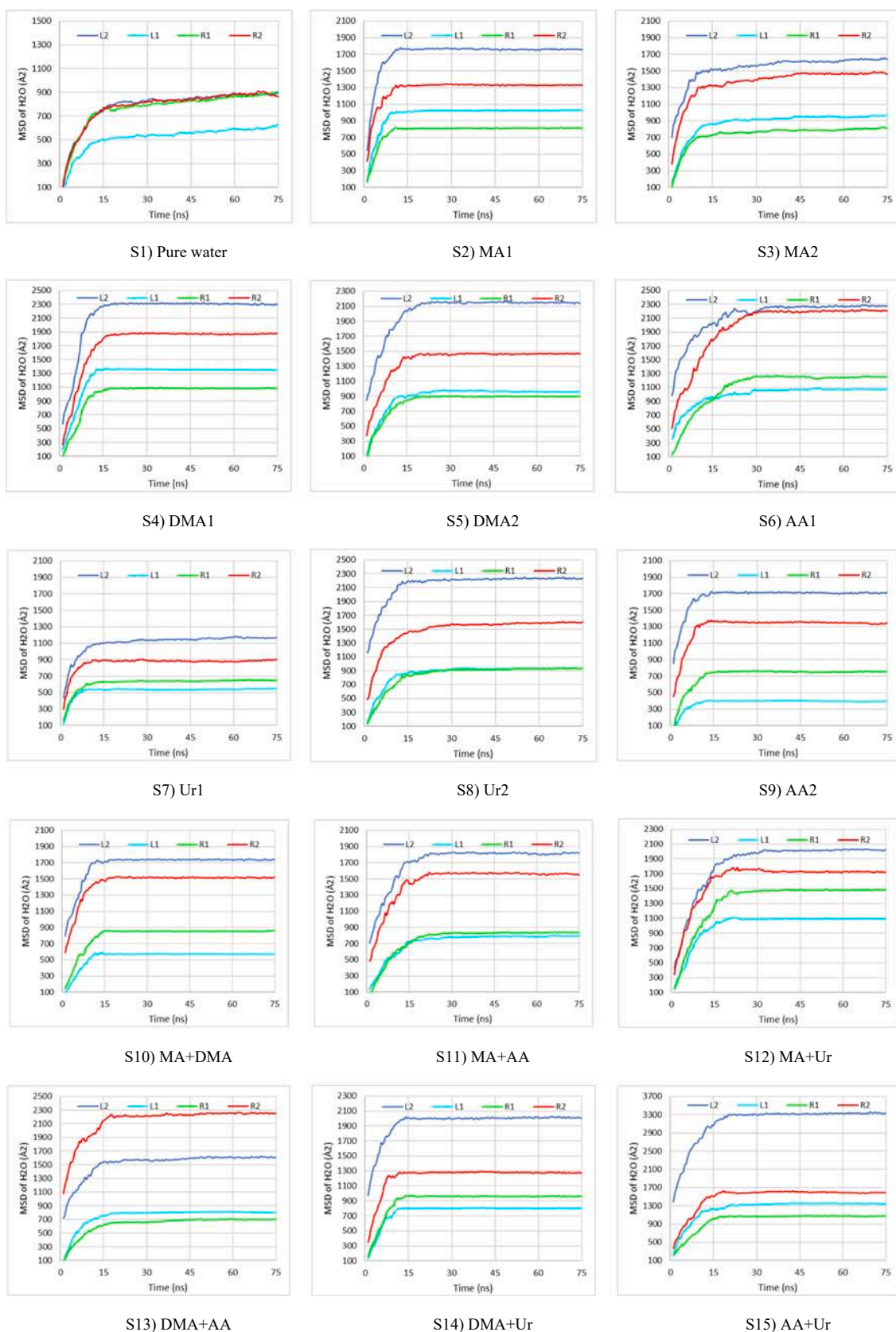**Fig. 5.** Total MSDs of both guest and host molecules.

S1) Pure water



S2) MA1



S3) MA2



S4) DMA1



S5) DMA2



S6) AA1



S7) Ur1



S8) Ur2



S9) AA2



S10) MA+DMA



S11) MA+AA



S12) MA+Ur



S13) DMA+AA



S14) DMA+Ur



S15) AA+Ur

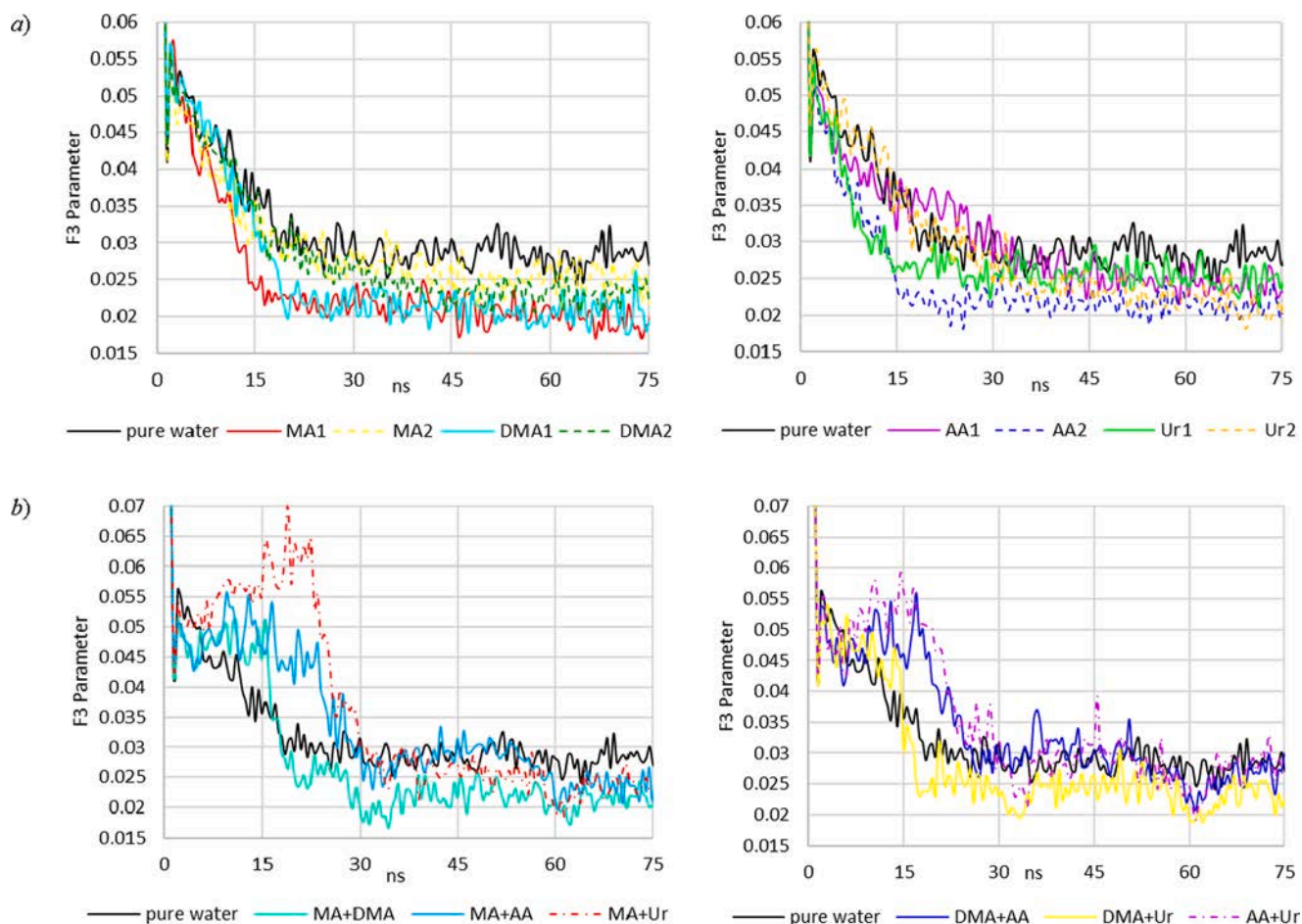**Fig. 6.** MSDs of $H_2O$ in different sections of the solution phase.

**Fig. 7.** $F_3$ order parameter of $CO_2 + CH_4$ hydrate including amines/urea: (a), single; (b), binary additives.

The $F_3$ parameter versus time for hydrates in the presence of single and binary amines/urea are shown in Fig. 7. The sharp reduction of the $F_3$ parameter for the system including MA1, AA2, and DMA1 implies that the water molecules at solution regions in the simulation box are converted into a hydrate-like amorphous state within around 15 ns, and 20 ns, 25 ns respectively. Moreover, considering one and two organic molecules in the system highlights that the concentration of these molecules can be one of the determinative key points. For example, unlike MA and DMA molecules, the inclusion of AA molecule with a higher concentration in the solution can create more promotion influences on the orientations of liquid water. Also, the presence of urea molecule can somewhat accelerate the formation of a hydrate network. In contrast, the utilization of combined amines or urea such as MA + AA, MA + Ur, and AA + DMA, AA + Ur operates completely in a different way. Up to the initial 30 ns of the simulation time, these components even inhibit the arrangements of water molecules toward being ordered but they showed a positive role in the growth rate after the mentioned time. However, the trend of the system with MA + DMA shows a lower $F_3$ value after around the initial 20 ns which indicates the promotion impacts of these components with a 20 ns time delay. This may also be valid when the mixed DMA + Ur was involved; however, its improvements are not credibly substantial.

Based on the above-mentioned analysis, it is inferred that the presence of MA1, DMA1, AA2, and MA + DMA are found to be more promotionally effective for the formation of $CO_2 + CH_4$ clathrate hydrate. Therefore, more evaluations to understand their impressions need to be carried out. To analyse the degree of the hydrates with these components which exhibited desirable improvements during the process of crystal growth, the four-body structural $F4\varphi$ order parameter as a
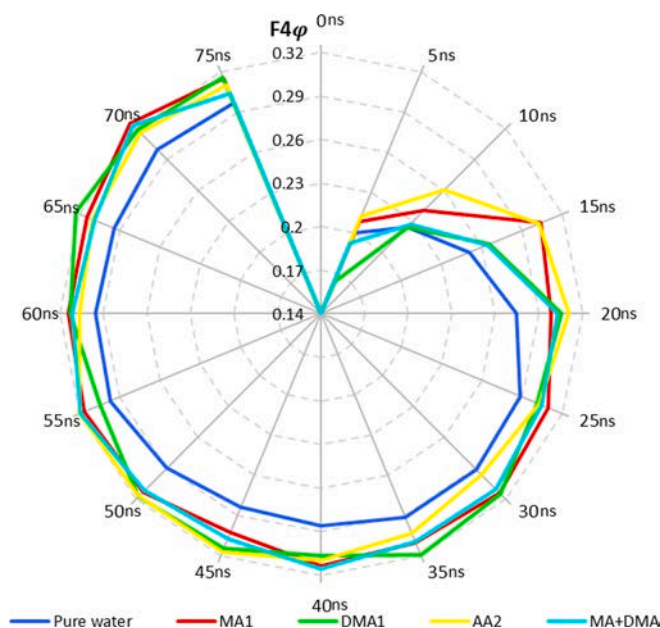


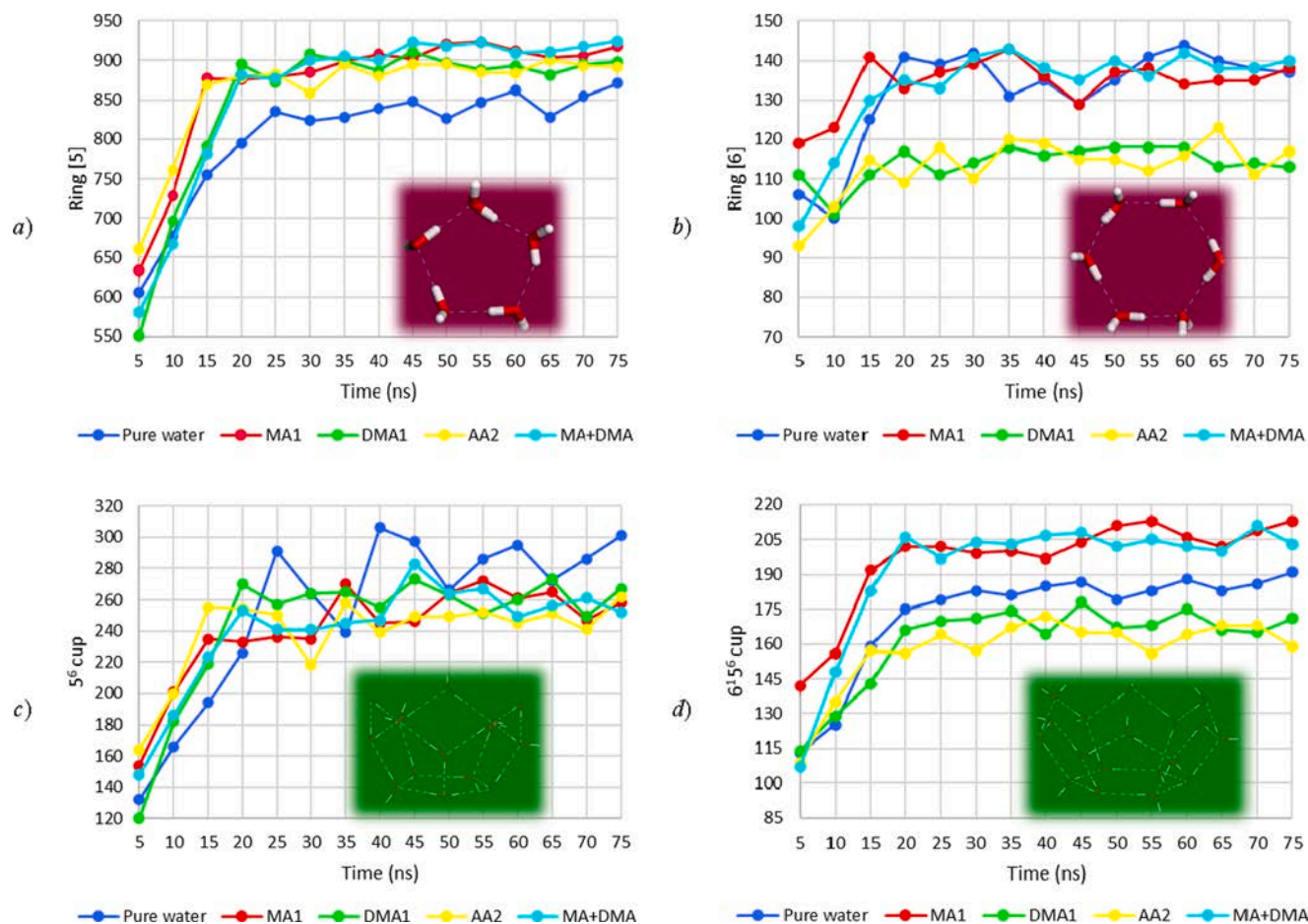**Fig. 8.** Four-order structural parameter ($F4\varphi$) of simulated cases.

**Fig. 9.** Number of formed rings and cups: (*a*), ring [5]; (*b*), ring [6]; (*c*), $5^6$ cups; and (*d*), $6^1 5^6$ cups during simulation time.

function of simulation time was applied. This parameter recognizes the tetrahedral networks of water which can be determined with:

$$F_{4\varphi} = \frac{1}{n} \sum_{i=1}^{n} cos3\varphi_i \tag{3}$$

Where n indicates the overall number of $H_2O - H_2O$ pairs with the O − O distance below 3.5 Å; $\varphi_i$ stands for the H-O…O-H torsion angle which is described in terms of the outer-most hydrogen atoms in the *i*th $H_2O - H_2O$ pair. the value of the $F_4$ parameter, in theory, varies in ranging between −0.4 and 0.7 in which ice, liquid, and hydrate phases can be about −0.4, −0.04, and 0.7 respectively [47]. Worth mentioning, this value for five and six-membered rings in hydrate-like structures would be lower. Fig. 8 exhibits four-order structural parameters of the systems including amine promoters and pure water with a time interval of 5 ns. The rising trend of this chart indicates the formation of the hydrate. It is displayed that the inclusion of the amines influences the kinetics of clathrate hydrate cages. As expected, at the beginning simulation times (e.g. 10 ns and 15 ns), the solution with AA2 and MA1 is substantially more than pure water. Also, the values for all amine systems approach together after 20 ns. The faster and higher increase in the $F_4$ parameter may reflect a more regular or less formation of amorphous fragments at the early stages and continuous growth of the hydrate layer.

### 3.6. Clathrate hydrate cage analysis

The clathrate growth multistep hypothesis has declared that the local concentration of guests at a supersaturated region of the solution can generate "blobs" known as the rate-limiting nucleation stage. These blobs then accelerate water molecules to solidify into cavities hosting guests. In the beginning, cages in an amorphous manner are stacked together. Then the amorphous cages transform into the clathrate configuration. This phenomenon also plays an important role in biological systems like non-polar side chains which induce water molecules to create an incomplete cage-like configuration. Hence, understanding the effects and mechanisms of studied amine promoters on clathrate cages is important to discovering better organic promoters. To do this, we employed an open-source computer code-named GRADE [48]. This code is based on a hierarchical algorithm that identifies the evolution of rings (made of five/six first-neighbour water molecules), cups (e.g. half cages formed by the connectivity of rings), and cages (bounded cups to form $5^{12}$, $6^2 5^{12}$, and $6^4 5^{12}$ cages). Fig. 9 (*a,b*) exhibits the number of formed rings and cups during the simulation time. As is displayed, the number of rings [5] increased from about 850 to over 900 when organic amines were introduced to the solution phase. This improvement is also evident at the initial step of simulation time (up to 20 ns). Although the utilization of MA1 and MA + DMA in the formation of the ring [6] gave the same results as pure water, DMA1 and AA2 decreased the quantity of the ring [6] by almost 11%. As Fig. 9 (*c,d*) shows, the tendency of the formed ring [5] in contributing to form $5^6$ cups of pure water is higher than the presence of amines while the propensity of the ring [6] to form $6^1 5^6$ cups in the studied amine systems (more specifically with MA1 and MA + DMA) is tangibly higher compared with pure water.

To form $5^{12}$ hydrate cages, two $5^6$ cups including 20 water molecules are required. The superscript 6 is the number of pentagonal rings. Also, two and four $6^1 5^6$ cups with 24 and 28 water molecules can respectively build $5^{12} 6^2$, and $5^{12} 6^4$ hydrate cages. Fig. 10 shows the quantities of identified cages by the GRADE algorithm. As is evident, up to 20 ns of
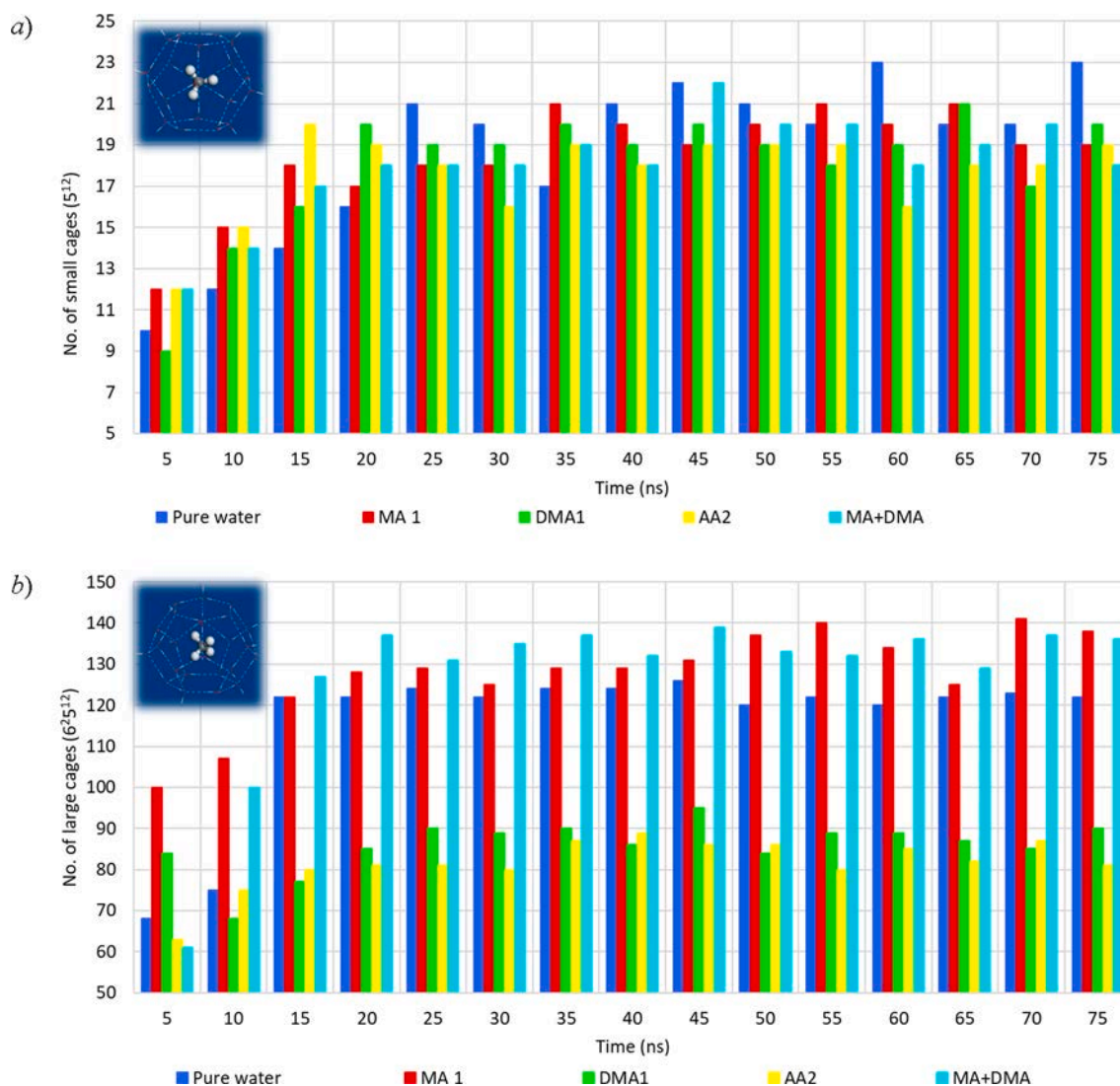
**Fig. 10.** Number of formed (*a*) small and (*b*) large cages during the simulation time.

the simulation time, the counted small cages for pure water are less than those comprising amines. However, by completing the simulations, at least 15% fewer $5^{12}$ cages with the presence of amines were obtained. Fig. 10 also reveals that although DMA1 and AA2 are disabled to induce water molecules in creating large cages, MA1 and MA + DMA can increase $5^{12}6^2$ cages by around 13%. Worth noting that dissimilar to the presence of organic molecules, approximately 3% of formed large cages of the solution phase using pure water is $5^{12}6^4$ (sII large cages). Since small and large cages of sI clathrate hydrate stoichiometrically possess 25% and 75% of the proportions in the unit-cell respectively, it can be deduced that the studied organic molecules by orienting near the amorphous-like water molecules induce them to form large ones rather than small cavities. This may also be caused by the size and propensity of these molecules.

To elucidate the roles of amines in hydrate growth, cage occupancy was also investigated. Fig. 11 shows the percentage of filled cages during hydrate formation with either amines or pure water. As the obtained results indicate, the presence of DMA1 and AA2 provides better orientations for guest molecules in which they can fill about 30% extra small cages compared to pure water. The inclusion of MA1 and MA + DMA can also increase the fractional occupancy of small cages by 10% to 15% respectively. Based on Fig. 11b, it can be found that a substantial proportion of large cages were filled by the gas molecules. Also, more fluctuations in the trend of amine systems compared to pure water show

that the mobility of $CO_2$ and $CH_4$ molecules is more substantial when such organic components are in the solution phase. Although the cage occupancy of DMA1 and AA2 systems is slightly lower than pure water, MA + DMA and more specifically MA1 can induce gas molecules to fill the large cages more efficiently.

### 3.7. Water and gas molecular distribution at the liquid–solid interface

Fig. 12 presents the changes in the density of components in two different cases at the solution-solid interface. The inclusion of the MA molecule in the solution phase significantly induces water molecules to arrange themselves in locations similar to the initial hydrate slab while such intention cannot be observed when pure water was used. The formation of a hydrate-like structure at the early simulation time (before 15 ns) is quite in line with the previous behaviour of MA1 in Fig. 5a. Also, the distribution of $CO_2$ and $CH_4$ molecules with or without the existence of MA molecule is entirely dissimilar. The concentration of almost all guest molecules utilizing pure water fluctuates close to the composition in the preliminary $CO_2$ + $CH_4$ hydrate. In contrast, the dispersion of both hydrate formers indicates the interactions of MA molecule with $CO_2$ and $CH_4$ molecules the effect of which, better separation can also be achieved. It seems that the MA molecule has a stronger binding with $CO_2$ in comparison with $CH_4$ in which $NH_2$ might be an electron-donating to the electro-negative N which improves the strength
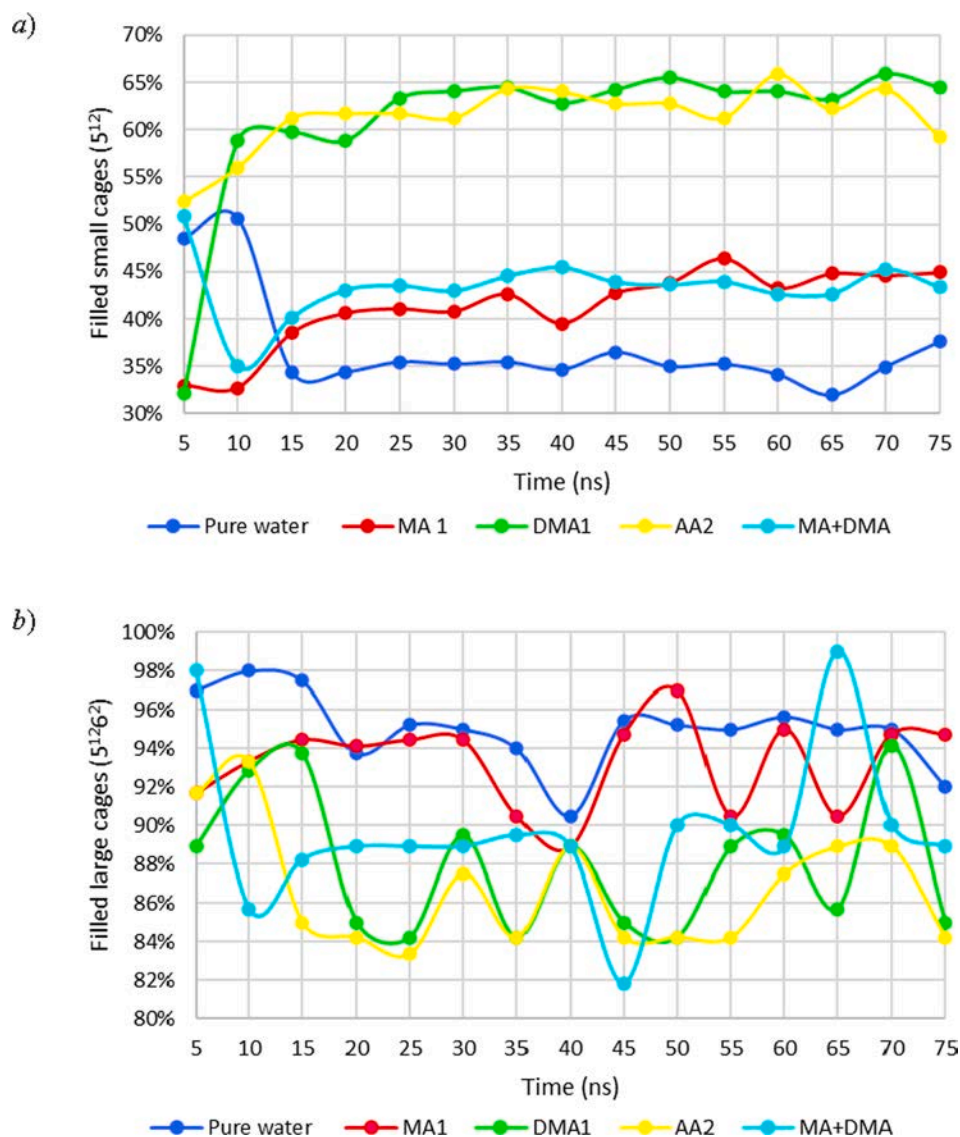
**Fig. 11.** Cage occupancy of (*a*) small and (*b*) large cages during simulation.

of electrostatic interaction. It can be assumed that the stronger the binding between functional groups of amine molecules, the higher the selectivity and better enrichment.

Fig. 13 exhibits the number of $CO_2$ and $CH_4$ molecules at the Z-axis of the simulation box at 75 ns. The regularity of guest molecules in the formed hydrate state in contact with the MA molecule certifies the proper distributions which directly influences the cage occupancy. Toward the Z-direction of the simulation box, almost every 6 Å interval in MA1 possesses a peak with 8 molecules while such specification cannot be observed in the pure water case. This specification is mostly valid for other simulations in which the promotion effects of amines were observed.

The interactions of studied molecules with $CO_2$ and $CH_4$ in the solution phase vary depending on the functional groups of these molecules. Therefore, it is expected to see the different compositions of these guest gases after starting the growth of the initial hydrate slab. Since the $CO_2$ hydrate compared to $CH_4$ can thermodynamically be formed at lower pressure (at a certain temperature), providing the selective solution layers in contact with the hydrate phase can help to upgrade the process recovery of the hydrate-based biogas separation. Therefore, the inclusion of organic components increases $CO_2$ molecules while decreasing $CH_4$ molecules. This occurs besides accelerating the process

of hydrate growth. Both of these characteristics can be recognized as the favourability of kinetic hydrate promoters. Table 4 tabulates the different deviations of $CO_2$ and $CH_4$ concentrations compared to the pure water in the solution layer interfaced with a solid hydrate state. To do so, two adjacent layers of solutions with a thickness of 10Å were considered. Taking into account the outcomes, it is evident that $CH_4$ molecules in the presence of MA molecule are more prone to participate in areas interfaced with the initial clathrate crystal while less contribution they have when DMA molecule was introduced. In contrast, the tendency of $CO_2$ molecules to locate themselves near the initial hydrate slab is evidently more than pure water once AA molecule was added. This is not only valid for the solution including Ur, but the inclusion of this molecule can reduce the number of $CH_4$ molecules at the hydrate-solution interface. From the studied binary organic molecules, it can be deduced that although MA + DMA and MA + Ur may desirably increase the concentration of $CO_2$ molecules at the interface, the effects of AA + Ur by enhancing the number of $CO_2$ molecules and declining $CH_4$ molecules can also be proper for the biogas split fraction. The influence of DMA + AA, DMA + Ur, and MA + AA is also inappreciable.

The addition of kinetic hydrate promoters can mostly reduce the induction time, and increase the rate of gas and liquid conversion to hydrate state and the gas consumption (GC) from the feed. However,
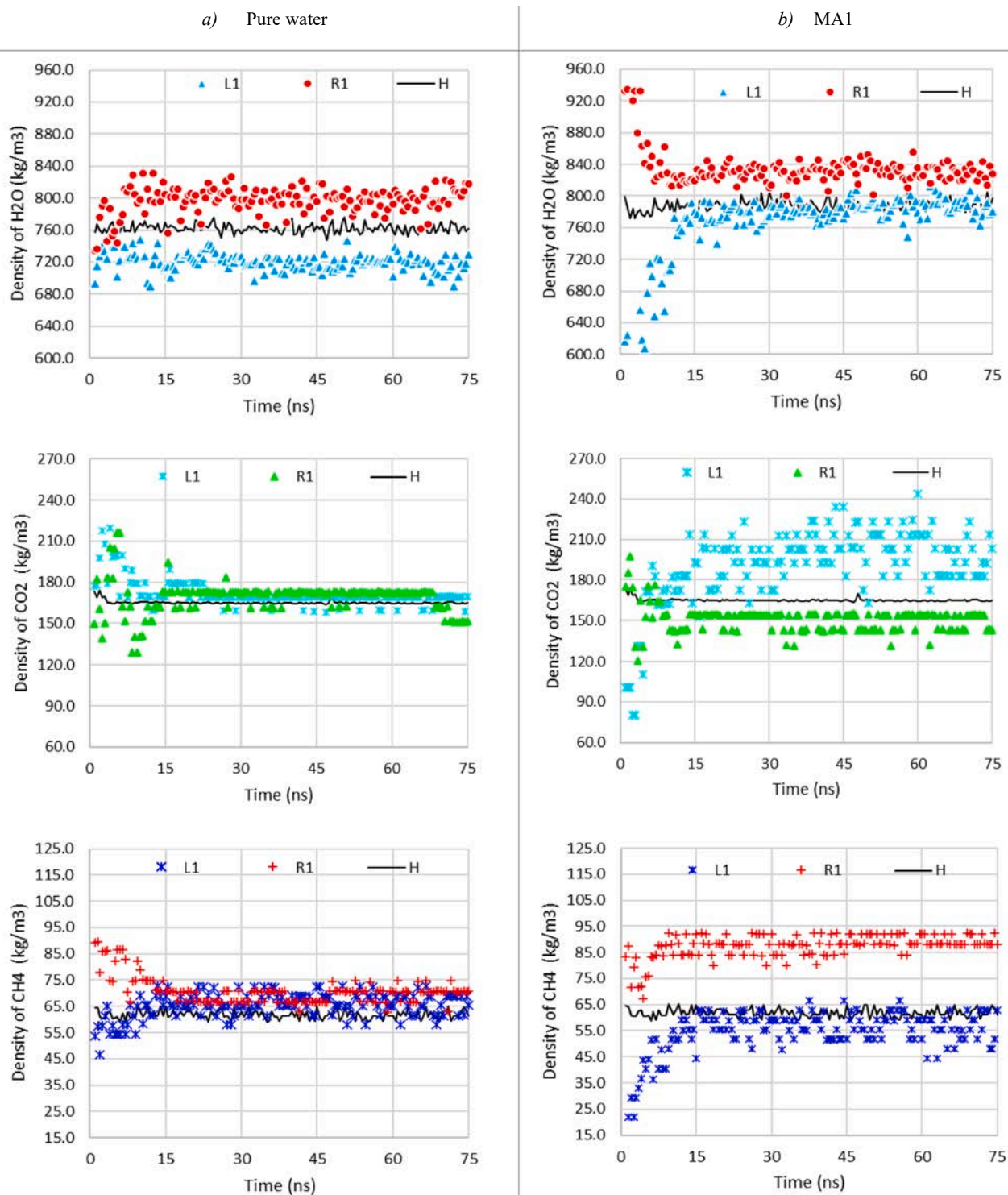
a)   Pure water

b)   MA1



**Fig. 12.** Density of water, CO₂, and CH₄ near the initial hydrate layer. (*a*), pure water; (*b*), in the presence of MA molecule.

their effects are not limited to these vital elements. The performance of hydrate-based purification technologies is directly relevant to the split fraction (S.F.: $CO_2$ in hydrate over feed) as well as the separation factor (S.Fr.: $CO_2$ in hydrate over remaining gas phase). Therefore, the higher S.F. and S.Fr. can result in more efficiency of such processes. Also, the number of enrichment stages (hydrate formation-dissociation steps) can be decreased wich results in lower cost impacts. Although the hydrate phase would capture $CO_2$ more than $CH_4$ molecules, the utilization of proper kinetic additives may facilitate the hydrate selectivity. The

impressions of kinetic promoters on $CO_2/CH_4$ selectivity relative to the pure water case for both studied in this work and reported in the literature are presented in Fig. 14. It should be noted that the layers interfaced with the initial hydrate were considered for determining the selectivity improvements. As is exhibited in Fig. 14 (*a*), the pure and mixture of these substances can improve or reduce the selectivity of formed hydrate. Between the simulated cases, pure Ur or mixed AA + Ur, and MA + DMA can positively raise the $CO_2/CH_4$ selectivity while pure MA or mixed DMA + AA ware found to possess negative impacts.
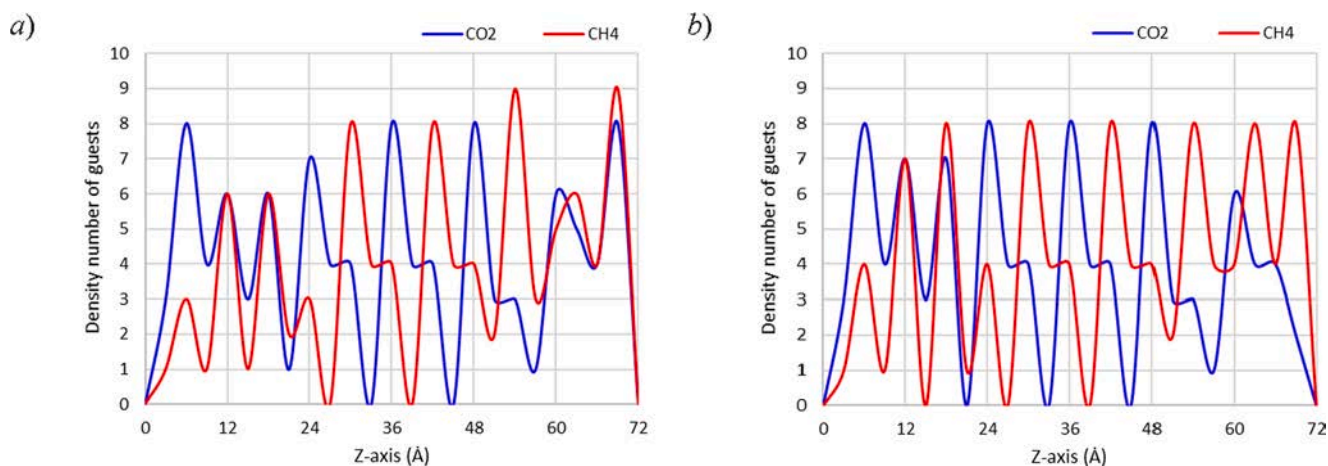
**Fig. 13.** The concentration distribution of guests for $CO_2$ and $CH_4$ hydrate with (*a*), pure water; (*b*), MA molecule.

**Table 4**
The difference percentages (D%) of $CO_2$ and $CH_4$ concentrations in comparison with pure water near the first solid–liquid interface (initial hydrate slab).

| Solution system | CO$_2$ | CH$_4$ | Solution system | CO$_2$ | CH$_4$ |
|---|---|---|---|---|---|
| MA1 | 6.5% | 12.1% | AA1 | 9.7% | −2.8% |
| MA2 | −4.5% | 16.7% | AA2 | 9.6% | 2.7% |
| DMA1 | 0.5% | −15.4% | Ur1 | 12.9% | −13.2% |
| DMA2 | 0.2% | −12.6% | Ur2 | 9.7% | −8.3% |
| MA + DMA | 25.8% | 0.2% | DMA + AA | 3.2% | 5.7% |
| MA + AA | 0.3% | −2.3% | DMA + Ur | 1.4% | −5.6% |
| MA + Ur | 12.9% | −0.1% | AA + Ur | 16.1% | −13.9% |

This can be observed in Fig. 14 (*b*) in which EXP-6 and EXP-8 indicate that although SDS reduces the ability of the solid phase in capturing $CO_2$ molecules, the combined SDS + THF acts differently. However, the effectiveness of either pure or mixed kinetic promoters is directly proportional to the operating circumstances.

## 4. Conclusion

Comprehending and controlling the kinetics of hydrate-based biogas formation may potentially accelerate this technology toward its large-scale industrial applications. To do so, the addition of promoters has become a subject of interest through experimental explorations. Although there have been various promising clathrate hydrate promoters, their incorporation from environmental criteria and sustainability points of view is not acceptable. Therefore, the most practical alternative would be the employment of organic promoters to meet both ecological and economic criteria. Accordingly, in this work, the effects of pure or binary organic amines and urea on the growth of biogas clathrate hydrate at a molecular scale using MD simulations have been carried out. The obtained results reveal that among the investigated organic molecules, biogas hydrate in the presence of MA, DMA, and their combination (MA + DMA) forms more rapidly than other molecules. Consistent with the recently reported experimental measurements, AA unlike MA or DMA needs more concentration to kinetically act as an efficient hydrate promoter. The binary mixture of Ur with studied amines in terms of providing an orderly formed clathrate network was found to be slightly less effective compared to the mixed
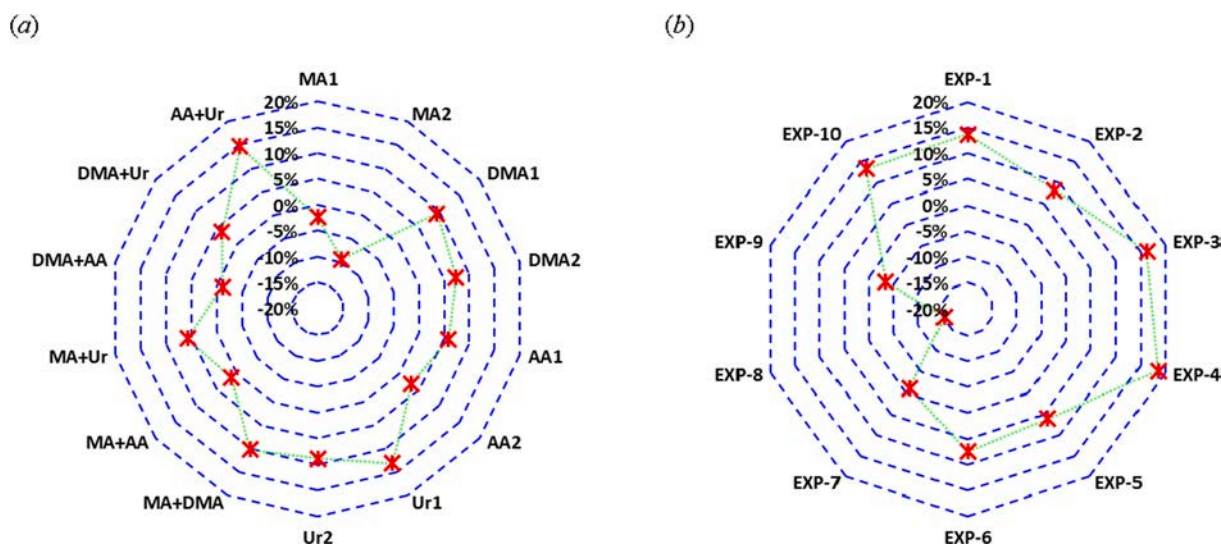


**Fig. 14.** $CO_2/CH_4$ selectivity improvement relative to pure water during the hydrate formation under the influence of different kinetic hydrate promoters. (*a*): obrained results from MD simulations at the microscopic scale (this work); (*b*): experimental measurements at the macroscopic scale reported in the literature; EXP-1: Al nanofluid (0.3 wt%) [49]; EXP-2: Al$_2$O$_3$ nanofluid (0.2 wt%) [50]; EXP-3: THF (5.6 mol%) + DMSO (1.6 mol%) [51]; EXP-4: TBAB (2.3 mol%) + DMSO (1.6 mol%) [51]; EXP-5: THF (1 mol%) + SL (500 ppm) [52]; EXP-6: THF (1 mol%) + SDS (500 ppm) [53]; EXP-7: SDBS (600 ppm) [54]; EXP-8: SDS (500 ppm) [54]; EXP-9: TBAB (5 wt%) + [C8min] BF4 (1000 ppm) [55]; EXP-10: Cyclooctane + tryptophan (1 wt%) [56].

amines. Cage analysis shows that the solution with MA + DMA and MA are more capable of building both sI clathrate cage types in comparison to pure water. These additives can also increase the mobility of guest molecules to fill the formed cavities. The concentration of $CO_2$ and $CH_4$ gas species at the solid-solution interface may also be changed once organic molecules are included. This would be a useful feature for increasing the recovery factor in the process of hydrate-based biogas purification besides enhancement of the hydrate formation kinetics. Although the established formation of hydrogen bonds of organic amines with water molecules was identified, more complex hydrogen bonds with the presence of urea molecule were observed.

## CRediT authorship contribution statement

## Declaration of Competing Interest

The authors declare that they have no known competing financial interests or personal relationships that could have appeared to influence the work reported in this paper.

## Data availability

Data will be made available on request.

## Acknowledgments

## References

[1] O.W. Awe, Y. Zhao, A. Nzihou, D.P. Minh, N. Lyczko, A Review of Biogas Utilisation, Purification and Upgrading Technologies, Waste and Biomass Valorization. 8 (2017) 267–283, https://doi.org/10.1007/s12649-016-9826-4.

[2] E.D. Sloan, C.A. Koh, Clathrate hydrates of natural gases, 3rd Ed., CRC Press, Taylor & Francis Group, Boca Raton, 2008.

[3] Y.-J. Lee, T. Kawamura, Y. Yamamoto, J.-H. Yoon, Phase equilibrium studies of tetrahydrofuran (THF) + $CH_4$, THF + $CO_2$, $CH_4$ + $CO_2$, and THF + $CO_2$ + $CH_4$ hydrates, J. Chem. Eng. Data. 57 (2012) 3543–3548, https://doi.org/10.1021/je300850q.

[4] H. Huang, S. Fan, Y. Wang, X. Lang, G. Li, Energy and exergy efficiency analysis for biogas De-$CO_2$ with tetra-n-butylammonium bromide hydrates, Energy. 265 (2023), 126365, https://doi.org/10.1016/j.energy.2022.126365.

[5] S.M. Jokar, D.A. Wood, S. Sinehbaghizadeh, P. Parvasi, J. Javanmardi, Transformation of associated natural gas into valuable products to avoid gas wastage in the form of flaring, J. Nat. Gas Sci. Eng. 94 (2021) 104078.

[6] S. Sinehbaghizadeh, A. Saptoro, A.H. Mohammadi, $CO_2$ hydrate properties and applications: A state of the art, Prog. Energy Combust. Sci. 93 (2022), 101026, https://doi.org/10.1016/j.pecs.2022.101026.

[7] S. Sinehbaghizadeh, J. Javanmardi, A.H. Mohammadi, Phase stability conditions of clathrate hydrates in the (methane + 3-methyl-1-butanol + water), (methane + 3,3-dimethyl-2-butanone + water) and (methane + 2,3-dimethyl-2-butene + water) systems: Experimental measurements and thermodynamic modeling, J. Chem. Thermodyn. 125 (2018) 64–70, https://doi.org/10.1016/j.jct.2018.05.006.

[8] S. Sinehbaghizadeh, J. Javanmardi, A. Roosta, A.H. Mohammadi, Estimation of the dissociation conditions and storage capacities of various sH clathrate hydrate

[9] S. Sinehbaghizadeh, A. Roosta, N. Rezaei, M.M. Ghiasi, J. Javanmardi, S. Zendehboudi, Evaluation of phase equilibrium conditions of clathrate hydrates using connectionist modeling strategies, Fuel. 255 (2019), 115649, https://doi.org/10.1016/j.fuel.2019.115649.

[10] S. Sinehbaghizadeh, J. Javanmardi, A. Roosta, A.H. Mohammadi, A fugacity approach for prediction of phase equilibria of methane clathrate hydrate in structure H, Phys. Chem. Res. 5 (2017) 465–481, https://doi.org/10.22036/pcr.2017.69958.1334.

[11] Z.-M. Xia, Z.-Y. Chen, X.-S. Li, Y. Zhang, K.-F. Yan, Q.-N. Lv, C.-G. Xu, J. Cai, Thermodynamic Equilibrium Conditions for Simulated Landfill Gas Hydrate Formation in Aqueous Solutions of Additives, J. Chem. Eng. Data. 57 (2012) 3290–3295, https://doi.org/10.1021/je300933y.

[12] C.-G. Xu, Y.-S. Yu, Y.-L. Ding, J. Cai, X.-S. Li, The effect of hydrate promoters on gas uptake, Phys. Chem. Chem. Phys. 19 (2017) 21769–21776, https://doi.org/10.1039/C7CP02173A.

[13] X. Sen Li, C.G. Xu, Z.Y. Chen, H.J. Wu, Tetra-n-butyl ammonium bromide semi-clathrate hydrate process for post-combustion capture of carbon dioxide in the presence of dodecyl trimethyl ammonium chloride, Energy. 35 (2010) 3902–3908, https://doi.org/10.1016/j.energy.2010.06.009.

[14] C. Sahu, A. Sircar, J.S. Sangwai, R. Kumar, Effect of Methylamine, Amylamine, and Decylamine on the Formation and Dissociation Kinetics of $CO_2$ Hydrate Relevant for Carbon Dioxide Sequestration, Ind. Eng. Chem. Res. 61 (2022) 2672–2684, https://doi.org/10.1021/acs.iecr.1c04074.

[15] S.E. Atakoohi, S.M. Sanatgar, K. Peyvandi, Effect of Albumin and Tryptone as environmental-friendly additives on methane hydrate formation rate: Efficacy of a protein on promotion or inhibition of hydrate growth, Environ. Prog. Sustain. Energy. (2022), https://doi.org/10.1002/ep.14057.

[16] G. Bhattacharjee, P. Linga, Amino acids as kinetic promoters for gas hydrate applications: A mini review, Energy & Fuels. 35 (2021) 7553–7571, https://doi.org/10.1021/acs.energyfuels.1c00502.

[17] Y. Youn, J. Seol, M. Cha, Y.-H. Ahn, H. Lee, Structural Transition Induced by $CH_4$ Enclathration and Cage Expansion with Large Guest Molecules Occurring in Amine Hydrate Systems, J. Chem. Eng. Data. 59 (2014) 2004–2012, https://doi.org/10.1021/je500167n.

[18] J. Seol, Selective Inclusion of Secondary Amine Guests in sH Hydrate Systems, J. Chem. Eng. Data. 66 (2021) 3335–3345, https://doi.org/10.1021/acs.jced.1c00388.

[19] X. Xu, C. Heath, B. Pejcic, C.D. Wood, $CO_2$ capture by amine infused hydrogels (AIHs), J. Mater. Chem. A. 6 (2018) 4829–4838, https://doi.org/10.1039/C8TA00602D.

[20] X. Wang, S. Yang, H. Zhang, X. Xu, C.D. Wood, W. Lipiński, Amine infused hydrogel-based $CO_2$ gas storage technology for $CO_2$ hydrate-based cold thermal energy storage, J. CO2 Util. 53 (2021), 101705, https://doi.org/10.1016/j.jcou.2021.101705.

[21] P. Thoutam, S. Rezaei Gomari, A. Chapoy, F. Ahmad, M. Islam, I. Ahmed, Enhancement of $CO_2$ capture through hydrate formation: the effect of tetrahydrofuran (THF) and tertiary amine solutions, Int. J. Environ. Sci. Technol. 19 (2022) 691–704, https://doi.org/10.1007/s13762-021-03315-0.

[22] S. Lee, Y. Ok, Y. Lee, D. Seo, S. Moon, Y. Park, Exploring the tuning patterns of cyclopentyl amine hydrate for potential application to $CH_4$ storage, J. Environ. Chem. Eng. 10 (5) (2022) 108402.

[23] S. Sinehbaghizadeh, A. Saptoro, S. Amjad-Iranagh, P. Naeiji, A.N.T. Tiong, A.H. Mohammadi, A comprehensive review on molecular dynamics simulation studies of phenomena and characteristics associated with clathrate hydrates, Fuel. 338 (2023), 127201, https://doi.org/10.1016/j.fuel.2022.127201.

[24] M. Maddah, M. Maddah, K. Peyvandi, Molecular dynamics simulation of methane hydrate formation in presence and absence of amino acid inhibitors, J. Mol. Liq. 269 (2018) 721–732, https://doi.org/10.1016/j.molliq.2018.08.105.

[25] F. Castillo-Borja, U.I. Bravo-Sánchez, R. Vázquez-Román, C.O. Díaz-Ovalle, Biogas purification via sII hydrates in the presence of THF and DMSO solutions using MD simulations, J. Mol. Liq. 297 (2020), 111904, https://doi.org/10.1016/j.molliq.2019.111904.

[26] S. Sinehbaghizadeh, A. Saptoro, S. Amjad-Iranagh, A.N. Tze Tiong, A.H. Mohammadi, Molecular Dynamics Simulation Studies on the Stability and Dissociation of Clathrate Hydrates of Single and Double Greenhouse Gases, Energy & Fuels. 36 (2022) 8323–8339, https://doi.org/10.1021/acs.energyfuels.2c01396.

[27] S. Sinehbaghizadeh, A. Saptoro, P. Naeiji, A.N.T. Tiong, A.H. Mohammadi, Insights into the synergistic effects of metal particles (Ag, Cu, and Fe) and urea on $CO_2$ clathrate hydrate growth using molecular dynamics simulations, Chem. Eng. Sci. 264 (2022), 118194, https://doi.org/10.1016/j.ces.2022.118194.

[28] J. Gou, K.-P. Choi, X. He, J. Ahn, Dimethylamine, Trimethylamine, and Biogenic Amine Formation in High-Pressure Processed Semidried Squid (Todarodes pacificius) during Refrigerated Storage, J. Food Sci. 75 (2010) M489–M495, https://doi.org/10.1111/j.1750-3841.2010.01731.x.

[29] D.K. Barupal, O. Fiehn, Generating the Blood Exposome Database Using a Comprehensive Text Mining and Database Fusion Approach, Environ. Health Perspect. 127 (9) (2019) 097008.

[30] T.A.P. Steve, C. Paul, Large-scale atomic/molecular massively parallel simulator, LAMMPS, Sandia Natl. Labs, Albuquerque, NM, 2012.

[31] F. Takeuchi, M. Hiratsuka, R. Ohmura, S. Alavi, A.K. Sum, K. Yasuoka, Water proton configurations in structures I, II, and H clathrate hydrate unit cells, J. Chem. Phys. 138 (12) (2013) 124504.

[32] Z. Duan, P. Kjeldsen, C. Scheutz, Trace gas composition in landfill gas at Danish landfills receiving low-organic waste, Waste Manag. 122 (2021) 113–123, https://doi.org/10.1016/j.wasman.2021.01.001.

[33] L. Martínez, R. Andrade, E.G. Birgin, J.M. Martínez, PACKMOL: A package for building initial configurations for molecular dynamics simulations, J. Comput. Chem. 30 (2009) 2157–2164, https://doi.org/10.1002/jcc.21224.

[34] J. Bai, X. Zhen, K. Yan, P. Li, S. Fang, C. Chang, The effect of additive molecular diameters on the hydrate-based $CO_2$ capture from simulated biogas, Fuel. 278 (2020), 118370, https://doi.org/10.1016/j.fuel.2020.118370.

[35] S. Takeya, A. Hachikubo, Distortion of the Host Water Cages of Structure I Gas Hydrates: Structural Analysis of C2H4 Hydrate by Powder X-ray Diffraction, J. Phys. Chem. C. 125 (2021) 28150–28156, https://doi.org/10.1021/acs.jpcc.1c09464.

[36] B.L. Eggimann, A.J. Sunnarborg, H.D. Stern, A.P. Bliss, J.I. Siepmann, An online parameter and property database for the TraPPE force field, Mol. Simul. 40 (2014) 101–105, https://doi.org/10.1080/08927022.2013.842994.

[37] J.L.F. Abascal, E. Sanz, R. García Fernández, C. Vega, A potential model for the study of ices and amorphous water: TIP4P/Ice, J. Chem. Phys. 122 (23) (2005) 234511.

[38] H. Frisch, M.J.E.A., Trucks, G.W., Schlegel, H.B., ScFrisch, M.J.E.A., Trucks, G.W., Schlegel, H.B., Scuseria, G.E., Robb, M.A., Cheeseman, J.R., Scalmani, G., Barone, V., Mennucci, B., Petersson, G. and Nakatsuji, H.useria, G.E., Robb, M.A., Cheeseman, J.R., Gaussian 09, revision D. 01, (2009).

[39] D.A. Case, T.E. Cheatham, T. Darden, H. Gohlke, R. Luo, K.M. Merz, A. Onufriev, C. Simmerling, B. Wang, R.J. Woods, The Amber biomolecular simulation programs, J. Comput. Chem. 26 (2005) 1668–1688, https://doi.org/10.1002/jcc.20290.

[40] H. Docherty, A. Galindo, C. Vega, E. Sanz, A potential model for methane in water describing correctly the solubility of the gas and the properties of the methane hydrate, J. Chem. Phys. 125 (2006) 74510, https://doi.org/10.1063/1.2335450.

[41] D.J.T. Allen, P. Michael, Computer simulation of liquids, Oxford University Press, 2017.

[42] A. Stukowski, Visualization and analysis of atomistic simulation data with OVITO–the Open Visualization Tool, Model. Simul. Mater. Sci. Eng. 18 (1) (2010) 015012.

[43] W. Humphrey, A. Dalke, K. Schulten, VMD: Visual molecular dynamics, J. Mol. Graph. 14 (1996) 33–38, https://doi.org/10.1016/0263-7855(96)00018-5.

[44] V. Masson-Delmotte, P. Zhai, A. Pirani, S. Connors, C. Péan, Y. Chen, L. Goldfarb, M.I. Gomis, "Climate change 2021: the physical science basis." Contribution of working group I to the sixth assessment report of the intergovernmental panel on climate change, 2021. https://doi.org/10.1017/9781009157896.

[45] R.S. DeFever, S. Sarupria, Nucleation mechanism of clathrate hydrates of water-soluble guest molecules, J. Chem. Phys. 147 (20) (2017) 204503.

[46] S.A. Bagherzadeh, P. Englezos, S. Alavi, J.A. Ripmeester, Molecular simulation of non-equilibrium methane hydrate decomposition process, J. Chem. Thermodyn. 44 (2012) 13–19, https://doi.org/10.1016/j.jct.2011.08.021.

[47] C. Moon, R.W. Hawtin, P.M. Rodger, Nucleation and control of clathrate hydrates: insights from simulation, Faraday Discuss. 136 (2007) 367, https://doi.org/10.1039/b618194p.

[48] F. Mahmoudinobar, C.L. Dias, GRADE: A code to determine clathrate hydrate structures, Comput. Phys. Commun. 244 (2019) 385–391, https://doi.org/10.1016/j.cpc.2019.06.004.

[49] S. Said, B. Mohamed, H. Jean-Michel, Investigation of the effects of Al nanoparticles on $CO_2$ separation from natural gas using gas hydrates, Energy Sources, Part A Recover. Util. Environ. Eff. 42 (2020) 2333–2345, https://doi.org/10.1080/15567036.2019.1651426.

[50] S. Said, V. Govindaraj, J.M. Herri, Y. Ouabbas, M. Khodja, M. Belloum, J.S. Sangwai, R. Nagarajan, A study on the influence of nanofluids on gas hydrate formation kinetics and their potential: Application to the $CO_2$ capture process, J. Nat. Gas Sci. Eng. 32 (2016) 95–108, https://doi.org/10.1016/j.jngse.2016.04.003.

[51] Z.-M. Xia, X.-S. Li, Z.-Y. Chen, G. Li, K.-F. Yan, C.-G. Xu, Q.-N. Lv, J. Cai, Hydrate-based $CO_2$ capture and $CH_4$ purification from simulated biogas with synergic additives based on gas solvent, Appl. Energy. 162 (2016) 1153–1159, https://doi.org/10.1016/j.apenergy.2015.02.016.

[52] J. Yi, D.-L.-L. Zhong, J. Yan, Y.-Y.-Y. Lu, Impacts of the surfactant sulfonated lignin on hydrate based $CO_2$ capture from a $CO_2/CH_4$ gas mixture, Energy. 171 (2019) 61–68, https://doi.org/10.1016/j.energy.2019.01.007.

[53] D.-L. Zhong, Z. Li, Y.-Y. Lu, J.-L. Wang, J. Yan, Evaluation of $CO_2$ removal from a $CO_2+CH_4$ gas mixture using gas hydrate formation in liquid water and THF solutions, Appl. Energy. 158 (2015) 133–141, https://doi.org/10.1016/j.apenergy.2015.08.058.

[54] M. Ricaurte, C. Dicharry, X. Renaud, J.-P. Torré, Combination of surfactants and organic compounds for boosting $CO_2$ separation from natural gas by clathrate hydrate formation, Fuel. 122 (2014) 206–217, https://doi.org/10.1016/j.fuel.2014.01.025.

[55] G. Yue, A. Liu, Q. Sun, X. Li, W. Lan, L. Yang, X. Guo, The combination of 1-octyl-3-methylimidazolium tetrafluorborate with TBAB or THF on $CO_2$ hydrate formation and $CH_4$ separation from biogas, Chinese, J Chem. Eng. 26 (2018) 2495–2502, https://doi.org/10.1016/j.cjche.2018.03.014.

[56] N. Gaikwad, G. Bhattacharjee, O.S. Kushwaha, J.S. Sangwai, P. Linga, R. Kumar, Effect of cyclooctane and L-tryptophan on hydrate formation from an equimolar $CO_2–CH_4$ gas mixture employing a horizontal-tray packed bed reactor, Energy & Fuels. 34 (2020) 9840–9851, https://doi.org/10.1021/acs.energyfuels.0c01511.

# Chapter 5 (Objective 3): Stability and dissociation of clathrate hydrates of pure/ mixed CO₂ hydrates with different structure-II (sII) thermodynamic hydrate promoters

As Figure 13 (step 5) of the chapter 1 indicated, the molecular effects of kinetic hydrate promoters (KHPs) on the pure/mixed $CO_2$ hydrate growth (formation) were investigated in chapters 3 and 4. In this chapter, a variety of properties and mechanisms associated with the influences of thermodynamic hydrate promoters (THPs) on pure/mixed $CO_2$ hydrate dissociation have been explored.

The suggested $CO_2$ hydrate-based methods mostly operate at moderate pressure conditions while with the addition of large hydrocarbons which can form sII clathrate hydrates, the significant reduction in the operating pressure for such methods can be observed. Therefore, these approaches will possess lower initial and operating costs which allow them to be utilized in a more extensive range of industrial applications. However, the effect of these substances on $CO_2$ hydrates during either stability or dissociation circumstances are dissimilar. For industrial applications such as secondary refrigeration as well as air conditioning, the higher stability at specific pressure-temperature conditions would be preferred while the easier hydrate dissociation with the lower required energy for the gas separation technologies would have been an advantage. Thus, it is essential to recognize the different characteristics of these components during the stability or dissociation phenomenon. In this chapter, the inclusion of different influences of sII THPs for $CO_2$ or $CO_2+CH_4$ hydrates at the molecular level was simulated.

In addition, the formation of nanobubbles after the hydrate dissociation was evaluated. In this regard, visualization software (VMD and Ovito) was employed to determine the position and dimension of generated nanobubbles after releasing gas molecules from the clathrate crystal. Based on the positions of all molecules, the regions of the final configuration where the gas concentration was over 80% were first specified in the simulation box. This step was followed by another determination where almost pure $CO_2$ and $NF_3$ molecules in the selected regions were presented. Finally, the dimension of these nanobubbles was roughly measured.

This chapter was published as a research paper in Energy & Fuels Journal:

# Molecular Dynamics Simulation Studies on the Stability and Dissociation of Clathrate Hydrates of Single and Double Greenhouse Gases

Saeid Sinehbaghizadeh, Agus Saptoro,* Sepideh Amjad-Iranagh, Angnes Ngieng Tze Tiong, and Amir H. Mohammadi*

Read Online

ACCESS | Metrics & More | Article Recommendations | Supporting Information

**ABSTRACT:** Comprehending and controlling the stability and dissociation of greenhouse gases hydrates are critical for a variety of hydrate-based industrial applications, such as greenhouse gas separation, sequestration, or utilization. Although the promotion effects of greenhouse F-gases (F-promoters) and new cyclic promoters on $CO_2$ hydrates have been acknowledged, the involved molecular mechanisms are poorly understood. This work was therefore conducted to investigate the intermolecular mechanisms of the properties of $CO_2$ and $NF_3$ hydrates using molecular dynamics (MD) simulation to better understand their stability and dissociation and the effects of thermodynamic conditions as well as cage occupancy. In addition, the stability of $CO_2/CO_2 + CH_4$ hydrates in the presence of seven thermodynamic hydrate promoters (THPs) from different molecular groups or substituents was evaluated. Results reveal that after the breakup of the hydrate, the propensity of $NF_3$ to form nanobubbles is more than that of $CO_2$ molecules. The relative concentration distribution of partially occupied hydrates was also found to be greater than that of completely filled by guest gases. MD simulation results of $CO_2$ double and mixed hydrates also show that the type of large molecular guests in the large cages plays a major role in the stabilization of the clathrate hydrate network. The structural properties, however, indicate that the resistance against being dissociated for $CO_2$ + promoter can be somewhat increased when half of the $CO_2$ molecules in small cages is replaced by $CH_4$. In addition, the existence of neopentyl alcohol in large cavities was found to facilitate the process of hydrate dissociation by making new hydrogen bonds between hydroxyl groups and water molecules. Among studied systems with THPs, cyclopentane, and cyclohexane in comparison with F-promoters seem to be more susceptible to maintaining the stability of $CO_2$ clathrate hydrate.
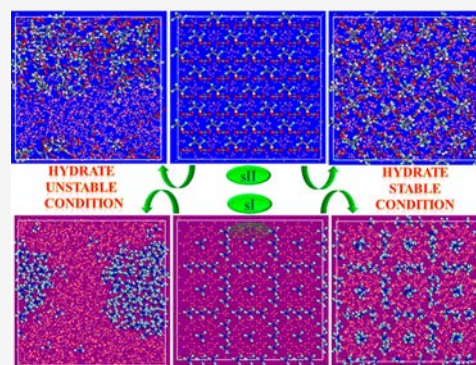
## 1. INTRODUCTION

Greenhouse gases (GHGs) known to science as "super-pollutants,"[1] emitted from fossil fuels and industries into the atmosphere, have increased unprecedentedly. The concentration of $CO_2$ in the atmosphere since the industrial revolution has increased from 280 ppm to a high level of 410 ppm. The prediction of the intergovernmental panel on climate change (IPCC) has determined that the atmospheric $CO_2$ concentration, global temperature, and sea level will experience further increase up to 570 ppm, 2 °C, and 38 cm, respectively by the end of the 21st century.[2] Additionally, strong fluorinated greenhouse man-made gases (F-gases), for example, chlorofluorocarbons (CFCs), with different physical and chemical properties due to their nonflammability, nontoxicity, high efficiency, and high molecular stability (resulting from strong C−F bonds) have gained great popularity for refrigeration and air conditioning aims. By replacing either one or two Cl atoms with F atoms or all four H atoms in $CH_4$, CFCs were first discovered. The F-gases share the fact that they have at least one fluorine (F) atom in

their molecular formula which enables them to have desirable properties for chemicals that serve as good refrigerants. However, the increasing concentrations of these components in the atmosphere have made the situation more critical. Despite knowing that these components were recognized as ozone-depleting substances, evidence counterintuitively shows the 5-fold growth of the use of F-gases at an "aggressive rate" from 2005 to 2025, while the radiative forcing impacts of hydrofluorocarbons (HFCs) caused by increasing their emission sources are already doubling every 5−7 years.[3,4] In terms of global warming potential (GWP), F-gases are mostly 140 to over 23,000 times more harmful than $CO_2$, and they

**Table 1. Characteristics of F-Gases Studied in This Work[8]**

| F-gas name | chemical formula | GWP | date widely commercialized | lifetime (years) | halocarbon |
|---|---|---|---|---|---|
| HFC-134a | $CHF_2CHF_2$ | 1300 | 1990s | 14 | yes |
| HCFC-141b | $CH_3CCl_2F$ | 782 | 1950s | 11 | yes |
| nitrogen trifluoride | $NF_3$ | 16,100 | 1990s | 500 | no |

possess high atmospheric stability with a lifetime of up to 50,000 years which induces large effects on the global temperature, given that the cooling aim among the F-gas processes deserves particular consideration and is responsible for 50−70% of total global F-gas emissions.[5] Generally, the literature classifies two distinct types of F-gases for cooling. Refrigeration refers to the use of cooling or freezing for hermetically sealed productions and for keeping fresh in the agriculture, pharmaceutical, and chemical industries[6] and stationary air conditioning which relates to air conditioners and fans in the buildings.[7] Table 1 shows some characteristics of F-gases (used in this work), adapted from the IPCC assessment report.[8]

To recover and minimize F-gases [e.g., HFCs, hydro-chlorofluorocarbons (HCFCs), and $NF_3$] and $CO_2$ emitted into the atmosphere, several technologies such as liquefaction, adsorption, and membrane processes have been developed.[9−11] However, sequestration or utilization methods after capturing stage may need to be implemented. In this regard, gas hydrates or clathrate hydrates as an innovative alternative have been suggested to apply in either hydrate-based GHG separation,[12] sequestration,[13] or utilization processes.[14] Clathrate hydrates are nonstoichiometric crystalline inclusion compounds, including hydrogen-bonded water cages and entrapped gas and/or some volatile liquid molecules (called guest molecules), which can be usually formed under prevailing pressure−temperature conditions. Three typical structures of the clathrate hydrates family are structure-I ($Pm3n$), structure-II ($Fd3m$), and structure-H ($P6/mmm$) which are mostly determined by the molecular properties and configuration of guests as well as interactions between the guest and the host (water molecules).[1] The typical tips of clathrate hydrate cages are small, medium, and large cages [S-cage, $5^{12}$; M-cage, $4^3 5^6 6^3$; and L-cage, $5^{12} 6^n$ ($n$ = 2, 4, 8 for sI, sII, and sH, respectively)]. Structure-I and -II consist of S- and L-cages with 46 and 136 water molecules, respectively, whereas structure-H includes S-, M-, and L-cages with 34 water molecules.[15]

The F-gases and $CO_2$ with the utilization of hydrate-based methods can be first separated from the gas mixture and then utilized in the other sections of the industry. For example, they can be applied for food and juice preservation, water treatment and desalination, heat recovery from power plants, and so forth.[14,16−18] Based on easy to form $CO_2$ hydrate than $H_2$, $CH_4$, and $N_2$ guests, the hydrate-based gas separation approach as a viable strategy has been widely investigated for the separation of biogas ($CO_2/CH_4$),[19] syngas ($CO_2/H_2$),[20] and flue gas ($CO_2/N_2$).[21] These technologies in comparison with conventional methods possess some advantages, for example, moderate operation conditions, simple process, and high environmental compatibility.[22] Somewhat more recently, to eliminate the remaining $CO_2$ and improve the $CO_2$ recovery, hybrid methods such as the combination of hydrate-membrane,[23] hydrate-cryogenic,[24] hydrate-absorption,[25] and hydrate-adsorption[26] methods have been designed. The process of capturing/separating GHGs can be followed by hydrate-based GHG utilization. For instance, because of the

large storage capacity available in a phase transition, the dissociation enthalpy of $CO_2$ hydrate (507 kJ/kg) is markedly higher than that of ice (333 kJ/kg). Hence, relying on endothermic hydrate dissociation, heat transfer can be efficiently achieved. A novel hydrate-based refrigeration process has shown that using $CO_2$ as working media, a relatively high coefficient of performance can be attained.[14] The presence of hydrates not only improves heat exchange and working time but also enhances the temperature difference between cold and hot fluids during the process of hydrate dissociation. $CO_2$ hydrate slurries due to transport energy with high heat exchange coefficients and relatively low viscosity are promising. The impact of hydrates on the heat exchanger efficiency under various flowrates and hydrate fractions has shown that the convective heat-transfer coefficients of hydrate slurries are 1.5 to 2.5 times greater than that of liquid water. Also, the heat exchanger performance for liquid water and hydrate slurry with a fraction equal to or greater than 9.5 wt % is almost 0.4−0.5 and 0.5−0.6, respectively. Moreover, a pressure drop for 5−8 wt. % $CO_2$ hydrate slurry was determined to be 2 times lower than that of water.[27] Hydrate-based methods for cold thermal energy storage and transport have recently been reviewed elsewhere.[28,29] In addition, for volatile compounds (e.g., aroma or substances like polyphenols and heat-sensitive vitamins), evaporation may impair the quality of products. In this respect, hydrate-based technologies during the concentration of fruit juices have shown the capacity to concentrate betanin, vitamin C, carotenoids, and polyphenols.[30] Since carbonated frozen dessert ($CO_2$ hydrate dessert) has a greater $CO_2$ concentration than carbonated beverages, it could be applied to carbonate the dessert or ice cream.[31] Also, it has been suggested that $CO_2$,[32,33] $SF_6$,[34] cyclopentane,[35] and refrigerant gases (HCFC-141b,[36,37] HFC-134a[17]) have proper potential for effluent concentration and desalination targets. This process was simply designed based on crystal formation in a saltwater solution followed by hydrate-saline water separation and then hydrate dissociation. Experimental explorations have shown that desalination, by using a new hybrid gas hydrate and capacitive deionization process at lower temperatures near the water freezing point, gives a higher efficiency in which 82% of impurities from saline water can be removed.[38,39] Besides, parallel experiments have suggested that utilizing $CO_2$ hydrate as a fire extinguishing agent to extinguish a flame requires a lower critical mass in comparison with ordinary ice.[40] Also, due to the fact that most F-gases can form clathrate hydrates at very low-stability conditions, using them in hydrate-based methods can be highly efficient.

Since the hydrate-based $CO_2$ separation/utilization methods have relatively high formation pressure, the inclusion of large-molecular guests (LMGs) as thermodynamic hydrate promoters (THPs) has been suggested.[41,42] These compounds can also increase the stability of the hydrate during the dissociation. Interestingly, most F-gases can act as a promoter for $CO_2$ hydrate. However, to develop applications of gas hydrates, understanding different specifications of F-gases and
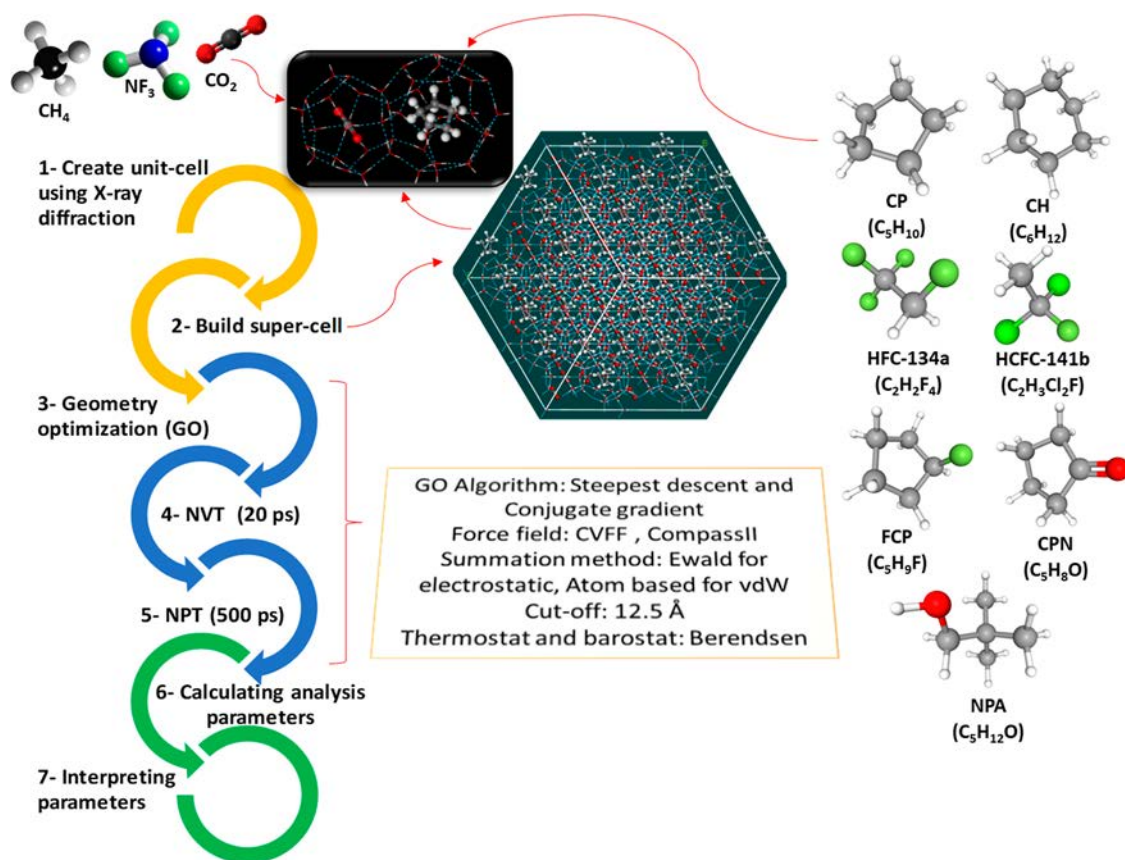
**Figure 1.** Main steps for MD simulation of clathrate hydrates.

$CO_2$ hydrates or in the presence of THPs at a microscopic scale would be essential. To analyze such characteristics, molecular dynamics (MD) simulations have been conducted in several studies. MD simulations have shown that the stability zones of HFC-32 sI hydrate and NMP + $CH_4$ sH double hydrate under high temperature or low pressure conditions are less stable than that of N-methylpiperidine (NMP) + HFC-32 sH hydrate. MD has also demonstrated that placing NMP in large cages can increase the guest-water hydrogen bonding of sH clathrate hydrate. Interestingly, compared to the non-hydrogen bonding state of NMP + $CH_4$ sH hydrate, the NMP + HFC-32 + watersystem does not lead to the destabilization of clathrate hydrate. According to MD results, there is a possibility that HFC-32 molecules, by relieving some strains in the large cavities, increase the stability of the double hydrate structure. Therefore, this phenomenon can be favorably applied to gas storage.[43] MD simulations of binary HFC-41 + pinacolone sH double hydrate have shown that although pinacolone molecules have weak hydrogen bonding with the water in the cages, its hydrate phase boundary can equilibrate at lower pressure conditions than either HFC-41 sI hydrate or HFC-41 + methylcyclohexane sH hydrate.[44] According to MD investigations, it was understood that the stability of double hydrates, namely, $CO_2$ + tetrahydrofuran (THF) sII hydrate, is different from that of $CO_2$ hydrate. Also, a greater hydrogen bonding probability for $CO_2$ + THF hydrate can be formed.[45] Moreover, synergistic hydrogen bonding interactions of $CO_2$ and THF with the water lattice may boost the injection of Bjerrum defects and water reorientation.[46] Although THF does reduce the storage capacity of $CO_2$ in the clathrate hydrate, it expedites $CO_2$ diffusion and stabilizes to lower pressures.[47,48]

It was also revealed that replacing the $CH_4$ molecules with $CO_2$ guests in the sII double hydrate increases the thermal expansion and isothermal compressibility but reduces the specific heat capacity.[49]

Studies pertinent to MD analyses for either $NF_3$ or $CO_2$ double/mixed hydrates (e.g., $CO_2$ + HFCs/new THPs) are scarce in the literature and mostly unexplored. This work, therefore, aims to investigate the phase stability and dissociation conditions of GHG hydrates such as $CO_2$ and $NF_3$ hydrates via MD simulation which helps to better understand the microscopic mechanisms involved. In addition, since the presence of different LMGs plays a leading role in the stability of $CO_2$ structure-II double hydrates, the molecular influences of seven LMGs, including greenhouse F-gases and promoters from different functional groups, on $CO_2$/$CO_2$ + $CH_4$ hydrates were evaluated. The results from this study can be fruitful for facilitating the development of large-scale hydrate-based processes of GHG storage, transportation, or utilization.

## 2. SIMULATION METHODOLOGY

The classical MD study of hydrate systems in the presence of different promoters was performed at the molecular level. The sI and sII were employed as the solid substrate for the simulation of hydrate crystalline. To build the initial configurations, unit cells of sI and sII clathrate hydrates were adopted from the work of Takeuchi et al.[50] Also, the lattice parameters for the initial cubic unit cell of sI and sII clathrate hydrates were set at 12.03 and 17.31 Å, respectively, and guest molecules were placed in the center of small and large cages. To prepare clathrate hydrates with 75% occupancy, two small

**Table 2. Summary of Hydrate Systems and Simulation Conditions of $CO_2/CO_2$ + $CH_4$ sII Hydrates in the Presence of Promoters[a]**

| hydrate guests | set | P (MPa) | T (K) | $T_{exp.}$ (K) | hydrate guests | set | P (MPa) | T (K) | $T_{exp.}$ (K) |
|---|---|---|---|---|---|---|---|---|---|
| $CO_2$ (66.7%) + HFC-134a (33.3%) | 1 | 1 | 273 | 283 | $CO_2$ (66.7%) + FCP (33.3%) | 1 | 1 | 273 | 283 |
| | 2 | | 293 | | | 2 | | 293 | |
| | 3 | 3 | 278 | 288 | | 3 | 3 | 277 | 287 |
| | 4 | | 298 | | | 4 | | 297 | |
| $CO_2$ (66.7%) + HCFC-141b (33.3%) | 1 | 1 | 278 | 288 | $CO_2$ (66.7%) + CPN (33.3%) | 1 | 1 | 269 | 279 |
| | 2 | | 298 | | | 2 | | 289 | |
| | 3 | 3 | 282 | 292 | | 3 | 3 | 275 | 285 |
| | 4 | | 302 | | | 4 | | 295 | |
| $CO_2$ (66.7%) + CH (33.3%) | 1 | 1 | 266 | 276 | $CO_2$ (66.7%) + NPA (33.3%) | 1 | 1 | 265 | 275 |
| | 2 | | 286 | | | 2 | | 285 | |
| | 3 | 3 | 271 | 281 | | 3 | 3 | 273 | 283 |
| | 4 | | 291 | | | 4 | | 293 | |
| $CO_2$ (66.7%) + CP (16.65%) + CH (16.65%) | 1 | 1 | 272 | 282* | $CH_4$ (33.33%) + $CO_2$ (33.33%) + CH (33.34%) | 1 | 1 | 266 | 276 |
| | 2 | | 282 | | | 2 | | 271 | |
| | 3 | | 292 | | | 3 | | 276 | |
| | 4 | 3 | 277 | 287* | | 4 | | 286 | |
| | 5 | | 297 | | | 5 | 3 | 271 | 281 |
| $CO_2$ (66.7%) + CP (33.3%) | 1 | 1 | 273 | 288 | | 6 | | 276 | |
| | 2 | | 278 | | | 7 | | 281 | |
| | 3 | | 283 | | | 8 | | 291 | |
| | 4 | | 288 | | $CH_4$ (33.33%) + $CO_2$ (33.33%) + CP (33.34%) | 1 | 1 | 273 | 293 |
| | 5 | | 298 | | | 2 | | 283 | |
| | 6 | | 308 | | | 3 | | 288 | |
| | 7 | 3 | 273 | 293 | | 4 | | 293 | |
| | 8 | | 283 | | | 5 | | 303 | |
| | 9 | | 293 | | | 6 | 3 | 288 | 298 |
| | 10 | | 303 | | | 7 | | 308 | |

[a]$T_{exp.}$: Experimental equilibrium temperature of hydrate at corresponding pressure in the presence of promoter (CPN,[58] NPA,[59] FCP,[60] HCFC141b,[61] CH,[62] HFC-134a,[63] and CP[41,42]). (*): Estimated from thermodynamic modeling.[64−67]

cages as well as four out of six large cages of sI clathrate hydrate were filled with guest molecules. The unit cell was then replicated three times in all directions to generate the initial hydrate slab. Also, the periodic boundary condition in three dimensions was considered, and the stable structure was geometrically optimized using both steepest descent and conjugate gradient methods.[51,52] In this approach, based on the direction of the energy downhill drop, a linear search was introduced so that in the opposite direction at which the gradient holds the highest value, geometry minimization with an adequate tolerance was performed. However, by applying this technique, it might experience considerable fluctuations to find a minimized energy structure. Therefore, this optimization was followed by performing the conjugate gradient method. By the usage of Ewald summation,[53] van der Waals and long-range Coulomb interaction terms were computed. To simulate the guest−guest, host−host, and guest−host interactions, CVFF and compass-II (for $NF_3$) force fields were employed.[54,55] The cutoff distance of 12.5 Å was considered for all interactions. To reach the targeted temperature in each set of simulations, the constant volume and constant temperature (NVT) ensemble for 20 ps was performed. This step was followed by the constant pressure and constant temperature (NPT) for 500 ps to investigate the stability and final configuration of clathrate hydrates.[56] Temperature and pressure were also controlled by

the Berendsen thermostat and barostat.[57] The main MD simulation steps of clathrate hydrates as well as guest molecules are exhibited in Figure 1.

Although the unary use of $CO_2$ molecules by filling the guest in both small and large cages is generally expected to attain maximal storage capacity, the inclusion of LMGs into the large cages of clathrate hydrate from an engineering perspective can be more feasible. In addition, such LMGs often play a major contribution in stabilizing the clathrate hydrate shape by shifting the thermodynamic phase equilibria to practically implementable milder P−T conditions. In this context, $CO_2/CO_2$ + $CH_4$ hydrates in the inclusion of two F-promoters (HFC-134a and HCFC-141b), large molecular alcohol such as neopentyl alcohol (NPA), and four cyclic promoters including cyclopentane derivatives such as fluorocyclopentane (FCP), cyclopentanone (CPN), cyclopentane (CP), and cyclohexane (CH) at the molecular level was simulated. It should be mentioned that $CO_2$ and $NF_3$ sI hydrates were simulated at 3/10 MPa and 273/283/293 K. In addition, simulations for the case of 75% cage occupancy filled by $CO_2$ and $NF_3$ molecules were performed at 3/10 MPa and 283 K. Also, the summary of simulation conditions and guest compositions in the initial configuration of $CO_2/CO_2$ + $CH_4$ sII hydrates in the presence of different promoters is presented in Table 2. To provide the initial simulations, all small cages were filled with $CO_2$ or $CH_4$
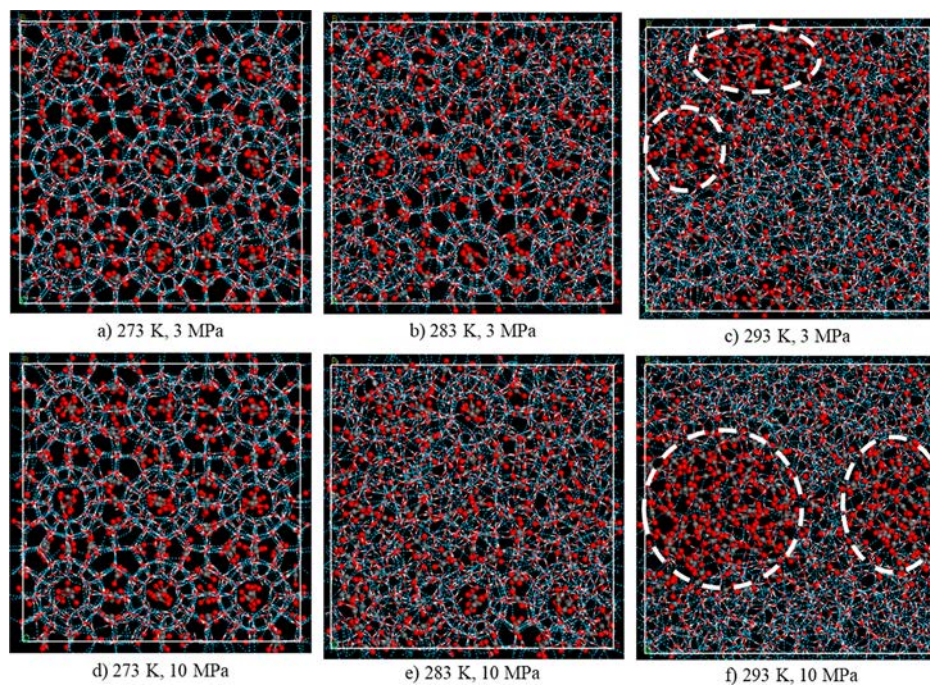
**Figure 2.** Final configuration of $CO_2$ sI hydrate at different $T-P$ conditions.
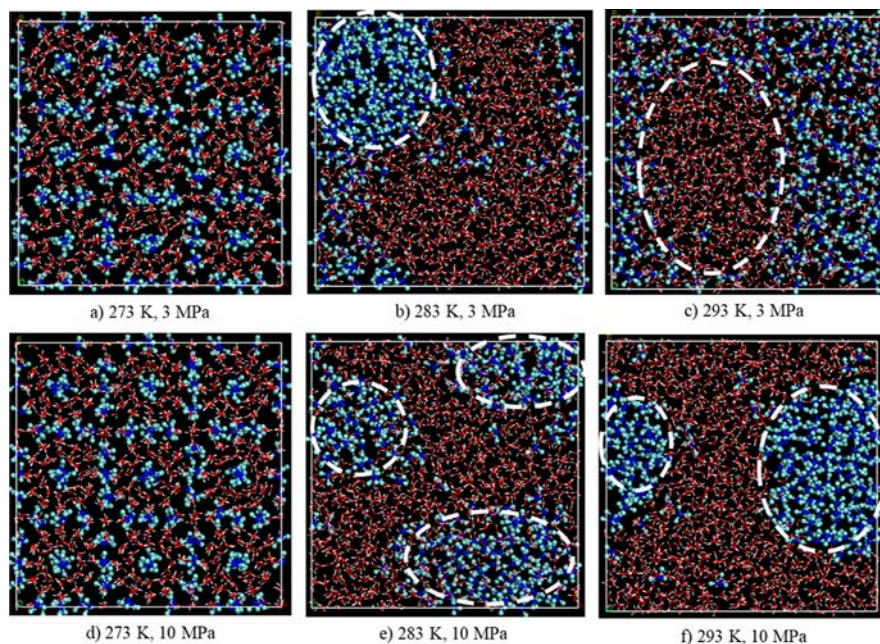


**Figure 3.** Final configuration of $NF_3$ sI hydrate at different $T-P$ conditions.

molecules, while the large ones were occupied by LMGs or F-gases. Therefore, the percentages in the table represent the proportion of hydrate formers in all filled cages of the sII clathrate hydrates (number of guest molecules in filled cages per total cages).

## 3. RESULTS AND DISCUSSION

In this work, hydrate systems such as (1) $CO_2$ hydrate and $NF_3$ hydrate and (2) mixed $CO_2$ hydrates, for example, $CO_2/$ $CO_2 + CH_4 + LMGs$, and $CO_2 + F$-gases, were simulated. Therefore, the first and second subsections below present the results of simulated pure and mixed gas hydrates, respectively.

This section covers the structural and thermodynamic characteristics of the simulated hydrates. Since the cage occupancy and pressure–temperature conditions contribute to the stability and dissociation of clathrate hydrates, their effects on analysis parameters such as lattice parameter, relative concentration, potential energy, diffusion coefficient, mean square displacement (MSD), and radial distribution function (RDF) are evaluated in the following subsections.

**3.1. Stability and Characterization of $CO_2$ and $NF_3$ Hydrates.** The final snapshots of $CO_2$ and $NF_3$ hydrates at 3/ 10 MPa and 273/283/293 K after 500 ps are depicted in Figures 2 and 3 respectively. It can be observed that the

**Table 3. Locations of RDF Peaks of $CO_2$ Hydrate in This Work and Those Reported in the Literature**

| locations of RDF peaks (Å) | T−P condition (K, MPa) | $g_{o-o}$ (r) | | | $g_{o-c}$ (r) | | | $g_{c-c}$ (r) | |
|---|---|---|---|---|---|---|---|---|---|
| | | 1st | 2nd | 3rd | 1st | 2nd | 3rd | 1st | 2nd |
| Liu et al.[69] | 260, 30 | 2.75 | 4.48 | 6.42 | | | | 4.17 | 6.49 |
| Kondori et al.[70] | 270, 5 | 2.75 | 4.50 | 6.53 | 4.22 | 6.81 | | 4.21 | 6.80 |
| Mahmoodi et al.[71] | 250, 30 | 2.75 | 4.55 | 6.55 | 4.05 | 6.85 | 8.15 | 4.15 | 6.75 |
| Chialvo et al.[72] | 270, 5 | 2.75 | 4.49 | 6.45 | 3.80 | 6.00 | 7.50 | | 6.71 |
| this work | 273, 3 | 2.75 | 4.53 | 6.51 | 4.09 | 6.83 | 8.07 | 4.16 | 6.79 |
| [a]AARD % | | 0.00 | 0.55 | 0.35 | 1.63 | 4.05 | 3.04 | 1.38 | 1.51 |

[a]AARD % $= \frac{1}{m}\sum_{i=1}^{m} \left| \frac{g_i - g_i^{\text{ref}}}{g_i^{\text{ref}}} \right| \times 100$.

structure of cages for Figure 2a,d is approximately consistent with the initial configuration in which $CO_2$ molecules keep themselves at the center of the cages, and hydrogen bonds (dash-lines) of water molecules experience inappreciable changes. Therefore, the $CO_2$ hydrate does not dissociate. In addition, a 10 K temperature increase brings about reducing the structural stability as exhibited in Figure 2b,e. However, the cage stability for case (b) is slightly higher than that for case (e). It should be pointed out that under the equilibrium condition, the $CO_2$ hydrate at 3 MPa is coexistent with $CO_2$ in the vapor phase ($H-L_{H_2O}-V_{CO_2}$), while it can be in equilibrium with $CO_2$ in the liquid phase ($H-L_{H_2O}-L_{CO_2}$) when the pressure exceeds 4.5 MPa. Since nanobubbles have significant impacts on the reformation and dissociation dynamics of clathrate hydrates, the evolution of gaseous bubbles composed of $CO_2$ and $NF_3$ from the hydrate phase after the dissociation was evaluated. It is worth mentioning that according to the standpoint of classical thermodynamic theories, nanobubbles can persist for a long time in liquids while participating in the hydrate processes. The objective of this work was to further understand the behaviors of $CO_2$ and $NF_3$ bubbles and their effects on the hydrate stability while producing gas from hydrates. As expected, by increasing the temperature to 293 K, cages of the hydrate structure disappear entirely. Therefore, $CO_2$ molecules are freely released from the cluster and accumulate into the nanobubbles as displayed in Figure 2c,f.

It is worth mentioning that the critical P−T conditions for $CO_2$ hydrate are 0.74 MPa and 304 K, whereas that for $NF_3$ hydrate are 0.05 MPa and 234 K. Also, $NF_3$ is a stable gas at room temperature. The stability of $NF_3$ hydrate under the same thermodynamic conditions as $CO_2$ hydrate is shown in Figure 3. It should be pointed out that the hydrate of $NF_3$ is more stable than $CF_4$,[68] but it seems to be less stable than $CO_2$. At 3/10 MPa and 273 K, the effect of pressure is not substantial, and the water structure of cages as well as $NF_3$ molecules remain unchanged. However, increasing the temperature to 283 K results in complete dissociation of $NF_3$ hydrate and creates the supersaturation condition in the water phase either at 3 or 10 MPa. At this stage, $NF_3$ molecules contribute to the formation of nanobubbles as shown in Figure 3b,e. However, the $NF_3$ bubble evolution for upper temperatures like 293 K may be dissimilar. The $NF_3$ bubbles in the case (f) of Figure 3 seem to be denser and slightly larger in size than in case (e). Unlike 10 MPa in case (f), the $NF_3$ molecules at 3 MPa in Figure 3c surround the water molecules which indicates the importance of pressure in the bubble formation. The density of the $NF_3$ bubbles appears to be larger than that of $CO_2$ bubbles. This might be caused by the higher solubility

of $CO_2$ than $NF_3$ in the water phase. The $CO_2$ and $NF_3$ concentrations at the liquid−bubble interface are also dissimilar. This difference would be originated from the diverse surface tension between guest and host molecules at the interface. The produced bubbles can grow in any direction; even so, due to a periodic boundary condition, the shape of the bubbles changes from spherical to cylindrical once the bubble's diameter is equal to the cell size.

Table 3 compares the locations of peaks in oxygen−oxygen, oxygen−carbon, and carbon−carbon RDFs of $CO_2$ hydrate in this work and previous studies. According to the magnitudes of average absolute relative deviation percentage (AARD %), the $g_{o-o}$, $g_{o-c}$, and $g_{c-c}$ are in agreement with the results available in the literature which shows that the structural configurations are nearly identical. Hence, the employed potential functions are capable to describe the host and guest interactions in the crystal hydrate.

Investigations suggest that under hydrate formation conditions, a small volume variation in a hydrate lattice (e.g., 1.5%) may result in significant differences in predicting the thermodynamic characteristics of clathrate hydrates. Also, to incorporate a variable hydrate volume, the vdWP model should be modified like the model proposed by Ballard and Sloan.[73] Therefore, systematic measurements on lattice parameters should be performed to accurately predict $CO_2$ hydrate properties at various thermodynamic conditions. In this work, the effects of pressure, temperature, and cage occupancy as main contributors to the lattice parameter were evaluated. The unit cell parameters for fully/partially occupied $CO_2$ and $NF_3$ hydrates under earlier mentioned P−T conditions are exhibited in Figure 4a,b respectively. Since the interactions of the guest molecules with the host water lattice as well as the guest molecular vibrational motions would significantly contribute to the lattice parameter, drawing a comparison before and after the hydrate dissociation phenomenon can be useful. Once the guest molecules escape from the water network and dissociate the clathrate hydrate, the phase is changed from a solid hydrate lattice to liquid and gas phases. Therefore, to understand the alteration of the unit cell parameter after experiencing the dissociation stage, for example, Figures 2c,f and 3b,c,e,f, an equivalent of the unit cell parameters of dissociated clathrate hydrates based on the dimension of the simulation box was calculated that is shown in Figure 4. As is evident, at the hydrate stability zone (273 K and 3/10 MPa), the effect of pressure is insignificant. The average lattice parameters for $CO_2$ and $NF_3$ hydrates from 0 to 500 ps are found to be 11.98 and 12.03 Å, respectively. By decreasing the $CO_2$ hydrate stability caused by a 10 K temperature increase, some fluctuations can be observed. However, in comparison with the preceding thermodynamic
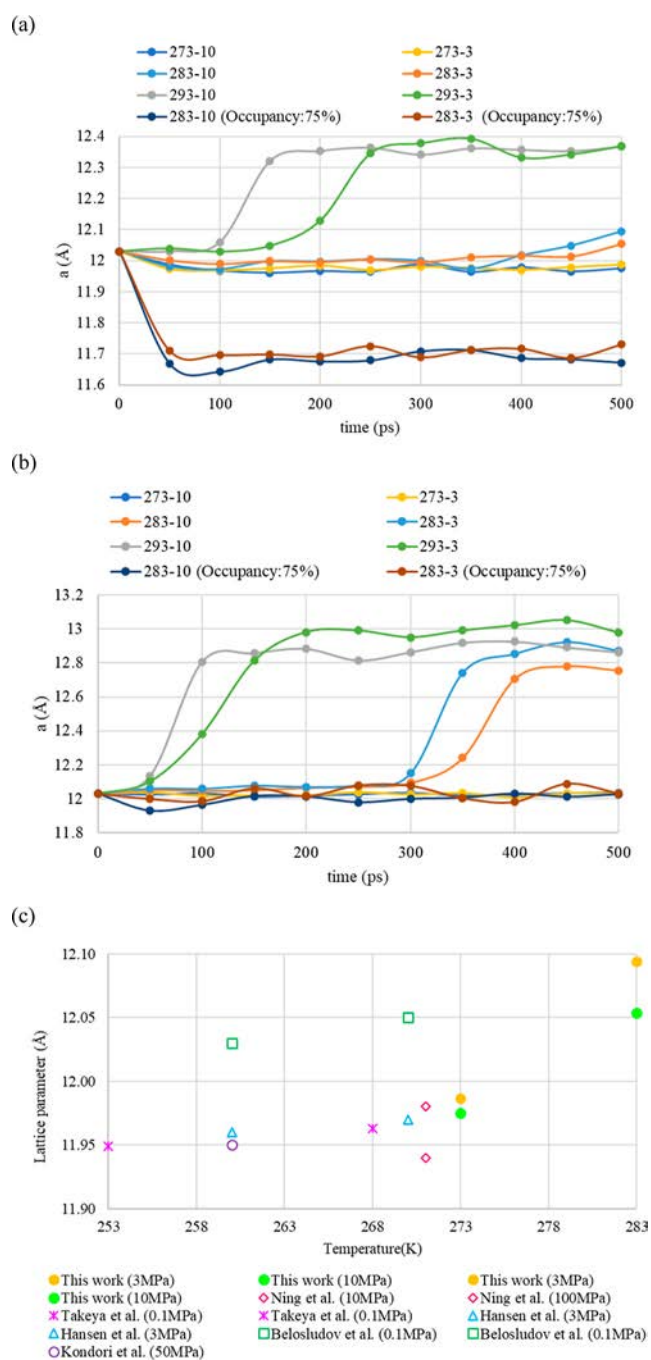
**Figure 4.** Unit cell parameter for (a) $CO_2$ hydrate and (b) $NF_3$ hydrate. (c) Comparison of the calculated lattice parameter of $CO_2$ sI hydrate with the theoretical and experimental data.[70,74−77]

conditions, the effects of pressure are more substantial which has a reverse impact on such fluctuations. According to simulation results for $NF_3$ hydrate at 283 K, it can be observed that the hydrate structure up to 300 ps can remain unchanged. This may imply that the simulation condition is near the equilibrium condition. Also, by comparing the trend of 100 and 75% cage occupancies, it can be inferred that the cage occupancy affects the equivalent of the initial lattice parameter for $CO_2$ hydrate in which 25% decrease in the total cage occupation leads to a 2.5% drop. However, this is not valid for $NF_3$ hydrate after the dissociation. The equivalent of the unit cell parameter for 75% $CO_2$ occupancy at 283 K is around 0.3

Å lower than the sI lattice parameter at 273 K; however, that for $NF_3$ almost remains constant. In addition, the equivalent of this parameter for $CO_2$ and $NF_3$ hydrates at 293 K is approximately 0.4 and 0.9 Å higher than the final value at 273 K, respectively. It seems that the guest−host interactions and the formation of nanobubbles after the clathrate hydrate dissociation for $NF_3$ in comparison with $CO_2$ would be the main causes of higher expansion. Therefore, the contraction because of 75% $NF_3$ occupancy and the expansion due to $NF_3$−water interactions and greater formed nanobubbles after the hydrate dissociation may compensate each other, so that the lattice parameter for $NF_3$ hydrate at 273 K and 100% occupancy is similar to that at 283 K and 75% occupancy. Figure 4c also compares the obtained lattice parameter of $CO_2$ hydrate at undissociated circumstances and theoretical as well as experimental data at different thermodynamic conditions. It seems that the impact of the pressure up to moderate ranges (e.g., 3−10 MPa) is lower than that of the high pressure. Additionally, near the threshold of hydrate dissociation (283 K), the direct and inverse proportional lattice parameters to temperature and pressure are found to be more substantial.

Monitoring the guest concentrations at different simulation time intervals can reflect the microscopic behavior of the molecules in the hydrate phase. The relative concentration distribution (RCD) of $CO_2$ and $NF_3$ molecules against the $z$ coordinate of the simulation box at five different consecutive time intervals is exhibited in Figure 5. The concentration profiles for cases (a) and (b) during the simulation time remains constant. In addition, the regular peaks indicate the uniformity of the cluster. Also, the higher and lower peaks represent the guest molecules in large and small cavities, respectively. Cases (c) and (d) display the RCDs of $CO_2$ and $NF_3$ hydrates at 283 K, respectively. As is evident, the aforesaid peaks are reduced as the simulation time proceeds. This change occurs more quickly for the $NF_3$ hydrate in which the cavities at the final time segment (400−500 ps) are dissociated completely. The trends of RCDs in cases (e) and (f) with the partial cage occupancy of 75% at 283 °C are relatively different. There is a fluctuation in the trend of RCDs for all time segments which demonstrates the transition state of hydrate cages before being dissociated. This implies the higher mobility of guest molecules in comparison with the full cage occupation; however, this phenomenon reduces the stability of the hydrate structure. Previously, it was shown that the stability of $CH_4$ hydrate can be decreased once the fractional occupancy is reduced from 100% to either 87.5% or 75%.[78] Based on cases (g) and (h), the RCDs of $CO_2$ and $NF_3$ molecules after the dissociation stage mostly fluctuate between 0.5 and 1.5. Moreover, the height of the first-time segment (0−100 ps) which refers to the hydrate state before the break-up of cages is slightly shorter than cases (a) and (b). It is essential to highlight that the smoother curves of $NF_3$ compared to $CO_2$ may manifest the higher concentration of guest molecules in bubbles after the dissolution stage as shown in Figures 2 and 3.

Since the guest−host van der Waals interactions as well as the hydrogen bonds between water molecules create the hydrate cages, changing the number of hydrogen bonds per guest gas molecule and the interactions between guest−host molecules alter the amount of clathrate hydrate enthalpy. Generally, the value of required heat to dissociate the hydrate network and generate 1 mole of gas molecule is the dissociation enthalpy of clathrate hydrate which can be represented by $G \cdot nH_2O(s) \rightarrow G(g) + nH_2O(l)$, where $n$
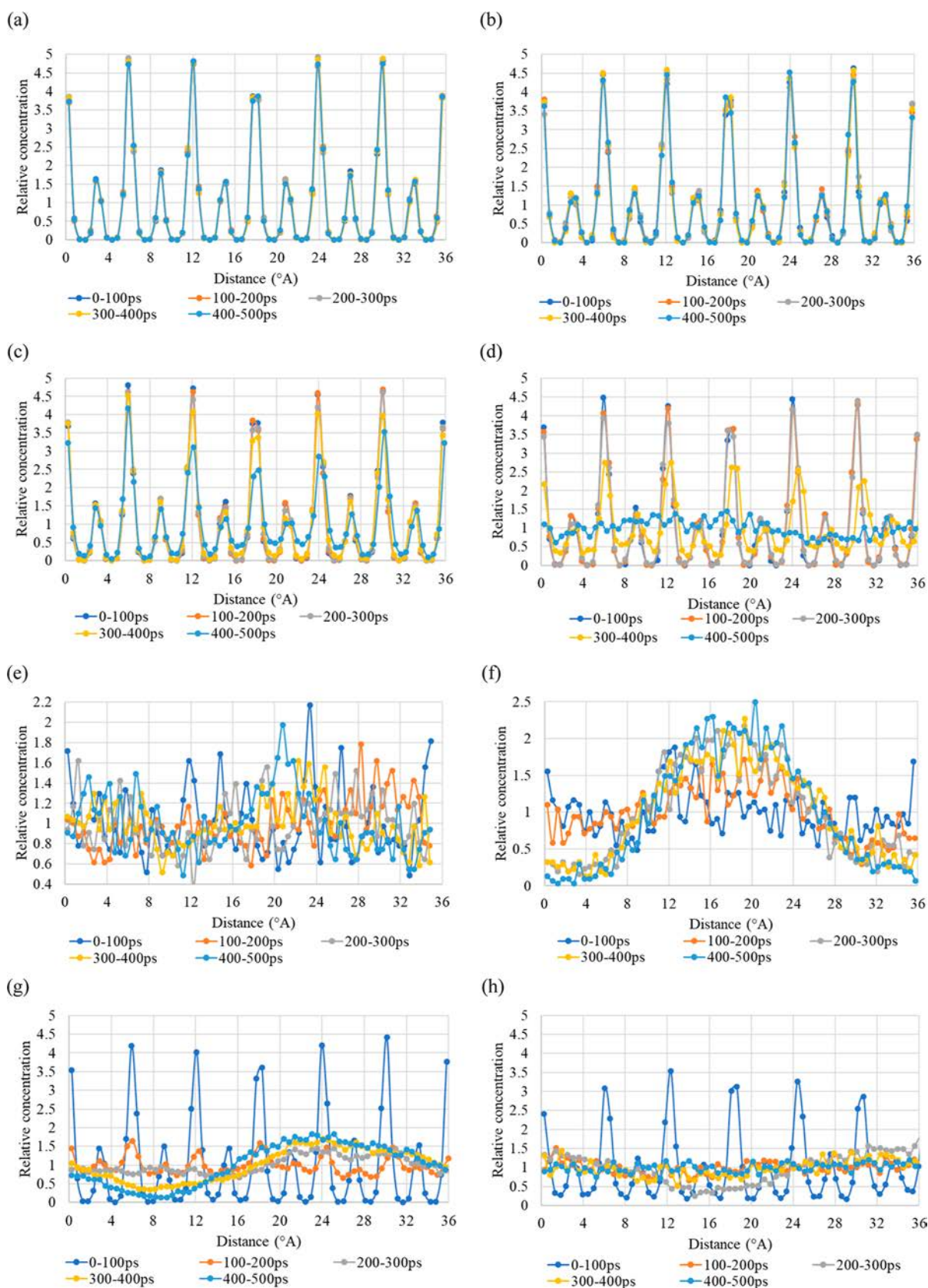
**Figure 5.** Relative concentration of $CO_2$ and $NF_3$ hydrates at 10 MPa and 273 K, (a,b); 10 MPa and 283 K, (c,d); 10 MPa and 293 K, (g,h), respectively. Cases (e,f) reflect the $CO_2$ and $NF_3$ hydrates with a cage occupancy of 75% at 10 MPa and 283 K.

refers to the hydration number and G denotes the guest gas molecules in the hydrate phase. Given that the structure of

$CO_2$ and $NF_3$ hydrates is sI, the number of hydrogen bonds and types of cages are the same. Therefore, guest−host

interactions only affect the dissociation enthalpy of $CO_2$ and $NF_3$ hydrates. The differential between the total enthalpies of the final and initial configurations of $CO_2$ and $NF_3$ hydrates is displayed in Figure 6. The lower values represent the
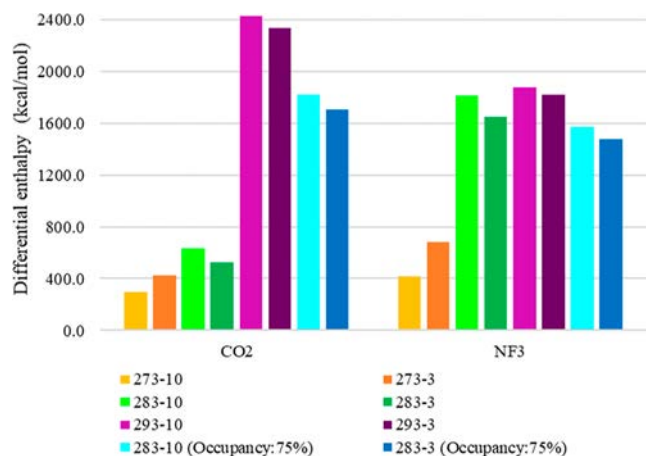


**Figure 6.** Differential between the total enthalpies of the final states and initial configurations of $CO_2$ and $NF_3$ hydrates.

insignificant changes in the hydrate structures, whereas the greater amounts illustrate the dissolution of the hydrate network. Since the number of guest molecules for the cases with partially filled cages is less than full occupation, their differential values are smaller. Based on the MD simulation results in this work, the molar enthalpies of dissociation for $CO_2$ and $NF_3$ hydrates at 3 MPa and 293 K are found to be 63.2 and 50.4 kJ/mol of gas, respectively, which are quantitatively in agreement with the values reported in the literature.[79]

The other criterion to monitor the process of clathrate hydrate phase transition would be the density alteration in the simulation. Figure 7 reveals the initial and final densities of $CO_2$ and $NF_3$ hydrates at different $P-T$ conditions. The
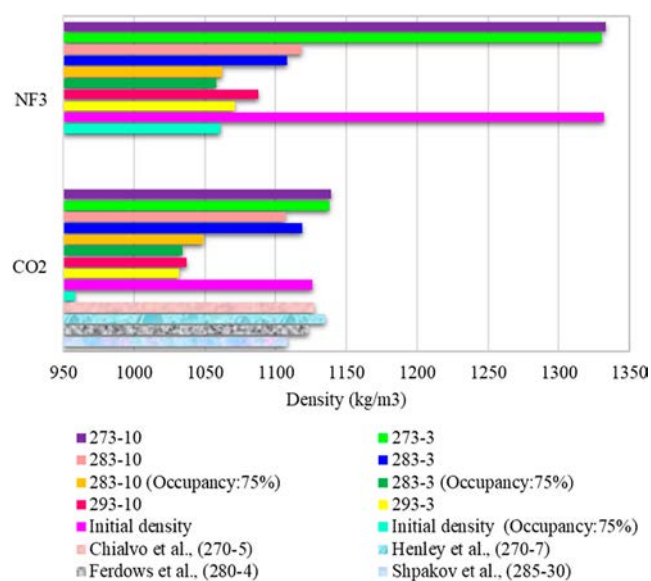


**Figure 7.** Densities of $CO_2$ and $NF_3$ hydrates at different $T-P$ conditions (K, MPa). (Texture symbols denote the data reported in the literature[72,80−82]).

obtained results for $CO_2$ hydrate are comparable with the experimental data reported in the literature. The sharp drops in this diagram indicate the change of hydrate phase into liquid and gas states. It should be noted that due to the empty cages of $CO_2$ hydrate for the case of 75% occupancy, the hydrogen bonds may affect the lattice parameter which is reduced to lower amounts as shown in Figure 4a. Thus, a higher final density compared to the initial structure is obtained. However, this is not observed for $NF_3$ hydrate (75% occupancy) which could be affected by the molecular size/shape of hydrate guests and their interactions with water. It should be noted that the initial dimensions of the simulation box for both cases, 100 and 75% occupancies, are the same, but the number of $CO_2$ molecules in the simulation box of 75% occupancy is lower than full occupation which results in a lower density. In addition, the initial and final densities of $CO_2$ and $NF_3$ hydrates in the case of 75% occupancy are found to be similar to the behaviors of lattice parameters of these clathrate hydrates. The final densities of $CO_2$ and $NF_3$ hydrates at 293 K show that the process of hydrate dissociation can influence the $NF_3$ hydrate more than the $CO_2$ hydrate.

To provide further analysis on dissociation behaviors, the diffusion coefficients of guest molecules at aforesaid thermodynamic conditions can be estimated. In certain nodes of simulation temperatures and pressures, the diffusion coefficient is generally determined as a function of the MSD of a specific component which is known as the Einstein relationship: $6D_t = MSD$, where $t$ and $D$ denote the simulation time and diffusion coefficient, respectively.[83] Based on this equation, the coefficient of diffusion can be defined as the average of MSDs. On the basis of this concept, the water molecules without movement vibrate around hydrate cages once the hydrate structure remains stable. Accordingly, the diffusion coefficients under the stable conditions are very low which is approximately equaivalent to the solid state. The $CO_2/CH_4$ exchange in the bulk crystalline without dissociating the hydrate phase requires guest molecular transformation between the cages such as the "cage hopping" phenomenon through the intercage plane (pentagonal and hexagonal of large and small cavities). Although hopping of the guest at low temperatures bears an enormous energy barrier, interstitial defects of the hydrate by lowering the energy barrier may accelerate the guest diffusion. The gas diffusivity in the stable hydrate is about $10^{-11}$ to $10^{-10}$ ($cm^2/s$), whereas in the case of intercage movements, it can be around $10^{-9}$ to $10^{-8}$ ($cm^2/s$). The $CO_2$ diffusion coefficients under the hopping events in the system with a high concentration of water vacancy at 273 and 278 K reported in the literature were found to be 101 and 255 $cm^2/s$, respectively.[84] Figure 8 shows the diffusion coefficients of $CO_2$ and $NF_3$ molecules in the simulation box. Under a stable situation, the guest diffusivities of both molecules are in the order of $10^{-10}$ ($cm^2/s$) which is in agreement with the values reported in the literature.[85] As was earlier shown in Figure 2b,e, the solid phase of $CO_2$ hydrate is partially dissociated on increasing the temperature to 283 K. Subsequently, the diffusion coefficient of $CO_2$ (on the threshold of being dissociated or partially disordered) markedly increases by 2 or 3 orders of magnitude to $10^{-8}$ to $10^{-7}$ ($cm^2/s$) which is exhibited in Figure 8. By the elevation of temperature or reducing the cage occupancy to 75%, the solid-state of $CO_2$ and $NF_3$ hydrates completely vanished. By the effect of such rapid molecular transformation, the coefficient of diffusion again experiences 2 or 3 orders of magnitude growth
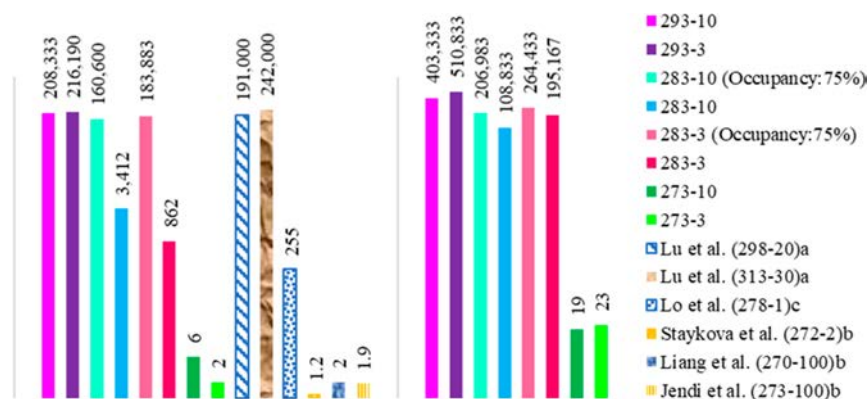
**Figure 8.** Diffusion coefficients of $CO_2$ and $NF_3$ hydrates at different $T-P$ conditions (K, MPa). (Texture symbols denote the data reported in the literature[84−88]). (a) Diffusion coefficient of $CO_2$ in water, (b) in solid hydrate phase, and (c) for cage hopping transfer of $CO_2$ molecules in the hydrate.

and increases to $10^{-5}$ ($cm^2/s$) which is quantitatively in agreement with experiments.[86] It should be noted that for all studied thermodynamic and fractional occupancies in this work, the $NF_3$ diffusivity after the hydrate dissociation is found to be higher than that of $CO_2$.

**3.2. Stability and Characterization of Promoted $CO_2$/ $CO_2 + CH_4$ Hydrates.** This section provides the simulation results of the mixed hydrate systems reported in Table 2. Therefore, the effects of seven different thermodynamic promoters on the $CO_2$ or $CO_2 + CH_4$ sII hydrates in terms of potential energy, RDF, MSD, and the diffusion coefficients of guest and host molecules are investigated. Generally, $CO_2$ under prevailing conditions can generate sI clathrate hydrate; however, $CO_2$ in the existence of liquid hydrocarbons with diameters between 6 and 7.5 Å, such as CP and CH, can form structure-II of clathrate hydrate.[15] It should be noted that $CO_2$ plus F-gases such as HFC-134a may exhibit heterogeneous azeotropic-like behavior derived from the structural phase transition of the mixed-gas hydrate. However, the Raman shifts indicate that a structural transition occurs in the high-concentration ranges of $CO_2$ in the hydrate phase.[89] It should be pointed out that the initial sII clathrate hydrates of the studied systems in this work under stable conditions as a function of simulation time are found to structurally remain unchanged. Figure 9 exhibits the final configuration of $CO_2 +$ CH hydrate after 500 ps. In cases (a) and (c), the hydrate is under thermodynamic stability, so that the crystalline structures remain unaltered while in agreement with the experimental evidence,[62] and the solid phase over the phase equilibrium of $CO_2 +$ CH hydrate is segregated as shown in cases (b) and (d). Interestingly, after the process of clathrate hydrate dissociation, the $CO_2$ bubbles are not generated, but CH molecules are surrounded by the $CO_2$ molecules. In addition, the final positions of CH and water molecules in Figure 9b,d are quite different. In the former snapshot (Figure 9b), CH molecules accumulate at the center of the simulation box, whereas in the latter snapshot, the majority of water molecules are located in the middle of that and CH molecules environ the water phase.

Under unstable thermodynamic conditions, the dissociation times for $CO_2$ hydrates in the inclusion of promoters such as HFC-134a, FCP, NPA, and HCFC-141b are estimated to be about 60, 70, 80, and 90 ps, respectively. This may indicate that the resistances against being dissociated for the aforementioned promoters are not appreciable. However, the
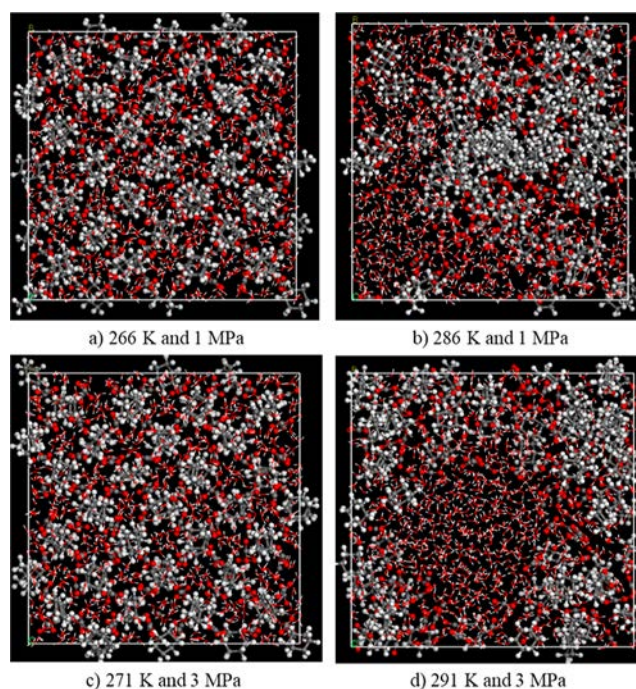


a) 266 K and 1 MPa       b) 286 K and 1 MPa

c) 271 K and 3 MPa       d) 291 K and 3 MPa

**Figure 9.** Final configuration of $CO_2 +$ CH sII hydrate at different $T-P$ conditions.

times of $CO_2$ hydrates dissociation in the inclusion of CPN, CH, and CP are found to be 120, 210, and 230 ps, respectively. This value for $CO_2$ hydrate at 293 K is determined to be nearly 110 ps. Therefore, considering the hydrate dissociation times for investigated thermodynamic promoters, it can be inferred that the existence of cyclic LMGs in large cavities can increase the structural stability of $CO_2$ sII hydrates, whereas the presence of fluorine atom in F-gases may reduce the firmness of the hydrate crystalline structure.

The lattice parameters of $CO_2$/$CO_2 + CH_4$ II hydrates in the inclusion of LMGs or F-gases as a function of temperature are displayed in Figure 10. As exhibited, this parameter is affected by the size and shape of guest type in both small and large cages as well as the $P-T$ conditions. Also, the greater diameter of LMGs or F-gases gives the higher lattice parameter. To identify the crystal structures of the cyclic compounds in clathrated hydrate systems with $CO_2$ using PXRD patterns, the lattice parameters for $CO_2 +$ CPN, $CO_2 +$
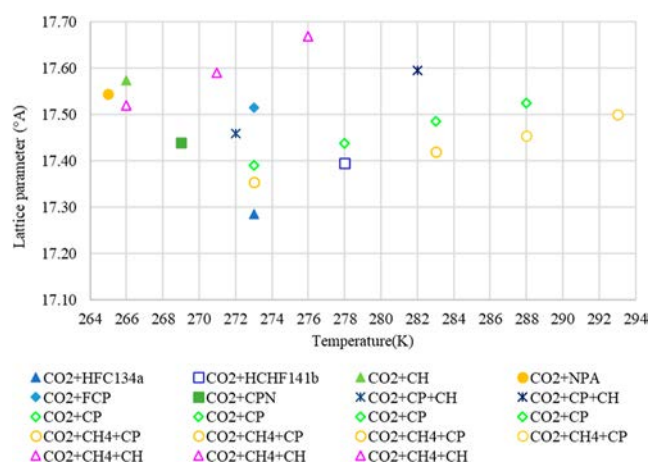
**Figure 10.** Calculated lattice parameters of $CO_2$ or $CO_2$ + $CH_4$ sII hydrates in the presence of LMGs or F-gases at 1 MPa and different temperatures.

CP, and $CO_2$ + THF sII clathrate hydrates were determined to be 17.30, 17.38, and 17.34 Å, respectively.[90,91] In addition, MD simulations have shown that the lattice parameter for $CO_2$ + THF hydrate using TIP4P/2005, OPLS-AA, and TraPPE force fields for water, THF, and $CO_2$ at 273 K and 0.1 MPa is approximately 17.47 Å.[49] Therefore, the obtained sII clathrate hydrate lattice parameters in this work are comparable with those experimentally or theoretically reported in the literature.

The potential energy reflects the van der Waals and long-range Coulomb interactions included in simulated systems. The differential between the potential energies (running average) of the final and initial configurations of simulated systems for $CO_2$/$CO_2$ + $CH_4$ hydrates in the presence of promoters are displayed in Figure 11. For the systems where the hydrate is thermodynamically stable, the potential energy of the final state exhibits significantly lower alteration in comparison with the unstable conditions. Under the equilibrium state, the rotation and vibration of guest molecules cannot disturb the water molecular hydrogen bonds. Therefore, the potential energy throughout the simulation varies around the equilibrium value. Also, the differential potential energies of stable cases are less or around 500 kcal/mol, while those of unstable circumstances are mostly over 1500 kcal/mol. This value for the $CO_2$ hydrates including HCFC-141b is the highest, whereas CP is the lowest. This may indicate that the presence of CP can properly maintain the structural stability rather than other studied promoters. However, this amount slightly increases once $CH_4$ or CH is included in the hydrate system. Moreover, case $CO_2$ + CP-6 hydrates indicates that the temperature increase after the dissociation process can markedly elevate the potential energy of the system. Also, the addition of promoters such as NPA in large cavities by making new hydrogen bonds between hydroxyl groups and water molecules may facilitate the hydrate dissociation. Generally, the new hydrogen bonds between guest and host molecules can enfeeble or disarrange the primary hydrogen bonds of the water network in the clathrate hydrate.

To analyze the hydrate stability either before or after the dissociation occurrence, the distance between atoms in water and guest molecules in phases can be monitored using the RDF. Figure 12a,b exhibits the RDFs between oxygen atoms of water and carbon atoms of $CO_2$ ($g_{o-c}(r)$) and promoters ($g_{o-p}(r)$), respectively. The RDFs represent the positions of each
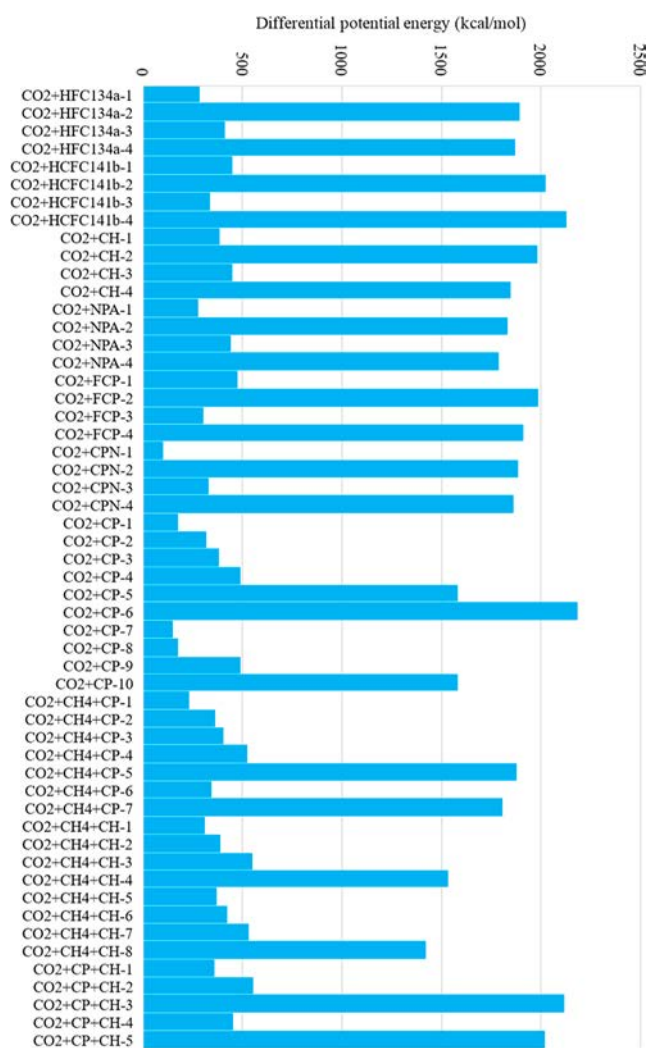


**Figure 11.** Differential between the potential energies of the final and initial configurations of simulated systems.

system before and after the dissociation. At distances less than an atomic diameter, the magnitudes of RDFs are zero. As is shown, the first peak in $g_{o-c}$ is located at 3.96 Å which is within ~0.05 Å of the average cavity radius of small $5^{12}$ (3.91 Å) cages in the sII clathrate hydrate.[15] This is also qualitatively consistent with the value reported for $CO_2$ + THF hydrate.[47] The height of peaks for hydrate systems under the stability zone is in the range of 4−4.8 Å. Between the hydrate systems including different LMGs and F-gases, CP and CH possess the highest peaks, whereas the lowest peak is for HCFC-141b. Also, the height of the peak after the breakup of hydrate cages reduces to a range between 3.5 and 1.3 Å. In this regard, the lowest peaks belong to the LMGs which have fluorine in their molecular structure (FCP, HFC-134a, and HCFH-141b). For HFC-134a and HCFC-141b, the RDFs hold different peak values because of dissimilar atoms of carbon in their molecules. Also, the first peak of NPA compared to four cyclic LMGs is unique. It should be noted that in the sII clathrate structure, the radius of large $5^{12}6^4$ cavities is 4.73 Å. The first peaks of $g_{o-p}$ for HFC-134a, and HCFH-141b occur at a distance of approximately 4.6 Å, while those for other LMGs are between 3.6 and 4.8 Å. Although there is some similarity between the peak arrangement of $g_{o-p}$ and $g_{o-c}$, the difference between the RDFs before and after hydrate dissolution is not substantial. In
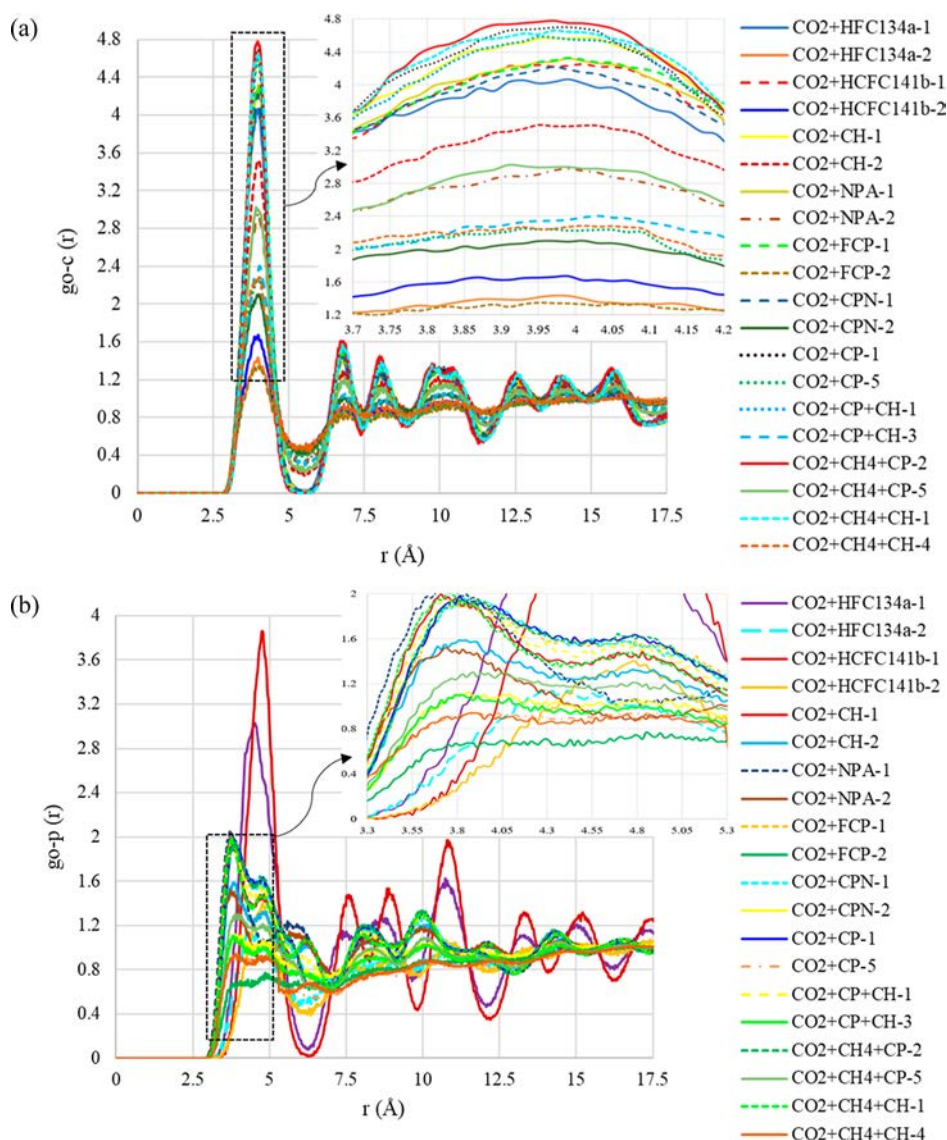
**Figure 12.** RDF between oxygen in $H_2O$ and carbon in $CO_2$ (a) and carbon promoters (b) below and above the equilibrium conditions.

addition, the heights of peaks for all systems after the dissociation reduce to a range of 0.6−1.6 Å.

Analysis of the dynamic properties of $CO_2$ sII hydrates helps to understand the time evolution of guest molecules in the solid phase. Figure 13 manifests the MSD for $CO_2$ and LMG molecules within sII hydrates below and above the equilibrium conditions. The results in Figure 13a,b demonstrate that $CO_2$ in the presence of F-promoters (HFC-134a, HCHC-141b, and FCP) moves faster. This behavior is followed by the systems encompassing NPA and CPN, while the presence of CP and CH gives the lowest MSD for $CO_2$ molecules, probably because of their weaker interactions with surrounding water molecules. Due to the relationship between movements of molecules with temperature, the slopes and values of the MSDs increase when the hydrates below the equilibrium curve are exposed to higher temperatures. Figure 13c,d displays that as $CO_2$ crystalline collapses, the MSD of $CO_2$ molecules drastically elevates by over 3 orders of magnitude. It is important to note that $CO_2$ molecules in the presence of CP and CH move slightly slower than other types of promoters. This may result from the symmetrical cyclic structure of these molecules. Also, by comparing MSDs in cases (c) and (d), it

can be inferred that the higher MSDs are related to the $CO_2$ hydrates in the presence of F-promoters. Figure 13e,f shows the MSDs of CP for $CO_2$ + CP and $CO_2$ + $CH_4$ + CP hydrates, respectively. To properly demonstrate the MSD alteration up to the hydrate equilibrium curve, Figure S1 displays the MSDs of the mentioned hydrates as a function of time at different thermodynamic conditions. As is shown, below the hydrate equilibrium curve, for example, $CO_2$ + CP-1 and $CO_2$ + CP-7, the lower temperature gives the MSD around 3.65 Å². However, on increasing the temperature up to the equilibrium state such as $CO_2$ + CP-4 or $CO_2$ + CP-9, MSD fluctuations and the values increase to nearly 3.8 Å². Also, MSD increases sharply once the temperature elevates to over the crystalline stability. The preceding expression is also valid for $CO_2$ + $CH_4$ + CP hydrate which indicates that the behavioral movements of the mixed gas in the hydrate state are similar to $CO_2$ + CP hydrate.

Table 4 recapitulates the diffusion coefficients of host and guest molecules of $CO_2$/$CO_2$ + $CH_4$ sII hydrates in the inclusion of different THPs. As is exhibited, before the thermodynamic stability conditions, the diffusion coefficients of guest and host molecules are not substantially increased by
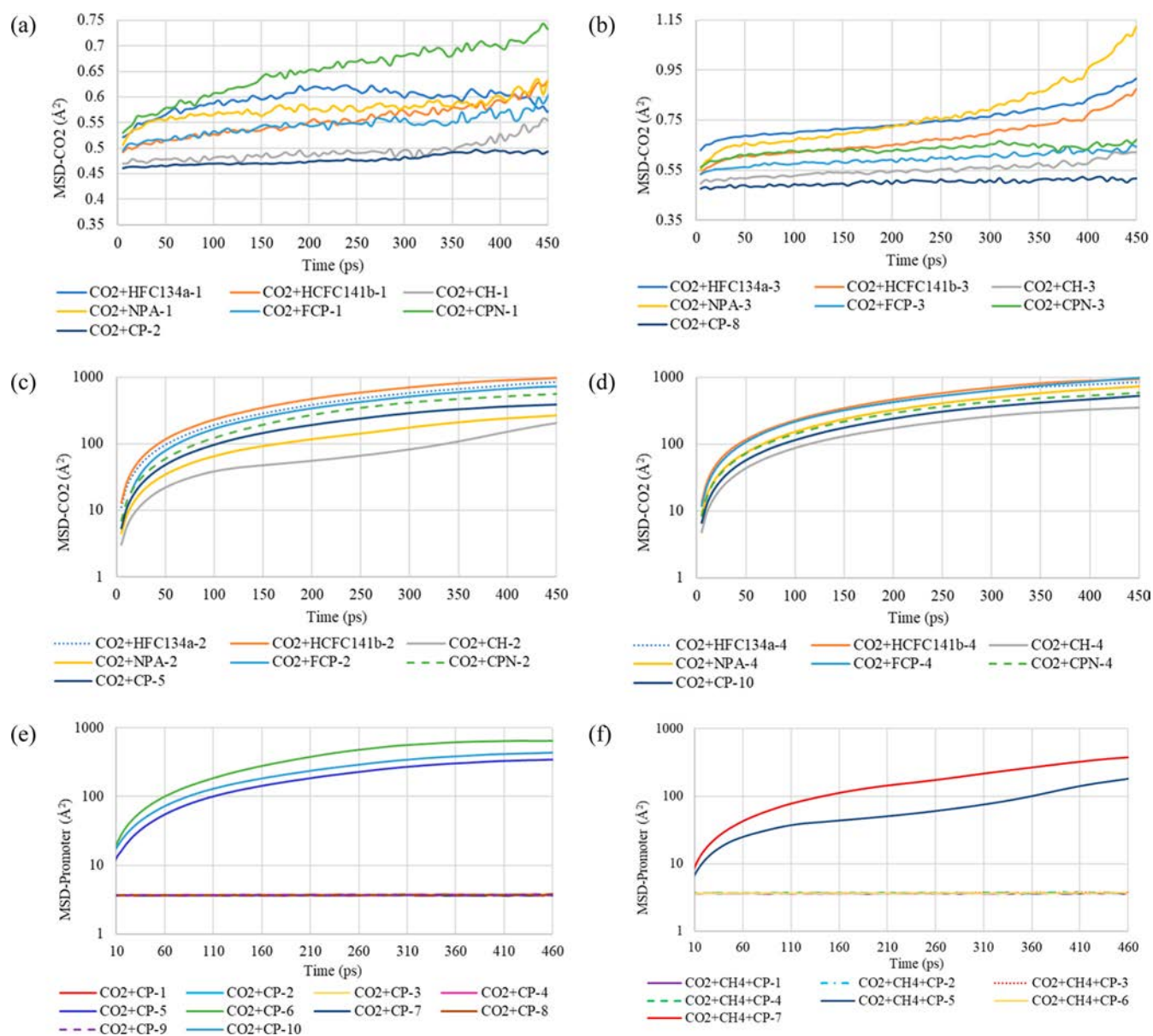
**Figure 13.** MSD-$CO_2$ for $CO_2$ hydrates in the presence of promoters at below equilibrium condition: (a) 1 and (b) 3 MPa; at above equilibrium condition: (c) 1 and (d) 3 MPa. The MSD-LMG for (e) $CO_2$ + CP hydrate and (f) $CO_2$ + $CH_4$ + CP hydrate.

the elevation of the temperature. This is due to the fact that increasing temperature gradually amplifies the water molecular vibrations in the hydrate cavities. In addition, the $CO_2$ diffusivity in the sII hydrates under the prevailing thermodynamic conditions is slightly higher than in the sI hydrate. This might be caused by the interactions between $CO_2$ and LMG molecules that exist in small and large cavities. It seems that the type of promoters and their molecular nature would be one of the contributors which influence the diffusion of other substances. For example, under 10 K subcooling, the diffusion coefficients of $CO_2$ in the presence of CP and NPA are 35 and 294 ($cm^2/s \times 10^{10}$), respectively. This is also valid for water molecules, but diffusivities of LMGs due to the greater sizes of large cages compared to small ones in the clathrate hydrates are mostly higher than those of $CO_2$. In addition, the lowest penetration of promoters in the hydrate state is for the presence of CP, while NPA possesses the highest diffusion coefficient. Similar behavior for the mixed gas hydrates or

mixed promoters can also be observed. Based on the results for the unstable conditions, the diffusion coefficients of components can be dramatically increased when the hydrate network is dissociated. This is attributed to the water's molecular rotations and movements instead of vibrations after the dissociation. Moreover, the diffusion coefficients of promoters above the hydrate equilibrium curve are less than those of water, $CO_2$, and $CH_4$. Furthermore, the diffusivities of guest and host molecules for $CO_2$ + F-promoters which have a fluorine atom in their molecular structures (FCP, HFC-134a, and HCFC-141b) are found to be higher than in other systems. This is also followed by the systems encompassing CPN and NPA.

## 4. CONCLUSIONS

In this study, the dynamic and structural properties of $CO_2$ and $NF_3$ sI clathrate hydrates systems at stable and unstable pressure−temperature conditions were explored. In addition,

**Table 4. Diffusion Coefficients of Host and Guests Molecules of sII Clathrate Hydrates (cm$^2$/s $\times$ 10$^{10}$)**

| hydrate guests | $D_{H_2O}$ | $D_{CO_2}$ | $D_{LMG}$ | hydrate guests | $D_{H_2O}$ | $D_{CO_2}$ | $D_{LMG}$ | $D_{CH_4}$ |
|---|---|---|---|---|---|---|---|---|
| CO$_2$ + HFC-134a-1 | 683 | 42 | 45 | CO$_2$ + CH$_4$ + CH-1 | 52 | 49 | 203 | 45 |
| CO$_2$ + HFC-134a-2 | 349,730 | 314,898 | 219,682 | CO$_2$ + CH$_4$ + CH-2 | 88 | 64 | 208 | 66 |
| CO$_2$ + HFC-134a-3 | 766 | 62 | 121 | CO$_2$ + CH$_4$ + CH-3 | 545 | 403 | 211 | 201 |
| CO$_2$ + HFC-134a-4 | 372,667 | 304,471 | 267,157 | CO$_2$ + CH$_4$ + CH-4 | 135,424 | 162,972 | 92,583 | 170,285 |
| CO$_2$ + HCFC-141b-1 | 66 | 320 | 34 | CO$_2$ + CH$_4$ + CH-5 | 67 | 55 | 188 | 64 |
| CO$_2$ + HCFC-141b-2 | 366,583 | 358,200 | 282,817 | CO$_2$ + CH$_4$ + CH-6 | 73 | 62 | 229 | 65 |
| CO$_2$ + HCFC-141b-3 | 263 | 48 | 61 | CO$_2$ + CH$_4$ + CH-7 | 980 | 405 | 247 | 438 |
| CO$_2$ + HCFC-141b-4 | 388,797 | 351,833 | 270,133 | CO$_2$ + CH$_4$ + CH-8 | 173,083 | 195,903 | 110,882 | 191,263 |
| CO$_2$ + CPN-1 | 177 | 78 | 147 | CO$_2$ + CH$_4$ + CP-1 | 27 | 26 | 94 | 30 |
| CO$_2$ + CPN-2 | 231,830 | 215,102 | 111,063 | CO$_2$ + CH$_4$ + CP-2 | 80 | 45 | 97 | 49 |
| CO$_2$ + CPN-3 | 237 | 44 | 168 | CO$_2$ + CH$_4$ + CP-3 | 86 | 46 | 107 | 57 |
| CO$_2$ + CPN-4 | 282,088 | 213,550 | 134,992 | CO$_2$ + CH$_4$ + CP-4 | 101 | 73 | 112 | 68 |
| CO$_2$ + FCP-1 | 102 | 53 | 158 | CO$_2$ + CH$_4$ + CP-5 | 84,281 | 94,352 | 79,864 | 107,176 |
| CO$_2$ + FCP-2 | 381,138 | 324,728 | 216,202 | CO$_2$ + CH$_4$ + CP-6 | 47 | 31 | 106 | 29 |
| CO$_2$ + FCP-3 | 295 | 58 | 149 | CO$_2$ + CH$_4$ + CP-7 | 140,467 | 171,649 | 92,897 | 162,252 |
| CO$_2$ + FCP-4 | 367,962 | 356,617 | 189,078 | CO$_2$ + CP + CH-1 | 58 | 47 | 178 | |
| CO$_2$ + NPA-1 | 212 | 48 | 326 | CO$_2$ + CP + CH-2 | 515 | 112 | 157 | |
| CO$_2$ + NPA-2 | 120,867 | 99,021 | 45,405 | CO$_2$ + CP + CH-3 | 116,449 | 112,615 | 75,618 | |
| CO$_2$ + NPA-3 | 381 | 224 | 294 | CO$_2$ + CP + CH-4 | 84 | 57 | 142 | |
| CO$_2$ + NPA-4 | 288,710 | 275,280 | 153,281 | CO$_2$ + CP + CH-5 | 145,354 | 131,279 | 83,298 | |
| CO$_2$ + CH-1 | 65 | 55 | 212 | CO$_2$ + CP-4 | 263 | 64 | 132 | |
| CO$_2$ + CH-2 | 67,683 | 71,245 | 40,867 | CO$_2$ + CP-5 | 194,809 | 146,797 | 87,149 | |
| CO$_2$ + CH-3 | 97 | 69 | 192 | CO$_2$ + CP-6 | 281,342 | 250,483 | 171,126 | |
| CO$_2$ + CH-4 | 199,350 | 197,867 | 109,333 | CO$_2$ + CP-7 | 11 | 2 | 20 | |
| CO$_2$ + CP-1 | 41 | 3 | 40 | CO$_2$ + CP-8 | 101 | 19 | 89 | |
| CO$_2$ + CP-2 | 49 | 35 | 78 | CO$_2$ + CP-9 | 180 | 79 | 151 | |
| CO$_2$ + CP-3 | 75 | 46 | 109 | CO$_2$ + CP-10 | 215,269 | 187,175 | 126,413 | |

the molecular behaviors of CO$_2$ double and mixed hydrates such as CO$_2$/CO$_2$ + CH$_4$ + promoters of sII clathrate hydrates were investigated. To study the process of hydrate dissociation, analysis parameters including RDF, lattice parameter, RCD, diffusion coefficient, hydrate density, potential energy, and dissociation enthalpy were utilized. According to the obtained MD results, the effect of temperature on the hydrate stability is found to be more than that of the pressure. The water molecules under the prevailing thermodynamic conditions vibrate around the guest molecules but keep the structure of hydrate cages intact, while the movements of both guest and host molecules increase with changing the temperature of the system. Once the guests overcome hydrogen bonds between the water molecules, they leave the cages and disturb the structure of the clathrate hydrate. Also, the partial occupancy of the cages by increasing the fluctuations in an ordered structure induces the process of hydrate dissociation. Therefore, CO$_2$ and NF$_3$ hydrates, regardless of the guest type, at 75% cage occupancy are more prone to change their structural form in comparison with 100% occupancy. The analysis of CO$_2$ + LMG hydrates demonstrate that the shape and type of LMG can markedly contribute to the clathrate hydrate stability. Generally, guest–water hydrogen bonding can weaken the water framework of clathrate hydrate. Therefore, NPA molecules in large cages can facilitate the process of CO$_2$ double hydrate dissociation by making new hydrogen bonds between hydroxyl groups and water molecules. Also, the structural analysis show that CO$_2$ in the presence of F-promoters (HFC-134a, HCHC-141b, and FCP) seems to be less stable than CO$_2$ sI hydrate. The effect of CPN is also moderate, while the most stable clathrate hydrate is for the presence of CP and CH in large cavities that helps CO$_2$

molecules stay in small cages. The simulation results of this work can be used to develop the performance of chemical additives in the optimization and management of hydrate-based CO$_2$ capture, storage, and utilization aims.

## ■ ASSOCIATED CONTENT

**ⓈI Supporting Information**

The Supporting Information is available free of charge at https://pubs.acs.org/doi/10.1021/acs.energyfuels.2c01396.

> MSD for sII hydrates under different prevailing thermodynamic conditions up to hydrate equilibrium curve (PDF)

## ■ AUTHOR INFORMATION

**Corresponding Authors**

**Agus Saptoro** − *Department of Chemical and Energy Engineering, Curtin University Malaysia, Miri 98009 Sarawak, Malaysia;* ⓞ orcid.org/0000-0002-1734-4788; Email: agus.saptoro@curtin.edu.my

**Amir H. Mohammadi** − *Discipline of Chemical Engineering, School of Engineering, University of KwaZulu-Natal, Durban 4041, South Africa;* ⓞ orcid.org/0000-0002-2947-1135; Email: amir_h_mohammadi@yahoo.com

**Authors**

**Saeid Sinehbaghizadeh** − *Department of Chemical and Energy Engineering, Curtin University Malaysia, Miri 98009 Sarawak, Malaysia*

**Sepideh Amjad-Iranagh** − *Department of Materials and Metallurgical Engineering, Amirkabir University of Technology, Tehran 15875-4313, Iran*

**Angnes Ngieng Tze Tiong** − *Department of Chemical and Energy Engineering, Curtin University Malaysia, Miri 98009 Sarawak, Malaysia*

Complete contact information is available at:
https://pubs.acs.org/10.1021/acs.energyfuels.2c01396

**Notes**
The authors declare no competing financial interest.

## ■ REFERENCES

(1) Ramanathan, V. Climate Change, Air Pollution, and Health: Common Sources, Similar Impacts, and Common Solutions. In *Health of People, Health of Planet and Our Responsibility*; Springer International Publishing: Cham, 2020; pp 49−59.

(2) Zheng, J.; Chong, Z. R.; Qureshi, M. F.; Linga, P. Carbon Dioxide Sequestration via Gas Hydrates: A Potential Pathway toward Decarbonization. *Energy Fuels* 2020, 34, 10529−10546.

(3) Zhang, H.; Xie, B.; Wang, Z. Effective Radiative Forcing and Climate Response to Short-Lived Climate Pollutants Under Different Scenarios. *Earths Future* 2018, 6, 857−866.

(4) Zaelke, D.; Borgford-Parnell, N. The Importance of Phasing down Hydrofluorocarbons and Other Short-Lived Climate Pollutants. *J. Environ. Sci. Stud.* 2015, 5, 169−175.

(5) Sovacool, B. K.; Griffiths, S.; Kim, J.; Bazilian, M. Climate Change and Industrial F-Gases: A Critical and Systematic Review of Developments, Sociotechnical Systems and Policy Options for Reducing Synthetic Greenhouse Gas Emissions. *Renew. Sustain. Energy Rev.* 2021, 141, 110759.

(6) Mota-Babiloni, A.; Makhnatch, P.; Khodabandeh, R. Recent Investigations in HFCs Substitution with Lower GWP Synthetic Alternatives: Focus on Energetic Performance and Environmental Impact. *Int. J. Refrig.* 2017, 82, 288−301.

(7) Hu, S.; Cabeza, L. F.; Yan, D. Review and Estimation of Global Halocarbon Emissions in the Buildings Sector. *Energy Build.* 2020, 225, 110311.

(8) Masson-Delmotte, V.; Zhai, P.; Pirani, A.; Connors, S.; Péan, C.; Chen, Y.; Goldfarb, L.; Gomis, M. I. *Climate Change 2021: The Physical Science Basis. Contribution of Working Group I to the Sixth Assessment Report of the Intergovernmental Panel on Climate Change*, 2021.

(9) Jovell, D.; Pou, J. O.; Llovell, F.; Gonzalez-Olmos, R. Life Cycle Assessment of the Separation and Recycling of Fluorinated Gases Using Ionic Liquids in a Circular Economy Framework. *ACS Sustain. Chem. Eng.* 2022, 10, 71−80.

(10) Ayittey, F. K.; Saptoro, A.; Kumar, P.; Wong, M. K. Energy-saving Process Configurations for Monoethanolamine-based CO2 Capture System. *Asia Pac. J. Chem. Eng.* 2021, 16, No. e2576.

(11) Ayittey, F. K.; Obek, C. A.; Saptoro, A.; Perumal, K.; Wong, M. K. Process Modifications for a Hot Potassium Carbonate-based CO2 Capture System: A Comparative Study. *Greenhouse Gases: Sci. Technol.* 2020, 10, 130−146.

(12) Ahn, C. K.; Kim, G.-H.; Lee, J. E.; Kim, K. S.; Kim, K. An SF6 Purification Process Utilizing Gas Hydrate Formation Developed for Electric Power Industry. *Sep. Purif. Technol.* 2019, 217, 221−228.

(13) Qureshi, M. F.; Dhamu, V.; Usadi, A.; Barckholtz, T. A.; Mhadeshwar, A. B.; Linga, P. CO2 Hydrate Formation Kinetics and Morphology Observations Using High-Pressure Liquid CO2 Applicable to Sequestration. *Energy Fuels* 2022, 1c03840 acs.energyfuels.

(14) Xie, N.; Tan, C.; Yang, S.; Liu, Z. Conceptual Design and Analysis of a Novel CO2 Hydrate-Based Refrigeration System with Cold Energy Storage. *ACS Sustain. Chem. Eng.* 2019, 7, 1502−1511.

(15) Sloan, E. D.; Koh, C. A. *Clathrate Hydrates of Natural Gases*, 3rd ed.; CRC Press, Taylor & Francis Group, Boca Raton, 2008.

(16) Rudolph, A.; El-Mohamad, A.; McHardy, C.; Rauh, C. Concentrating Model Solutions and Fruit Juices Using CO2 Hydrate Technology and Its Quantitative Effect on Phenols, Carotenoids, Vitamin C and Betanin. *Foods* 2021, 10, 626.

(17) Usman, M.; Rehman, Z.; Seong, K.; Song, M. H. Vacuum Degassing of Aqueous Tetrafluroethane (R134a) Solution during Seawater Desalination Utilizing Gas Hydrate. *Desalination* 2021, 498, 114754.

(18) Obara, S. y.; Tanaka, R. Waste Heat Recovery System for Nuclear Power Plants Using the Gas Hydrate Heat Cycle. *Appl. Energy* 2021, 292, 116667.

(19) Lim, J.; Choi, W.; Mok, J.; Seo, Y. Kinetic CO2 Selectivity in Clathrate-Based CO2 Capture for Upgrading CO2-Rich Natural Gas and Biogas. *Chem. Eng. J.* 2019, 369, 686−693.

(20) Yu, Y.-S.; Xu, C.-G.; Li, X.-S. Crystal Morphology-Based Kinetic Study of Carbon Dioxide-Hydrogen-Tetra-n-Butyl Ammonium Bromide Hydrates Formation in a Static System. *Energy* 2018, 143, 546−553.

(21) Zheng, J.; Bhatnagar, K.; Khurana, M.; Zhang, P.; Zhang, B.-Y.; Linga, P. Semiclathrate Based CO2 Capture from Fuel Gas Mixture at Ambient Temperature: Effect of Concentrations of Tetra-n-Butylammonium Fluoride (TBAF) and Kinetic Additives. *Appl. Energy* 2018, 217, 377−389.

(22) Jokar, S. M.; Wood, D. A.; Sinehbaghizadeh, S.; Parvasi, P.; Javanmardi, J. Transformation of Associated Natural Gas into Valuable Products to Avoid Gas Wastage in the Form of Flaring. *J. Nat. Gas Sci. Eng.* 2021, 94, 104078.

(23) Feyzi, V.; Mohebbi, V. Hybrid Hydrate-Membrane Post-Combustion CO2 Capture: A Conceptual Process Design and Analyses. *Ind. Eng. Chem. Res.* 2020, 59, 13132−13142.

(24) Surovtseva, D.; Amin, R.; Barifcani, A. Design and Operation of Pilot Plant for CO2 Capture from IGCC Flue Gases by Combined Cryogenic and Hydrate Method. *Chem. Eng. Res. Des.* 2011, 89, 1752−1757.

(25) Xu, C.; Li, X.; Cai, J.; Chen, Z. Hydrate-Based Carbon Dioxide Capture from Simulated Integrated Gasification Combined Cycle Gas. *J. Nat. Gas Chem.* 2012, 21, 501−507.

(26) Mu, L.; Zhang, Q.; Cui, Q. Experimental Study on CO2 Capture from Simulated Flue Gas with an Adsorption−Hydration Method. *Ind. Eng. Chem. Res.* 2021, 60, 3411−3420.

(27) Dufour, T.; Hoang, H. M.; Oignet, J.; Osswald, V.; Fournaison, L.; Delahaye, A. Experimental and Modelling Study of Energy Efficiency of CO2 Hydrate Slurry in a Coil Heat Exchanger. *Appl. Energy* 2019, 242, 492−505.

(28) Wang, X.; Zhang, F.; Lipiński, W. Carbon Dioxide Hydrates for Cold Thermal Energy Storage: A Review. *Sol. Energy* 2020, 211, 11−30.

(29) Yin, Z.; Zheng, J.; Kim, H.; Seo, Y.; Linga, P. Hydrates for Cold Energy Storage and Transport: A Review. *Adv. Appl. Energy* 2021, 2, 100022.

(30) Claßen, T.; Seidl, P.; Loekman, S.; Gatternig, B.; Rauh, C.; Delgado, A. Review on the Food Technological Potentials of Gas Hydrate Technology. *Curr. Opin. Food Sci.* 2019, 29, 48−55.

(31) Peters, T. B.; Smith, J. L.; Brisson, J. G. Transfer Process Limited Models for CO2 Perception in CO2 Hydrate Desserts. *J. Food Eng.* 2013, 115, 285−291.

(32) Yang, M.; Song, Y.; Jiang, L.; Liu, Y.; Li, Y. CO2 Hydrate Formation Characteristics in a Water/Brine-Saturated Silica Gel. *Ind. Eng. Chem. Res.* 2014, 53, 10753−10761.

(33) Kang, K. C.; Linga, P.; Park, K.-n.; Choi, S.-J.; Lee, J. D. Seawater Desalination by Gas Hydrate Process and Removal Characteristics of Dissolved Ions. *Desalination* 2014, 353, 84−90.

(34) Seo, Y.; Moon, D.; Lee, C.; Park, J.-W.; Kim, B.-S.; Lee, G.-W.; Dotel, P.; Lee, J.-W.; Cha, M.; Yoon, J.-H. Equilibrium, Kinetics, and Sspectroscopic Studies of SF6 Hydrate in NaCl Electrolyte Solution. *Environ. Sci. Technol.* 2015, 49, 6045−6050.

(35) Tanaka, M.; Tsugane, K.; Suga, D.; Tomura, S.; Ohmura, R.; Yasuda, K. Simultaneous Crystallization of Cyclopentane Hydrate and Sodium Chloride for Desalination and Salt Manufacture. *ACS Sustain. Chem. Eng.* **2021**, *9*, 9078−9084.

(36) Karamoddin, M.; Varaminian, F. Water Desalination Using R141b Gas Hydrate Formation. *Desalin. Water Treat.* **2014**, *52*, 2450−2456.

(37) Wang, Y.; Lu, J.; Qi, J.; Lang, X.; Fan, S.; Yu, C.; Li, G. High Selectivity $CO_2$ Capture from Biogas by Hydration Separation Based on the Kinetic Difference in the Presence of 1,1-Dichloro-1-Fluoroethane. *Energy Fuels* **2021**, *35*, 10689−10702.

(38) Maniavi Falahieh, M.; Bonyadi, M.; Lashanizadegan, A. A New Hybrid Desalination Method Based on the $CO_2$ Gas Hydrate and Capacitive Deionization Processes. *Desalination* **2021**, *502*, 114932.

(39) Ho-Van, S.; Bouillot, B.; Douzet, J.; Babakhani, S. M.; Herri, J. M. Cyclopentane Hydrates − A Candidate for Desalination? *J. Environ. Chem. Eng.* **2019**, *7*, 103359.

(40) Hatakeyama, T.; Aida, E.; Yokomori, T.; Ohmura, R.; Ueda, T. Fire Extinction Using Carbon Dioxide Hydrate. *Ind. Eng. Chem. Res.* **2009**, *48*, 4083−4087.

(41) Herslund, P. J.; Daraboina, N.; Thomsen, K.; Abildskov, J.; von Solms, N. Measuring and Modelling of the Combined Thermodynamic Promoting Effect of Tetrahydrofuran and Cyclopentane on Carbon Dioxide Hydrates. *Fluid Phase Equilib.* **2014**, *381*, 20−27.

(42) Bai, J.; Zhen, X.; Yan, K.; Li, P.; Fang, S.; Chang, C. The Effect of Additive Molecular Diameters on the Hydrate-Based CO2 Capture from Simulated Biogas. *Fuel* **2020**, *278*, 118370.

(43) Kondo, Y.; Alavi, S.; Murayama, K.; Ruiz, A.; Takeya, S.; Ohmura, R. Effect of Help-Guest Size and Hydrogen Bonding on the Stability of N-Methylpiperidine Structure H Clathrate Hydrate. *J. Phys. Chem. C* **2020**, *124*, 5978−5986.

(44) Kondo, Y.; Alavi, S.; Takeya, S.; Ohmura, R. Characterization of the Clathrate Hydrate Formed with Fluoromethane and Pinacolone: The Thermodynamic Stability and Volumetric Behavior of the Structure H Binary Hydrate. *J. Phys. Chem. B* **2021**, *125*, 328−337.

(45) Alavi, S.; Ripmeester, J. A. Effect of Small Cage Guests on Hydrogen Bonding of Tetrahydrofuran in Binary Structure II Clathrate Hydrates. *J. Chem. Phys.* **2012**, *137*, 54712.

(46) Moudrakovski, I. L.; Udachin, K. A.; Alavi, S.; Ratcliffe, C. I.; Ripmeester, J. A. Facilitating Guest Transport in Clathrate Hydrates by Tuning Guest-Host Interactions. *J. Chem. Phys.* **2015**, *142*, 74705.

(47) Phan, A.; Schlösser, H.; Striolo, A. Molecular Mechanisms by Which Tetrahydrofuran Affects $CO_2$ Hydrate Growth: Implications for Carbon Storage. *Chem. Eng. J.* **2021**, *418*, 129423.

(48) Inkong, K.; Yodpetch, V.; Veluswamy, H. P.; Kulprathipanja, S.; Rangsunvigit, P.; Linga, P. Hydrate-Based Gas Storage Application Using Simulated Seawater in the Presence of a Co-Promoter: Morphology Investigation. *Energy Fuels* **2022**, *36*, 1100−1113.

(49) Fang, B.; Ning, F.; Cao, P.; Peng, L.; Wu, J.; Zhang, Z.; Vlugt, T. J. H.; Kjelstrup, S. Modeling Thermodynamic Properties of Propane or Tetrahydrofuran Mixed with Carbon Dioxide or Methane in Structure-II Clathrate Hydrates. *J. Phys. Chem. C* **2017**, *121*, 23911−23925.

(50) Takeuchi, F.; Hiratsuka, M.; Ohmura, R.; Alavi, S.; Sum, A. K.; Yasuoka, K. Water Proton Configurations in Structures I, II, and H Clathrate Hydrate Unit Cells. *J. Chem. Phys.* **2013**, *138*, 124504.

(51) Meza, J. C. Steepest Descent. *Wiley Interdiscip. Rev. Comput. Stat.* **2010**, *2*, 719−722.

(52) Arias, T. A.; Payne, M. C.; Joannopoulos, J. D. Ab Initio Molecular-Dynamics Techniques Extended to Large-Length-Scale Systems. *Phys. Rev. B: Condens. Matter Mater. Phys.* **1992**, *45*, 1538−1549.

(53) Frenkel, D.; Smit, B. *Understanding Molecular Simulation*; Academic Press: San Diego, 2000.

(54) Dauber-Osguthorpe, P.; Roberts, V. A.; Osguthorpe, D. J.; Wolff, J.; Genest, M.; Hagler, A. T. Structure and Energetics of Ligand Binding to Proteins:Escherichia Coli Dihydrofolate Reductase-Trimethoprim, a Drug-Receptor System. *Proteins Struct. Funct. Genet.* **1988**, *4*, 31−47.

(55) Sun, H. COMPASS: An Ab Initio Force-Field Optimized for Condensed-Phase ApplicationsOverview with Details on Alkane and Benzene Compounds. *J. Phys. Chem. B* **1998**, *102*, 7338−7364.

(56) Andersen, H. C. Molecular Dynamics Simulations at Constant Pressure and/or Temperature. *J. Chem. Phys.* **1980**, *72*, 2384−2393.

(57) Berendsen, H. J. C.; Postma, J. P. M.; van Gunsteren, W. F.; DiNola, A.; Haak, J. R. Molecular Dynamics with Coupling to an External Bath. *J. Chem. Phys.* **1984**, *81*, 3684−3690.

(58) Song, J.; Sun, Z.-G.; Li, R.; Dai, M.-L. Effect of HFE254 or Cyclopentanone on Phase Equilibrium Dissociation Conditions for Carbon Dioxide Hydrate. *J. Chem. Eng. Data* **2021**, *66*, 2177−2181.

(59) Moon, S.; Ahn, Y.-H.; Kim, H.; Hong, S.; Koh, D.-Y.; Park, Y. Secondary Gaseous Guest-Dependent Structures of Binary Neopentyl Alcohol Hydrates and Their Tuning Behavior for Potential Application to $CO_2$ Capture. *Chem. Eng. J.* **2017**, *330*, 890−898.

(60) Matsumoto, Y.; Makino, T.; Sugahara, T.; Ohgaki, K. Phase Equilibrium Relations for Binary Mixed Hydrate Systems Composed of Carbon Dioxide and Cyclopentane Derivatives. *Fluid Phase Equilib.* **2014**, *362*, 379−382.

(61) Wang, M.; Sun, Z.-G.; Li, C.-H.; Zhang, A.-J.; Li, J.; Li, C.-M.; Huang, H.-F. Equilibrium Hydrate Dissociation Conditions of $CO_2$ + HCFC141b or Cyclopentane. *J. Chem. Eng. Data* **2016**, *61*, 3250−3253.

(62) Mohammadi, A. H.; Richon, D. Phase Equilibria of Clathrate Hydrates of Methyl Cyclopentane, Methyl Cyclohexane, Cyclopentane or Cyclohexane+carbon Dioxide. *Chem. Eng. Sci.* **2009**, *64*, 5319−5322.

(63) Lee, H.; Park, C.; Lee, E.; Lee, J. D.; Kim, Y. Effect of HFC-134a as a Promoter of $CO_2$ Hydrate: Phase Equilibrium, Dissociation Enthalpy and Kinetics. *J. Chem. Eng. Data* **2017**, *62*, 4395−4400.

(64) Sinehbaghizadeh, S.; Roosta, A.; Rezaei, N.; Ghiasi, M. M.; Javanmardi, J.; Zendehboudi, S. Evaluation of Phase Equilibrium Conditions of Clathrate Hydrates Using Connectionist Modeling Strategies. *Fuel* **2019**, *255*, 115649.

(65) Sinehbaghizadeh, S.; Javanmardi, J.; Roosta, A.; Mohammadi, A. H. Estimation of the Dissociation Conditions and Storage Capacities of Various SH Clathrate Hydrate Systems Using Effective Deterministic Frameworks. *Fuel* **2019**, *247*, 272−286.

(66) Sinehbaghizadeh, S.; Javanmardi, J.; Mohammadi, A. H. Phase Stability Conditions of Clathrate Hydrates in the (Methane + 3-Methyl-1-Butanol + Water), (Methane + 3,3-Dimethyl-2-Butanone + Water) and (Methane + 2,3-Dimethyl-2-Butene + Water) Systems: Experimental Measurements and Thermodynamic Modeling. *J. Chem. Thermodyn.* **2018**, *125*, 64−70.

(67) Sinehbaghizadeh, S.; Javanmardi, J.; Roosta, A.; Mohammadi, A. H. A Fugacity Approach for Prediction of Phase Equilibria of Methane Clathrate Hydrate in Structure H. *Phys. Chem. Res.* **2017**, *5*, 465−481.

(68) Davidson, D. W.; Garg, S. K.; Ratcliffe, C. I.; Tse, J. S.; Gough, S. R. Characterization of a Clathrate Hydrate of Nitrogen Trifluoride. *Can. J. Chem.* **1984**, *62*, 1229−1235.

(69) Liu, N.; Zhu, H.; Zhou, J.; Yang, L.; Liu, D. Molecular Dynamics Simulations on Formation of $CO_2$ Hydrate in the Presence of Metal Particles. *J. Mol. Liq.* **2021**, *331*, 115793.

(70) Kondori, J.; James, L.; Zendehboudi, S. Molecular Scale Modeling Approach to Evaluate Stability and Dissociation of Methane and Carbon Dioxide Hydrates. *J. Mol. Liq.* **2020**, *297*, 111503.

(71) Mahmoodi, M. H.; Manteghian, M.; Naeiji, P. Study the Effect of Ag Nanoparticles on the Kinetics of $CO_2$ Hydrate Growth by Molecular Dynamics Simulation. *J. Mol. Liq.* **2021**, *343*, 117668.

(72) Chialvo, A. A.; Houssa, M.; Cummings, P. T. Molecular Dynamics Study of the Structure and Thermophysical Properties of Model SI Clathrate Hydrates. *J. Phys. Chem. B* **2002**, *106*, 442−451.

(73) Ballard, L.; Sloan, E. D. The next Generation of Hydrate Prediction IV. *Fluid Phase Equilib.* **2004**, *216*, 257−270.

(74) Takeya, S.; Muromachi, S.; Yamamoto, Y.; Umeda, H.; Matsuo, S. Preservation of $CO_2$ Hydrate under Different Atmospheric Conditions. *Fluid Phase Equilib.* **2016**, *413*, 137−141.

(75) Ning, F. L.; Glavatskiy, K.; Ji, Z.; Kjelstrup, S.; Vlugt, T. J. Compressibility, Thermal Expansion Coefficient and Heat Capacity of $CH_4$ and $CO_2$ Hydrate Mixtures Using Molecular Dynamics Simulations. *Phys. Chem. Chem. Phys.* **2015**, *17*, 2869−2883.

(76) Hansen, T. C.; Falenty, A.; Kuhs, W. F. Lattice Constants and Expansivities of Gas Hydrates from 10 K up to the Stability Limit. *J. Chem. Phys.* **2016**, *144*, 054301.

(77) Belosludov, R. V.; Zhdanov, R. K.; Bozhko, Y. Y.; Gets, K. V.; Subbotin, O. S.; Kawazoe, Y.; Belosludov, V. R. Lattice Dynamics Study of the Thermal Expansion of $C_3H_8$-, $CH_4$-, $CF_4$-, $CO_2$-, Xe-, and $N_2$-Hydrates. *Energy Fuels* **2020**, *34*, 12771−12778.

(78) Kondori, J.; Zendehboudi, S.; James, L. New Insights into Methane Hydrate Dissociation: Utilization of Molecular Dynamics Strategy. *Fuel* **2019**, *249*, 264−276.

(79) Sabil, K. M.; Witkamp, G.-J. J.; Peters, C. J. Estimations of Enthalpies of Dissociation of Simple and Mixed Carbon Dioxide Hydrates from Phase Equilibrium Data. *Fluid Phase Equilib.* **2010**, *290*, 109−114.

(80) Shpakov, V. P.; Tse, J. S.; Tulk, C. A.; Kvamme, B.; Belosludov, V. R. Elastic Moduli Calculation and Instability in StructureI Methane Clathrate Hydrate. *Chem. Phys. Lett.* **1998**, *282*, 107−114.

(81) Ferdows, M.; Ota, M. Density of $CO_2$ Hydrate by Monte Carlo Simulation. *Proc. Inst. Mech. Eng., Part C* **2006**, *220*, 691−696.

(82) Henley, H.; Thomas, E.; Lucia, A. Density and Phase Equilibrium for Ice and Structure I Hydrates Using the Gibbs−Helmholtz Constrained Equation of State. *Chem. Eng. Res. Des.* **2014**, *92*, 2977−2991.

(83) Allen, M. P.; Tildesley, D. J. *Computer Simulation of Liquids*; Oxford University Press, 2017.

(84) Lo, H.; Lee, M.-T.; Lin, S.-T. Water Vacancy Driven Diffusion in Clathrate Hydrates: Molecular Dynamics Simulation Study. *J. Phys. Chem. C* **2017**, *121*, 8280−8289.

(85) Liang, S.; Liang, D.; Wu, N.; Yi, L.; Hu, G. Molecular Mechanisms of Gas Diffusion in $CO_2$ Hydrates. *J. Phys. Chem. C* **2016**, *120*, 16298−16304.

(86) Lu, W.; Guo, H.; Chou, I. M.; Burruss, R. C.; Li, L. Determination of Diffusion Coefficients of Carbon Dioxide in Water between 268 and 473K in a High-Pressure Capillary Optical Cell with in Situ Raman Spectroscopic Measurements. *Geochim. Cosmochim. Acta* **2013**, *115*, 183−204.

(87) Jendi, Z. M.; Servio, P.; Rey, A. D. Molecular Mobility in Carbon Dioxide Hydrates. *Mol. Syst. Des. Eng.* **2017**, *2*, 500−506.

(88) Staykova, D. K.; Kuhs, W. F.; Salamatin, A. N.; Hansen, T. Formation of Porous Gas Hydrates from Ice Powders: Diffraction Experiments and Multistage Model. *J. Phys. Chem. B* **2003**, *107*, 10299−10311.

(89) Suzuki, S.; Yasuda, K.; Katsuta, Y.; Matsumoto, Y.; Hashimoto, S.; Sugahara, T.; Ohgaki, K. Isothermal Phase Equilibria for the $CO_2$ + 1,1,1,2-Tetrafluoroethane and $CO_2$ + 1,1-Difluoroethane Mixed-Gas Hydrate Systems. *J. Chem. Eng. Data* **2013**, *58*, 780−784.

(90) Choi, S.; Park, J.; Park, J. H.; Kim, S.-C.; Won, S. O.; Kang, Y. T. Study on $CO_2$ Hydrate Formation Characteristics with Promoters for $CO_2$ Capture and Cold Thermal Energy Transportation. *J. Clean. Prod.* **2021**, *295*, 126392.

(91) Hong, S.; Moon, S.; Lee, Y.; Lee, S.; Park, Y. Investigation of Thermodynamic and Kinetic Effects of Cyclopentane Derivatives on $CO_2$ Hydrates for Potential Application to Seawater Desalination. *Chem. Eng. J.* **2019**, *363*, 99−106.
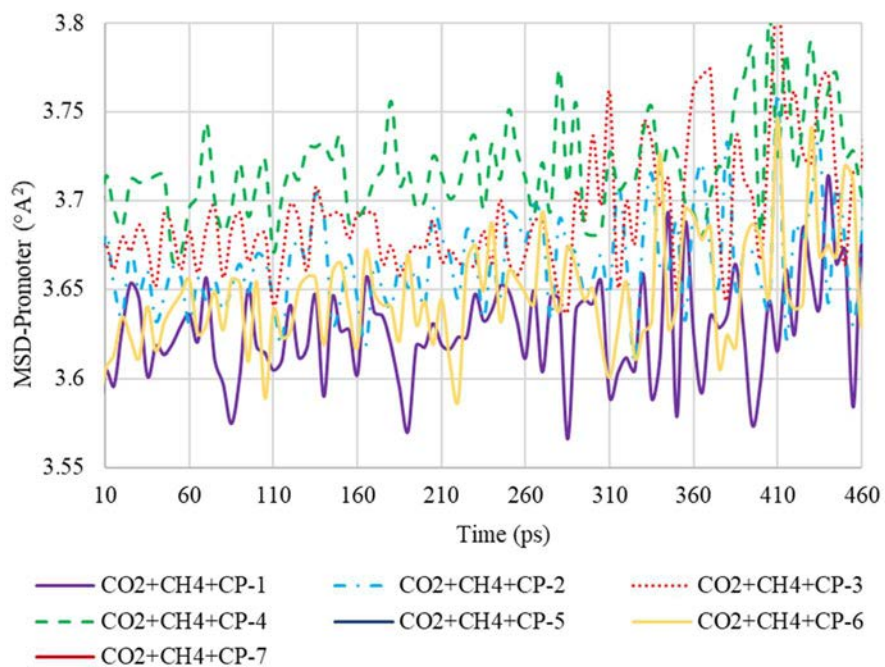
# Supporting Information

(a)
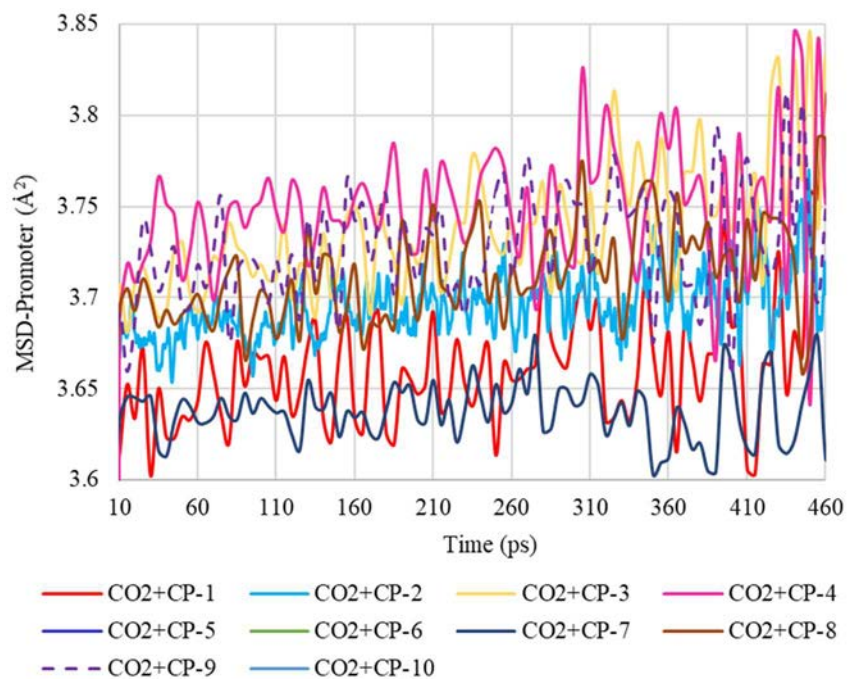


(b)



Figure S1: The MSD-LMG for (a) $CO_2$+CP and (b) $CO_2$+$CH_4$+CP hydrates at different thermodynamic conditions up to hydrate equilibrium curve.

# Chapter 6 (Objective 4): Stability and dissociation of clathrate hydrates of pure/ mixed CO₂ structure-H (sH) hydrates in the existence of different amino acids and sH thermodynamic hydrate promoters

As Figure 13 (step 5) of the chapter 1 indicated, the positive and negative effects of different sI and sII thermodynamic hydrate promoters (THPs) during the hydrate stability and the dissociation were discussed in the previous chapter. Hence, this chapter deals with the influences of sH hydrate promoters, amino acids and the role of gas species. The selected sH hydrate promoters as liquid hydrocarbons belongs to different molecular groups such as alkanes, alkenes, and cylcoalkanes. Also, amino acids were chosen frm polar and nonpolar types.

Since the clathrate hydrates have been categorized into three various structures (sI, sII, sH), their properties such as operating conditions, storage capacities, and thermophysical/ mechanical characteristics are unique. Between these structures, the experimental evidence suggests that sH hydrates would be an appropriate alternative for $CO_2$ hydrate-based applications. This structure can be formed when the liquid hydrocarbons larger than those studied in the previous chapter are presented in the system. Hence, in this chapter, the effects of sH thermodynamic hydrate promoters (THPs) on the stability and the dissociation of pure/ mixed $CO_2$ hydrates were investigated.

This chapter was published as a research paper in Energy & Fuels Journal:

Sinehbaghizadeh, S., Saptoro, A., Amjad, S., Mohammadi, A.H. Molecular dynamics insights into the stability and dissociation of structure-H clathrate hydrates in the presence of different amino acids, gas species and sH hydrate formers, *Energy & Fuels Journal,* 2023, 37 (14),10550-10566, ACS.

# Molecular Dynamics Simulations of the Stability and Dissociation of Structure-H Clathrate Hydrates in the Presence of Different Amino Acids, Gas Species, and sH Hydrate Formers

Saeid Sinehbaghizadeh, Agus Saptoro,* Sepideh Amjad-Iranagh,* and Amir H. Mohammadi*

ACCESS | 📊 Metrics & More | 📖 Article Recommendations

**ABSTRACT:** Hydrate-based technologies for $CO_2$ capture and storage or utilization (CCSU) have been perceived as a novel and effective option to arrest increasing concentrations of $CO_2$ in the atmosphere. In this regard, structure-H (sH) of the clathrate hydrates in terms of the operating conditions and storage capacity would be a proper alternative. In addition, the utilization of organic amino acids is able to improve the features of $CO_2$ hydrate-based approaches. However, the microscopic influences of such components on $CO_2$ sH hydrates are mostly unexplored, and the effects of associated gas species as well as sH large guests at the molecular level still need to be studied. This work investigates the stability and dissociation of $CO_2$ sH hydrates in the existence of $CH_4$, $N_2$, $H_2$, amino acids, and various large molecular guest substances via classical molecular dynamics (MD) simulations. Results reveal that the hydroxyl of amino acids, by attaching to the surrounding water molecules of the sH hydrate, weakens the hydrogen bonds of the water molecules in the sH clathrate. Also, the effects of such a physical approach are relevant to the operating conditions. Unlike $CH_4$ and $N_2$, the presence of $H_2$ molecules significantly induces the mobility of molecules in the clathrate network, which was even intensified when double cage occupancy for $H_2$ molecules was considered. This may be due to the significantly lower molecular weight of this molecule in comparison with either $CH_4$ or $N_2$. Moreover, in comparison to full occupation, the partial occupancy of small cages can contribute to the distribution of water molecules in the sH clathrate hydrate. Among investigated sH hydrate formers, adamantane and 1,1-dimethyl cyclohexane were identified as the most stable sH hydrates, which suggests that the cyclic hydrocarbons with larger carbon numbers may help large cages remain integrated.
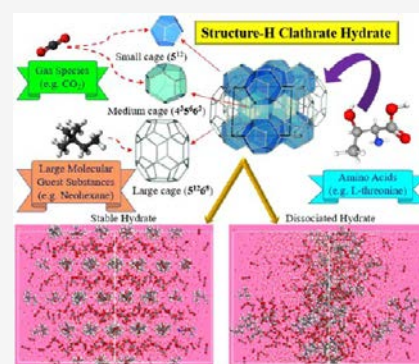
## 1. INTRODUCTION

As a promising mitigation, carbon capture and sequestration & utilization (CCSU) technologies are being developed to reduce the $CO_2$ emissions from different industrial sources. To date, several methods such as membranes, cryogenic process, absorption, and adsorption have been employed. In this regard, one of the newly suggested technologies to split $CO_2$ from the gas mixture is the utilization of hydrate-based method.[1] Clathrate hydrates (gas hydrates) are ice-like crystalline compounds in which gas and/or some volatile liquid molecules, known as guests, are trapped within a lattice of water molecules as hosts, forming a solid structure that can be stable at high pressures and low temperatures. The guest molecules are located inside the water molecules through hydrogen bonds between them which create cage-like shapes. There are different clathrate hydrate structures, the most common of which are structure I (sI), sII, and sH. They can be formed based on molecular characteristics such as the diameter of guest molecules and their molecular structure. The crystal of sI and sII hydrates is the cubic shape containing two tips of the cages, while that of sH hydrates is a hexagonal form including

three types of clathrate hydrate cages.[2] To form sH clathrate hydrates, two different guests are required: the gas species (known as help gas) capable of forming sI or sII (e.g., $CO_2$, $N_2$, $CH_4$, $H_2$) and the presence of large molecular guest substances (LMGSs) with a molecular diameter ranging between 7.5 Å to over 9 Å.

Since the pressure of $CO_2$ hydrate formation is less than other associated gas species, e.g., $CH_4$, $N_2$, and $H_2$, this component, through the hydrate formation and dissociation stages, can simply be eliminated from either industrial emitted gases like flue gas or fuel and landfill gases.[3] The $CO_2$ separation stage can be followed by the next steps such as $CO_2$ transportation, sequestration, or utilization using the suggested hydrate-based processes. Recently, we have reviewed

**Table 1. Summary of the Investigated $CO_2$ sH Hydrates Including Different Amino Acids, Gas Species, and sH Hydrate Formers[a]**

| case NO. | | simulated sH hydrates |
|---|---|---|
| C1 | $CO_2$ sH hydrates | $CO_2$ + 11DMCH (1,1-dimethyl cyclohexane) |
| C2 | | $CO_2$ + 2MCHN (2-methyl cyclohexanone) |
| C3 | | $CO_2$ + 223TMB (2,2,3-trimethyl butane) |
| C4 | | $CO_2$ + Ad. (adamantane) |
| C5 | | $CO_2$ + Cy. (cyclooctane) |
| C6 | | $CO_2$ + NH (neohexane) |
| C7 | $CO_2$ + NH sH hydrate + amino acids | $CO_2$ + NH + Gly. (glycine, nonpolar) |
| C8 | | $CO_2$ + NH + Ser. (serine, polar) |
| C9 | | $CO_2$ + NH + L-thr. (L-threonine, polar) |
| C10 | | $CO_2$ + NH + L-val. (L-valine, nonpolar) |
| C11 | | $CO_2$ + NH + Leu. (leucine, nonpolar) |
| C12 | mixed sH hydrates | $CO_2$ (50%) + $CH_4$ (50%) + NH |
| C13 | | $CO_2$ (50%) + $CH_4$ (50%) + Cy. |
| C14 | | $CO_2$ (80%) + $N_2$ (20%) + NH |
| C15 | | $CO_2$ (80%) + $N_2$ (20%) + Cy. |
| C16 | | $CO_2$ (50%) + $CH_4$ (50%) + NH + Cy. |
| C17 | | $CO_2$ (45%) + $CH_4$ (45%) + NH (90% occupancy) |
| C18 | | $CO_2$ (75%) + $N_2$ (15%) + NH (90% occupancy) |
| C19 | | $CO_2$ (98%) + $H_2$ (2%) + NH |
| C20 | | $CO_2$ (96%) + $H_2$ (4%) + NH (double $H_2$ occupancy) |

[a]Percentages refer to the number of gas molecules in both small and medium cavities of sH hydrates.

a large number of $CO_2$ hydrate applications and their characteristics at either macroscopic or molecular scales.[4,5] These methods, due to the higher melting enthalpy in comparison with conventional coolants, can be designed for secondary refrigeration systems.[6] Such methodologies can also be used for wastewater treatment, e.g., removing salt ions and effluent concentration.[7] Also, introducing viable hybrid approaches including hydrate formation−dissociation stages with more efficiency than their standalone utilizations have been newly developed.[8−11] Moreover, different gas species can be stored within the crystalline structures of the hydrates, which make them a potentially attractive option for storage and transportation. The use of gas hydrates for gas storage has several advantages over traditional methods, including a suitable storage capacity, low environmental impact, and low cost.[12] However, the stability of the gas hydrates can be affected by changes in temperature and pressure, which can lead to the release of the trapped gases. Between the three structures, sH clathrate hydrate has more potential for gas storage due to its higher storage capacity.[13] Owing to the fact that $CO_2$ sH hydrate formers can generate hydrates at lower operating conditions than $CO_2$ sI hydrate, they require notably lower energy for the process of $CO_2$ hydrate formation.[14−16] However, toward being industrialized, the dissociation of $CO_2$ sH hydrates for the above-mentioned applications could be explored in more detail. For example, with the inclusion of organic and biodegradable additives like amino acids, the dissociation stage needs to be analyzed.[17−19]

Amino acids are mostly labeled as the monomer blocks of proteins that can be found in the human diet. The makeup of these components is often an organic side chain, an amino group, and a carboxyl group.[19,20] Considering their side chains, they can be categorized into nonpolar (hydrophobic) and polar (hydrophilic) classifications.[21−23] On the basis of the hydropathy scale, amino acids with more hydrophobicity possess the greater hydropathy index. For example, the side chain and hydropathy index of some amino acids (studied in

this work) are presented here in the parenthesis: nonpolar glycine (H, −0.4); polar serine (HO−$CH_2$, −0.8); polar L-threonine (CH(OH)$CH_3$, −0.7); nonpolar Leucine ($CH_2$CH-($CH_3$), 3.8); and nonpolar L-valine (CH($CH_3$)$_2$, 4.2). Hence, the first three components would be slightly hydrophilic, while the last two materials are the most hydrophobic. However, this rule has some exceptions. Taking L-tryptophan as an instance, it tends to get close to the hydrophilic end of the spectrum, while it is still categorized between hydrophobic amino acids.[24−27] From an environmental perspective, these substances possess the advantage of being biodegradable and less expensive than the synthetic chemicals mostly offered as kinetic hydrate promoters (KHPs).[28] Since these components can be used as efficient KHPs, their impacts on the hydrate stability and during the dissociation would also be substantial.[29,30] Amino acids have the potential to improve the stability, selectivity, and transport properties of clathrate hydrates, which could have important applications in energy storage, gas separation, and other areas. They can also be used to selectively capture certain gases in clathrate hydrates, which could be useful for gas separation technologies.[31] For example, certain amino acids have been found to preferentially help to form clathrate hydrates with $CO_2$ over $CH_4$.[32,33]

Besides the experimental explorations of $CO_2$ hydrates in the presence of additives at the macroscopic scale, analysis at the molecular level would either verify/complete the previous investigations or reveal new findings toward further improvements. In this regard, to comprehend the effects of bio-friendly amino acids on $CH_4$[34−38] and $CO_2$[39] sI hydrate formation and dissociation mechanisms, some studies using molecular dynamics (MD) simulations have been performed. Also, we recently employed MD simulations to understand the growth and dissociation of $CO_2$ clathrate hydrates in the existence of various thermodynamic and kinetic promoters.[40,41] Since organic, eco-friendly components such as amino acids can play a positive role in hydrate applications and sH hydrates would also be the proper alternative for such aims,
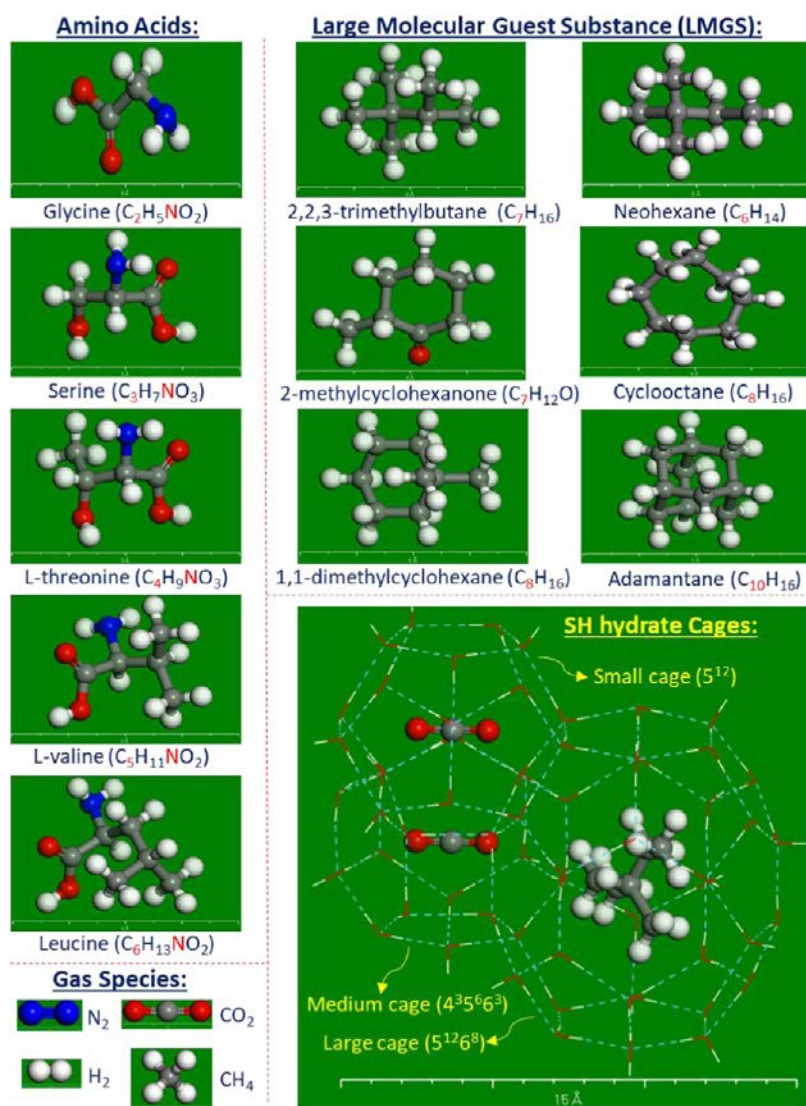
**Figure 1.** Molecular structure of gas species, sH hydrate formers, amino acids, and sH hydrate cages.

comprehending the impressions of these components on the stability and dissociation of sH clathrate hydrates would be crucial. However, they are still poorly understood at a molecular level. In addition, $CH_4$, $N_2$, and $H_2$ gas species in the process of sH hydrate-based $CO_2$ separation from the flue, fuel, and landfill gases play a significant role in either the stability or during the dissociation stage. In such processes, the effects of sH hydrate formers would also be substantial. Hence, in this work, the role of five organic amino acid additives, the impressions of $CH_4$, $N_2$, and $H_2$ gases mixed with $CO_2$ and six various sH hydrate formers on the stability and dissociation of sH clathrate hydrates using MD simulations were investigated.

## 2. SIMULATION METHODOLOGY

In this research, the classical MD simulations, using Newton's law for computing the equation of motion and obtaining the position of each particle as a function of time, were utilized. The dynamic and thermodynamic properties using statistical mechanics were then determined. Although the protons of water molecules have been specified by X-ray diffraction, they cannot be specified unambiguously while the positions of hydrogen atoms are disordered. Therefore, the initial

orientation of oxygen and hydrogen atoms of water molecules in sH clathrate hydrates were constructed from the work by Takeuchi et al.,[42] which determined their cartesian coordinates by satisfying the Bernal−Fowler ice rule and net zero dipole moment. To create the simulation box, a $4 \times 4 \times 4$ supercell with 2176 water molecules and the dimension of 42.3 Å $\times$ 40.6 Å $\times$ 48.8 Å was built. A unit cell of the sH hydrate is hexagonal and computationally more time-consuming in MD simulations, while a considered supercell here is orthogonal hexagonal, for which the periodic boundary conditions can be properly implemented. A unit cell of hexagonal sH has 34 water molecules and $P6/mmm$ space group symmetry, which includes three $5^{12}$ small cages, two $4^3 5^6 6^3$ medium cages, and one $5^{12} 6^8$ large cages.[43] Hence, the simulation box can contain 320 gas molecules in both small and medium cavities as well as 64 large guests in the large cavities. In this work, the characteristics of $CO_2$ sH hydrates at various operating conditions were investigated. Table 1 summarizes the list and composition of studied $CO_2$ sH hydrates in the presence of different amino acids, gas species, and sH hydrate formers. To evaluate the influences of amino acids, one molecule of these substances was located in one of the large cages of the $CO_2$ + NH sH clathrate hydrate. In addition, to implement the
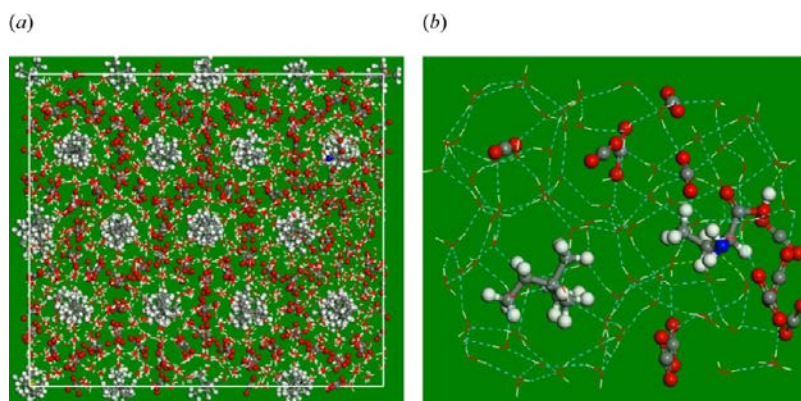
**Figure 2.** Final configuration of the $CO_2$ + NH sH hydrate in the presence of L-thre. at 5 MPa and 273.15 K after 500 ps.

same thermodynamic conditions for simulations including mixed $CO_2$ with $CH_4$, $N_2$, and $H_2$ sH hydrates, the measured phase equilibrium conditions of these hydrates were considered as a basis for their combined mixtures.[44−47]

The molecular structure of investigated gas species, sH hydrate formers, amino acids, and sH clathrate hydrate cavities are demonstrated in Figure 1. After providing the initial configuration, geometry optimization, and energy minimization using both conjugate gradient and steepest descent algorithms were carried out. Then, using the NVT ensemble (constant volume and temperature), the simulation box to reach the targeted temperature was equilibrated for 40 ps. As the canonical ensemble, the NVT approach would be successful when conformational searches of models without periodic boundary conditions are implemented. Also, due to the absence of coupling to a pressure bath, this ensemble under the periodic boundary conditions provides the advantage of less trajectory perturbation. The temperature of the simulation box was adjusted using the Berendsen method, which can be expressed by[48]

$$\lambda = \sqrt{1 + \frac{\Delta t}{\tau_T}\left(\frac{T_0}{T} - 1\right)} \tag{1}$$

In this equation, $\tau_T$ and $\Delta t$ resemble the time step (ps) and a characteristic relaxation time, respectively; $T_0$ refers to the target temperature in K. Finally, by employing the NPT ensemble (constant temperature and pressure) for 500 ps, the production phase of the MD simulations was performed. The Berendsen method to adjust the pressure and temperature with a decay constant of 0.1 ps was utilized. In the periodic systems, the pressure of the simulation box by adjusting the volume through the vector position of particles was controlled. Via the below scaling factor, the coordinates of each particle for each step were scaled by[48]

$$\mu = \left[1 + \frac{\Delta t}{\tau_P}\lambda(P_0 - P)\right]^{1/3} \tag{2}$$

where $P_0$ and $P$ are instantaneous and target pressures, respectively. Also, the units of pressure and compressibility in the above equation are in Pascal. As shown, the compressibility of the system ($\lambda$) and relaxation time ($\tau_T$) were used to perform the scaling factor calculations ($\mu$). The interactions between guests, hosts, and guest−host molecules were modeled using the consistent valence force field (CVFF) as given below[49−52]

$$E_{\text{total}} = \sum_b D_b[1 - e^{-\alpha(b-b_0)}] + \sum_\theta H_\theta(\theta - \theta_0)^2$$
$$+ \sum_\varnothing H_\varnothing[1 - S\cos(n\varnothing)] + \sum_X H_X X^2$$
$$+ \sum_b \sum_{b'} F_{bb'}(b - b_0)(b' - b_0')$$
$$+ \sum_\theta \sum_{\theta'} F_{\theta\theta'}(\theta - \theta_0)(\theta' - \theta_0')$$
$$+ \sum_b \sum_\theta F_{b\theta}(b - b_0)(\theta - \theta_0)$$
$$+ \sum_\varnothing F_{\varnothing\theta\theta'}\cos\varnothing(\theta - \theta_0)(\theta' - \theta_0') + \sum_X F_{XX'}XX'$$
$$+ \sum \varepsilon\left[\left(\frac{r_{ij}^o}{r_{ij}}\right)^{12} - 3\left(\frac{r_{ij}^o}{r_{ij}}\right)^6\right] + \frac{q_i q_j}{\varepsilon r_{ij}} \tag{3}$$

where F, H, and D denote the force constants; $X$, $\varnothing$, $\theta$, and $b$ stand for the out-of-plane parameter, dihedral angle, bond angle, and bond length, respectively; $n$ and $S$ are the nonnegative integer coefficient and sign convention coefficient variables for the dihedra, respectively; $\varepsilon$ is the well-depth in van der Waals; and $r_{ij}$ refers to the length from atom $i$ to atom $j$. The first four terms of this equation are the diagonal of the valence of the force field, while terms five to nine are the cross terms that show the couplings via the deformation of internal coordinates. The term $\alpha$ in the previous equation can be expressed by[53]

$$\alpha = \sqrt{\frac{K_0}{2D_0}} \tag{4}$$

where $D_0$ and $K_0$ stand for the equilibrium well-depth and the force constant, respectively. In addition, the Ewald summation was used to compute the long-range Coulomb and van der Waals interactions. Also, a cutoff distance of 12.5 Å was set to determine the van der Waals interactions between host−guest molecules in the simulation box. All MD simulations were performed using Materials Studio software.[54]

## 3. RESULTS AND DISCUSSION

The guest and host molecules under the thermodynamically stable zone have vibrations and rotations while keeping their positions in the hydrate crystals constant. The addition of amino acids inside the sH clathrate hydrate by creating several
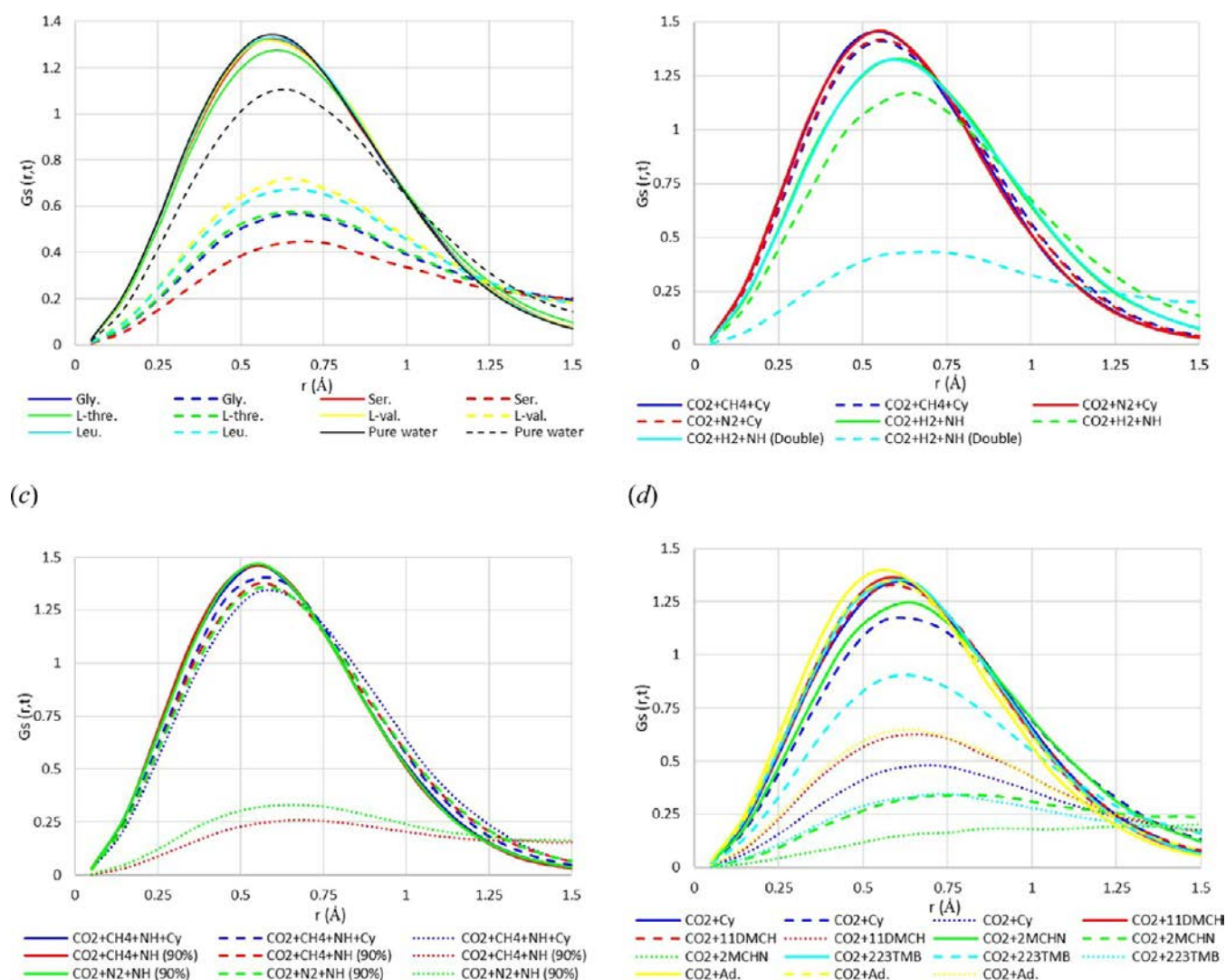
**Figure 3.** Self-space–time correlation function of water molecules in the simulation box. (a) $CO_2$ + NH hydrate in the existence of amino acids; (b, c) mixed-gas sH hydrates; and (d) $CO_2$ hydrates with different sH hydrate formers (solid, dashed, and dotted lines display SSTCF at 273.15, 283.15, and 293.15 K, respectively).

hydrogen bonds with surrounding water molecules can impose weakening forces on the stability of local cages in the sH hydrate. Figure 2 displays the final configuration of the $CO_2$ + NH sH hydrate in the presence of L-threonine at 5 MPa and 273.15 K. Although, the clathrate hydrate structure could keep its regular arrangements, partial disruption occurred in the region around L-threonine, as shown in Figure 2b. Hydroxyl of L-threonine is more likely to bind to the water surface of the local cages. Probably it tends to strengthen the local water ordering due to its long alkyl side chain, resulting in a local perturbation that destructed the hydrogen bonds between local cages of water molecules and releases some $CO_2$ molecules from centers of small and medium cavities.

This phenomenon was intensified when the movements of water molecules due to the increasing temperature to 283.15 K were induced, which led to the total dissociation of the sH hydrate quite sooner than the absence of L-threonine. The same scenario was also observed when the other amino acids were included in the system. To realize the behavior of these components as well as small and large guests in sH clathrate hydrates, the following subsections deal with their applicable characteristics.

## 3.1. Dynamical and Structural Properties of sH Hydrates.
Dynamical properties of hydrates can reveal the ability of molecules in the structure to undergo phase transitions upon changes in temperature or pressure. Gas hydrates can lose their structural water molecules under heating or exposure to thermodynamic inhibitors, resulting in a change in their crystal structure and properties. Another dynamic property of hydrates is the ability of the guest molecules to move or rotate within the host lattice. This motion can be characterized by various spectroscopic techniques. The frequency and extent of this motion can provide information on the binding interactions between the host and guest molecules, as well as the strength of the crystal lattice. However, the other possible option would be the utilization of MD simulations. Hydrates can also exhibit interesting properties related to their thermal conductivity. The existence of guest molecules in the crystal structure can influence the thermal properties of gas hydrates. Therefore, the dynamical features of water, gas, and large guest molecules in the hydrate phase are essential for comprehending the behavior and properties of these compounds, as well as their potential applications. In molecular dynamics simulations of gas
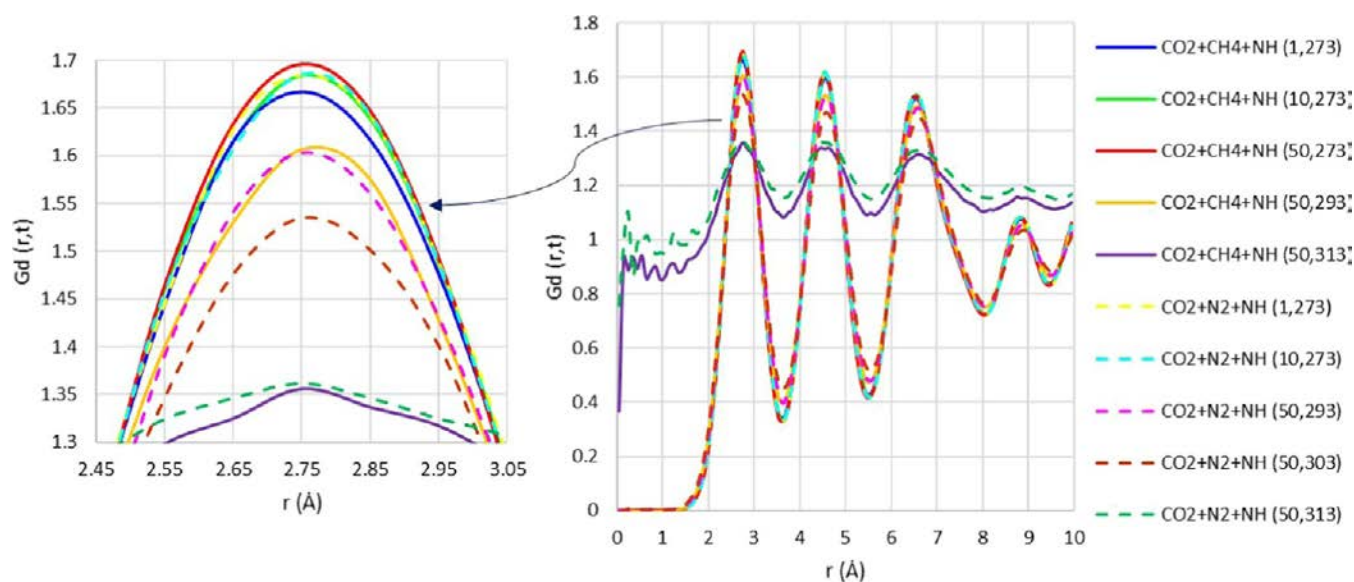
**Figure 4.** Distinct space−time correlation function of water molecules in the simulation box (the solid line displays the $CO_2$ + $CH_4$ + NH hydrate and the dashed line indicates the $CO_2$ + $N_2$ + NH hydrate).

hydrates, the space−time correlation function is a mathematical quantity used to describe how the velocities and positions of atoms or molecules in the system are correlated in space and time. This correlation function is commonly used to investigate the dynamical properties of gas hydrates, such as diffusion and vibrational motions within the clathrate cages formed by the host water molecules. By calculating the correlation function for the positions and velocities of the guest molecules, it is possible to obtain information about their diffusion coefficients and vibrational spectra, which are essential for understanding the behavior of gas hydrate systems in natural environments and for the development of gas hydrate technologies. The space−time correlation function or the van Hove function describes the time evolution of spatial correlations between atoms. The probability at the specified time $t$ can be given by $G(r,t)$, where an atom will be located at a distance $r$ away from the location occupied by an atom at an earlier time zero. This parameter can be considered as the self ($G_s$) and distinct ($G_d$) part of the space−time correlation function, which is presented in the following equation

$$G_s(r, t) = \frac{1}{N} \left\langle \sum_i \delta(r + r_i(0) - r_i(t)) \right\rangle \tag{5}$$

$$G_d(r, t) = \frac{1}{N} \left\langle \sum_i \sum_{i \neq j} \delta(r + r_i(0) - r_j(t)) \right\rangle \tag{6}$$

where $N$ denotes the number of atoms or molecules in the simulation box, $\delta$ is the ith particle displacement from its position at time 0 to time $t$, and $\langle \rangle$ denotes the ensemble average over all possible initial configurations of the system. The correlation function is typically calculated for a range of values of $r$, the distance between particle pairs, and $t$, the time lag between the two positions being correlated. The function can provide dynamic information such as the time scales of vibrational motion and diffusion. Also, the self and distinct normalization property of the space−time correlation function can be described by the following equations

$$\int G_s(r, t) dr = 1 \text{ and } \int G_d(r, t) dr = N - 1 \tag{7}$$

Figure 3 shows the self-space−time correlation function (SSTCF) of water molecules as a function of time at 5 MPa and 273.15, 283.15, and 293.15 K. The contributions of the oxygen−oxygen correlation function in all simulations possess a peak of around 0.6 Å. As case (a) exhibits, the peaks at 273.15 K are almost the same for pure water and amino acids (except L-threonine), while they experienced a reduction when a 10 K temperature increase was imposed. It is very likely that amino acids that have low hydrophobicity such as serine, glycine, and L-threonine play more inhibition effects on the dissociation of sH hydrates. Gas species and sH hydrate formers also play a vital role in the structure and stability of sH clathrate hydrates. Other factors such as the composition of gas molecules can also affect the hydrate's stability. The effects of guest gases and full/partial cage occupancy are revealed in Figure 3a,b. Although the SSTCF of hydrates including the mixture of $CO_2$ with either $CH_4$ or $N_2$ have some similarities, the presence of $H_2$ reduced the hydrate stability, which even intensified when double cage occupancy in small cages was considered. In comparison with full occupancy, sH hydrates with 90% small cage occupation have similar trends at 273.15 and 283.15 K but act differently at 293.15 K. This may be due to the lower resistivity of small empty cages against the dissociation conditions. The results of the $CO_2$ + $CH_4$ hydrate with NH + Cy. at 293.15 K reveals that the simultaneous presence of branched and cyclic sH promoters can significantly support the stability of the sH clathrate. By continuing this simulation, it was found that the dissociation time occurred at 625 ps, which is quite longer than using a single NH or Cy. sH hydrate formers. Such maintenance of the hydrogen-bonded water network may be due to their different molecular structures, which may provide the antiresonance behavior against disturbing movements of water molecules at 293.15 K. As Figure 3d shows, the type of sH hydrate formers has the most impact on structural stability. In addition, the large guests consisting of C and H in the cyclic form are found to be more
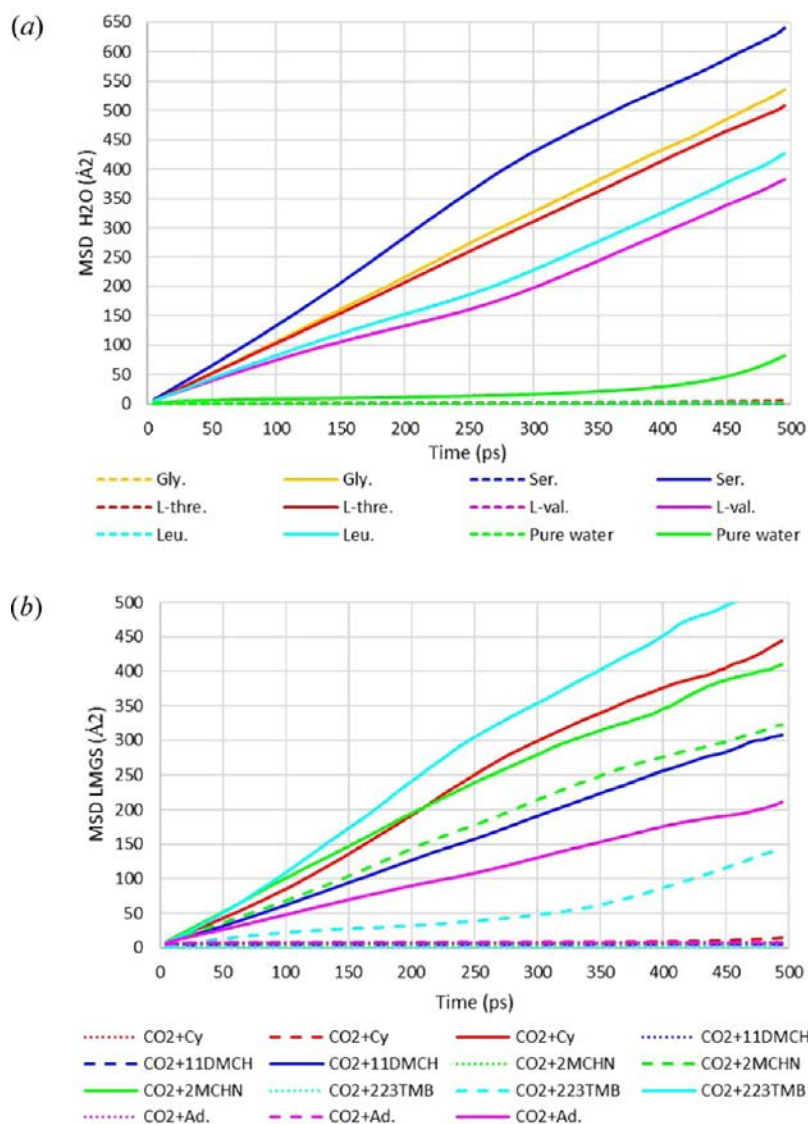
**Figure 5.** MSDs of molecules: (a) water molecules (dashed and solid lines represent MSDs at 5 MPa and 273.15 and 283.15 K, respectively) and (b) LMGS molecules (dotted, dashed, and solid lines represent MSDs at 5 MPa and 273.15, 283.15, and 293.15 K, respectively).

capable of deactivating the disturbance movements of water molecules in the large cavities.

The distinct space−time correlation function (DSTCF) for water molecules is a measure of the correlations between the water molecules due to their interactions with each other. This quantity is important for understanding the properties of water in the hydrated state. The intermolecular correlation of water molecules is manifested in Figure 4, which exhibits the DSTCF. The motion of each molecule may be affected by the presence of neighboring molecules, which interact with each other through hydrogen bonds. It is worth noting that the operating conditions have an insignificant impact on the peak values until the sH crystalline network can keep itself intact. Also, at prevailing hydrate temperature conditions (e.g., 273.15 K), the effects of pressure at a constant temperature on $CO_2$ mixed with $CH_4$ and $N_2$ are not the same, which may be due to the different molecular shapes of these gas species.

The other parameter to analyze the dynamical properties of components in the system can be studied by the mean squared displacement (MSD), which determines the average displacement of atoms as a function of a specific time. Moreover, it is commonly used to describe the diffusion of molecules in a fluid or gas. The MSD for gas hydrates models the motion of individual molecules within the structure. This parameter can be defined as the average of the squared displacement of each molecule from its initial position over a given period. The average squared displacement in an equilibrium ensemble is independent of time. The MSD can level off to a specific value if the particle in the system is bound, while the MSD (in the diffusive regime) would be linear in time. The MSD and the diffusion coefficient ($D$) can be expressed by the following equations[55]

$$MSD = \frac{1}{N} \sum_{i=1}^{N} |R^i(t) - R^i(t_0)|^2 \tag{8}$$

$$D = \frac{1}{6} \lim_{\Delta t \to \infty} \frac{dMSD}{d\Delta t} \tag{9}$$

where $N$ and $R^i$ are the total number and position of particles. In gas hydrates, the motion of the guest molecules is restricted by the lattice of water molecules, and the MSD can provide

**Table 2. Diffusion Coefficient ($\times 10^{10}$ cm$^2$/s) of Different sH Hydrates at 5 MPa[a]**

| sH hydrate system | at 273.15 K | | | | at 283.15 K | | | |
|---|---|---|---|---|---|---|---|---|
| | H$_2$O | CO$_2$ | LMGS | AA/G | H$_2$O | CO$_2$ | LMGS | AA/G |
| CO$_2$ + NH | 7 | 3 | 5 | | 1017 | 950 | 513 | |
| CO$_2$ + NH + Gly. | 17 | 15 | 3 | 92 | 10,839 | 10,298 | 6814 | 5312 |
| CO$_2$ + NH + Ser. | 26 | 13 | 9 | 311 | 13,247 | 13,193 | 9152 | 4183 |
| CO$_2$ + NH + L-thre. | 86 | 49 | 14 | 109 | 10,285 | 10,096 | 7088 | 3971 |
| CO$_2$ + NH + L-val. | 16 | 6 | 3 | 203 | 7390 | 13,503 | 4386 | 2804 |
| CO$_2$ + NH + Leu. | 12 | 8 | 5 | 85 | 8264 | 7995 | 5022 | 2654 |
| CO$_2$ + CH$_4$ + Cy | 2 | 2 | 2 | 2 | 3 | 2 | 3 | 3 |
| CO$_2$ + CH$_4$ + NH + Cy | 2 | 1 | 3 | 1 | 4 | 2 | 2 | 2 |
| CO$_2$ + N$_2$ + Cy | 3 | 2 | 2 | 3 | 3 | 2 | 3 | 5 |
| CO$_2$ + CH$_4$ + NH (90%) | 8 | 1 | 4 | 1 | 57 | 5 | 8 | 44 |
| CO$_2$ + N$_2$ + NH (90%) | 9 | 2 | 2 | 3 | 52 | 17 | 25 | 11 |
| CO$_2$ + H$_2$ + NH | 7 | 3 | 2 | 6 | 426 | 375 | 152 | 2157 |
| CO$_2$ + H$_2$ + NH (Double) | 13 | 5 | 2 | 369 | 14,190 | 14,355 | 10,485 | 68,520 |
| CO$_2$ + 11DMCH | 4 | 3 | 1 | | 8 | 5 | 3 | |
| CO$_2$ + 2MCHN | 9 | 6 | 4 | | 13,921 | 11,368 | 6707 | |
| CO$_2$ + 223TMB | 6 | 3 | 1 | | 420 | 4287 | 2468 | |
| CO$_2$ + Ad. | 5 | 3 | 2 | | 12 | 5 | 2 | |
| CO$_2$ + Cy. | 8 | 4 | 2 | | 345 | 312 | 101 | |

[a]AA/G denotes the diffusion coefficient of amino acids (AA) or the other gas species (G) such as CH$_4$, N$_2$, and H$_2$ in the system.

information about the diffusivity of the guest molecules within the sH clathrate. The MSD may also be affected by the temperature and pressure conditions, as well as the composition of the gas and water molecules. Understanding the MSD for gas hydrates is also important not only for hydrate-based applications but also for predicting the behavior of these compounds in natural gas hydrate reservoirs and developing technologies to extract gas hydrates from deposits. The MSDs of water (in the CO$_2$ + NH hydrate without/with amino acids) and that of LMGSs (in different CO$_2$ sH hydrates) at diverse operating conditions are shown in Figure 5. The MSD alterations in all simulations are insignificant when the clathrate hydrate structure can keep itself stable. This minor change of MSDs may be attributed to just a vibration of both host and guest molecules without leaving the position of sH clathrate hydrate crystals. However, they acted differently as the temperature increased to 283.15 and 293.15 K. As Figure 5a exhibits, the order of MSD growth is serine > glycine > L-threonine > leucine > L-valine > pure water. It is well established that the inclusion of amino acids boosts the rate of water MSD during the simulation time. Due to the contribution of electrostatic and van der Waals interactions within regions where amino acids and water molecules interact with each other, the first breakage of the cages in the hydrate network occurred from the local cages around these molecules and then extended across the simulation box. It seems that amino acids with shorter side chains in their molecular structure are more prone to facilitate the rate of sH hydrate dissociation and the movements of water molecules. Also, an alkyl chain length of Leucine and L-valine may determine the kinetic performance of these molecules in interacting with water molecules. The MSDs of sH large guests in Figure 5b also reveal that the shape, size, and type of these molecules would be determinative in the stability of CO$_2$ sH clathrate hydrates. Between studied LMGSs, the MSD of 2-methyl cyclohexanone and 2,2,3-trimethyl butane at 283.15 K showed different behavior in comparison with other large molecules. Also, adamantane and 1,1-dimethyl cyclohexane possess lower MSDs when the simulations were performed at 293.15 K.

Apparently, the LMGSs with higher carbon numbers in the molecular structure are more capable of enhancing the crystalline form of the large cavities.

Mass transfer in gas hydrates occurs by diffusion mechanisms, which refer to the movement of guest molecules through the hydrate lattice or the liquid water phase surrounding the hydrate particles. The diffusion coefficient of gas hydrates is a complex phenomenon that depends on multiple factors, and it can vary widely depending on the compositions and conditions of the formed hydrate. The diffusion coefficient of gas hydrates at low and high pressures is generally similar once the hydrate phase can become quite stable. The temperature also affects the diffusion coefficient, as higher temperatures tend to increase the mobility of the guest molecules in the hydrate structure. Generally, smaller and more mobile guests tend to diffuse more quickly in the hydrate structure than larger ones. The diffusion coefficient of simulated sH hydrates at 5 MPa and 273.15 and 283.15 K are reported in Table 2. Although the presence of amino acids at 273.15 K cannot disintegrate the surrounding network of water molecules, they actively vibrate inside the clathrate hydrate so that they possess a higher diffusion coefficient than H$_2$O, CO$_2$, and NH. However, the disruption of amino acids between the hydrogen-bonded clathrate hydrate occurred at 283.15 K, which was followed by the destruction of the sH hydrate. These molecules, in comparison with their absence, can also greatly increase the diffusion coefficient of other components in the system. The effects of 90% cage occupancy on the diffusion can also play a prominent role when the temperature is elevated from 273.15 to 283.15 K. This is also valid for the entrapped CO$_2$ + H$_2$ + NH hydrate in which H$_2$ molecules in small cavities can significantly induce the movements of CO$_2$ and water molecules more than NH molecules. Although the impression of double H$_2$ molecules in small cavities on other components at 273.15 K was not considerable, they dramatically influenced the stability of the clathrate hydrate network at 283.15 K. The diffusion coefficients of CO$_2$ sH hydrates with different large guests at 273.15 K are quite similar together. However, clathrate
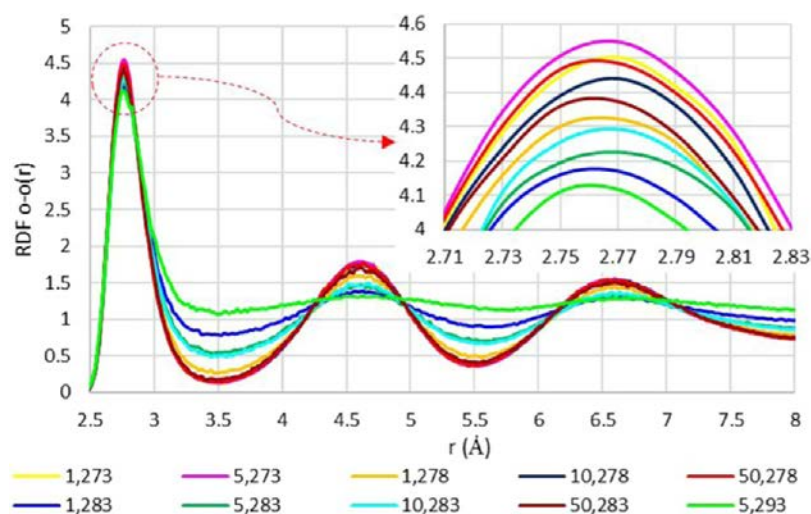
**Figure 6.** RDF of the $CO_2$ + NH clathrate hydrate at various P−T (MPa, K) conditions.



**Figure 7.** Final density of pure/mixed $CO_2$+NH hydrates under different thermodynamic conditions.

hydrates including 2-methyl cyclohexanone and 2,2,3-trimethyl butane experienced total dissociation as the temperature was elevated by 10 K.

The radial distribution function (RDF or $g_{\alpha\beta}$) is a way to describe the spatial arrangement of molecules in a system by quantifying the probability of finding particles positioned from a certain particle in a specified distance. In the case of analyzing gas hydrates, the RDF can provide insight into the structure of the hydrate lattice, as well as the interactions between the guest and water molecules.[56] This parameter typically exhibits peaks at certain distances, corresponding to the distances between adjacent water molecules in the hydrate lattice. The height and shape of the peaks can reveal

information about the water molecular arrangements as well as guest molecules within the cages. This parameter can be calculated by analyzing the positions of two atoms as follows

$$g_{\alpha\beta}(r) = \frac{V}{N_\alpha N_\beta}\left(\sum_{i=1}^{N_\alpha} \frac{n_i\beta(r)}{4\pi r^2 \Delta r}\right) \tag{10}$$

where $n_i\beta(r)$ refers to the overall number of $\beta$ at $r$ distance from $\alpha$ and $N$ and $V$ represent the number of particles and volume of the simulation box, respectively. The RDF of oxygen−oxygen in the $CO_2$ + NH clathrate hydrate under various pressure and temperature conditions is exhibited in Figure 6. Three peaks at 2.76, 4.57, and 6.56 Å denote the
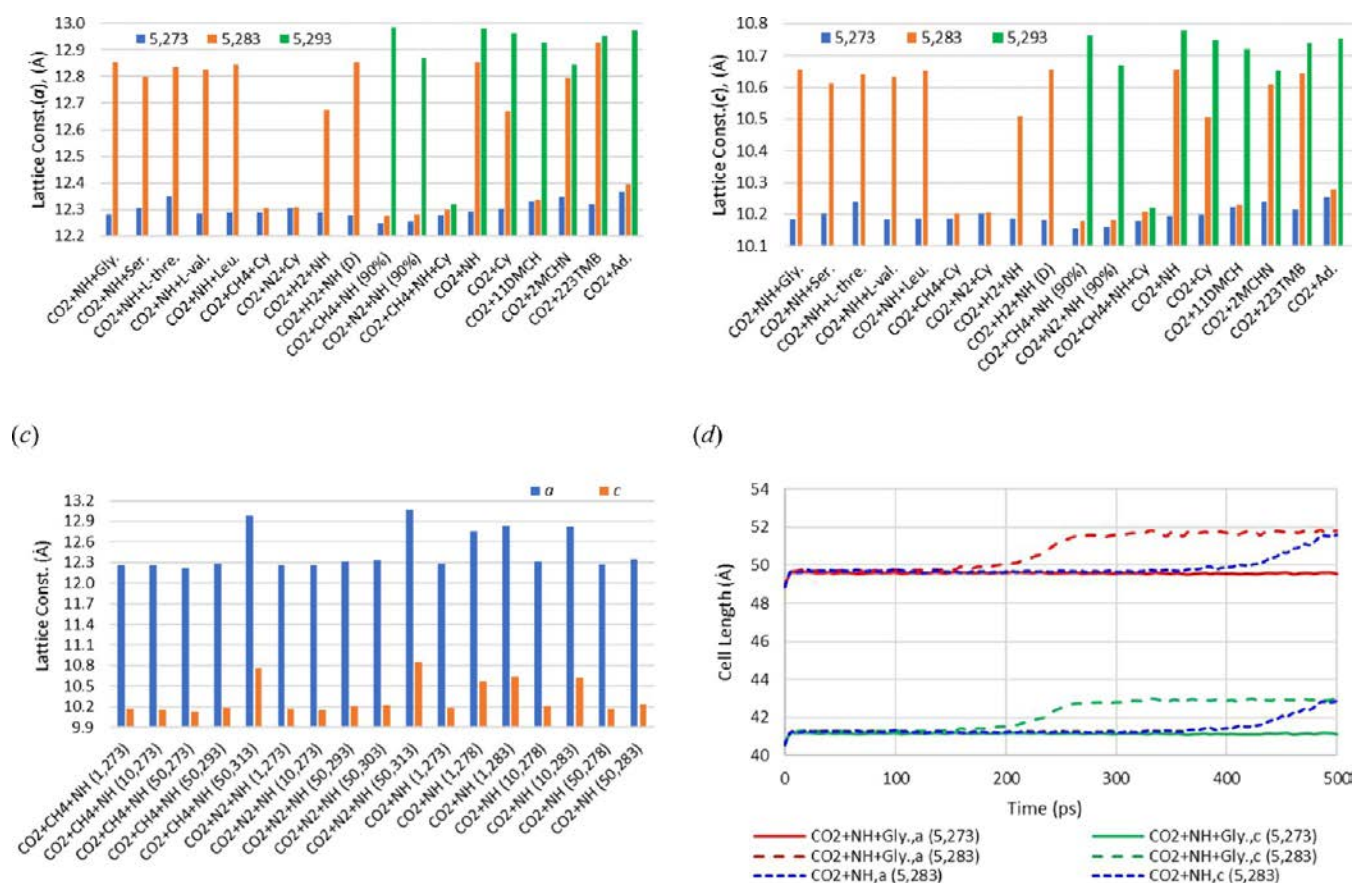
(c)



(d)



**Figure 8.** sH hydrate lattice constants: (a–c) simulated sH hydrates at different pressure-temperature conditions and (d) evolution of the cell length of the $CO_2$ + NH hydrate without/with glycine.

length corresponding to the oxygen–oxygen pairs of nearest, tetrahedral, and hexagonal rings of water molecules, respectively. The RDF at low temperatures possesses a higher peak, indicating an expansion of the hydrate lattice. This is because the guest gas molecules occupy shorter volumes at lower temperatures, leading to an increase in the average distance between the gas and water molecules. At higher temperatures, it shifts toward lower values, indicating compression of the hydrate lattice due to the increased thermal motion of the molecules. In contrast, the increase in pressure gives the higher height of the peak. In addition, the lower height of the peak may demonstrate that the network of water molecules is more prone to leave the regular positions of the clathrate hydrates. Also, the second and third peaks at 1 MPa and 283.15 K, as well as 5 MPa and 293.15 K, almost disappeared, which shows the disintegration of water cages in the structure of the hydrate.

**3.2. Thermodynamic and Thermophysical Properties of sH Hydrates.** The density alteration of sH hydrates would be a proper criterion for monitoring the stability and process of the clathrate hydrate dissociation. Generally, decreasing temperature (or increasing pressure) causes the water molecules in the hydrate lattice to become more ordered, resulting in a decrease in the volume occupied by the guest molecules and an increase in the density. Figure 7 displays the alteration of pure/mixed $CO_2$ + NH clathrate hydrates at diverse operating conditions. At the clathrate hydrate stability conditions, the sH hydrate densities including $N_2$ and $CH_4$ guests reduced slightly from over 1100 kg/m³ to less than that

due to the lower molecular weight of such gas species. As is shown, the densities of the $CO_2$ + NH hydrate are almost similar and close together when the structure of the guest–host network can hold its solidity. However, it experienced a significant reduction to less than 1000 kg/m³ by implementing unstable circumstances. The same description can be applied to the other simulated sH hydrates. Apparently, the combination of NH and Cy. can more effectively enhance the stability of large cavities. In addition, the mixture of $CO_2$ with either $CH_4$ or $N_2$ in the small molecules showed less significant alteration in the strength of structural stability against unsteady thermodynamic conditions.

The structural characteristics of sH clathrate hydrates can be analyzed in terms of structural configuration and guest molecules. The lattice parameter is a measure of the size of the unit cell in a crystal lattice that is an essential factor in evaluating the properties of hydrates, particularly in terms of their stability and storage capacity. This parameter can vary depending on the guests in the hydrate structure and the conditions under which it is formed. The size and shape of molecules fitted in small, medium, and large cages are important factors that influence the cage shape and size of the clathrate hydrate lattice. Generally, the larger molecular diameter of guests will cause the cages to expand, resulting in a larger unit-cell size of the sH clathrate hydrate. Decreasing the energy parameter between guest and host interactions may also increase the lattice parameter of hydrates. The X-ray diffraction analysis revealed that the dimension of lattice constants for the hexagonal sH clathrate hydrate is $a$:12.26 Å and $c$:10.17 Å.[57]
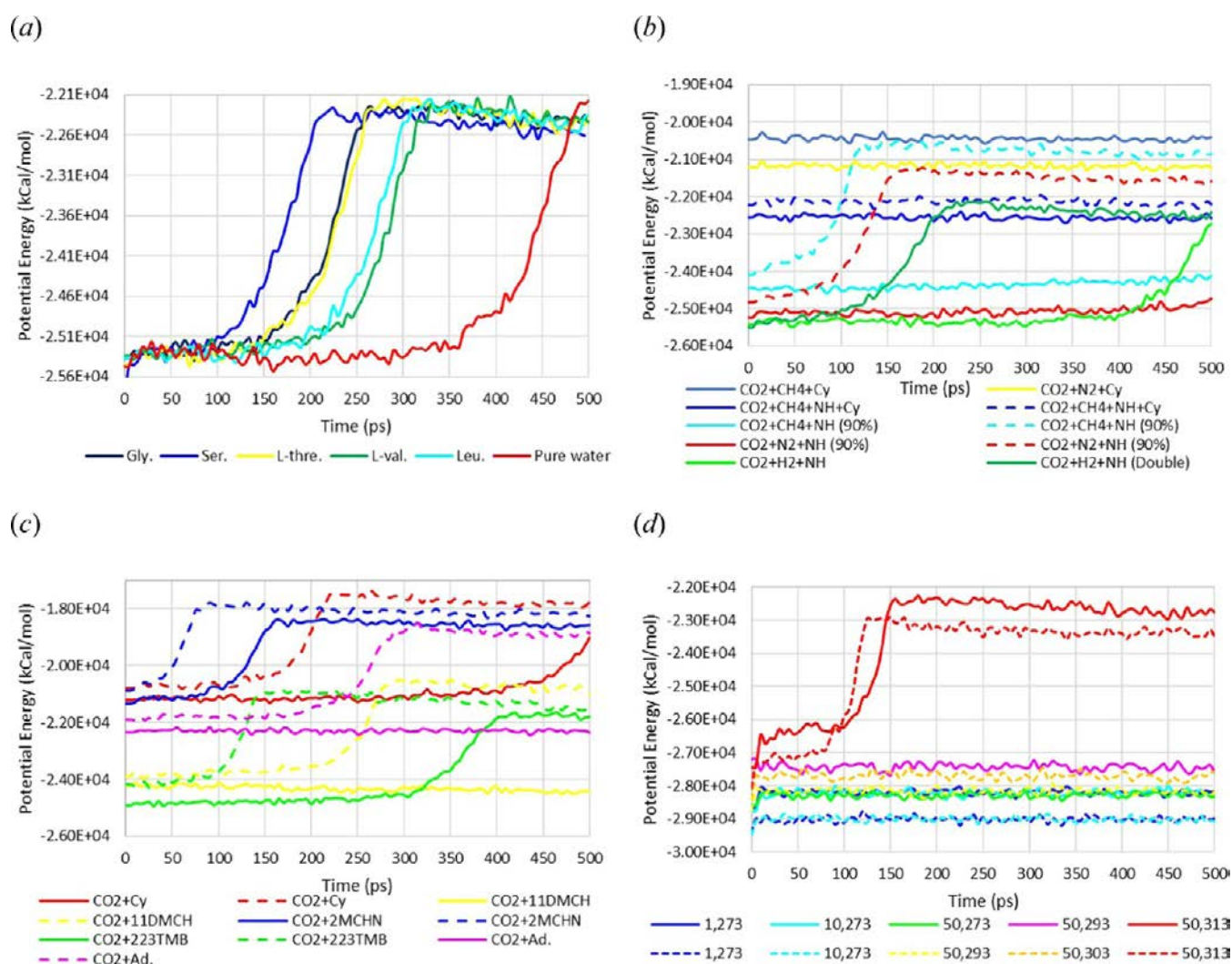
**Figure 9.** Potential energy of (a) the $CO_2$ + NH hydrate with amino acids; (b) sH hydrates of mixed gases; (c) $CO_2$ hydrates with different sH hydrate formers (solid and dashed lines display PE at 283.15 and 293.15 K, respectively), and (d) potential energy of $CO_2$ + $CH_4$ + NH (solid lines) and $CO_2$ + $N_2$ + NH (dashed lines) at different P−T conditions.

Also, molecular modeling considering the ice rules and a net zero dipole moment from the least potential energy for the protons determined $a$:12.21 Å and $c$:10.14 Å.[42] Figure 8 demonstrates the lattice parameters of simulated sH hydrates under various thermodynamic conditions. As displayed in Figure 8a,b, the obtained results for sH hydrates under the thermodynamic stability conditions (e.g., 5 MPa and 273.15 K) are in agreement with reported values in the literature. It can be realized that sH hydrates including smaller gas species as well as large molecular guests possess lower unit-cell parameters. For example, $a$ parameters for $CO_2$ + NH, $CO_2$ + $N_2$ + NH, and $CO_2$ + Ad. are estimated at 12.35, 12.38, and 12.46, respectively. Moreover, the presence of amino acids mostly increased the lattice constant of the $CO_2$ + NH hydrate. Figure 8c reveals the impressions of temperature and pressure on the sH clathrate lattice parameter. For instance, the lattice constant ($a$) of $CO_2$ + $CH_4$ + NH at 273.15 K and 1, 10, and 50 MPa is calculated to be 12.36, 12.35, and 12.31, respectively. The lattice constant with increasing temperature experienced a significant increase once the arrangement of the clathrate lost its regular form and guest molecules were released from the sH clathrate cages. As Figure 8d shows, the

dissociation of the sH hydrate with glycine occurred quite sooner than its absence. Also, the expansion of the simulation box caused by the clathrate hydrate destruction simultaneously took place for both $a$ and $c$ lattice constants.

Potential energy (PE) analysis of the hydrate structure during the phase transition may reveal the clathrate hydrate stability and how the guest and water molecules interact with each other. Figure 9 depicts the PE of simulated systems as a function of time. By comparing the PEs in Figure 9a, it can be found that the increase in the PE is due to an increase in the long-range Coulomb and van der Waals interactions. The existence of amino acids shifted the PE alteration to around the first half of the simulation time. As displayed in Figure 9b, the PE of sH hydrates at 283.15 K before the deformation phenomenon because the rotation of the guests in the central cages varies around the equilibrium values. However, the inclusion of $H_2$ molecules motivated the mobility of other components, which led to the PE growth before the end of simulation time. The PE results of $CO_2$ + $CH_4$ hydrates, as displayed in Figure 9c, revealed that 10% empty of small cage occupancy influenced the PE of the hydrate network. It is also clear that the type of large guest is one of the contributors to
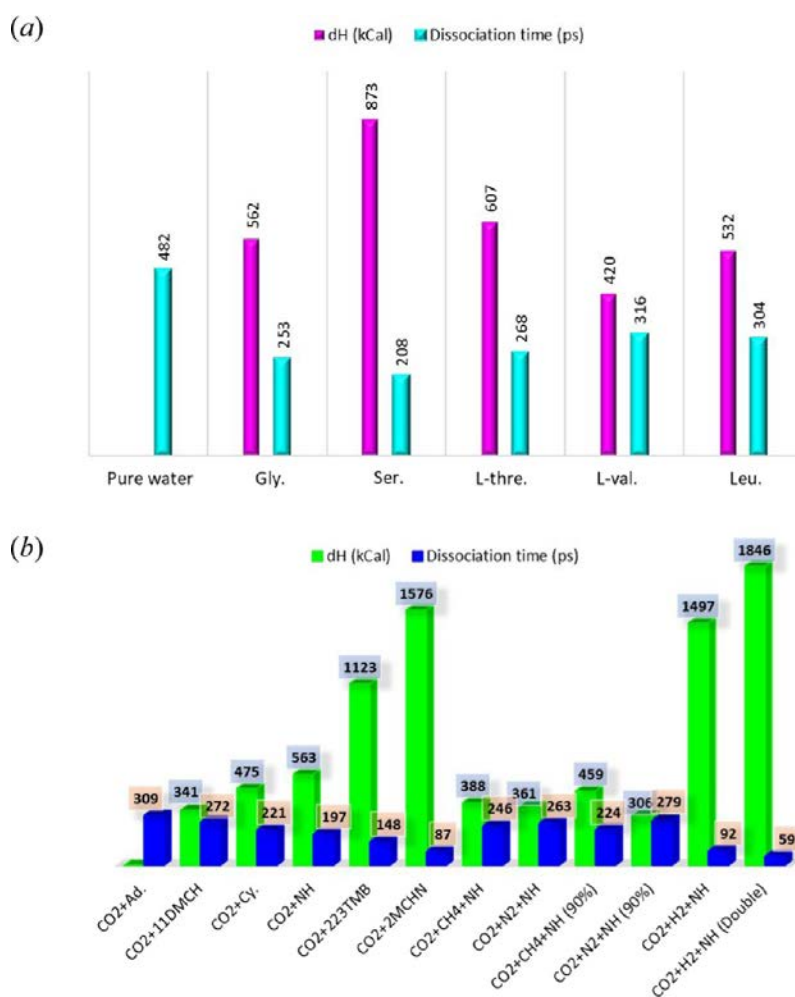
**Figure 10.** Dissociation time and differential of final enthalpy of sH hydrates in comparison with (a) the $CO_2$ + NH hydrate (at 5 MPa, 283.15 K) and (b) the $CO_2$ + Ad. hydrate (at 5 MPa, 293.15 K).
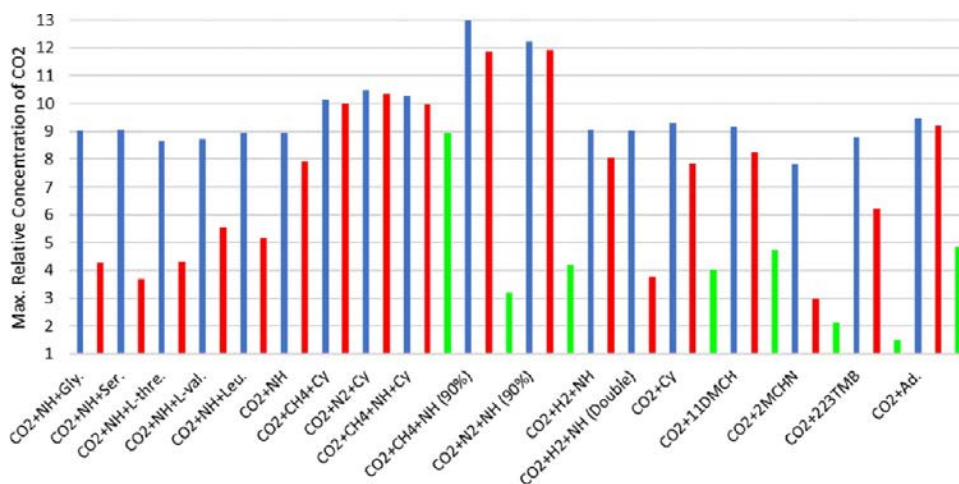


**Figure 11.** Maximum relative concentration of $CO_2$ molecules at 5 MPa and 273.15, 283.15, and 293.15 K in blue, red, and green, respectively.

sH hydrate dissociation. As Figure 9d shows, the PE for $CO_2$ + $CH_4$ + NH and $CO_2$ + $N_2$ + NH hydrates at high pressure and far away from the water freezing point can still oscillate around specific extents without a tangible change.

The dissociation enthalpy of hydrates due to the higher heat capacity seems to be markedly more than ice. This parameter refers to the amount of energy required to break the intermolecular forces holding the guest molecules within the hydrate cavities, causing the guest to be released from the hydrate. Hence, this phenomenon can be used for hydrate-based phase change applications. Generally, the alteration enthalpy of gas hydrates varies depending on the composition of guests and the clathrate hydrate structures. Figure 10 reveals the dissociation time and differential of final enthalpy of
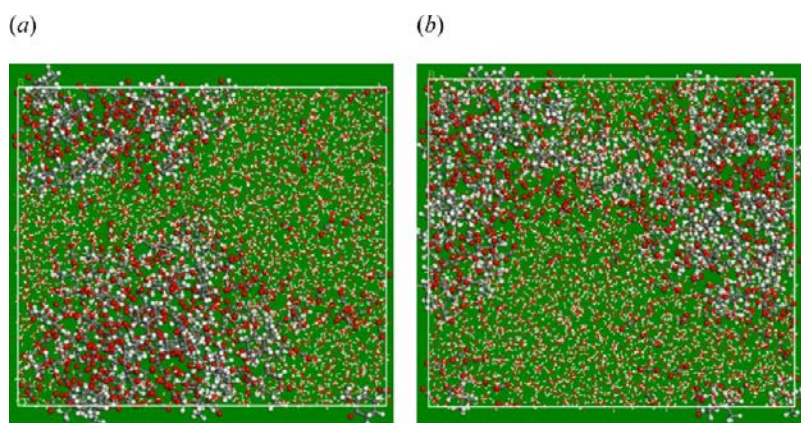
**Figure 12.** Final configuration of (*a*) $CO_2$ + 2-methyl cyclohexanone and (*b*) $CO_2$ + 2,2,3-trimethyl butane sH hydrates at 5 MPa and 293.15 K.

**Table 3. Definition of the Thermodynamic Quantities Obtained from Fluctuation Analysis**

| quantity | name | definition | units | quantity | name | definition | units |
|---|---|---|---|---|---|---|---|
| $\beta_S$ | adiabatic compressibility | $-\frac{1}{V}\left(\frac{\partial V}{\partial P}\right)_S$ | $\frac{1}{MPa}$ | $\chi$ | Grüneisen parameter | $-\frac{V}{C_V}\left(\frac{\partial P}{\partial T}\right)_V = -\frac{V}{C_V}\Delta_V$ | - |
| $\beta_T$ | isothermal compressibility | $-\frac{1}{V}\left(\frac{\partial V}{\partial P}\right)_T$ | $\frac{1}{MPa}$ | $\varphi_S$ | Isenthalpic Joule−Thomson coefficient | $\left(\frac{\partial T}{\partial P}\right)_H = \frac{V(T\alpha_P - 1)}{C_P}$ | $\frac{K}{MPa}$ |
| $\alpha_P$ | thermal expansion coefficient | $-\frac{1}{V}\left(\frac{\partial V}{\partial T}\right)_P$ | $\frac{1}{K}$ | $\varphi_T$ | isothermal Joule−Thomson coefficient | $\left(\frac{\partial H}{\partial P}\right)_T = -\mu C_P$ | $Å^3$ |
| $\gamma_V$ | thermal pressure coefficient | $-\left(\frac{\partial P}{\partial T}\right)_V$ | $\frac{MPa}{K}$ | $\omega$ | sonic velocity | $\left(\frac{C_P P}{C_V \rho}\right)^{1/2}$ | $\frac{m}{s}$ |

various sH hydrates in the simulation box (dH) compared to the base cases: $CO_2$ + NH and $CO_2$ + Ad. hydrates. As is evident, there is a relevance between the time for total hydrate destruction and differential enthalpies of the final configuration. In other words, the more unstable the thermodynamic condition, the more the difference between the final enthalpies from the base cases. It seems that the influences of amino acids, e.g., polar molecules with shorter side chains on the $CO_2$ + NH hydrate, are more substantial. Figure 10*b* shows that the most calculated dH compared to $CO_2$ + Ad. are for the systems comprising $H_2$, 2-methyl cyclohexanone, and 2,2,3-trimethyl butane molecules. The final dHs of $CO_2$ + NH including $CH_4$ and $N_2$ are also slightly lower than their absence, which indicates better hydrate stability.

Analyzing the relative concentration of $CO_2$ molecules can uncover the thermodynamic effects on the composition of gas hydrates. The unitless concentration profile determines the concentration of molecules in layers of the simulation box; however, it is relatively a random distribution. The range of this parameter can be between zero (when there are no particles in the layer) to the total number of resided particles in the same layer of the simulation box. Therefore, the total number in the box is equal to the summation of all layers. By computing the density of the guest molecules in the hydrate lattice in comparison with those in the hydrate phase as a function of pressure and temperature, the relative concentration in sH hydrates can be obtained. The maximum relative concentration (Max. RC) of $CO_2$ molecules for the simulated sH hydrates across the z-coordinate of the simulation box is presented in Figure 11. This parameter under the stability conditions for pure $CO_2$ sH hydrates is approx. 9, while it significantly reduced as the water network changed its initial configuration. Moreover, the addition of amino acids can intensify the Max. RC due to the destructive interactions with the water molecules. It can be concluded that there is an

inverse proportion of the Max. RC and the temperature increase. For example, the Max. RC of the $CO_2$ + $CH_4$ + NH + Cy. hydrate at 273.15, 283.15, and 293.15 K was calculated around 10.3, 10.0, and 8.9, respectively. The fraction of cage occupancy can also influence the RC of $CO_2$ molecules. This parameter for $CO_2$ + $CH_4$ + NH with 90% small cage occupation at 273.15 and 283.15 K is found to be 12.9 and 11.8, respectively. This implies that the combination of temperature increase and the fractional occupancy may impose the combined negative effects on structural water molecules of the clathrate hydrate. The max. RC for $CO_2$ sH hydrates including 2,2,3-trimethyl butane and 2-methyl cyclohexanone at 293.15 K is determined at about 1.5 and 2.1, respectively, which is the lowest compared to other $CO_2$ sH hydrates. It can be stated that these molecules may have inducing interactions with $CO_2$ molecules, which promote their quick release of them from the medium and small cages. Figure 12 shows the final configuration of these hydrates after experiencing total clathrate hydrate dissociation. The separation of both guest-type molecules from the water network while mixing can be observed in this figure.

Investigating thermophysical properties of sH hydrates come into play for several gas hydrate applications. These parameters may sometimes be difficult to quantify using experiments; therefore, applying classical molecular dynamics would be more convenient. The relation of ensemble fluctuations of thermodynamic quantities is a significant result of statistical mechanics. The thermodynamic quantities such as adiabatic/isothermal compressibility, thermal expansion/pressure coefficient, isenthalpic/isothermal Joule−Thomson coefficient, Gruneisen parameter, and sonic velocity can be obtained from such fluctuation analysis. It measures how the quantity responds to other quantity changes, as presented in Table 3. Commonly, the relationships between experimentally meas-

**Table 4. Fluctuation Properties of Different sH Hydrates at 273.15 K and 5 MPa[a]**

| sH hydrate system | $\beta_S$ | $\beta_T$ | $\alpha_P$ | $\gamma_V$ | $\chi$ | $\varphi_S$ | $\varphi_T$ | $\omega$ |
|---|---|---|---|---|---|---|---|---|
| $CO_2$ + 11DMCH | 1.268 | 1.548 | 345 | 2.229 | 1.927 | −35 | 5.729 | 3.336 |
| $CO_2$ + 2MCHN | 1.215 | 1.404 | 318 | 2.265 | 1.974 | −32 | 5.281 | 3.387 |
| $CO_2$ + 223TMB | 1.136 | 1.347 | 329 | 2.442 | 2.073 | −33 | 5.463 | 3.363 |
| $CO_2$ + Ad. | 1.296 | 1.616 | 371 | 2.296 | 1.884 | −37 | 5.961 | 3.254 |
| $CO_2$ + Cy. | 1.139 | 1.529 | 338 | 2.211 | 1.968 | −34 | 5.613 | 3.328 |
| $CO_2$ + NH | 1.065 | 1.158 | 313 | 2.703 | 2.252 | −31 | 5.198 | 3.462 |
| $CO_2$ + NH + Gly. | 0.988 | 1.218 | 325 | 2.748 | 2.290 | −34 | 5.613 | 3.553 |
| $CO_2$ + NH + Ser. | 0.945 | 1.194 | 328 | 2.668 | 2.224 | −35 | 5.729 | 3.585 |
| $CO_2$ + NH + L-thre. | 0.973 | 1.177 | 323 | 2.743 | 2.286 | −33 | 5.530 | 3.514 |
| $CO_2$ + NH + L-val. | 0.965 | 1.184 | 317 | 2.677 | 2.231 | −32 | 5.264 | 3.507 |
| $CO_2$ + NH + Leu. | 0.943 | 1.163 | 319 | 2.743 | 2.286 | −32 | 5.297 | 3.494 |
| $CO_2$ + $CH_4$ + Cy. | 1.108 | 1.256 | 288 | 2.293 | 1.911 | −22 | 3.620 | 3.418 |
| $CO_2$ + $CH_4$ + NH + Cy. | 1.129 | 1.285 | 279 | 2.171 | 1.809 | −21 | 3.471 | 3.362 |
| $CO_2$ + $CH_4$ + NH | 1.065 | 1.121 | 271 | 2.417 | 2.015 | −20 | 3.338 | 3.552 |
| $CO_2$ + $CH_4$ + NH (90%) | 0.955 | 1.195 | 232 | 1.941 | 1.617 | −16 | 2.690 | 3.659 |
| $CO_2$ + $N_2$ + Cy. | 0.919 | 0.984 | 273 | 2.774 | 2.312 | −17 | 2.873 | 3.664 |
| $CO_2$ + $N_2$ + NH | 0.896 | 0.963 | 263 | 2.731 | 2.276 | −16 | 2.707 | 3.687 |
| $CO_2$ + $N_2$ + NH (90%) | 0.834 | 0.912 | 244 | 2.675 | 2.230 | −12 | 2.059 | 3.769 |
| $CO_2$ + $H_2$ + NH | 0.942 | 1.012 | 276 | 2.727 | 2.273 | −18 | 2.923 | 3.656 |
| $CO_2$ + $H_2$ + NH (double) | 0.917 | 0.994 | 281 | 2.827 | 2.356 | −13 | 2.175 | 3.621 |

[a]$\beta_s$ ($\times10^{-4}$ $MPa^{-1}$): adiabatic compressibility; $\beta_T$ ($\times10^{-4}$ $MPa^{-1}$): isothermal compressibility; $\alpha_p$ ($\times10^{-6}$ $K^{-1}$): thermal expansion coefficient; $\gamma_V$ (MPa/K): thermal pressure coefficient; $\chi$: Gruneisen parameter; $\varphi_S$ ($\times10^3$ K/MPa): isenthalpic Joule−Thomson coefficient; $\varphi_T$ ($\times10^{-4}$ $Å^3$): isothermal Joule−Thomson coefficient; and $\omega$ ($\times10^3$ m/s): sonic velocity.

urable quantities and fluctuations are ensemble-dependent, so various formulas must be applied to obtain any given property.

Obtained results of fluctuation properties calculated from MD simulations are summarized in Table 4. Based on the phase equilibrium curve of the studied sH hydrates, all of these hydrate systems can be in the stable region of the equilibrium curves at 5 MPa and 273.15 K so that they can remain stable. Hence, this P−T condition was selected to determine some thermodynamic/thermophysical characteristics of all systems. As is shown, the thermal expansion and compressibility of sH gas hydrates can be affected by both guest−host and host−host interactions. Also, compared to guest−host coupling interactions, the host−host interaction deterministically contributes to the thermal characteristics of sH crystalline clathrates. The inclusion of amino acids due to generating a local disturbance in the hydrogen-bonded network slightly influences the thermal parameters of the $CO_2$ + NH hydrate. Such behavior can also be observed when either 90% cage occupancy or double occupation is simulated. Also, fundamental properties for comprehending the nature of sH hydrates such as sonic velocity and thermal pressure coefficient are closely related to isobaric expansibility, isothermal compressibility, and the entropy of hydrate dissociation. The ratio between the isothermal compressibility and isobaric thermal expansivity gives the thermal pressure coefficient. The Gruneisen parameter is also a dimensionless thermodynamic parameter that can be formulated in terms of phonon nonlinearities. To understand how thermodynamic circumstances influence the thermal and vibrational properties by a volume change, this parameter can be applied. The Gruneisen parameter for most of the studied sH clathrate hydrates at 5 MPa and 273.15 K is found to be between about 1.6 and 2.3, while the higher value for the ice Ih is expected. The Joule−Thomson coefficient, known as the Joule−Kelvin coefficient, describes the rate of change of temperature with respect to pressure during a process of gas expansion or compression. It is calculated at

constant enthalpy through the partial derivative of the temperature concerning pressure. The Joule−Thomson coefficient is often used to predict the conditions of fluids under which hydrates will form through a throttling process. Therefore, this parameter for the circulation of hydrate slurry in different hydrate-based applications would be practical. As Table 4 shows, the lower isothermal Joule−Thomson coefficient for the mixed-gas sH hydrates is observed. Sonic velocity can also be defined by thermal expansivity, isothermal compressibility, and adiabatic compressibility. This characteristic of gas hydrates can vary depending on several factors such as the composition of the guests and the hydrate structure. Normally, gas hydrates have a lower sonic velocity compared to ice. Moreover, $CH_4$ hydrates have a higher sonic velocity compared to $CO_2$ hydrates due to the differences in molecular weight and composition. Additionally, the sonic velocity of structure-H may be lower than other clathrate hydrate structures.

## 4. CONCLUSIONS

This work investigated the impressions of amino acids, small and large guests, on the stability and dissociation process of $CO_2$ sH hydrates by using MD simulations, and the outcomes may potentially contribute to identifying the molecular mechanisms involved in $CO_2$ sH hydrates and their characteristics useful for the industrial hydrate-based applications. The obtained results demonstrated that the hydroxyl in amino acids tends to be located near the surface of oxygen and hydrogen atoms simultaneously. Therefore, the inclusion of organic amino acids by approaching the sH hydrate surface, increasing the diffusion coefficient of guest and host molecules, and accelerating the dissociation in the system can induce the sH hydrate dissociation. This may reduce the required energy for the dissociation stage of such hydrate-based technologies. Between the studied amino acids, the order of facilitating sH hydrate dissociation was found to be serine > glycine > L-

threonine > Leucine > L-valine. Also, the side chain and hydrophobicity of amino acids play a critical role in clathrate hydrate structural changes. Additionally, the type of guests can contribute to the clathrate alteration of sH hydrates, which corresponds to the operating circumstances. The combination of $CO_2$ with either $CH_4$ or $N_2$ was also recognized as more stable than with $H_2$ at the same thermodynamic conditions. Although the presence of $H_2$ molecules on the structural integration at the hydrate stable zone is not substantial, they stimulate the mobility of other molecules as the temperature increases. This phenomenon was also expedited when double $H_2$ molecules inside the small cavities were considered. Simulations of sH hydrates with 90% occupancy of small cages showed that the resistivity of hydrogen bonds between the water molecules can be slightly reduced due to the empty cages in the sH clathrate hydrate. Moreover, it may promote the local vibrations of host molecules, which can result in partial dissociation in the clathrate hydrate framework. The role of large molecular guests is identified as a highly effective contributor in which the hybrid inclusion of neohexene and cyclooctane gave more balanced sH clathrate hydrate than their standalone usage. Between the studied large guests, the most stable hydrate framework was found to be in the existence of 1,1-dimethyl cyclohexane and adamantane, while the lowest was recognized for 2-methyl cyclohexanone and 2,2,3-trimethyl butane sH hydrate formers. It is more likely that in preserving sH large cages against perturbations in water molecules, the large hydrocarbons including eight to ten carbon numbers are more effective than those comprising six or seven carbon numbers. Also, the large guests with a cyclic molecular structure seem to have more guest−host stability interactions in comparison with the branched molecules. In addition, the oxygen atom in the structure of their molecular can reduce the stability of sH clathrate hydrates. This may occur owing to the creation of hydrogen bonds with neighbor water molecules.

## AUTHOR INFORMATION

### Corresponding Authors

**Agus Saptoro** − *Department of Chemical and Energy Engineering and Curtin Malaysia Research Institute, Curtin University Malaysia, Miri, Sarawak 98009, Malaysia;* ⓘ orcid.org/0000-0002-1734-4788; Email: agus.saptoro@curtin.edu.my

**Sepideh Amjad-Iranagh** − *Department of Materials and Metallurgical Engineering, Amirkabir University of Technology, Tehran 15875-4313, Iran;* ⓘ orcid.org/0000-0002-3220-7992; Email: amjad_i_s@aut.ac.ir

**Amir H. Mohammadi** − *Discipline of Chemical Engineering, School of Engineering, University of KwaZulu-Natal, Howard College Campus, Durban 4041, South Africa; Department of Chemical Engineering, Faculty of Engineering and the Built Environment, Cape Peninsula University of Technology, Bellville Campus, Bellville 7535, South Africa;* ⓘ orcid.org/0000-0002-2947-1135; Email: amir_h_mohammadi@yahoo.com

### Author

**Saeid Sinehbaghizadeh** − *Department of Chemical and Energy Engineering, Curtin University Malaysia, Miri, Sarawak 98009, Malaysia*

Complete contact information is available at:
https://pubs.acs.org/10.1021/acs.energyfuels.3c01312

### Notes

## REFERENCES

(1) Ma, Z. W.; Zhang, P.; Bao, H. S.; Deng, S. Review of Fundamental Properties of $CO_2$ Hydrates and $CO_2$ Capture and Separation Using Hydration Method. *Renewable Sustainable Energy Rev.* **2016**, *53*, 1273−1302.

(2) Sloan, E. D.; Koh, C. A. *Clathrate Hydrates of Natural Gases*, 3rd Ed.; CRC Press, Taylor & Francis Group: Boca Raton, 2008.

(3) Li, L.; Fan, S.; Yang, G.; Chen, Q.; Zhao, J.; Wei, N.; Meng, W.; Fan, J.; Yang, H. Continuous Simulation of the Separation Process of $CO_2/H_2$ by Forming Hydrate. *Chem. Eng. Sci. X* **2020**, *7*, No. 100067.

(4) Sinehbaghizadeh, S.; Saptoro, A.; Mohammadi, A. H. $CO_2$ Hydrate Properties and Applications: A State of the Art. *Prog. Energy Combust. Sci.* **2022**, *93*, No. 101026.

(5) Sinehbaghizadeh, S.; Saptoro, A.; Amjad-Iranagh, S.; Naeiji, P.; Tiong, A. N. T.; Mohammadi, A. H. A Comprehensive Review on Molecular Dynamics Simulation Studies of Phenomena and Characteristics Associated with Clathrate Hydrates. *Fuel* **2023**, *338*, No. 127201.

(6) Xie, N.; Tan, C.; Yang, S.; Liu, Z. Conceptual Design and Analysis of a Novel $CO_2$ Hydrate-Based Refrigeration System with Cold Energy Storage. *ACS Sustainable Chem. Eng.* **2019**, *7*, 1502−1511.

(7) Ngan, Y. T.; Englezos, P. Concentration of Mechanical Pulp Mill Effluents and NaCl Solutions through Propane Hydrate Formation. *Ind. Eng. Chem. Res.* **1996**, *35*, 1894−1900.

(8) Mu, L.; Zhang, Q.; Cui, Q. Experimental Study on $CO_2$ Capture from Simulated Flue Gas with an Adsorption−Hydration Method. *Ind. Eng. Chem. Res.* **2021**, *60*, 3411−3420.

(9) Wang, X.; Yang, S.; Zhang, H.; Xu, X.; Wood, C. D.; Lipiński, W. Amine Infused Hydrogel-Based $CO_2$ Gas Storage Technology for $CO_2$ Hydrate-Based Cold Thermal Energy Storage. *J. $CO_2$ Util.* **2021**, *53*, No. 101705.

(10) Wang, L.; Zhang, Y.; Xie, H.; Lu, X.; Wen, X.; Liu, Z.; Zhou, H.; Liu, Z.; Xu, Y. Effect of Voltage and Initial Temperature on Thermodynamics and Kinetics of $CO_2$ Hydrate Formation in an Electrostatic Spraying Reactor. *Energy* **2022**, *239*, No. 122384.

(11) Xu, G.; Xu, C.-G.; Wang, M.; Cai, J.; Chen, Z.-Y.; Li, X.-S. Influence of Nickel Foam on Kinetics and Separation Efficiency of Hydrate-Based Carbon Dioxide Separation. *Energy* **2021**, *231*, No. 120826.

(12) Wang, Y.; Yin, K.; Lang, X.; Fan, S.; Li, G.; Yu, C.; Wang, S. Hydrogen Storage in SH Binary Hydrate: Insights from Molecular Dynamics Simulation. *Int. J. Hydrogen Energy* **2021**, *46*, 15748−15760.

(13) Khokhar, A. A.; Gudmundsson, J. S.; Sloan, E. D. Gas Storage in Structure H Hydrates. *Fluid Phase Equilib.* **1998**, *150–151*, 383−392.

(14) Sinehbaghizadeh, S.; Javanmardi, J.; Roosta, A.; Mohammadi, A. H. Estimation of the Dissociation Conditions and Storage Capacities of Various SH Clathrate Hydrate Systems Using Effective Deterministic Frameworks. *Fuel* **2019**, *247*, 272−286.

(15) Sinehbaghizadeh, S.; Javanmardi, J.; Mohammadi, A. H. Phase Stability Conditions of Clathrate Hydrates in the (Methane + 3-Methyl-1-Butanol + Water), (Methane + 3,3-Dimethyl-2-Butanone + Water) and (Methane + 2,3-Dimethyl-2-Butene + Water) Systems: Experimental Measurements and Thermodynamic Modeling. *J. Chem. Thermodyn.* **2018**, *125*, 64−70.

(16) Sinehbaghizadeh, S.; Javanmardi, J.; Roosta, A.; Mohammadi, A. H. A Fugacity Approach for Prediction of Phase Equilibria of Methane Clathrate Hydrate in Structure H. *Phys. Chem. Res.* **2017**, *5*, 465−481.

(17) Bai, J.; Zhen, X.; Xie, G.; Li, P.; Fang, S.; Chang, C.; Gu, X. Kinetics Investigation of Hydrate-Based $CO_2$ Capture from Simulated Flue Gas by Using an Improved Combinatorial Promoter. *Energy Fuels* **2018**, *32*, 10822−10829.

(18) Srivastava, S.; Kollemparembil, A. M.; Zettel, V.; Claßen, T.; Gatternig, B.; Delgado, A.; Hitzmann, B. Experimental Investigation of $CO_2$ Uptake in $CO_2$ Hydrates Formation with Amino Acids as Kinetic Promoters and Its Dissociation at High Temperature. *Sci. Rep.* **2022**, *12*, No. 8359.

(19) Rehman, A. N.; Bavoh, C. B.; Lal, B.; Sabil, K. M.; Sangwai, J. S. Insights on $CO_2$ Hydrate Formation and Dissociation Kinetics of Amino Acids in a Brine Solution. *Ind. Eng. Chem. Res.* **2022**, *61*, 13863−13876.

(20) Burla, S. K.; Tulluru, B.; Prasad, P. S. R. Collective Impact of Amino Acids on Clathrate Hydrates of the $CO_2$ + $CH_4$ Gas Mixture. *Energy Fuels* **2022**, *36*, 10618−10626.

(21) Bavoh, C. B.; Lal, B.; Osei, H.; Sabil, K. M.; Mukhtar, H. A Review on the Role of Amino Acids in Gas Hydrate Inhibition, $CO_2$ Capture and Sequestration, and Natural Gas Storage. *J. Nat. Gas Sci. Eng.* **2019**, *64*, 52−71.

(22) Bhattacharjee, G.; Linga, P. Amino Acids as Kinetic Promoters for Gas Hydrate Applications: A Mini Review. *Energy Fuels* **2021**, *35*, 7553−7571.

(23) Roosta, H.; Dashti, A.; Mazloumi, S. H.; Varaminian, F. Inhibition Properties of New Amino Acids for Prevention of Hydrate Formation in Carbon Dioxide−Water System: Experimental and Modeling Investigations. *J. Mol. Liq.* **2016**, *215*, 656−663.

(24) Sa, J.-H.; Lee, B. R.; Park, D.-H.; Han, K.; Chun, H. D.; Lee, K.-H. Amino Acids as Natural Inhibitors for Hydrate Formation in $CO_2$ Sequestration. *Environ. Sci. Technol.* **2011**, *45*, 5885−5891.

(25) Kamei, N.; Tamiwa, H.; Miyata, M.; Haruna, Y.; Matsumura, K.; Ogino, H.; Hirano, S.; Higashiyama, K.; Takeda-Morishita, M. Hydrophobic Amino Acid Tryptophan Shows Promise as a Potential Absorption Enhancer for Oral Delivery of Biopharmaceuticals. *Pharmaceutics* **2018**, *10*, No. 182.

(26) Veluswamy, H. P.; Lee, P. Y.; Premasinghe, K.; Linga, P. Effect of Biofriendly Amino Acids on the Kinetics of Methane Hydrate Formation and Dissociation. *Ind. Eng. Chem. Res.* **2017**, *56*, 6145−6154.

(27) Sa, J.-H.; Kwak, G.-H.; Han, K.; Ahn, D.; Lee, K.-H. Gas Hydrate Inhibition by Perturbation of Liquid Water Structure. *Sci. Rep.* **2015**, *5*, No. 11526.

(28) Pires, J. P.; da Silva Ramos, A.; Mattos, C. F.; Ketzer, M.; Lourega, R. V. Analysis of the Effect of Organic Salts Derived from L-Phenylalanine Amino Acid as Kinetic Promoters/Inhibitors of $CO_2$ Hydrates. *Energy Fuels* **2021**, *35*, 8095−8101.

(29) Kiran, B. S.; Bhavya, T.; Prasad, P. S. Synergistic and Antagonistic Effects of Amino Acids in Clathrate Hydrates of Greenhouse Gases. *Chem. Eng. J. Adv.* **2021**, *7*, No. 100117.

(30) Bharathi, A.; Nashed, O.; Lal, B.; Foo, K. S. Experimental and Modeling Studies on Enhancing the Thermodynamic Hydrate Inhibition Performance of Monoethylene Glycol via Synergistic Green Material. *Sci. Rep.* **2021**, *11*, No. 2396.

(31) Pandey, J. S.; Daas, Y. J.; Solms, N. V. Screening of Amino Acids and Surfactant as Hydrate Promoter for $CO_2$ Capture from Flue Gas. *Processes* **2020**, *8*, No. 124.

(32) Gaikwad, N.; Bhattacharjee, G.; Kushwaha, O. S.; Sangwai, J. S.; Linga, P.; Kumar, R. Effect of Cyclooctane and L-Tryptophan on Hydrate Formation from an Equimolar $CO_2$−$CH_4$ Gas Mixture Employing a Horizontal-Tray Packed Bed Reactor. *Energy Fuels* **2020**, *34*, 9840−9851.

(33) Prasad, P. S. R.; Sai Kiran, B. Clathrate Hydrates of Greenhouse Gases in the Presence of Natural Amino Acids: Storage, Transportation and Separation Applications. *Sci. Rep.* **2018**, *8*, No. 8560.

(34) Maddah, M.; Maddah, M.; Peyvandi, K. Molecular Dynamics Simulation of Methane Hydrate Formation in Presence and Absence of Amino Acid Inhibitors. *J. Mol. Liq.* **2018**, *269*, 721−732.

(35) Bhattacharjee, G.; Choudhary, N.; Kumar, A.; Chakrabarty, S.; Kumar, R. Effect of the Amino Acid L-Histidine on Methane Hydrate Growth Kinetics. *J. Nat. Gas Sci. Eng.* **2016**, *35*, 1453−1462.

(36) Hu, Y.; Wang, S.; Yang, X.; He, Y. Examination of Amino Acid Inhibitor Effect in Methane Hydrate Dissociation via Molecular Dynamics Simulation. *J. Mol. Liq.* **2021**, *325*, No. 115205.

(37) Zhu, J.; Li, X.; Liu, Z.; Sun, X.; Zhao, L.; Shi, Y.; Zhou, G.; Rui, Z.; Lu, G. Effect of Biofriendly Amino Acids on Methane Hydrate Decomposition: Insights from Molecular Dynamics Simulations. *Fuel* **2022**, *325*, No. 124919.

(38) Hussain, H. H.; Husin, H. The Effect of Synergistic Amino Acids-Ionic Liquids in Methane Hydrate Inhibition by COSMO-RS Application. *J. Mol. Liq.* **2021**, *321*, No. 114837.

(39) Liu, N.; Zhou, J.; Hong, C. Molecular Dynamics Simulations on Dissociation of $CO_2$ Hydrate in the Presence of Inhibitor. *Chem. Phys.* **2020**, *538*, No. 110894.

(40) Sinehbaghizadeh, S.; Saptoro, A.; Amjad-Iranagh, S.; Tze Tiong, A. N.; Mohammadi, A. H. Molecular Dynamics Simulation Studies on the Stability and Dissociation of Clathrate Hydrates of Single and Double Greenhouse Gases. *Energy Fuels* **2022**, *36*, 8323−8339.

(41) Sinehbaghizadeh, S.; Saptoro, A.; Naeiji, P.; Tiong, A. N. T.; Mohammadi, A. H. Insights into the Synergistic Effects of Metal Particles (Ag, Cu, and Fe) and Urea on $CO_2$ Clathrate Hydrate Growth Using Molecular Dynamics Simulations. *Chem. Eng. Sci.* **2022**, *264*, No. 118194.

(42) Takeuchi, F.; Hiratsuka, M.; Ohmura, R.; Alavi, S.; Sum, A. K.; Yasuoka, K. Water Proton Configurations in Structures I, II, and H Clathrate Hydrate Unit Cells. *J. Chem. Phys.* **2013**, *138*, No. 124504.

(43) Jin, Y.; Kida, M.; Nagao, J. Structure H Clathrate Hydrates in Methane−Halogenic Large Molecule Substance−Water Systems. *J. Phys. Chem. C* **2019**, *123*, 17170−17175.

(44) Beltrán, J. G.; Servio, P. Equilibrium Studies for the System Methane + Carbon Dioxide + Neohexane + Water. *J. Chem. Eng. Data* **2008**, *53*, 1745−1749.

(45) Lee, Y.; Lee, D.; Lee, J. W.; Seo, Y. Enclathration of $CO_2$ as a Co-Guest of Structure H Hydrates and Its Implications for $CO_2$ Capture and Sequestration. *Appl. Energy* **2016**, *163*, 51−59.

(46) Servio, P.; Lagers, F.; Peters, C.; Englezos, P. Gas Hydrate Phase Equilibrium in the System Methane-Carbon Dioxide-Neohexane and Water. *Fluid Phase Equilib.* **1999**, *158−160*, 795−800.

(47) Uchida, T.; Ohmura, R.; Ikeda, I. Y.; Nagao, J.; Takeya, S.; Hori, A. Phase Equilibrium Measurements and Crystallographic Analyses on Structure-H Type Gas Hydrate Formed from the $CH_4$−$CO_2$−neohexane−water System. *J. Phys. Chem. B* **2006**, *110*, 4583−4588.

(48) Berendsen, H. J. C.; Postma, J. P. M.; van Gunsteren, W. F.; DiNola, A.; Haak, J. R. Molecular Dynamics with Coupling to an External Bath. *J. Chem. Phys.* **1984**, *81*, 3684−3690.

(49) Hagler, A. T.; Lifson, S.; Dauber, P. Consistent Force Field Studies of Intermolecular Forces in Hydrogen-Bonded Crystals. 2. A Benchmark for the Objective Comparison of Alternative Force Fields. *J. Am. Chem. Soc.* **1979**, *101*, 5122−5130.

(50) Lange, J.; de Souza, F. G.; Nele, M.; Tavares, F. W.; Segtovich, I. S. V.; da Silva, G. C. Q.; Pinto, J. C. Molecular Dynamic Simulation of Oxaliplatin Diffusion in Poly(Lactic Acid- Co -Glycolic Acid). Part A: Parameterization and Validation of the Force-Field CVFF. *Macromol. Theory Simul.* **2016**, *25*, 45−62.

(51) Gaedt, K.; Holtje, H.-D. Consistent Valence Force-Field Parameterization of Bond Lengths and Angles with Quantum Chemicalab Initio Methods Applied to Some Heterocyclic Dopamine D3-Receptor Agonists. *J. Comput. Chem.* **1998**, *19*, 935−946.

(52) Zhang, Z.; Kusalik, P. G.; Guo, G.-J.; Ning, F.; Wu, N. Insight on the Stability of Polycrystalline Natural Gas Hydrates by Molecular Dynamics Simulations. *Fuel* **2021**, *289*, No. 119946.

(53) Kondori, J.; James, L.; Zendehboudi, S. Molecular Scale Modeling Approach to Evaluate Stability and Dissociation of Methane and Carbon Dioxide Hydrates. *J. Mol. Liq.* **2020**, *297*, No. 111503.

(54) Shankar, U.; Gogoi, R.; Sethi, S. K.; Verma, A.Introduction to Materials Studio Software for the Atomistic-Scale Simulations. In *Forcefields for Atomistic-Scale Simulations: Materials and Applications*; Springer, 2022; pp 299−313.

(55) Liang, S.; Kusalik, P. G. Explorations of Gas Hydrate Crystal Growth by Molecular Simulations. *Chem. Phys. Lett.* **2010**, *494*, 123−133.

(56) Alavi, S.; Shin, K.; Ripmeester, J. A. Molecular Dynamics Simulations of Hydrogen Bonding in Clathrate Hydrates with Ammonia and Methanol Guest Molecules. *J. Chem. Eng. Data* **2015**, *60*, 389−397.

(57) Mehta, A. P.; Sloan, E. D. Improved Thermodynamic Parameters for Prediction of Structure H Hydrate Equilibria. *AIChE J.* **1996**, *42*, 2036−2046.

# Chapter 7 (Objective 5): The effects of associated gas impurities on the formation of biogas hydrate and the kinetical modelling

As Figure 13 (step 5) of the chapter 1 indicated, the influences of kinetic hydrate promoters (KHPs) on pure/mixed $CO_2$ hydrate formation were discussed in chapters 3 and 4; while the effects of thermodynamic hydrate promoters (THPs) were investigated in chapters 5 and 6. This chapter deals with the impressions of different gas species on $CO_2$ hydrate formation and how gas impurities can affect the process of hydrate growth. The kinetics of the simulated hydrate systems have also been predicted by developing a kinetical model.

To purify the biogas and split it into reach $CH_4$ and remaining gases mostly $CO_2$, the effects of gas impurities such as $H_2S$, $SO_2$, $N_2$, and $H_2$ using hydrate-based methods are substantial. Although these components exist in the biogas stream as a trace, they can change the properties of the process of hydrate formation. For example, these gas species can alter the fraction of cage occupancy and operating formation conditions. Moreover, there is a close relationship between the amount of fraction of dissolved bases in the liquid water and the growth rate. Hence, the kinetics of the biogas hydrate formation considering the gas dissolution needs to be understood. In this chapter, the influence of the gas impurities which are mostly present as a trace in the biogas during the hydrate formation was studied.

In addition, kinetic two-parametric modelling for the growth rate of biogas hydrate based on various ranges of gas dissolution, operating conditions, and gas compositions was provided. The current kinetic model has been developed based on irreversible and non-equilibrium thermodynamics and the concept of the thermodynamic natural path to determine the hydrate formation kinetics. Generally, the irreversible processes that take place in non-equilibrium systems can be described in terms of the thermodynamic forces and flows such as the irreversible flow of heat. Hence, this model may bridge the gap between the mass action mechanistic approach and the non-mechanistic irreversible thermodynamic approach. The assumptions of this work are also according to the classical kinetic approach in which a stoichiometric hydrate formation proceeds from an initiation state to an equilibrium state. The driving force for the chemical reaction has been considered as chemical affinity where the rate of decay of the chemical affinity can control the observed hydrate growth reaction velocity. Also, the natural path velocity can be derived directly from thermodynamic considerations and can be correlated with the empirical data.

This chapter was submitted as a research paper in Energy Journal:

Sinehbaghizadeh, S., Saptoro, A., Amjad, S., Mohammadi, A.H. Understanding the influences of different associated gas impurities and the kinetic modelling of biogas hydrate formation at the molecular scale. *Energy Journal*, 2023, 282, 128893, Elsevier.
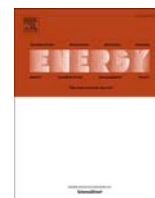
# Understanding the influences of different associated gas impurities and the kinetic modelling of biogas hydrate formation at the molecular scale

Saeid Sinehbaghizadeh [a],[*], Agus Saptoro [a],[b],[*], Sepideh Amjad-Iranagh [c], Amir H. Mohammadi [d]

[a] Department of Chemical and Energy Engineering, Curtin University Malaysia, CDT 250 Miri, Sarawak 98009, Malaysia
[b] Curtin Malaysia Research Institute, Curtin University Malaysia, CDT 250, Miri 98009, Sarawak, Malaysia
[c] Department of Materials and Metallurgical Engineering, Amirkabir University of Technology, Tehran, 15875-4313, Iran
[d] Discipline of Chemical Engineering, School of Engineering, University of KwaZulu-Natal, Howard College Campus, King George V Avenue, Durban 4041, South Africa

## A B S T R A C T

The biological degradation of organic waste generates biogas that mostly comprises a mixture of $CH_4$ and $CO_2$. The separation of $CO_2$ and other gas impurities from $CH_4$ using a hydrate-based technique has recently gained interest as an option. The captured $CO_2$ and impurities can then be sequestered in natural gas hydrate (NGH) geological sites leading to an exchange of the in situ $CH_4$ hydrate over to $CO_2$-dominated hydrate and a simultaneous $CH_4$ release from these huge natural sources of energy in permafrost sediments. Consequently, the effects of associated gas impurities such as $SO_2$, $H_2S$, $N_2$, and $H_2$ on either hydrate-based biogas purification or residual sequestration in NGH deposits need to be well-understood. In this work, the influence of different biogas compositions on the process of clathrate hydrate formation using molecular dynamics (MD) simulations was investigated. Additionally, a kinetic model for predicting the progress of biogas crystal growth based on the formation of the number of hydrogen bonds as well as total energy is proposed. The results elucidate that the concentration of dissolved gas in liquid water at the solid-solution interface is one of the key controllers of the growth rate but it has less impact on the filling percentage of formed both types the clathrate hydrate cages. The presence of $H_2S$ and $SO_2$ molecules was found to slightly increase the formation of biogas hydrate. On the other hand, $N_2$, and $H_2$ molecules reduce the rate of biogas hydrate generation.

## 1. Introduction

Landfill gas or biogas is a mixture of gases generated from the biological degradation of organic waste in biowaste treatment plants. The main proportion of landfill gas includes a mixture of 25–50 mol% of $CO_2$ and 50–75 mol% of $CH_4$, however, it contains the other associated gas species such as $N_2$ and the trace of $H_2S$, $H_2$, and $SO_2$ in which their concentrations depend on the type of the feedstock. Therefore, the removal of $CO_2$ and other impurities as well as $CH_4$ enrichment in the production phase would be a part of biogas processing [1]. Although both $CO_2$ and $CH_4$ are greenhouse gases and need to be controlled, the other unfavorable components known as impurities such as $H_2S$ and $SO_2$ can reduce the quality of final production. Up to now, different processes have been designed to perform biogas processing. For example, separation with membranes, cryogenic fractionation, adsorption with molecular sieves or activated carbons, physical absorption with methanol or glycols, or chemical absorption with carbonates and amines are some

of these methods that have been previously developed in the industrial division [2]. However, the main disadvantages of these technologies are the required high energy costs as well as different ranges of environmental impacts [3,4]. Recently, to develop the process of either $CO_2$ or impurity separation from gas emissions, hydrate-based methods have been introduced. Gas hydrate, or clathrate hydrate are ice-like crystalline compounds in which the guest molecules (gas and/or some volatile liquid molecules) at a proper thermodynamic state are encapsulated through the hydrogen-bonded water molecules as a host [5]. Some investigations indicate that the utilization of hydrate technologies is a more cost-effective and environmentally friendly alternative in comparison with conventional methods [6–8]. In addition, $CO_2$ sequestration by injecting $CO_2$ into the geological hydrate zones e.g. natural gas hydrates present on the floor of oceans or permafrost, and at the same time producing the $CH_4$ (known as replacement phenomenon) would be the next step after performing the hydrate-based biogas purification. We recently overviewed a large proportion of suggested hydrate-based

---

**Table 1**
Number of gas molecules in the solution phase for different cases of the simulations.

| Solution: | Full saturation (100%) | | | | Partial saturation (75%) | | | | Partial saturation (50%) | | | |
|---|---|---|---|---|---|---|---|---|---|---|---|---|
| Case: | **C1** | **C2** | **C3** | **C4** | **C5** | **C6** | **C7** | **C8** | **C9** | **C10** | **C11** | **C12** |
| **CH$_4$** | 32 | 64 | 60 | 28 | 24 | 48 | 44 | 20 | 16 | 32 | 30 | 14 |
| **CO$_2$** | 96 | 64 | 60 | 92 | 72 | 48 | 44 | 68 | 48 | 32 | 30 | 46 |
| **H$_2$S** | – | – | 4 | 4 | – | – | 4 | 4 | – | – | 2 | 2 |
| **SO$_2$** | – | – | 4 | 4 | – | – | 4 | 4 | – | – | 2 | 2 |
| Solution: | **Full saturation (100%)** | | | | **Partial saturation (75%)** | | | | **Partial saturation (50%)** | | | |
| Case: | **C13** | **C14** | **C15** | **C16** | **C17** | **C18** | **C19** | **C20** | **C21** | **C22** | **C23** | **C24** |
| **CH$_4$** | 60 | 60 | 60 | 56 | 44 | 44 | 44 | 40 | 30 | 30 | 30 | 28 |
| **CO$_2$** | 60 | 60 | 60 | 56 | 44 | 44 | 44 | 40 | 30 | 30 | 30 | 28 |
| **H$_2$S** | – | – | – | 4 | – | – | – | 4 | – | – | – | 2 |
| **SO$_2$** | – | – | – | 4 | – | – | – | 4 | – | – | – | 2 |
| **N$_2$** | 8 | – | 4 | 4 | 8 | – | 4 | 4 | 4 | – | 2 | 2 |
| **H$_2$** | – | 8 | 4 | 4 | – | 8 | 4 | 4 | – | 4 | 2 | 2 |

technologies as well as their characteristics, strengths, weaknesses, prospects, and challenges [9]. Understanding how associated impurities can affect the growth of biogas hydrate would be vital from two aspects: the process of gas separation and permanent unfavorable gas sequestration in natural gas hydrate locations. The gas impurities may also contribute to the leakage and disposal of $CO_2$ in backing into the ocean after the sequestration. The observation by X-ray diffraction analysis (XRD) and Raman spectroscopy revealed that a small fraction of impurities can influence the conversion rate of the hydrate formation [10]. Worth mentioning that in case of splitting $CO_2$ and other impurities, they can be sequestered by injecting them into the hydrate sediments. The process of gas exchange can occur through a cage opening without the melting down of the solid phase. Hence, a technology for coupled $CH_4$ production from these resources and long-term $CO_2$ storage in natural hydrate sediments with considering environmental safety may

be feasible [11,12].

Besides the macroscopic findings using laboratory equipment, investigation of $CO_2$+$CH_4$ hydrate formation and analyzing the effects of impurities at a molecular level can aid to comprehend the microscopic mechanisms involved in the processes of mentioned methods [13–18]. MD simulations have revealed that $H_2S$ and $SO_2$ impurities would have higher stability in the clathrate hydrate in comparison with $CO_2$ molecules. Therefore, increasing the concentration of such impurities in the feed can lead to a decrease in the rate of capturing/storing pure $CO_2$. In contrast, these components would ease the thermodynamic state of the hydrate formation. Hence, the pretreatment for removing $H_2S$ and $SO_2$ impurities from the captured $CO_2$ before storing it in the depleted natural gas deposits may not be required. However, the presence of $H_2S$ and $SO_2$ impurities in the reach $CO_2$ stream may increase the probability of water acidification as well as a corrosive influence on the rocks of the
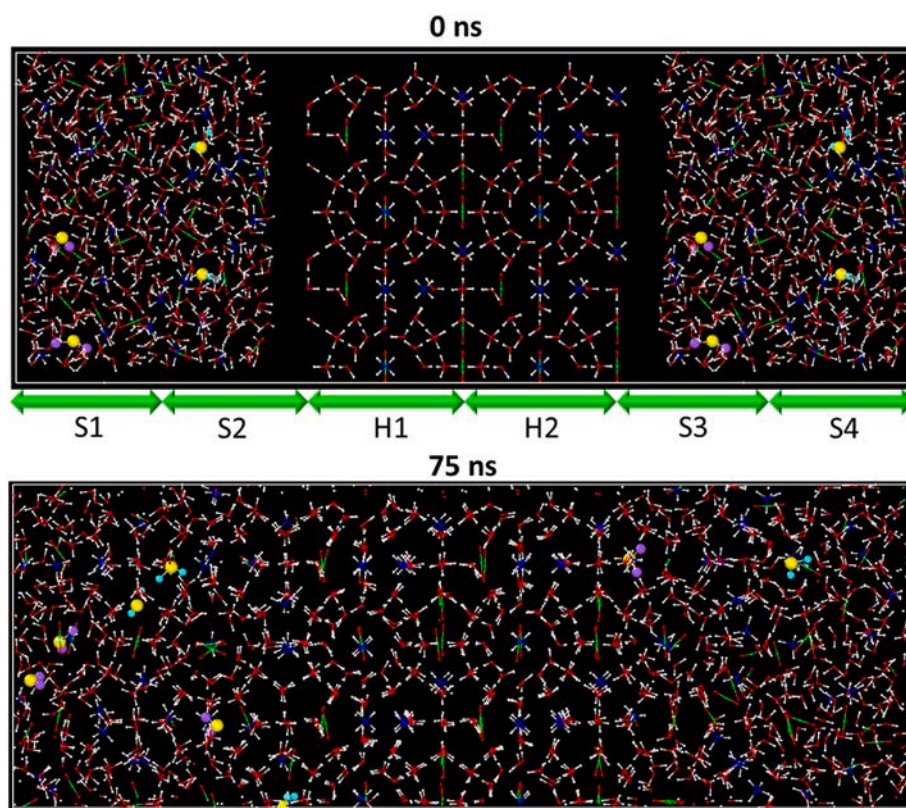


**Fig. 1.** Discretization of simulation box for case C3 in the Z-direction into the different layers; S and H indicate solution and hydrate phases, respectively; water, $CO_2$, and $CH_4$ molecules are in red and white, green and red, dark blue and white colors, respectively; $SO_2$ and $H_2S$ are also in purple and yellow, light blue and yellow, respectively.

sediments [19]. Density functional theory (DFT) calculations showed that associated gases like $SO_2$ and $H_2S$ by increasing the bulk modulus and reducing Young's modulus as well as shear modulus can alter the mechanical characteristics of the formed hydrates [20]. Therefore, the structural stability due to increasing elastic strain against force-induced deformation may be enhanced [21,22]. The occupancy ratio and the adsorption isotherm analysis of small and large cages using combined MD simulations and Grand canonical Monte Carlo (GCMC) showed that $SO_2$ molecules tend to fill the large cavities but $H_2S$ has no preference to occupy the cage types. Also, single occupancy would be the dominant scenario for the distribution of these gas molecules. Moreover, the potential of these gas species in replacing $CH_4$ from natural gas hydrates was confirmed [23].

Although some MD studies to evaluate the effects of gas impurities have been conducted, the impressions of these components on the cage occupancy, growth rate, gas distribution in the hydrate phase, and the importance of dissolved gas in the water phase are still poorly understood. In this work, the growth properties of $CO_2+CH_4$ hydrate and the impressions of gas impurities such as $H_2S$, $SO_2$, $N_2$, and $H_2$ (similar to the biogas composition) with the utilization of molecular dynamics (MD) simulations have been carried out. In addition, a kinetic model to predict the process of $CO_2+CH_4$ hydrate formation without/with impurities for the simulated systems based on the MD analysis parameters has been developed.

## 2. Simulation methodology

In this study, to analyse the effects of different biogas compositions and the presence of associated impurities such as $H_2S$, $SO_2$, $N_2$, and $H_2$, different gas compositions were considered. Since the main proportion of biogas is $CO_2$ and $CH_4$ which is in a range between 50/50 and 75/25 mole percent for $CO_2/CH_4$, the upper and lower of this range were selected as base cases. Hence, the number of these molecules in cases 1 and 2 (C1, C2) is based on the mentioned values. Regarding the other simulated cases, between 3 mole % and 9 mole % gas impurities (e.g. $SO_2$, $H_2S$, $N_2$, $H_2$) were considered to investigate the influences of these components during biogas hydrate formation. Table 1 summarizes the number of initial gas molecules in the water phase for 24 studied cases. The initial simulation box was constructed with $2 \times 2 \times 2$ hydrate supercells (including 368 water molecules and 64 gas molecules) surrounded by two equal solutions. The process of hydrate formation is started by dissolving gas molecules in the water phase which creates the solution phase in contact with the solid phase. However, considering separate layers for water and gas phases to achieve the final solution requires a long simulation time (e.g. hundreds of nanoseconds or even over a microsecond). Therefore, similar to the hydrate growth MD studies reported in the literature, the step of gas dissolution in the water phase was ignored and a solution phase was considered to start the simulations [24,25]. The initial solution phase was built using the Packmol code [26] which is a computer program designed to generate initial configurations and uses a random placement algorithm to position the gas and water molecules within the simulation box.

Experimental evidence using X-ray diffraction has proven that biogas can form sI clathrate hydrate [10]. So that the maximum number of gas and water molecules for the solution phase would be 128 and 736 molecules if 100% conversion of the solution phase to the clathrate hydrate occurs. Therefore, three different scenarios: 100%, 75%, and 50% including 128, 96, and 64 gas molecules between liquid water were considered. It should be noted that since the simulation box indicates the initial growth of the biogas hydrates at the nano-scale of the solid-solution interface, the stoichiometric composition of sI hydrate was considered as the basis for all simulations.

Fig. 1 exhibits the initial configuration as well as segments of the simulation box. To better detect the evolution of molecular positions in the surrounding phase, both solid and solution phases were segmentized into equal sections.

**Table 2**
Operating conditions for the simulated hydrate cases.

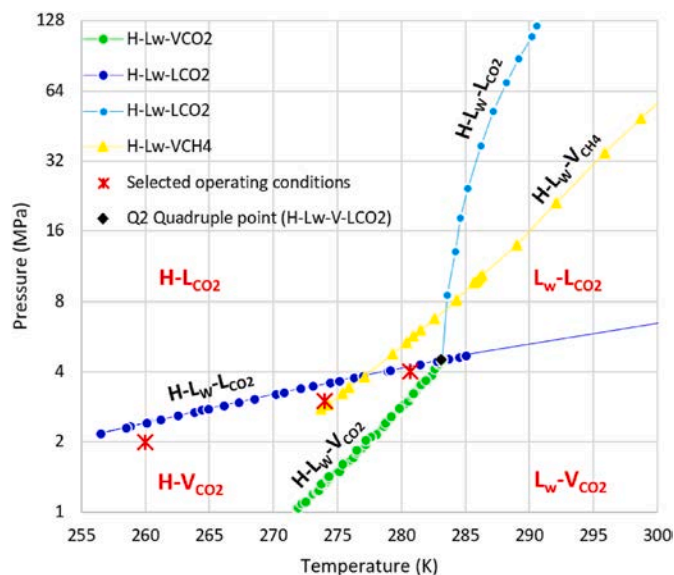| Cases | Operating conditions | 260 K, 2 MPa | 274 K, 3 MPa | 281 K, 4 MPa |
|-------|---------------------|--------------|--------------|--------------|
| | C1 to C4 | ✓ | ✓ | ✓ |
| | C5 to C8 | - | ✓ | ✓ |
| | C9 to C12 | - | ✓ | ✓ |
| | C13 to C16 | ✓ | ✓ | - |
| | C17 to C24 | - | ✓ | - |



**Fig. 2.** Phase coexistence of $CO_2$ hydrate in equilibrium with liquid and vapor/gas phase.

The MD simulations were implemented by employing the LAMMPS software [27] which is an open-source package. The interactions of water molecules were modeled using TIP4P-Ew potential [28] while the TRAPPE force field was utilized for $CO_2$, $CH_4$, and $N_2$ molecules [29]. Also, the rigid Kamath and Ribeiro potentials were applied for $H_2S$, and $SO_2$ molecules, respectively [30,31]. To simulate the molecular interactions of $H_2$ with other components, Alavi potential model was utilized [32]. In addition, the Lorentz-Berthelot combining rules were employed to describe the cross lennard jones (L-J) parameters between water and guest molecules. Also, by utilizing the SHAKE algorithm, the angles of water molecules and bond lengths were constrained. The SHAKE algorithm can be used in MD simulations to maintain the structural integrity of water molecules. It allows for larger integration time steps by constraining bond lengths and angles within predefined limits. This improves computational efficiency without sacrificing accuracy and enables accurate representation of water behavior in scientific investigations. To proceed with the simulations, an integration time step of 1 fs was set. The sum of long-range Coulomb and the van der Waals potentials with a precision of $1 \times 10^{-4}$ k-space cutoff was calculated using the Ewald summation method. Moreover, a spherical cutoff of 11.0 Å was set for all intermolecular interactions. In order to perform an energy minimization step, the steepest descent algorithm was applied. Then by conducting the NVT ensemble, the simulations were performed for 40 ps? This step was followed by implementing the NPT ensemble. As a production phase for all simulations, this step was continued up to 75 ns. Simulated cases were conducted at three various pressure and temperature operating conditions where the gas phase can be in equilibrium with the hydrate phase. As is presented in Table 2, the feasible operating conditions for the hydrate-based bigas purification were selected for the simulations. The operating conditions were chosen from the hydrate-vapor region of the $CO_2+CH_4$ phase coexistence
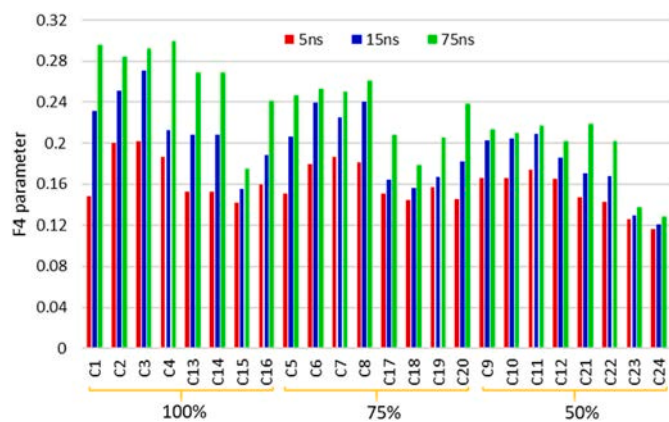
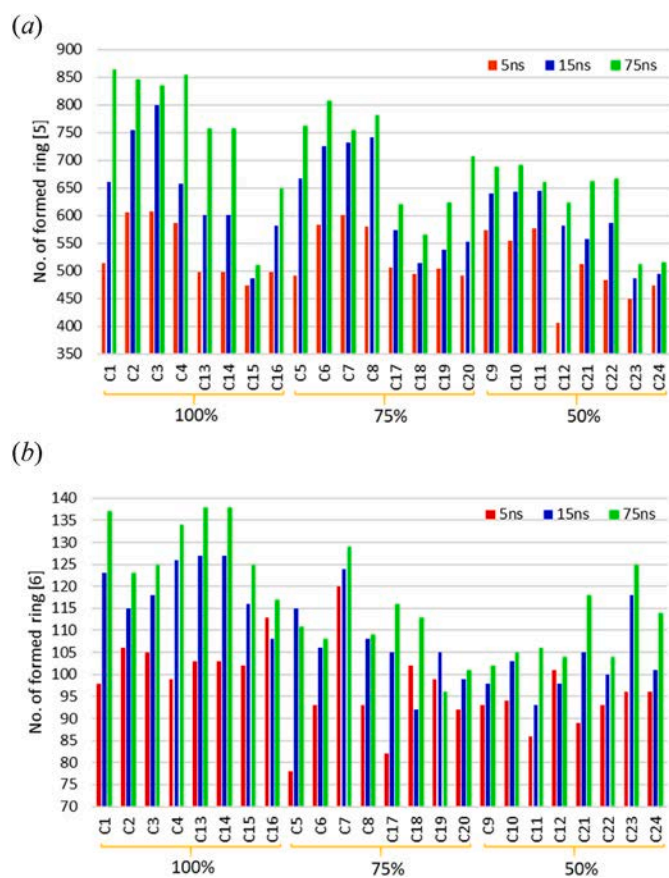**Fig. 3.** F4 parameter of studied all simulation cases at 274 K and 3 MPa.



**Fig. 4.** Formed pentagon and hexagon rings of all simulated cases at 274 K and 3 MPa.

diagram as is shown in Fig. 2.

## 3. Results and discussion

### 3.1. Effects of impurities on biogas hydrate growth

To confirm the growth of gas hydrates in all performed simulations, the structural F4 order parameter was computed. This parameter is used in gas hydrate simulations to quantify the structural order of the formed crystalline shape. It measures the fraction of water molecules involved in a nearly perfect tetrahedral arrangement. Higher F4 values indicate greater tetrahedral order, providing insights into higher gas hydrate
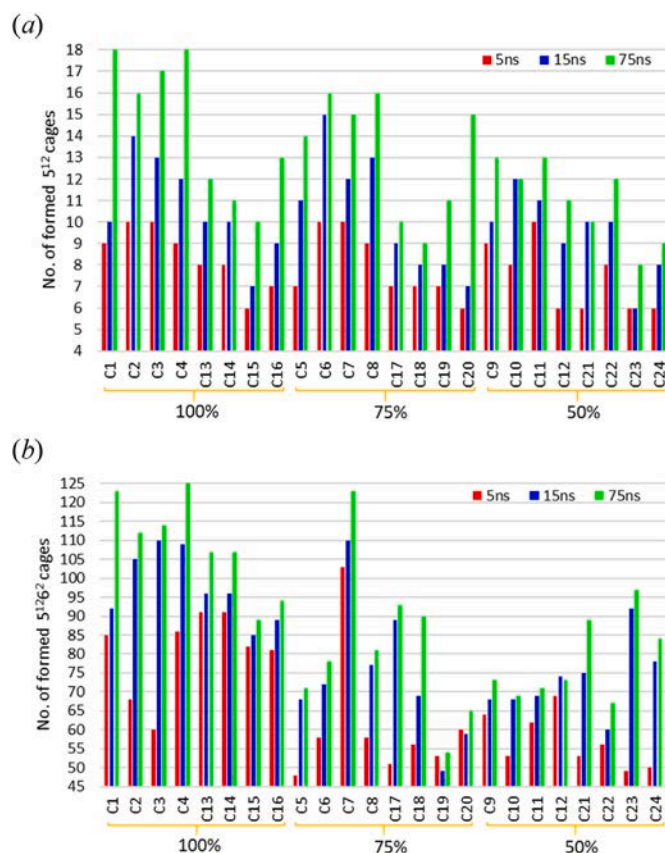


**Fig. 5.** Number of formed hydrate cages at 274 K and 3 MPa; (*a*), small cages; and (*b*), large cages.

formation and stability. Fig. 3 shows the extent of F4 as a function of three simulation times in which the higher F4 parameter indicates faster hydrate formation. As is evident, the number of gas molecules dissolved in the liquid water significantly contributes to the increasing rate of the F4 parameter. Also, the difference between values at 5 ns and 15 ns for 100% and 75% saturation of gases in water are mostly more than that for 50% which highlights the importance of the mixing phenomenon at the hydrate-solution interface. By comparing C1 to C4 cases, it can be deduced that the impressions of $H_2S$ and $SO_2$ impurities are quite relevant to the $CO_2/CH_4$ ratio in the system. Although these impurities in C3 facilitated the hydrate formation rate, they were less effective when 50% dissolved gas was considered. Also, the trace presence of mixed $N_2$ and $H_2$ (C15) reduced the clathrate growth in comparison with either $N_2$ or $H_2$ (C13 and C14). This may be due to their dissimilar mobilities which might prevent the arrangement of local cages. However, the combination of $SO_2$, $H_2S$, $N_2$, and $H_2$ in C16 compensated for the negative influence of this phenomenon. The average F4 parameter for 100%, 75%, and 50% dissolved gases in the solution phase are found to be 0.27, 0.23, and 0.19, respectively. This may indicate the linear-like relationship of hydrate growth with the dissolved gases in the system.

The positions of water molecules to form pentagon and hexagon rings ([5,6]) would be vital for generating the small and large cages by connecting these rings. Fig. 4 demonstrates the number of formed rings at 5 ns, 15 ns, and 75 ns which are quite consistent with the obtained results for the F4 parameter. The average number of formed pentagon rings for 100%, 75%, and 50% gas saturation are 760, 703, and 628 and that also for hexagon rings are 129, 110, and 108, respectively. It seems that the number of gas molecules at the solid-liquid interface can markedly affect the formed rings. Although the number of pentagon rings for all studied cases at 75 ns was increased, that of hexagon rings e. g. (C5, C9, C19) was reduced or at least close together as the simulations
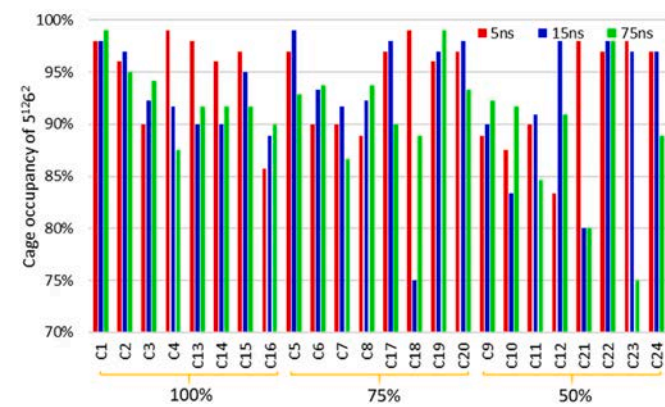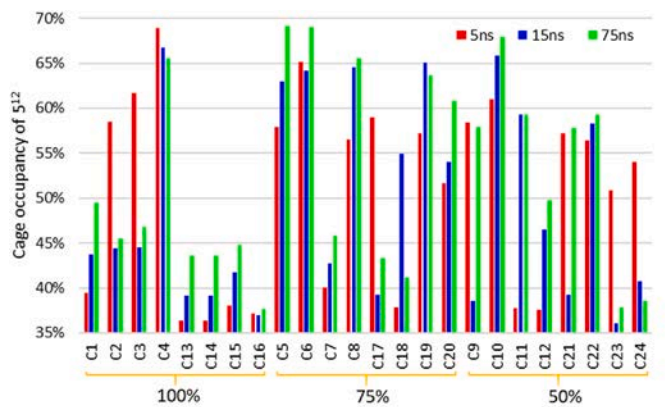
**Fig. 6.** Cage occupancy of performed simulation cases at 274 K and 3 MPa.
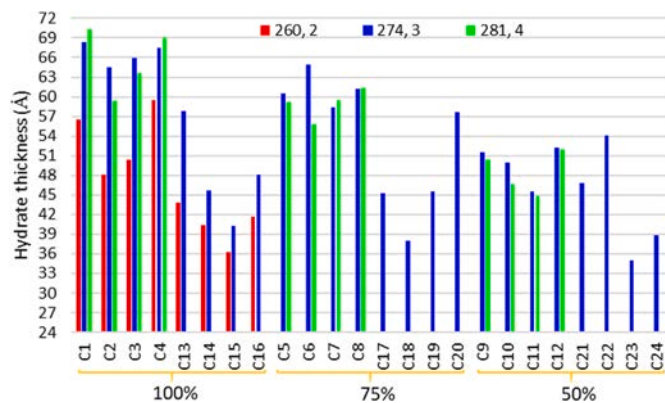


**Fig. 7.** Final hydrate thickness of all performed simulations at three different thermodynamic conditions.

proceeded from 15 ns to 75 ns. This may be due to the reduction of concentration of gas species in the liquid phase which would be the main driving force of the hydrate growth.

The number of formed rings may either quantitatively or qualitatively contribute to the formation of small and large hydrate cages. Fig. 5 exhibits the extent of generated $5^{12}$ and $5^{1,2}6^2$ hydrate cavities as a function of three simulation times. Under 100% gas saturation, the presence of $H_2S$, $SO_2$, $N_2$, and $H_2$ gases reduces the number of generated cavities, however, their effects are not the same. By comparing C3 with C2 it can be seen that the existence of impurities such as $H_2S$ and $SO_2$ molecules can slightly decrease the number of cages while the negative impressions of $N_2$ and $H_2$ molecules (such as C13 and C14) for the conversion of the solution phase to the hydrate are higher. This may be even more when both molecules are in the system (C15) but the
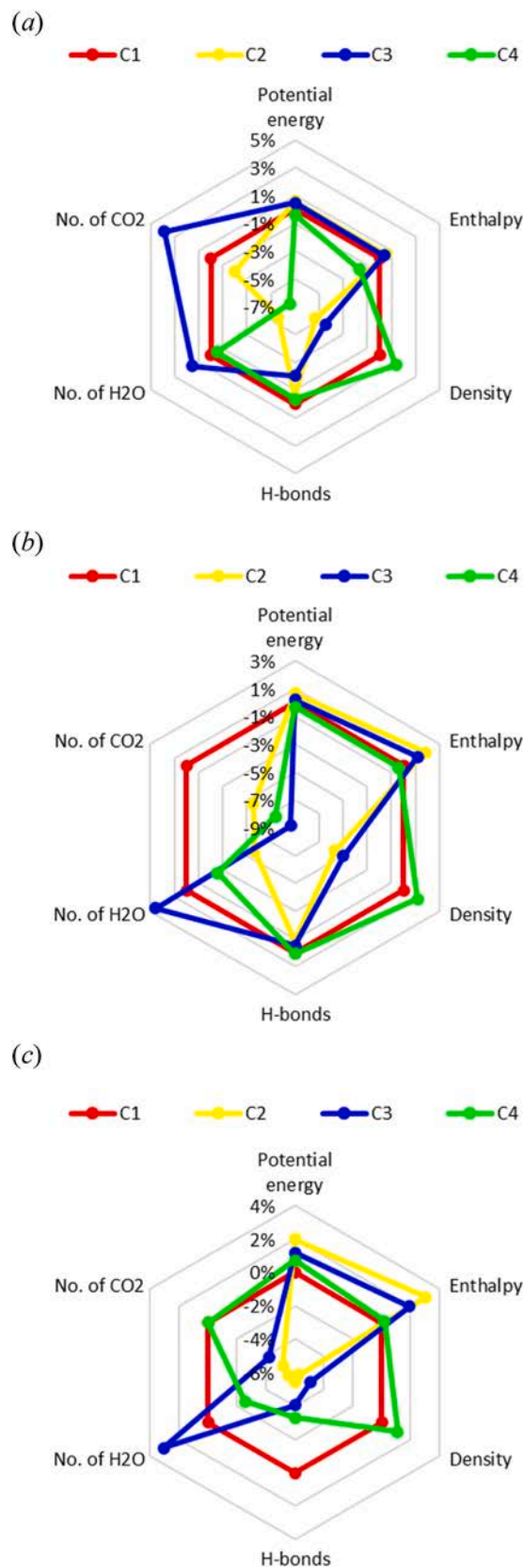


**Fig. 8.** The average alteration of characteristics of C1 to C4 cases under the influence of thermodynamic circumstances at initial 25 ns; (*a*), at 260 K, 2 MPa; (*b*), at 274 K, 3 MPa; (*c*), at 281 K, 4 MPa.

inclusion of $SO_2$ and $H_2S$ to a certain extent can compensate for these negative impacts. By making a comparison of these simulated cases at 75% dissolved gases in the liquid water, it can be observed that the effects of impurities on the biogas hydrate formation are lower.

The proportion of cage occupancies would be proportional to the species of components in biogas. Fig. 6 exhibits the percentages of evaluated cases as a function of simulation time. For $5^{12}$ cages, the existence of $H_2S$ and $SO_2$ increased the filled cavities while $N_2$ and $H_2$ molecules showed the opposite impressions. Since the decrease of dissolved gas molecules from 100% to either 75% or 50% reduces the number of both small and large cavities, the slower cage occupancy for the latter cases can be observed. The average percentages of final occupancy for 100%, 75%, and 50% cases are found to be 67%, 69%, and 66% respectively. Therefore, it can be deduced that the kinetics of filling cages with gas molecules is consistent with the number of gas molecules in the liquid phase but the fraction of cage occupancy is mostly independent.

Fig. 7 shows the hydrate thickness of all performed simulations at 75 ns. The average thickness of final crystal at 260 K, 274 K, and 281 K are estimated around 45.1 Å, 57.3 Å, and 55.8 Å respectively. It should be noted that the selected thermodynamic conditions are within the hydrate-vapor/gas region of the $CO_2+CH_4$ phase coexistence diagram. It seems that the moderate pressure condition at temperatures near the water freezing point would give the fastest speed for the formation of biogas clathrate hydrates. Also, the reduction of dissolved gas in the water phase from 100% to 75% and 50% resulted in an 8% and 21% average reduction in the crystal growth, respectively. The formed hydrates in cases such as C16, C20, and C24 are found to be higher than C15, C19, and C23. This indicates that the presence of $H_2S$ and $SO_2$ molecules may somewhat restrict the repulsive interactions of $N_2$ and $H_2$ molecules between the water molecules.

The composition and concentration of gas species in the solution phase would have determinative effects on the process of hydrate formation. There are several characteristics at the interface between solid and mixed gas-liquid phases that can be altered by the interactions of these molecules. Fig. 8 exhibits the percentage changes of different properties of layers beside the solid-solution interface for C2, C3, and C4 cases in comparison with C1 at 75 ns. The changes in the number of $CO_2$ and water molecules were compared by considering the initial concentration of the hydrate slab. As is shown, the number of both guest and host molecules, potential energy (PE), total enthalpy (TE), and formed hydrate density can be changed by different gas compositions and thermodynamic operating conditions. The lower energy parameters and higher number of hydrogen bonds as well as density can give a more regular hydrate formation. It can also be deduced that the balanced distribution of $CO_2$ and water molecules resulted in slightly higher hydrate growth.

## 3.2. Kinetic modelling of biogas hydrate formation

The hydrate formation process is initiated by the gas dissolution in the water phase. Then the nucleation phenomenon takes place which is followed by the crystal growth. The time to occur the two first steps is markedly more than the occurrence of the final stage. In this study, the kinetic modelling was developed based on the non-equilibrium and irreversible thermodynamics natural path [33,34]. The overall entropy can be considered by the summation of entropy alteration due to the irreversible processes which result in the uncompensated transformation ($d_iS$) and the exterior interaction ($d_e$) [35]:

$$dS = d_iS + d_eS \tag{1}$$

in the chemical process of hydrate growth, the thermodynamic flows and forces can contribute to the non-equilibrium thermodynamic path where uncompensated released heat within femtosecond intervals leads to the generation of entropy as below [35]:

**Table 3**
Regerssed parameters of the model for all studied simulated cases.

| Basis of regression | | No. of H-bonds | | Total energy | |
|---|---|---|---|---|---|
| Cases | | $n$ | $k$ | $n$ | $k$ |
| 260 K, 2 MPa | C1 | −1.0598 | $3.54 \times 10^{-22}$ | −1.0602 | $9.24 \times 10^{-23}$ |
| | C2 | −1.0807 | $2.46 \times 10^{-22}$ | −1.0667 | $9.11 \times 10^{-23}$ |
| | C3 | −1.0119 | $2.94 \times 10^{-22}$ | −1.0701 | $9.04 \times 10^{-23}$ |
| | C4 | −1.0280 | $2.85 \times 10^{-22}$ | −1.0595 | $9.25 \times 10^{-23}$ |
| | C13 | −0.9149 | $1.99 \times 10^{-22}$ | −1.0539 | $9.30 \times 10^{-23}$ |
| | C14 | −0.9584 | $4.84 \times 10^{-22}$ | −1.0443 | $9.49 \times 10^{-23}$ |
| | C15 | −0.8651 | $2.19 \times 10^{-22}$ | −1.0358 | $9.66 \times 10^{-23}$ |
| | C16 | −0.9843 | $4.37 \times 10^{-22}$ | −1.0553 | $9.28 \times 10^{-23}$ |
| 274 K, 3 MPa | C1 | −0.9519 | $3.70 \times 10^{-22}$ | −0.9841 | $1.56 \times 10^{-23}$ |
| | C2 | −1.1291 | $2.17 \times 10^{-22}$ | −1.0004 | $1.52 \times 10^{-23}$ |
| | C3 | −1.1120 | $2.28 \times 10^{-22}$ | −1.0043 | $1.50 \times 10^{-23}$ |
| | C4 | −0.8824 | $4.59 \times 10^{-22}$ | −0.9893 | $1.55 \times 10^{-23}$ |
| | C5 | −1.0627 | $2.61 \times 10^{-22}$ | −0.9886 | $1.55 \times 10^{-23}$ |
| | C6 | −1.0544 | $2.67 \times 10^{-22}$ | −0.9920 | $1.54 \times 10^{-23}$ |
| | C7 | −1.0181 | $2.93 \times 10^{-22}$ | −0.9909 | $1.54 \times 10^{-23}$ |
| | C8 | −0.9619 | $3.61 \times 10^{-22}$ | −0.9931 | $1.54 \times 10^{-23}$ |
| | C9 | −1.0812 | $2.31 \times 10^{-22}$ | −1.0392 | $9.60 \times 10^{-23}$ |
| | C10 | −1.0959 | $2.24 \times 10^{-22}$ | −1.0279 | $9.84 \times 10^{-23}$ |
| | C11 | −0.8726 | $4.39 \times 10^{-22}$ | −1.0528 | $9.32 \times 10^{-23}$ |
| | C12 | −1.0286 | $2.55 \times 10^{-22}$ | −1.0167 | $1.01 \times 10^{-23}$ |
| | C13 | −1.0539 | $2.59 \times 10^{-22}$ | −1.0581 | $9.28 \times 10^{-23}$ |
| | C14 | −0.9429 | $3.70 \times 10^{-22}$ | −1.0485 | $9.41 \times 10^{-23}$ |
| | C15 | −0.8971 | $3.88 \times 10^{-22}$ | −1.0314 | $9.76 \times 10^{-23}$ |
| | C16 | −1.1342 | $2.03 \times 10^{-22}$ | −1.0582 | $9.28 \times 10^{-23}$ |
| | C17 | −0.8710 | $4.45 \times 10^{-22}$ | −1.0434 | $9.51 \times 10^{-23}$ |
| | C18 | −0.9322 | $3.74 \times 10^{-22}$ | −1.0379 | $9.63 \times 10^{-23}$ |
| | C19 | −1.0252 | $2.77 \times 10^{-22}$ | −1.0393 | $9.60 \times 10^{-23}$ |
| | C20 | −0.9540 | $3.50 \times 10^{-22}$ | −1.0368 | $9.65 \times 10^{-23}$ |
| | C21 | −0.8745 | $4.31 \times 10^{-22}$ | −1.0363 | $9.66 \times 10^{-23}$ |
| | C22 | −0.9957 | $2.93 \times 10^{-22}$ | −1.0342 | $9.70 \times 10^{-23}$ |
| | C23 | −0.7090 | $3.11 \times 10^{-22}$ | −1.0296 | $9.80 \times 10^{-23}$ |
| | C24 | −0.7071 | $4.58 \times 10^{-22}$ | −1.025 | $9.80 \times 10^{-23}$ |
| 281 K, 4 MPa | C1 | −1.0335 | $2.91 \times 10^{-22}$ | −1.0671 | $9.10 \times 10^{-23}$ |
| | C2 | −0.9947 | $3.24 \times 10^{-22}$ | −1.0727 | $8.99 \times 10^{-23}$ |
| | C3 | −1.0902 | $2.46 \times 10^{-22}$ | −1.0790 | $8.88 \times 10^{-23}$ |
| | C4 | −0.8854 | $4.55 \times 10^{-22}$ | −1.0623 | $9.20 \times 10^{-23}$ |
| | C5 | −0.9726 | $3.42 \times 10^{-22}$ | −1.0612 | $9.22 \times 10^{-23}$ |
| | C6 | −1.0536 | $2.66 \times 10^{-22}$ | −1.0685 | $9.07 \times 10^{-23}$ |
| | C7 | −0.9652 | $3.45 \times 10^{-22}$ | −1.0655 | $9.13 \times 10^{-23}$ |
| | C8 | −0.9738 | $3.45 \times 10^{-22}$ | −1.0609 | $9.22 \times 10^{-23}$ |
| | C9 | −1.1194 | $1.19 \times 10^{-22}$ | −1.0351 | $9.68 \times 10^{-23}$ |
| | C10 | −1.1513 | $1.10 \times 10^{-22}$ | −1.0464 | $9.45 \times 10^{-23}$ |
| | C11 | −0.9448 | $9.65 \times 10^{-22}$ | −1.0516 | $9.35 \times 10^{-23}$ |
| | C12 | −0.9366 | $8.41 \times 10^{-22}$ | −1.0216 | $9.97 \times 10^{-23}$ |

$$d_iQ = Td_iS = Ad\vartheta \tag{2}$$

where $\vartheta$ stands for the reaction advancement term, $d_iQ$ denotes uncompensated heat, and $A$ is the affinity in the system [36]. The affinity is relevant to the irreversible chemical process that naturally takes place. This variable constantly declines with the conversion of the solution phase into hydrate crystalline and finally it converges to zero once the growth process approaches the equilibrium circumstance. Hence, the process of the conversion rate ($r = \frac{d\vartheta}{dt} = kA^n$) can be described from the following equation [37,38]:

$$\frac{d_iQ}{dt} = T\frac{d_iS}{dt} = A\frac{d\vartheta}{dt} = kA^{n+1} > 0 \tag{3}$$

The parameters $n$ and $k$ are the parameters that can be obtained from the growth characteristics those the affinity would act as the driving force for them. In this work, the properties such as the number of formed hydrogen bonds (H-bonds), and total energy were employed, however, the number of gas molecules that participate in the clathrate growth from the solid-solution interface may also be used. Hence, the reaction advancement term and the affinity of the growth process to specify the mentioned parameters of the kinetic modelling can be specified through the following equations [39,40]:
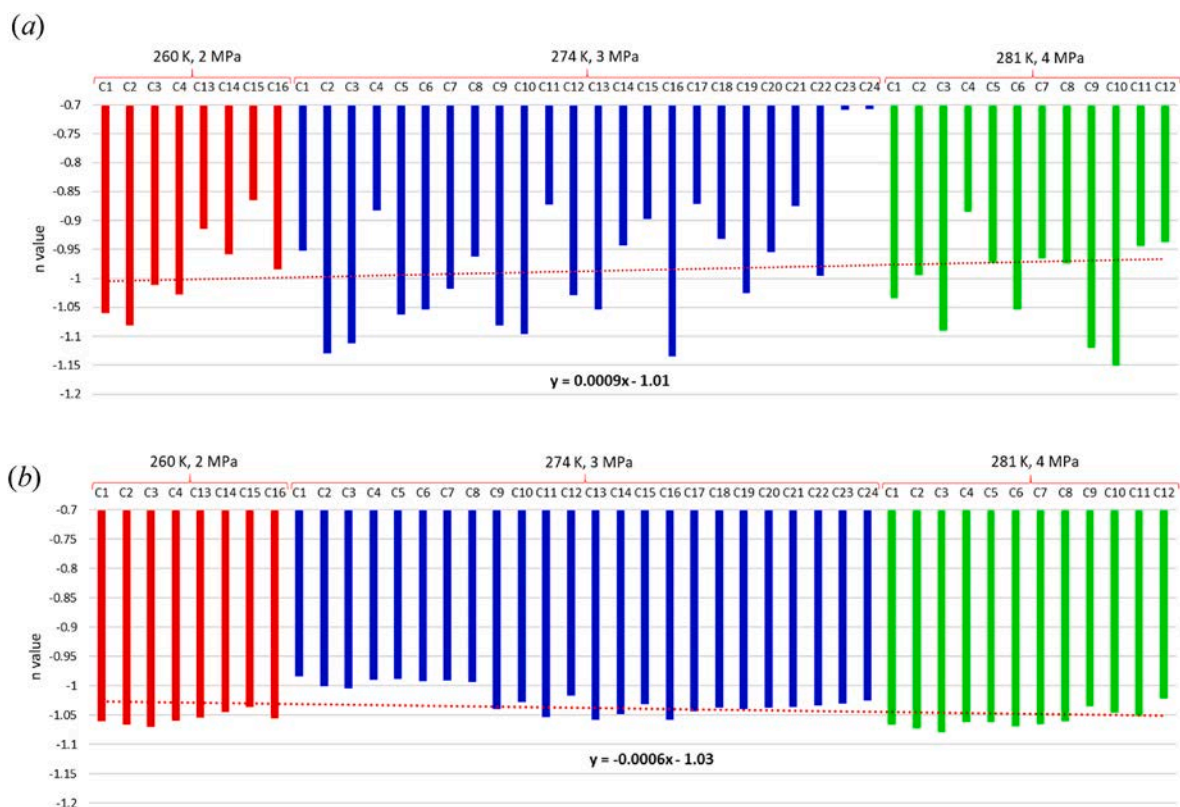
**Fig. 9.** The regression $n$ value based on: ($a$), the growth of the number of H-bonds; and ($b$), the total energy of the simulation box.

$$\vartheta_i = \frac{X_i - X_1}{X_f - X_1}, and \; A_i = -RTln \sum \vartheta_i \qquad (4)$$

where $X_i$, $X_1$, and $X_f$ stand for the No. of H-bonds or value of total energy of the system at each simulation time, initial and the final times, respectively. The two determinative parameters of the kinetic model can be given by calculating the below logarithm correlation:

$$ln\left(\frac{d\vartheta_i}{dt}\right) = \ln k + n \ln A \qquad (5)$$

Table 3 shows the results of parameters $n$ and $k$ obtained from the number of formed H-bonds and the total energy of the system during the hydrate formation.

As Fig. 9 shows, the average of the parameter $n$ regressed from proceeded hydrogen bonds, and the decline of the total energy is found to be around −1.01 and −1.03, respectively. It should be noted that the range of obtained values for the former and latter based on generating entropy and uncompensated heat is −0.71 to −1.15 and −0.98 to −1.08, respectively. Moreover, the parameter $k$ of the model for all studied cases as reported in Table 3 are in similar orders of magnitude. Also, the operating conditions and the number of gas molecules in the system would be proportional to the growth kinetics of the system as they influence the driving force. In addition, since the rate of formed H-bonds in the semi-regular regions from the interface toward the solution phase would be not the same as with the decline of total energy, the values of the model parameters are slightly different.

The driving force of the hydrate growth in the system determines the process of affinity. Fig. 10 exhibits the alteration of hydrate growth affinity and the decay rate for case C1 as a function of simulation time. As is evident, the affinity reduces quickly with progressing the hydrate formation, so that, it is inversely proportional to the simulation time. Therefore, it can be deduced that the affinity would be a reverse function of the natural logarithmic correlation of the elapsed time. This may also indicate that the process of biogas hydrate formation would be

analogous to the natural path in which a chemical reaction starts to proceed until approaching the equilibrium state.

## 4. Conclusion

Despite many efforts to remove unfavorable impurities during the cleaning process of biogas, these impurities may still be part of the emitted gases. However, with the utilization of hydrate-based technology, $CO_2$ along with most of these gas species can be captured in the hydrate phase at thermodynamic equilibrium formation conditions lower than that of $CH_4$ hydrate formation circumstances. This study investigated the effects of biogas compositions including various impurities such as $SO_2$, $H_2S$, $N_2$, and $H_2$ gases on the formation of clathrate biogas hydrate. The performed MD simulations reveal that the ratio of $CO_2/CH_4$ in the feed can alter the cage occupancy, growth rate, and gas distribution in the hydrate phase. The presence of gas impurities in the system may slightly increase the arrangement rate of water molecules toward being organized in the clathrate form. In addition, decreasing the gas concentration in the solution phase to 75% and 50% in comparison with the entrapped gas molecules in the initial hydrate results in an 8% and 21% reduction in the growth rate respectively. However, their effects on the fraction of the cage occupancy of the formed cavities are found to be insignificant. The performed simulations at three different temperature-pressure conditions, where the vapor phase is in equilibrium with the hydrate phase, show that the growth rate at 274 K and 3 MPa would be higher than either 260 K and 2 MPa or 281 K and 4 MPa. Hence, the influence of the operating conditions on the role of impurities would be substantial. Further, the growth mechanisms in all cases occur based on two consecutive steps: the diffusion of the gas molecules from the bulk of the solution phase to the solid-liquid interface, followed by the reordering of the water molecules in agreement with the initial hydrate slab. In addition, a kinetic model based on the thermodynamic natural pathway through the increasing formation of hydrogen bonds and decreasing the total energy in the simulation box was developed.
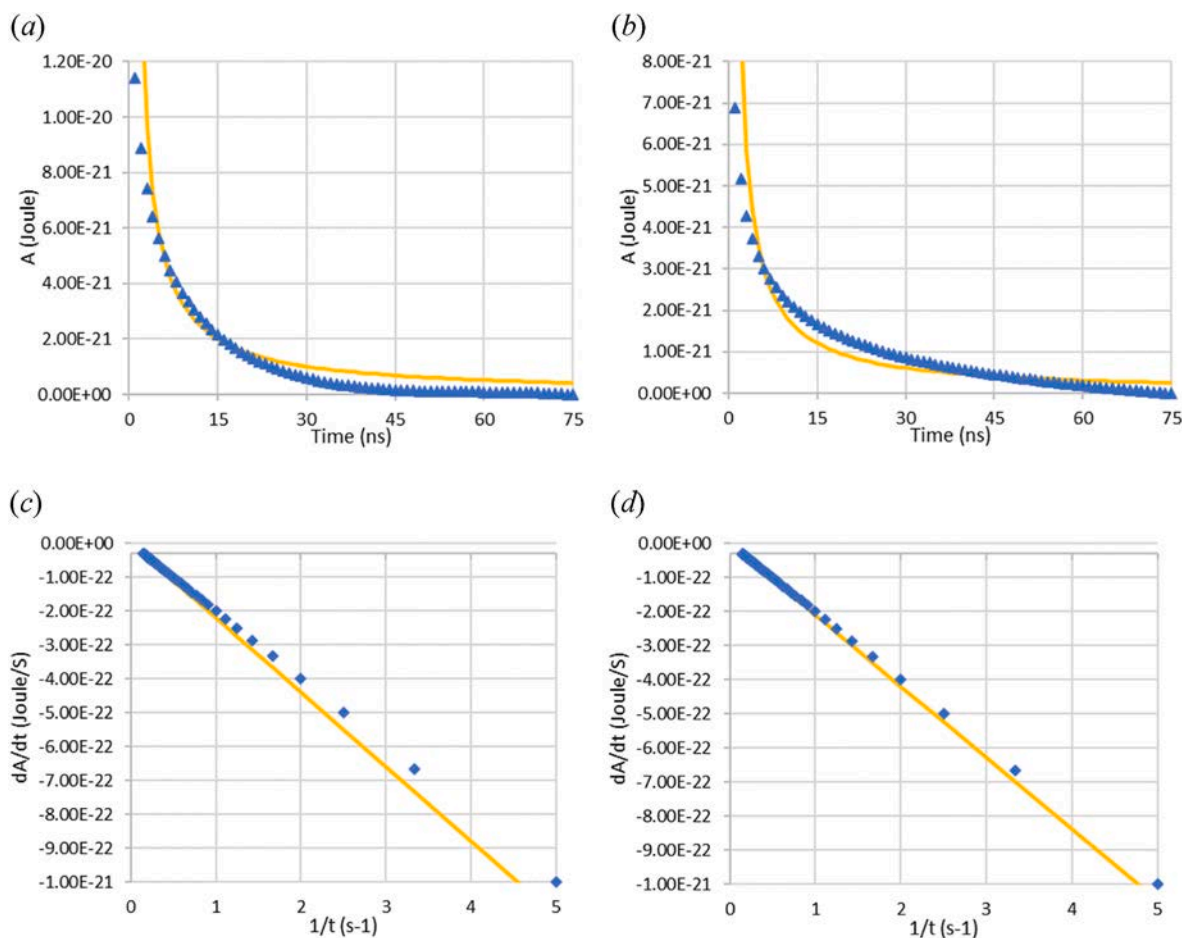
**Fig. 10.** The evolution of hydrate growth affinity (A) and the decay rate (dA/dt) for simulated case C1 at 274 K and 3 MPa. (*a*) and (*c*) is based on the number of H-bonds, and (*b*) and (*d*) is according to the total energy. The solid line shows the regression results.

The affinity and decay rate of the model demonstrate that the progress of the hydrate formation is driven by the concept of a thermodynamic driving force which analogously follows the proceeding process based on a natural path.

## CRediT authorship contribution statement

**Saeid Sinehbaghizadeh:** Conceptualization, Methodology, Software, Investigation, Data curation, Visualization, Formal analysis, Validation, Writing – original draft. **Agus Saptoro:** Conceptualization, Methodology, Resources, Writing – review & editing, Supervision, Funding acquisition. **Sepideh Amjad-Iranagh:** Methodology, Resources, Writing – review & editing. **Amir H. Mohammadi:** Writing – review & editing, Supervision.

## Declaration of competing interest

The authors declare that they have no known competing financial interests or personal relationships that could have appeared to influence the work reported in this paper.

## Data availability

Data will be made available on request.

## Acknowledgments

The first author is grateful to Curtin University Malaysia for

## References

[1] Li Y, Alaimo CP, Kim M, Kado NY, Peppers J, Xue J, Wan C, Green PG, Zhang R, Jenkins BM, Vogel CFA, Wuertz S, Young TM, Kleeman MJ. Composition and toxicity of biogas produced from different feedstocks in California. Environ Sci Technol 2019;53:11569–79. https://doi.org/10.1021/acs.est.9b03003.
[2] Khan MU, Lee JTE, Bashir MA, Dissanayake PD, Ok YS, Tong YW, Shariati MA, Wu S, Ahring BK. Current status of biogas upgrading for direct biomethane use: a review. Renew Sustain Energy Rev 2021;149:111343. https://doi.org/10.1016/j.rser.2021.111343.
[3] Gkotsis P, Kougias P, Mitrakas M, Zouboulis A. Biogas upgrading technologies – recent advances in membrane-based processes. Int J Hydrogen Energy 2023;48: 3965–93. https://doi.org/10.1016/j.ijhydene.2022.10.228.
[4] Golmakani A, Ali Nabavi S, Wadi B, Manovic V. Advances, challenges, and perspectives of biogas cleaning, upgrading, and utilisation. Fuel 2022;317:123085. https://doi.org/10.1016/j.fuel.2021.123085.
[5] Sloan ED, Koh CA. Clathrate hydrates of natural gases. third ed. Boca Raton: CRC Press, Taylor & Francis Group; 2008.
[6] Skiba S, Chashchin D, Semenov A, Yarakhmedov M, Vinokurov V, Sagidullin A, et al. Hydrate-based separation of the $CO_2 + H_2$ mixtures. Phase equilibria with isopropanol aqueous solutions and hydrogen solubility in $CO_2$ hydrate. Int J Hydrogen Energy 2021;46:32904–13. https://doi.org/10.1016/j.ijhydene.2021.07.112.
[7] Li X-Y, Ge B-B, Yan J, Lu Y-Y, Zhong D-L, Englezos P, et al. Review on hydrate-based $CH_4$ separation from low-concentration coalbed methane in China. Energy Fuel 2021;35:8494–509. https://doi.org/10.1021/acs.energyfuels.1c00359.
[8] Xu C-G, Xie W-J, Chen G-S, Yan X-X, Cai J, Chen Z-Y, et al. Study on the influencing factors of gas consumption in hydrate-based $CO_2$ separation in the presence of CP by Raman analysis. Energy 2020;198:117316. https://doi.org/10.1016/j.energy.2020.117316.

[9] Sinehbaghizadeh S, Saptoro A, Mohammadi AH. $CO_2$ hydrate properties and applications: a state of the art. Prog Energy Combust Sci 2022;93:101026. https://doi.org/10.1016/j.pecs.2022.101026.

[10] Beeskow-Strauch B, Schicks JM, Spangenberg E, Erzinger J. The influence of $SO_2$ and $NO_2$ impurities on $CO_2$ gas hydrate formation and stability. Chem Eur J 2011; 17:4376–84. https://doi.org/10.1002/chem.201003262.

[11] Kvamme B, Iden E, Tveit J, Veland V, Zarifi M, Qorbani K. Effect of $H_2S$ content on thermodynamic stability of hydrate formed from $CO_2/N_2$ mixtures. J Chem Eng Data 2017;62:1645–58. https://doi.org/10.1021/acs.jced.7b00027.

[12] Tung Y-T, Chen L-J, Chen Y-P, Lin S-T. In situ methane recovery and carbon dioxide sequestration in methane hydrates: a molecular dynamics simulation study. J Phys Chem B 2011;115:15295–302. https://doi.org/10.1021/jp2088675.

[13] Sinehbaghizadeh S, Saptoro A, Amjad-Iranagh S, Naeiji P, Tiong ANT, Mohammadi AH. A comprehensive review on molecular dynamics simulation studies of phenomena and characteristics associated with clathrate hydrates. Fuel 2023;338:127201. https://doi.org/10.1016/j.fuel.2022.127201.

[14] Sinehbaghizadeh S, Saptoro A, Amjad-Iranagh S, Tiong ANT, Mohammadi AH. Molecular dynamics simulation studies on the stability and dissociation of clathrate hydrates of single and double greenhouse gases. Energy Fuel 2022;36:8323–39. https://doi.org/10.1021/acs.energyfuels.2c01396.

[15] Sinehbaghizadeh S, Saptoro A, Naeiji P, Tiong ANT, Mohammadi AH. Insights into the synergistic effects of metal particles (Ag, Cu, and Fe) and urea on $CO_2$ clathrate hydrate growth using molecular dynamics simulations. Chem Eng Sci 2022;264: 118194. https://doi.org/10.1016/j.ces.2022.118194.

[16] Sinehbaghizadeh S, Saptoro A. Molecular dynamics simulations of $CO_2$ clathrate hydrate in the presence of organic components. In: MATEC Web Conf. 377; 2023, 01008. https://doi.org/10.1051/matecconf/202337701008.

[17] Sinehbaghizadeh S, Saptoro A, Naeiji P, Mohammadi AH. Molecular dynamics simulations to investigate the effects of organic amines on biogas clathrate hydrate formation. J Mol Liq 2023;382:122015. https://doi.org/10.1016/j.molliq.2023.122015.

[18] Sinehbaghizadeh S, Saptoro A, Amjad-Iranagh A, Mohammadi AH. Molecular dynamics simulations of the stability and dissociation of structure-H clathrate hydrates in the presence of different amino acids, gas species, and sH hydrate formers. Energy Fuel 2023;37:10550–66. https://doi.org/10.1021/acs.energyfuels.3c01312.

[19] Nohra M, Woo TK, Alavi S, Ripmeester JA. Molecular dynamics Gibbs free energy calculations for $CO_2$ capture and storage in structure I clathrate hydrates in the presence of $SO_2$, $CH_4$, $N_2$, and $H_2S$ impurities. J Chem Thermodyn 2012;44:5–12. https://doi.org/10.1016/j.jct.2011.08.025.

[20] Zong X, Cheng G, Qiu N, Huang Q, He J, Du S, et al. Structures and mechanical properties of $CH_4$, $SO_2$, and $H_2S$ hydrates from density function theory calculations. Chem Lett 2017;46:1141–4. https://doi.org/10.1246/cl.170333.

[21] Shi Q, Cao P, Han Z, Ning F, Gong H, Xin Y, Zhang Z, Wu J. Role of guest molecules in the mechanical properties of clathrate hydrates. Cryst Growth Des 2018;18: 6729–41. https://doi.org/10.1021/acs.cgd.8b01017.

[22] Xu K, Yang L, Liu J, Zhang Z, Wu J. Mechanical properties of $CH_4$–$CO_2$ heteroclathrate hydrates. Energy Fuel 2020;34:14368–78. https://doi.org/10.1021/acs.energyfuels.0c02430.

[23] Qiu N, Bai X, Xu J, Sun N, Francisco JS, Yang M, Huang Q, Du S. Adsorption behaviors and phase equilibria for clathrate hydrates of sulfur and nitrogen containing small molecules. J Phys Chem C 2019;123:2691–702. https://doi.org/10.1021/acs.jpcc.8b05962.

[24] Mahmoodi MH, Manteghian M, Naeiji P. Study the effect of Ag nanoparticles on the kinetics of $CO_2$ hydrate growth by molecular dynamics simulation. J Mol Liq 2021;343:117668. https://doi.org/10.1016/j.molliq.2021.117668.

[25] Phan A, Schlösser H, Striolo A. Molecular mechanisms by which tetrahydrofuran affects $CO_2$ hydrate growth: implications for carbon storage. Chem. Eng. J. 2021: 129423. https://doi.org/10.1016/j.cej.2021.129423.

[26] Martínez L, Andrade R, Birgin EG, Martínez JM. PACKMOL: a package for building initial configurations for molecular dynamics simulations. J Comput Chem 2009; 30:2157–64. https://doi.org/10.1002/jcc.21224.

[27] Plimpton S. Fast parallel algorithms for short-range molecular dynamics. J Comput Phys 1995;117:1–19. https://doi.org/10.1006/jcph.1995.1039.

[28] Horn HW, Swope WC, Pitera JW, Madura JD, Dick TJ, Hura GL, Head-Gordon T. Development of an improved four-site water model for biomolecular simulations: TIP4P-Ew. J Chem Phys 2004;120:9665–78. https://doi.org/10.1063/1.1683075.

[29] Eggimann BL, Sunnarborg AJ, Stern HD, Bliss AP, Siepmann JI. An online parameter and property database for the TraPPE force field. Mol Simulat 2014;40: 101–5. https://doi.org/10.1080/08927022.2013.842994.

[30] Kamath G, Lubna N, Potoff JJ. Effect of partial charge parametrization on the fluid phase behavior of hydrogen sulfide. J Chem Phys 2005;123:124505. https://doi.org/10.1063/1.2049278.

[31] Ribeiro MCC. Molecular dynamics simulation of liquid sulfur dioxide. J Phys Chem B 2006;110:8789–97. https://doi.org/10.1021/jp060518a.

[32] Alavi S, Ripmeester JA, Klug DD. Molecular-dynamics study of structure II hydrogen clathrates. J Chem Phys 2005;123:24507. https://doi.org/10.1063/1.1953577.

[33] Kondepudi DK. Introduction to modern thermodynamics. Chichester: Wiley; 2008.

[34] Naeiji P, Varaminian F, Rahmati M. The kinetic modeling of methane hydrate growth by using molecular dynamic simulations. Int J Heat Mass Tran 2019;142: 118356. https://doi.org/10.1016/j.ijheatmasstransfer.2019.07.006.

[35] Garfinkle M. The thermodynamic natural path in chemical reaction kinetics. Discrete Dynam Nat Soc 2000;4:145–64. https://doi.org/10.1155/S1026022600000145.

[36] Sato N. Chemical energy and exergy: an introduction to chemical thermodynamics for engineers. Elsevier Science & Technology Books; 2004.

[37] Shi L, He Y, Lu J, Liang D. Effect of dodecyl dimethyl benzyl ammonium chloride on $CH_4$ hydrate growth and agglomeration in oil-water systems. Energy 2020;212: 118746. https://doi.org/10.1016/j.energy.2020.118746.

[38] Shi L, Ding J, Liang D. Enhanced $CH_4$ storage in hydrates with the presence of sucrose stearate. Energy 2019;180:978–88. https://doi.org/10.1016/j.energy.2019.05.151.

[39] Roosta H, Khosharay S, Varaminian F. Experimental study of methane hydrate formation kinetics with or without additives and modeling based on chemical affinity. Energy Convers Manag 2013;76:499–505. https://doi.org/10.1016/j.enconman.2013.05.024.

[40] Naeiji P, Arjomandi A, Varaminian F. Amino acids as kinetic inhibitors for tetrahydrofuran hydrate formation: experimental study and kinetic modeling. J Nat Gas Sci Eng 2014;21:64–70. https://doi.org/10.1016/j.jngse.2014.07.029.

# Chapter 8: Conclusion and Recommendations

Molecular dynamics (MD) simulations of $CO_2$ hydrates have various industrial applications. The key areas of these simulations are mostly practical in gas separation or carbon capture and storage (CCS), hydrate-based desalination and food industries, cold energy storage and secondary refrigeration, gas storage and transformation, and also a wide range of processes in sustainable technologies. MD simulations of $CO_2$ hydrates in the presence of thermodynamic and kinetic hydrate promoters can help to understand the interactions between the promoters and water and gas species, as well as their impact on the formation, stability, and properties of hydrates. These simulations also provide insights into the promotion mechanisms and determine practical characteristics which allow researchers to optimize promoter compositions and conditions for efficient processes. These investigations can also aid to evaluate the effectiveness of promoters in capturing/ storing $CO_2$ emissions. Therefore, by selecting the proper design and optimized promoter systems based on the operating conditions, the enhanced efficiency of processes with lower energy requirements would be feasible.

## 8.1 Conclusions

New insights from the performed MD simulations in this thesis answered several open-ended questions in the research topic that other approaches have insufficiently addressed. Hence, the findings here from the molecular scale can be considered in further experimental measurements at macroscopic investigations. To reduce the operating conditions of the hydrate formation reactors as well as accelerate the rate of the clathrate formation, the addition of strong kinetic/ thermodynamic hydrate promoters would significantly contribute to the initial investments in such technologies. For example, the inclusion of effective kinetic promoters would enhance the conversion rate by several times. In another instance, the formation pressure of $CO_2$ hydrate in the absence and presence of cyclopentane (CP) or HCFC-141b at 279 K can be decreased from 4 MPa to 0.2 MPa. This can markedly affect the costs of the initial investments such as equipment, instrumentations, materials, etc. Therefore, it is essential to reveal the positive and negative aspects of these promoters. In this thesis, the newly suggested promoters which can act as strong additives for pure and mixed $CO_2$ clathrate hydrates during the formation and dissociation. Hence, the effects of these components as well as gas species on the aforementioned phenomena which are the basis of $CO_2$ hydrate-based processes in different industries using MD simulations have been investigated. The main findings and conclusions of this dissertation which can be considered for these technologies can be categorized as follows:

**Objective 1 (Chapter 3): The effects of single/ synergistic kinetic hydrate promoters (KHPs) on Pure $CO_2$ hydrate formation**

To help the hydrate-based applications, the increasing rate of $CO_2$ hydrate formation is highly critical. The results of this work highlighted that the combination of promoters from different types possesses various mechanisms, therefore, they can improve the rate of hydrate formation in comparison with their absence but not at the same time. For example, it was found that the urea by dragging around side water molecules helps them be in the locations of clathrate crystalline

cages; while the inclusion of Ag and Cu metal particles by increasing the thermal conductivity and Brownian motions can enhance the water molecular movements and $CO_2$ dissolution in the water phase. The addition of both metal particles and urea imposes all mentioned mechanisms in the solution phase. The performed simulations indicated that this combination can increase the growth rate of $CO_2$ hydrate up to 5 times so that it would help the process of hydrate formation reactor. Also, at moderate pressure conditions, the temperatures close to the water freezing point may give a higher efficiency. The P-T conditions and concentrations of additives can be the main determinative items along which the combination of mechanisms can be adjusted, therefore, optimized conditions can be attained.

## Objective 2 (Chapter 4): The effects of single/ synergistic organic kinetic hydrate promoters (KHPs) on mixed $CO_2$ hydrate formation

To promote the hydrate-based methods, introducing environmentally friendly promoters could either enhance the formation or improve the recovery rates. The simulations elucidated that studied amine molecules can affect the distribution of $CO_2$ and $CH_4$ molecules during the conversion of the solution phase to a clathrate-like state which could be a useful feature to intensify the split fraction of hydrate-based processes. Also, the mixture of molecules including short-chain amines can more efficiently upgrade the process of biogas separation through hydrate. Therefore, it can be suggested that, for further developments of hydrate formation reactors, combining the successful organic hydrate promoters with mechanical methods e.g. spraying, water jet method can be designed. Also, since the optimized concentration of promoters in the solution phase and at the solid-liquid interface can play a critical role in the rate of the solution conversion to the hydrated state, developing/ designing proper concentration controllers to control the concentration of components more specifically promoters could be considered.

## Objective 3 (Chapter 5): The effects of single/ synergistic thermodynamic hydrate promoters (THPs) on pure/ mixed structure-I/ II $CO_2$ hydrate stability and dissociation

Once $CO_2$ is captured in the hydrate phase, the dissociation stage in hydrate-based processes should be performed. This step also exists in hydrate-based $CO_2$ utilization methods (e.g. air conditioning, secondary refrigeration, and fire extinguishment aims). In this regard, controlling the stability and dissociation would be critical. MD simulations revealed that between studied thermodynamic promoters, the components which include fluorine in their molecular structure are not suitable for hydrate-based applications if they have higher stability; this is also valid for the promoters that create the hydrogen bonds with water molecules of the clathrate crystals. In contrast, simple cyclic components like cyclopentane and cyclohexane would be the better option for these applications. For example, if $CO_2$ hydrate preservation e.g. transportation is desired, the former components would be the better alternative while the latter can be utilized for the process of hydrate-based air conditioning. Therefore, the aforementioned additives may better help $CO_2$ hydrates be more stable, more efficient, and safer during the processes of these applications. Also, the lower occupancy of the cages by $CO_2$ molecules can induce the process of hydrate dissociation, however, the main contributor would be the shape and type of thermodynamic promoters.

## Objective 4 (Chapter 6): The effects of single/ synergistic thermodynamic hydrate promoters (THPs) on pure/ mixed sH $CO_2$ hydrate stability and dissociation

Between the three clathrate hydrate structures, structure-H (sH) in terms of the operating conditions and storage capacity would be a proper alternative. In terms of utilizing amino acids as

organic kinetic promoters, they can affect the characteristics of the formed hydrate at the dissociation stage. The MD simulations showed that the hydroxyl of amino acids by attaching to the surrounding water molecules of the sH hydrate weakens the hydrogen bonds of the water molecules in the sH clathrate. This can be a useful feature for the purification of the gas mixture and for removing $CO_2$. Also, unlike $CH_4$ and $N_2$, the presence of $H_2$ molecules significantly induces the mobility of molecules in the clathrate network which was intensified when double cage occupancy for $H_2$ molecules was considered. Hence, the required energy for the mixed gas species including $N_2$ and $H_2$ would be different. Moreover, among investigated sH hydrate formers, Adamantane and 1,1-dimethyl cyclohexane were identified as the most stable sH hydrates which suggests that the cyclic hydrocarbons with larger carbon numbers (e.g. 8 to 10) may better help large cages remain integrated.

## Objective 5 (Chapter 7): The effects of different associated gas impurities and kinetic modelling of biogas hydrate formation

$CO_2$ and impurities can be captured from biogas in the clathrate hydrate. This can be followed by sequestering in the natural gas hydrate (NGH) geological sites which leads to an exchange of the in situ $CH_4$ hydrate over to $CO_2$-dominated hydrate and a simultaneous $CH_4$ release from these huge natural sources of energy in permafrost sediments. Therefore, for both steps, the effects of associated gas impurities such as $SO_2$, $H_2S$, $N_2$, and $H_2$ would be important. The results elucidated that the concentration of dissolved gas in liquid water at the solid-solution interface is one of the controllers of the growth rate but has less impact on the filling percentage of formed both types the clathrate hydrate cages. Although the presence of $H_2S$ and $SO_2$ molecules can slightly increase the formation of biogas hydrate, $N_2$, and $H_2$ molecules reduce the biogas hydrate generation. Also, a developed kinetic model based on the formation of the number of hydrogen bonds as well as total energy is found to be accurate for predicting the progress of biogas crystal growth.

## 8.2 Recommendations for future work

To address the fundamental issue of $CO_2$ emissions, there has been an increased call to develop novel technologies. To capture, sequester, or utilization of $CO_2$, different hydrate-based approaches have been suggested. In this regard, the experimental measurements, process designs, and MD simulations of previous research at macroscopic, mesoscopic, and microscopic levels convey the message that, although effectible progress has been achieved, coordinated studies on different limitations of the gas hydrate applications to find feasible approaches are still required. Therefore, in light of these investigations, the following suggestions can be taken into consideration.

### 8.1.1    Suggestions for performing further MD simulations (at molecular scale):

1) Since the synergistic hydrate promoters from organic components, nanoparticles, and nanosheets can be coupled using chemical preparation e.g. oxidation, sulfonation, reduction stages, or physical preparation to produce new more efficient promoters at the laboratory, the theoretical preparation and utilization of these components to understand their effects on different clathrate hydrate phenomena at the molecular scale can be investigated.

2) Using MD simulations, additional MD studies on the synergistic impacts of different promoters and inhibitors (such as KHP+THP and KHI+THI) on clathrate or semiclathrate hydrates to clarify the relationship between hydrate formation and additives can be conducted. These evaluations may aid to understand the specifications which contribute to enhancing the performance parameters of HBCC/S/U or other hydrate-relevant applications. Besides, MD simulation studies on

heterogeneous nucleation with fast mass transfer in the hydrate growth, describing memory effects and the role of nanobubbles in hydrate nucleation could be the further intriguing aspects.

3) To analyze the effects of hydrate formation methods, surface tension, and grain wettability on permeability in hydrate-bearing sediments, more research should be carried out. Also, more MD simulations to understand some gas hydrate phenomena such as memory effect and self-preservation at different environmental or operating conditions need to be carried out. Moreover, despite several experimental suggestions to utilize the semiclathrate hydrates in different processes of hydrate-based applications e.g. secondary refrigeration and air conditioning aims, the least proportion of MD simulations is for this type of gas hydrates. Therefore, a manifold of MD explorations to reveal the molecular mechanisms of semiclathrate hydrate promoters can be conducted.

4) Heterogeneous nucleation MD simulations with fast mass transfer in the hydrate formation, and analyzing the role of nanobubbles during the nucleation phase can be considered for further research. In addition, although some MD simulations in porous media have been performed, studying the systems simultaneously including mixed minerals e.g. kaolinite, quartz, montmorillonite, and kaolinite can help to assess the effects of these components on gas hydrate phenomena. In this respect, to evaluate the influences of permeability and wettability on hydrate-bearing sediments, more MD studies should be carried out.

5) Discrepancies between MD simulations and experimental outcomes in terms of consistency with the real condition can be assessed by providing simulations of the phenomena at larger scales. Therefore, a better understanding of the mutual relationship among mechanisms can be achieved.

### 8.1.2 Suggestions for performing further experimental measurements (at macroscopic scale):

1) Considering the suggested application of $CO_2$ hydrate as a fire-extinguishing agent and the high dissociation enthalpy of $CO_2$ semiclathrate (e.g. $CO_2$+TBAB), new investigations should be conducted. In addition, the performance of $CO_2$ hydrate extinguishers in terms of operational design could be evaluated. Also, toward energy-saving, hydrate-based hybrid technologies have shown a good potential to become industrialized but the industrial feasibility of such designs still needs to be examined. In addition, the coefficient of performance (COP) of the hydrate cold storage exhibits a strong capacity but more analysis on the combination of renewable energy techniques and hydrate cold storage to discover a competent process design in future exploration could be implemented.

2) The formation rate of gas hydrate without active agitation to boost gas-liquid mixing is not appreciable. Moreover, the performance of promoters in the continuous operation of the static reactors needs to be examined. Conclusively, to overcome these shortcomings further investigations should be carried out. In the case of long distances between $CO_2$ capture plants and $CO_2$ sequestration sites, the costs of $CO_2$ transportation may be higher than capturing process. To facilitate $CO_2$ transportation, various aspects associated with the performance and safety of $CO_2$ transportation were discussed elsewhere. Thus, investigations on the mobility and transport efficiency of hydrate slurry in future explorations can be considered.

3) For further developments of hydrate formation reactors, combining the successful hydrate promoters with mechanical methods e.g. spraying, jet method, can be designed. Also, developing concentration controllers to control the concentration of components more specifically promoters at the solid-liquid interface. Also, since the rate of hydrate formation is

directly proportional to the concentration of promoters, dissolved gas in the water phase, and the operating conditions, designing new methods to coordinate the system by these variables needs to be performed.

4) Commercial exploitation of natural gas hydrates in sediments and reservoirs is still technologically challenging. Based on exhaustive reviews focused on the interaction of climate change and $CH_4$ hydrates in the sediments of marine continental, permafrost areas, and the arctic ocean, the risk of collapse of marine sediments while releasing $CH_4$ gases under harsh engineering conditions can exacerbate greenhouse warming. As a result, to avoid engineering failures that may lead to damaging the marine ecosystem during $CO_2$ sequestration and $CH_4$ production from NGH, accurate strategies need to be implemented. Because of the influences of fluid flow characteristics which can affect the field stability, migration in reservoirs must be attentively analyzed. Also, comprehending the hydrodynamics of $CO_2$ injection is highly crucial for $CO_2/CH_4$ replacement in NGH. To improve the safety of operation, a risk assessment scheme by evaluating mechanisms that may induce the generation of leakage paths in $CO_2$ geological sites must also be developed.

# Appendix A1

## Nomenclature

| | | | |
|---|---|---|---|
| GWP | Global Warming Potential | DN$_2$Cl | N-dodecylpropane-1,3-diamine hydrochloride |
| IGCC | Integrated Gasifier Combined Cycle | HTABr | Hexadecyl-Trimethyl-Ammonium Bromide |
| CCS | Carbon Capture and Storage/ Sequestration | NPE | Nonyl Phenol Ethoxylates |
| IPCC | International Panel on Climate Change | LAE | Lauryl Alcohol Ethoxylates |
| GIIP | Gas Initially In Place | SDS | Sodium Dodecyl Sulfate |
| HBGS | Hydrate-Based Gas Separation | SL | Sulfonated Lignin |
| HBCC | Hydrate-Based Carbon Capture | SHS | Sodium Hexadecyl Sulfate |
| NGH | Natural Gas Hydrate | STS | Sodium Tetradecyl Sulfate |
| COC | Cyclic Organic Compounds | SDBS | Sodium Dodecyl Benzene Sulfonate |
| T/KHI | Thermodynamic/Kinetic Hydrate Inhibitor | DMSO | Di-Methyl Sulf-Oxide |
| T/KHP | Thermodynamic/Kinetic Hydrate Promoter | TMS | Tetra-Methylene Sulfone |
| LMGS | Large Molecule Guest Substance | SWNT | Single-Walled carbon Nano-Tube |
| G.C. | Gas Consumption | MWCNT | Multi-Walled Carbon Nano-Tube |
| S.Fr. | Split Fraction | Na-MMT | Sodium Mont-Morillonite |
| S.F. | Separation Factor | SW-CNTs | Single-Walled Carbon Nano-Tubes |
| COP | Coefficient of Performance | SAMs | Self-Assembled Monolayers |
| LHTS | Latent Heat Thermal Storage | TMS | Tetra-Methylene Sulfone |
| CTES | Cold Thermal Energy Storage | EO | Ethylene Oxide |
| PCM | Phase Change Materials | LHA | Leonardite Humic Acid |
| ZLD | zero liquid discharge | TMO | Tri-Methylene-Oxide |
| HBPR | hydrate-based pollutant removal | FA | FormAldehyde |
| TBAF | Tetra-n-Butyl-Ammonium Fluoride | CB | CycloButane |
| TAAC | Tetra-Amyl-Ammonium Chloride | MWCNT | Multi-Walled Carbon Nano-Tube |
| DTAC | Dodecyl Trimethyl Ammonium Chloride | THT | Tetrahydrothiophene |
| TBMAC | Tri-n-Butyl-Methyl-Ammonium Chloride | THF | TetraHydroFuran |
| TBANO$_3$ | Tetra-n-Butyl Ammonium Nitrate | ACF | Auto-Correlation of the Fluctuations |
| TBAB | Tetra-n-Butyl-Ammonium Bromide | AOP | Angular Order Parameter |
| TBAC | Tetra-n-Butyl-Ammonium Chloride | APDF | Angular probability distribution function |
| TBPB | Tetra-n-Butyl-Phosphonium Bromide | CGMC | Grand Canonical Monte Carlo |
| TBPC | Tetra-n-Butyl-Phosphonium Chloride | DFT | Density Functional Theory |
| MEG | Mono-Ethylene Glycol | DWC | Dodecahedral Water Cluster |
| GdmCl | Guanidinium chloride | FSICA | Face-Saturated Incomplete Cage Analysis |
| NH$_4$Cl | Ammonium chloride | HCACF | Flux AutoCorrelation Function |
| LAE2 | Lauryl alcohol ethoxylate-2 | MCG-OP | Mutually Coordinated Guest Order Parameter |
| [EMIM]BF$_4$ | 1-Ethyl-3-methylimidazolium tetrafluoroborate | MCG | Mutually Coordinated Guest |
| [C8min] BF$_4$ | 1-methyl-3-octylimidazolium tetrafluoroborate | MSD | Mean Square Displacement |
| PDMAEMA | poly(di-methyl-amino-ethyl-meth-acrylate), | NEMD | Non-Equilibrium Molecular Dynamics |
| Gly-zw | zwitterionic glycine | PMF | Potential of Mean Force |
| DTACl | Dodecyl-Trimethyl-Ammonium Chloride | OACF | Orientation Auto-Correlation Function |
| ENP | Ethoxylated Nonyl Phenol | QLD | Quasi-harmonic Lattice Dynamics |
| LABS | Linear Alkyl-Benzene Sulfonate | TCF | Time Correlation Function |
| SDBS | Sodium Dodecyl-Benzene-Sulfonate | VACF | Velocity Auto-Correlation Function |
| DBSA | Dodecyl-Benzene-Sulfonic Acid | RDF | Radial Displacement Function |
| DTAC | Dodecyl-Trimethyl-Ammonium Chloride | RACF | Rotational Auto-Correlation Function |
| DTAB | Dodecyl-Trimethyl-Ammonium Bromide | RPMD | Ring Polymer Molecular Dynamics |
| CTAB | Cetyl-Trimethyl-Ammonium Bromide | RMSF | Root Mean Square Fluctuation |
| ENP | Ethoxylated Nonyl-Phenol | RPMD | Ring Polymer Molecular Dynamics |
| DAH | Dodecyl-Amine Hydrochloride | MFPT | Mean First-Passage Time |

# Appendix A2

## Fundamental equations

| | |
|---|---|
| **Bonded energy** | $U_{bonded} = U_{bond}(r_{ij}) + U_{angle}(\theta_{ijk}) = k_1(r_{ij} - r_0)^2 + k_2(\theta_{ijk} - \theta_0)^2$ |
| **Non-bonded energy** | $U_{non-bonded} = U_{LJ}(r_{ij}) + U_{Elec}(r_{ij})$ <br><br> $= 4\mathcal{E}_{ij}\left[\left(\dfrac{\sigma_{ij}}{r_{ij}}\right)^{12} + \left(\dfrac{\sigma_{ij}}{r_{ij}}\right)^{6}\right] + \dfrac{q_i q_j}{4\pi\mathcal{E}_0 r_{ij}}$ |
| **Mixing rule for L-J parameters** | $\sigma_{ij} = \dfrac{\sigma_i + \sigma_j}{2} , \mathcal{E}_{ij} = \sqrt{\mathcal{E}_i \mathcal{E}_j}$ |
| **Verlet Algorithm** | $r(t + \Delta t) = 2r(t) - r(t - \Delta t) + \dfrac{d^2 r(t)}{dt^2}\Delta t^2$ <br><br> $v(t) = \dfrac{1}{\Delta t^2}[r(t + \Delta t) - r(t - \Delta t)]$ <br><br> $\dfrac{dr(t)}{dt}\left(t + \dfrac{\Delta t}{2}\right) = \dfrac{dr(t)}{dt}\left(t - \dfrac{\Delta t}{2}\right) + \dfrac{d^2 r(t)}{dt^2}\Delta t$ <br><br> $r(t + \Delta t) = r(t) + \dfrac{dr(t)}{dt}(t + \dfrac{\Delta t}{2})\Delta t$ |
| **Tip4P-ice force field** | $U(r_N, q_N) = 4\mathcal{E}_{ij}\left[\left(\dfrac{\sigma_{ij}}{r_{ij}}\right)^{12} + \left(\dfrac{\sigma_{ij}}{r_{ij}}\right)^{6}\right] + \dfrac{e^2}{4\pi\mathcal{E}_0}\sum_{i,j}\dfrac{q_i q_j}{r_{ij}}$ |
| **TraPPE force field** | $U(r_N, q_N) = \sum \dfrac{q_i q_j}{4\pi\varepsilon r_{ij}} + \sum_{i<j}^{vdW-sites} U_{vdW}(r_{ij}, q_i, q_j) + \sum_{dihedrals} u_{dih}(\emptyset)$ <br><br> $+ \sum_{angles}\dfrac{k_\theta}{2}(\theta - \theta_{eq})^2 + \sum_{bonds}\dfrac{k_l}{2}(l - l_{eq})^2$ <br><br> $+ \sum_{molecules}^{vdW-sites} U_{pol}(q_a, q_b, r_{ab}) + \sum_{dihedrals} u_{gp}$ |
| **CVFF force field** | $E_{total} = \sum_b[k_2(b - b_0)^2 + k_3(b - b_0)^3 + k_4(b - b_0)^4] + \sum_\theta[k_2(\theta - \theta_0)^2 + k_3(\theta - \theta_0)^3 + k_4(\theta - \theta_0)^4] + \sum_\emptyset[k_1(1 - \cos\emptyset) + k_2(1 - \cos2\emptyset) + k_3(1 - \cos3\emptyset)] + \sum_\chi[k_2\chi^2] + \sum_{b,b'}[k(b - b_0)(b' - b'_0)] + \sum_{b,\theta}[k(b - b_0)(\theta - \theta_0)] + \sum_{b,\emptyset}(b - b_0)[k_1\cos\emptyset + k_2\cos2\emptyset + k_3\cos3\emptyset] + \sum_{b,\emptyset}(\theta - \theta_0)[k_1\cos\emptyset + k_2\cos2\emptyset + k_3\cos3\emptyset] + \sum_{b,\theta}k(\theta' - \theta'_0)(\theta - \theta_0) + \sum_{\theta,\theta,\emptyset}k(\theta' - \theta'_0)(\theta - \theta_0)\cos\emptyset + \sum_{i,j}\dfrac{q_i q_j}{r_{ij}}\sum_{i,j}\mathcal{E}_{ij}\left[2\left(\dfrac{r_{ij}^o}{r_{ij}}\right)^9 - 3\left(\dfrac{r_{ij}^o}{r_{ij}}\right)^6\right]$ |

| | |
|---|---|
| **COMPASS-II force field** | $E_{total} = \sum_b D_b\left[1 - e^{-\alpha(b-b_0)}\right] + \sum_\theta H_\theta(\theta - \theta_0)^2 + \sum_\emptyset H_\emptyset[1 - Scos(n\emptyset)] + \sum_X H_X X^2 + \sum_b \sum_{b'} F_{bb'}(b - b_0)(b' - b_0') + \sum_\theta \sum_{\theta'} F_{\theta\theta'}(\theta - \theta_0)(\theta' - \theta_0') + \sum_b \sum_\theta F_{b\theta}(b - b_0)(\theta - \theta_0) + \sum_\emptyset F_{\emptyset\theta\theta'} cos\emptyset(\theta - \theta_0)(\theta' - \theta_0') + \sum_X F_{XX'} XX + \sum \varepsilon\left[\left(\frac{r_{ij}{}^o}{r_{ij}}\right)^{12} - 3\left(\frac{r_{ij}{}^o}{r_{ij}}\right)^6\right] + \frac{q_i q_j}{\varepsilon r_{ij}}$ |

# Appendix A3

| Example of LAMMPS code for $CO_2$ hydrate in the presence of Cu+Ag+Fe metal particles and Urea molecule. |
| --- |

```
####################
#      Initialization   # The following commands specify the unit and styles for calculations.
####################
units              real
atom_style         full
bond_style         harmonic
angle_style        harmonic
dihedral_style charmm
boundary       p p p
neighbor       2.0 bin
neigh_modify    delay 0 every 1 check yes
velocity       all create 260 1234 rot yes mom yes dist gaussian
timestep 1.0
thermo             500000
####################
# Atom Definition     # The following commands separate the atoms based on atom types.
####################
read_data          data.data
lattice        fcc 1
read_restart   file.restart.10000000
group          HYD id < > 1298 2595
group          SOL1 id < 1299
group          SOL2 id > 2594
group          SOL union SOL1 SOL2
group          H2O type 1 2
group          CO2 type 3 4
mass           1 1.008    # H
mass           2 15.999   # O.3
mass           3 12.011   # C.1
mass           4 15.999   # O.2
mass           5 107.868  # Ag
mass           6 63.546   # Cu
mass           7 55.845   # Fe
mass           8 12.011   # C.2  # Urea: CO(NH2)2
mass           9 14.007   # N
mass           10 15.999  # O.4
mass           11 1.008   # H2
########################
#   TIP4P-ice + TraPPE   # The following commands specify the force fields for calculations.
########################
pair_style     lj/cut/tip4p/long 2 1 1 1 0.1577 11.0
pair_modify    tail yes
kspace_style   pppm/tip4p 1.0e-5
################
#    Coefficients  # The intermolecular coefficients between atoms are specified in the below commands.
################
pair_coeff         1 1 0.000 0.000      # H-H2O
pair_coeff         2 2 0.21084 3.1668  # O-H2O
pair_coeff         3 3 0.054 2.8        # C-CO2
pair_coeff         4 4 0.157 3.05       # O-CO2
pair_coeff         5 5 4.5618 2.955     # Ag
```

```
pair_coeff        6 6 4.7217 2.616    # Cu
pair_coeff        7 7 2.9010 2.32     # Fe
pair_coeff     8 8 0.1050 3.75        # C.2
pair_coeff     9 9 0.1700 3.25        # N
pair_coeff     10 10 0.2100 2.96      # O.4
pair_coeff     11 11 0.000 0.000      # H2
pair_coeff     2 3 0.1064 2.9834   # O-H2O + C-CO2
pair_coeff     2 4 0.1819 3.1084   # O-H2O + O-CO2
pair_coeff     2 5 0.9807 3.0609   # O-H2O + Ag
pair_coeff     2 6 0.9978 2.8914   # O-H2O + Cu
pair_coeff     2 7 0.7821 2.7434   # O-H2O + Fe
pair_coeff     2 8 0.1488 3.4584   # C.2 + O-H2O
pair_coeff     2 9 0.1893 3.2084   # N + O-H2O
pair_coeff     2 10 0.2104 3.0634  # O.4 + O-H2O
pair_coeff     3 4 0.0918 2.9250   # C-CO2 + O-CO2
pair_coeff     3 5 0.4947 2.8775   # C-CO2 + Ag
pair_coeff     3 6 0.5033 2.7080   # C-CO2 + Cu
pair_coeff     3 7 0.3945 2.5600   # C-CO2 + Fe
pair_coeff     3 8 0.0751 3.2750   # C.2 + C-CO2
pair_coeff     3 9 0.0955 3.0250   # N + C-CO2
pair_coeff     3 10 0.1061 2.8800  # O.4 + C-CO2
pair_coeff     4 5 0.8463 3.0025   # O-CO2 + Ag
pair_coeff     4 6 0.8610 2.8330   # O-CO2 + Cu
pair_coeff     4 7 0.6749 2.6850   # O-CO2 + Fe
pair_coeff     4 8 0.1284 3.4000   # C.2 + O-CO2
pair_coeff     4 9 0.1634 3.1500   # N + O-CO2
pair_coeff     4 10 0.1816 3.0050  # O.4 + O-CO2
pair_coeff     5 6 4.6410 2.7855   # Ag + Cu
pair_coeff     5 7 3.6378 2.6375   # Ag + Fe
pair_coeff     5 8 0.6921 3.3525   # C.2 + Ag
pair_coeff     5 9 0.8806 3.1025   # N + Ag
pair_coeff     5 10 0.9787 2.9575  # O.4 + Ag
pair_coeff     6 7 3.7010 2.4680   # Cu + Fe
pair_coeff     6 8 0.7041 3.1830   # C.2 + Cu
pair_coeff     6 9 0.8959 2.9330   # N + Cu
pair_coeff     6 10 0.9957 2.7880  # O.4 + Cu
pair_coeff     7 8 0.5519 3.0350   # C.2 + Fe
pair_coeff     7 9 0.7023 2.7850   # N + Fe
pair_coeff     7 10 0.7805 2.6400  # O.4 + Fe
pair_coeff     8 9 0.1336 3.5000   # C.2 + N
pair_coeff     8 10 0.1485 3.3550  # C.2 + O.4
pair_coeff     9 10 0.1889 3.1050  # N + O.4
# Bond Coeffs  (bond coefficients of molecules are as below)
bond_coeff     1 0.0 0.9572        # H2O  (H-O)
bond_coeff        2 1029.0 1.16    # CO2  (C-O)
bond_coeff     3 376.0 1.38        # Urea (C-N)
bond_coeff     4 500.0 1.277       # Urea (C-O)
bond_coeff     5 438.0 0.9896      # Urea (H-N)
# Angle Coeffs  (angle coefficients of all molecules are as follow)
angle_coeff    1 00.0 104.5        # H2O  (H-O-H)
angle_coeff       2 56.0 180.0     # CO2  (C-O-C)
angle_coeff    3 30.0 120.0        # Urea (C-N-H)
angle_coeff    4 35.0 120.0        # Urea (H-N-H)
angle_coeff    5 80.0 122.9        # Urea (N-C-O)
angle_coeff    6 80.0 114.2        # Urea (N-C-N)
# Dihedral Coeffs  (dihedral coefficients for urea molecule are as below)
```

```
dihedral_coeff  1 2.50 2 180 0      # Urea (O-C-N-H)
dihedral_coeff  2 2.50 2 180 0      # Urea (N-C-N-H)  % x-C-N-x
#dihedral_coeff  3 1.00 2 180 0     # Urea           % x-x-N-H
#dihedral_coeff  4 10.5 2 180 0     # Urea           % x-x-C-O
###########################
#   Computational Parameters  # After the above calculations, the following analysis is determined.
###########################
# No. of hydrogen bonds
# RDF
# Diffusion coefficient
# Thickness of the hydrate growth (Å/ ns)
# MSD
# F3 order parameter
# No. of CO2 molecules in hydrate phase
# No. of water molecules in hydrate phase
# potential energy profile
#########################################
#              Sketch of simulation            # The simulation box is divided into 6 segments.
#  1(S) #  2(S) #  3(H) #  4(H) #  5(S) #  6(S) #
#########################################
region    totalbox block -1.20 24.79 -0.99 24.77 -0.12 71.36 # Total Simulation box
region    box1 block -1.20 24.79 -0.99 24.77 -0.12 11.76      # Solution 1 of 4
region    box2 block -1.20 24.79 -0.99 24.77 11.76 23.52      # Solution 2 of 4
region    box3 block -1.20 24.79 -0.99 24.77 23.52 35.55      # Hydrate 1 of 2
region    box4 block -1.20 24.79 -0.99 24.77 35.55 47.58      # Hydrate 2 of 2
region    box5 block -1.20 24.79 -0.99 24.77 47.58 58.52      # Solution 3 of 4
region    box6 block -1.20 24.79 -0.99 24.77 58.52 71.88      # Solution 4 of 4
group     no type 2    # No. of oxygen of H₂O
group     nc type 3    # No. of carbon of CO₂
group     re-1 region totalbox
group     re-2 region box1
group     re-3 region box2
group     re-4 region box3
group     re-5 region box4
group     re-6 region box5
group     re-7 region box6
group     nc1 intersect nc re-1
group     nc2 intersect nc re-2
group     nc3 intersect nc re-3
group     nc4 intersect nc re-4
group     nc5 intersect nc re-5
group     nc6 intersect nc re-6
group     nc7 intersect nc re-7
group     no1 intersect no re-1
group     no2 intersect no re-2
group     no3 intersect no re-3
group     no4 intersect no re-4
group     no5 intersect no re-5
group     no6 intersect no re-6
group     no7 intersect no re-7
# No. of CO2 and H2O in different regions (the number of molecules in each segment is determined)
variable   nco21 equal count (nc, box1)
variable   nco22 equal count(nc,box2)
variable   nco23 equal count(nc,box3)
variable   nco24 equal count(nc,box4)
variable   nco25 equal count(nc,box5)
```

```
variable    nco26 equal count(nc,box6)
variable    nco27 equal count(nc,totalbox)
variable    nh2o1 equal count(no,box1)
variable    nh2o2 equal count(no,box2)
variable    nh2o3 equal count(no,box3)
variable    nh2o4 equal count(no,box4)
variable    nh2o5 equal count(no,box5)
variable    nh2o6 equal count(no,box6)
variable    nh2o7 equal count(no,totalbox)
# Density of different regions (density of each segment is calculated here)
variable    d1 equal mass(re-1)/(vol*1.0e-24*6.02e23)
variable    d2 equal mass(re-2)/(vol*1.0e-24*6.02e23)/6
variable    d3 equal mass(re-3)/(vol*1.0e-24*6.02e23)/6
variable    d4 equal mass(re-4)/(vol*1.0e-24*6.02e23)/6
variable    d5 equal mass(re-5)/(vol*1.0e-24*6.02e23)/6
variable    d6 equal mass(re-6)/(vol*1.0e-24*6.02e23)/6
variable    d7 equal mass(re-7)/(vol*1.0e-24*6.02e23)/6


# Potential energy (potential energy of each segment is computed by the below commands)
compute    per1 re-1 pe/atom
compute    pe1 re-1 reduce sum c_per1
compute    per2 re-2 pe/atom
compute    pe2 re-2 reduce sum c_per2
compute    per3 re-3 pe/atom
compute    pe3 re-3 reduce sum c_per3
compute    per4 re-4 pe/atom
compute    pe4 re-4 reduce sum c_per4
compute    per5 re-5 pe/atom
compute    pe5 re-5 reduce sum c_per5
compute    per6 re-6 pe/atom
compute    pe6 re-6 reduce sum c_per6
compute    per7 re-7 pe/atom
compute    pe7 re-7 reduce sum c_per7
```

# MSD of $CO_2$ and $H_2O$ (MSD of $CO_2$ and $H_2O$ are calculated by the following commands)

```
compute    m_s_d all msd
compute    m_s_dc nc msd
compute    m_s_do no msd
```

# MSD of $CO_2$ in different regions (MSD of $CO_2$ in segments is determined by the below commands)

```
compute    m_s_dnc1 nc1 msd
compute    m_s_dnc2 nc2 msd
compute    m_s_dnc3 nc3 msd
compute    m_s_dnc4 nc4 msd
compute    m_s_dnc5 nc5 msd
compute    m_s_dnc6 nc6 msd
compute    m_s_dnc7 nc7 msd
```

# MSD of $H_2O$ in different regions (MSD of $H_2O$ in segments is determined by the below commands)

```
compute    m_s_dno1 no1 msd
compute    m_s_dno2 no2 msd
compute    m_s_dno3 no3 msd
compute    m_s_dno4 no4 msd
compute    m_s_dno5 no5 msd
compute    m_s_dno6 no6 msd
compute    m_s_dno7 no7 msd
```

# Computation of the pressure in each direction is performed by the below commands:

```
compute    peratom1 re-1 stress/atom
compute    p re-1 reduce sum c_peratom1[1] c_peratom1[2] c_peratom1[3]
```

```
variable    press equal -(c_p[1]+c_p[2]+c_p[3])/(3*vol)
variable    pressxx equal -(c_p[1])/(vol)
variable    pressyy equal -(c_p[2])/(vol)
variable    presszz equal -(c_p[3])/(vol)
compute     peratom2 re-2 stress/atom
compute     pp re-2 reduce sum c_peratom2[1] c_peratom2[2] c_peratom2[3]
variable    press2 equal -(c_pp[1]+c_pp[2]+c_pp[3])/(3*vol)
variable    press2xx equal -(c_pp[1])/(vol)
variable    press2yy equal -(c_pp[2])/(vol)
variable    press2zz equal -(c_pp[3])/(vol)
compute     peratom3 re-3 stress/atom
compute     ppp re-3 reduce sum c_peratom3[1] c_peratom3[2] c_peratom3[3]
variable    press2 equal -(c_ppp[1]+c_ppp[2]+c_ppp[3])/(3*vol)
variable    press3xx equal -(c_ppp[1])/(vol)
variable    press3yy equal -(c_ppp[2])/(vol)
variable    press3zz equal -(c_ppp[3])/(vol)
compute     peratom4 re-4 stress/atom
compute     pppp re-4 reduce sum c_peratom4[1] c_peratom4[2] c_peratom4[3]
variable    press2 equal -(c_pppp[1]+c_pppp[2]+c_pppp[3])/(3*vol)
variable    press3xx equal -(c_pppp[1])/(vol)
variable    press3yy equal -(c_pppp[2])/(vol)
variable    press3zz equal -(c_pppp[3])/(vol)
###########
#   thermo   # To display the outputs every 0.5 ns, the following commands are defined:
###########
thermo_style custom step temp press lx ly lz vol etotal ke enthalpy c_m_s_d[4] c_m_s_dc[4] c_m_s_do[4] c_m_s_dnc1[4]
c_m_s_dnc2[4] c_m_s_dnc3[4] c_m_s_dnc4[4] c_m_s_dnc5[4] c_m_s_dnc6[4] c_m_s_dnc7[4] c_m_s_dno1[4] c_m_s_dno2[4]
c_m_s_dno3[4] c_m_s_dno4[4] c_m_s_dno5[4] c_m_s_dno6[4] c_m_s_dno7[4] v_nco21 v_nco22 v_nco23 v_nco24 v_nco25
v_nco26 v_nco27 v_nh2o1 v_nh2o2 v_nh2o3 v_nh2o4 v_nh2o5 v_nh2o6 v_nh2o7 c_pe1 c_pe2 c_pe3 c_pe4 c_pe5 c_pe6 c_pe7
v_d1 v_d2 v_d3 v_d4 v_d5 v_d6 v_d7
thermo_modify    flush yes
dump           1 all xyz 500000 dump.xyz
dump_modify      1 element H1 O2 C3 O4 Ag5 Cu6 Fe7 C8 N9 O10 H11
################## By the below commands, the constraints such as shake, spring, and momentum
# Fix Commands    # algorithms are conducted. Then NVT and NPT ensembles are conducted:
##################
fix          1 all shake 1.0e-4 10 0 b 1 2 a 1   # to provide the rigidity of water and CO₂
fix          2 HYD spring/self 10.0
fix          3 all momentum 1 linear 1 1 1
fix          4 SOL npt temp 275 275 100.0 iso 30.0 30.0 100.0   # operating condition 3 MPa, 275 K ###
run          500000      # 0.5 ns
unfix        4
fix          5 all nvt temp 275 275 100.0
run          40000       # 40 ps
unfix        5
fix          6 all npt temp 275 275 100.0 iso 30.0 30.0 100.0
restart      5000000 file.restart
run          500000000   # 500 ns
# END OF CODE #
```

# Appendix A4

The list of employed analysis parameters in this thesis is tabulated in below table.

| No. | Analysis parameters | Chapter 3 | Chapter 4 | Chapter 5 | Chapter 6 | Chapter 7 |
|---|---|---|---|---|---|---|
| 1 | Hydrate growth thickness | ✓ | | | | ✓ |
| 2 | Potential energy (PE) | ✓ | ✓ | ✓ | ✓ | ✓ |
| 3 | Three-body structural order ($F_3$) | ✓ | ✓ | | | ✓ |
| 4 | Number of hydrogen bonds (H-bonds) | ✓ | ✓ | | | ✓ |
| 5 | Mean squared displacement (MSD) | ✓ | ✓ | ✓ | ✓ | |
| 6 | Radial distribution function (RDF) | ✓ | | ✓ | ✓ | |
| 7 | Guest molecular distribution | ✓ | | | | ✓ |
| 8 | Water molecular distribution | ✓ | | | | ✓ |
| 9 | Total energy (TE) | ✓ | ✓ | ✓ | | |
| 10 | Four-order structural parameter (F4φ) | | ✓ | | | ✓ |
| 11 | Number of ring [5] and ring [6] | | ✓ | | | ✓ |
| 12 | Number of cup ($5^{12}$) and cup ($6^1 5^6$) | | ✓ | | | |
| 13 | Number of formed small and large cages | | ✓ | | | ✓ |
| 14 | Percentages of filled hydrate cages by gases | | ✓ | | | ✓ |
| 15 | Density number for water/ gas molecules | | ✓ | | | ✓ |
| 16 | Differential percentages of gas concentration (near solid-liquid interface) | | ✓ | | | ✓ |
| 17 | Gas selectivity improvement | | ✓ | | | ✓ |
| 18 | Total density | ✓ | | ✓ | ✓ | |
| 19 | Differential enthalpy (or Dissociation enthalpy) | | | ✓ | ✓ | |
| 20 | Diffusion coefficient of components/ water | | | ✓ | ✓ | |
| 21 | Determination of nanobubbles | | | ✓ | | |
| 22 | Lattice parameter | | | ✓ | ✓ | |
| 23 | Relative concentration | | | ✓ | ✓ | |
| 24 | Dissociation time | | | ✓ | ✓ | |
| 25 | Self-space-time correlation function (SSTCF) | | | | ✓ | |
| 26 | Distinct space-time correlation function (DSTCF) | | | | ✓ | |
| 27 | Adiabatic compressibility* | | | | ✓ | |
| 28 | Isothermal compressibility* | | | | ✓ | |
| 29 | Thermal expansion coefficient* | | | | ✓ | |
| 30 | Thermal pressure coefficient* | | | | ✓ | |
| 31 | Grüneisen parameter* | | | | ✓ | |
| 32 | Isenthalpic Joule-Thomson coefficient* | | | | ✓ | |
| 33 | Isothermal Joule-Thomson coefficient* | | | | ✓ | |
| 34 | Sonic velocity* | | | | ✓ | |
| 35 | Hydrate growth affinity (A) | | | | | ✓ |
| 36 | Affinity decay rate (dA/dt) | | | | | ✓ |

*: These thermodynamic quantities were determined from fluctuation analysis.

Note: The overall list of analysis parameters those which have been introduced in the literature are summarized in Figure 11 of 1$^{st}$ chapter.

# Appendix A5

Contributions of the authors of chapters 1 to 7 are as follows:

<u>Research output 1 (Chapter 1):</u>

| Contributors | Statement of contribution |
|---|---|
| Saeid Sinehbaghizadeh | Conceptualization, methodology, analysis and writing original draft |
| Agus Saptoro | Supervision, Review on a manuscript and editing |
| Amir Hossein Mohammadi | Supervision, Review on a manuscript and editing |

<u>Research output 2 (Chapter 2):</u>

| Contributors | Statement of contribution |
|---|---|
| Saeid Sinehbaghizadeh | Conceptualization, methodology, analysis and writing original draft |
| Agus Saptoro | Supervision, Review on a manuscript and editing |
| Sepideh Amjad-Iranagh | Review on a manuscript and editing |
| Parisa Naeiji | Review on a manuscript and editing |
| Angnes Ngieng Tze Tiong | Review on a manuscript and editing |
| Amir Hossein Mohammadi | Review on a manuscript and editing |

<u>Research output 3 (Chapter 3):</u>

| Contributors | Statement of contribution |
|---|---|
| Saeid Sinehbaghizadeh | Conceptualization, methodology, analysis and writing original draft |
| Agus Saptoro | Supervision, Facility, Review on a manuscript and editing |
| Parisa Naeiji | Review on a manuscript and editing |
| Angnes Ngieng Tze Tiong | Review on a manuscript and editing |
| Amir Hossein Mohammadi | Review on a manuscript and editing |

<u>Research output 4 (Chapter 4):</u>

| Contributors | Statement of contribution |
|---|---|
| Saeid Sinehbaghizadeh | Conceptualization, methodology, analysis and writing original draft |
| Agus Saptoro | Supervision, Facility, Review on a manuscript and editing |
| Parisa Naeiji | Review on a manuscript and editing |
| Amir Hossein Mohammadi | Review on a manuscript and editing |

<u>Research output 5 (Chapter 5):</u>

| Contributors | Statement of contribution |
|---|---|
| Saeid Sinehbaghizadeh | Conceptualization, methodology, analysis and writing original draft |
| Agus Saptoro | Supervision, Review on a manuscript and editing |

| Sepideh Amjad-Iranagh | Facility, Review on a manuscript and editing |
| Angnes Ngieng Tze Tiong | Review on a manuscript and editing |
| Amir Hossein Mohammadi | Review on a manuscript and editing |

Research output 6 (Chapter 6):

| Contributors | Statement of contribution |
| --- | --- |
| Saeid Sinehbaghizadeh | Conceptualization, methodology, analysis and writing original draft |
| Agus Saptoro | Supervision, Review on a manuscript and editing |
| Sepideh Amjad-Iranagh | Facility, Review on a manuscript and editing |
| Amir Hossein Mohammadi | Review on a manuscript and editing |

Research output 7 (Chapter 7):

| Contributors | Statement of contribution |
| --- | --- |
| Saeid Sinehbaghizadeh | Conceptualization, methodology, analysis and writing original draft |
| Agus Saptoro | Supervision, Facility, Review on a manuscript and editing |
| Sepideh Amjad-Iranagh | Facility, Review on a manuscript and editing |
| Amir Hossein Mohammadi | Review on a manuscript and editing |

# Copyright Permission

The following pages contain the right granted by Elsevier and ACS to the first author of the publications (Chapters 1, 2, 3, 4, 5, 6, and 7) to represent the contribution in this thesis.

## CCC
**RightsLink**

### CO2 hydrate properties and applications: A state of the art

**Author:** Saeid Sinehbaghizadeh,Agus Saptoro,Amir H. Mohammadi

**Publication:** Progress in Energy and Combustion Science

**Publisher:** Elsevier

**Date:** November 2022

*© 2022 Elsevier Ltd. All rights reserved.*

### Journal Author Rights
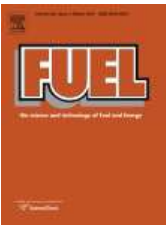
Please note that, as the author of this Elsevier article, you retain the right to include it in a thesis or dissertation, provided it is not published commercially. Permission is not required, but please ensure that you reference the journal as the original source. For more information on this and on your other retained rights, please visit: https://www.elsevier.com/about/our-business/policies/copyright#Author-rights

BACK                                                                 CLOSE WINDOW

**CCC**

**RightsLink**

### A comprehensive review on molecular dynamics simulation studies of phenomena and characteristics associated with clathrate hydrates

**Author:**
Saeid Sinehbaghizadeh,Agus Saptoro,Sepideh Amjad-Iranagh,Parisa Naeiji,Angnes Ngieng Tze Tiong,Amir H. Mohammadi

**Publication:** Fuel

**Publisher:** Elsevier

**Date:** 15 April 2023

## Journal Author Rights

BACK                                                                           CLOSE WINDOW

**CCC**

**RightsLink**

⌂ Home      ? Help ˅      💬 Live Chat      👤 Sign in      👤⁺ Create Account
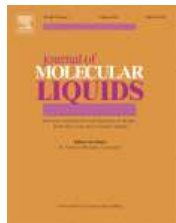
## Insights into the synergistic effects of metal particles (Ag, Cu, and Fe) and urea on CO2 clathrate hydrate growth using molecular dynamics simulations

**Author:**
Saeed Sinehbaghizadeh,Agus Saptoro,Parisa Naeiji,Angnes Ngieng Tze Tiong,Amir H. Mohammadi

**Publication:** Chemical Engineering Science

**Publisher:** Elsevier

**Date:** 31 December 2022

### Journal Author Rights

BACK                                                                    CLOSE WINDOW

CCC

**RightsLink**

## Molecular dynamics simulations of the effects of organic amines on biogas clathrate hydrate formation

**Author:** Saeed Sinehbaghizadeh,Agus Saptoro,Parisa Naeiji,Amir H. Mohammadi

**Publication:** Journal of Molecular Liquids

**Publisher:** Elsevier

**Date:** Available online 6 May 2023

### Journal Author Rights

BACK                                                                    CLOSE WINDOW

## Molecular Dynamics Simulation Studies on the Stability and Dissociation of Clathrate Hydrates of Single and Double Greenhouse Gases

**ACS Publications**
Most Trusted. Most Cited. Most Read.

**Author:** Saeid Sinehbaghizadeh, Agus Saptoro, Sepideh Amjad-Iranagh, et al

**Publication:** Energy & Fuels

**Publisher:** American Chemical Society

**Date:** Aug 1, 2022

*Copyright © 2022, American Chemical Society*

## Molecular Dynamics Simulations of the Stability and Dissociation of Structure-H Clathrate Hydrates in the Presence of Different Amino Acids, Gas Species, and sH Hydrate Formers

**ACS** Publications
Most Trusted. Most Cited. Most Read.

**Author:** Saeid Sinehbaghizadeh, Agus Saptoro, Sepideh Amjad-Iranagh, et al

**Publication:** Energy & Fuels

**Publisher:** American Chemical Society

**Date:** Jul 1, 2023

*Copyright © 2023, American Chemical Society*

### PERMISSION/LICENSE IS GRANTED FOR YOUR ORDER AT NO CHARGE

BACK                                                                                      CLOSE WINDOW

**CCC**

RightsLink

## Understanding the influences of different associated gas impurities and the kinetic modelling of biogas hydrate formation at the molecular scale

**Author:** Saeid Sinehbaghizadeh,Agus Saptoro,Sepideh Amjad-Iranagh,Amir H. Mohammadi

**Publication:** Energy

**Publisher:** Elsevier

**Date:** 1 November 2023

*© 2023 The Authors. Published by Elsevier Ltd.*

### Journal Author Rights